Soil Dynamics and Earthquake Engineering

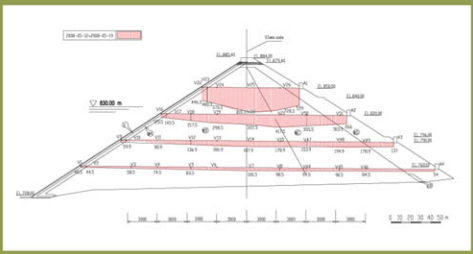

Geotechnical Special Publication No. 201

Edited by *Maosong Huang*
Xiong (Bill) Yu
Yu Huang

ASCE
G-I GEO-INSTITUTE ASCE

GEOTECHNICAL SPECIAL PUBLICATION NO. 201

SOIL DYNAMICS AND EARTHQUAKE ENGINEERING

PROCEEDINGS OF SESSIONS OF GEOSHANGHAI 2010

June 3–5, 2010
Shanghai, China

HOSTED BY
Tongji University
Shanghai Society of Civil Engineering, China
Chinese Institution of Soil Mechanics and Geotechnical Engineering, China

IN COOPERATION WITH
Alaska University Transportation Center, USA
ASCE Geo-Institute, USA
Deep Foundation Institute, USA
East China Architectural Design & Research Institute Company, China
Georgia Institute of Technology, USA
Nagoya Institute of Technology, Japan
Transportation Research Board (TRB), USA
The University of Newcastle, Australia
The University of Illinois at Urbana-Champaign, USA
The University of Kansas, USA
The University of Tennessee, USA
Vienna University of Natural Resources and Applied Life Sciences, Austria

EDITED BY
Maosong Huang
Xiong (Bill) Yu
Yu Huang

Published by the American Society of Civil Engineers

Library of Congress Cataloging-in-Publication Data

GeoShanghai International Conference (2010)
Soil dynamics and earthquake engineering : proceedings of the GeoShanghai 2010 International Conference, June 3-5, 2010, Shanghai, China / edited by Maosong Huang, Xiong (Bill) Yu, Yu Huang.
p. cm. -- (Geotechnical special publication ; 201)
Includes bibliographical references and index.
ISBN 978-0-7844-1102-5
1. Soil dynamics--Congresses. 2. Earthquake engineering--Congresses. 3. Engineering geology--Congresses. 4. Soil structure interaction--Congresses. I. Huang, Maosong. II. Yu, Xiong, 1974- III. Huang, Yu, 1973- IV. American Society of Civil Engineers. V. Title.

TA711.A1G47 2010
624.1'762--dc22 2010012085

American Society of Civil Engineers
1801 Alexander Bell Drive
Reston, Virginia, 20191-4400

www.pubs.asce.org

Any statements expressed in these materials are those of the individual authors and do not necessarily represent the views of ASCE, which takes no responsibility for any statement made herein. No reference made in this publication to any specific method, product, process, or service constitutes or implies an endorsement, recommendation, or warranty thereof by ASCE. The materials are for general information only and do not represent a standard of ASCE, nor are they intended as a reference in purchase specifications, contracts, regulations, statutes, or any other legal document. ASCE makes no representation or warranty of any kind, whether express or implied, concerning the accuracy, completeness, suitability, or utility of any information, apparatus, product, or process discussed in this publication, and assumes no liability therefore. This information should not be used without first securing competent advice with respect to its suitability for any general or specific application. Anyone utilizing this information assumes all liability arising from such use, including but not limited to infringement of any patent or patents.

ASCE and American Society of Civil Engineers—Registered in U.S. Patent and Trademark Office.

Photocopies and reprints.
You can obtain instant permission to photocopy ASCE publications by using ASCE's online permission service (http://pubs.asce.org/permissions/requests/). Requests for 100 copies or more should be submitted to the Reprints Department, Publications Division, ASCE, (address above); email: permissions@asce.org. A reprint order form can be found at http://pubs.asce.org/support/reprints/.

Copyright © 2010 by the American Society of Civil Engineers.
All Rights Reserved.
ISBN 978-0-7844-1102-5
Manufactured in the United States of America.

Preface

This special publication contains 43 technical papers cover a variety of topics of interest to soil dynamics and earthquake engineering. These papers are classified into three groups. The first group of papers is on the *dynamic soil-structural interactions* under seismic loads. The topics of papers cover important issues such as the dynamic responses of earth dams, pile and pile groups, soil nailing, tunnel, landfills and shallow foundations. A theme paper provides a thorough analyses and discussion on the seismic responses of high earth dam observed during the recent Wenchuan earthquake, one of the most catastrophic earthquakes. Due to the large number of papers in this group, this group is arranged into two subgroups in this book. The second group of papers is on the *dynamic properties of soils and rocks*. These papers include both experimental study and numerical simulations of the soil dynamic properties. A few papers describe the study of soil dynamic behaviors under special loading path and saturation conditions. The third group of papers is on the *seismic zoning and earthquake hazard assessment*. These include the use of different testing methods and analyses algorithms to assess the seismic hazards for certain regions or for specific engineering structures.

Each paper published in this ASCE Geotechnical Special Publication (GSP) was evaluated by two or more reviewers and the editors. The authors of the accepted papers have addressed all the reviewers' comments to the satisfaction of the editors. All published papers are eligible for discussion in the Journal of Geotechnical and Geoenvironmental Engineering, and are also eligible for ASCE awards.

The papers in this publication were presented during the GeoShanghai International Conference held in Shanghai, China, June 3 – 5, 2010. This conference was hosted by Tongji University, Chinese Institution of Soil Mechanics and Geotechnical Engineering and the Shanghai Society of Civil Engineering, China in cooperation with ASCE Geo-Institute, Transportation Research Board of National Academics, East China Architectural Design & Research Institute Co., LTD., Deep Foundations Institute, University of Kansas, University of Illinois at Urbana-Champaign, Vienna University of Natural Resources and Applied Life Sciences, Nagoya Institute of Technology, Georgia Institute of Technology, University of Newcastle, Alaska University Transportation Center, University of Tennessee.

We are thankful to Professor Jian-min Zhang from the Tsinghua University, who gave the keynote speech on the Lessons from Damages to High Embankment Dams in the May 12, 2008 Wenchuan Earthquake. Thanks are extended to Professor Yongsheng Li, conference chair of GeoShanghai, Professors Imad Al-Qadi and Baoshan Huang who were instrumental in organizing the GeoShanghai Conference

and provided important guidance during the organization of the Soil Dynamics Track. We wish to thank the chair of Technical Coordination council of ASCE Geo-Institute, Prof. Kevan Sharp, and the council members for their support to the Publication of the GSPs as proceedings of this conference. Thanks are also due to Donna Dickert at ASCE and Carol Bower at ASCE Geo-Institute.

Xiong (Bill) Yu
Case Western Reserve University,
Cleveland, OH, USA

Maosong Huang
Tongji University, Shanghai, China

Yu Huang
Tongji University, Shanghai, China

January 28, 2010

Acknowledgements

The editors would like to thank the following individuals who reviewed one or more papers for this geotechnical special publication:

Names

Shahid Ahmad
Scott Brandenberg
Yonggui Chen
Jason DeJong
Vincent Drnevich
Jürgen Grabe
Russell Green
Yingcai Han
Jie Huang
Takeshi Kodaka
Steve Kramer
Guoming Lin
Zhen Liu
Yan Liu
John S. McCartney
Chadi Mohtar
Scott Olson
Angelica M. Palomino
Tong Qiu
Glenn Rix
Adrian Rodriguez-Marek
Timothy Stark
Jonathan Stewart
Junliang Tao
Ryosuke Uzuoka
Zhiliang Wang
Judy Wang
Zhaohui Yang
Atsushi Yashima
Bin Ye
Guanlin Ye
Xinbao Yu
Xiong Yu
Bin Zhang[1]
Bin Zhang[2]
Feng Zhang
Limin Zhang
Xiong Zhang
Guoping Zhang

In producing this Geotechnical Special Publication, the editors also would like to acknowledge the assistance of Donna Dickert at ASCE and Carol Bower at ASCE Geo-Institute.

This page intentionally left blank

Contents

Keynote Paper

Lessons from Damages to High Embankment Dams in the May 12, 2008 Wenchuan Earthquake **1**
Jian-Min Zhang, Ze-Yan Yang, Xi-Zhang Gao, and Zhao-Xia Tong

Dynamic Soil-Structure Interactions: Part I

Axial Vibration of Partially Embedded Pile Groups in Layered Soil **32**
Q. Ren and M. S. Huang

Model Test Study on Dynamic Responses of Loess Slope by Dynamic Compaction **38**
Zhong Zhou, Bao-chen Liu, and Xiao-li Yang

Nonlinear Dynamic Behaviour of Pile Foundations in Horizontal Vibration **50**
Bappaditya Manna and Dilip Kumar Baidya

Seismic Performances of Pile Groups in Inclined Soil Layers Subjected to Strong Motions **56**
Mingwu Wang, Teteso Tobita, and Susumu Iai

Dynamic Response of Railway Track Rested on Transversely Isotropic Poroelastic Media **64**
Ye Zhou, Ganbin Liu, and Rongyue Zheng

Dynamic Analysis for Foundation of Vibrating Equipments Considering Soil-Structure Interaction **71**
Y. C. Han

Cumulative Effects of Soil Nailing under Cyclic Load Considering Bottom Boundary Conditions of Facing **77**
Fangcai Zhu, Xingui Liao, Jianhua Li, and Yue Yang

A Scale Model Test on Dynamic Soil-Tunnel Interactions **85**
Nina Liu, Yang Liu, Dongdong Han, Yuming Men, and Jianbing Peng

Effect of Soil Flexibility on Dynamic Behavior of Building Frames Resting on Strip Foundation **92**
G. Narayana, H. Sharada Bai, and A. Manish

3D Finite Element Analysis of a Ship Grounding Problem **101**
G. Qiu and J. Grabe

Pile Responses under Seismic Earth Pressures of Lateral Spread Using Wave Equation Analysis **109**
Bor-Shiun Lin, Der-Wen Chang, and Hsing-Chuan Ho

Dynamic Analysis of Municipal Solid Waste Landfills in Central Asia **118**
Xue-tao Wang, B. G. Tensay, and Wei Wu

Dynamic Soil-Structure Interactions: Part II

Different Failure Modes of a Clay Foundation-Embankment System Corresponding to Different Incident Seismic Waves..... 125
Kentaro Nakai, Toshihiro Noda, and Akira Asaoka

Numerical Investigation into the Arrangement of Clay Core on the Seismic Performance of Earth Dams 131
Tensay G. Berhe, Xue-tao Wang, and W. Wu

Soil-Water Coupled Finite Deformation Analysis of Seismic Deformation and Failure of Embankment on Horizontal and Inclined Ground 139
Masaki Nakano, Takayuki Sakai, Toshihiro Noda, and Akira Asaoka

Deformation Analyses of River Dike on Liquefiable Ground Affected by Different Earthquake Motions..... 145
Hiroshi Yokawa, Atsushi Yashima, Masata Sugito, Kazuhide Sawada, Masumitsu Kuse, Akinori Tanabe, and Osamu Nakayama

Elastic Response of Soil-Structure Systems Subjected to Near-Fault Rupture Directivity Pulses..... 153
Zeynab Azarhoosh and G. Reza Ghodrati Amiri

Seasonal Freezing Effects on the Dynamic Behavior of Highway Bridges 162
Zhaohui "Joey" Yang, Qiang Li, Gang Xu, and J. Leroy Hulsey

Seismic CPTu to Assist the Design on Existing Foundations..... 169
Xiong (Bill) Yu, Jian Fang, and Guoming Lin

Effects of Damping and Dynamic Soil Mass on Footing Vibration 178
H. V. Phuong Truong

Ground Vibration Caused by Dynamic Excitation on Pile Foundation 185
Xuecheng Bian, Guang Song, Yunmin Chen, and Hirokazu Takemiya

Dynamic Properties of Soils and Rock

Modeling of Cyclic Plane Strain Response of Toyoura Sand..... 194
Md. Raquibul Hossain, Mohammed Saiful Alam Siddiquee, and Syed Ishtiaq Ahmad

Dynamic Property of Mucky Soil of Subgrade under Cyclic Load 206
Ganbin Liu and Qianzheng Kai

Relevance Vector Machine for Evaluating Seismic Liquefaction Potential Using Shear Wave Velocity 212
Pijush Samui and T. G. Sitharam

Numerical Analysis on Co- and Postseismic Behavior of Sandy/Clayey Soil Ground Improved by Sand Compaction Pile Method 218
Hidekatsu Takeuchi, Toshihiro Noda, and Akira Asaoka

FDTD Simulation of GPR Electromagnetic Wave 225
Jingwei Zhang, Yuancheng Guo, and Jia Li

Cyclic Shear Strength of Clay under Simple Shear Condition..... 234
Takeshi Kodaka, Kazuo Itabashi, Hiroki Fukuzawa, and Shinjoro Kato

Effect of Cyclic Loading Frequency on Dynamic Properties of Marine Clay 240
Minmin Jiang, Zhengyin Cai, Pei Cao, and Dan Liu

Influence of Soil Saturation on the Free Field Response of Liquefiable Soils 246
Hanbing Bian, Ali Daouadji, Yun Jia, and Isam Shahrour

Numerical Analysis of Wave Propagation in Two-Phase Soil Medium..... 252
Anna Borowiec

Undrained Long-Term Cyclic Degradation Characteristics of Offshore Soft Clay..... 263
Shuai Li and Maosong Huang

Study of Effects of Fines Content on Liquefaction Properties of Sand 272
Yong Wang and Yanli Wang

Laboratory Flume Static and Dynamic Experiment for Rock Avalanches..... 278
K. Ugai, Q. Yang, F. Cai, Q. Xu, A. Ahmed, Z. Su, and M. Yamada

Seismic Zoning and Ground Characterization

Near Surface Soil Characterisation by Passive Ambient Noise HVSR Method 288
Pavlick Harutoonian, Ben Chapman, Christopher Neil Young, Chin Jian Leo, and Ju Jia Zou

Modeling and Seismic Response Analysis of a Reclaimed Artificial Ground 294
Toshihiro Noda, Akira Asaoka, and Kentaro Nakai

The Application of the H/V Spectral Ratio Technique for Estimating the Site Characterization in the South of Iran 300
Mehdi Mokhberi, Mohammad Davoodi, and Ebrahim Haghshenas

Efficient Algorithm Proposed to Generate Non-Uniform Ground Motion on Canyon Sites 309
Reza Tarinejad and Mohammad T. Ahmadi

Earthquake Response Analysis of Soil Layers Using HFTD Approach 320
A. Asgari and M. H. Bagheripour

Earthquake Induced Liquefaction Potential of Reclaimed Areas of Dhaka City..... 326
Mohammad Shariful Islam and Md. Tanvir Hossain

Seismic Hazard Assessment of Bandar Abbas for Seismic Retrofitting 332
G. Ghodarti Amiri, S. A. Razavian Amrei, and B. Mohebi

Effect of Amplification on Seismic Stability of Tailings Dam..... 340
Sanjay S. Nimbalkar and Deepankar Choudhury

Indexes

Author Index..... 347

Subject Index..... 349

This page intentionally left blank

Lessons from Damages to High Embankment Dams in the May 12, 2008 Wenchuan Earthquake

Jian-Min Zhang [1], Ze-Yan Yang [2], Xi-Zhang Gao [3], Zhao-Xia Tong [4]

[1]Professor, State Key Laboratory of Hydroscience and Engineering, School of Civil Engineering, Tsinghua University, Beijing, P.R.China, 100084; zhangjm@tsinghua.edu.cn

[2]Senior Engineer, Water Resources and Hydropower Planning & Design General Institute, Beijing, P.R.China, 100120;

[3]Senior Engineer, Sichuan Investigation Design and Research Institute of Water Resources and Hydropower, Chengdu, Sichuan Province, P.R.China, 610072;

[4]Assistant Professor, School of Transportation Science and Technology, Beihang University, Beijing, P.R.China, 100191; tongzx@buaa.edu.cn

ABSTRACT: Five embankment dams with the height over 100m experienced the May 12, 2008 Wenchuan earthquake with a magnitude of Ms 8.0. Damages to the Bikou loam-core-wall earth-rockfill dam and especially to the Zipingpu concrete face rockfill dam (CFRD) were induced by the great earthquake, despite no significant damages to the other three dams. The Zipingpu CFRD with the maximum dam height of 156m is the highest embankment dam located in the high seismic intensity region during the Wenchuan earthquake and is also the first CFRD experiencing strong shallow earthquake of IX-X degrees in the world. In this paper, the engineering properties, earthquake-induced damages and monitoring results of the Zipingpu CFRD are described in details. Its aseismic characteristics are analyzed from the following aspects: 1) basic features of earthquake damages, 2) deformation characteristics, 3) evaluation of earthquake damages, 4) aseismic performance, 5) ground motion, 6) weak parts of seismic resistance, and 7) repairability performance. A brief introduction to the damage to the Bikou dam is also made. These are expected to be beneficial to the understanding of the seismic behavior of high embankment dams subjected to strong earthquakes.

INTRODUCTION

Seismicity of China

China is located between two large active belts in the world and is one of the countries suffered from the most frequent and devastating earthquake disasters. Since the 20th century, about 35% strong earthquakes with the magnitude greater than 7.0 occurred in the mainland of China occupying 7% of the total land area of the world. Among these earthquakes, there are three strong earthquakes with the magnitude greater than 8.5[1].

During the late 20th century, the number of people died due to the earthquakes reaches 2.85 hundred thousand accounting for 54% of the total death caused by various natural disasters. During the great Tangshan earthquake with the magnitude of Ms 7.8 in 1976, about 2.4 hundred thousand people died and the direct economic loss exceeded 10 billion RMB.

In the mainland of China, there are two evident seismic belts. One passes through the center of the country from north to south and the other passes through the north China region from east to west. The following two obvious seismic characteristics are produced due to the differences of the geological structure and crustal movement among these different regions. Firstly, the seismic intensity is higher in the west than the east whether in time or space distribution. Taking 107° east longitude to be the boundary line, the earthquake energy released in the west of the mainland of China occupies 90% of the total energy released in the whole mainland with the rest of 10% in the east. Secondly, earthquakes in China are mostly of shallow focal depth, high magnitude, wide distribution and high frequency of occurrence. According to the historical records, the destructive earthquakes have occurred almost in all the provinces of China, of which 18 provinces, municipalities directly under the Central Government and Autonomous Regions were subjected to earthquakes with the magnitude greater than 7.0 and 10 were subjected to earthquakes with the magnitude greater than 8.0[1].

Challenges to seismic safety of high embankment dams in China

The embankment dam has the advantages of good adaptability to different topographic and geologic conditions, wide availability of materials, simple and fast construction and etc.. With the rapid development of construction machinery and technologies, the embankment dams have been widely adopted in the world with the obvious superiority in the synthetic economic index. It was reported by the International Committee on Large Dams (ICOLD) in 2003 that the total number of dams higher than 15m was 49,697 in 140 countries, among which there were 25,800 in China and the embankment dams accounted for over 80%[2, 3].

The embankment dam has become the major type of high dams in the world during the recent multi-decades. In the countries outside China, there are 9 dams over the height of 250m completed, among which 5 dams are the embankment dams and 2 dams are the ones over the height of 300m. In China, most of the high dams built are embankment dams. Listed in Table 1 and 2 are some high embankment dam projects over the height of 150m completed, under construction and in design.

China is rich in hydropower resources and about 70% of the total hydropower resources are concentrated in southwest and northwest of China. However, these regions are well known for the high seismic intensity and frequency of earthquake occurrence. Most of high embankment dams in China are built in such high seismic intensity regions. Table 3 shows the embankment dams with the height over 100m built in the regions with the seismic intensity of Ⅷ-Ⅸ degrees and the seismic safety becomes a control factor in the design for some of them[4,5]. Before the Wenchuan earthquake, only some embankment dams below the height of 100m were subjected to severe earthquake damage. In the great Tangshan earthquake, for example, the sand and

Table 1. Embankment dam projects over the height of 150m completed in China

No.	Name of project	Province (region)	River	Dam height (m)	Year of completion
1	Xiaolangdi	Henan	Yellow	160.0	2000
2	Tianshengqiao No.1	Guangxi	Nanpanjiang	178.0	2000
3	Hongjiadu	Guizhou	Liuconghe	179.5	2005
4	Zipingpu	Sichuan	Mingjiang	156.0	2006
5	Jilintai No.1	Xinjiang	Kashe	157.0	2006
6	Sanbanxi	Guizhou	Qingjiang	185.5	2007
7	Shuibuya	Hubei	Qingjiang	233.0	2008
8	Tankeng	Zhejiang	Xiaoxi	162.0	2009
9	Pubugou	Sichuan	Daduhe	186.0	2009

Table 2. Embankment dam projects over the height of 150m under construction and in design in China

No.	Name of project	Province (region)	River	Dam height (m)	Situation of completion
1	Shuangjiangkou	Sichuan	Daduhe	314.0	Under construction
2	Lianghekou	Sichuan	Yalongjiang	295.0	Under construction
3	Nuozhadu	Yunnan	Lancangjiang	261.5	Under construction
4	Cihaxia	Qinghai	Yellow	253.0	In design
5	Aertashe	Xinjiang	Yerqianghe	162.8	In design
6	Daliushu	Ningxia	Yellow	156.0	In design
7	Malutang	Yunnan	Panlongjiang	154.0	Under construction

gravel upstream face of the 65m high Baihe dam of the Miyun reservoir suffered from a large slide with the area of 60,000 m^2, the length of 900m and the volume of 150,000 m^3 due to the seismic liquefaction [4]. Some embankment dams in the other countries were also damaged during strong earthquakes such as the large slides of the upstream surface of the Lower San Fernando dam of 43.2m in height during the San Fernando earthquake of Ms 6.6 in 1971[6] and the failure of the concrete face slabs of the Pantabangan CFRD of 107m in height during the Philippines earthquake of Ms 7.7 in 1990[7].

The seismic safety of high embankment dams has received high attention from the government officials and engineers of China since the 80th of the last century. The key

construction technologies of high embankment dams have been included in the national scientific and technical research programs of the 6th 5-year plan starting from the earlier 1980s to the 11th 5-year plan continuously. Consequently substantial achievements have been obtained [9-15]. Seismic safety design of high embankment dams has been reasonably considered from dynamic response analysis to aseismic technologies. However, the seismic safety is still one of the key problems puzzling the design and construction of high embankment dams in China owing to the following four reasons.

Table 3. Embankment dam projects over the height of 100m with the seismic intensity of Ⅷ-Ⅸ degrees in China[5]

No.	Name of project	Province (region)	Dam height (m)	Aseismic criterion	Peak acceleration of bedrock(gal)	Situation of construction
1	Yelei	Sichuan	125.5	50 years, 2%	450.0	Completed, 2005
2	Zipingpu	Sichuan	156.0	100 years, 2%	392.0	Completed, 2006
3	Jilintai No.1	Xinjiang	157.0	100 years, 2%	462.0	Completed, 2006
4	Qiapuqihai	Xinjiang	105.0	100 years, 2%	435.6	Completed, 2006
5	Jiudianxia	Gansu	135.5	50 years, 2%	283.9	Completed, 2008
6	Jijin	Xinjiang	134.7	50 years, 5%	361.0	Under construction
7	Cihaxia	Qinhai	253.0	100 years, 2%	266.0	In design
8	Kensiwate	Xinjiang	129.7	50 years, 2%	477.0	In design
9	Aertashe	Xinjiang	162.8	100 years, 2%	320.6	In design

Firstly, very few high embankment dams with the height over 100m have experienced the strong earthquake action although many embankment dams have been built in the strong earthquake regions in the worldwide. Therefore, the efficiency of the current seismic design theories, experiences and measures has not been fully verified. Especially design engineers lack comprehensive understanding of the real seismic behaviors of high embankment dams with the height over 200-300m under strong earthquake actions and their earthquake-resistant performance.

Secondly, the main methods used currently for the seismic safe design of embankment dams are based on pseudo-static concept although earthquake response analysis is required for the important embankment dams in the high intensity regions according to the design codes of China. For most of super high embankment dams with the height over 200-300m under construction or in design in China, the geological conditions in their dam site are very complex and the dam shapes are varied. Therefore, the seismic safety requirements for these dams should be higher. The previous seismic safety design methods, criteria and measures used for the 100m-level embankment dams cannot be simply extended to the super high embankment dams with the height of 200-300m.

Thirdly, the theories and methods for the dynamic response analysis and damage

process evaluation of high embankment dams under strong seismic excitation are far from mature due to complexity of the physical and mechanical properties of dam construction materials, random and hard-predictability of earthquake occurrence and difficulties of the ground motion simulation. Furthermore, the verification of the current theories and methods is still dependent mainly on the post-earthquake site investigation, numerical simulation and simple model tests. The ability to predict and evaluate the mechanical behavior and damage process of high embankment dams under a seismic excitation is far from meeting the requirements of project design and construction.

Finally, the devastating secondary disasters may be induced once the occurrence of the earthquake-induced failure accident of high embankment dams. Therefore, the seismic safety of high embankment dams is required to be ensured absolutely.

The above reasons imply that how to guarantee the seismic safety for high embankment dams and especially for super high embankment dams with the height of 200-300m has become one of the unprecedented and challenging problems faced by the design engineers and researchers of China.

Key problems in seismic analysis and design of high embankment dams

The pseudo-static method is widely adopted for the seismic design of embankment dams in China according to specifications for seismic design of hydraulic structures (DL5073-2000)[15]. In the pseudo-static method, the seismic action is simplified as an inertial force system added on the design objects after the static analysis. Therefore, the pseudo-static method is a very simplified approach used to approximately solve the dynamic problems and the key of its application lies in the determination of the design acceleration. In the pseudo-static analysis the accumulation effect of dynamic loading application can be reflected in some extent, however it is not able to consider the dynamic properties of dam construction materials, the dynamic responses of high embankment dam systems and various dynamic coupling effects within the structure system of high embankment dams. The pseudo-static method is only suitable for the seismic design of structures with small design acceleration and dynamic interactions. It cannot be used in the situation with obvious reduction of soil stiffness and even occurrence of soil liquefaction during earthquakes. In the specifications for seismic design of hydraulic structures (DL5073-2000), the pseudo-static method is specified to be used only for the embankment dams with the height lower than 150m and no sufficient basis can be supplied to verify whether it can be used for super high embankment dams with the height of 200m to 300m. For such high embankment dams with high design seismic intensity, the specifications for seismic design of hydraulic structures (DL5073-2000) require to conduct the dynamic response analysis and the corresponding guide has been given in its appendix.

The equivalent linear analysis based on viscoelastic constitutive models is the main method used currently for the dynamic response analysis of high embankment dams. This method is convenient and accepted by design engineers because of more and more experiences in the determination of the model parameters and the evaluation of the seismic safety as well as abundant experimental data related with the analysis. However, it has some obvious shortages in the following aspects. Firstly, it cannot be used to reasonably evaluate the seismically-induced residual seismic deformation of the dam

body, which is of extreme importance for the seismic design of high embankment dams. To overcome this shortage, two approximate approaches are used to evaluate the seismically-induced residual deformation of embankment dams. One is the Newmark sliding block analysis based on the yield acceleration concept and the other one is the global deformation method based on the strain potential concept proposed by Serff et al. [16,17]. However, in the above two approaches dynamic response analysis and residual deformation calculation are artificially separated. Secondly, in most of the dynamic response analysis only the residual deformation induced by the seismic deviatoric strain is considered without that by the seismic volumetric strain. Yet the seismic volumetric deformation due to dilatancy in cyclic shearing cannot be ignored, which may be the main reason for the earthquake-induced residual deformation of high embankment dams. It is therefore very necessary to develop a rational dynamic deformation analysis used for evaluating the effects of both the seismic volumetric and deviatoric strains with degree of high accuracy. Finally, the equivalent linear analysis is hard to be effectively used in the evaluation of large deformation developed after the dynamic failure or in the local region of the dam body and foundation where soil liquefaction is induced.

From the theoretical point of view, a reasonable dynamic response should be the true 3D nonlinear analysis based on cyclic elasto-plastic constitutive models of the rockfill materials and various interfaces suitable for high embankment dams. Advances in this field have achieved in the past decades, however new developments are relatively slow. One of the most important reasons is the shortage of necessary theoretical and experimental tools to reveal and evaluate the complicated seismic behaviors of high embankment dams, and also to verify and improve the effectiveness of the existing theories, methods and technologies. Many key problems, such as 3D seismic wave input, cyclic elasto-plastic constitutive models truly representing the material properties and efficient numerical methods, have still not been solved yet. The results obtained from most of the current dynamic response analysis for high embankment dams are shown to be significantly different due to the differences of the adopted constitutive models, assumptions and solving techniques. The rationality and efficiency of the existing methods need to be fully verified, before they are used for the practical seismic response analysis and earthquake-resistant design of high embankment dams. In addition, only small number of high embankment dams in the worldwide experienced the strong seismic actions. The records showing the relationship of the earthquake response with the seismic damages for high embankment dams in high seismic intensity regions are very few. These never benefit the improvements of the seismic design level for high embankment dams. Therefore, on the one hand great efforts need to be paid to solving the above key problems in the seismic analysis and design of high embankment dams; On the other hand special attention should be put on the field investigation on the seismic performance and damages of high embankment dams experiencing strong earthquakes.

High embankment dams experiencing the Wenchuan earthquake

On May 12, 2008, a major earthquake with magnitude Ms 8.0 occurred in the Wenchuan County, Sichuan Province, China. The focal depth of the Wenchuan earthquake was 15km and the maximum epicentral intensity reached XI degrees, which made it to be strong shallow earthquake. The Wenchuan earthquake was induced due to

the sudden movement of the Yingxiu-Beichuan fault of the Longmenshan structural zone. The rupture began from the epicenter of the Wenchuan County and transmitted toward the north by east direction with the velocity of 3km/s. The rupture length was about 300km and the total time lasted 120s. Meanwhile, the upward movement of the upper side along the fault plan aggravated the already serious damages[18].

As shown in Table 4, five embankment dams with the height over 100m experienced this major earthquake and were damaged at different levels [19]. No obvious deformation was induced for the Yelei dam and slight damages to the Yaoji and Shuiniujia dams were mainly presented as the settlement and horizontal deformation of the dam body since the seismic intensity experienced by these three dams was relatively low during the Wenchuan earthquake.

Table 4. 100m-level embankment dams subjected to the Wenchuan earthquake[19]

No.	Name of project	River	Dam height (m)	Dam type	Year of completion	Seismic intensity(degree)	
						Design intensity	Experienced intensity
1	Zipingpu	Minjiang	156.0	CFRD	2005	8	＞9
2	Bikou	Bailongjiang	101.8	LCWERD	1976	7.5	9
3	Shuiniujia	Huoxihe	108	GCWRD	2007	8	7
4	Yaoji	Baoxinghe	123	GCWRD	2007	8	7
5	Yelei	Nanwanghe	123.5	BCCWRD	2006	9	6

Note that: 1) Experienced intensity means the maximum intensity obtained from Seismic Intensity Distribution Map of the Ms 8.0 Wenchuan earthquake (Version 2.0) published by China Seismological Bureau; 2) CFRD =Concrete Face Rockfill Dam, LCWER=Loam-Core-Wall Earth-Rockfill Dam, GCWRD=Gravel-Core-Wall Rockfill Dam, BCCWRD=Bituminous-Concrete-Core-Wall Rockfill Dam

The Zipingpu concrete face rockfill dam (CFRD) with the maximum dam height of 156m is the highest one located in the high seismic intensity region during the great Wenchuan earthquake of May 12, 2008. It was shaked strongly since the seismic acceleration experienced during the Wenchuan earthquake far exceeded the original design acceleration, which made it to become the first high CFRD bearing the IX-X seismic intensity in the world. Due to the Zipingpu CFRD is the highest embankment dam close to the epicenter and generating faults, its safety has great influences on the Dujiangyan City and the Chengdu plain and therefore its damages and safety state have received extremely high attention from all parts of society. It is one of the most important projects among the damage investigation of large-medium sized hydraulic projects in the seismic disastrous areas [20].

Presented in the following are the damage investigation and aseismic property analysis of the Zipingpu dam and the Bikou dam with emphasis on the Zipingpu dam experiencing the strong shallow earthquake. The experiences and lessons from the aseismic properties of the high embankment dams are very helpful for understanding the aseismic performance of high embankment dams, establishing the theories and methods of dynamic analysis, improving the level of seismic evaluation and design, and promoting the development of aseismic measures and damage detection technologies.

THE ZIPINGPU CFRD

General Description of Project

The Zipingpu hydraulic project, situated in 60km northwest of Chengdu City, Sichuan Province, is the lowest one among the upstream hydropower cascade development of the Minjiang River. Its downstream is the Dujiangyan City and the Chengdu Plain, 9km away from the Dujiangyan City. According to the design codes of China, the Zipingpu hydraulic project belongs to the first-class large-sized water control project with the main functions of irrigation and water supply, as well as the comprehensive benefits in power generation, environmental protection and tourism. The normal water level of the reservoir is 877m with its total storage capacity of 1.112 billion m^3 and total installed capacity of 760MW. The Zipingpu hydraulic project mainly consists of CFRD, spillway, the No.1 and No. 2 flood discharge and flushing tunnels, flushing and emptying tunnel and hydropower system. It was completed in June 2006. The general layout of the Zipingpu CFRD with the maximum height of 156.0m is shown in Fig. 1. The dam crest is 634.8m in length and 884.00m in elevation. As one of the several high CFRDs with the height over 150m built during the new century in China, the latest technologies and experiences obtained for the high CFRDs in the worldwide have been adopted in the design and construction of the Zipingpu CFRD [18-32].

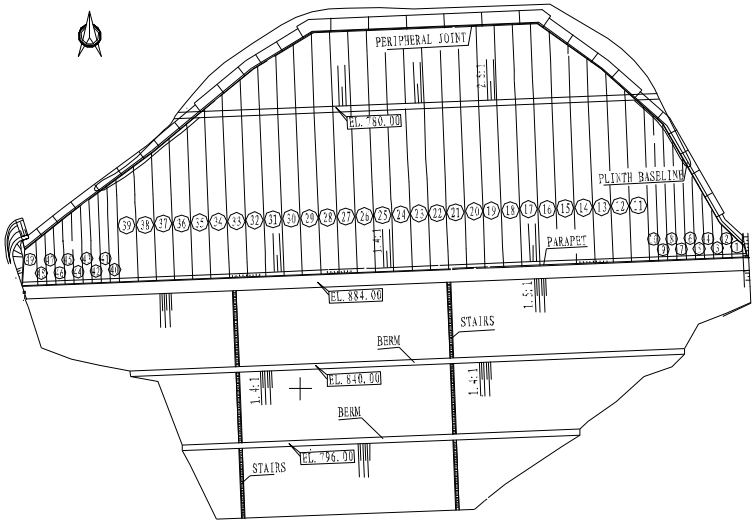

FIG. 1. General layout of the Zipingpu CFRD

1) The dam site is located in the downstream of the Shajinba section of the Minjiang River and the valley is unsymmetrical V shape. Considering the importance of the Zipingpu project, the riverbed overburden within the range of the plinth foundation to 100m upstream of the dam axis and the right bank terrace overburden were excavated

completely. The gravel layer with 300m in length, 140-200m in width and 8-14m in thickness was remained in the downstream riverbed with the remove of all the overhead layer and sand lens. The plinth foundation of the Zipingpu CFRD was built on the rock masses and the effective measures had been taken to deal with the poor geologies such as the shear and crushed zones. In addition, the technologies of extending seepage path and filter protection were used behind the plinth foundation.

2) The dam axis of the Zipingpu CFRD approaches the east west direction and the inter-angle between the dam axis and the Minjiang River is about 60-70°. Its right abutment is connected with the open spillway, which belongs to the soft and hard joints. The length height ratio of the Zipingpu CFRD exceeds 4.0, which makes it to be the CFRD built on a wide and gentle valley. The upstream and downstream dam slopes are designed based on mature experiences. The zoning of the dam section is mainly based on the experiences and lessons learnt from the design and construction of various high dams such as Aguamierba, Xinge and Tianshengqiao No.1 dams built in China and the other countries. Taking the deformation and settlement of the dam as the dominant control, the zoning of the main and secondary rockfills is set in the downstream of the dam axis with the gentle connection slope of 1:0.5, as shown in Fig. 2.

3) Rockfill materials are mainly comprised of medium-hard and hard limestones. Sand gravels are used in the local regions. The original rock masses of the Zipingpu CFRD have good compaction performance. By controlling the main, secondary and downstream rockfills with high density and similar compaction parameters, the completed dam body almost has the similar density, which makes it have high stability to resist the deformation, sliding and failure of seepage. According to the site measurement, the porosity of rockfill materials is about 18%-19% with the corresponding dry density of 2.20 t/m^3 to 2.27 t/m^3 and that of the sand gravel materials is about 14% with the corresponding dry density of 2.36t/m^3. Table 5 shows the technical properties of the materials used in the Zipingpu dam. It can be seen from the table that the dam body has high shear strength and compression modulus. The permeability increases gradually from the upstream to the downstream. Each parameter measured in the field reaches or exceeds the design requirements.

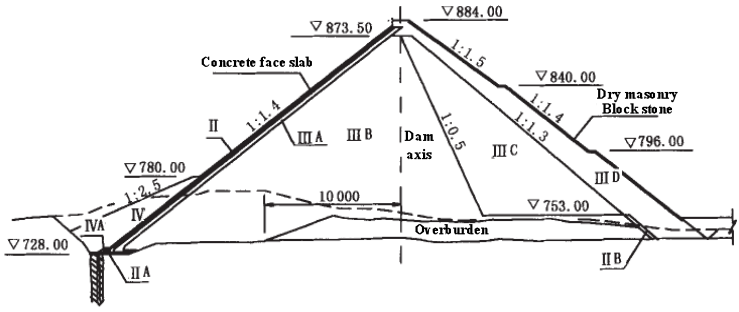

Ⅱ-cushion zone; ⅡA-special cushion zone; ⅡB-filtration zone; ⅢA-transition zone; ⅢB-main rockfill zone; ⅢC-secondary rockfill zone; ⅢD-downstream rockfill zone; Ⅳ-weighting protection zone; ⅣA-auxiliary anti-seepage zone; Ⅵ-downstream slope protection zone.

FIG. 2. Typical cross section of the Zipingpu CFRD

Table 5. Technical parameters of materials used in the Zipingpu dam[21-23]

Materials	Strength parameters in lab tests (°)			Compression modulus (MPa)		Permeability (cm/s)	
	linear	Non-linear		Lab test	Calculation on in-situ data	Lab test	In-situ test
	φ	φ_0	$\Delta\varphi$				
Cushion material	38~42	59.5	12.1	155~359	——	$A\times10^{-2}$~$A\times10^{-3}$	$1.89\sim6.7\times10^{-3}$
Transition material	38~41	58.9	12.57	210~241	——	$A\times10^{-1}$	0.24~0.71
Rockfill material	39~40	57.61	11.89	168~245	125~210	$A\times10^{-0}$~$A\times10^{-1}$	1.1~3.8
Sand and gravel material	——	——	——	——	——	——	$2.2\sim2.5\times10^{-2}$

4) The design parameters of the concrete face slab and the plinth foundation are determined based on the existing experiences. There are 48 vertical joints with 29 compression joints and 19 tension joints for the concrete face slabs. Proper measures are taken for the water-seal joints of the dam body. No seam is arranged for the vertical compression joints of the slabs and their joint interface are brushed with bitumen emulsion. The width of the tension joints and the perimeter joints is 12.5mm filled with the asphalt fir board. The bottom and top of all the joints are installed with the copper seals and GB plastic fillings protected by ethylene propylene diene monomer composite board. The concrete face slabs of the dam are constructed by three stages. The elevations for the first and second stages are 796.00m and 845.00m respectively and their joints are treated as the construction joints.

5) The design seismic intensity of the Zipingpu dam is Ⅷ degrees and various aseismic measures have been taken. The lower part of the downstream slope is steeper than the upper part by setting the slopes below and above the berm (EL.840.00m) of 1:1.4 and 1:1.5 respectively as shown in Fig. 2. The secondary rockfill zone is close to the downstream of the dam axis and a gentle interface line is arranged between the main and secondary rockfill zones. All the rockfill materials are compacted to have high density. It is confirmed from the analysis that the slope stability of the Zipingpu CFRD is relatively high for the seismic condition[24]. To protect the slopes, the masonry stones are placed on parts of the downstream slope crest and the downstream of each berm.

6) Each rockfill layer filled is 90cm thick, which is compacted to be 80cm by adding the water amount of about 15% and then rolling eight times with 25t automatic vibratory roller. Pre-settlement is conducted before the cast of the concrete face slabs.

7) According to the monitor data, the maximum settlement of the Zipingpu dam after the construction of the dam body is known to occur at the dam axis with the elevation of 790.00m, indicating that the dam body was almost homogenous. The maximum settlement reached 88.1cm on June 26, 2005, accounting for 0.56% of the dam height. The downstream-ward horizontal displacement was induced due to the water storage. When the water level of the reservoir reached 874m close to the normal water level in

Oct., 2006, the displacements at various monitoring points were found to change suddenly, showing that the deformation of the dam was adjusted significantly under the water pressure and then gradually tended to be stable.

Seismic intensity at the damsite

The Zipingpu dam lies in the southeast direction of the epicenter of the Wenchuan earthquake and the footwall of the generating fault. It is about 17km away from the epicenter and 8km from the surface rupture zone. During the earthquake, strong shaking of the dam body was induced so that the people on the dam could not stand. According to the seismic intensity distribution map of the Ms 8.0 Wenchuan earthquake shown in Fig. 3, the seismic intensity at the damsite reaches IX-X degrees. Based on the acceleration curves without calibration (shown in Fig. 4) measured by the seismograph on the downstream slope crest of the dam body, the peak accelerations along the directions of the dam axis, vertical and river are 2.06g，2.06g and 1.65g respectively. It can be inferred that the peak ground input acceleration of the dam may be higher than 0.5g. The main shock lasted for almost 1 minute during the Wenchuan earthquake.

The design seismic intensity of the Zipingpu dam is Ⅷ degrees, which is one degree

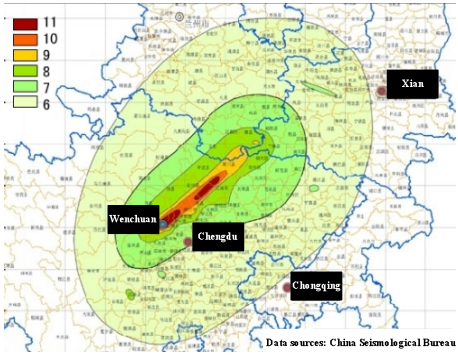

FIG. 3. Seismic intensity distribution map of the Ms 8.0 Wenchuan earthquake

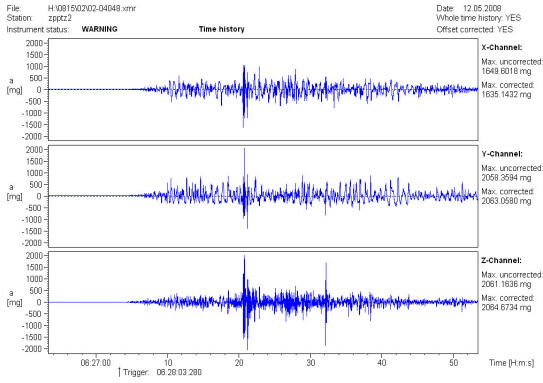

FIG. 4. Measured acceleration curve

higher than its basic seismic intensity of Ⅶ degrees by considering the scale and importance of this project. The adopted dynamic peak acceleration with an exceeding probability of 2% in 100 years is 0.26g. Thus it can be seen clearly that the seismic intensity and dynamic peak acceleration experienced by the Zipingpu dam during the Wenchuan earthquake are significantly higher than the aseismic design standard. According to the No.1 modification of seismic ground motion parameter zonation map of China, the horizontal peak acceleration with an exceeding probability of 10% in 50 years has been adjusted to be 0.20g and the corresponding basic seismic intensity for the damsite is VIII degrees. After the review of the authorized institute[32], the China Seismological Bureau approved officially that the horizontal peak ground accelerations with the exceeding probabilities of 2% and 1% in 100 years are 0.392 g and 0.485g respectively, and moreover, the vertical acceleration is taken as two thirds of the horizontal acceleration.

Major earthquake damages

When the Wenchuan earthquake occurred, the reservoir was half-filled with the water level before the dam of 828.74m, close to the dead water level of 817.00m. Two generator units were in normal operation (each with the capacity of 130 MW). Earthquake-induced damage to the Zipingpu CFRD was observed in the following main aspects.

1）Major geological hazards

Small number of rolling stones and landslides were induced on the slopes above the open line of both banks. The left bank talus slope in front of the dam deformed greatly after the earthquake. Three small-scale landslides named D1, D2 and D3, as shown in Fig. 5, occurred at the leading edge of the Denzhanping with the elevation of 845.00-890.00m. The materials collapsed in these landslides were crushed stone and clay. The volumes for landslides of D1, D2 and D3 reached 600, 400 and 150m^3 respectively. Meanwhile, multiple continuous cracks were found on the lateral side of roadway at the elevation of 890.00m [31], as shown in Fig. 6. No other failures were found and the talus slope was in

the overall stable state. According to the post-earthquake survey, the seismic surge of the Zipingpu reservoir swelled to 2-3m during the earthquake, causing heavy casualties of the fishermen on both banks. However, the safety of the dam was not affected and no liquefaction was found in the overburden layer of the dam foundation.

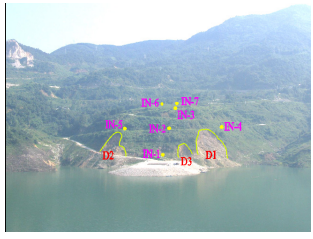

FIG. 5. Landslides in talus slope[31]

FIG. 6. Surface cracks[31]

2) Dam crest

The vertical joints in the middle of the wave wall deformed due to squeeze and the squeezing damages of the structure joints were induced in different extents by flaking off or bulging of the cover concrete shown in Fig. 7. The joints of the wave wall on the right bank dam crest were in extrusion state with traces of crushing failure. Those on the left bank dam crest were pulled open and also had traces of crushing failure. Dislocation and cracks were induced on the junction of the dam. The dislocation between the crests of the right bank wave wall and the spillway was 10cm. The soft and hard joints between the pavement and the retaining wall crest of the spillway settled 20cm presented in Fig. 8. The maximum width of cracks in the junction of the left bank dam crest reached 60mm, as shown in Fig. 9. Meanwhile, the junctions between the wave walls Nos. 4-25 and the sidewalk were pulled open and the seams between the pavement and the wave wall were widen with the maximum width of 3cm. The original elevation of the wave wall crest was 885.40m and reduced to 884.38m with the maximum settlement of 1.02m. The 500m long sidewalk on the downstream side of the dam crest was damaged with the separation of the curb and pavement. As shown in Fig. 10, most of the concrete guard columns in the downstream side of the dam crest collapsed by falling on the downstream slope or dam crest except those next to the right bank. The damage length of the concrete guard columns was about 550m and the distance of each collapsed concrete column away from their original roots along the dam axis was given in Fig. 11. Almost all the collapsed concrete columns were broken from their roots and their collapse directions were almost perpendicular to the dam axis by pointing to upstream or downstream in some order.

FIG. 7. Squeezing damages of the vertical joints of the wave wall

FIG. 8. Dislocations in the junction of the right bank

FIG. 9. Cracks in the junction of the left bank

FIG. 10. Collapse of the concrete guard columns

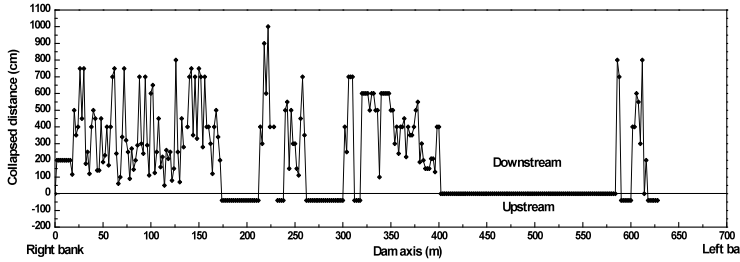

Fig.11 Collapsed distances of the downstream concrete guard columns

3) Upstream surface (anti-seepage system)

Fig.12 shows the upstream surface of the Zipingpu CFRD after the Wenchuan earthquake. The arching, bulging, detaching and cracking with a few penetrating cracks were induced for the upstream face slabs Nos. 3-8, 10-12, 15, 17-25, 27, 28 and 36. The maximum dislocation of the vertical joint between the face slabs Nos. 5 and 6 reached 35cm and the concretes on both sides of these two slabs suffered from squeezing damages at EL. 880.40m to 845.00m with the elevation difference of 35m. The dislocation of the vertical joint between the face slabs Nos. 23 and 24 extended from the top of the slabs to the underwater elevation of 791.00m with the maximum value of 15cm and their damaged length accounted for 60% of the total length of the slabs. As shown in Fig.13, the face slab No. 23 suffered from squeezing damage with the longitudinal width of 50-170cm. According to the borehole inspection at EL. 843.00m, the damaged depth of the concrete slab No. 23 was 320mm with the separation void of 50mm. The conformal mesh reinforcement at the interfaces of the slabs was separated from the concrete protective layer. The stress steel bars in the middle of the slab were bended. Meanwhile, the obvious dislocations were induced on the construction joints of the second- and third-phase slabs at EL. 845.00m such as the dislocation of 150-170 mm for the slabs Nos. 5-12, 120-150 mm for the slabs Nos. 14-23, and 20-90 mm for the slabs Nos. 30-42, as shown in Fig.14 [32]. Among them, the dislocation occurred for the slabs Nos. 5-12 was the horizontal dislocation with the total length of 340 m, and moreover, cracks were induced for the slabs Nos. 30-34 and Nos. 39-42 on the second- and third-

phase construction joints at EL. 845.00m.

Fig.12 Upstream surface of the Zipingpu dam after the Wenchuan earthquake

a) Longitudinal squeezing damages joints

b) Excavation of the damaged longitudinal joints

FIG. 13. Damages to the No.23 face slab

a) Dislocation of the construction joints

b) Excavation of the construction joints

FIG. 14. Damages to the second- and third-phase construction joints at EL. 845m

4) Downstream slope

The downstream slope after the Wenchuan earthquake was shown in Fig. 15. In the downstream surface of the dam, the masonry stones below the curb of the dam crest slide towards the downstream side with the maximum width of 65cm as shown in Fig. 16. Two large pieces of paved rock blocks were uplifted significantly in the region of the downstream side of the spillway with the length of 100m, the elevation difference of 35m and the DAM0+200~0+400 at EL. 880.00-820.00m. The masonry stones outside the

berm at EL. 840.00m and 796.00m were also damaged. The paved rock blocks at DAM0+251~0+371 with EL. 780.00-790.00m were uplifted and loosen. A few of blocks were scattered on the slope below the berm at EL. 840.00m.

FIG. 15. Downstream slope after the Wenchuan earthquake

FIG. 16. Downstream-ward slide of the masonry stones

Major monitoring results

1) Exterior deformation

According to the monitoring data, the exterior deformation of the dam body after the Wenchuan earthquake was presented in Figs. 17 and 18 by comparing those in April 2008.

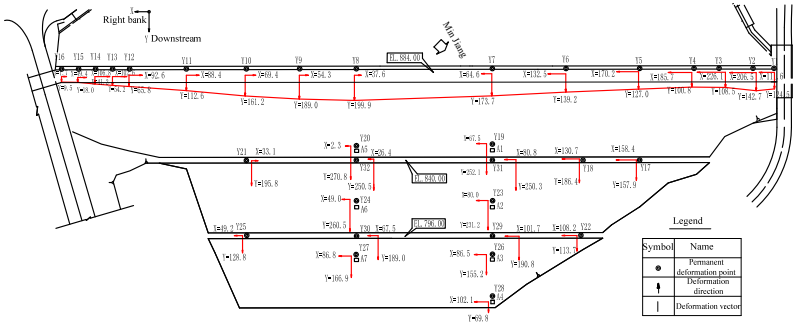

FIG. 17. Earthquake-induced horizontal increment displacements compared with those in April 2008 (Downstream planar graph, unit: mm)

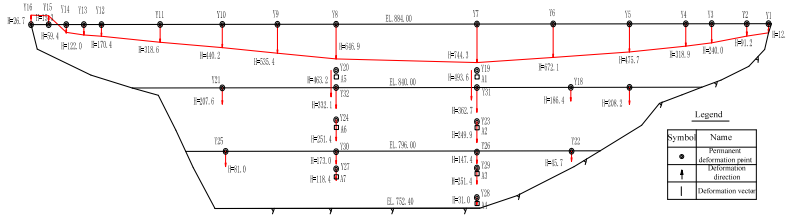

FIG. 18. Earthquake-induced vertical increment displacements compared with those in April 2008 (Downstream planar graph, unit: mm)

Both the upstream and downstream surfaces moved toward the downstream side with the maximum value of 270.8 mm occurred at the observation house A5 (Measuring Point Y20). Along the dam axis, it can be seen from Figs.17 and 18 that both left and right sides of the dam crest exhibited riverbed-ward displacements and the downstream surface moved to the right bank in general. The maximum displacement of the right bank to the riverbed with the value of 106.8mm occurred at the measuring point Y14 installed on the right side of the wave wall, and moreover, the maximum displacement of the left bank to the riverbed reached 158.4mm and occurred at the measuring point Y17 on the left side of the berm at EL. 840.00m. During the Wenchuan earthquake, large amount of settlement was induced in a short time and the maximum settlement was observed at the measuring point Y7, which was installed in the middle of the wave wall. The measured maximum settlement was 744.3mm on May 17, 2008 and increased to 760mm after 45 day, which indicated that the settlement rate was lowered rapidly after the earthquake as shown in Fig. 19.

2) Interior Deformation

The cross section DAM0+251 inside the dam is the main monitoring section for the transverse deformation and the cross section DAM0+371m is the auxiliary monitoring section. The horizontal displacement of the main monitoring section at EL. 760.00m pointed to the downstream. Compared with that on May.12, 2008, the maximum displacement reached 179.9mm occurred at the observation point H33, which was installed 90m downstream away from the dam axis. And the horizontal displacements at other observation points were in the range of 146-165.5mm. The monitor data at EL. 850.00m, 820.00m, 790.00m and the auxiliary monitoring section were not obtained due to these displacements induced by the earthquake beyond the measurement range of the apparatus.

Presented in Figs. 20 and 21 are the measured settlement results of the main and auxiliary cross sections compared with those on May 12, 2008. The maximum settlement of 810.3mm was occurred at the central point of the dam axis with EL. 850.00m of the main monitoring section. And it had a slight fluctuation due to the aftershocks, yet approached to a constant value of 812.5mm on June 22, 2008.

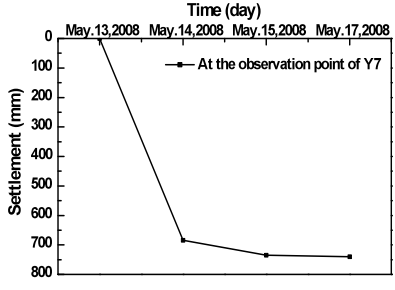

FIG. 19. Measured settlement of the dam crest after the Wenchuan earthquake

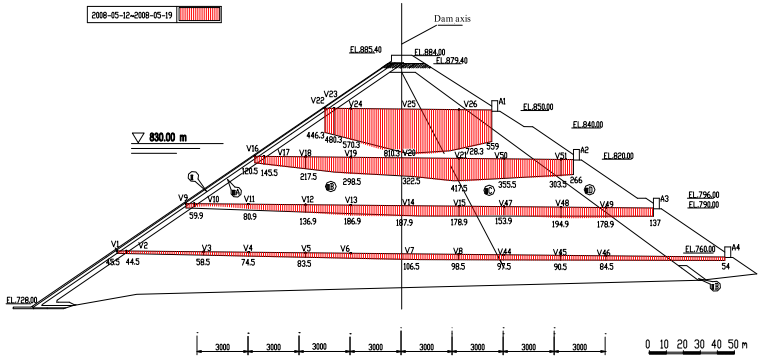

FIG. 20. Vertical displacements of the monitoring section DAM0+251 observed from May 12, 2008 to May 19, 2008

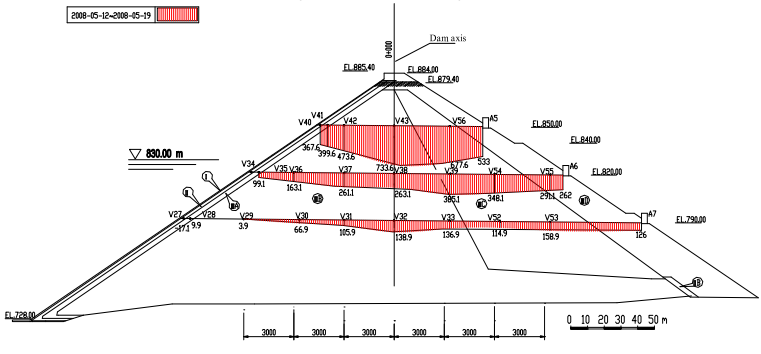

FIG. 21. Vertical displacement of the monitoring section DAM0+371 observed from May 12, 2008 to May 19, 2008

3) Joint displacement

During the Wenchuan earthquake, the peripheral joints were deformed. The peripheral joint at EL. 833.00m of the left abutment (the observation point Z2) was induced a settlement of 92.85mm, an opening of 57.85mm and a shear displacement of 13.42mm on May 13, 2008. That at the riverbed of the right abutment with EL. 745.00m (the observation point Z9) reached a settlement of about 53.65mm, an opening of 26.97mm and a shear displacement of 103.77mm on May 18, 2008. In addition, the displacements of the peripheral joints at some observation points were beyond the allowable value of the joint meters.

The joints between concrete slabs were found to deform due to the seismic shaking. Because of the complex stress conditions of the slabs, both the tensile and compressive deformations were observed at the joints between the slabs by the joint meters. However, all these deformations did not exceed the allowed ranges of watertight materials.

4）Separation between the concrete slab and the cushion layer

The data measured by gap meters installed under face slabs showed that the separation void between the face slab and the cushion layer occurred during the earthquake. Due to the limitation of the observation points, the whole separation status of the face slabs was hard to be presented and thus the post-earthquake site borehole inspection was conducted. Eighteen face slabs at 5 elevations (EL. 833.00m, 843.00m, 847.00m, 860.00m, 878.00m or 879.00m) were drilled to investigate the separation between the concrete slab and the cushion layer. It was found that above EL. 845.00m, the separation was produced in all face slabs Nos. 1-23 and the face slabs Nos. 24-49 were partially separated on their top. At EL. 879.00m, larger separation of 230mm occurred at the top of the face slab No. 6. Despite the separation of 210mm for the face slab No.15, 180mm for No. 19 and 170mm for three slabs Nos.17, 21 and 23, the separation for the other slabs was below 120mm. Below EL. 845.00m, no other face slabs suffered from separation except the face slab No.6, which was induced the separation of 20mm at EL. 833.00m.

5）Seepage

The monitoring data of the osmometers inside the dam body and the bypass seepage indicated that no significant variation was found on the measured water pressure head and water level in the bypass seepage observation hole by comparing those of pre- and post-earthquake. The pre-earthquake seepage amount was 10.38L/s at the water level of 826.00m on May 10, 2008. After the Wenchuan earthquake, the maximum leakage amount reached 16.91L/S at the water level of 829.00m on May 20, 2008 and it remained around 20L/s in June, as shown in Fig. 22. The seeping water was turbid with silt in the first two days after the earthquake and became clear afterwards.

The seepage of the dam increased due to the earthquake, however the increased amount was not so large. Compared with the similar projects in the worldwide, the overall seepage of the Zipingpu CFRD was relatively low, which indicated that the post-earthquake seepage control system was still effective and the overall structure of the dam was safe and stable.

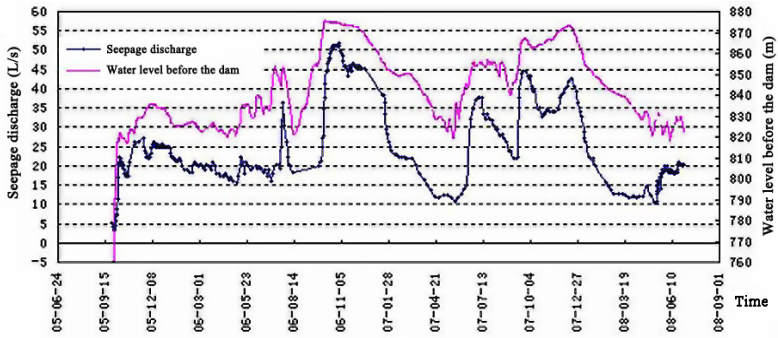

FIG. 22. Evolution of seepage amount of the weir behind the dam

Aseismic property analysis

1）Basic features of earthquake-induced damages

During the Wenchuan earthquake, the ground shaking experienced by the Zipingpu dam was much stronger than the seismic design standard. The dam crest suffered significant damages and deformation, and larger seismic subsidence and horizontal displacement of the dam body were induced. Meanwhile, the seepage control system was damaged severely resulting from the squeezing damage, separation and dislocation of the upstream face slabs. The large areas of the rockfills in the downstream slopes were loosened and overturned, and small number of rolling stones was found on the slopes of both banks. The overall seismic damages along the dam height can be summarized in the following main aspects: (1) The damages to the upstream surface were heavier than those to the downstream surface; (2) The damages to the upper part of the dam were more serious than those to the lower part; (3) The damages to the dam above the water level were greater than those below the water level; (4) The damages to the left bank face slabs were more severer than those to the right bank face slabs.

2）Deformation characteristics

Under the strong seismic action, the dam body experienced great changes in shaking deformation. As a result of the aftershocks and redistribution of the stress-deformation in the dam body, it was observed that the deformation of the dam tended to be stable. The surface of the dam body showed the downstream-ward deformation. Along the dam axis direction, the dam crest deformed horizontally from both banks to the valley and the deformation of the downstream slope pointed to the right bank. Whether on the dam surface or inside the dam, obvious settlements were produced. The lower the elevation was, the smaller the displacements and separation were. Generally, the dam body was densified (contracted) during the earthquake, and moreover, the lower the elevation was, the smaller the densification occurred.

3）Evaluation of earthquake damages

Due to avoiding the active faults and the branch faults, the site of the Zipingpu dam was not subjected to direct damages caused by co-seismic dislocation of the active faults. After experiencing the strong ground motion which was 1-2 degrees above the design seismic intensity, the basic water storage function of the dam was not affected greatly and the upstream and downstream slopes remained stable and safe, although part of the dam crest and upstream seepage control system suffered from the damage and deformation. In addition, despite the serious damages to the local parts of the dam such as the dam crest, the upstream face slabs and watertight joints, the damage to the whole dam body was slight.

4）Aseismic performance analysis

The upstream slope had good stability owing to the protection of the concrete face slabs and the action of hydraulic pressure. No obvious damages were found for the masonry slope protection in the downstream side of the dam crest which could prevent the rockfill from flying. Two large pieces of the slope protection rock blocks were loosened and overturned due to the earthquake, but no large sliding was produced. These indicated that the downstream slope remained stable. The upstream slope protected by the concrete face slabs, the downstream slope with gentle upper portion and steep lower portion, and the rockfills with higher shear strength had good stability to resist sliding under the strong seismic action.

The maximum settlement measured by the water-tube settlement gauge on the major monitoring section was 812.5mm, which made up 0.52% of the maximum dam height. The maximum settlement of the wave wall on the dam crest was measured by the measuring point Y7 with the value of 760mm, accounting for 0.49% of the maximum dam height. The elevation of the wave wall crest was reduced by 1.02m and the total settlement of the dam crest accounted for about 0.65% of the maximum dam height. Therefore, the settlements whether inside the dam body or at the dam crest did not exceed 1% of the maximum dam height. The zoning of the dam with relatively similar density and the rockfills with high compression modulus had high capacity to resist deformation during the strong seismic motion.

According the field investigation and analysis, no liquefaction and large deformation were found in the overburden layer of the dam foundation, which indicated that the treatments of excavating the sand lens from the overburden layer and retaining the gravel layer were effective.

Although the concrete face slabs near the watertight joints and the vertical joints suffered from severe damages, the downstream seepage was not increased significantly, showing that the face slabs and watertight joints designed in accordance with the current engineering experiences had strong aseismic capacity. Based on the monitoring results of the seepage amount and seepage pressure on the dam foundation, the post-earthquake seepage increase may be induced due to the following two reasons: one was the squeezing damages of the underwater face slabs and the other was the seepage from the bedrock fissure or the cracks of anti-seepage curtain during the earthquake. The seeping water was turbid with silt in the first two days after the earthquake and became clear afterwards, which revealed that the rockfill dam functioned well in filtration and protection. The modern CFRD seepage control system and rockfills with good permeability had high stability of seepage.

Compared with the Kegaodianshan CFRD with the height of 84m in Chile, which experienced four strong earthquakes, the Zipingpu CFRD showed the similar aseismic performance. However, the dam height and experiencing seismic intensity for the Zipingpu CFRD were higher. The investigation and analysis show that high CFRDs with good design and construction quality, especially with the construction of thin layer and heavy rolling, can withstand the damages caused by major earthquakes.

5）Ground motion

The peak acceleration of the bedrock in the original design was 0.26g. Based on the measured records of the acceleration history shown in Fig. 4, the real peak response acceleration of the dam crest was inferred to reach or be close to 2.0g and that of the dam foundation might be above 0.50g far beyond the design peak acceleration.

The Zipingpu dam suffered relatively minor seismic damages although its site was very close to the epicenter and seismogenic fault. It could be found that the location of the dam site at the footwall of the generating fault was beneficial for the seismic resistance. Meanwhile, according to the measured acceleration records, the acceleration along the river direction was smaller than those along the dam axis and vertical directions, which also helped the aseismic capacity of the dam body.

The dam axis of the Zipingpu CFRD approached the EW direction and its dam site was located in the southeast direction of the main shock point. The inter-angle between the dam axis and the main shock direction was small. The right bank and the upstream side

were the seismic input direction and the seismic motions along the dam axis and vertical directions were obvious. Different from the existing seismic input mode specified in the seismic design code of China, the seismic input type of the Zipingpu CFRD significantly intensified the dynamic interaction between the dam and the abutment leading to the dislocation and non-uniform deformation of the dam near the abutment. The phenomena of the more serious damages to the upstream surface than the downstream surface and the heavier damages to the left bank slabs than the right bank slabs might be related to the seismic input direction of the right bank and the upstream side, the wave propagation and the dynamic interaction. In addition the whiplash effect was clearly shown by the more serious damages to the upper portion of the dam than the lower portion. The obvious effect of traveling waves was found based on the damages to the concrete guard columns and the non-uniform and regular distribution of the dam crest damages under the earthquake. Subjected to the strong seismic motion, the rockfills were densified generally producing the vibration densification effects despite the loosened local surfaces.

6）Weak parts of aseismic resistance

The soft-hard joints between the right bank abutment and spillway, watertight joints and construction joints were weak parts for CFRDs to resist the earthquake. Therefore, the soft-hard joints in the dam body should be reduced as possible and researches on the aseismic performance of vertical compression joints and construction joints should be strengthened. Furthermore, the following measures may be helpful to advance the aseismic properties. For example, the vertical joints should be designed to be flexible and deformation-absorbable. The vertical joints instead of horizontal joints should be adopted for the construction joints.

7）Repairability performance

The earthquake damages to the Zipingpu dam could be repaired and were also easy to be repaired. By the end of October, 2008, except the crest railings and the downstream surface, all the other damages to the dam had been repaired basically and the reservoir had started to store water with the upstream water level of 860.00m. The whole project was in normal operation. Compared with the earth core dams, the face slabs and watertight joints of CFRDs were repairable and easy to be repaired. The repaired Zipingpu dam is evaluated to have high aseismic capacity.

THE BIKOU LOAM-CORE-WALL EARTH-ROCKFILL DAM

General Description of Project

The Bikou hydraulic project, located at 3km upstream of the Bikou Town, Wen County, Gansu Province, is the earliest cascade in the main stream of the Bailongjiang river. The main function of the Bikou hydraulic project is power generation accompanied with various benefits in flood control, irrigation and fishery. The project mainly consists of the loam-core-wall earth-rockfill dam, spillway, flood discharge tunnels, flushing tunnel and hydropower system. The total installed capacity of the Bikou project is 300MW with its total storage capacity of 0.521 billion m^3. It began construction in May, 1969 and generated power in Mar., 1976 with the total completion in the year of 1983.

The typical cross section of the Bikou loam-core-wall earth-rockfill dam with the maximum height of 101.8m is presented in Fig. 23. Its dam crest is 297.36m long and

11.5m wide with the construction of 5.3m high L-type concrete wave wall. The left abutment of the Bikou dam is connected with the bank slope and its right abutment is connected with the side wall of the spillway. The water level variation area of the upstream slope above EL. 680.00 is protected with 0.2m thick cast-in-place concrete boards. The 40cm×40cm×40cm prefabricated concrete blocks and 3m×5m gravel-filled concrete frames are adopted for the downstream slope protection above and below EL. 691.00m respectively. The core wall of the Bikou dam is filled with heavy-middle silty loam and silty clay with the clay content of 30%, plastic index of 14, water content of 16%-19%, dry density of 1.7 t/m^3-1.71 t/m^3 and permeability lower than i×10^{-7}cm/s. The core wall crest is 5.0m wide and its maximum bottom width is 49.0m. The foundation of the core wall in the riverbed is built on the sand gravel overburden layer and two concrete cutoff walls are constructed under the core wall with the maximum depths of 42.5m and 68.5m and widths of 1.3m and 0.8m respectively. The total filling volume of the Bikou dam is 3.89 million m^3, among which the core wall is 4.84 hundred thousand m^3 and the dam shell is 3.3 million m^3.

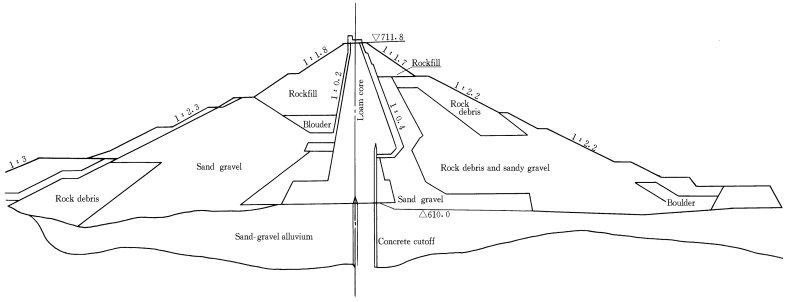

FIG. 23. Typical cross section of the Bikou dam

No Holocene active faults and strong earthquake records had been found in the dam site of the Bikou hydraulic project before the 2008 Wenchuan earthquake. The seismic activity was very small and the earth crust was relatively stable. The basic seismic intensity for the Bikou project is 6.0 degrees and the design intensity for the Bikou dam is 7.5 degrees, 1.5 degrees above the basic seismic intensity. The peak acceleration is 0.15g with the corresponding design intensity of Ⅶ degrees in the design code. According to the seismic intensity distribution map of the Ms 8.0 Wenchuan earthquake newly published by China Seismological Bureau in Fig. 3, the original design intensity of Ⅶ degrees for the Bikou damsite should be adjusted to Ⅷ degrees. The peak acceleration of the Bikou project area is also increased to 0.20g after the Wenchuan earthquake based on the No.1 modification of seismic ground motion parameter zonation map of China approved on June 11, 2008.

Major earthquake damages

When the Wenchuan earthquake occurred on May 12, 2008, the water level before the Bikou dam was 691.41m, 12.59m lower than the normal water level of 704.00m and the downstream water level was 617.13m. The upstream and downstream water level variations were 3.0-4.0m and 0.2m respectively during the earthquake. The major damages to the Bikou dam during the Wenchuan earthquake are described as follows[5,35].

1) Dam crest

Although small number of transverse joints between the wave wall sections were deformed locally, the surfaces of the upstream transverse joints were in good condition. It was observed that asphalt inside the downstream transverse joints was squeezed out and no large damages were induced. As shown in Fig. 24, one crack running through the left and right banks occurred between the wave wall and the upstream horizontal concrete slope protection, which extended from the width of 5cm in left bank to 0.3cm in the middle and then to 4cm in right bank. It was induced mainly due to the settlement with the maximum value of 9cm. Meanwhile, there were 6 cracks between the wave wall and the downstream slope resulted from the deformation of the junctions between the concrete blocks. The main deformation type was the tension accompanied with the vertical settlement. Among the above cracks, the crack in the connection section of the downstream horizontal concrete board of the wave wall and the downstream concrete slope protection was 21.27m long and 1.5cm-26cm wide shown in Fig. 25.

Penetrating cracks between the dam crest concrete pavement and the side wall of the right bank spillway occurred, which should be tension cracks by surface observation and were 5-9cm wide as shown in Fig. 26. In the connection part of the right bank dam crest and the bank slope, irregular tension cracks running through the upstream and the downstream were induced, which was presented in Fig. 27.

FIG. 24. Crack between the wave wall and the upstream slope

FIG. 25. crack between the horizontal concrete board of the wave wall and the downstream slope protection

FIG. 26. Cracks between the dam crest pavement and the spillway

FIG. 27. Cracks between the right bank dam crest and the bank slope

2) Upstream slope

The upstream slope of the Bikou dam after the Wenchuan earthquake was shown in Fig. 28. It can be seen that its upstream slope above the water surface was smooth and no obvious arching, depression and cracks were observed on the upstream concrete protective face. The water surface before the Bikou dam was clear and quiet, and no bubbles, turbidity and vortexes were observed after the earthquake.

3) Downstream slope

The downstream slope of the Bikou dam was generally smooth. Local rupture, crack and uplift were induced on the stair steps, prefabricated concrete block, concrete frames and drains, which had no influences on the whole safety of the downstream slope yet.

The prefabricated concrete block slope protection above EL. 691.00m was relatively smooth and no obvious depression and bulging were observed. Local concrete blocks were uplifted due to the long-term deformation of the downstream slope. The concrete frame slope protection below EL. 691.00m was also smooth and local concrete frames were ruptured and uplifted as Fig. 29 shown. The transverse ribs (Numbers 3-4 in a row) of concrete frames close to both dam slopes within EL. 691.00m-670.00m and those (Number 5 in a row) in the left side of the middle stair below EL. 670.00m were ruptured due to squeeze.

FIG. 28. The upstream surface of the Bikou dam after the Wenchuan earthquake

FIG. 29. Rupture of the concrete frame

FIG. 30. Deformation of the drain

The downstream-ward deformation with the horizontal value of 3cm was induced for the drain in the left side of the berm at EL. 691.00m due to the settlement of the upper dam surface. The upstream side of the drain beside the berm at EL. 670.00m suffered from the downstream-ward squeezing deformation of 4cm-11cm in the horizontal direction, which occurred near the maximum profile within the range between the left bank and right bank stairs. As shown in Fig. 29, the upstream side of the drain beside the zigzag dam road at EL. 670.00-650.00m was subjected to the downstream-ward deformation with the maximum horizontal deformation of 25cm, which occurred in the middle of the dam road (below half of the dam height at the maximum profile). The obvious squeeze deformation was induced for the drain at the toe of the dam slope with the residual section of 5cm in width resulting from the deformation of the upper dam slope. Generally the deformation of the lower drain is larger than that of the upper drain, which was not induced only by the seismic action. According to the site enquiry and investigation, the above deformations of the drains were produced before the Wenchuan earthquake. Due to lack of the pre-earthquake deformation data, the influence of the seismic action was not able to be exactly evaluated, however the deformation of the drains was indeed increased due to the Wenchuan earthquake.

Major monitoring results

The main surface deformations of the Bikou dam were the settlements with the maximum value of 24.2cm occurred at the left dam crest. The settlement of the impervious core wall is lower than that of the dam crest. The maximum settlement of the impervious core wall was 16.4cm, which was produced at its left crest corresponding to the maximum settlement position of the dam crest.

The upstream-ward horizontal deformation of the dam crest was induced generally with the maximum value of 15.4cm occurred at the left dam crest. The deformation of the downstream slope pointed to the downstream side with the maximum value occurred at half of the dam height, among which the maximum deformation was 4.9cm at EL. 691.00m (two-thirds of the dam height), 7.1cm at EL. 670.00m (half of the dam height) and 4.2cm at EL. 650.00m (one-thirds of the dam height) .

The pre- and post-earthquake monitoring results of the piezometric tubes behind the Bikou dam indicated that the water heads at most of the piezometric tubes had almost no change or little change and no obvious seepage was induced due to the Wenchuan earthquake.

CONCLUSIONS AND REMARKS

Five embankment dams with the height over 100m experienced the great Wenchuan earthquake with magnitude Ms 8.0. Despite the very slight damages to the other three embankment dams, significant damages to the Bikou dam were induced especially to the Zipingpu CFRD. As the highest embankment dam within the strong seismic zone during the Wenchuan earthquake, the Zipingpu dam becomes the first CFRD with the height over 150m experiencing the strong shallow earthquake of IX-X degrees in the world, which makes the earthquake cases of CFRD rise from 80m level to 150m level in height.

Several key experiences and lessons can be learned from the field investigation and analysis of the high embankment dams and especially the Zipingpu CFRD subjected to the Wenchuan earthquake as follows.

1) The site of the Zipingpu dam was kept away from the active faults and branch faults and it was also located in the footwall of the generating fault, which is beneficial for the dam body to resist the strong earthquake motion. The designed layout, cross-section, filling materials and aseismic measures for the Zipingpu CFRD are reasonable and conformable to the dam height accompanied with high construction quality. Therefore, the Zipingpu dam suffered minor damages as a whole, though serious damages were induced in some local parts. It had high stability in deformation, sliding and seepage under strong earthquake motion. The damages to the Zipingpu dam were acceptable and could be easily repaired. The high embankment dams designed according to the modern design theories, methods and speculations are safe and stable as a whole, yet the understanding of the aseismic performance of the high embankment dams is far from enough and should be further investigated.

2) The seismic input under the strong shallow earthquake showed the complicated three-dimensional features of directionality, distribution non-uniformity, predominance of transverse and vertical peak acceleration components, long duration and strong shaking of seismic motion, unignorable compression wave effect and etc. It should be pointed out specially that the seismic input mode of the Zipingpu dam in the Wenchuan earthquake had an apparent difference with that suggested in the speculations. The uniform input of massless foundation used usually can hardly simulate the above features of high CFRDs under a strong shallow earthquake, which requires further discussions and researches.

3) The obvious dynamic interaction was observed from the damages to the Zipingpu CFRD during the Wenchuan earthquake. Especially the predominance of the seismic motion along the dam axis aggravated the dynamic interaction between the dam body and the abutment. The significant deformation and dislocation settlements were induced around the both abutments. The squeezing damages to the face slabs near the steep left abutment were more obvious than the gentle right abutment. In addition, the peripheral joints of concrete slabs were deformed. Researches on the dynamic interactions between the abutment, foundation and high embankment dam body are one of the key issues to improve the seismic response analysis capacity of high embankment dams.

4) The damages to the high embankment dams under the strong earthquakes mainly appeared as seismic deformation, especially non-uniform residual deformation and discontinuous contact deformation. The deformation of the Zipingpu dam body manifested as seismic densification with the local negative dilatancy. In the meantime, the significant discontinuous contact deformation occurred between the rockfill and concrete, the rockfill and bedrock as well as the face slabs and cushion materials. All these deformations not only depend on the dynamic and static mechanical behaviors of the dam construction materials and structures, also on the cyclic effect, whiplash effect, traveling wave effect, seismic densification effect and boundary constraint effect caused during the earthquakes. In the viscoelastic dynamic analysis used widely for the seismic design, however, the empirical formulas are still adopted to estimate the residual deformation, and correspondingly, there exist obvious deficiencies in the cyclic constitutive models of various rockfills and interfaces, computation model of the dam

structure-foundation system, and numerical methods of dynamic response. Therefore, the developments from viscoelastic dynamic analysis to 3D elastoplastic dynamic analysis are required urgently.

5) The key to the seismic safety and aseismic measures of high embankment dams is the control of the earthquake-induced deformation. The damage investigation of the Zipingpu dam indicates that high embankment dams have very strong aseismic capacity, but still lack of rational index, theories and methods of quantitative evaluation in the seismic design. More attention in the future should be paid to understanding and establishing the internal relationship of the seismic safety of high embankment dam with the earthquake-induced deformation, seepages, damages and local failures. More rational methods and standards of seismic evaluation should be developed together with the effective aseismic measures such as the reinforcement measures of the downstream slope close to dam crest and the aseismic property improvement of the watertight and construction joints of the concrete faced slabs.

Lessons from the investigation and analysis on the damages to high embankment dams in the great Wenchuan earthquake provide a sufficient evidence for the following recognition and challenging problems: (1) Evaluation of earthquake-induced deformation has become the most important entry in the seismic design of high embankment dams; (2) Numerical analysis of dynamic response is playing an indispensable role in the evaluation of the seismic deformation behavior and aseismic safety of high embankment dams although there exist some unignorable deficiencies; (3) Control of seismically-induced deformation is one of the most important and difficult earthquake geotechnical engineering problems for high embankment dams. Greater efforts are further required to cope with challenging and solving these earthquake-induced dam geotechnical problems by means of higher scientific and technical standards.

ACKNOWLEDGMENTS

The authors appreciate the support of the National Basic Research Program of China (No. 2007CB714108) and the National Natural Science Foundation of China (No.50979046). The authors wish to express their sincere appreciation to the Sichuan Investigation Design and Research Institute of Water Resources and Hydropower which was in charge of the design of the Zipingpu project and offered helpful supports in the field investigation of the damage to the Zipingpu CFRD just after the Wenchuan earthquake and valuable design materials in the preparation of this paper. The authors also want to give their heartfelt thanks to Professor Zuyu Chen of the China Institute of Water Resources & Hydropower Research for his valuable comments.

REFERENCES

[1] Zhang, G.M., Ma, H.S., Wang, H., and Li, L. (2004). "Active tectonic blocks and strong earthquakes in the continent of China." *Science in China Series D: Earth Sciences*, Vol. 34 (7): 591-599. (in Chinese)

[2] Jia, J.S., Yuan Y.L. and Li, T.J. (2004). "Statistics of high dams built in the world and China in 2003." China Water Resources, 13: 25-33. (in Chinese)

[3] Zhang, J.-M. and Zhang, B.Y. (2004). "Geotechnical aspects of high embankment

dams in China." Keynote lecture, *Proceedings of the 12th Asian Regional Conf. on Soil Mechanics and Geotechnical Engineering*, Leung, C.F. et al.(eds). Vol. 2: 1197-1214.

[4] Chen, H.Q. (2000). "Earthquake resistance of large dams." *Large dams in China: a fifty-year review,* Pan J.Z. and He J.(eds): 723-795.

[5] Guan, Z.C. (2009). "Seismic protection basis and selection standard of high embankment dams." *Water Resources Planning and Design,* Vol. 5: 1-3. (in Chinese)

[6] Seed, H.B., Lee, K. L., Idriss, I. M., et al. (1975) . "The slides in the San Fernando dams during the earthquake of February 9, 1971." *Journal of the Geotechnical Engineering,* Vol.101(GT7): 651-688.

[7] Nai, D.J., Mei, P.J., Zhao, S.L., et al. (1992). "Lesson from seismic affect on large dam." *International Hydropower*, Vol. 44(3): 37-39, 50.(in Chinese)

[8] Han, G.C. and Kong, X.J . (1995). "Aseismic studies of concrete faced rockfill dams: state of the art." *Journal of Dalian University of Technology*, Vol. 36 (6): 708-719. (in Chinese)

[9] Zhang, J.-M. and Wang, J.H. (1999). "Advances in soil dynamics and geotechnical earthquake engineering." State-of-the-art lecture, *Proceedings of the 8th China National Conference on Soil Mechanics & Geotechnical Engineering*, International Academic Publishers: 44-55. (in Chinese)

[10] China Institute of Water Resources and Hydropower Research.(1986). "Key technical research for the construction of high embankment dams." *General report of the 6th 5-year national scientific and technical research program* (No.15-1-1). (in Chinese)

[11] China Institute of Water Resources and Hydropower Research.(1990). "Key technical research on the construction of high soil-impervious embankment dams." *General report of the 7th 5-year national scientific and technical research program.* (in Chinese)

[12] China Institute of Water Resources and Hydropower Research.(1995). "Key aseismic problem research of high embankment dams." *General report of the 8th 5-year national scientific and technical research program* (No. 85-208-02-04). (in Chinese)

[13] China Institute of Water Resources and Hydropower Research. (1996). "Nonlinear dynamic response method and damage investigation of embankment dams." *General report of National Natural Science Foundation Program.* (in Chinese)

[14] China Institute of Water Resources and Hydropower Research. (2000). "Large-scale shaking table model test and dynamic response analysis of concrete face dams in strong earthquake region." *General report of the 9th 5-year national scientific and technical research program* (No. 96-221-02-03). (in Chinese)

[15] China Institute of Water Resources and Hydropower Research. (2000). "Specifications for seismic design of hydraulic structures (DL5073-2000)." (in Chinese)

[16] Newmark, N.M. (1965). "Effects of earthquakes on dams and embankments." *Rankine Lecture, Geotechnique*, Vol. 15 (2): 139-160.

[17] Serff, N., Seed, H.B., Makdisi, F.I., and Chang, C.K. (1976). "Earthquake Induced Deformations of Earth Dams. " *Report No. EERC/76-4, Earthquake Engineering Research Center*, University of California, Berkeley.

[18] Li, Y.H., Wang, P., and Cao, R. (2009). Preliminary damage investigation of high

embankment dams during the Wenchuan earthquake. *Analysis and Investigation on Seismic Damages of Projects Subjected to the Wenchuan earthquake*, 427-434. (in Chinese)

[19] Water Resources and Hydro-power Planning & Design General Institute. (2009). "A report on damage investigation and preliminary analysis of large and medium-sized hydropower projects (over 30MW) within the Wenchuan earthquake disaster area." (in Chinese)

[20] Chengdu Hydroelectric Investigation & Design Institute of SPC. (2009). "A preliminary design report on risk control and reinforcement of the Zipingpu hydraulic project (Geological part)." (in Chinese)

[21] Wu, C.G. (2006). "Embankment quality control of CFR dam in Zipingpu project." *Sichuan Water Power*, Vol. 25(1): 12-14. (in Chinese)

[22] Liu, Y. (2003). "Study on construction material for concrete faced rockfill dam at Zipingpu project." *Sichuan Water Power*, Vol. 22(2): 63-71. (in Chinese)

[23] Song Y.G., Deng L.S, Cai D.W, et al. (2006)., "Monitoring for concrete faced rockfill sam settlement during construction of Zipingpu project." *Sichuan Water Power*, Vol. 25(1): 21-27.(in Chinese)

[24] Zhang, J.-M. and Luo, G. (2000). "Numerical analysis on stress-displacement and seismic response of the Zipingpu CFRD and its aseismic safety assessment." (Submitted to the Sichuan Investigation Design and Research Institute of Water Resources and Hydropower), *Research Report of Department of Hydraulic Engineering, Tsinghua University.* (in Chinese)

[25] Luo, G. and Zhang, J.-M. (2004). "3-D seismic response analysis for Zipingpu concrete faced rockfill dam." *The Fifth International Conf. on Case Histories in Geotechnical Engineering*, USA, No.2.11.

[26] Li, H., Song, Y.G., and Deng, L.S. (2006). "Solutions of key technical problems for concrete faced rockfill dam at Zipingpu project." *Sichuan Water Power*, Vol.25 (1): 4-11. (in Chinese)

[27] Song, S.W. and Cai, D.W. (2009). "Earthquake damage phenomena and deformation monitoring analysis for concrete faced rockfill dam at Zipingpu project during the Wenchuan earthquake." *Chinese Journal of Rock Mechanics and Engineering*, Vol.28 (4): 841-849. (in Chinese)

[28] Zhao, J.M., Liu, X.S., and Wen, Y.F. (2009). "Analysis of earthquake damage of the Zipingpu dam in the Wenchuan earthquake and the study proposal on the anti-earthquake and disaster reduction of high earth-rock dam." *Water Power*, Vol.35 (5):11-14. (in Chinese)

[29] Yang, Z.Y., Zhang, J.-M., and Gao, X.Z. (2009). "A primary analysis of seismic behavior and damage of the Zipingpu CFRD during the Wenchuan earthquake." *Water Power*, Vol.35 (7): 30-33. (in Chinese)

[30] China Earthquake Disaster Prevention Center, Institute of Earthquake Prediction, China Seismological Bureau. (2009). "Check report on aseismic safety evaluation of the dam site of the Zipingpu hydraulic project, Minjiang River, Sichuan Province." (in Chinese)

[31] Wang, J.L., Xu, X.T., Wang, X.L., and Huang, X.F. (2009). "Monitoring analysis of influence of Wenchuan 8.0 earthquake on talus slope stability at left bank in front dam of the Zipingpu hydraulic project." *Chinese Journal of Rock Mechanics and*

Engineering, Vol.28 (6): 1279-1287. (in Chinese)

[32] Guan, Z.C. (2009). "Investigation of the 5.12 Wenchuan earthquake damages to the Zipingpu Water Control Project and an assessment of its safety state." *Science in China Series E: Technological Sciences*, Vol.52 (4): 820-834.

[33] Jiang, G.C., Fu, Z.A., and Feng J.J. (1996). "Concrete face slab dam engineering.", *Hubei Science & Technology Press.* (in Chinese)

[34] Chen, H.Q., Xu, Z.P, and Li, M. (2008) . "The Wenchuan earthquake and seismic safety of large dams." *Journal of Hydraulic Engineering,* Vol.33 (10):1158-1167. (in Chinese)

[35] HydroChina Xibei Engineering Corporation. (2008). "Preliminary report on the seismic damage investigation of the Bikou hydraulic project during the 5.12 Wenchuan earthquake." (in Chinese)

Axial Vibration of Partially Embedded Pile Groups in Layered Soil

Q. REN [1], M. S. Huang [2]

[1]Ph.D, Deparment of Civil Engineering, University of Shanghai for Science and Technology, Shanghai 200093, China; renqing1976@163.com

[2]Director, Professor, Department of Geotechnical Engineering, Tongji University, Shanghai 200092, China; mshuang@tongji.com

ABSTRACT: In this paper, a simplified analytical method was developed for the axial harmonic response of partially embedded pile groups in layered soil. Based on pile-to–pile interaction factors, transfer matrix method was used to setup the dynamic model of partially embedded pile groups. A comprehensive parameter study focused on the influence of length ratio(L_1/L_2), pile spacing(s/d) and vibration frequency(f) on the dynamic response of pile groups, and following conclusions could be got: (1) the increase of length ratio(L_1/L_2) would reduce vertical dynamic impedance of single and pile groups; (2) the pile-pile interaction factors vary with the pile spacing and vibration frequency, and will be seriously weaken for length ratio (L_1/L_2); (3) the length ration (L_1/L_2) has evident influence on dynamic response of pile foundations with the rise of vibration frequency.

INTRODUCTION

Pile foundations as a kind of reliable and effective support system has been widely used in marine engineering. As for pile groups, the complexity of their dynamic behavior stemming from the environmental loads (e.g. wave, wind, and machine vibration) and pile-soil interaction has restricted further research in this field.

Over the past 35 years, most of scholars focused on dynamic response of totally embedded pile groups (Kaynia and Kausel,1982, Gazetas，1993). Very few papers (as far as author know) discussed the dynamic characteristics of partially embedded pile groups. Doyle and Pavlovi (1982) firstly studied the natural response of a beam supported by an elastic foundation. The natural frequencies are compared with the extreme cases where the pile is either completely supported by, or fully detached from, the elastic foundation. Ronald (1985) calculated the dynamic vibration of single bar partially embedded in half space by integration approach. A series of Green's functions are derived for calculating displacement and internal force of pile. Lee (1999) and Budkowska (1997) concerned on the sensitivity analysis of a beam resting on Winkler type foundation. Catal(2006) adopted Timoshenko-beam model to analyze the free vibration of semi-rigid connected and partially embedded piles with the effects of the bending moment, axial and shear force.

The work reported here was motivated by needs to find the influence of partially embedded pile on the response of pile groups. To this end, Timoshenko-beam model and

a hybrid formulation is presented, based on the sub-structure method and dynamic Winkler beam model. The dynamic Winkler beam model is formulated by considering the interaction between passive pile and surrounding soil.

Single Pile Model

The whole pile is divided into two parts: the first part is rigid connected to cap and the second part is assumed to be friction pile fully contacted with surrounding soils, which can be represented by distributed independent spring (Wikler assumption) and damping (Gazetas and Makris, 1991) (fig.1).

(1) First part of pile

The dynamic equilibrium of an infinitesimal piece of an elastic pile yields:

$$\frac{d^2 w_i^1(z)}{dz^2} + (\frac{\lambda_1}{h_i})^2 w_i^1(z) = 0 \qquad (1)$$

in which

$$\lambda_1 = h_i [m_p \omega^2 / E_p A_p]^{1/2} \qquad (2)$$

where h_i, E_p and A_p are pile element height, elastic modulus and cross area of pile. The solution of Eqn(1) is

$$w_i^1(z) = A_i \cos \lambda_i \frac{z}{h_i} + B_i \sin \lambda_i \frac{z}{h_i} \qquad (3)$$

in which, A and B is integration constant determined by boundary conditions. The relation between bottom and top displacements and forces for each pile segment (layer) *i* can be expressed as:

$$\begin{Bmatrix} w_i^1(h_i) \\ N_i^1(h_i) \end{Bmatrix} = [t_1^1] \begin{Bmatrix} w_i^1(0) \\ N_i^1(0) \end{Bmatrix} \qquad (4)$$

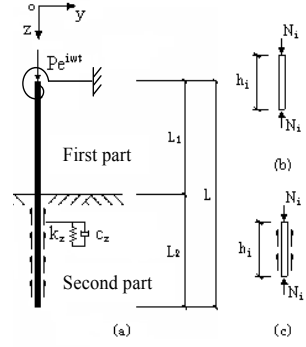

Fig.1 Vertical vibration of partially embedded single pile

where

$$[t_1^1]_i = \begin{bmatrix} \cos \lambda_{1i} & \frac{h_i \sin \lambda_{1i}}{E_p A_p \lambda_{1i}} \\ -\frac{E_p A_p \lambda_{1i} \sin \lambda_{1i}}{h_i} & \cos \lambda_{1i} \end{bmatrix} \qquad (5)$$

Applying transfer matrix approach, axial force $N^1(\,)$ and displacement $w^1(\,)$ for both top and tip of first part of pile have following relationship:

$$\begin{Bmatrix} w^1(L_1) \\ N^1(L_1) \end{Bmatrix} = [T_1^1] \begin{Bmatrix} w^1(0) \\ N^1(0) \end{Bmatrix} \qquad (6)$$

where

$$[T_1^1] = [t_1^1]_i [t_1^1]_{i-1} \cdots [t_1^1] \qquad (7)$$

(2) Second part of pile

For *n* soil layers, (similar process was omitted) while imposing the continuity condition at each interface, leads to:

$$\begin{Bmatrix} w^2(L_2) \\ N^2(L_2) \end{Bmatrix} = [T_2^1] \begin{Bmatrix} w^2(0) \\ N^2(0) \end{Bmatrix} \tag{8}$$

in which, $N^2(\,)$ and $w^2(\,)$f are displacement and axial force of the second part of pile.

$$[T_2^1] = [t_2^1]_n [t_2^1]_{n-1} \cdots [t_2^1]_1 \tag{9}$$

where

$$[t_2^1] = \begin{bmatrix} \cos\lambda_i & \dfrac{h_i \sin\lambda_i}{E_p A_p \lambda_i} \\ -\dfrac{E_p A_p \lambda_i \sin\lambda_i}{h_i} & \cos\lambda_i \end{bmatrix} \tag{10}$$

in which,

$$\lambda_i = h_i[(m_p\omega^2 - k_{zi} - i\omega c_{zi})/E_p A_p]^{1/2} \tag{11}$$

Based on the continuity condition, $w^1(L_1) = w^2(0)$ and $N^1(L_1) = N^2(0)$ then

$$\begin{Bmatrix} w(L) \\ N(L) \end{Bmatrix} = [T_2^1] \cdot [T_1^1] \begin{Bmatrix} w(0) \\ N(0) \end{Bmatrix} = [T^1] \begin{Bmatrix} w(0) \\ N(0) \end{Bmatrix} \tag{12}$$

in which $w(\,)$ and $N(\,)$ are displacement and axial force of the whole pile.

Enforcing boundary conditions of pile tips, impedance of partially embedded single pile can be got:

$$\Re^s = \frac{N(0)}{w(0)} = -\frac{T^1(1,1)K_b + T^1(2,1)}{T^1(1,2)K_b + T^1(2,2)} \tag{13}$$

$$K_b = -G_b(c_{w1} + ic_{w2})w(L) \tag{14}$$

in which G_b, c_{w1} and c_{w2} are shear modulus and impedance functions of pile tip's soil, respectively.

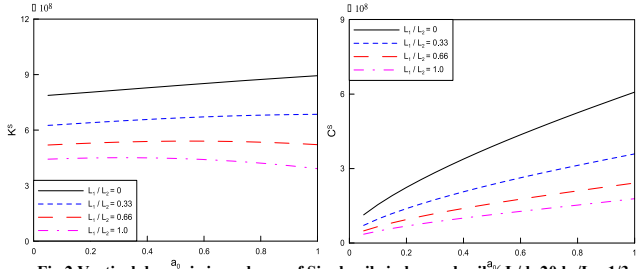

Fig.2 Vertical dynamic impedance of Single pile in layered soil[a]**(L/d=20,h_1/L_2=1/3, E_p/E_{s1}=1000, ν s=0.40, ρ p/ ρ s2=1.25, ρ s1/ ρ s2=0.8, β s1=0.10, β s2=0.05)**

Eqn(14) are plotted in Fig.2. It is apparent that impedances (K_s and C_s) of single pile decrease evidently with increment of length ratio (L_1/ L_2). The damping (C_s) for single pile with different length ratios are relative close compared with stiffness (K_s) in low frequencies. This also happens in uniformed layer.

Dynamic Pile-Pile Interaction Model

Gazetas et.al (1991) proposed an approximate method to calculate axial vibration of pile groups in half space based on Beam-on-Winkler-Foundation (BWF) model, takes into account of the interaction between the passive pile and surrounding soil. The proposed method was further improved for layered soils by Mylonakis and Gazetas (1998), as well as authors (2007). The pile-soil-pile system is shown in Fig.3. Two identical piles embedded in the layered soil with length L and diameter d under harmonic load $Pe^{i\omega t}$. The response of the receiver pile (pile2) to the oscillations of the source pile is not identical to the response of the free-field soil at the location of receiver pile due to interaction between the passive pile and surrounding soil. Let s be the distance between two piles, the free-field displacement as location of pile2 can be expressed as following

$$w_s(z,t)=w_s(z)e^{i\omega t}=\psi(s)w_{11}^2(z)e^{i\omega t} \qquad (15)$$

where w_{11} is displacement amplitude of pile 1 and $\psi(s)$ is the attenuation function.

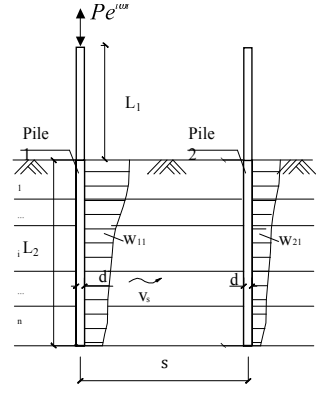

Fig.3 Vertical dynamic interaction between two piles

The dynamic equilibrium of an infinitesimal piece of passive pile in *n* layered soil, yields:

$$\frac{d^2w_{21}^2(z)_i}{dz^2}+\frac{\lambda_i^2}{h_i^2}w_{21}^2(z)_i=\frac{-(k_{zi}+i\omega c_{zi})\psi(s)w_{11}^2(z)_i}{E_pA_p} \qquad (16)$$

Starting from the bottom layer *n*, the similar scheme as above section is repeated layer, layer-by-layer until reaching the pile top, the axial force and displacement between passive pile top and tip can be written as

$$\begin{Bmatrix} w_{21}^2(L_2) \\ N_{21}^2(L_2) \end{Bmatrix}=[T_2^1]\begin{Bmatrix} w_{21}^2(0) \\ N_{21}^2(0) \end{Bmatrix}+[T_2^2]\begin{Bmatrix} w_{11}^2(0) \\ N_{11}^2(0) \end{Bmatrix} \qquad (17)$$

where, $[T^1]$ and $[T^2]$ are the transfer matrix. According to the definition of interaction factor

$$\alpha(s)=\frac{w_{21}(0)}{w_{11}(0)}=-\frac{T_v(1,1)K_b+\Re^s K_b T_v(1,2)+T_v(2,1)+\Re^s T_v(2,2)}{T(1,1)K_b+T(2,1)} \qquad (18)$$

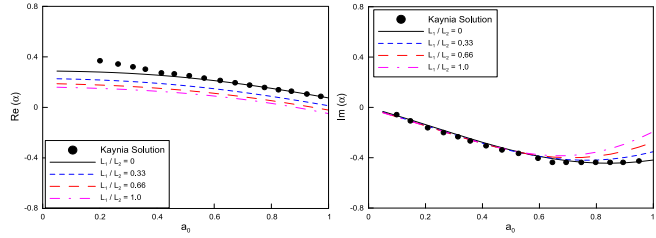

Fig.4 Pile-pile interaction factors in layered soil (s/d=2, L/d=20, h1/L_2=1/3, E_p/E_{s1}=1000, ν $_s$=0.40, ρ **p/ ρ $_{s2}$=1.25, ρ $_{s1}$/ ρ $_{s2}$=0.8, β $_{s1}$=0.10, β $_{s2}$=0.05)**

Eqns (5) are plotted in Figs.4, the interaction factors α in 2-layered soil by the proposed simplified method are plotted against results of BEM (Kaynia and Kausel, 1982). Notice the oscillatory behavior of the interaction factors with frequency. The length ratios (L_1/ L_2) have evident influence on pile-pile interaction factors, especially in real part. And the degenerated solution of present simplified method has a good accordance with BEM solution almost in the whole range of frequencies.

Dynamic Response of Pile Groups

The superposition method, based on pile-pile interaction factors, is one of the most effective approaches developed in the last decades for calculating dynamic response of floating pile groups with rigid caps. A parametric study, which is focused on the effects of pile spacing and length ratio on impedance of pile groups, and well known results (Kaynia and Kausel, 1982) are presented here. Now, the displacements of piles, $\{w\}$ can be expressed as

$$\begin{Bmatrix} w_1 \\ w_2 \\ \cdots \\ w_n \end{Bmatrix} = \frac{1}{K_p^s} \begin{bmatrix} 1 & \alpha_{12} & \cdots & \alpha_{1n} \\ \alpha_{21} & 1 & \cdots & \alpha_{2n} \\ & \cdots & & \\ \alpha_{n1} & \alpha_{n2} & \cdots & 1 \end{bmatrix} \begin{bmatrix} N_1 \\ N_2 \\ \cdots \\ N_n \end{bmatrix} \tag{19}$$

or

$$[N] = K_p \{w\} \tag{20}$$

in which, $[K_p] = K_p^s [\alpha]^{-1}$ is the stiffness matrix of pile groups in the whole pile-cap system, $[N]$is the load distributed onto the individual pile heads.

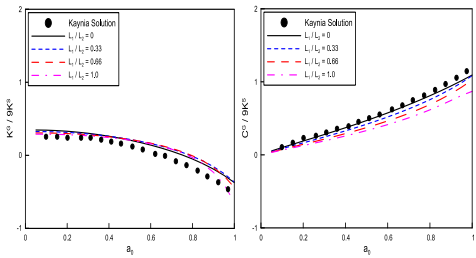

Fig.5 Vertical dynamic impedance of 3×3 Pile groups in layered soil (s/d=2, L/d=20, h_1/L_2=1/3, E_p/E_{s1}=1000, ν_s=0.40, ρ_p/ρ_{s2}=1.25, ρ_{s1}/ρ_{s2}=0.8, β_{s1}=0.10, β_{s2}=0.05)

In Fig.5-6, the axial dynamic impedance of a 3×3 pile group are plotted in terms of the so-called group efficiency factor (defined as the dynamic impedance of the pile group divided by the sum of the individual static stiffness of the pile). It is noted that the group factors of partially embedded pile groups are smaller than that of the totally embedded pile solution and rigorous solution (Kausel and Kaynia, 1982). When pile spacing is 5 and length ratio is larger than 0.33, the dynamic character of partially embedded pile groups is similar as a shallow foundation, since the partially embedded pile groups has relative larger deformation and soil has no confinement on movement of the first part of pile.

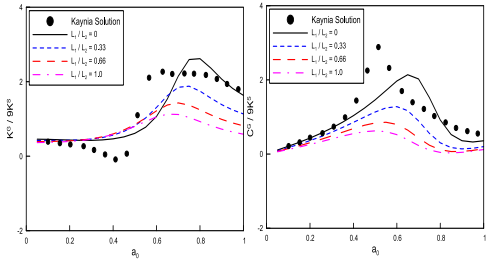

Fig.6 Vertical dynamic impedance of 3×3 **Pile groups in layered soil (s/d=5, L/d=20, h_1/L_2=1/3, E_p/E_{s1}=1000, ν_s=0.40, ρ_p/ρ_{s2}=1.25, ρ_{s1}/ρ_{s2}=0.8, β_{s1}=0.10, β_{s2}=0.05)**

CONCLUSIONS

A simplified studied model has been proposed for direct analysis of partially embedded pile groups subjected to vertical dynamic loading in the service ability state. Based on pile-to–pile interaction factors, sub-structure method is used to form the global stiffness matrix of pile-cap-soil system. Through comprehensive parameter study, it is pointed out that partially embedded piles have evident influence on the dynamic response of pile group. It is very important for engineer to notice the partially embedded pile in practical design.

REFERENCES

Kaynia, A.M. and Kausel, E. (1982). "Dynamic stiffness and seismic response of pile groups." *R. Dept. of Civil Engineering., MIT, Cambridge, Mass*.

Gazetas, G. and Fan K, Kaynia A. (1993). "Dynamic response of pile groups with different configuration." *J. Soi1. Dyn. Earthq. Engrg.,* Vol. 12: 239-257.

Doyle, P.F and Pavlovi, M.N. (1982). "Vibration of beams on partial elastic foundations." *J.Earthq. Engng. & Struct. Dynamics.,* Vol.10:663-674.

Ronald, Y.S.Pak. (1985). "Dynamic response of a partially embedded bar under transverse excitations." *R. NO.EERL 85-04-12, California*.

Lee, B.K., Jeong, J.S. Fan, L.G. and Jin, T.K. (1999). "Free vibrations of tapered piles embedded partially in Winkler type foundations." *J. KSCE. Civil. Engrg.*, Vol. 3(2): 195-203.

Budkowska, B.B. and Szymczak, C. (1997). "Initial post-buckling behavior of piles partially embedded in soil." *J. Computers & Structures.*, Vol. 62(5):831-835.

Catal, H.H. (2006). "Free vibration of semi-rigid connected and partially embedded piles with the effects of the bending moment, axial and shear force." *J. Engineering Structures.,* Vol. 28:1911-1918.

Gazetas, G. and Makris, N. (1991). "Dynamic pile-soil-pile interaction: Part Ⅰ: Analysis of axial vibration." *J.Earthquake Engrg Struc Dyn.,* Vol.20:115-132.

Mylonakis, G. and Gazetas, G. (1998). "Vertical vibration and additional distress of grouped piles in layered soil." *J. Soils and Foundations.,* Vol.38(1):1-17.

Wu Zhi-ming., Huang Mao-song. and Ren, Q. (2007). "Vertical vibration and internal forces of pile groups in layered soil." *J. Tongji University (Natural Science).* Vol. 35(1):21-26.

Model Test Study on Dynamic Responses of Loess Slope by Dynamic Compaction

ZHOU Zhong，LIU Bao-chen and YANG Xiao-li

Civil Architechural Engineering College, Central South University, Changsha Hunan 410075, China, Tel: +86-13319541496; E-mail: zhongzhou78@yahoo.com.cn

ABSTRACT: This article has accomplished the model test for 1:20 loess slope, investigated the law of similitude, boundary condition treatment and so on in the model test, studied the change rules of dynamic properties and dynamic response rules for loess slope in dynamic compaction. Results show that the amplitude of dynamic response for loess slope in dynamic compaction fades out rapidly with the impact loading effect; the vibration cycle is less than 1s and the major frequency is between 25~45 Hz that no superimposed vibration will occur. The amplification effect on radial acceleration is more obvious for loess slope in dynamic compaction, the vertical vibration prevails at lower part of slope while radial vibration prevails at upper part of slope. There is amplification effect for response amplitude on impact vibration of on the ridge of loess slope. There is obvious amplification effect on slope for input acceleration along the slope, especially the most obvious amplification effect at the top of slope. The test results have favorable influence on revealing the rules of dynamic response for loess slope in dynamic compaction, and provide instructive reference for the engineering design and construction for the loess region.

INTRODUCTION

The dynamic compaction, also called dynamic consolidation, was originally as a method for foundation stabilization, created by France Menard Technical Corporation in 1969. This method usually rams the foundation by strong impact energy and strong shock wave, which are produced by free falling of rammer, it compacts, presses and consolidates the earth of a certain depth under the ramming level, to raise the strength of foundation soil, reduce the soil compressibility, improve the anti-liquefaction conditions for sandy clay and eliminate the soaking settlement of soaking loess, hence, it improves the engineering properties for the foundation soil. At first, the dynamic compaction was only used to deal with sandy clay and gravels foundation, and with background of experience and scientific and modernized progress of construction method, it has been applied to more and more types of foundations, even to the dynamic compaction for undersea and underwater soft soil stratum with special treatment. The dynamic compaction is characterized by good performance in reinforcement, wide applications, simple equipments, convenient operation, short construction period, conservation of materials and low cost of

construction expenses that it has been widely used in the engineering field[1~5].

In engineering construction, the building (structure) might have breaks or cracks to influence its normal service owing to soaking settlement of the foundation, as we have not paid much attention to the soaking settlement for the loess that proper measures have not been taken. Therefore, it is required that the soaking settlement of loess should be solved for the engineering construction in the area where soaking settlement of loess prevails. The dynamic compaction has good performances in dealing with soaking settlement of soil, reducing deformation and improving strength, all of which make it rapidly developed and promoted, especially in Shanxi, Shanxi, Gansu and so on, the dynamic compaction has already been the major method to deal with soaking settlement of loess, moreover, with the improvement of equipments and ramming energy, its capability in depth continues to increase to more than 10m.

However, there might be some threat to the safety for the construction site and adjacent structures owing to large shock wave produced during dynamic compaction. In the past few years, many scholars home and abroad have taken a series of studies on the influence of dynamic compaction on adjacent buildings and put forward the safety vibration distance, formula of vibration attenuation and so on[6~9]. Still by far, there have been not many issues on influence of dynamic compaction dynamic on dynamic response for loess construction site, especially for adjacent slope. Therefore, this article, through indoor model test, investigates the response rules of acceleration, speed, transient displacement and amplification effect for loess in dynamic compaction, and provides instructive reference to engineering design and construction in the area of loess.

1. Schematic design for model test

The objective for this test is to investigate the dynamic response (acceleration, speed and displacement) of loess slope in dynamic compaction, find out the rules of dynamic response on the slope and at different position in the slope and the amplification effect of dynamic response for loess construction slope; investigate the change rules of stress and deformation at different position of the loess slope in dynamic compaction, and analyze the influence mechanism on stability for loess slope in dynamic response.

1.1 Physical and mechanical properties for soil sample

The soil sampled at the opening of Lujiaya Tunnel on Zheng-Xi Passenger Dedicated Line is used in the test, the soil sample is mostly sandy loess and after normal indoor test for physical and mechanical properties, its average indicators of physical and mechanical properties are included in Table 1. The maximum dry density and best water content are calculated by heavy compaction test

Table 1 Basic Physical and Mechanical Properties for Soil Sample

Liquid limit w_L (%)	Plastic limit w_P (%)	Specific gravity G_s	Natural water content w (%)	Optimum water content w_{op} (%)	Maximum dry density $\rho_{d\max}$ ($g.cm^{-3}$)	Dynamic cohesive strength C_d (kPa)	Dynamic internal friction angle ϕ_d (^{0})
24.7	16.5	2.71	10.34	11.4	1.96	50	23.2

1.2 Schematic design for model test

The test model and compacting function are designed on the law of similitude for geometric and kinematic similarity, the loess fillers are selected same as the prototypes. The geometric similarity ratio is 1:20 that the similarity relations for each physical property are obtained on Bockingham π Theory. It is impossible to create a model strictly based on the law of similitude, hence, there are many restrictions in the materials for the model, especially in quality density. The gravity can be ignored if the gravity influence is less than the influence of dynamic load on dynamic response, therefore, the gravity-ignored model is adopted.

The loess acquired in the field will be filled and compacted by layer on specified compactness and according to the dimensions of the model. The model has a slope ratio of 1:1 and a slope height of 1m, which equals to 20m of the prototype. The acceleration transducers and displacement measuring points are arranged in and on the slope in the process of filling, the ramming will be carried out with the strength in design at the specified point, and in such ramming process, the propagation rules of impact vibration for the slope are measured by the acceleration transducers and the vertical and horizontal deformations are measured at the measuring point and on the slope surface. Also in such ramming process, the propagation rules of impact vibration for embankment are measured by the acceleration transducers and the slope displacements are measured by the dial indicators. The size of model and the layout of measuring points refer to Figure 1, a pair of horizontal and vertical acceleration transducers are arranged respectively at each point from A1-A8, the horizontal dial indicators SH1-SH3 and vertical dial indicators SV1-SV3 are arranged on the slope indicated on in the figure, there are 16 acceleration transducers and 6 dial indicators in total. The spacing between compacting point D1 and D2 is 0.4m, which equals to 8m for the prototype.

The slope, as a semi-infinite body, has no limit in theory, however in the model test, the model shall be placed in a dimensional container. In this way, there is some error in test results owing to wave reflection on the ridge and change in the form of system vibration, which is the so-called “model box effect”. The successful stimulation for soil boundary conditions, is the model in the container, under dynamic action, deforms in the same way as that for the prototype in a free field, which can reduce the boundary influence. The common solution is to increase the size and add vibration-absorbing materials of some thickness on the rigid walls of model box, the materials shall have a large damping factor and a certain rigidity to prevent large deformation. This distance of the compacting point away from both sides of the model box is 0.6m, which equals to 12m of the prototype, based on the Bornitz ground vibration attenuation formula, the amplitude fading rate at 12m is 10.6%. An 8mm particle plastic board will be installed on the bottom and the 3 sides, other than the side with tempered glass, as to reduce the reflection effect of the model box.

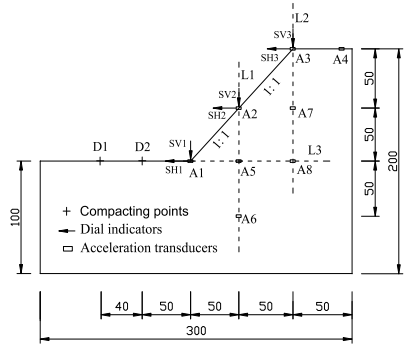

FIG. 1 Model dimensions and layout for measuring points (cm)

1.3 Testing devices and main instruments and equipments

① Model box

The self-developed model box, which frame is made of channel steel by welding and consists of 1 bottom plate and 3 side plates, among which a transparent toughened glass is installed to observe the inside deformation of the slope, a grid network is marked on the toughened glass to observe the displacement of soil. Inside net dimensions for model box: Length×Width×Height=3.0m×1.2m×2.0m, and its weight is 1.5t. A flat-bottom circular hammer, of 25kg heavy and 20cm in diameter, is hoisted by dead pulley with a hoisting height of 1.5m to simulate dynamic compaction in the field, according to the compacting point on embankment in design. Calculated on the law of similitude, it equals to 100kN hammer, 30m distance of fall and 3000 kN·m ramming energy.

② Acceleration acquisition system

The high-sensitivity micro acceleration transducers (18 pcs) manufactured by Germany IMC Integration Measuring & Control Co., Ltd, and SPARTAN multi-channel data acquisition and analysis system will be adopted.

③ Slope displacement

The developing and change rules for horizontal and vertical displacement on slope are measured by dial indicator in dynamic compaction.

1.4 Procedures for model test

Prepare and set the acceleration transducer and dynamic testing devices before model test. In order to prevent damage on acceleration transducer and wires owing to vibration of dynamic compaction, a transducer box of welding steel plates is manufactured, a combined pipe sleeve of thin steel pipe and solid plastic pipe, 20cm for each section, are adopted to make the wires flexible and bear the vibration impact. The formal test procedures are as follows:

1) Prepare slope fillers. Screen the loess fillers to eliminate agglomerations, gravels and impurities, the soil will be prepared on best water content of 11.4%, covered by colorful cloth and stored for more than 2d to achieve uniform water content for the fillers.

2) Build slope by layer. The thickness of each layer is 10cm, the fillers are weighted, filled and compacted on 80% compactness to the design mark, and in this way, to the pre-

set elevation. When the fillers are compacted to the slope above ground, the slope will be built after some wood plates are needed to form a staircase-shape support. The filling of each layer shall be uniform and even.

3) In layered filling, the acceleration transducers are embedded and the wires of transducer are arranged, according to the positions indicated in Figure 1, to be uniform in outlet direction for connection with data analyzer.

4) The compacting point, height and position for dead pulleys of hammer will be confirmed based on design scheme after filling is completed.

5) Set the dynamic testing devices and check the one-to-one relation between acceleration transducer and channel of dynamic testing device, draft a corresponding block diagram for measuring point and testing device.

6) According to Figure1, install the dial indicators to ensure no influence at position for the fixed magnetic pedestal of dial indicator owing to vibration of model box, then measure the initial displacement at measuring point on slope after the installation is completed. The test models for linear slope and staired slope after measuring points are arranged refer to Figure 2.

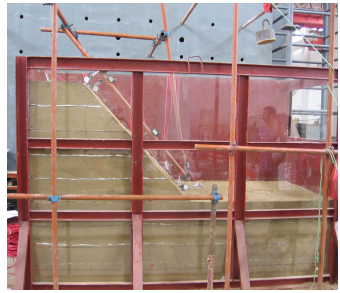

FIG. 2 Model of loess slope

7) Start test on pre-set working conditions. 1 commander, 2 persons for readings and 2 persons for hammer hoisting and auxiliary operations, 1 person for slope deformation test and photographing are assigned in the test, the commander will guide the test in an unified manner to ensure all personnel act in unison, and to avoid error measuring of dynamic impact signal and abnormal situations.

8) The road embankment will be excavated by layer after compacting test. After excavation of embankment , check each measuring point and the quality of wires, crash the agglomerated soil and water the soil on specified water content, then screen the soil according to the previous procedures after the soil is placed for 2d, fill the road embankment by layer for the test of next working condition.

9) The professional analysis software, famos4.0, will be used for the measured dynamic data, and the statistical analysis and sorting are required for the processed data. based on the test results, the test scheme for the next working condition will be evaluated or adjusted if necessary, and the quality of the testing system and testing devices shall be checked.

2. Result analysis for model test

The scheme for model test of dynamic response for loess slope in dynamic compaction

will be carried out according to the specified procedures. Based on the law of similarity, the values in model test are calculated to prototype values that all of the following test values are calculated prototype values.

2.1 Change rules of compacting settlement over ramming number

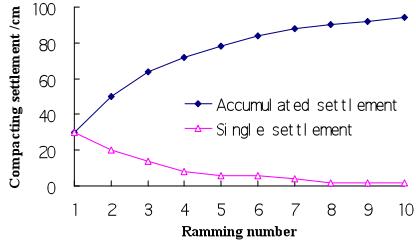

FIG. 3 Relation of compacting settlement over ramming number

Figure 3 is the relation curve of accumulated settlement and single settlement over ramming number for D1 ramming point. We can see from the figure that the accumulated settlement increases with the ramming number, however, in a slowing way of increase rate, the maximum compacting settlement is 94cm; the single settlement decreases with the increase of ramming number that the settlement of the last 2 rammings is 2cm.

2.2 Change curve of slope displacement

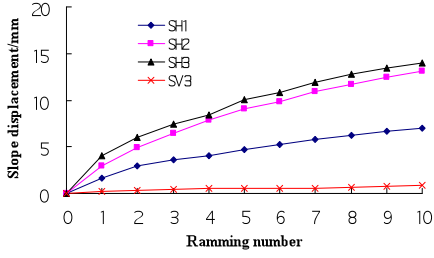

FIG. 4 Change curve of slope displacement over ramming number

Figure 4 is the change curve over ramming number, plotted by the readings of dial indicator, measured for the slope displacement on the linear slope D1, the horizontal displacement indicates the distance away from the slope and the vertical displacement indicates the downward displacement. We can see from the figure that the slope displacement increases with the ramming number, however in a slowing way of increase rate, the horizontal displacement is more than the vertical displacement that the horizontal displacement increases at foot, middle and top of the slope in a fast way of increase rate, the maximum horizontal displacements are 7.0mm, 13.1mm and 14.0mm respectively. The vertical displacement is relatively small that the maximum vertical displacement at the top of slope is 0.82mm. From these points, we can see that the horizontal displacement is the major factor for this kind of slope in dynamic compaction.

2.3 Typical oscillogram on actual measurement

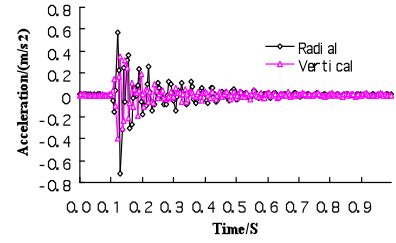

(a) Time-history curve for acceleration

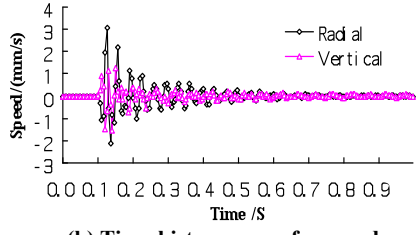

(b) Time-history curve for speed

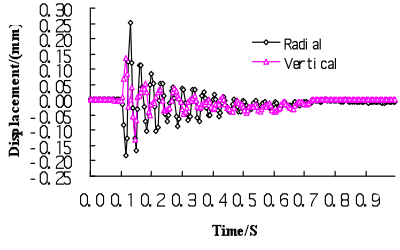

(c) Time-history curve for transient displacement

FIG. 5 Time-history curve for dynamic response

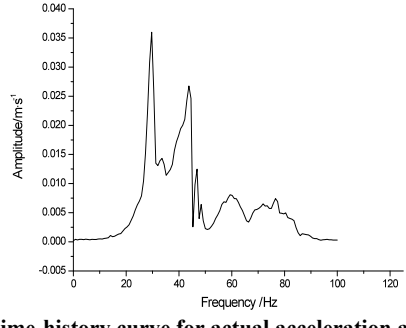

FIG. 6 Time-history curve for actual acceleration amplitude

The results of model test for dynamic compaction indicate that the waveform is basically similar except for the wave amplitude of dynamic compaction. 2 acceleration

transducers are arranged at each measuring point to measure the vertical and radial accelerations. Figure 5 shows the time-history curve of dynamic response for the third ramming at A2 measuring point on D1, the speed and transient displacement are calculated by integrative approach in data processing for the acceleration oscillogram. Based on the analysis on actual measurements, the change rules for vibration transmission of dynamic compaction can be described that: the vertical and radial acceleration, speed and transient displacement are produced by impact loading effect and then rapidly fade out, the vibration cycle is less than 1s; the radial value for dynamic response is more than vertical value at the same point, which corresponds to the measuring values on slope dial indicators. The peaks of vertical and radial acceleration for A2 are 0.39m/s^2 and 0.72m/s^2, the peaks of vertical and radial speed are 1.55 and 3.08mm/s, while the vertical and radial transient displacements are 0.14mm and 0.25mm respectively.

The frequency-spectrum analysis indicates that the frequency of dynamic compaction is low, usually between 25~45 Hz for major frequency (See Figure 6). In field construction of dynamic compaction, 10 times of ramming are needed continuously at each compacting point and there are “several minutes” between 2 rammings, however, the waveform analysis has shown that the lasting time of vibration is less than 1s, therefore, the vibration effect will not be superimposed.

2.4 Change rules of acceleration over ramming number

As for the single compacting test, the soil is compacted and the acceleration increases with the ramming number. The acceleration reaches the peak when the ramming number reaches a certain value; the acceleration will maintain at the peak if the ramming continues. Hence, the relation curve of vertical and radial acceleration peaks over ramming number for A3 measuring point in D1 compacting is plotted (Figure 7). We can see from the Figure 4-11 that, the effective energy of compaction decreases with the increase of ramming number, much energy is propagated in wave outward and the surrounding vibration is aggravated, the peak of vibration acceleration increases, however, in a slowing way of increase rate, and the radial acceleration peak is more than the vertical acceleration peak.

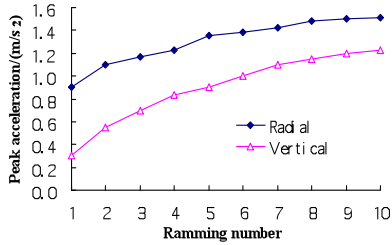

FIG. 7 Relation curve of acceleration peak over ramming number

2.5 Change rules for acceleration along slope

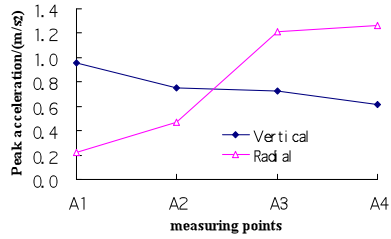

FIG. 8 Change rules of acceleration peaks along slope

The change curve for vertical and radial acceleration peaks at each point for the fifth impact of D1 compacting are shown in Figure 8, we can see from the figure that, the radial acceleration is less than the vertical acceleration at the lower part of slope that the vertical vibration prevails at this part of slope; the radial acceleration is more than the vertical acceleration at the upper part of slope that the radial vibration prevails at this part of slope. Compare with the vertical acceleration, the radial acceleration increases from foot to top of the slope, which shows there is more obvious amplification effect for slope on radial acceleration.

2.6 Relation between distance of compacting point and acceleration measuring point

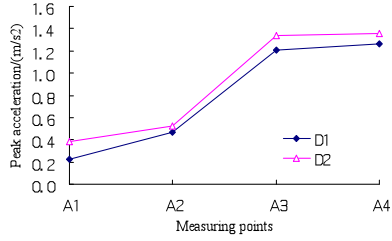

FIG. 9 Relation curve for acceleration measuring point over distance of compacting point

Figure 9 is the curve for the relation between radial acceleration peak and distance of compacting point for each point on slope in the fifth impact of the two compacting points, the distance for each point away from the D1 compacting point is 8m farther than D2 on slope. We can see from the figure that, the radial acceleration peak increases with the slope, the D2 acceleration peaks at each point are averagely 0.11m/s^2 larger than D1 acceleration peaks.

2.7 Change rules for acceleration in the slope

The acceleration amplitude at the same vertical point (L1 and L2 sections) increases from bottom to top, the amplification effect of radial vibration is obvious with a fast increase, there is little change in vertical vibration and the dynamic response of slope increases from bottom to top in a gradual way (See Figure 10). The acceleration amplitude at the same horizontal point (L3 section) decreases from the surface to the inside of the slope, the vertical vibration fades out in a fast way and there is little change in radial vibration (See Figure 11).

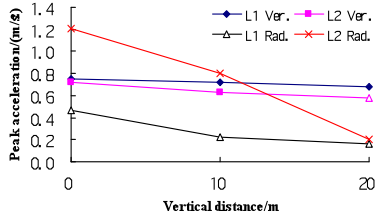

FIG. 10 Change rules of acceleration peak in vertical direction in slope

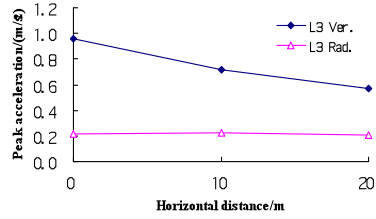

FIG. 11 Change rules of acceleration peak in horizontal direction in slope

2.8 Change rules for acceleration amplification coefficient over slope height

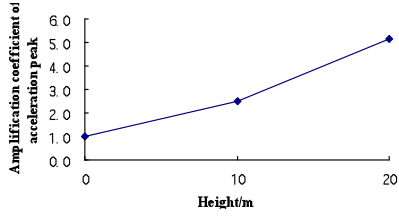

FIG. 12 Amplification coefficient of acceleration peak at each point on slope

As to describe the response rules of slope acceleration in dynamic compaction, the ration of response acceleration peak to acceleration peak of corresponding point is defined as the amplification coefficient of acceleration peak. The test results indicate that there are similar rules of slope response acceleration for the model under different compacting conditions, the amplification effect of vertical acceleration peak for the fifth impact of D1 compacting is described as follows. Figure 12 indicates the change rules of the amplification coefficient of vertical acceleration peak at each point on slope. We can see from the figure that, there is obvious amplification effect for slope on dynamic compaction. The amplification coefficient of acceleration peak increase along the slope that the upper part of slope has a larger amplitude, there is a rapid increase at the slope shoulder and the maximum amplification coefficient of acceleration peak is 5.2.

3. CONCLUSION

This article has accomplished the large model test for 1:20 loess slope, investigated the law of similitude, boundary condition treatment and so on in the model test, studied the

change rules of dynamic properties and dynamic response rules for loess slope in dynamic compaction. And then we have reached the following conclusions:

(1) The accumulated settlement increases with the ramming number, however in a slowing way of increase rate.

(2) In dynamic compaction, there is little change in the displacement on loess slope, while the horizontal displacement at foot, middle and top of slope increases, while the vertical displacement decreases in a gradual way.

(3) The amplitude of dynamic response for loess slope in dynamic compaction fades out rapidly with the impact loading effect; the vibration cycle is less than 1s and the major frequency is between 25~45 Hz that no superimposed vibration will occur.

(4) The amplification effect on radial acceleration is more obvious for loess slope in dynamic compaction, the vertical vibration prevails at lower part of slope while radial vibration prevails at upper part of slope.

(5) There is amplification effect for response amplitude on impact vibration of on the ridge of loess slope.

(6) There is obvious amplification effect on slope for input acceleration along the slope, especially the most obvious amplification effect at the top of slope.

It is a complex issue for the dynamic response of loess slope in dynamic compaction that, the characteristics and change rules for dynamic response need further studies. However, the test in this article, have provided rich test data on theory verification and data analysis, improvement or proposing of reasonable calculation model and analysis method. The test results have favorable influence on revealing the rules of dynamic response for loess slope in dynamic compaction, and provide instructive reference for the engineering design and construction for the loess region.

Acknowledgments

The authors appreciate the support of the National Science Foundation of China (Project 50908234).

REFERENCES

[1] FEI Xiang-ze, WANG Zhao, ZHOU Zheng-bing.(2002). “Experimental research of dynamic compaction of loess[J]”. **Rock and Soil Mechanics**, Vol. 23(4)：437-441.

[2] ZOU Li-hua, ZHAO Jian-chang, CHEN Quan-hong. (2005). “Experiment study on vibration to improve collapsible loess with dynamic compaction[J]”. **Chinese Journal of Rock Mechanics and Engineering**, Vol. 24(18): 3393-3397.

[3] ZHANG Meng-xi, WANG Yu-ling, FENG Jian-long. (2004). “Engineering properties of loess disturbed and geo-environmental damage due to dynamic consolidation[J].” **Rock and Soil Mechanics**, Vol. 25(12): 1903-1909.

[4] Leonards G A，Cutter W A，Holtz R D. (1998). “Dynamic compaction of granular soil[J].” Journal of Geotechnical Engineering, Division, ASCE, Vol. 106(1)：257–264.

[5] YU Ke-ping, CHENG Xia, SHE Xue-sen. (2003). “Model test of loess embankment treated by dynamic compaction[J].” **Journal of Changan University(Natural Science Edition)**, Vol. 23(4)：22-24.

[6] XU Guang-xing, YAO Ling-kan, GAO Zhao-ning et al. (2009). “Large-scale shaking table model test study on dynamic characteristics and dynamic responses of

slope[J].” **Chinese Journal of Rock Mechanics and Engineering**, Vol. 27(3)：624-632.

[7] Shen C K, Kim Y S, Bang S, et al. (1982). “Centrifuge modeling of lateral earth support[J].” **.Journal of Geotechnical Engineering. ASCE**. Vol. 108（9）: 1150-1164.

[8] TAMRAKAR S B, TOYOSAWA Y, ITOH K, HORII N, KUSAKABE S. (2005). “Failure mechanism of slopes in the centrifuge using in-flight excavator[C]”//International Symposium Landslide Hazard in Orogenic Zone from the Himalaya to Island Arc in Asia, Nepal, 2005: 255–264.

[9] TAMRAKAR S B, MITACHI T, TOYOSAWA Y, ITOH K, AIRKI T. (2005). “Measurement of slope movement during the slope excavation of small size full scale model [C]” //International Symposium Landslide Hazard in Orogenic Zone from the Himalaya to Island Arc in Asia, Nepal, 2005: 265–274.

Nonlinear Dynamic Behaviour of Pile Foundations in Horizontal Vibration

Bappaditya Manna[1], and Dilip Kumar Baidya[2]

[1]Lecturer, Department of Civil Engineering, National Institute of Technology, Rourkela, Orissa - 769008, India; bd_manna@yahoo.com

[2]Professor, Department of Civil Engineering, Indian Institute of Technology, Kharagpur, West Bengal - 721302, India; baidya@civil.iitkgp.ernet.in

ABSTRACT: Horizontal vibration tests are performed on reinforced concrete single pile (L/d = 20) and group piles (L/d = 20 and s/d = 2, 3, 4) under varying levels of harmonic excitation acting above the center of gravity of the pile cap-loading system. The observed response curves display marked nonlinearity as the natural frequencies decreases with increasing intensity of excitation for both horizontal and rocking mode of vibrations. The measured response is compared with linear elastic and nonlinear solutions of Novak's continuum approach. To account for the nonlinear response of the piles, provisions are made for yielding of soil around the piles by introducing the weak boundary zone concept. Different separation length between the pile and top soil is also considered for different excitation intensities in the nonlinear analysis. It is found that a close agreement can be achieved between theoretical predictions and measured response curves by allowing for boundary zone and separation between pile and soil. It is also found that the boundary zone parameters, pile-soil separation, pile-soil-pile interaction and the embedded effect of the pile cap play a major role in the coupled dynamic response of pile foundation.

INTRODUCTION

Pile foundations are widely used in weak soil deposits for supporting various structures. In addition to static loads, pile-supported foundations and structures are exposed to dynamic loads such as machine-induced vibrations, moving traffic, ocean waves and earthquakes.

A number of approaches are available to account for nonlinear dynamic pile-soil interaction. Novak & Sheta (1980) proposed an approximate approach, which includes a weak cylindrical zone or inner boundary zone around the pile. Veletsos & Dotson (1988) proposed a scheme that can account for the mass of the boundary zone. To predict the pile group behaviour the method of interaction factors was developed for dynamic response by some researchers (Kaynia & Kausel 1982). With the emergence of the new rather abstract theories for dynamic analysis of piles, it became necessary to verify their validity by means of experiments. Some researchers (Novak & Grigg 1976) conducted

the dynamic experiments on small prototype single piles and pile groups in the field.

In this paper a comprehensive study involving both dynamic testing of pile foundation and theoretical analysis is presented. The coupled vibration tests were carried out on reinforced concrete single pile and groups piles of different length (L) and spacing (s). Frequency versus amplitude curves of piles were experimentally established in the field for different excitation intensities. The test results are compared with the results obtained by continuum approach of Novak using both linear elastic solutions and nonlinear solutions. The influences of various boundary zone parameters, pile-soil separation, pile-soil-pile interaction and embedded effect of pile cap on the coupled dynamic response of piles are also studied.

METHODOLOGY OF COUPLED VIBRATION TEST

The site was located adjacent to Hangar, at Indian Institute of Technology, Kharagpur Campus, India. The soil properties were determined by in-situ and laboratory tests. Two different in situ tests were conducted, namely, standard penetration tests (SPT) to determine N value and cross hole seismic tests for determining the shear wave velocity (or shear modulus) of soil layer.

The piles were constructed in the field by bored cast-in-situ method. The diameter (d) of the pile was 0.1 m. In the present study, one single pile (L = 2.0 m) and three sets of 2 × 2 group piles (L = 2.0 m and s = 2d, 3d and 4d) were used. The dimension of pile cap was 0.57 m × 0.57 m × 0.25 m. Tests were carried out for two different embedded depths (h) of pile cap: Case 1 - Pile cap embedded into soil (h = 0.175 m); Case 2 - No contact of pile cap with soil (h = 0).

Forced vibration tests were conducted on piles subjected to coupled vibration. The mass of the system was controlled using steel ingots or test body attached to the pile cap. Steel ingots were mounted first on to the pile cap. Then the Lazan type mechanical oscillator was mounted on the steel ingots to produce the excitation forces above the C.G. of the pile cap-loading system. In this arrangement, both horizontal and rocking vibrations were generated simultaneously by the oscillator. Whole set up was connected so that it acts as a single unit. The mechanical oscillator was connected by means of a flexible shaft with a DC motor and its speed was controlled by a speed control unit. The vibration measuring equipment consisted of two piezoelectric acceleration pickups and the associated vibration meter. The horizontal component was measured using one pickup connected to the side of the foundation at the level of center of gravity (C.G.), while the rocking amplitudes were measured simultaneously by another pickup mounted vertically on the axis of the pile cap. The complete experimental setup is shown in Fig. 1.

The oscillator was run slowly through a motor using speed control unit. Thus the pile was subjected to vibration in the horizontal direction. Two different static loads (W_s = 10 kN and 12 kN including the weight of the pile cap and oscillator) were used. For each static load, tests were conducted with four different eccentric moments ($W{\cdot}e$ = 0.187 N m, 0.278 N m, 0.366 N m, and 0.450 N m, where W is the weight and e is eccentric distance of the rotating masses of the oscillator, respectively).

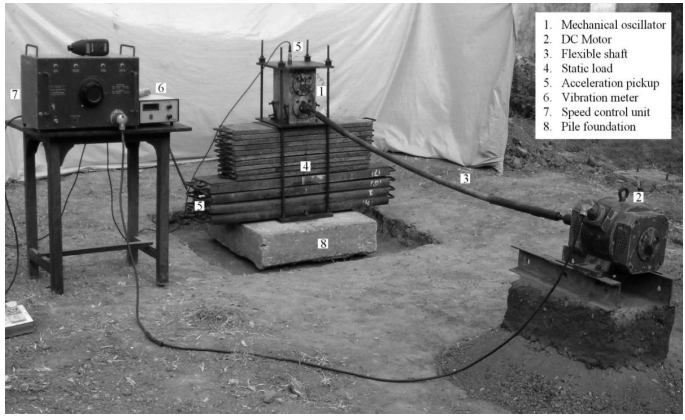

FIG. 1. Setup of coupled vibration test on small prototype pile

TEST RESULTS

The frequency versus amplitudes curves were recorded from the dynamic tests for both horizontal and rocking response. A set of response curves were obtained with different excitation level for each static load. It is observed that the observed response curves display nonlinearity as the resonant frequencies decreases with increasing excitation intensity and also the amplitudes are not proportional to the excitation intensity. Two resonant peaks are observed at two different frequencies for both horizontal and rocking component. The effects of static loads on the dynamic response of piles are studied and it is observed that both the resonant frequency and amplitude decreases as the static load increases.

The variations of resonant frequency and amplitude are observed for different *s/d* ratio of pile groups and it is found that the resonant frequency increases and the resonant amplitude decreases with increasing pile spacing. It is also found that the embedded pile cap (Case 1) produced higher resonant frequencies of pile than the no contact condition of pile cap (Case 2). However, the resonant amplitudes are higher for Case 2 as compared to Case 1.

THEORETICAL STUDY

In this study the continuum approaches by Novak & Aboul-Ella (1978) are used to analyses the dynamic behavior of single piles. In this approach, the stiffness and damping are calculated assuming that the soil is perfectly bonded to the pile. In nonlinear analysis for determining the impedance of single piles, the continuum approach is extended with a weak cylindrical boundary zone (Novak & Sheta 1980) around the pile. To account approximately for the effect of slippage and nonlinearity it is assumed that an embedded cylindrical body is surrounded by a linear viscoelastic medium composed of two parts - an outer infinite region and an inner weak layer surrounding the cylindrical body. Soil

nonlinearity, as well as the weakened bond and slippage are presumed to be accounted for by a reduced soil shear modulus and increased soil damping of the inner soil layer. The soil reactions of such composite medium can be substituted into the theory described in linear analysis (Novak & Aboul-Ella 1978) for calculation of stiffness and damping constants of piles embedded in layered media. The group stiffness and damping are calculated using the superposition method described in Novak & Mitwally (1990). With the stiffness and damping of single and group pile, the coupled horizontal and rocking component of pile under horizontal excitation can be calculated using the computer program DYNA5 which employs the previous theoretical approach.

THEORY VERSUS EXPERIMENT

In linear analysis, a perfect bonding between pile and soil is assumed and no weak zone is considered around the pile. Comparison of experimental response curves and the theoretical predictions are shown in Figs. 2(a) and (b) for group pile (L/d = 20, s/d = 4, W_s = 12 kN, Case 1). It can be seen from Fig. 2 that the agreement between the theoretical predictions and the experimental results is not fairly good. The predicted values of first and second natural frequencies are higher than the experimental results. The linear theory underestimates the resonant amplitude of piles in most of the cases.

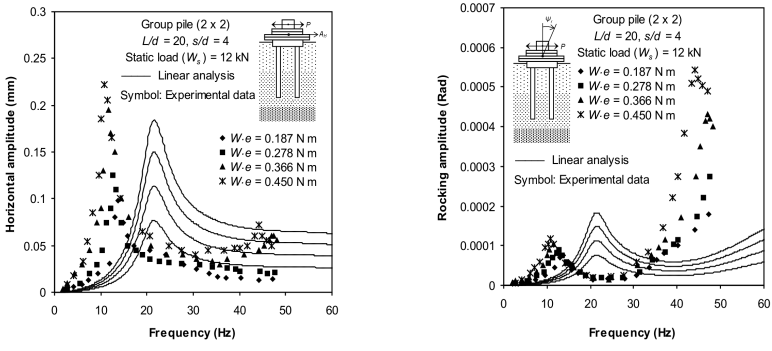

FIG. 2. Comparison of experimental results with that obtained by linear theory for group pile: (a) Horizontal Component, (b) Rocking Component

In nonlinear analysis, the boundary-zone concept was incorporated into the linear-elastic based mathematical model. The soil parameter in the weakened zone and different separation length for different excitation intensities are adjusted so that the nonlinear theoretical response curves approach the observed results. In no contact condition of pile cap, the separation between pile and soil is 2.1d (= 0.21 m) for We = 0.187 N m and 3.0d (= 0.30 m) for We = 0.450 N m. It is found that the length of separation (l_s) is more for no contact condition of pile cap (Case 2) than the embedded pile cap (Case 1) condition. For instance, the pile separation length is 2.4d for Case 1 and 3.0d for Case 2 for the strongest excitation (We = 0.450 N m). Typical comparison between the experimental response

curves and theoretical predictions by nonlinear analysis are shown in Figs. 3(a) and (b) for single pile (L/d = 20, W_s = 12 kN, Case 2) for both horizontal and rocking component, respectively.

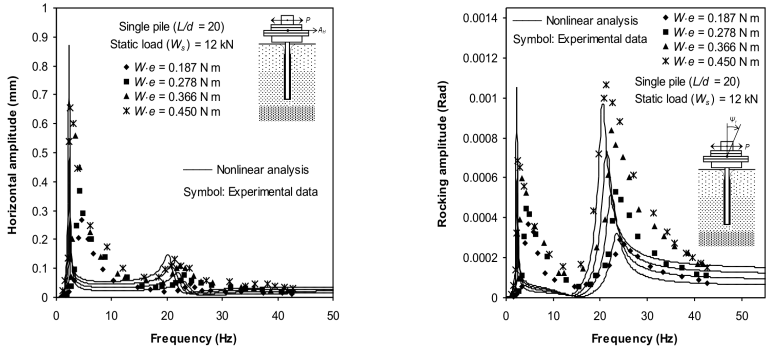

FIG. 3. Comparison of experimental results with that obtained by nonlinear theory for single pile: (a) Horizontal Component, (b) Rocking Component

It can be seen from Fig. 3 that the nonlinear theory provides a good estimate of resonant frequency for of coupled vibration. It can also be seen that the nonlinear model predicts the resonant amplitudes reasonably well for both first and second modes of vibration. It can be said that the inclusion of boundary zone and separation of pile with soil improves the agreement between the theoretical predictions and experimental results as compared to the linear theory.

STIFFNESS AND DAMPING OF PILE

The stiffness and damping of group pile (2 × 2, L/d = 20, s/d = 4, Case 2) obtained by nonlinear analysis for horizontal and rocking mode with different excitation intensities are shown in Figs. 4(a) and (b). It can be observed from Fig. 4 that pile stiffness decreases with increasing excitation intensities. The reduction in stiffness of the pile group with increasing excitation intensity is mainly due to development and growth of weak zone of soil around the pile. On the other hand, the pile damping increases significantly as the frequency approaches to zero. It can be noted that the damping of pile group for horizontal and rocking vibration reduces as the excitation intensity increases. These characteristics of pile stiffness and damping are due to the development and spread of the weak soil zone and the soil-pile separation effects.

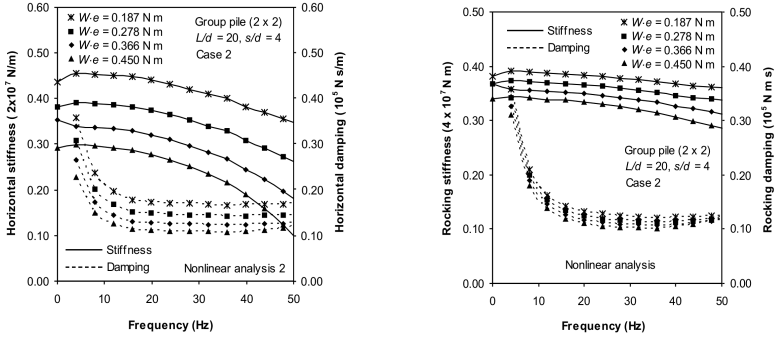

FIG. 4. Stiffness and damping of group pile obtained from nonlinear analysis: (a) Horizontal stiffness and damping, (b) Rocking stiffness and damping

CONCLUSIONS

This paper describes coupled vibration test of piles in the field subjected to harmonic loading to study the frequency amplitude behaviour of piles. The observed pile response exhibit typical nonlinear behavior. Many parameters, namely, exciting intensities, static load, embedment of pile cap and *s/d* ratios have an influence on the dynamic response of pile foundation. The measured response curves of piles have been compared with two different approaches, namely, linear analysis and nonlinear analysis using the continuum approach of Novak. The theoretical analysis based on the linear theory is found inadequate to predict the nonlinear response of piles under coupled vibration. The nonlinear theoretical model with boundary zone and pile-soil separation predicts the resonant frequency and amplitude of piles reasonably well for both horizontal and rocking modes of vibration.

REFERENCES

Kaynia, A. M. and Kausel, E. (1982). "Dynamic behavior of pile groups." *In: Proc. 2nd Int Conf Num Meth Offshore Piling*, Austin, Texas, 509-532.

Novak, M. and Aboul-Ella, F. (1978). "Impedance functions of piles in layered media." *J. Engrg. Mech.*, ASCE, Vol. 104(3): 643-661.

Novak, M. and Grigg, R. F. (1976). "Dynamic experiments with small pile foundations." *Can. Geotechnical J.,* Vol. 13: 372-385

Novak, M. and Mitwally, H. (1990). "Random response of offshore towers with pile-soil-pile interaction." *J. Offshore Mechanics and Arctic Engrg*, 112: 35-41.

Novak, M. and Sheta, M. (1980). "Approximate approach to contact problems of piles." *Proc: Dynamic Response of Pile Foundations: Analytical Aspects,* M. O'Neill et al., eds., ASCE, New York, 53–79.

Veletsos, A.S. & Dotson, K. W. (1988). "Vertical and torsional vibration of foundations in inhomogeneous media." *J. Geotechnical Engrg*, 114(9): 1002-1021.

Seismic Performances of Pile Groups in Inclined Soil Layers Subjected to Strong Motions

Mingwu Wang[1], Teteso Tobita [2], Susumu Iai [2]

[1]Professor, School of Civil Engineering, Hefei University of Technology, Hefei, China 230009; geotechnics@foxmail.com
[2]Associate Professor, DPRI, Kyoto University, Kyoto, Japan, 611-0011; tobita@ geotech.dpri.kyoto-u.ac.jp
[2]Professor, DPRI, Kyoto University, Kyoto, Japan, 611-0011; Iai@ geotech.dpri.kyoto-u.ac.jp

ABSTRACT: In order to insure the safety of pile groups on the inclined soils in the earthquake prone area, analysis of seismic performances of pile groups in the inclined soil layers is of prime importance. Centrifuge tests of 50g and responding numerical simulations are conducted to investigate the seismic performances of pile foundation under strong ground shaking conditions. Moreover, detailed discussions and comparisons between numerical modeling and centrifuge tests are included. These centrifuge test model consisted of a model pile foundation of 2×2, 10 times diameter spacing on an inclined dry or saturated layer of slope angle = arctg(1/2). Effective stress analysis method based on a multiple shear mechanism is employed for conducting the numerical predictions and validation. It is concluded that the measured and computed responses of acceleration, displacement are in good agreement. The physical and numerical models both indicate that the lateral displacements of pile groups are much larger in laterally spreading soils than in dry soils. The dynamic centrifuge test and the numerical simulation method proposed in this paper is reliable and applicable for analyzing seismic performance of soil-pile system in inclined soils subjected to strong motions.

INTRODUCTION

Soil liquefaction is the extreme manifestation of the pore pressure increase when saturated soil deposits are subjected to earthquake loading. When soil liquefaction occurs, the strength and stiffness of the soil decreases and the ability of the soil deposit to support foundations of buildings is reduced (Finn et al. 2002). It leads to the large lateral spreading and post-liquefaction displacement of foundation, which often control design of pile foundation in weak liquefiable soils. Although the behaviour of pile in liquefiable deposits have been studied by many researches, the seismic response of soil-pile system in inclined liquefiable soils subjected to strong motion has not been clarified. Consequently, the seismic design of pile foundations in these liquefiable soils poses very difficult problems, and the research of this topic, a focus problem for the geotechnical

engineers throughout the world, is potentially very significant.

In the absence of field data, centrifuge model test is a good method used to investigate the above problem (Wang et al. 2005b). On the other hand, numerical simulation can make up for these shortcomings of centrifuge test, such as boundary effect and variation of acceleration within model, and validate the results of centrifuge test (Wang et al. 2005a; 2008). The objective of this study is to investigate the performance of pile foundation in an inclined liquefiable soil layer subjected to strong motion using centrifuge tests and numerical simulations, and to provide a basis for the seismic design of pile foundation subjected to a strong motion in inclined liquefiable soils, which are of much non-linear and large deformation.

CENTRIFUGE TESTS

Testing Equipment

All centrifuge tests are conducted at the DPRI Centrifuge of Kyoto University, using the rigid container box and model piles and silica sand as research tools. The DPRI Centrifuge has an in-flight radius of 2.5m, and its maximum centrifugal acceleration for static test is 200 g, and for dynamic test is 50g. A rectangular rigid container with internal dimensions of 150(W)×450(L)×300 mm(H) was used in the centrifuge tests.

For each test, a complete set of response time histories were recoded during and after shaking, in the form of acceleration at 3 locations(at sand surface and pile top and container base), pile strain at 22 locations, horizontal displacement at 1 location by the side of pier surface, and pore pressure at 2 locations for saturated model. A data acquisition system was installed on the centrifuge to minimize electric noise. Digitals signals from the on-board computer were transferred to the computer in the controlled room via wireless communications.

Model Pile and Model Soil

The model pile foundation was a 2×2 pile group. The model pile was made of brass pipe of an outside diameter 7.0 mm, length 360 mm and thickness 0.9 mm, clamped to a pile cap at pile head. A pile plate fixed on the top of pile cap has dimensions of 83(W) × 83(L) × 12mm (H), in model units. To simplify the analysis, model pile's tips were fixed to the container base to simulate a fixed-based condition.

The soil profile is comprised of one layer silica sand of about ranging from 7.5 m through 15 m thick with an inclined angle = arctg (1/2) resting on stiff bedrock at prototype scale. The sand is a uniformly grade fined sand with coefficient of uniformity of 1.8 and mean grain size of 0.15mm. The specific gravity of the sand is Gs=2.63. The maximum and minimum porosity is 1.2 and 0.7, respectively. In the saturated model, the soil is saturated with de-aired metolose solution, having 50 times the viscosity of water such that the deposit has the prototype permeability of sand. The ground is assumed to be of uniformly deposited sand of which density is 1.46 g/cm^3 and 1.86 g/cm^3, respectively for 60% and 90% relative density sand deposit.

Centrifuge Model

Two types of model, saturated model and dry model were carried out to investigate the seismic performances of pile group in the inclined soils during earthquake. The main features and parameters of each test were listed in the Table 1. Figure 1 shown the scenario prototype input motion applied to the base of each model (See Table 1 for the exact acceleration level applied to each model). The programmed motion was excited parallel to the base of the container.

Table 1. Centrifuge Model Tests

Model	Relative Density of Soils (%)	Peak Value of Input Motion (m/s^2)
Dry Model	90	11.63
Saturated Model	60	8.46

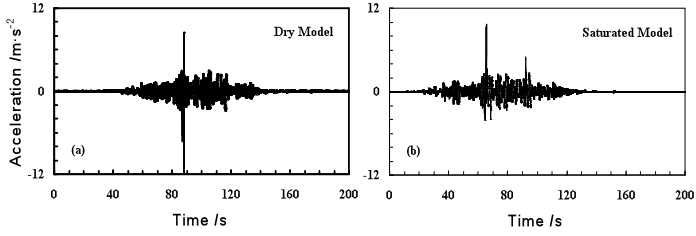

FIG. 1. Base motion of two models.

NUMERICAL SIMULATIONS

To validate and analyze the results of centrifuge tests, numerical modeling based on the effective stress analysis method has conducted using the program FLIP (Finite element analysis program for LIquefaction Process). The constitutive model used for the analysis was incorporated in the program FLIP. The constitutive model is based on multiple inelastic shear springs defined in the deviator strain space, which takes into account the effect of rotation of principal stress axis directions. The excess pore water pressure (EPWP) generation due to dilatancy is modeled using the concept of liquefaction front, which is defined in the equivalent normalized stress space. The more detailed illumination was expounded in references (Iai et al. 1992; Wang et al. 2005a).

The finite element mesh used in the analysis for the saturated model was shown in Figure 2. The finite element model consists of 2486 nodes and 4106 elements. Pile was modeled with linear beam elements. The mesh for the dry model was similar to saturated model. The seawater was modeled as incompressible fluid. The super-structure mass was treated as a rigid body and was represented by a concentrated mass. The soil-pile

interaction spring element was used. To simulate the conditions of centrifuge test, the both sides and bottom boundary conditions were simulated as shown in Figure 2. The locations of output elements and output nodes responding to the sensors in the centrifuge tests indicated as shown in Figure 2.

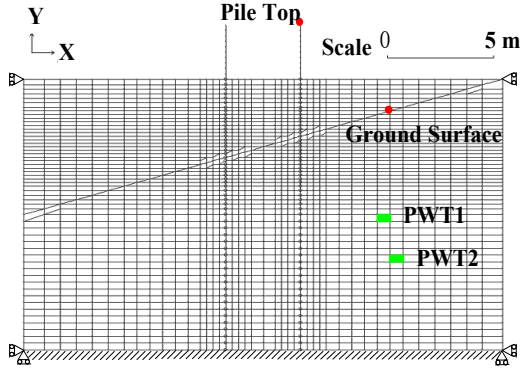

FIG. 2. Mesh for the simulation.

Table 2. Parameters of Soil Layer for the Numerical Simulation

Model	Density (g/cm^3)	Soil Porosity	G_{ma} (kPa)	K_{ma} (kPa)	ϕ_f (°)
Dry Model	1.46	0.45	1.328×10^5	3.462×10^5	42
Saturated Model	1.86	0.47	0.932×10^5	2.426×10^5	40

Note: K_{ma}: initial bulk modulus of soil skeleton at confining pressure of 98 kPa; G_{ma}: initial shear modulus at confining pressure of 98 kPa; φ_f: effective friction angle

The seismic response analysis was performed for 200 s for two models with a time intervals of 0.1s for the saturation model and 0.01 s for dry model , respectively, using Wilson- method (θ=1.4). Rayleigh damping of α=0.0, β=0.002 was used. Before the dynamic response analysis, a static analysis was performed with gravity to simulate the initial stress acting in situ before the earthquake.

RESULTS AND COMPARISONS

Results of analysis shown in Figs. 3, 4, and 5 were given at prototype scale.

Dry Model

Figure 3 illustrated the measured and computed time histories of displacement, accelerations at pile top and sand surface for the dry model. It may be seen that there was a closely agreement between the centrifuge test and numerical modelling. Moreover, the comparison between the measured and computed maximum value of displacement and acceleration was also good. It was observed in the test that the maximum lateral displacement at pile top is about 0.56 m (at prototype model scale), and the residual displacement is minor. The peak value of acceleration responses did not decreased obviously with the shaking.

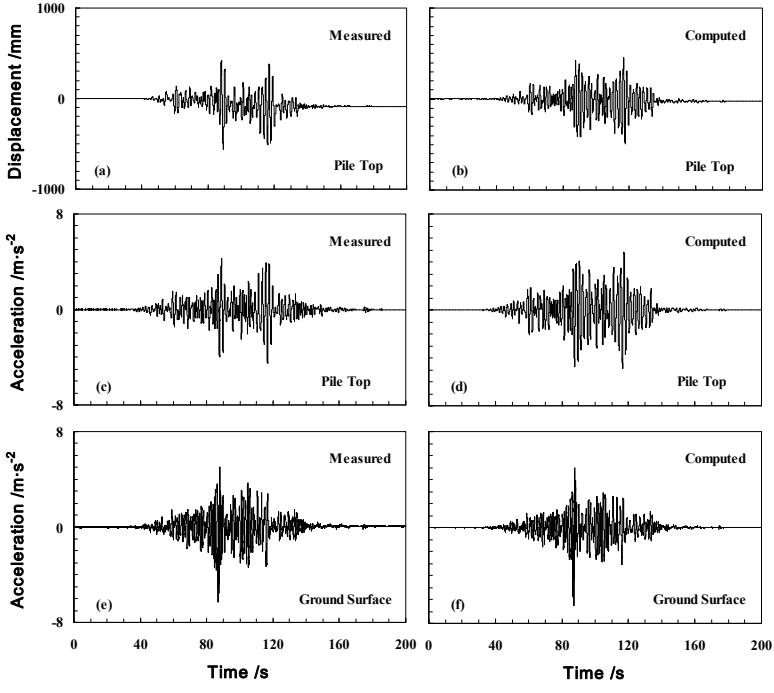

FIG. 3. Comparison between measured and computed responses of dry model.

Saturated Model

The measured and computed time histories of displacement, accelerations, and excess pore water pressures at pile head and sand deposit of different depths are depicted in the Figures 4, and 5. The permanent prototype lateral displacement of test was much more than 0.80 m for the laser displacement transducer (LDT) overflowed (See Fig. 4(a)). The predicted value at prototype scale shown in Fig. 4-b was 1.59m. That was much more

than dry model. It may be seen that the observed displacement time history before the LDT overflowed was in closely agreement with that of the computed (See Fig. 4 (a) and (b)). The measured and computed acceleration waveforms at the pile top and sand surface were in generally agreement, moreover, the computed maximum acceleration value of sand surface were almost same as the measured maximum value.

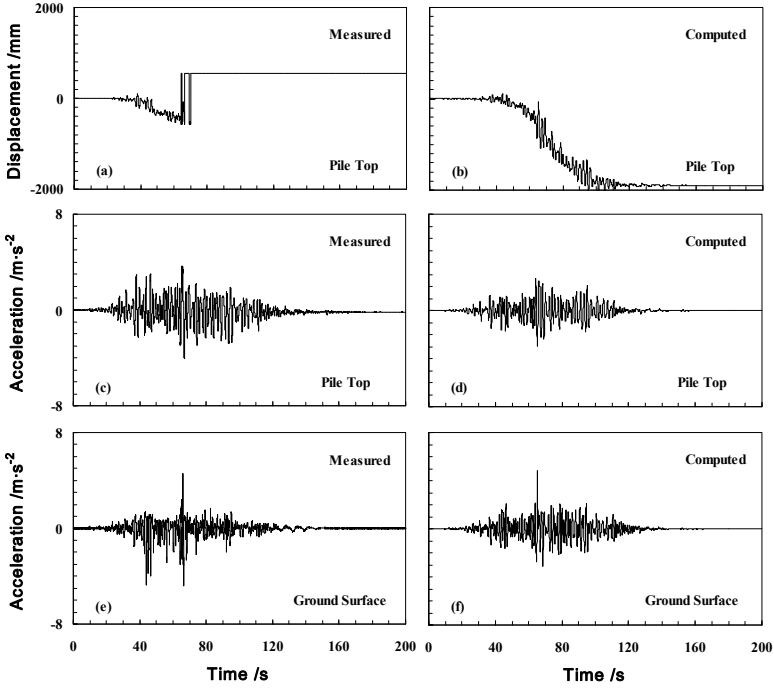

FIG. 4. Time histories of displacement and acceleration in the saturated model.

Recorded excess pore pressures during the shaking respectively were shown in Figure 5 at prototype depths of 5.5 and 8.2 m in the soil profile, in which the alphabets PWT1 and PWT2 shown in the figures indicate the locations shown in Figure 2. It was clearly seen that the saturated sand at two depths was shown to have completely liquefied when the pore water pressure reaches the initial effective stress of about 46 and 69 kPa after 60s period of shaking, and responding displacements were much larger. It was also concluded that the triggering of liquefaction increases with the decreasing relative density of soil deposit. It was observed in the test that the liquefaction occurred first near the surface and works its way downward.

Based on the above results and comparisons, it is concluded that the permanent lateral displacement of saturated model at pile top was much more than that of dry model. The

amplitude of acceleration at pile top and ground surface attenuated in saturated when the soil layer was liquefied, but in the dry model they were not observed. In a word, the lateral spread and liquefaction played a role of seismic performances of pile groups on inclined liquefiable soils. These results also shown that for the saturated model and the dry model, there is a good agreement of responses of displacement, acceleration and pore pressure between the centrifuge test and numerical modeling. The system identification procedure employed here to investigate the dynamic response, is very helpful to understand better the liquefaction process and seismic behavior of pile foundation under strong shaking condition.

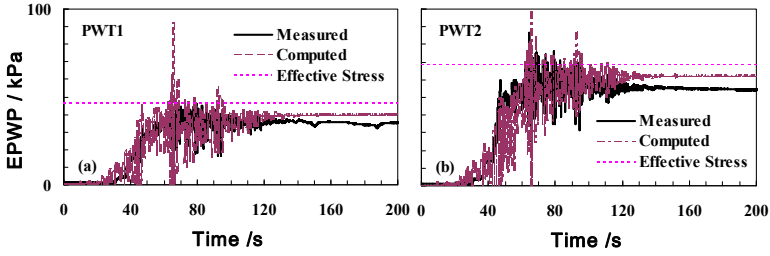

FIG. 5. Comparison between measured and computed responses of EPWP.

CONCLUSIONS

This paper presented centrifuge model tests and numerical simulations, which simulated the effect of strong ground shaking on the pile foundation structure in inclined soils. Results as well as detailed interpretations and discussions were presented. Some major conclusions may be drawn from these results as follows:

1) This study presented demonstrates that centrifuge modeling can simulate realistically seismic response of soil-pile system in the inclined soil layer. The FLIP has potential ability to simulate the seismic behavior of pile foundation in inclined liquefiable ground during the strong ground shaking.

2) The measured values of acceleration and displacement at pile top, excess pore pressures in the ground are in good agreement with the predicted values. The displacement of pile and ground are much larger in the saturated model than in the dry model.

3) It is found that for the saturated model, numerical model predicts, which are in good agreement with the centrifuge tests

4) The problem of soil-pile interaction in inclined liquefiable soil is a very complex problem. Extensive and further studies are needed to evaluate further the performance and validity of centrifuge test and numerical modeling, such as the comparison of seismic responses between in a horizontal soil layer and in the inclined soil layer.

ACKNOWLEDGMENTS

This research was supported by Science and Technological Fund of Anhui Province for Outstanding Youth (No. 08040106830) and National Natural Sciences Foundation, China (No. 40702049), the supported is gratefully appreciated. The authors would also like to express their sincere thanks to Technician Shimizu and graduate student Nakayama for their assistance throughout centrifuge tests.

REFERENCES

Finn, W.D.L. and Fujita, N. (2002). " Piles in liquefiable soils: seismic analysis and design issues." *Soil Dynamics and Earthquake Engineering*, Vol. 22 (9-12): 731-742.

Iai, S., Matsunaga, Y., Kameoka, T. (1992). "Strain space plasticity model for cyclic mobility." *Soils Foundations*, Vol. 32 (2):1-15.

Kagawa, T., Sato, M., Minowa, M., and et al. (2004). "Centrifuge simulations of large-scale shaking table tests: case studies." Journal of Geotechnical and Geoenvironmental Engineering,; 130(7): 663-672.

Wang, M., Iai, S., Tobita T. (2005a). "Numerical modeling for dynamic centrifuge model test of the seismic behaviors of pile-supported structure." *Chinese Journal of Geotechnical Engineering*, Vol. 27 (7): 738-741.

Wang, M., and Li L. (2008). "Effective stress analysis of liquefaction-induced uplift of shallow duct-type underground RC structures." *Journal of Vibration Engineering*, Vol. 21 (3):286-290.

Wang, M., Tobita, T., Iai, S. (2005b). "Centrifuge modeling of soil-pile interaction in liquefiable soils subjected to strong motion." *Chinese Journal of Rock Mechanics and Engineering*, Vol. 24 (S2): 5555-5560.

Dynamic Response of Railway Track Rested on Transversely Isotropic Poroelastic Media

Zhou Ye, Liu Ganbin*, Zheng Rongyue
Faculty of Architectural, Civil Engineering and Environment, Ningbo University, Zhejiang Ningbo 315211. Liugb76@163.com

ABSTRACT: Based on Biot's wave equation, the dynamic response of a transversely isotropic saturated soil under train load was studied with Fourier transform technique. In this application, the track, including the rails, rail pad, sleepers and ballast, is modeled as an infinite layered beam structure. Analytical solutions for displacement, stress and pore pressure are derived in the form of integral. Numerical results are obtained by using the inverse Fourier transform and are used to analyze the influence of the anisotropic parameter of the ground on the ground vibration and pore pressure. It is shown that the anisotropy of stratum has great influence on the behavior of soil-track system.

INTRODUCTION

With the development of railway, the ground vibration due a moving load has drawn more and more attentions. There have been numerous investigations concerning the dynamic response of ground subjected to a moving load since the 1950s. Alabi(1992) represented a moving train by a set of concentrated, moving vertical forces for low speeds. Based on Biot's theory, the three-dimensional analytical solution for the dynamic response of a half-space porous medium subjected to a point load applied on the surface and moving with constant speed has been proposed by Lu and Jeng(2007).

However, soils are deposited through a process of sedimentation over a long period of time, anisotropy soils are often modeled as transversely isotropic saturated poroelastic media from the standpoint of practical considerations in engineering. This paper intends to analyze the effects of anisotropic parameter on ground vibration and pore pressure.

CALCULATION MODEL

The model considered is shown in Fig.1. The rails are modeled as a single Euler beam with mass per unit length of track m_R and bending stiffness EI. The sleepers are modeled as a distributed mass m_S per unit length of track. The rail pads are represented as a distributed vertical spring stiffness k_P between the rail beam and the sleeper mass. The ballast is modeled as an elastic layer with a width b and a mass per unit length m_B. For the ballast layer, only the vertical stiffness k_B is taken into account.

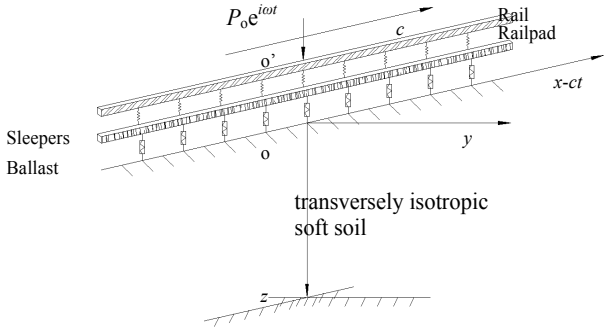

FIG. 1. Diagram of the model of track on soft soil foundation.

The moving load is assumed harmonic with an angular frequency ω and an amplitude P_0. c is the speed of the moving load. The vertical displacements of the rail beam and the sleeper mass are denoted by $w_R(x,t)$, $w_S(x,t)$, respectively, and the vertical displacement at the centerline in the contact plane(i.e.,the x-axis) by $w_G(x,t)$. The contact force in the contact plane is $F_3(x,t)$.

The plane Oxy represents the ground surface, below which the ground consists of transversely isotropic saturated poroelastic layer. The layer overlies a rigid foundation. The material constants of layer are two Young's modulus E_V and E_H, two Poisson ratios v_{HH} and v_{HV}, shear modulus G_V, solid grains and fluid densities ρ_s and ρ_l, porosity n, viscosity coefficient of fluid η_w, soil permeability k_s, bulk modulus of soil particle, fluid and soil skeleton K_s, K_f and K_b.

GOVERNING EQUATIONS

The differential equations of motion of the railway have been proposed by Sheng et al (1999). For the rail beam

$$EI\frac{\partial^4 w_R(x,t)}{\partial x^4}+m_R\frac{\partial^2 w_R(x,t)}{\partial t^2}+k_p[w_R(x,t)-w_S(x,t)]=\delta(x-ct)P_0e^{i\omega t} \quad (1)$$

Where δ(.) is the Dirac-delta function.

For the sleeper mass

$$m_S\frac{\partial^2 w_S(x,t)}{\partial t^2}+k_p[w_S(x,t)-w_R(x,t)]=-F_2(x,t) \quad (2)$$

and for the ballast layer a linear spring stiffness with a consistent mass approximation is used so that

$$\frac{m_B}{6}\begin{bmatrix}2&1\\1&2\end{bmatrix}\begin{Bmatrix}\dfrac{\partial^2 w_S(x,t)}{\partial t^2}\\[2ex]\dfrac{\partial^2 w_G(x,t)}{\partial t^2}\end{Bmatrix}+k_B\begin{bmatrix}1&-1\\-1&1\end{bmatrix}\begin{Bmatrix}w_S(x,t)\\w_G(x,t)\end{Bmatrix}=\begin{Bmatrix}F_2(x,t)\\-F_3(x,t)\end{Bmatrix} \quad (3)$$

where $F_2(x,t)$ is the force per unit length of track between the sleeper mass and the ballast.

The differential equations of motion of the ground are as follows(1956).

$$C_{11}\frac{\partial^2 u_1}{\partial x^2}+C_{12}\frac{\partial^2 u_2}{\partial x\partial y}+C_{13}\frac{\partial^2 u_3}{\partial x\partial z}-\alpha\frac{\partial p}{\partial x}+C_{66}\frac{\partial^2 u_1}{\partial y^2}+C_{66}\frac{\partial^2 u_2}{\partial x\partial y}+C_{44}\frac{\partial^2 u_1}{\partial z^2}+C_{44}\frac{\partial^2 u_3}{\partial x\partial z}=\rho\ddot{u}_1+\rho_l\ddot{w}_1 \quad (4)$$

$$C_{66}\left(\frac{\partial^2 u_1}{\partial x\partial y}+\frac{\partial^2 u_2}{\partial x^2}\right)+C_{12}\frac{\partial^2 u_1}{\partial x\partial y}+C_{11}\frac{\partial^2 u_2}{\partial y^2}+C_{13}\frac{\partial^2 u_3}{\partial y\partial z}-\alpha\frac{\partial p}{\partial y}+C_{44}\left(\frac{\partial^2 u_2}{\partial z^2}+\frac{\partial^2 u_3}{\partial y\partial z}\right)=\rho\ddot{u}_2+\rho_l\ddot{w}_2 \quad (5)$$

$$C_{44}\left(\frac{\partial^2 u_1}{\partial x\partial z}+\frac{\partial^2 u_3}{\partial x^2}\right)+C_{44}\left(\frac{\partial^2 u_2}{\partial y\partial z}+\frac{\partial^2 u_3}{\partial y^2}\right)+C_{13}\frac{\partial^2 u_1}{\partial x\partial z}+C_{13}\frac{\partial^2 u_2}{\partial y\partial z}+C_{33}\frac{\partial^2 u_3}{\partial z^2}-\alpha\frac{\partial p}{\partial z}=\rho\ddot{u}_3+\rho_l\ddot{w}_3 \quad (6)$$

$$p=M\left(-\frac{\partial w_1}{\partial x}-\frac{\partial w_2}{\partial y}-\frac{\partial w_3}{\partial z}\right)-\alpha M\left(\frac{\partial u_1}{\partial x}+\frac{\partial u_2}{\partial y}+\frac{\partial u_3}{\partial z}\right) \quad (7)$$

where u_i and w_i are the displacement of the solid skeleton and the fluid, p is the pore pressure. α, M are the Biot's parameters accounting for the compressibility of the grains and the fluid. They can be given by $\alpha=1-K_b/K_s$, $M=K_s^2/(K_d-K_b)$, $K_d=K_s(1+n(K_s/K_f-1))$, C_{ij} are elastic constants, they can be expressed as follows

$C_{11}=E_H\left(1-\nu_{HV}^2E_H/E_V\right)/\left(1+\nu_{HH}\right)\Delta$, $C_{12}=E_H\left(\nu_{HH}+\nu_{HV}^2E_H/E_V\right)/\left(1+\nu_{HH}\right)\Delta$,

$C_{13}=E_H\nu_{HV}/\Delta$, $C_{33}=E_V\left[+2\nu_{HV}^2E_H/\left(E_V\Delta\right)\right]$, $C_{44}=G_V$, $C_{66}=E_H/2\left(1+\nu_{HH}\right)$,

$\Delta=1-\nu_{HH}-2\nu_{HV}^2E_H/E_V$.

CALCULATION METHOD

Now applying the single spatial Fourier transform pairs and the double spatial Fourier transform pairs

$$\overline{f}(\xi)=\int_{-\infty}^{\infty}f(x)e^{-i\xi x}dx,\quad f(x)=\frac{1}{2\pi}\int_{-\infty}^{\infty}\overline{f}(\xi)e^{i\xi x}d\xi \quad (8)$$

$$\overline{f}(\xi,\eta)=\int_{-\infty}^{\infty}\int_{-\infty}^{\infty}f(x,y)e^{-i(\xi x+\eta y)}dxdy,\quad f(x,y)=\frac{1}{4\pi^2}\int_{-\infty}^{\infty}\int_{-\infty}^{\infty}\overline{f}(\xi,\eta)e^{i(\xi x+\eta y)}d\xi d\eta \quad (9)$$

to equations (1)-(3) and (4)-(7), and define $e_h=\xi\overline{u}_1+\eta\overline{u}_2$, $\beta=1/\left(m\Omega^2-i\quad b\right)$ and $\Omega=\omega-\xi c$, yields

$$\overline{F}_3(\xi,t)=\frac{A_1^2\overline{w}_G(\xi,t)+A_1A_2P_0}{Q}-A_3\overline{w}_G(\xi,t) \quad (10)$$

$$\begin{bmatrix}C_{44} & & \\ & C_{33} & \\ & & M\beta\end{bmatrix}\frac{\partial^2}{\partial z^2}\begin{bmatrix}\overline{e}_h\\ \overline{u}_3\\ \overline{p}\end{bmatrix}+\begin{bmatrix}b_1 & & \\ b_2 & & b_3\\ & b_4 & \end{bmatrix}\frac{\partial}{\partial z}\begin{bmatrix}\overline{e}_h\\ \overline{u}_3\\ \overline{p}\end{bmatrix}+\begin{bmatrix}b_5 & & b_6\\ & b_7 & \\ b_8 & & b_9\end{bmatrix}\begin{bmatrix}\overline{e}_h\\ \overline{u}_3\\ \overline{p}\end{bmatrix}=\begin{bmatrix}0\\0\\0\end{bmatrix} \quad (11)$$

where $A_1=\frac{1}{6}m_B\Omega^2+k_b$, $A_2=k_P/\left(EI\eta^4-\Omega^2m_R+k_P\right)$, $A_3=-\frac{1}{3}m_B\Omega^2+k_b$,

$Q=A_3-\Omega^2m_s+k_P-A_2k_P$, $b_1=\left(-C_{13}i-C_{44}i\right)\left(\xi^2+\eta^2\right)$, $b_2=-C_{44}i-C_{13}i$, $b_3=\beta\Omega^2\rho_l-\alpha$,

$b_4=\alpha M-\rho_l\beta M\Omega^2$, $b_5=-C_{11}\xi^2-C_{11}\eta^2+\rho\Omega^2-\rho_l^2\beta\ ^4$, $b_6=\left(\alpha i-i\rho_l\beta\Omega^2\right)\left(\xi^2+\eta^2\right)$,

$b_8=iM\rho_l\beta\Omega^2-i\alpha M$, $b_7=-C_{44}\xi^2-C_{44}\eta^2+\rho\Omega^2-\rho_l^2\beta\ ^4$, $b_9=1-\beta M\left(\xi^2+\eta^2\right)$.

Assuming the general solutions of equations (11) in the form

$$\left[\bar{e}_h \quad \bar{u}_3 \quad \bar{p}\right]^T = \left[C_1 \quad C_2 \quad C_3\right]^T \exp\left(\lambda z\right) \tag{12}$$

One can obtain the following characteristic equation

$$a_1\lambda^6 + a_2\lambda^4 + a_3\lambda^2 + a_4 = 0 \tag{13}$$

where $a_1 = C_{33}C_{44}M\beta$, $a_2 = C_{33}C_{44}b_9 + b_7C_{44}M\beta - C_{44}b_3b_4 + C_{33}b_5M\beta - b_1b_2M\beta$, $a_3 = C_{44}b_7b_9 + C_{33}b_5b_9 + b_5b_7M\beta - b_3b_4b_5 + b_1b_5b_8 - b_1b_2b_9 + b_2b_4b_6 - C_{33}b_6b_8$ $a_4 = b_5b_7b_9 - b_6b_7b_8$, and λ_1, λ_2, λ_3, λ_4, λ_5, λ_6 are the roots of the characteristic equation, $\lambda_1 = -\lambda_4$, $\lambda_2 = -\lambda_5$, $\lambda_3 = -\lambda_6$.

Substituting the roots into the Eq.(12) yields

$$\bar{p} = \sum_{i=1}^{6} C_i e^{\lambda_i z} \qquad e_h = \sum_{i=1}^{6} C_i h_i e^{\lambda_i z} \qquad \bar{u}_3 = \sum_{i=1}^{6} C_i r_i e^{\lambda_i z} \tag{14}$$

where $r_s = \dfrac{\left[\bar{b}_2 b_6\lambda_s - b_3\lambda_s\left(C_{44}\lambda_s^2 + b_5\right)\right]}{\left(C_{33}\lambda_s^2 + b_7\right)\left(C_{44}\lambda_s^2 + b_5\right) - b_1b_2\lambda_s^2}$, $h_s = \dfrac{-b_1\lambda_s r_s - b_6}{C_{44}\lambda_s^2 + b_5}$, $(s = 1,2,3,4,5,6)$.

According to $e_h = \xi\bar{u}_1 + \eta\bar{u}_2$, (4), (5), (14), $\bar{u}_1$ is obtained as follows

$$\bar{u}_1 = \sum_{i=1}^{6} C_i W_i e^{\lambda_i z} \tag{15}$$

where $W_s = \dfrac{C_{13}i\xi\lambda_s r_s + C_{44}i\xi\lambda_s r_s + C_{12}\xi h_s + C_{66}\xi h_s - \alpha i\xi + i\rho_l\beta\xi\Omega^2}{C_{44}\lambda_s^2 + C_{12}\xi^2 + C_{66}\xi^2 - C_{11}\xi^2 - C_{66}\eta^2 + \rho\Omega^2 - \rho_l^2\beta^4}$, $(s = 1,2,3,4,5,6)$

According to the constitutive relations $\sigma_z = C_{13}\left(u_1 + u_2\right) + C_{33}u_3 - \alpha p$ and $\sigma_{xz} = C_{44}\left(\partial u_1/\partial z + \partial u_3/\partial x\right)$, the following stresses are obtained

$$\bar{\sigma}_z = \sum_{i=1}^{6} C_i N_i e^{\lambda_i z} \qquad \bar{\sigma}_{xz} = \sum_{i=1}^{6} C_i M_i e^{\lambda_i z} \tag{16}$$

where $N_s = -iC_{13}h_s + C_{33}\lambda_s r_s - \alpha$, $M_s = C_{44}\lambda_s W_s - C_{44}i\xi r_s$, $(s = 1,2,3,4,5,6)$

FORMULATION OF THE BOUNDARY VALUE PROBLEM

There are six unknown parameter in equations (14), (15), (16) and are related to each other via the following boundary conditions. Coupling of the ground with the railway track can be carried out by taking into account the continuity of the displacements and the equilibrium of the stresses in the plane of contact between them, i.e.,

$$\bar{w}_G\left(\xi, t\right) = \bar{u}_3\big|_{z=0} \;;\; \bar{\sigma}_{33}\Big|_{Z=0} = -\frac{\sin(\eta b)}{\eta b}\bar{F}_3\left(\xi\right) \tag{17}$$

Substituting equations (10) into equation (17), yields

$$\bar{\sigma}_{33}\Big|_{Z=0} = -\frac{\sin(\eta b)}{\eta b}\left(\frac{\left(A_1^2\bar{u}_3\big|_{z=0} + A_1A_2P_0\right)}{Q} - A_3\bar{u}_3\big|_{z=0}\right) \tag{18}$$

As only the vertical load is applied over the surface of the soft soil layer and the layer overlies a rigid foundation, so that

$$\bar{\sigma}_{13}\Big|_{z=0} = 0 \;;\; \bar{u}_1\big|_{z=H} = 0 \;;\; \bar{u}_3\big|_{z=H} = 0 \tag{19}$$

An additional boundary condition is now introduced by considering the surface of the layer as permeable or impermeable.

For the permeable surface

$$\overline{p}\big|_{z=0} = 0\,,\ \frac{\partial \overline{p}}{\partial z}\Big|_{z=H} = 0 \tag{20}$$

For the impermeable surface

$$\frac{\partial \overline{p}}{\partial z}\Big|_{z=0} = 0\,,\ \frac{\partial \overline{p}}{\partial z}\Big|_{z=H} = 0 \tag{21}$$

By substitution of equations (14), (15), (16) into the stress and displacement boundary conditions, one can obtain six homogeneous equations in the following matrix form.

$$[E][Q]=[F] \tag{22}$$

where $[Q]=[C_1 \quad C_2 \quad C_3 \quad C_4 \quad C_5 \quad C_6]^T$; $[F]=[f_1 \quad 0 \quad 0 \quad 0 \quad 0 \quad 0]^T$. The elements of matrices $[E]$ are given as follows: $e_{1i} = N_i + A_1^2 r_i \dfrac{\sin(\eta BR)}{Q\eta BR} - A_3 r_i \dfrac{\sin(\eta BR)}{\eta BR}$, $e_{2i} = r_i e^{\lambda_i H}$, $e_{3i} = W_i e^{\lambda_i H}$ for surface permeable, $e_{4i} = 1$; for surface impermeable, $e_{4i} = \lambda_i$, $e_{5i} = \lambda_i e^{\lambda_i H}$, $e_{6i} = M_i$ $(i = 1,2,3,4,5,6)$.

By solving equations (22), the expression of vertical displacement of ground surface and pore pressure in soft soil can be found.

NUMERICAL RESULTS

In this section, the influence of anisotropic parameter on ground vibration and pore pressure is investigated. For all the results presented, the inverse Fourier transform has been carried out using the IFFT algorithm. To compute the inverse Fourier transform accurately using a discrete transform, the integrals must be truncated at sufficiently high values to avoid distortion of the results by aliasing, while the mesh of calculated function values must be fine enough to well represent the detail of the functions(Jones, *et al*,1998).

In order to carry out example calculations, the material parameters of the ground model are given in Table 1. The ground model has a 5m layer of soil with a stiffer half-space substratum. Parameters for a typical railway track that have been used are presented in Table 2. The load has an unit amplitude and a frequency of 16Hz.

Table 1. The Parameters for Soft Soil Foundation

E_V(MPa)	E_H(MPa)	v_{HH}	ρ(kg/m^3)	ρ_l(kg/m^3)	η_w
2.5	3	0.3	1816	1000	0.01
v_{HV}	G_V(MPa)	n	α	M(MPa)	k(m^{3}kg^{-1}s)
0.3	80	0.4	0.9	24500	1×10^{-7}

Table 2. The Parameters for the Railway

EI(Nm^2)	m_R(kg/m)	m_S(kg/m)	m_S(kg/m)	k_P(Pa)	k_B(Pa)	b(m)
1.26×10^7	120	490	1200	3.5×10^8	3.15×10^8	0.1

In Fig.2, It can be seen that the amplitude of the vertical displacement decreases as the Horizontal Young's Modulus E_H increases for the impermeable surface and permeable surface. The influence of Poisson ratio v_{HH} on vertical displacement is indicated in Fig.3,

with increasing Possion ratio v_{HH}, the vertical displacement decreases, and v_{HH} has slightly effect on vertical displacement.

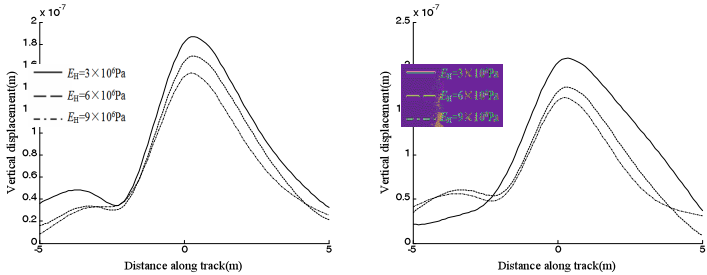

(a) surface permeable (b) surface impermeable

FIG. 2 Effect of transverse Young's modulus of soft soil on surface vibration

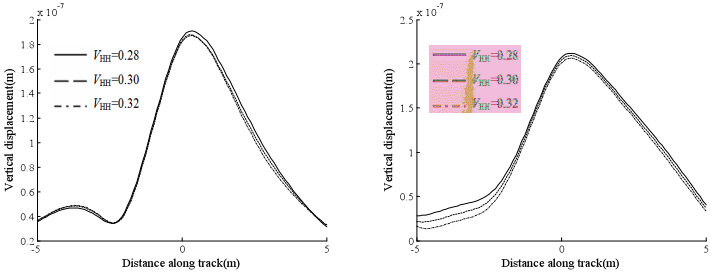

(a) surface permeable (b) surface impermeable

FIG. 3 Effect of passion ratio v_{HH} of soft soil on surface vibration

The curves of pore pressure are shown in Figure.4 and Fig.5 for different values of Horizontal Young's Modulus E_H and Poisson ratio v_{HH}. As can be seen from Fig.4 and Fig.5, the pore pressure varies significantly with the E_H ,it decreases with the increase of E_H. The influence of Possion ratio v_{HH} on pore pressure is negligible.

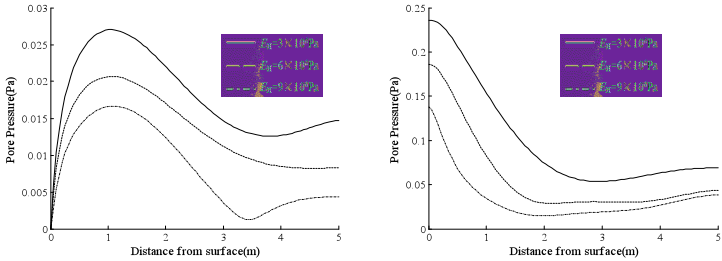

(a) surface permeable (b) surface impermeable

FIG. 4 Effect of transverse Young's modulus of soft soil on pore pressure

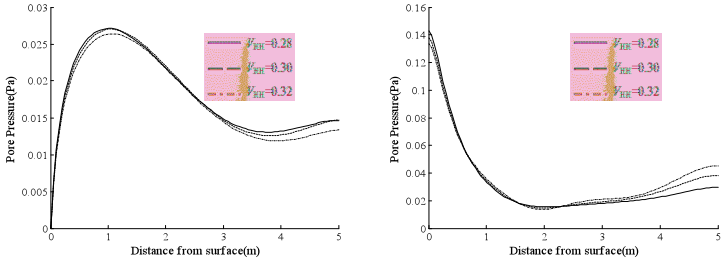

(a) surface permeable (b) surface impermeable

FIG.5 Effect of passion ratio υ_{HH} of soft soil on pore pressure

CONCLUSIONS

The IFFT method has been used in the analysis of the dynamic response of a transversely isotropic saturated soil subjected to a moving load with a constant speed. Numerical results show that soil anisotropy has great influence on the behavior of soils. The influence of the horizontal Young's modulus E_H on the vertical displacement and pore pressure is remarkable. The influence of Possion ratio ν_{HH} on the vertical displacement and pore pressure is negligible.

ACKNOWLEDGMENTS

The Project Supported t Supported by Ningbo city Natural Science Foundation of China (2007A610062) and Scientific Research Fund of Zhejiang Provincial Education Department (20070961).

REFERENCES

Alabi B. (1992). "A Parametric Study on Some Aspects of Ground-borne Vibrations due to Rail Traffic.". *J Sound Vibr*, Vol,153 (1): 77-87.

Lu,J.F, Jeng,D.S. (2007). "A half-space saturated poro-elastic medium subjected to a moving point load." *International Journal of Solids and Structures* ,Vol, 44 (2):573-586.

Sheng X., Jones D.V., Petyt M. (1999). "Ground vibration generated by a load moving along a railway track.". *Journal of Sound and Vibration*, Vol,288(1):129-156.

Biot M.A.(1956). "Theory of propagation of elastic waves in a fluid-saturated porous solid. I-Low-frequency range." *The Journal of the Acoustical Society of America* Vol,28(2):168-178.

Jones D.V., *et al*. (1998). "Ground vibration in the vicinity of a moving harmonic rectangular load on a half-space." *European Journal of Mechanics. A/Solids* Vol,17:153-166

Dynamic Analysis for Foundation of Vibrating Equipments Considering Soil-Structure Interaction

Y. C. Han, F. CSCE

Principal Specialist, Fluor, 1075 W. Georgia Street, Vancouver, BC, Canada V6E 4M7, yingcai.han@fluor.com

ABSTRACT: The dynamic analysis and design for a large pump foundation are investigated with different design options. The nonlinearity of soil is considered approximately using the boundary zone model with non-reflective interface. The impedances (stiffness and damping) and the dynamic response of foundation are generated from a computer program DYNAN. The amplitudes calculated might be larger than the allowable vibration limit, if the design of foundation is not reasonable. Three options of the foundation design are considered: shallow block foundation, deep block foundation, and cast-in-place concrete piled foundation. The stiffness and damping of foundation, dynamic response, and construction cost are compared with the different types of foundation. The ground water is very shallow in the construction site, and the level of water even closes to the surface. The effects of groundwater on dynamic response of foundation are discussed.

INTRODUCTION

With the recent progress, the importance of soil-structure interaction, or soil-pile-structure interaction, has been recognized widely. Now the real problem is how to account for the interaction in practice and how to account for the nonlinear properties of soil. A comprehensive method should be not only advanced in theory but also verified in tests and applications.

In this study, the dynamic behavior is investigated for a large pump foundation. The amplitudes calculated might be larger than the allowable vibration limit, if the design of foundation is not reasonable. To reduce the damage of vibration, three options of the foundation design are considered: shallow block foundation, deep block foundation, and cast-in-place concrete piled foundation.

The groundwater is very shallow in the construction site, and the level of water even closes to the surface. The effects of groundwater on dynamic response of foundation are discussed.

SOIL – STRUCTURE INTERACTION CONSIDERING NON-LINEAR PROPERTIES OF SOIL

For the dynamic soil - pile interaction, many efforts have been spent on the numerical analysis using the finite element method (FEM) or boundary element method. However, it is too complex, especially for group piles in nonlinear soil. A rigorous approach for the nonlinearity of a soil-foundation system is extremely difficult and time consuming.

Both theoretical and experimental studies have shown that the dynamic response of piles

is very sensitive to the properties of the soil in the vicinity of the pile shaft (Han and Novak, 1988). The validation of impedance function method is confirmed by dynamic tests on piles in the field (Han 1997).

Novak and Sheta (1980) proposed including a cylindrical annulus of softer soil (an inner weakened zone or so called boundary zone) around the pile in a plane strain analysis. One of the simplifications involved in the original boundary zone concept was that the mass of the inner zone was neglected to avoid the wave reflections from the interface between the inner boundary zone and the outer zone. To overcome this problem, Velestsos and Dotson (1988) proposed a scheme that can account for the mass of the boundary zone. Some of the effects of the boundary zone mass were investigated by Novak and Han (1990) who found that a homogeneous boundary zone with a non-zero mass yields undulation impedance due to wave reflections from the fictitious interface between the two media.

The ideal model for the boundary zone should have properties smoothly approaching those of the outer zone to alleviate wave reflections from the interface. Consequently, Han and Sabin (1995) proposed such a model for the boundary zone with a non-reflective interface. DYNAN program has been developed based on such a model (2003), details see www.ensoftinc.com.

The group effect of piles is accounted for using the method of interaction factors. The vertical static interaction factors are based on Poulos and Davies (1980). The horizontal static interaction factors are due to El-Sharnouby and Novak (1986). The dynamic interaction factors are derived from the static interaction factors multiplied by a frequency variation, and the frequency variation of interaction factors is based on the charts of Kaynia and Kausel (1982).

It should be explained that the foundations (or caps on piles) are assumed to be rigid. In most cases, the superstructures are flexible rather than rigid. By means of a substructure method, the dynamic response of the superstructure is calculated using a finite element program, such as SAP2000, and the stiffness and damping of the foundation can be generated from the computer program. With this procedure, the seismic or dynamic response of the structure can be calculated in time domain or frequency domain (see Han, 2001). This method has already been applied in practice (see Han et al, 1999).

DYNAMIC RESPONSE OF PUMP FOUNDATION

The soil properties in the location of vibrating equipments are described based on the geotechnical report. In the top 7 m, the type of soil is light brown medium sand with SPT N value of 26 to 33. From depth of 7 to 12 m, it is very dense sand. From depth of 12 to 16.5 m, it is hard clay. The ground water is very shallow, about 2 m, even closes to the surface in some season. The effects of liquefaction were discussed by Han and Wang (2008).

The weight of pump is 290 kN and motor is 180 kN, with operating speed of 507 rpm. The layout of foundation for the vibrating equipments is shown in Fig.1.

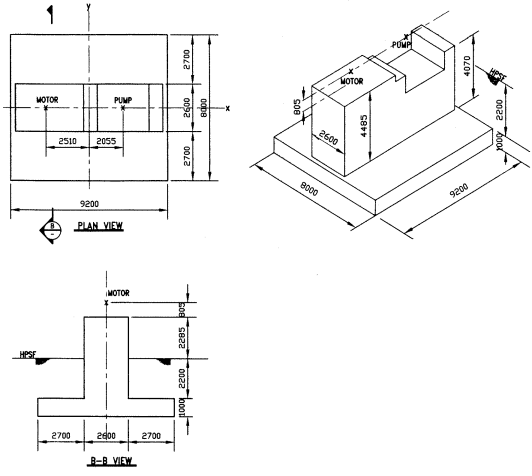

Fig. 1 Layout of pump foundation

In this case, the unbalanced force is 2.3 KN for pump and 1.5 KN for motor, and the shallow foundation was considered in the original design. The base slab is 9.5 m x 5.0 m with thickness of 0.6 m. The base slab was embedded into soil 0.9 m.

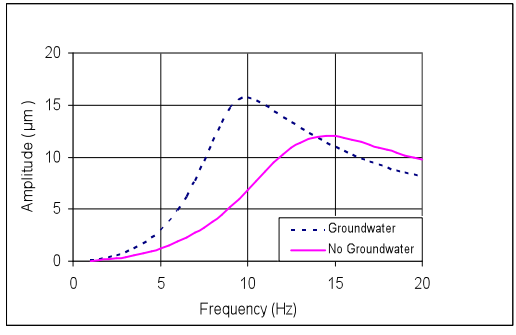

Fig. 2 Effect of groundwater on dynamic response of pump foundation

However, the level of groundwater is shallow and the buoyant forces of soil have to be considered under the foundation. The buoyant density of soil should be used rather than the natural density in this case. The reaction mass of foundation under the buoyant forces will different from that case without the groundwater. The effects of groundwater on dynamic response of foundation is calculated and shown in Fig. 2. It should be explained that there are six degrees of freedom for the foundation vibration, three translations and three rotations. The horizontal vibration is discussed only here.

From Fig. 2, it can be seen that the dynamic response of foundation with ground water (dash line) is higher than those without the groundwater (real line) in the lower

frequency domain. The amplitude of horizontal vibration is 13.3 μm calculated with groundwater and 4.5 μm calculated without the groundwater at the operating speed of 507 rpm (8.45 Hz).

The allowable vibration limit is peak-to-peak value of 0.9 mil (23 μm) for centrifugal machine operating at 507 rpm. That is, the allowable vibration limit is 11.5 μm. The amplitude of horizontal vibration calculated in the case with groundwater is larger than the vibration limit. The machine operation will be not in order with the groundwater raised up although the foundation is workable in the case without the groundwater.

DIFFERENT DESIGN OPTIONS FOR PUMP FOUNDATION

To reduce the vibration, a design option of deep block foundation is considered. The base slab is changed as 9.2 m x 8.0 m with thickness of 1.0 m, and the embedment is increased to 2.2 m as shown in Fig. 1. Since the soil blocks above the base slab can service as reaction mass in the foundation vibration, the total reaction mass is increased sufficiently. The amplitude calculated is 4.4 μm at the operating speed, and meets the vibration limit. This option is workable.

For comparison, the option of pile foundation is also considered. 12 cast-in-place concrete piles with diameter of 3 feet (0.914 m) are used, with pile length of 15 m. The spacing of piles is 3.0 m.

In the dynamic analysis, the shear wave velocity of soil is 200 m/s within the depth of 10 m, and 350 m/s below the depth of 10 m. Both cases of with groundwater and without groundwater are considered. The amplitude of horizontal vibration calculated is 5.2 μm at the operating speed.

The dynamic response of deep block foundation and pile foundation are shown in Fig. 3. The peak value of amplitude is 15.7 μm and the frequency corresponding to the peak value is 10 Hz for the shallow block foundation as shown in Fig. 2. The peak value of amplitude is 5.6 μm and the frequency corresponding to the peak value is 6.5 Hz for the deep block foundation as shown in Fig.3. With the soil above base slab added to the total reaction mass, the peak value of amplitude is reduced and the resonant frequency becomes lower. With the option of deep block foundation, the construction cost is lower than that for pile foundation and vibration damage is reduced. The advantage of embedment is mobilized in the design of pump foundation. With the advanced design of foundation, the construction cost is saved and dynamic response is reduced.

The dynamic response is calculated using the computer program for the option of pile foundation, and the construction cost is estimated. The embedment of pile cap is 0.9 m and the effect of embedment is accounted for. The shear modulus of side soil is reduced since the confining pressure becomes low closed to the surface. Two layers of side soil are included, and the thickness of each layer is 0.3 m. The shear wave velocities of 100 m/s and 150 m/s are used in the two layers.

The peak value of amplitude is 5.6 μm and the frequency corresponding to the peak value is 10 Hz as shown in Fig. 3. By comparison with the option of shallow block, the dynamic response is reduced sufficiently, and meets the vibration limit.

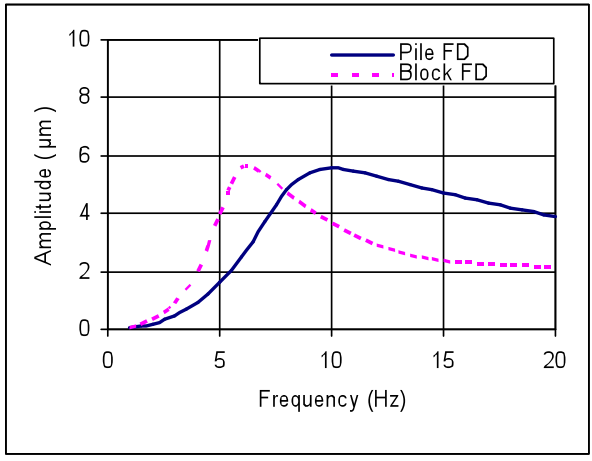

Fig. 3 Dynamic response (horizontal vibration) for deep block foundation and pile foundation

In this study, three options of foundation design are described, shallow block, deep block and pile foundation. The parameters are shown in Table 1, including mass, stiffness and damping of foundation. It can be seen that the mass of deep block is three times of that for shallow block. With the mass increased, the peak value of amplitude is reduced and the frequency corresponding to the peak value also reduced. Due to the effect of embedment, the rocking stiffness and damping in three directions are increased significantly. The mass of soil block above base slab is accounted for as the reaction mass, so the construction cost is saved.

Table 1. Parameters of Foundation at 507 rpm (f = 8.45 Hz)

Option of Foundation	Mass	Stiffness			Damping		
	(Mg)	K_x (kN/m)	K_z (kN/m)	K_φ (kN.m/ra)	C_x (kN/m/s)	C_z (kN/m/s)	C_φ (kN.m/rd/s)
Shallow	220	0.85×10^6	0.97×10^6	1.70×10^7	1.19×10^4	1.67×10^4	1.07×10^5
Deep Block	671	1.04×10^6	1.09×10^6	2.58×10^7	2.38×10^4	2.84×10^4	2.57×10^5
Pile	371	1.11×10^6	1.59×10^6	7.94×10^7	2.46×10^4	6.48×10^4	6.03×10^5

Where, K_x, K_z, and K_φ are stiffness in the horizontal, vertical and rocking directions, and C_x, C_z, and C_φ are damping constants in the respective directions.

As for the pile foundation, the rocking stiffness is increased almost five times by comparison with the shallow block foundation. The damping is also increased significantly. The horizontal and vertical stiffness are increased, but not too much. With the option of pile foundation, the dynamic response is reduced sufficiently.

CONCLUSIONS

The following conclusions are suggested based on three options of foundation design.

The vibration amplitude of shallow block foundation is higher than the allowable vibration limit as the groundwater raise up.

The vibration damage can be reduced significantly using the deep block foundation. With the effect of embedment, the rocking stiffness and damping are increased greatly. The soil block above the base slab can service as the reaction mass, so the vibration amplitude is reduced and the construction cost is saved.

The vibration amplitudes can be reduced by the pile foundation, since the rocking stiffness and damping are increased significantly. However, the construction cost is expensive using the pile foundation in this project.

REFERENCES

DYNAN 2.0 for Windows, Dynamic analysis of shallow and deep foundations, Ensoft. 2003. www.ensoftinc.com.

El-Sharnouby, H.and Novak. (1986). "Flexibility Coefficients and Interaction Factors For Pile Group Analysis", Canadian Geotechnical J., 23(4), P441- 450.

Han, Y. C. and Wang, S.T. (2008). "Non-linear analysis of soil-pile-structure interaction under seismic loads", 14th World Conference on Earthquake Engineering, Beijing, China.

Han, Y.C., Wang, S., Chan, P., and Sprinkhuysen, A. (1999). "Design of an Elevated Compressor Table Top Structure Considering Soil-Pile-Structure Interaction". Annual Conf. CSCE, Regina, Saskatchwan, P291-300.

Han, Y.C. (1997). "Dynamic Vertical Response of Piles in Nonlinear Soil". J. of Geotech. And Geoenvir. Engineering, ASCE, 123(8), 710-716.

Han, Y.C. and Sabin, G. (1995). "Impedances for Radially Inhomogeneous Soil Media with Non-reflective Boundary". J. of Eng. Mechanics, ASCE, 121(9), 939-947.

Han, Y.C. and Novak, M. (1988). "Dynamic Behavior of Single Piles under Strong Harmonic Excitation". Canadian Geotechnical Journal, 25(3), 523-534.

Han, Y.C. (2001). "Dynamic Soil-Pile-Structure Interaction". *4th Int. Conf. On Recent Advances In Geot. Earthq. Eng. & Soil Dynamics,* San Diego, CA, Paper 6.04.

Kaynia, A.M. and Kausel, E. (1982). "Dynamic Behavior of Pile Groups". 2nd Int. Conf. On Num. Methods in Offshore Piling, Austin, TX, P509-532.

Novak, M. and Sheta, M. (1980). "Approximate Approach to Contact Problems of Piles". ASCE National Convention, Florida, P53-79.

Novak, M. and Han, Y.C. (1990). "Impedances of Soil Layer with Boundary Zone", J. of Geotechnical Engineering, ASCE, 116(6), 1008-1014.

Poulos, H.G. and Davies, E.H. (1980). "Pile Foundations Analysis and Design". John Wiley and Sons, P. 397.

Veletsos, A.S. and Dotson, K.W. (1988). "Vertical and Torsional Vibration of Foundation in Inhomogeneous Media". J. Geotech. Eng., ASCE, 114(9), 1002-1021.

Cumulative Effects of Soil Nailing under Cyclic Load Considering Bottom Boundary Conditions of Facing

ZHU Fangcai[1] LIAO Xingui[2] LI Jianhua[1] YANG Yue[1]

(1 Institute of Geotechnical Engineering, Hunan University of Technology, Zhuzhou 412008, China; 2 Second Construction Company, Zhongtian Construction Group CO. LTD, Hangzhou 310008, China)

ABSTRACT: Based on laboratory study, cumulative effect of soil nailing under cyclic load is studied. The cyclic load is produced by a multi-channel load system, from experimental results, displacement of facing increases considerably after a certain load number, then keep almost constant, which indicates attenuation of accumulation effect. Thereafter, in order to compare with laboratory results, through ADINA system, based on Mohr-Coulomb criteria, a plain strain finite element model(FEM) is built. From both experimental and calculation results, considering different stiffness and boundary constraints at the bottom of facing, displament of facing is smaller with concrete facing(greater stiffness), which is than with wood facing(smaller stiffness), similarly, displacement of facing is smaller with fixed bottom than with free one, moreover, load frequency has pronounced influence on displacement of facing.

KEY WORDS: soil nailing; cyclic load; displacement of facing; load frequency

Compared with behaviour of slopes under static load, characteristics of slope deformation is different under dynamic load. Safety factor can be approximately computed through pseudo-static approach, whereas, deformation is vital to safety of slopes, especially considering dynamic behaviour, cyclic load, as a typical kind of dynamic load, cumulative effect can not be neglected. Dynamic bearing capacity of soil nailing is studied through prototype experiments(Zeng, 2003), cumulation effect of strain of soil nails is analyzed with explosive loading(YU, 2006). It is often stated that anchored and geosynthetic slopes are of large seismic-bearing capacity (White, 1994; Jahanandish, 2005; CAI, 1995; Koseki, 2006), however, due to cumulative deformation effect, these slopes may failed under cyclic load(Aurelian, 2009; Mark, 2000). Through elastic analysis, constraint condition of facing exerts great influence on bending moment and its inner force(WANG, 2008). There are few experiments of cumulative deformation of soil nailing under cyclic load, the author(ZHU, 2009) have studied cumulative effect of soil nailing with wood facing, in this paper, by comparing cumulative effect of deformation, an experiment with reinforced concrete facing will be studied.

1 Physical parameters of the model

Clay from a residential terrain of zhuzhou city in Hunan of China is used as filling material, of which typical parameters are shown in table 1, clay is first air-dried, then grinded and screened with a 5mm sieve

Table 1. Physical parameters of fill material for soil nailing

Liquid limit (%)	Plastic limit (%)	Specific gravity	Optimum water content (%)	Maximum dry density (g/cm^3)
32.4	15.2	2.69	20.8	1.754

2 Introduction to the experiments

Traffic load is very complex including horizontal and vertical ones, for convenience and representation, it is simplified as regular form, such as sine wave, rectangular wave, pulse wave, in this study, it is simplified as sine wave. A multi-channel automatic load system with 2 static actuators and 2 dynamic actuators, is used in the experiments. In this study, the size of the model box is length×width×height = 1200mm×800mm×1400mm, the frame is set up with steel plates and angle irons, the model box is shown in figure 1. For elimination of side friction, side wall is firstly smeared with thin motoroil, then a layer of plastic film is spread above.

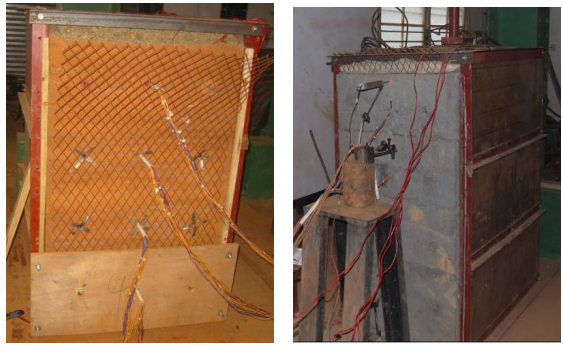

FIG.1. Arrangement of soil nailing

Clay is filled in the box layer by layer with 20mm height, soil nails and earthpressure cells are prepositioned, thereafter wood plates are removed, then a piece of wiremesh is hung from the top, M20 cementmortar with 30mm thick is casted as concrete facing with 28 days curing, at the top surface, pebbly sand with 70mm thickness is laid, and a ribbed steel plate with size of 1000mm×600mm×15mm is laid above. Layout of soil nails and centimeters is shown in figure 2.

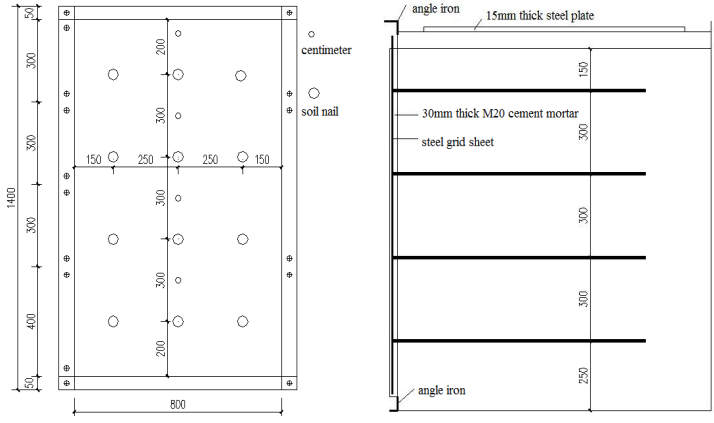

FIG.2. Layout of soil nails and centimeters (unit: mm)

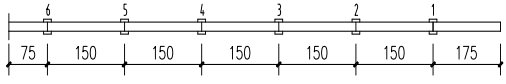

FIG.3. Layout of strain gauges (unit: mm)

Soil nails are ordinary stainless steel hollow tubes, of which elastic modulus is 210Gpa, diameter is 19mm, wall thickness is 0.6mm, length is 950mm with strain gauges pasted above, which are shown in figure 3. For protection of strain gauges, on which a layer of epoxy resin is covered, in order to simulation of roughness, a thin layer of standard sand is laid above.

The load is exerted with sine wave form, of which frequency is 2Hz produced by a multi channel loading system. Cumulative effect with three ranges including 10-30kN ，30-50kN and 50-70kN of cyclic load, are studied.

3 Experimental results and analysis

Final load number is 10000, related parameters are shown in table 2.

Table 2. Parameters of two phsical models

	Facing material	**thickness**	**Moudulus of facing**	**Fixed mode of bottom**	**Layout of soil nails**
Physical model of this study	M20 cement mortar	30mm	20GPa	Free horizontal boundary	4 rows with 3 colomns
Physical model(ZHU, 2009)	Wood facing	12mm	9.77GPa	Hinged with model box	3 rows with 1 colomn

3.1 Cumulative effect of displacement of facing

The displacement of facing is shown in figure 4, along with load number, initially displacement increases sharply, while arriving at a certain number about 100, increases slowly and keep almost constant.

a) 10-30kN b) 30-50kN

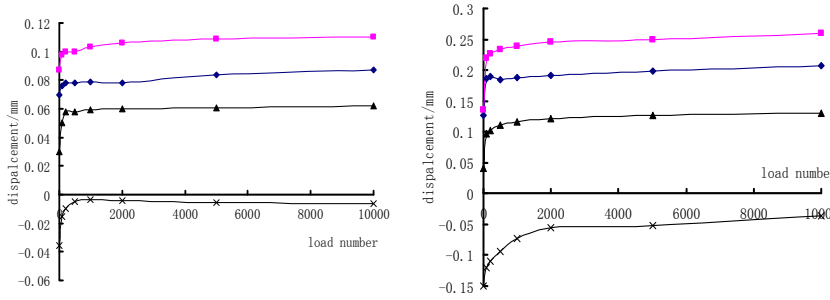

FIG.4. Cumulative effect of facing displacement

3.2 Displacement form of facing

Displacement of facing with different constraints and stiffness is shown in figure 5. From the figure, both position of maximum value and final displacement of facing is prone to influenced by its stiffness, the position of maximal displacement with wood facing is approximately at 2/3 height, whereas almost at middle height with concrete facing.

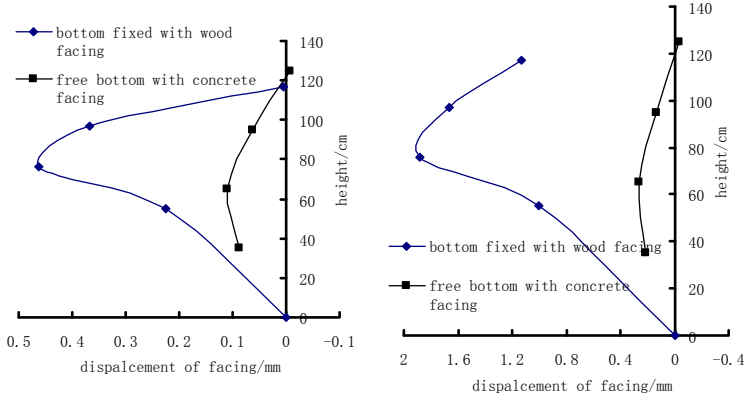

a) 10-30kN b) 30-50kN

FIG.5. Displacement of facing with different materials

4 Finite element analysis

Deformation analysis methods of anchored slopes can be divided into equivalent one (Jahanandish, 2005) and decoupling one (ZHANG, 2007). In the former, strengthening structure and soils are totally considered as an anisotropical compound material, whereas, the latter one is commonly adopted, in which action of soil nails is seperately considered through finite element method. ADINA as a commercial FEM software is adopted in the analysis, where soil nails and filling clay are considered linear elastic and elastic-plastic.

4.1 Calculation results

From calculation results, displacement form of facing is determined by facing stiffness, with free bottom, displacement value and form along facing height is similar as experiments' results as shown in figure 5 and 6.

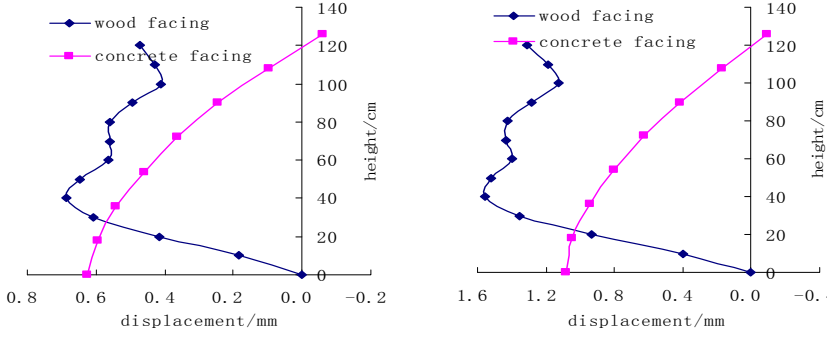

a) 10-30kN b) 30-50kN

FIG.6. Calculated results with wood and concrete panel under different range of cyclic load

The displacement of facing under cyclic load and static load are compared in figure 7. Cyclic magnitude load is 10kN, of which frequency is 2Hz and cyclic number is 10000. Displacement form of facing under cyclic load is similar to that under static load. While mean value of cyclic load is less then 20kN, displacement of facing is almost equal to that under static load, or it is larger than that under static load, it seems that along with increase of load, increase magnitude of displacement of facing becomes large, as shown in figure 7.

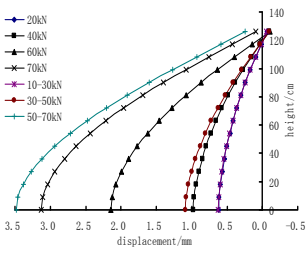

FIG.7. Facing displacement under cyclic load and static load

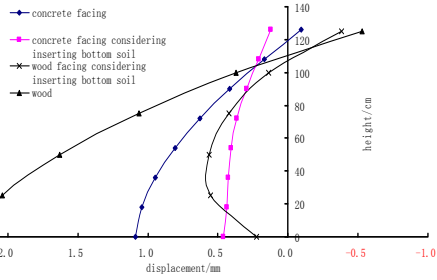

FIG.8. Facing displacement with different bottom constraint conditions

From figure 7, if with free bottom boundary of facing, it seems that maximal displacement of facing is close to that at the bottom. In order to study influence of constraint condition at the bottom of facing on displacement of facing, a calculation model, in which soil layer is deepen 1.5m downwards and 1.5m excavation towards with wood and concrete facing respectively, the calculation results are shown in figure 8, there is pronounced decrease while with fixed boundary at the bottom of facing, moreover, maximal displacement is almost at the middle of height.

4.2 Displacement of facing under cyclic load of different load frequencies

In order to study influence of load frequencies on displacement of facing, displacement of facing with 5 kinds of frequencies including 0Hz(static load), 2Hz, 4Hz, 8Hz, 16Hz, is researched, the load range is 30-50kN and cyclic number is 10000, which is shown in figure 9 and 10. Along with increase of load frequencies, displacement of facing demonstrates approximate linear increase.

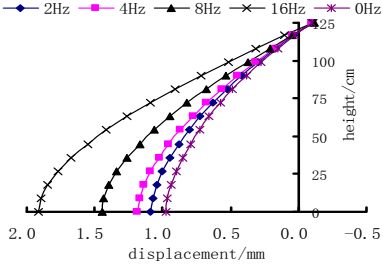

FIG.9 Displacement of facing under displacement of different load frequencies

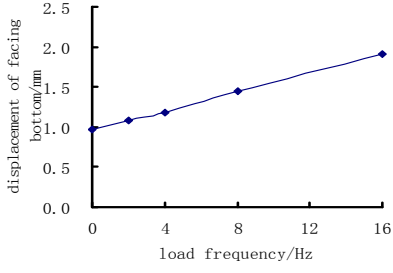

FIG.10 Relationship between bottom of facing and load frequency

5 CONCLUSIONS

The cumulative displacement of facing under the influence of dynamic loading are studied using model test and Finite Element Analyses. The effects of factors, including the magnitude and frequency of loading, the constraint conditions at the bottom boundary of facing, are analyzed. The following conclusions are drawn based on this study:

1) There are pronounced effect of dynamic loading on the cumulative lateral displacement at the initial loading cycles; the effects of loading cycles decreases with the increasing load numbers; the critical loading cycle is about 100.

2) The boundary conditions at the bottom of facing have great effects on the shape and magnitude of displacement of facing; the maximum displacement appear at bottom for the free facing condition; it appears in the middle when the bottom is constrained.

3) The FEM results indicate that the displacement of facing increases with the increase of load frequency for the range of load frequency investigated.

ACKNOWLEDGEMENTS

The authors would like to thank the fund of Hunan Natural Science Foundation of China(05JJ40120, 06JJ3002), Science fund project of China National Packaging Corporation(04ZBKJB008) and Zhuzhou Construction Bureau of Hunan Province of China(2005).

REFERENCES

ZENG Xianming, DU Yunhe, LI Shimin(2003). "Testing study of prototype and model comparison on resisting dynamical load with soil nail supporting." *Chinese Journal of Rock Mechanics and Engineering*，Vol. 22(11): 1 892－1 897.(in Chinese)

YU Xiaojin, YU Xuewen, ZHANG Yu(2006). "Analysis of the Effect of Cumulation of Transient Strain on Soil Nail in Several Cases." *Journal of East China Jiaotong University*, Vol. 23(4): 1-4. (in Chinese)

White D M, Holtz R D(1997). "Performance of geosynthetic-reinforced slopes and walls during the Northridge, California earthquake of Jannuary 17, 1994." *Earth reinforcement*(Ochiai, Yasufuku and Omine(eds), Balkema, Rotterdam, 965-972

Jahanandish M, Keshavarz A(2005). "Seismic bearing capacity of foundations on reinforced soil slopes." *Geotextiles and Geomembranes*, Vol. 23:1-25.

CAI Zhenqi, Bathurst R J(1995). "Seismic response analysis of geosynthetic reinforced soil segmental retaining walls by finite element method." *Computers and Geotechnics*, Vol. 17: 523-546

Koseki J, Bathurst R J, Güler E(2006). "Seismic stability of reinforced soil walls." *8th international conference of geosynthetics,*Yokohama, Japan, 18-22, September, 1-28

Aurelian C T, Toshitaka K, Roy S(2009). "Earthquake-induced displacements of gravity retaining walls and anchor-reinforced slopes." *Soil Dynamics and Earthquake Engineering*, Vol.29: 428-437

Mark R T, Mladen V(2000). "Dynamic Failure Mechanism of Soil-Nailed Excavation

Models in Centrifuge." *Journal of Geotechnical and Geoenvironmental Engineering*, Vol. 126(3): 227-235

WANG Lifeng, ZHU Xiangrong(2008). "Analysis of displacement and inner force in soil-nailing walls." *Rock and Soil Mechanics*, Vol. 29(2): 437-441. (in Chinese)

ZHU Fangcai, LIAO Xingui, LI Jianhua(2009). "Laboratory model test of soil nailed wall under cyclic load in unsaturated compacted soils." *Chinese Journal of Rock Mechanics and Engineering*, Vol. 28(suppl.1): 2994-3000. (in Chinese)

ZHANG Zhonglin(2007). "The FEM analysis of composite soil nailed wall in construction process and earthquake action." LanZhou: LanZhou University of Technology, 2007. (in Chinese)

A Scale Model Test on Dynamic Soil-tunnel Interactions

Nina Liu[1], Yang Liu[2], Dongdong Han[3], Yuming Men[4], Jianbing Peng[5]

[1]PhD candidate, instructor Department of Geological Engineering, Chang'an University, 126 Yangta Road, Xi'an China, 710054, dcdgx16@chd.edu.cn

[2]Master degree student, Department of Geological Engineering, Chang'an University, 126 Yangta Road, Xi'an China, 710054, yangliu1106@hotmail.com

[3]Master degree students, Department of Geological Engineering, Chang'an University, 126 Yangta Road, Xi'an China, 710054, yatongdongdong@163.com

[4]Director, Department of Geological Engineering, Chang'an University, 126 Yangta Road, Xi'an China, 710054, yumingmen@163.com

[5]Director, Department of Geological Engineering, Chang'an University, 126 Yangta Road, Xi'an China, 710054, Jianbinpen@chd.edu.cn

ABSTRACT: Soil-structure interactions are important for the safety of the underground structures under earthquake loads. In this paper, model tests were conducted on 1/60 scaled model of the prototype Xi'an metro tunnel. The seismic response data including the acceleration, the displacement and the dynamic soil pressure between the tunnel and soil were measured by testing the scaled model on a shaking table. From the test result, it is concluded that 1) the effects of tunnel and soil interactions are important for the bulk dynamic responses; 2) the soil pressure and the acceleration changed with the seismic inputs. The soil pressure at the top of the tunnel increased while the pressure at the bottom decreased; 3) the acceleration of the tunnel is greater than the adjacent soils.

INTRODUCTION

To utilize the underground space in cities, more and more research has been focused on the soil and underground structure interactions (Zhao, 1994). The field survey conducted in Xi'an for the past 40 years revealed 14 ground fissures crossing the current metro tunnel site (Shi et al, 2009). Xi'an is known for its loess deposit and has a history of strong earthquakes. Therefore, designing the infrastructure to overcome the challenging from the ground fissures, earthquake activities and loess deposit is important for the safety of the Metro system (Huang et al., 2009).

Scale model experiments were conducted to study the soil-tunnel interactions. The model was 1/60 of the prototype. Soils used in the model test were taken from the construction site. Ground motions from the El Centro earthquake, the Wenchuan earthquake, synthetic Xi'an earthquakes and a sinusoidal wave were individually input to the shaking table during the experiments.

EXPERIMENT SETUP

The size of the model box was 1.5m×1.0m×0.6m, which was constraint by the capacity of the shaking table. The photo of the box is shown in Fig. 1(a). In order to reduce the rigid boundary effect by the box, plastic materials, pieces of woods and nails were attached to the inside of the container. This is shown in Fig. 1(b), indicating different materials in parallel to each other. The seismic excitation by the shaking table was in the direction of walls B and D. Therefore, plastic, pieces of wood and nails were installed on Walls B and D to reduce the friction between the soil and box. There were pieces of woods and nails on Walls A and C to make sure the soil and the box are moving together. (Hashashm et al., 1998; Hou, 2005)

(a) (b)

FIG. 1 (a) the model box (b) the materials inside of the box

Following the Bingham principle, the model tunnel was as close as possible to the prototype tunnel; the soil used in the model box was the same as that at the site; and most importantly, the space relationship between soil and tunnel in the model was similar to the actual conditions. The size and weight of the model were designed to the capacity of the shaking table. The size of the model tunnel was 1/60 of the actual tunnel. The material used for the model tunnel was Plexiglass, with an elastic modules $Es = 3.0\times10^3 MPa$, density $\gamma = 1.19\times10^3 kg/m^3$, and poison ratio 0.35. Fig. 2 shows the model tunnel (a) and the compensator ring (d). (Li et al., 2009)

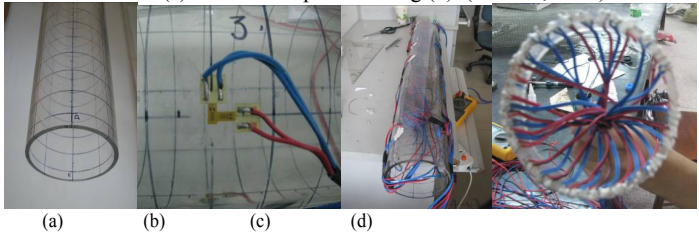

(a) (b) (c) (d)

FIG. 2 (a) the model tunnel (b) the sensor of the strain (c) the location of the strain sensors on the tunnel (d) compensators

The FIG. 3 show the dynamic sensors used in the experiments to measure the acceleration and the soil pressure.

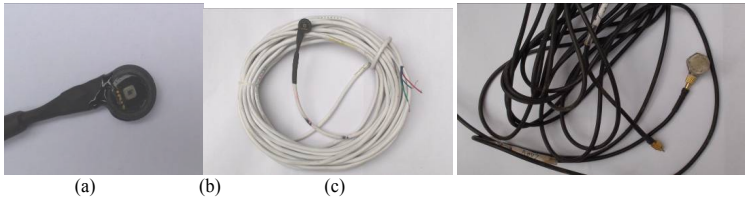

(a) (b) (c)

FIG. 3 (a, b) the soil pressure sensor (c) the acceleration sensor

INSTRUMENTATION

The shaking table was fabricated by the MTS Systems Corporation, Minneapolis, Minnesota USA. The size of the shaking table is 1.5m×1.0m.

The dynamic measuring system for acceleration, soil pressure and displacement is IMC Mess-System GmbH. Three instruments were used to measure the strain: SDY2400, DH5923 and YE6262B Dynamic Measuring System. Figure 4 below shows the pictures of the dynamic measuring system.

(a) (b) (c) (d)

FIG. 4 the Dynamic Measuring System(a) SDY2400 (b) DH5923 (c) YE6262B (d) IMC Mess-System GmbH

TEST PROCEDURES

According to the field survey in Xi'an, the ground fissures run almost perpendicular to the metro tunnel. So in the model box (see Fig. 5 (a)), the tunnel was aligned perpendicular to the fissures and the direction of the shaking table. As shown in Fig. 5 (b), the ground fissure was made of silver sand. Each layer of soil to the south of the ground fissure was compacted just one time whereas each layer to the north was compacted 3 times to match the ground fissure caused by un-uniform settlement displacement in the actual site.

(a) (b) (c)

FIG. 5 (a) the location of fissure (b) the fissure filled with silver sand (c) the model box

THE LOADING PROCESSES

In the test the earthquake ground input to the shaking table included the synthetic

Xi'an earthquakes, El Centro earthquake and Wenchuan earthquake. The synthetic Xi'an earthquakes are for the geological characters of Xi'an. The El Centro earthquake wave was recorded from the Empire Valley, US in 1940 and was used widely in earthquake research. The record was revised to match with the geological characters of the Xi'an metro site. The 2008 Wenchuan earthquake was a major seismic disaster and affected most parts of China. The seismic record of Wenchuan earthquake was used to determine the model responses from the long period earthquake activity. The characteristics of 18 different seismic loading were listed in Table 1.

Table1. The loading process

No.	The dynamic wave	The peak acceleration of the shaking table(m/s^2)
1	synthetic Xi'an earthquake	0.28
2	El Centro earthquake wave	0.3
3	Sine wave	1.0
4	synthetic Xi'an earthquake	0.5
5	El Centro earthquake wave	0.58
6	Sine wave	0.7
7	synthetic Xi'an earthquakes	0.9
8	El Centro earthquake wave	0.8
9	synthetic Xi'an earthquake	1.0
10	Sine wave	1.5
11	El Centro earthquake wave	2.0
12	synthetic Xi'an earthquake	2.0
13	Sine wave	2.0
14	El Centro earthquake wave	2.4
15	synthetic Xi'an earthquake	2.5
16	Sine Wave	2.6
17	synthetic Xi'an earthquake	3.0
18	Wenchuan earthquake wave	3.0

The observations during the loading period are described as follows: after 200 hours the soil in the south part of the box was lower than the soil in the north part. As Fig. 6 (a) shows, along the ground fissure, there was a settlement caused by the movement of the south and north part of the soil.

After the 12th loading process, the settlement of the south part was measured 1.0 mm, and along the surface of the fault, some granules of soil could be observed; After the 13th loading process, the settlement of the south part became 1.5mm, and from the fault there were other fissures going out perpendicular to the south part (Fig. 6 (c)); After the 14th loading process, the settlement of the south part became 2.0mm; After the18th loading process, the soil in the south of the box cracked into several pieces (Fig. 6 (d)).

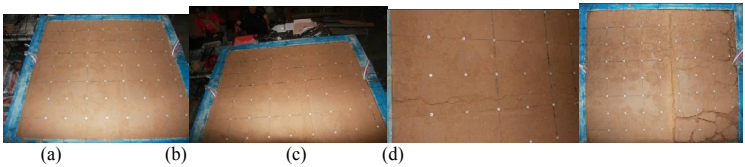

(a) (b) (c) (d)

FIG6 (a) the fault of the fissure (b) the damage after 12th loading process (c) the damage after 13th loading process (d) the damage after 18th loading process

There were four soil pressure sensors placed in the model box, i.e., SP001, SP003, SP004 and SP005 attached outside of the tunnel. There were five acceleration sensors in the model box, two inside the tunnel and three in the soil as shown in FIG. 7. The locations of the soil pressures and acceleration sensors were determined from the finite element simulation of the model box to obtain the complete dynamic response at different points of the tunnel and soil (Shi et al 2009; Liu et al 2009).

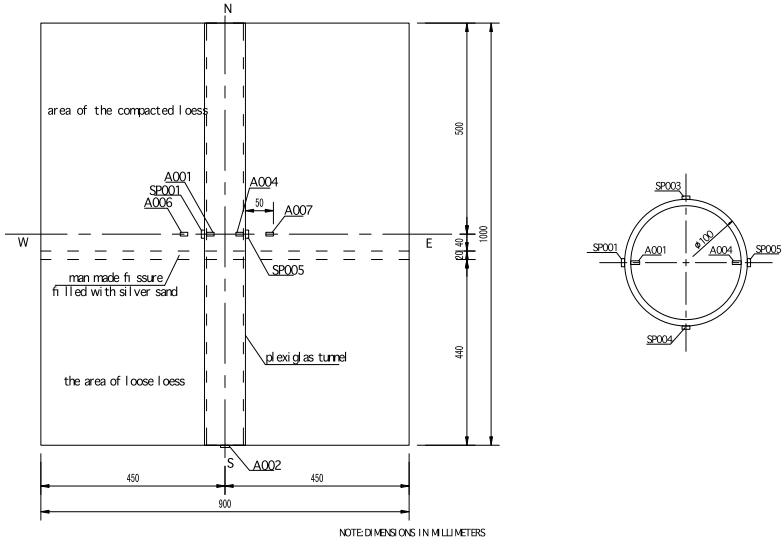

(a) (b)

FIG. 7 (a) the profile of the model box (b) the location of the soil pressure and acceleration sensors

The 9th loading stage is the synthetic Xi'an earthquake wave and the peak acceleration of the shaking table is 1.0m/s^2. The data of the 9th loading process had good quality. Therefore most analyses in this paper were based on data from this loading process.

The FIG. 8 shows the soil pressure taken during the 9th loading process. From the soil pressure time history of SP001, SP003, SP004 and SP005, the four points have the similar acceleration time history and the accelerations outside the tunnel were different from each other. The measurement indicated that the maximum soil pressure was located

at SP001, reaching a value of -81.8Mpa, the negative sign stands for compression. At each location the soil pressure fluctuated from time to time. The soil pressure at SP003 located at the top of tunnel became a little greater after the earthquake wave, increasing from -77Mpa to -76.5Mpa, whereas the soil pressure of SP004 decreased from -78.4Mpa to -78.6Mpa. The increase of soil pressure at SP005 was insignificant.

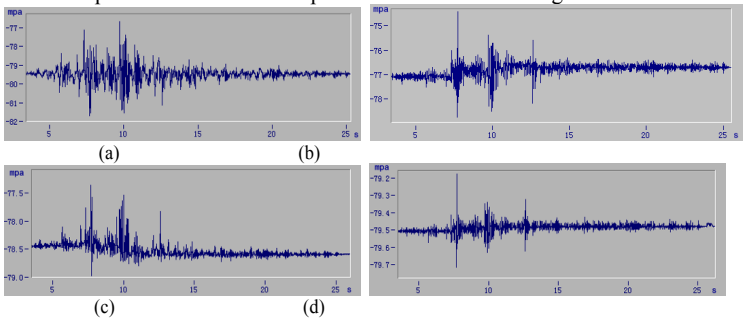

FIG8 (a) the soil pressure of SP001 (b) the soil pressure of SP003 (c) the soil pressure of SP004 (d) the soil pressure of SP005

FIG. 9 below shows the acceleration data taken from the 9th loading process.

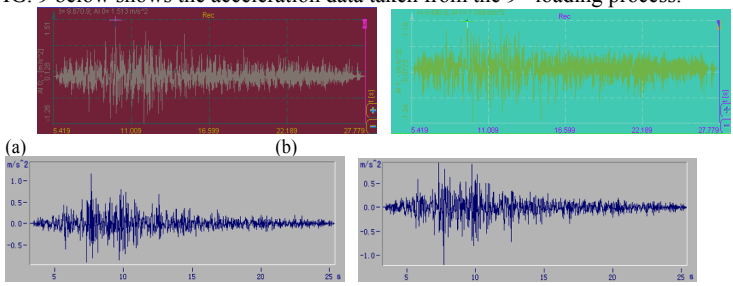

FIG. 9 (a) acceleration of A001 (b) acceleration of A002 (c) acceleration of A006 (d) acceleration of A007

The acceleration sensors A001 and A006 were on the same side of the box, where A001 being inside the tunnel and A006 in the soil. The acceleration time history of A001 was similar to that of A006, but the magnitude of peak accelerations of A006 was smaller than those of A001. It showed that the accelerations of the tunnel were bigger than the accelerations of soil around the tunnel. The acceleration sensor A002 was on the shaking table, the time history of A002 showed the motion of the shaking table. Comparing A002 with the time history of synthetic Xi'an earthquake wave indicated that the ground motion followed the synthetic Xi'an earthquake wave. This validated that the shaking table inputted the earthquake excitation correctly. A006 and A007 were on the opposite sides of the tunnel with equal distance to the tunnel, from the data of FIG.9 (c) and (d), the accelerations of A006 and A007 are similar to each other.

CONCLUSIONS

The results of the experiments indicated:

1. The model in the test matches with the reality of the site. The materials and the conditions in the model closely represent the prototype metro tunnel. The test would indicate that the interaction between the soil and underground structure was as expected.

2. The soil pressure on the tunnel and in the soil changed with time. The time intervals of pressure change were similar to that of the earthquake loading. The soil pressure at the top of the tunnel increased while the pressure at the bottom decreased.

3. The acceleration of the tunnel is greater than the adjacent soils.

ACKNOWLEDGMENTS

Thanks to the National Natural Science Foundation (40772183, 40534021) and the Shaanxi Natural Science Foundation (2005D04), China Geology Survey (1212010641403) and Youth Foundation of Chang'an University (0305-1001).

REFERENCES

Zhao, Y. (1994). Random vibration for seismic analysis of multiply supported nuclear piping. Case Western Reserve University.

Shi Yuling, Men Yuming, Pen Jianbing, Liu Yang et al. (2009). Analysis on Xi an ground-fissure destruction to Chang an Road overpass. The Chinese Journal of Geological Hazard and Control. Vol. 20(2), pp. 65-69.

Huang Qiangbing, Peng Jianbing, Fan Hongwei, Yang Peimin, Men Yuming (2009). Metro tunnel hazards induced by active ground fissures in Xi'an and relevant control measures. Chinese Journal of Geotechnical Engineering. Vol. 31(10), pp. 1525-1532.

Huo, H. (2005). Seismic design and analysis of rectangular underground structures, Purdue University.

Hashashm, Y.M.A., Tseng, W.S. and Krimotat, A. (1998). Seismic Soil-structure Interaction Analysis for Immersed Tube tunnel Retrofit. Geotechnical Earthquake Engineering and Soil Mechanics, Vol. III 2, pp. 1380-1391.ASCE Geotechnical Special Publication No.75.

Li Jie; Yue Qingxia; Chen Jun (2009) Research on shaking-table test and finite element numerical simulation of utility tunnel. Journal of Earthquake Engineering and Engineering Vibration. Vol 29 (4), pp. 41~45.

Shi Yuling; Men Yuming; Peng Jianbing; Huang Qiangbing; Liu Hongjia; Chen Liwei (2008). Numerical simulation of ground-fissure cracking and extending in Xi an. Hydrogeology & Engineering Geolog. Vol. 2008(6), pp. 56-60.

Liu Nina; Men Yuming; Liu Yang (2009). Model Test of Soil and Metro-tunnels Interaction in Earthquake Activities. Journal of Earth Sciences and Environment Vol 31(3), pp. 295-298.

Effect of Soil Flexibility on Dynamic Behavior of Building Frames Resting on Strip Foundation

Narayana, G[1]; Sharada Bai, Dr. H[2] ; Manish, A[3]

[1]Asst. Professor, Dept. of Civil Engineering, S.J.C.Institute of Technology, VTU, Chickaballapur-562 101, Karnataka, India ,narayanag@rediffmail.com Contact No: +91-09980923307
[2]Professor of civil engineering, Dept. of Civil Engineering, U V C E, Bangalore University, Bangalore-560056 sharadaj29@yahoo.com Contact No: +91-09341213638
[3]StructuralEngineer,NaveenConsultant,Bangalroe-560050,Karnataka,Indiamanish.chajed@gmail.com Contact No: +91-09036529063.

ABSTRACT: The effect of soil flexibility is generally ignored in seismic design of buildings. The design is generally carried out based on the results of dynamic analysis considering fixed base condition. Flexibility of soil causes lengthening of lateral natural periods due to overall decrease in lateral stiffness. Such lengthening may considerably alter the seismic response of the building frames. It is therefore, necessary that the dynamic inter relationship between soil and structure to be taken into account in the seismic analysis of structures. In order to evaluate the seismic response of a structure, at a given site, the dynamic properties of the combined soil structure system must be established. Due to the differences in responses of a rigidly supported structure and elastically supported structure, it is essential to study the effect of soil flexibility on structure for safety and economy. The seismic load acts during a very small interval of time. Hence, during the action of such loads, instead of consolidation settlement, the instantaneous settlement is expected to occur. This behavior of soil can be conveniently simulated using a set of elastic springs. This study has been carried out for numerous building frames resting on strip foundations and comparison between the nature of change in lateral natural periods and base shears due to the incorporation of soil flexibility relative to that at fixed base condition has been presented. Such study may help to provide guidance to assist more accurately the seismic vulnerability of the building frames resting on strip foundations and may be useful for seismic design.

Key words: Soil structure interaction, Natural period, Base shear, Strip footing.

INTRODUCTION

It has been a common practice to consider the analysis of structure and foundation separately. Typical load distributions within the building frames is calculated based on the assumption that the base of structure is fixed i.e., assumption made that the foundation transfer the load by direct bearing on solid rocky stratum.There is no doubt about a simplifying assumption and is generally applicable if the superstructure is much more flexible/compliant than the underlying soil stratum upon which the foundation rest. However, when the reverse is true i.e., assuming that the structure is much stiffer than the soil medium, then the response of structure can be significantly influenced by the flexibility of soil.

When structure is subjected to a seismic force during an earthquake. As waves from an earthquake reach a structure, they produce motions in the structure itself. These motions depend on the structure's vibrational characteristics and the building or structural layout. For the structure to react to the motion, it needs to overcome its own inertia, which results in an interaction between the structure and the soil. Such an interdependent behaviour between soil and structure regulating overall response is referred as soil flexibility in the present context. In other words, Soil-structure interaction is the phenomenon that involves the analysis of the relationship between the structure and the soil and how it affects the motion the structure experiences during an earthquake.

Analyzing the structure as a fixed base condition proves to be lower estimation of response quantities as highlighted in few earlier researches**.** Soil flexibility may decrease the overall stiffness of the structural systems and hence may increase in natural period of system. So such increase in lateral natural period may considerably alters the response of building frames under the seismic forces. Hence present study has been carried out for dynamic response of building frames resting over Strip foundation incorporating soil flexibility (equivalent springs) with that of a fixed base under the influence of various parameters.

SCOPE OF THE PRESENT STUDY

Modeling and Analysis method

Buildings are modeled using ETABS Nonlinear 9.1.4.,Superstructure of building frame is idealized as 3 dimensional space frames (Fig.1) with two noded beam elements with slab modeled as membrane element with rigid diaphragm. Soil is modeled as Winkler's model (springs) [Fig.2 & Fig.3] as per which three translational and three rotational springs about three mutually perpendicular directions have been considered to simulate the effect of soil flexibility. Dynamic analyses (Response Spectrum Method) is carried out as per IS 1893-2002 (part 1) for structure modeled with rigid and flexible base.

Description of Building Model

For the present study, Two bay Two bay – one, two and four storied reinforced concrete moment resisting frame buildings are chosen (without considering stiffness of infill). The storey height of base story is 4.5m (Termed Ratio of Base storey to higher stories Hr=1.5 henceforth) and is kept at 3m for all the other stories in the model. In order to introduce certain amount of unsymmetry in the structures considered, the independent spans of the 2bay 2 bay structure is taken as 6m and 3m (henceforth referred as Ratio of higher to lower span Sr=2). No parapets on the roof storey but all-round one brick infill masonry wall (230 mm thick) in the floor stories, is considered in the structure. The building is modeled as bare frame. However masses of the walls are included. To study the effect of soil flexibility, lumped mass spring model is used. The stiffness of the springs is used to represent soil flexibility.

Input Design Data for the Buildings

The material properties considered are: Young's modulus of M25 concrete, E= 25×10^6 kN/m2,Density of Reinforced Concrete= 25 kN/m^3,Density of brick masonry= 20 kN/m^3, Dead load intensities Like Floor finishes = 1.5 kN/m^2,Roof finishes= 1.5 kN/m^2,Live load intensities on Roof = 1.5 kN/m^2 and on Floor = 3.0 kN/m^2,Member properties taken are Thickness of Slab=120mm,Column size =350 mm × 500 mm, Beam size=250 mm × 600 mm, Thickness of wall=230 mm, Earthquake live load on slab as per clause 7.3.1 and 7.3.2 of IS: 1893-2002 (Part 1) is calculated as:Roof (clause 7.3.2)= 0,Floor (clause 7.3.1) =0.25 × 3.0 = 0.75 KN/m^2,Type of use=office, Response spectra = as per 1893(part 1)2002, Importance factor =1,Response factor = 5. The foundation dimensions were designed for gravity load and all its design combinations, using STAAD ETC software package.

Soil Parameters Considered

The type of soil considered is sandy clay **(Bowles, 1988)** classified as soft, medium and stiff soil based on dynamic shear modulus. Properties of soil types considered in this study are Stiff(Type-I),Medium(Type-II)and Soft (Type-III) with Poisson Ratio μ=0.5 for all, Mass Density p=2000 kg/m^3,1700 kg/$m^3$and 1400 kg/m^3, Shear Wave Velocity v=1400 m/s,700 m/s and 150 m/s, Shear Modulus G=3920000 KN/m^2, 833000 KN/m^2 and 31500 KN/m^2, Elastic Modulus E=11760000 KN/m^2, 2499000 KN/m^2 and 94500 KN/m^2 respectively.

MATHEMATICAL MODELING OF BUILDING FRAMES AND FOUNDATIONS.

3 D space frame model

Super structure of the building frame is idealized as 3-dimensional space frame (Fig.1)with two nodded beam elements with 6 degrees of freedom at each joint. Any torsional effects are automatically considered in this model. The ground motions are applied in X, Y or Z directions individually. The slab modeled as membrane element with rigid diaphragm

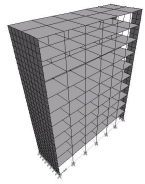

FIG.1. 3D model

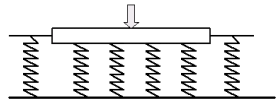

FIG.2. Winkler Model

Modeling of floor diaphragms

Slabs are considered as rigid supports; these are analyzed and designed for gravity loads separately from the frame system. The floor slabs is adequately represented in 3D model of the structure so that their Dead loads and live loads are properly accounted for. Under seismic load, floor slabs play an important role of transmitting inertial loads to the frame and tying together element of the latter into a 3D entity. To perform these roles, slabs are adequately connected with their supporting beams, walls and columns. The slabs are modeled in two ways either as rigid or flexible floor diaphragms. In present study 3D space frame with rigid diaphragms for slabs were considered for modeling in ETABS.

Modeling of soil-foundation.

The flexibility of soil is usually modeled by inserting the discrete spring- dashpot elements between the foundation members and the soil medium. The spring constants are determined from elastic half space solution. Another important effect in soil modelling is soil damping. The damping was calculated for a Strip footing -soil spring system due to large variation in foundation sizes. The calculation showed that for such a strip-soil spring system, the overall soil damping was not more than 5% of the critical damping. Hence 5% of critical damping is considered in each mode of vibration for all the cases in the present study.

Within the ambit of linear elasticity, In the present study Winkler springs model was used**.** In Winkler's model, the soil mass is represented by a series of linear independent springs (Fig.2). Hence the shear resistance of soil is not taken into account and the reaction force acting on foundation at any point is directly proportional to the foundation settlement at that point. The pressure settlement relation is given as

$$P_i = K_s W_i$$

Where,

P_i = pressure at any point I
W_i = settlement at the point i
K_s = coefficient of sub grade reaction of the soil or
Unit sub grade modulus

In addition, stiffness coefficient $K_{ii,}$ which is defined as load per unit deformation, is given by

$$K_{ii} = K_s \, Lb$$

Where 'Lb' is the area over which p_i is acting.

Idealization of soil in present study:

The function of the foundation media is to resist the forces applied to it by the base of the buildings. During earthquake, a rigid base may be subjected to displacement in six degrees of freedom, and the resistance of soil may be expressed by the six corresponding resultant force component. Hence the structural behavior of the elastic half space is represented completely by a set of force displacement relationships defined for these degrees of freedom. To simulate the static behavior of soil-structure system, it is evident that the foundation medium could be modeled by six linear springs acting in rigid base degrees of freedom. Appropriate static spring constants can be evaluated for the elastic half space by the method of continuum mechanics.

To analyze the soil-foundation-structure systems under dynamic loading, the impedance functions associated with a rigid mass less foundation are often used. Translations of foundation in two mutually perpendicular principal horizontal directions and vertical direction as well as rotations of the same about these three directions are considered in the present study.

Calculation of Stiffness' of Elastic Springs for strip foundation

FIG.3. Strip footing and Spring notations

The flexibility of soil is usually modeled by inserting the discrete spring elements between the foundation members and the soil medium(**Winkler springs model).** The spring constants are determined from elastic half space solution. The following expressions as recommended in **ATC-40** can account for the flexible behavior of soil below the Rectangular Strip footing.

$$K_{hx} = \frac{Gb}{(2-\nu)}[6.8(l/b)^{0.65}+2.4][1+(0.33+1.34/(1+(l/b))(e/b)^{0.08}]$$

$$K_{hy} = \frac{Gb[6.8(l/b)^{0.65}+0.8(l/b)+1.6][1+(0.33+1.34/(1+l/b))(e/b)^{0.08}]}{(2-\nu)}$$

$$K_{v} = \frac{Gb\,[3.1(l/b)^{0.75}+1.6][1+(0.25+0.25(b/l))(e/b)^{0.8}]}{(1-\nu)}$$

$$K_{rx} = \frac{Gb^3[3.2\,(l/b)+0.8][1+e/b+1.6(e/b)^2/(0.35+l/b)]}{(1-\nu)}$$

$$K_{ry} = \frac{Gb^3[3.73(l/b)^{2.4}+0.27][1+e/b+1.6(e/b)^2/(0.35+(l/b)^4)]}{(1-\nu)}$$

$$K_t=Gb^3[4.25(l/b)^{2.45}+4.06][1+(1.3+1.32(b/l))(e/b)^{0.9}]$$

G-Shear modulus, **b& l**- width and length of the Strip footing, **ν**-Poisson ratio

The stiffness values so obtained at the Center of Gravity (CG)of the footing are distributed all the springs as series or parallel connections according to the respective directions. Finally, the springs are connected with each other using rigid links

RESULTS AND DISCUSSION

In this paper only Fundamental natural period and Base shear obtained from Interaction analysis are compared with Non-interaction(NI)analysis(Non interaction-Fixed base and Interaction-considering Soil flexibility)

Lateral Natural Period : Storeys wise variation in plot of natural period is as shown in Table-1, Fig. 4 and Fig.5. It is evident from these figures that the natural period is relatively higher as number of storeys is increased. The natural period of 2 bay 2bay structure considered for a particular number of storeys, varies negligibly with the shear modulus.(Fig.5).Also the lower values of lateral natural period was observed for non interaction(NI) case compared to interaction case for all storeys with different types of soils.

Change in Base Shear: Table-2,Fig.6 and Fig.7 shows the resulting base shear for different number of storeys and types of soil. It is seen from the figure that increase in number of storeys increases the base shear in all the types of soil. Also observed is the decrease in base shear values from soil type soft to stiff which is more effective for 4 storeys than one and two storied structures. No change in base shear observed for stiff soil compared to NI case, where as a maximum change of 66.37% is observed for soft soil with 4 storeys structure.

Table 1:- Variations in Fundamental natural period (secs), in Zone V of IS1893:2002

Type of Frame	Fixed (*NI*)	Spring (Interaction-*I*)			% change from fixed base $\frac{NI-I}{NI}x100$		
		stiff	medium	soft	Type I	Type II	Type III
2bay2bay 1 story (Sr=2)	0.191	0.1911	0.1912	0.2035	0.052	0.105	6.54
2 bay 2 bay 2 story (Hr=1.5;Sr=2)	0.5889	0.5916	0.5892	0.6045	0.458	0.051	2.65
2 bay 2 bay 4 story (Hr=1.5;Sr=2)	1.0201	1.0203	1.0205	1.0309	0.019	0.039	1.058

Table 2:- Variation in Base Shear (KN) in Zone V of IS1893:2002

Type of Frame	Fixed (*NI*)	spring (Interaction-*I*)			% change from fixed base $\frac{NI-I}{NI}x100$		
		stiff	medium	soft	Type I	Type II	Type III
2bay2bay 1 story (Sr=2)	114.70	114.70	114.70	114.70	0.000	0.000	0.000
2 bay 2 bay 2 story (Hr=1.5;Sr=2)	286.64	286.64	308.80	308.80	0.000	7.73	7.73
2 bay 2 bay 4 story (Hr=1.5;Sr=2)	332.87	332.87	451.48	553.80	0.000	35.63	66.37

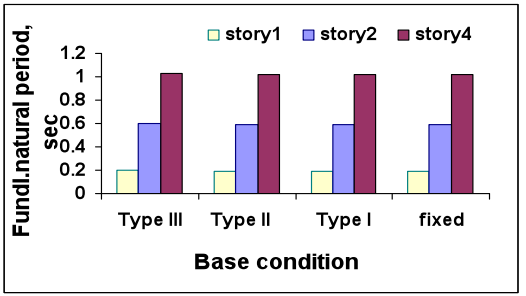

FIG.4. Variation in Fundamental(Fundl.) Natural Period [2x2 (Sr=2,Hr=1.5),Zone 5]

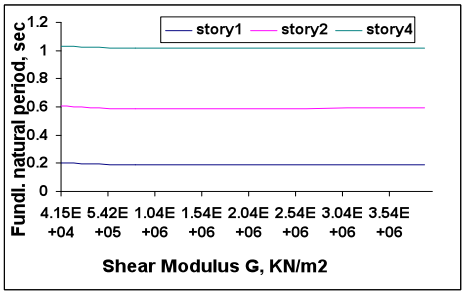

FIG.5. Variation in Fundamental Natural Period [2x2(Sr=2;Hr=1.5,Zone 5]

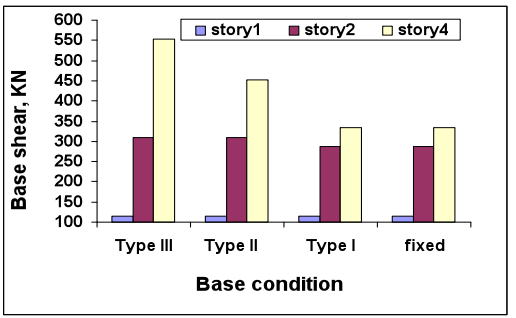

FIG.6. Variation in Base Shear [2x2 (Sr=2,Hr=1.5),Zone 5]

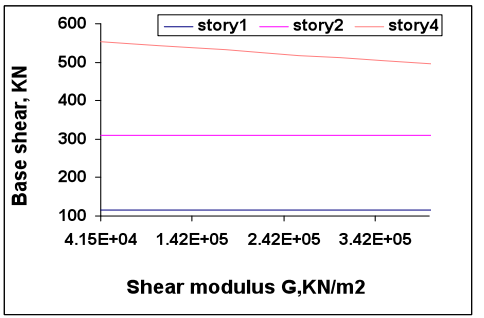

FIG.7. Variation in Base Shear [2x2(Sr=2;Hr=1.5,Zone 5]

CONCLUSIONS

The present study makes an effort to evaluate the effect of soil flexibility on dynamic characteristics of building frames resting on Strip foundation, namely the Lateral natural period and Seismic base shear.

Fundamental Natural period

The fundamental natural period of a structure increases with increase in number of storeys and as stiffness of soil decreases. The fundamental natural period of a particular structure considering interaction is more than that of non-interaction values**,** the maximum percentage increase being 6.54% with respect to NI for Type III(Soft soil) is observed.

Base shear

Base shear values for the Interaction case is found to be effective for Type-II(medium soil) and Type-III (soft soil)Soil type with 2 storeys and above. The Base shear values increases with increase in number of storeys in all the types of soil and a maximum value of 66.37% is observed for Type III soil and 4 storeys structure.

REFERENCES

Gazetas.G, (1991).“Formula and Charts for impedance of surface and embedded foundations” *Journal of Geotechnical Engineering*, American Society of Civil Engineers 117(9) 1363-1381.

ATC-40 (Applied technology council) “Seismic evaluation and retrofit of concrete buildings” Volume 1.

Koushik Bhattacharya, Sekhar Chandra Dutta.(2004) “Assessing lateral period of building frames incorporating soil flexibility” *Journal of sound and vibrations* 269795-821.

Edward L Wilson, (2004). “Static & Dynamic analysis of structures” 4th edition, *Computers & Structures Inc.,*

J.E. Bowles, (1996), “Foundation Analysis and Design” 5th Edition, *McGraw-Hill International Editions*, Civil Engineering Series, New York,.

IS:1893(part 1):2002,”Criteria for Earthquake Resistant Design of Structures” Part 1- General provisions and buildings, fifth revision, Bureau of Indian Standards, New Delhi, India.

Sekhar Chandra Dutta, Koushik Bhattacharya, RanaRoy(2004) “Response of low-rise buildings under seismic ground excitation incorporating soil-structure interaction” *Journal of soil dynamics and earthquake engineering* 24893-914.

Chandrashekar.A,Jayalakshmi B.R,Katta Venkataramana(2005) “Dynamic soil-structure interaction effects on multi storied RCC frames” *Proceedings of International Conference on Advance to structural dynamics and its application* 7-9 December , ICASDA, 454-467.

3D finite element analysis of a ship grounding problem

G. Qiu[1] and J. Grabe[1]

1. Institute for Geotechnical and Constructional Engineering, Hamburg University of Technology, Germany; g.qiu@tuhh.de

ABSTRACT: The ever expanding world trade necessitates larger container ships and increases the demand for sea transports. However, the increasing occurrence of shipping accidents, such as ships running aground, threaten the safety of freights and ships. Due to the complex contact mechanisms between ships and structures or the ground, it is very difficult to predict the collisional force and stopping distance when applying classical mechanical theory. In the related project 'Hochdonn' of BAW (Federal Waterways Engineering and Research Institute, Germany) collision experiments were performed to analyze the impact mechanisms in grounding problems. This paper describes the simulation of the collision of the ship "Gerda" with a sandbank using a coupled Eulerian-Lagrangian (CEL) method. Numerical analysis were conducted and compared with the experimental results.

INTRODUCTION

During the last century there has been an increase in frequency of ships colliding with bridges spanning over inland waterways (Stede, 1997). Due to the dramatic increase in dead weight load and the speed of inland ships, the old bridges over inland waterways are at risk.

Meier-Dörnberg (1984) undertook theoretical and experimental studies to determine the collisional force and the stopping distance of a grounding ship. His studies are based on the principle of conservation of momentum as well as the assumption of a rigid embankment. However, accident damage analyses have shown that ships always penetrate the banks of waterways (Kauther, 2007). A prediction of the path of penetration is impossible using the theory after Meier-Dörnberg. In order to develop models to predict impact force and stopping distance as a function of the ship's velocity as well as the bow types of the ship and the geometry of the embankment, small scale model tests (Kauther, 2007) and field tests (Schuppener et al., 2006) were performed by BAW (Federal Waterways Engineering and Research Institute). In this paper, a coupled Eulerian-Lagrangian (CEL) method is applied to simulate a field test with the ship

"Gerda" previously undertaken by BAW.

NUMERICAL METHOD

During the collision between ship and embankment large deformations can occur within the soil. The use of classic FE methods that are based on Lagrangian formulation often leads to contact problems and distortion of the FE-mesh. To deal with these problems the coupled Eulerian-Lagrangian method (CEL) (Noh, 1964) came into consideration. Qiu et al. (2009) analyzed two benchmarks of geotechnical problems using the CEL-method and concluded that it is well suited to solve geotechnical problems involving large deformations. In this paper, the numerical simulations are carried out using the CEL-method with the commercial software Abaqus.

There are two ways to describe the movement of the small volumetric element as a function of time: Lagrangian description and Eulerian description (s. FIG. 1).

Lagrangian description: The movement of the continuum is specified as a function of the material coordinates and time. This is a particle description that is often applied in solid mechanics. In simulations using the Lagrangian formulation, the nodes of a Lagrangian mesh move with the material. Therefore the interface between two parts is precisely tracked and defined. In these simulations large deformations of one part may lead to unpromising mesh and element distortions.

Eulerian description: The movement of the continuum is specified as a function of the spatial coordinate and time. This is a field description that is often applied in fluid mechanics. In the Eulerian analysis, an Eulerian reference mesh which remains undistorted is needed to trace the motion of the material in the Eulerian domain. Materials can move through an Eulerian mesh. The advantage of the Eulerian formulation is that no element distortions occur; the disadvantage is that numerical diffusion can happen in case of two or more materials in the Eulerian domain.

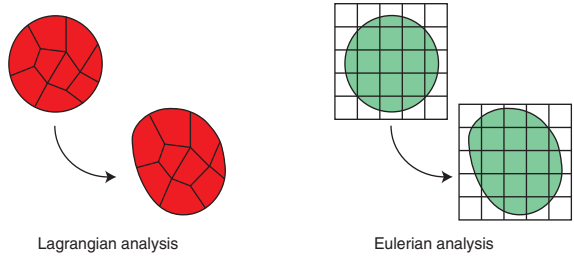

FIG 1 . Deformation of a continuum in Lagrangian analysis (left) and Eulerian analysis (right)

A coupled Eulerian-Lagrangian (CEL) method that attempts to capture the advantages both of the Lagrangian and the Eulerian method is implemented in Abaqus/Explicit (Dassault Systèmes, 2008). In the analysis with this CEL method the Eulerian material is tracked as it flows through the mesh by computing its Eulerian volume fraction (EVF). Each Eulerian element is designated a percentage, which represents the portion of that

element filled with a material. If an Eulerian element is completely filled with a material, its EVF is 1; if there is no material in an element, its EVF is 0. Contact between Eulerian materials and Lagrangian materials is enforced using a general contact that is based on a penalty contact method. A general contact algorithm does not enforce contact between the Lagrangian elements and the Eulerian elements. The Lagrangian elements can move through the Eulerian mesh without resistance until they encounter an Eulerian element filled with material (EVF ≠ 0). Seeds are created on Lagrangian edges and faces while anchor points are created on the Eulerian material surface. The penalty method approximates hard pressure-overclosure behavior. This method allows small penetration of the Eulerian material into the Lagrangian domain. The contact force F_P which is enforced between seeds and anchor points is proportional to the penetration distance d_P.

$$F_P = k_P d_P, \tag{1}$$

where k_P is the penalty stiffness which depends on the Lagrangian and Eulerian material properties.

For the ship grounding problem, a Lagrangian mesh is used to discretize the ship, and an Eulerian mesh is used to discretize the soil. The interface between ship and soil can be represented using the boundary of the Lagrangian domain. Meanwhile the Eulerian mesh, which represents the soil that may undergo large deformations, eliminates the problems regarding mesh and element distortions.

NUMERICAL SIMULATION OF A SHIP COLLISION

In this section, a three-dimensional finite-element model is presented to investigate the collision of the ship "Gerda" with an embankment.

The test ship "Gerda" has a width of B = 8 m and an overall length of L = 66.5 m. With a draught of h_0 = 1.9 m, it has a tonnage of m = 900 t. In order to save computational time only half of the bow is simulated. The geometry and mesh of the bow are shown in FIG. 2. The ship is modeled as a discrete rigid body using 4-node bilinear quadrilateral elements. The center of mass is located in the middle of the ship and 0.5 m from the bottom. This ship has an initial velocity of 2.64 m/s and is running aground on a gravel sand embankment with an inclination of 1:3.

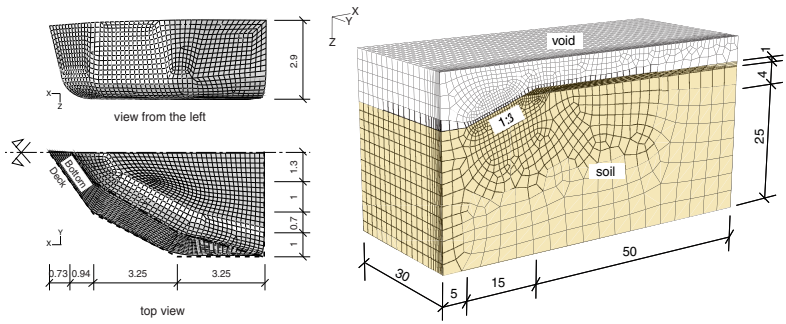

FIG. 2. Geometry and mesh of the ship "Gerda" (left) and the embankment (right);

unit [m]

The embankment is modeled as an Eulerian domain, which is meshed using an 8-node linear brick, multi-material elements with reduced integration and hourglass control. The Eulerian domain is divided into two parts: the initial soil material and the absence of material (void) (s. FIG. 2). The water table is 1.0 m below the top of the embankment. The gravel sand has a specific weight of γ = 24.6 kN/m^3 and an effective unit weight of γ' = 14.6 kN/m^3. After Jaky (1948), the initial lateral stress coefficient K_0 is set to 0.42 for the gravel sand with a friction angle φ_c of 36°. In this paper a hypoplastic constitutive law is used to describe the soil. The theory of hypoplasticity was developed at the University of Karlsruhe, especially by Kolymbas (1991) and Gudehus (1996). Over time, the constitutive model was further improved by Wu (1992) and Bauer (1992). The calculations in this paper are based on the version of von Wolffersdorf (1996) with the extended concept of intergranular strain (Niemunis and Herle, 1997). The hypoplastic parameters of the gravel sand can be found in Table 1.

Table 1. Hypoplastic parameters of the Hochstetten gravel after Herle (1997)

Parameters	φ_c [°]	h_s [MPa]	n [-]	e_{d0} [-]	e_{c0} [-]	e_{i0} [-]	α [-]	β [-]
Value	36	32000	0.18	0.26	0.45	0.50	0.10	1.80
Parameters	R [-]	m_R [-]	m_T [-]	β_r [-]	χ [-]			
Value	$1 \cdot 10^{-4}$	5.0	2.0	0.50	6.0			

The contact between the soil material in the Eulerian domain and the ship meshed with Lagrangian elements is described using the "general contact" algorithm, which enforces the use of the penalty contact method. This contact method works without discrete contact elements. The "general contact" algorithm with the finite-sliding formulation, which allows arbitrary motion of the surface, is well suited to simulate highly nonlinear processes with large deformations. The frictional behavior between soil and ship is described using the linear-elastic, ideal plastic formulation stated by Coulomb. According to the results of shear tests conducted by BAW, the friction angle δ between ship and embankment is determined to be 32°, which leads to a friction coefficient of tan δ = 0.62.

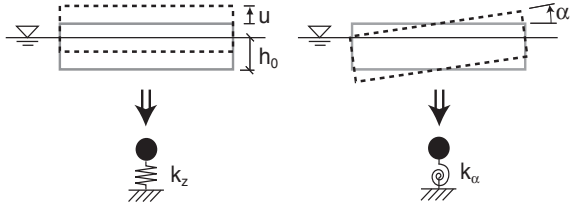

FIG. 3. Simplification of the buoyancy behavior using a linear spring (left) and a torsional spring (right)

Kauther and Schuppener (2007) investigated the buoyancy behavior of different ship types. From their work it can be concluded that it is sufficient and appropriate to simplify the ship geometry by using a cuboid to estimate changes in buoyancy. As long as the ship's bow is not lifted too far out of the water the correlation between the moment of buoyancy and the pitch angle can be fitted by a linear function. In the simulations for the present study the water is not taken account of study. In order to take buoyancy into account, one linear spring in the vertical direction and one torsional spring are assembled in the centroid (reference point) of the ship (s. FIG. 3).

The motion of a rigid ship can be divided into translation and rotation. The translational part of the buoyancy A_z can be calculated by:

$$A_z = \frac{mg}{h_0} u, \tag{2}$$

where m is the mass of the ship, h_0 is the draught and u is the translation of the ship in vertical direction. Then the spring constant in vertical direction can be calculated by:

$$k_z = \frac{mg}{h_0}. \tag{3}$$

The moment of the rotational part of the buoyancy M_α can be calculated by:

$$M_\alpha = \gamma_w \alpha \frac{BL^3}{12}, \tag{4}$$

where γ_w is the weight of the water, B is the width, L length and α the rotation angle of the ship. This can be converted to:

$$M_\alpha = \frac{mgL^2}{12h_0} \alpha. \tag{5}$$

As long as the ship's bow is not lifted too far out of the water, the torsional spring constant can be calculated by:

$$k_\alpha = \frac{mgL^2}{12h_0}. \tag{6}$$

RESULTS

In the field test, accelerations in the horizontal and vertical direction are measured using two sensors, which are assembled at the bow and stern of the ship "Gerda". From the measured acceleration the displacement of the contact point and the contact force are identified as shown by Schuppener et. al. (2006). In this section the results from the numerical simulation are compared with the results from the experiment in FIG. 5 and 6.

FIG. 4 shows the contour plot of vertical stress distribution at the end position after the collision. An increase of vertical stress is clearly visible under the bottom of the bow. During the collision the ship penetrates into the embankment. The soil is moved upwards and sideways as a result.

As can be seen from FIG. 5, the numerical results agree well with the measured displacements of the contact point. After the collision the ship stops within 2.4 s. According to the results of the field test the final stopping distance is 3.83 m in the horizontal direction and 0.85 m in the vertical direction. The numerical simulation shows a final stopping distance of 3.96 m in the horizontal direction and 0.77 m in the vertical

direction. Using the analytical method after Meier-Dörnberg (1984) a horizontal stopping distance of 3.1 m and a vertical stopping distance of 0.99 m are calculated. The prediction of the numerical solution is more accurate than the theoretical solution in this case.

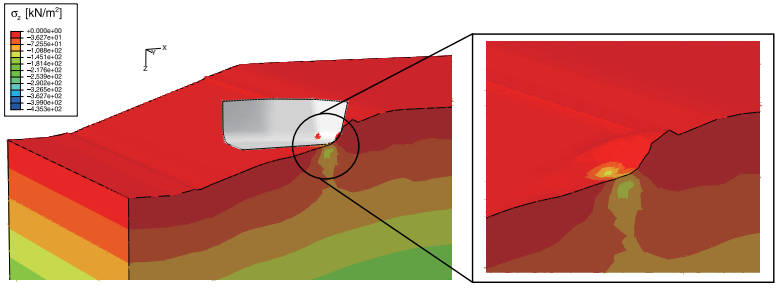

FIG. 4. Contour plot of vertical stress distribution and deformation of the embankment

During the first 0.5 s, the vertical displacements are close to zero. This means that the ship first penetrates horizontally into the soil after contact with the embankment. The assumption of a rigid bank after Meier-Dörnberg (1984) is inappropriate.

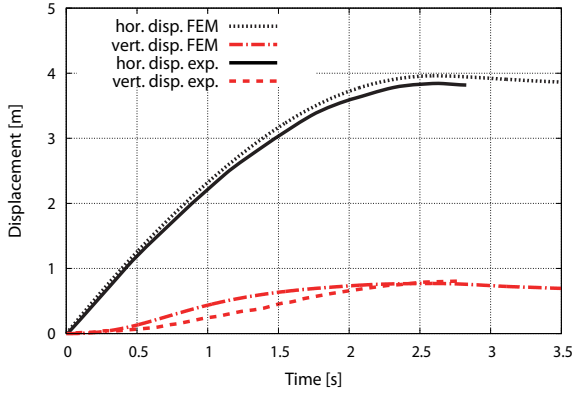

FIG. 5. Comparison of contact point displacements from numerical analyses and experimental test data according to BAW

FIG. 6 shows the contact forces predicted by the numerical simulation and from the experiment. It can be determined form both, that the maximum contact force in the vertical and horizontal direction is about 1200 kN. Good agreement of vertical contact force between the numerical results and the experimental data can be observed. The curves of horizontal contact force show some discrepancies. Two different phases can be distinguished regarding the numerical results: a dynamic phase (0 – 0.8 s) and a quasi-

static phase (after 0.8 s). In the dynamic phase a dramatic impact of the ship into the soil occurs. The reaction force in this phase depends on the ship's velocity and the type and stiffness of bow. The higher the velocity of the ship is, the higher the reaction force. The dynamic phase regarding a ship with a sharp and soft bow is less distinct than with a pontoon type and stiff bow. In the numerical model the ship is discretized as a rigid body. Therefore, the reaction presented by the FE solution is much more vigorous compared to the field test. In the quasi-static phase the reaction force consists of the passive earth pressure from the embankment and the friction between the ship and the soil. The kinetic energy decreases with increasing penetration distance until the ship stops.

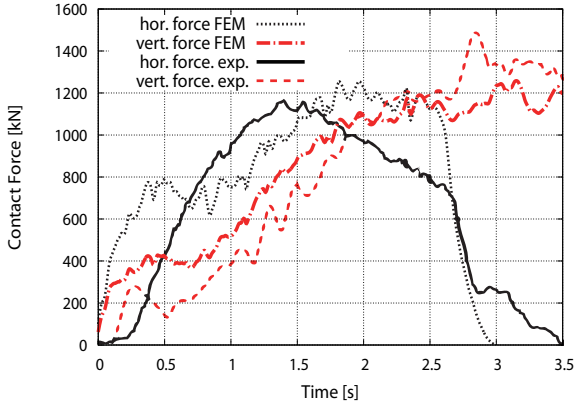

FIG. 6. Comparison of the horizontal and vertical contact force from FEM simulation with experiment test data according to BAW

CONCLUSIONS

A 3D FE model using a Coupled Eulerian-Lagrangian method is used to recalculate the collision experiment of BAW with the test ship "Gerda". The stopping distance and the reaction force that are indicated by the numerical simulation match the field test results very well. Compared to the conventional analytical method the application of the FE method enables the prediction of the slope of the stopping path. Moreover, the stopping distance can be predicted more precisely using FE method compared to the conventional analytical method.

ACKNOWLEDGMENTS

The authors would like to thank the German Research Foundation (DFG) for funding the present project in the framework of the post-graduate program GRK 1096 "Seaports for container ships of future generations".

REFERENCES

Bauer, E. (1992). "Zum mechanischen Verhalten granularer Stoffe unter vorwiegend ödometrischer Beanspruchung." *Dissertation, Institut für Bodenmechanik und Felsmechanik der Universität Karlsruhe*, Heft 130.

Dassault Systèmes, (2008). "ABAQUS, Version 6.8EF Documentation".

Feddersen, G. and Lehmann, E. (2007). "The Effects to a Container Ship due to Soft Grounding." *4th ICCGS. Hamburg, Germany.*

Gudehus, G. (1996). "A comprehensive constitutive equation for granular materials." *Soils and Foundations*, 36(11): 1-12.

Herle, I., 1997. "Hypoplastizität und Granulometrie einfacher Korngerüste." *Dissertation, Institut für Bodenmechanik und Felsmechanik der Universität Karlsruhe*, Heft 142.

Jaky, J. (1948). "Pressure in silos." *Proc 2nd International Conference on Soil Mechanics and Foundation Engineering*, Rotterdam, Vol. 1: 103-107.

Kauther, R. and Schuppener, B. (2007). "Physical modeling of ship collisions with waterway embankments." *4th ICCGS, Hamburg, Germany.*

Kolymbas, D. (1991). "Computer-aided design of constitutive laws." *International Journal for Numerical and Analytical Methods in Geomechanics,* Vol. 15: 593-604.

Meier-Dörnberg, K.-E. (1984). "Theoretische und experimentelle Untersuchungen zur Ermittelung statischer Ersatzlasten für den Anprall von Schiffen an Bauwerken." *TU-Darmstadt.*

Niemunis, A. und Herle, I. (1997). "Hypoplastic model for cohesionless soils with elastic strain range. " *Mechanics of frictional and cohesive materials,* 2(4):279-299.

Noh, W., 1964. "CEL: A time-dependent, two-spacedimensional, coupled Eulerian-lagrangian code. " *Methods in Computational Physics*, Vol. 3 Fundamental Methods in Hydrodynamics, pp. 117–179.

Qiu, G., Henke, S. and Grabe, J. (2009). "Applications of Coupled Eulerian-Lagrangian method to geotechnical problems with large deformations." *Proceeding of SIMULIA Customer Conference 2009, London, UK*: 420-435.

Schuppener, B., Kauther, R., Kramer, H. and Vorbau, J. (2005). "Schiffsanfahrungen an Uferböschungen." *Veröffentlichungen des Grundbauinstitutes der TU Berlin*, Heft Nr. 38, Berlin 2005, 79-102.

Schuppener, B., Kauther, R., Kramer, H. and Vorbau, J. (2006). "Ship collisions with sloped banks of waterways – an approach to determine the stopping distance." *Proceedings of the 31st PIANC-Congress, Estoril, Portugal.*

Stede, J. (1997). "Binnenschifffahrtsunfälle 1991 bis 1996." *St.BA, Wirtschaft und Statistik 12.*

von Wolffersdorff, P.-A. (1996). "A hypoplasic relation for granular material with a predefined limit state surface." *Mechanics of cohesive-fractional materials,* 1:251-271.

Wu, W. (1992). "Hypoplastizität als mathematisches Modell zum mechanischen Verhalten granularer Stoffe." *Dissertation, Institut für Bodenmechanik und Felsmechanik der Universität Karlsruhe*, Heft 129.

Pile Responses under Seismic Earth Pressures of Lateral Spread using Wave Equation Analysis

Bor-Shiun Lin[1], Der-Wen Chang[2], and Hsing-Chuan Ho[1]

[1]Research Engineer, Geotechnical Enigineering Research Center, Sinotech Engineering Consultants, Taiwan, corresponding author: bosch.lin@sinotech.org.tw
[2] Professor, Department of Civil Engineering, Tamkang University, Tamsui, Taiwan

ABSTRACT: This study presents a simplified method to conduct the behavior of pile foundations due to lateral spreading. Wave equation analysis applied to model the pile behavior under seismic motions. According to the concept of force-based method, the authors suggest to adopt the dynamic earth pressure in the wave equation analysis. Numerical procedures were validated with the well-documented cases of damaged piles in 1995 Kobe earthquake. In the meantime, comparing the numerical results with the case histories, one can again evaluate the damaged features of piles and distinguish the actual failure pattern of piles. The predictions and the observations were found in good correspondences.

INTRODUCTION

During the 1964 Niigata Earthquake, Showa Bridge with 12 spans and the length of 307 m was damaged. After the earthquake, excavation survey of one pile of the piers of Showa Bridge indicated that the bending failure occurred at depth of 7m to 8m due to lateral spreading along Shinano River (Hamada, 1992). Similarly, in the 1995 Kobe Earthquake, many of the quay walls along the coastline of Kobe moved up to several meters toward the sea as a result of lateral spreading (Tokimatsu and Asaka, 1998). They were damaged by the extreme soil mobility in spite of the types of structures. In consequence, Yasuda (2004) had reported that there are only two conditions to encounter this disaster. Namely, those are ground flow on the gentle slopes and ground flow behind quay walls. The above mechanisms are studied by laboratory tests and numerical analyses (Abdoun and Dobry, 2002; Rolline et al., 2005). When piles are subjected to lateral spreading, lateral forces are exerted directly on the embedded depth of piles in liquefied layer. There are generally two methods to analyze this task. The first method is called “Force-based method”. It applied the earth pressure immediately to piles based on empiricism or the means of viscous flow (Chaudhuri et al. 1995). The second method was called “Displacement-based method”. The observed or computed lateral displacements of ground are transmitted by soil springs to act on the whole pile system (Tokimastu and Asaka, 1998; Chang and Lin, 2003; Cubrinovski and Ishihara, 2004). The latter method has advantages on choosing the adequate soil spring model to fit with complexity of the

soil stratum. It can also consider the nonlinear material effects. On the contrary, the force-based method will not only simply define the parameters of soils and have an explicit numerical procedure to effectively obtain the solutions, but it can involve the geography including level and sloping ground.

In terms of static design for pile foundations, the current mechanism of failure assumes that the soil pushes the pile. The Japanese Road Association Code (JRA, 1996) has incorporated this concept as shown in Figure 1. The code advises civil engineers that the non-liquefied layer acts passive pressure on the piles and liquefied layer offers thirty percents of overburden pressure when designing piles against bending failure due to lateral spread. Other codes such as USA code (NEHRP, 2000) and Eurocode 8, part 5 (1998) also have specifications about the problem (Bhattacharya et al., 2005). In the other hand, Tokimatsu (2003) investigated that the equivalent earth pressure acting on the pile during liquefaction in shaking table tests can be defined as the seismic passive pressures subtracting the seismic active pressures. This concept was also verified with the centrifuge tests by Haigh and Madabhushi (2005). This study utilized the dynamic earth pressure to reveal the effects of liquefaction-induce lateral spreading. It acted directly on the pile to calculate the response of system by means of wave equations (Chang and Lin, 2003). Based on case studies from Japan, the failure patterns of the piles would be discussed and the results showed the reliability of the simplified method.

NUMERICAL PROCEDURES

The Winkler foundation model is often used in analyzing the deformation behaviors of the pile foundations. For solutions of the dynamic Winkler foundation model, or the so-called beam on dynamic Winkler foundation (BDWF) model, the wave equation analysis, initially proposed by Smith (1960), has been suggested for the driven piles. Such analysis is also applicable in the pile integrity tests to interpret the seismic data from the tests. Overview of the relevant analyses can be found in Prakash and Puri (1988), Poulos (1989), Prakash and Sharma (1990) and Chang and Lin (2003). For discrete models of the soils, both of the conventional load-displacement curves (t-z, q-z and p-y equations) and the Novak's dynamic impedance functions were widely used in practice. Nevertheless, some parameters of soil are hardly defined while using the above soil spring model to analyze the response of piles. In this paper, the authors suggest to use the dynamic earth pressures in the analysis to simulate the lateral spread effects based on the concept of forced-based method. The time history of earthquake records for the site of interest is selected and the dynamic coefficients of the earth pressures for the modified M-O method (Zhang et al., 1998) is calculated. Liquefaction potential of the site (Tokimatsu and Yoshimi, 1983) is evaluated for the limited pore water pressure ratio (ru) at various depths. Thereafter, ru would reduce the soil properties for corresponding influences. The lateral spread forces can be computed and applied onto the pile for the solutions. Figure 2 illustrates the numerical procedures required for such analysis.

DERIVATIONS OF WAVE EQUATION FOR PILE FOUNDATIONS

Wave equation of a single pile under lateral loads can be derived based on force equilibrium of the pile segments shown in Figure 1 as follows,

$$EI\frac{\partial^4 u(x,t)}{\partial x^4}+\rho A\frac{\partial^2 u(x,t)}{\partial t^2}+P_x\cdot\frac{\partial^2 u(x,t)}{\partial x^2}=P(x,t) \quad (1)$$

where u is the lateral pile displacement relative to the soil, E is the Young's modulus of the pile, is the moment inertia of the pile, is mass density of the pile, A is the cross-sectional area of the pile, is the superstructure loads, is the time-dependent loads due to laterally spreading at various depths, x is ordinate variable, and t represents for time. Using explicit finite difference schemes, the discrete form of Eq. (1) can be written as:

$$u(i,j+1)=\frac{1}{A_1}\begin{bmatrix}-u(i+2,j)+(4-B_1)\cdot u(i+1,j)\\+(2A_1+2B_1-6)\cdot u(i,j)\\+(4-B_1)\cdot u(i-1,j)-u(i-2,j)\\-A_1\cdot u(i,j-1)+C_1\end{bmatrix} \quad (2)$$

where $A_1=\frac{\rho A\Delta x^4}{EI\Delta t^2}$; $B_1=\frac{P_x\Delta x^2}{EI}$; $\frac{P(x,t)\Delta x^4}{EI}$. For the initial condition, $u(i,j)$ and $u(i,j-1)$ are set to be zero. The above equation can only calculate the responses along piles under lateral loads except the head and tip of pile. With proper boundary conditions, the other equations can then be derived.

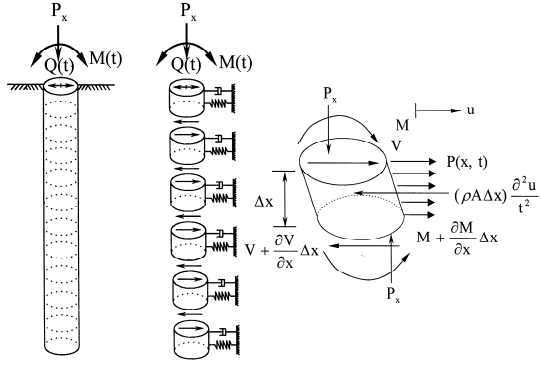

FIG. 1 Discrete system of the single pile.

Presuming that a long pile is at rest initially, and no shears and moments are applied at the tip. The governing equations at the pile tip and the corresponding difference formula at the pile tip and adjacent node are obtained individually. While the liquefaction-induced dynamic earthquake pressures are computed, the pile responses at various depths can be solved through the above formulations.

DYNAMIC EARTH PRESSURE

Since Mononobe and Okabe introduce the concept of dynamic lateral pressure, many reports and practical works have been conducted in this manner (Ishibahi et al., 1994; Richard et al., 1993; Soubra and Regenass, 2000). Tokimatsu (1999) and Uchida and Tokimatsu (2005) suggested the factors affecting the response of pile in the saturated

sand by the shaking table tests. They suggest that the total earth pressure acting on the foundation when neglecting the friction between foundation and soil is define as:

$$P_E = P_{EP} - P_{EA} = Q - F \tag{3}$$

where P_E is total earth pressure, P_{EP} and P_{EA} are earth pressures on the active and passive sides, Q is shear force at the pile head, and F is total inertial force from the superstructure and foundation. In addition, Haigh and Madabhushi (2005) have verified that the adjacent stresses of single piles subjected to lateral spreading forces would range between the active state and the passive state through the centrifuge modeling.

Based on the Mononobe-Okabe method, Zhang et al. (1998) successfully derivates the time-dependent the coefficients of earth pressure under active and passive states that involves the motions of soils and foundations. One can also modified the plane strain model of soil wedge to extend it for the three dimensions. The descriptions and formulations of the coefficients of active and passive earth pressures are as follows:

Active state:

$$K_{EA} = \frac{2\cos^2(\phi - \beta - i)}{\cos^2(\phi - \beta - i)(1+R) + \cos i \cos^2\beta \cos(\delta_{mob} + \beta + i)(1-R)I_{E.1}} \tag{4}$$

$$\delta_{mob} = \frac{1}{2}(1-R)\delta_a \tag{5}$$

$$R = \max\left[-1, -\left(\frac{|\Delta_r|}{\Delta_a}\right)^{0.5}\right] \quad (\Delta_a = aH, a = 0.001 - 0.005) \tag{6}$$

$$I_{E.1} = \left[1 + \sqrt{\frac{\sin(\phi + \delta_{mob})\sin(\phi - \alpha - i)}{\cos(\delta_{mob} + \beta + i)\cos(\beta - \alpha)}}\right]^2 \tag{7}$$

Passive state:

$$K_{EP} = 1 + \frac{1}{2}(R-1)\left[\frac{\cos^2(\phi + \beta - i)}{\cos i \cos^2\beta \cos(\delta_{mob} - \beta + i)I_{E.2}} - 1\right] \tag{8}$$

$$\delta_{mob} = \frac{1}{2}(R-1)\delta_p$$

$$R = \min\left[3, 3\left(\frac{|\Delta_r|}{\Delta_p}\right)^{0.5}\right] \quad (\Delta_p = bH, b = 0.05 - 0.1) \tag{9}$$

$$I_{E.2} = \left[1 - \sqrt{\frac{\sin(\phi + \delta_{mob})\sin(\phi + \alpha - i)}{\cos(\delta_{mob} - \beta + i)\cos(\beta - \alpha)}}\right]^2 \tag{10}$$

where $i (= \tan^{-1}[k_h/(1-k_v)])$ is angle of seismic coefficients, k_h is horizontal seismic coefficient, k_v is vertical seismic coefficient, ϕ is friction angle of sand, R is lateral strain constraint, β is inclined angle of the foundation with respect to the vertical, α is slope of the ground surface behind the foundation with respect to the horizontal, H is

the length of foundation, $I_{E.1}$ and $I_{E.2}$ are influenced factors, δ_{mob} is the mobilized foundation friction angle, δ_a and δ_p are friction angles of sand at the active and passive states, Δ_r is relative displacement between soil and foundation, Δ_a and Δ_p are reference relative displacements in active and passive states.

MODEL CORRECTIONS

A potentially liquefiable soil is defined as a soil having the possibility of excess pore pressure generation during earthquake shaking. In general, pore water pressure ratio represents the state of liquefaction in design. To controlling the excess pore water pressure actually, some researchers suggests the relationships between the safety factor against liquefaction and the pore water pressure ratio (r_u) by the regression method (Tokimatsu and Yoshimi, 1983). The empirical equation is given by

$$r_u = \frac{1}{2} + \frac{1}{\pi}\sin^{-1}(2F_L^{\frac{1}{\alpha\beta}} - 1) \tag{11}$$

where α, β are the experienced constants, and F_L is the safety factor of liquefaction. Eq. (24) has been used by the authors in obtaining the maximum pore water ratios at various depths of the site susceptible to liquefaction.

For lateral spreading induced by the liquefaction, the soil properties such as the unit weights and the friction angles of the soils could be corrected based on the calculated pore water pressure ratios. There are two ways depicting the weakness of soils during liquefaction. Those equations are given by

$$\gamma'_s = \gamma_s(1 - r_u) \tag{11}$$

$$\phi'_{eff} = \tan^{-1}[(1 - r_u)\tan\phi'] \tag{12}$$

where γ'_s is the unit weight of the soil, γ_s is the effective unit weight of the soil, ϕ' is the friction angle of the soil, and ϕ'_{eff} is the effective friction angle of the soil. According to the geometry of pile, the lateral forces at various depths are determined by

$$P_E = (\gamma'_s \underset{i}{Z} K_E)\cdot(B) \tag{13}$$

where $\underset{i}{Z}$ is the corresponding depth of node, K_E is the equivalent dynamic coefficients of earth pressure (i.e. $K_E = K_{EP} - K_{EA}$), and B is the loaded width of the pile body ($=\pi d/2$, where d is the pile diameter).

CASE STUDIES

The damaged cases of foundation piles during the 1995 Kobe earthquake are studied based on the wave equation analysis in the following paragraphs. The cases are all near the coastline or waterfront and the foundations locate on the gentle slope. It has been noted that the damages to piles are caused by lateral spreading form in-situ investigations. In this paper, the dynamic earth pressures from the lateral spreading of the liquefied layers are generated and used to model the forces exerting on piles where the deformations of piles occur accordingly. The results would show the pattern of failure to piles and the validity of methodology.

Mikagehama is a man-made island in the port area of Kobe where a number of liquefied propane gas (LPG) and oil tanks. During the 1995 Kobe Earthquake, the soils underlying the foundation of tank occur liquefaction. The quay wall moved seaward and lateral spreading of the backfill soils damage the piles supporting the tank. Oil-storage tank TA72 is chosen to be a target, which located in the west part of the island and about 20m from the waterfront. Figure 2 illustrate the cross sectional view of tank and underlying pile foundations. The tank has a diameter of 14.95 m and its storage capacity is about 2450 kl. It is supported on 69 precast concrete piles each with the length of 23 to 24 m and the diameter of 45 cm. The water table is estimated at the depth of 2 to 3 m. Sand compaction pile has been conducted to increase the SPT-N values of the Masado layer around the outside of Tank TA72. According to the relation between the bending moment (M) and curvature (Φ), the cracking bending moment (M_{cr}), the yield bending moment (M_y) and the ultimate bending moment (M_u) are 105 kN-m, 200 kN-m, and 234 kN-m respectively. The ultimate shear strength is 232 kN in regard to ACI (1998). Ishihara and Cubrinovski (2004) have utilized bore-hole cameras and inclinometers to inspect the damages of the piles. Their results for pile No. 2 is shown in FIG 2. The main failure field of piles locates at depth of 8 to 14 m that the piles develop many cracks. Moreover, pile No. 2 has scraped wounds due to large deformations and sheared off at depth of 10.5 m where lateral spreading of liquefied soils develops the weak interface.

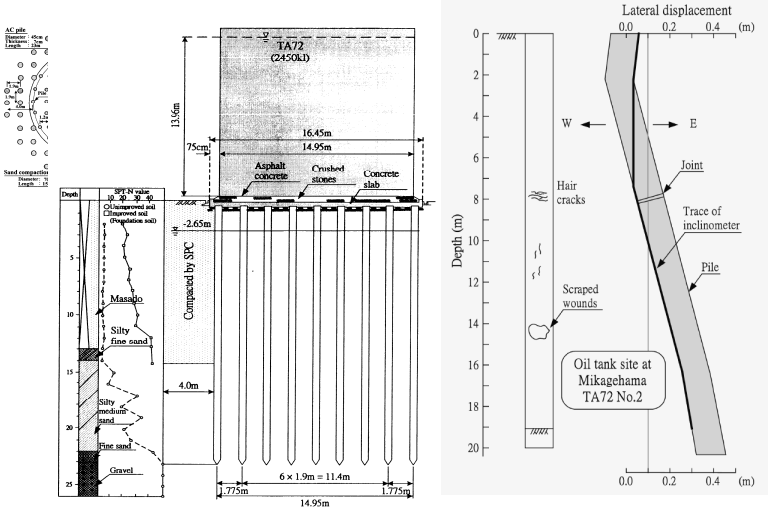

FIG 2. Cross sectional view of Tank TA 72 and its foundation (from Ishihara and Cubrinovski, 2004)

In this study, the length of pile is assumed to be 24 m with the diameter of 45 cm. Seismic record of the NS-component of 1995 Kobe Earthquake is adopted. Its peak ground acceleration reaches 0.88 g. According to the field data, distributions of pore water ratio pressure (r_u) versus the depths can be estimated by evaluating the liquefaction potential of that site and substitute the factor of safety to Eq. (11). The value of r_u is

approximately 27% for the depth of 1 to 2 m over the water table. However, the values of r_u range from 70% to 90% beneath the water table. With all the required data and incorporating with the modified M-O model, the dynamic coefficients of earth pressure are computed. In the meantime, the unit weight of the soil is reduced by r_u. When obtaining those dynamic earth forces to insert and execute the wave equation analysis, the time histories of displacements along the pile can be calculated. The displacement of the pile head oscillates significantly with time, but the peak value is smallest. As the depth increases, the peak displacement of pile becomes larger. Those peak displacements along the pile are shown in FIG 3. The maximum value among them occurs at the pile tip about 52.7 cm and the maximum relative displacement between the pile top and the pile bottom is estimated about 44.7 cm. The deformed shape of the pile is similar to pile No. 2. In the same way, FIG 3 show the time histories of bending moments and shear forces, and those peak values along the pile. It can be found that the maximum bending moments exceeds the ultimate bending moment at the depths of 2 to 23 m that would be dangerous zone to cause the pile damages. With regards to the shear failure, the weak interface will exist at a depth of 11 m, in which the maximum shear force is close to the ultimate to be sheared off. The above observations are agreeable to the field investigations reported by Ishihara and Cubrinovski (2004).

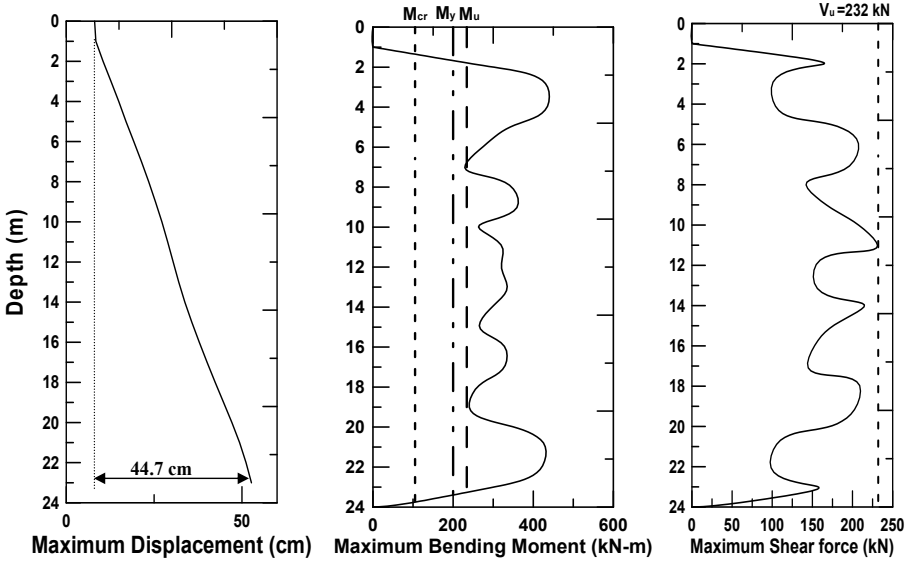

FIG 3. Maximum lateral response along the pile (Tank TA 72)

SUMMARY AND CONCLUSIONS

This paper employs the dynamic earth pressure with the discrete the wave equations of piles to model the effects of lateral spreading. A couple of case studies both show that the

lateral spreading would be a major cause to damage the piles. Through the wave equation analysis, we can capture the deformations and the failure patterns of piles. The following conclusions were drawn:

1. The wave equation analysis can be used to model the pile responses under the lateral spread due to earthquake.
2. The modified M-O model (Zhang et al., 1998) incorporating with reduction methods for soil parameters were successfully used to represent for the dynamic earth pressures of the lateral spread.
3. As a result of case studies, the deformed shapes of piles due to lateral spreading are similar to the field investigations. In addition to that, the numerical results fit well with the actual damage features of the piles.

REFERENCES

Abdoun, T. and Dobry, R., (2002) "Evaluation of Pile Foundation Response to Lateral Spreading," Soil Dynamics and Earthquake Engineering, Vol. 22, No. 9, pp. 1051-1058.

American Concrete Institute (1995), "Building Code Requirements for Structural Concrete", ASCE, USA.

Bhattacharya, S., Bolton, M.D. and Madabhushi, S.P.G. (2005), "A Reconsideration of the Safety of Piled Bridge Foundation in Liquefiable Soils", Soils and Foundations, JGS, Vol. 45, No. 4, pp. 13-25.

Chang, D.W. and Lin, B.S. (2003), "Wave Equation Analyses on Seismic Responses of Grouped Piles", Procds., 12th Asian Regional Conf. on Soil Mechanics and Geotechnical Engineering, Singapore, August, pp. 581-586.

Chaudhuri, D., Toprak, S., and O'Rourke, T.D. (1995), "Pile Response to Lateral Spread: a Benchmark Case", Lifeline Earthquake Engineering, Procds., 4th U.S. Conference, San Francisco, California, pp. 1-8.

Curbrinovski, M and Ishihara, K. (2004), "Simplified Method for Analysis of Pile Undergoing Lateral Spreading in Liquefied Soils", Soils and Foundations, JGS, Vol. 44, No. 5, pp. 119-133.

Haigh S.K. and Madabhushi S.P.G. (2005) "The effects of pile flexibility on pile-loading in laterally spreading slops", Proc. Int. Workshop Simulation and Seismic Performance of Pile Foundations in Liquefied and Laterally Spreading Ground, ASCE, 14 p.

Hamada M.（1992）, "Large Ground Deformations and Their Effects on Lifelines：1964 Niigata Earthquake," in Case Studies of Liquefaction and Lifeline Performance During Past Earthquakes, Vol. 1, Japanese Case Studies, Technical Report NCEER-92-0001, NCEER, Buffalo, NY, USA.

Hamada, M. and Wakamatsu, K. (1998), "A Study on Ground Displacement Caused by Soil Liquefaction", JSCE, Journal of Geotechnical Engineering, No. 596/III-43, pp. 189-208.

Ishibashi, I., Osada, M. and Uwabe, T. (1994), "Dynamic Lateral Pressures due to Saturated Backfills on Rigid Walls", Journal of Geotehnical Engineering, Vol. 120, No. 10, pp. 1747-1767.

Ishihara, K. and Cubrinovski, M. (2004), "Case Studies on Pile Foundations undergoing

Lateral Spreading in Liquefied Deposits", Proceeding of 5th International Conference on Case Histories in Geotechnical Engineering, New York, Paper SOAP 5.

Japanese Road Association (JRA) (1996), Specification for Highway Bridges, Part V, Seismic Design.

Poulos, H.G., (1989). "Cyclic axial loading analysis of piles in sand", Journal of Geotechnical Engineering, ASCE, Vol. 115, No. 6, 1989, pp. 836-852.

Prakash, S. and Puri, V.K., (1988). Foundations for Machines: Analysis and Design, John Wiley and Sons, Canada.

Prakash, S. and Sharma, H.D., (1990). Pile Foundations in Engineering Practice, John Wiley and Sons, Canada.

Richard, R., Elms, D. G. and Budhu, M. (1990), "Soil Fluidization and Foundation behavior', Proc. 2nd International Conference Recent Advance in Geotechnical Engineering and Soil Dynamics, Rolla 1, pp. 719-223.

Richard, R., Elms, D. G. and Budhu, M. (1993), "Seismic Bearing Capacity and Settlement of Foundations", Journal of Geotechnical Engineering Division, ASCE, Vol. 119, No. 4, pp. 662-674.

Rollins, K. M., Lane, J. D., and Gerber T. M. (2005), "Measured and Computed Lateral Response of a Pile Group in Sand", Journal of Geotechnical Engineering and Geoenvironmental Engineering, ASCE, Vol. 131, No.1, pp. 103-114.

Smith, E. A. L. (1960), "Pile Driving Analysis by the Wave Equation", Journal of Soil Mechanics and Foundation Divisions, ASCE, Vol. 86, No. SM4, pp. 35-61.

Soubra, A. H. and Regenass, P. (2000), "Three-dimensional Passive Earth Pressure by Kinematical Approach", Journal of Geotechnical and Geoenvironmental Engineering, Vol. 126, No. 11, pp. 969-978.

Tokimatsu, K. (1999) "Performance of pile foundations in laterally spreading soils", Procds, 2nd Int. Conf. Earthquake Geotechnical Engineering, Vol. 3, pp. 957-964.

Tokimatsu, K. and Asaka, Y. (1998) "Effects of Liquefaction-induced ground displacement on pile performance in the 1995 Hyogoken-Nambu earthquake," Soils and Foundations, Special Issue, No. 2, pp. 163-178.

Tokimatsu K. and Yoshimi Y. (1983), "Empirical Correlation of Soil Liquefaction Based on SPT N-Value and Fines Content", Soil and Foundations, JSSMFE, Vol. 23, No.4, pp. 56-74.

Tokimatsu, K. (2003), "Behavior and Design of Pile Foundations Subjected to Earthquakes", Procds., 12th Asian Regional Conf. on Soil Mechanics and Geotechnical Engineering, Singapore, August.

Uchida, A. and Tokimatsu, K. (2005), "Comparison of current Japanese design for pile foundations in liquefiable and laterally spreading ground", Proc. Int. Workshop Simulation and Seismic Performance of Pile Foundations in Liquefied and Laterally Spreading Ground, ASCE, 10 p.

Yasuda, S. (2004) "Development of Countermeasure Methods against Liquefaction-induced Flow after the 1995 Hyogoken-Nambu in Japan", Taiwan-Japan Joint Workshop on Geotechnical Hazards from Large Earthquakes and Heavy Rainfall, Taiwan.

Zhang, J. M., Shamoto, Y., and Tokimatsu, K. (1998), "Seismic Earth Pressure for Retaining Walls under Any Lateral Displacement", Soils and Foundations, Vol. 38, No. 2, pp. 143-163.

Dynamic Analysis of Municipal Solid Waste Landfills in Central Asia

Xue-tao Wang[1], B. G. Tensay[2] and Wei Wu[3]

[1]Doctor, Institute of Geotechnical Engineering, University of Natural Resources and Applied Life Sciences, Vienna, Feistmantelstrasse 4, A1180 Vienna, Austria; xuetao.wang@boku.ac.at
[2]Doctor, Institute of Geotechnical Engineering, University of Natural Resources and Applied Life Sciences, Vienna, Feistmantelstrasse 4, A1180 Vienna, Austria; gebremedhinberhe.tensay@boku.ac.at
[3]Professor, Institute of Geotechnical Engineering, University of Natural Resources and Applied Life Sciences, Vienna, Feistmantelstrasse 4, A1180 Vienna, Austria; wei.wu@boku.ac.at

ABSTRACT: The dynamic analyses of the landfill slopes were carried out on typical landfills (Bishkek) in Kyrgyzstan. The site investigation consists of boreholes, geotechnical laboratory tests and geophysical tests in field. Based on the results of the site investigation, dynamic analyses of the selected landfills were carried out with the finite-difference program FLAC3D and QUAKE/W. Features, advantages and disadvantages of these programs are discussed and the results of the response analysis of the selected landfills, subjected to an earthquake with a peak ground acceleration of 0.5g, are presented in this paper. The results of the analysis showed that the slope instabilities will occur approximately after 12 seconds of shaking.

INTRODUCTION

Municipal solid waste landfills subjected to strong ground motions may cause severe environmental damages or possess various risks, such as groundwater and soil contamination, threat of human lives or damage to operational facilities. The paper presents the results of stability analyses of Municipal Solid Waste (MSW) landfill slopes in Kyrgyzstan with the consideration of strong ground motion that were carried out under the NISMIST project. One of the objectives of the project NISMIST is the analysis of the dynamic behaviors of municipal solid waste landfills in the seismically active regions of the New Independent States (NIS) of Central Asia.

Bishkek landfill

Bishkek landfill is situated in the northern part of the Chu River valley and about 15 km away from the Bishkek city at a former brickworks site. Bishkek region lies on the north central of Kyrgyzstan, bordered by the northern foot of the North Tien Shan Mountains often considered as one of the seismically most active region of Central Asia. The landfill site is located on foothill plain at an elevation of 725 - 800 m above mean sea level.

SITE INVESTIGATION

The site investigation consists of boreholes, geotechnical laboratory tests and geophysical tests in field. Figure 1 shows the geological setting of the Bishkek landfill site. In addition to the boreholes, the geophysical investigation of the land fill site is also carried out using the ambient noise technique. This investigation was aimed to evaluate some dynamic characteristics of waste and loess deposits. Both disturbed and undisturbed soil samples were taken to the laboratory and various soil properties were determined. Shear tests and triaxial consolidation tests were also conducted. The basic soil parameters at the landfill sites are presented in tables 1 and 2. Table 1 shows the test results for both soil layers of the landfill. Table 2 shows the soil parameters used in the analysis. The values in Table 2 are taken from Table 1 as well as from Literature. Test results which are far from truth are ignored. According the USCS (Unified Soil Classification System), the loess is ML.

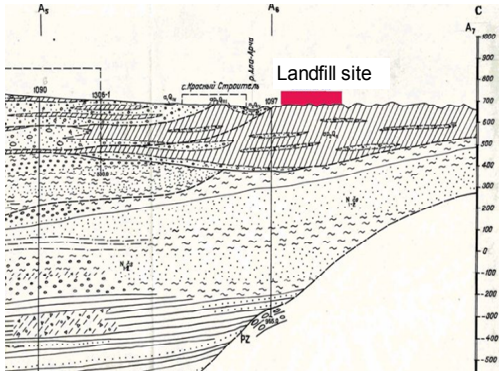

FIG. 1. Geological setting of Bishkek landfill

Table 1. Basic soil parameters of landfill site

Soil parameters	Units	Bishkek landfill site
Density (Natural condition)	(kN/m³)	15.0-16.2
Density (saturated condition)	(kN/m³)	N.A.
Porosity at usual loading (n)	-	0.83-0.92
Moisture content (ω)	(%)	9-13
Liquid limit	(%)	26.5-27.7
Plastic limit	(%)	18.5-19.5
Natural compressibility	(1/kPa)	< 6
Compressibility at saturated condition	(1/kPa)	6-80
Shear strength	(kPa)	8.5
Friction angle (ϕ)	(°)	21-27
Cohesion (c)	(kPa)	2-6

Table 2. Characteristic soil parameters used in dynamic analysis

Soil parameters	Bishkek landfill site	
	Waste	Loess
E (MPa)	8.5	10
Poisson's ratio ν	0.3	0.4
Density (kg/m^3)	750	1650
Cohesion c (kPa)	10	14
Friction angle φ (°)	23	20

DYNAMIC ANALYSIS USING NUMERICAL MODELING

The dynamic analysis of landfills can be performed using different numerical methods. Here the analysis is performed using the FLAC3D and QUAKE/W software.

FLAC3D (Fast Lagrangian Analysis of Continua in three dimension) is a three-dimensional explicit finite-difference program. FLAC3D simulates the behavior of three-dimensional structures built of soil, rock or other materials that undergo plastic flow when their yield limits are exceeded.

QUAKE/W is the part of the software GeoStudio. GeoStudio applications can be used to model almost any geotechnical problem. QUAKE/W is a geotechnical finite element program for the analysis of earth structures.

The landfill is modeled using the equivalent linear elastic in the case of the QUAKE/W and equivalent non linear model was used in the case of FLAC3D. The shear modulus reduction and damping coefficient curves for both soils are defined while executing the dynamic analysis in both programs. The Sigmoidal hysteretic damping with three parameters is used in the FLAC analysis. The parameters indicated in the Table 2 are some of the many used.

FLAC3D modeling

FLAC3D is used here to estimate the response of these existing landfill subjected to an earthquake with a peak ground acceleration (PGA) value of 0.5g.

The model of the Bishkek landfill grid consists of two block groups namely loess (soil) and waste (landfill) as shown in Figure 2. The loess layer has a uniform thickness of 30 meters. The x-displacements and z-displacements of the Bishkek landfill are shown in Figures 3 and 4. The faces at the boundaries of the model represent the free-field boundaries used in the dynamic analysis.

A maximum displacement of 1.6 m is expected in the x-direction at the bottom of the slope of the landfill. The calculations stopped after 12 seconds of the total 16 seconds shaking because of the unacceptable mesh distortion. The analysis shows that the slope is considered to be instable after 12 seconds under the assumed PGA of 0.5g. A maximum settlement of 1 m occurred in the middle of the modelled landfill body.

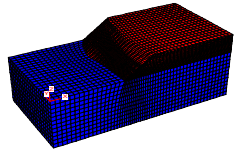

FIG. 2. Geometry of Bishkek landfill with the strata from top to bottom: waste (top), loess (bottom)

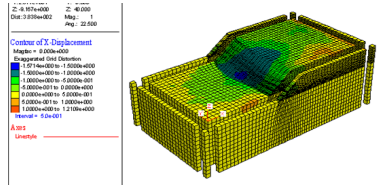

FIG. 3. Displacements of Bishkek landfill in the x-direction.

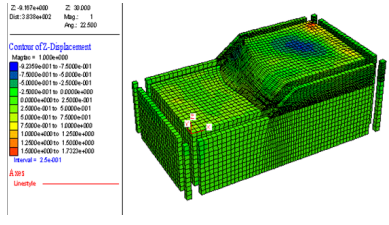

FIG. 4. Displacements of Bishkek landfill in the z-direction.

QUAKE/W Modeling

The earthquake record used in QUAKE/W is same as that used in FLAC3D modelling. The same material properties are used in the analysis as in FLAC3D analysis. Figure 5 shows the finite element mesh together with the boundary conditions of Bishkek landfill. Figure 6 shows the distorted model of the Bishkek landfill.

FIG. 5. Finite element mesh and boundary conditions of Bishkek landfill.

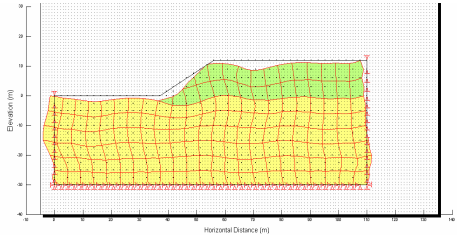

FIG. 6. The distorted model of Bishkek landfill.

The maximum displacement in x-direction at the bottom of the landfill is 1.8 cm. The maximum settlement of 1.7 cm occurred at the middle of the modelled landfill body. Moreover, the amplification or attenuation characteristics of the soil and waste layers were also investigated. Figure 7 and Figure 8 show the acceleration amplitude for the top (red line) and the bottom (black line) of the waste material and loess material respectively.

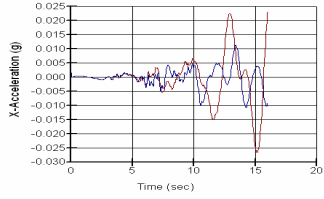

FIG. 7. Acceleration histories at the top (red line) and at the bottom (blue line) of the wastes at Bishkek landfill.

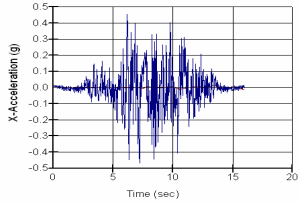

FIG. 8. Acceleration histories at the top (red line) and at the bottom (blue line) of the loess deposits of Bishkek landfill.

From the above figures, it can be concluded that the loess material attenuates the input motions whereas the waste material amplifies the input motions. Moreover, a factor of safety of 1.3 is resulted from the analysis. This means the landfill slope will not fail in case of an earthquake having an equivalent magnitude 0.5g (PGA).

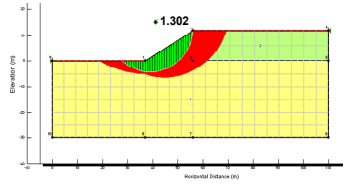

FIG. 9. A factor of safety calculation of the Bishkek landfill.

The dynamic analysis of the landfill from the QUAKE/W shows a stable condition using the factor of safety of 1.0 as reference for failure. The reason for this small reference value is the soil strength parameters of the waste used in the calculations are reduced significantly. In fact this can be also seen from the maximum displacements obtained from this calculation. They are in the order of *cm* that does not violate the serviceability of the landfill.

However, large displacement values in the order of meters were obtained from the FLAC3D calculations. Moreover, the failure of the slope occurred at the 12th second.

The basic difference for the results of the two codes is attributed from the difference in the material modeling (equivalent linear elastic in the case of QUAKE/W and equivalent non-linear in the case of FLAC3D) and the analysis used (2-D in the case of the QUAKE/W and 3-D in the case of the FLAC3D). And as the modeling used in the FLAC3D analysis are close to reality, the landfill is prone to failure when there is occurs an earthquake of similar magnitude.

CONCLUSIONS

The results of dynamic analysis using QUAKE/W and FLAC3D are quite similar except the displacement magnitudes, which show significant variations. This could be because QUAKE/W uses equivalent linear material behaviour whereas FLAC3D handles the problem using the equivalent non-linear material behaviour. Therefore, the values of the displacements obtained from FLAC3D analysis are considered to be more realistic. The basic findings from the numerical analysis of landfills are:

- There is considerable plastic flow of the landfill material with FLAC3D.
- The results showed that the input acceleration is significantly attenuated by the soil layer immediate to the input level and the attenuated response is amplified by the waste material.
- Both analyses showed maximum displacements starting from 12 seconds of the input motion.
- The Bishkek landfill can withstand an earthquake magnitude of 0.5g (PGA).
- As the results of the analyses show, remedial measurements are required in case of large earthquakes.

ACKNOWLEDGMENTS

The NISMIST project (Contract 516732) is funded by the EU Sixth Framework Program within the International Cooperation (INCO) especially for Russia and New Independent States (Call identifier FP6-2003-INCO-Russia + NIS-1). The first author wishes to thank Otto Pregl Foundation for Geotechnical Fundamental Research for the generous financial support.

REFERENCES

Anderson, D.G. and Kavazanjian, Jr. E. (1995). "Performance of Landfills Under Seismic Loading" *Proceedings of the Third International Conference on Recent Advances in Geotechnical Earthquake Engineering and Soil Dynamics*, University of Missouri-Rolla, Vol. 3, St. Louis, Missouri, USA, p. 277-306.

Bray, J.D. Rathje, E.M., Augello, A.J. and Merry, S.M. (1998). "Simplified Seismic Design Procedure for Geosynthetic-Lined, Solid-Waste Landfills" *Geosynthetics International*, Vol. 5, Nos. 1-2, p. 203-235.

Kavazanjian, E. Jr. and Matasovic, N. (1995). "Seismic analysis of solid waste landfills." *Proceedings, Geoenvironment* 2000, ASCE specialty conference, New Orleans, Louisiana.

Makdisi, F.I. and Seed, H.B. (1978). "Simplified Procedure for Estimating Dam and Embankment Earthquake-Induced Deformation." J*ournal of the Geotechnical Engineering Division*, Vol. 104, No. GT7, p. 849-867.

Thusyanthan, N.I., Madabhushi, S.P.G., Singh, S., Haigh, S. and Brennan, A. (2004). "Seismic behaviour of Municipal Solid Waste (MSW) landfills" *13th World Conference on Earthquake Engineering Vancouver*, B.C., Canada, August 1-6, Paper No. 2702.

Different Failure Modes of a Clay Foundation-embankment System Corresponding to Different Incident Seismic Waves

Kentaro NAKAI[1], Toshihiro NODA[2] and Akira ASAOKA[3]

[1] Assistant Professor, Department of Civil Engineering, Nagoya University, Furo, Chikusa, Nagoya, JAPAN, 464-8603; nakai@civil.nagoya-u.ac.jp
[2] Professor, Department of Civil Engineering, Nagoya University, Furo, Chikusa, Nagoya, JAPAN, 464-8603; noda@civil.nagoya-u.ac.jp
[3] Professor, Department of Civil Engineering, Nagoya University, Furo, Chikusa, Nagoya, JAPAN, 464-8603; asaoka@civil.nagoya-u.ac.jp

ABSTRACT: In recent years, damage to embankments from earthquakes has been frequently reported. In this paper, the deformation and failure behavior of an embankment constructed on a weak clay foundation during and after an earthquake is investigated using numerical analysis, ***GEOASIA***, assuming a 40 g centrifugal field. The main conclusions obtained were as follows. 1) Although the embankment remained stable without large deformation during the earthquake, a slip plane subsequently penetrated through the embankment, resulting in delayed failure (circular arc slip). 2) The deformation behavior (failure mode) of the foundation and embankment varies greatly depending on the characteristics of the incident seismic motions.

INTRODUCTION

In recent years, damage to embankments and embankment-foundation systems resulting from earthquakes has been frequently reported. Attention to earthquake damage tends to be focused on liquefaction of sandy foundations, but large deformation and unstable behavior during and after earthquakes has been observed many times in weak clay foundations. The main methods for understanding the behavior in an earthquake are model tests and numerical analysis. However, there are many problems with model tests, such as it is not being possible to produce foundations with a developed skeletal structure as in naturally deposited foundations and the effects of the side walls of the test containers, particle size, and time scales for vibration and water seepage phenomena not scaling properly, so it is comparatively difficult to evaluate the validity of the solutions of numerical analyses. By using model tests with clear initial conditions and boundary conditions as verification data for numerical analysis, more accurate modeling is possible.

To date, the authors have simulated the results of centrifugal model tests of foundation–embankment systems conducted at 40g centrifugal field, using the analysis

program ***GEOASIA*** (Asaoka et al., 2002, Noda et al., 2008) and evaluated and verified the reliability of the program and the validity of the material constants set for the foundations and initial and boundary conditions by comparing the results obtained from tests and analyses (Nakai et al., 2009). The objective of this paper is to investigate by numerical analysis the deformation and failure behavior of a foundation during and after an earthquake, assuming the foundation soil is very weak clay and leaving all other analysis conditions except the initial conditions of the foundation soil unchanged. In particular, 2 different types of seismic wave were input, and the deformation behavior of the foundation–embankment system was compared. ***GEOASIA*** carries out static or dynamic coupled water–soil finite deformation analysis (Noda et al., 2008) and uses the SYS Cam-clay model (Asaoka et al., 2002) as the constitutive model for the soil skeleton. This constitutive model is capable of describing sands and clays as well as intermediate soils that are mixtures of the two within the same theoretical framework using the skeletal structure (structure, overconsolidation, anisotropy) of the soil and the differences in its behavior.

ANALYSIS CONDITIONS

The analysis conditions were all determined by reference to centrifugal model tests (for details, refer to Nakai et al., 2009). The analysis was carried out assuming a 40 g gravitational field, but all analysis results, etc., are shown as values converted to the actual scale in a 1 g field. **Fig. 1** shows the finite element mesh before input of the earthquake. The foundation was 10 m high (8 m of clay, 2 m of sand) and 80 m long, and the soil was assumed to be uniform in the horizontal direction. The embankment was 11 m wide and 6 m high at the crest and had a 1:1.5 slope at the bottom. It was constructed by adding the separately created embankment (water-soil two-phase elasto-plastic finite elements) on top of the saturated clay foundation all at once and was treated as a saturated soil. The water pressure at the top surfaces of the foundation and the embankment was always zero (atmospheric pressure condition), and the side and bottom surfaces were set as undrained boundaries.

The earthquake motions were as in model tests using a fixed soil tank, so the accelerations shown in **Fig. 2** were input in the horizontal direction to all finite element nodes on the side and bottom surfaces, and the calculations were continued until the settlement converged.

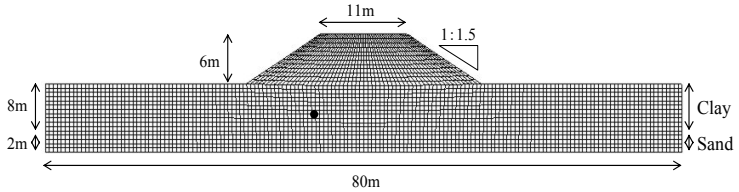

Fig. 1 Finite element mesh after embankment construction

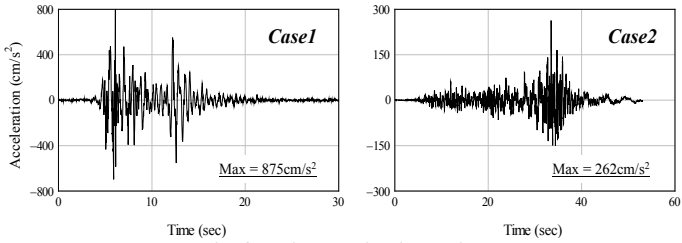

Fig. 2 Incident seismic motions

Table 1 shows the elasto-plastic properties of each layer used in the analysis immediately after construction of the embankment (material constants and initial values). The embankment was an intermediate soil that was a mixture of sand and clay, and the degree of compaction was assumed to be approximately 90%. Actually embankment soil is in a partially unsaturated condition, but in the case of numerical analysis, embankment was assumed to be completely saturated. So, the soil particle density was converted to smaller value so as the embankment load becomes equivalent to the actual embankment. The structure of the upper clay layer was assumed to be very highly developed and weak, and the lower sand layer was assumed to be very dense.

Table 1 Elasto-plastic properties used in the analysis

	Embankment	Clay	Sand
Elasto-plastic parameters			
Critical state index M	0.75	1.10	1.00
NCL intercept N	1.88	1.612	2.00
Compression index $\tilde{\lambda}$	0.052	0.060	0.050
Swelling indes $\tilde{\kappa}$	0.008	0.025	0.012
Poisson's ratio ν	0.20	0.30	0.30
Evolution parameters			
Degradation index of structure a ($b=c=1.0$)	0.8	0.8	2.0
Ratio of $-D_v^p$ to $\|D_s^p\|$ c_s	0.65	0.3	1.0
Degradation index of OC m	0.028	1.2	0.06
Rotational hardening index br	30.0	0.001	3.5
Limitation of rotational hardening m_b	0.96	1.0	0.7
Soil particle density ρ_s (g/cm3)	2.30	2.754	2.60
Mass permeability index k (cm/s)	2.0×10^{-3}	2.0×10^{-7}	1.0×10^{-3}
Initial conditions			
specific volume v_0	1.70	1.77	1.70
stress ratio η_0	0.30	0.43	0.55
degree of structure $1/R^*_0$	1.30	30.0	1.00
degree of Overconsolidation $1/R_0$	2000 ～ 7500	1.8 ～ 22.7	2900 ～ 3200
degree of anisotropy ζ_0	0.30	0.43	0.55

ANALYSIS RESULTS

Delayed failure behavior after the earthquake

Fig. 3 shows the distribution of shear strain right before the earthquake, 60 seconds and 10 hours after start of the earthquake, and after convergence of the consolidation settlement when inputting the Case 1 seismic wave. During the earthquake, shear strains are generated in the clay layer directly below the embankment and are particularly large at the boundary with the sand layer. On the other hand, it can be seen that the shear strain within the embankment is small. After the earthquake, shear strain gradually develops in the clay layer directly below the embankment and eventually extends to the embankment. At about 10 hours after start of the earthquake, the shear strain extending from the clay foundation penetrates to the crest of the embankment, and at the same time, a circular arc slip failure occurs in the embankment. **Fig. 4** shows the mean effective stress distributions for the same time points shown in **Fig. 3**. After the earthquake, the mean effective stress in areas without an embankment is reduced, but near the boundary between the embankment and the clay layer, the mean effective stress increases (some negative pressure is generated). This gradually dissipates after the earthquake, but ultimately a discontinuity occurs in the clay layer on both sides of the area of the circular arc slip.

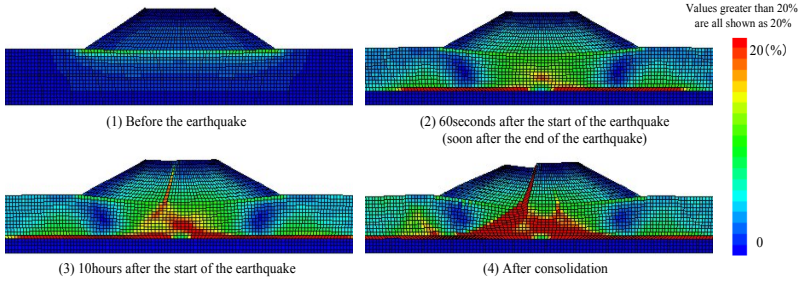

Fig. 3 Shear strain distribution (Case 1)

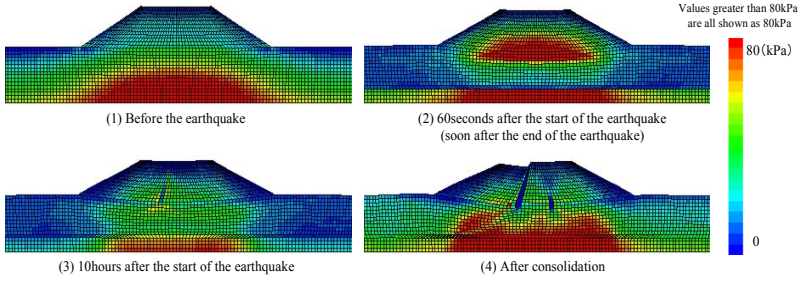

Fig. 4 Mean effective stress distribution (Case 1)

Fig. 5 shows the behavior of a soil element (in **Fig. 1**, ●) near the slip surface in the clay layer. This soil element maintains a highly developed structure and preserves the stress state on the outside of the normally consolidated line (NCL). After start of the earthquake, the mean effective stress initially increases along with repetitions of "hardening associated with elasto-plastic swelling" and unloading. The mean effective stress then decreases along with repetitions of "hardening associated with plastic compression" and unloading. After the earthquake, the compression hardening indicated by (a→b) initially changes to "softening associated with plastic expansion" (b→c) as a result of occurrence of plastic expansion due to dissipation of overconsolidation and reduction of the hardening/softening boundary line Ms; this results in s M > η . As a result of this water absorption and softening in the clay layer, the shear strain extends and causes the occurrence of a circular arc slip that penetrates into the embankment.

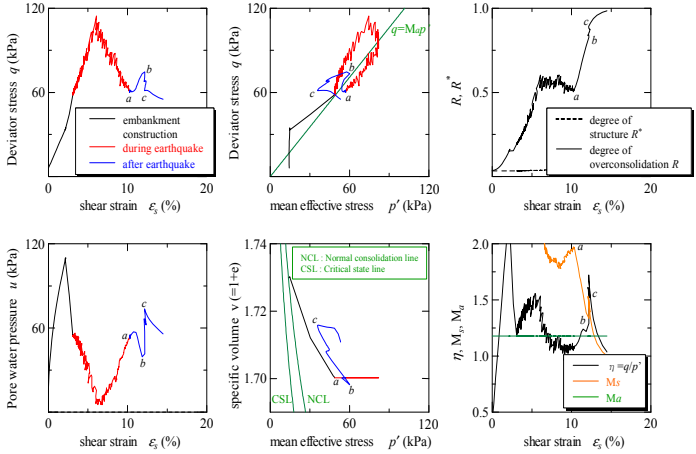

Fig. 5 Behavior of clay element directly below the embankment

Effect of differences in the seismic wave on the deformation behavior of the foundation–embankment system

Fig. 6 shows the distribution of shear strain right before the earthquake, 60 seconds, 8 hours, and 15 hours after start of the earthquake, and after convergence of the consolidation settlement when inputting the Case 2 seismic wave. With the Case 1 seismic wave, a single slip occurred on the left side of the embankment, but with the Case 2 seismic wave, after a slip occurred on the right side of the embankment, a further slip failure extended to the left side in a circular arc form. This suggests that the foundation and embankment deformation behavior (failure mode) varies greatly depending on the characteristics of the incident seismic motions.

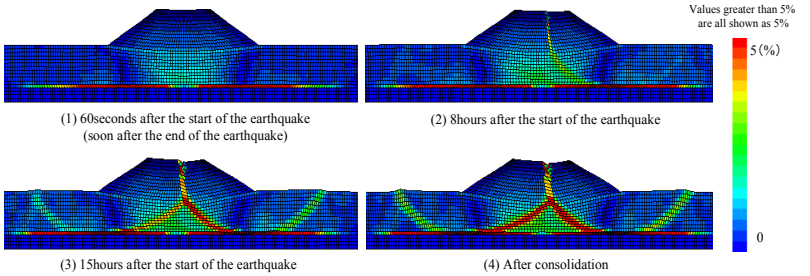

Fig. 6 Shear strain distribution (Case 2)

CONCLUSIONS

The behavior of an hypothetical embankment built on a weak clay foundation was investigated during and after an earthquake by simulating centrifugal model tests by numerical analysis using ***GEOASIA***. The conclusions obtained were as follows.

1) Although the embankment remained stable without large deformation during the earthquake, shear strain extended due to softening associated with plastic expansion caused by dissipation of overconsolidation after the earthquake, and a slip plane subsequently penetrated through the embankment, causing delayed failure (circular arc slip).
2) The deformation behavior (failure mode) of the foundation and embankment varies greatly, especially after the earthquake, depending on the characteristics of the incident seismic motions.

ACKNOWLEDGMENTS

This work was supported by JSPS, KAKENHI (Grant-in-Aid for Scientific Research (S):21226012).

REFERENCES

Asaoka, A., Noda, T., Yamada, E., Kaneda, K. and Nakano, M. (2002). "An elasto-plastic description of two distinct volume change mechanisms of soils" *Soils and Foundations*, Vol. 42(5): 47-57.

Noda, T., Asaoka, A. and Nakano, M. (2008). "Soil-water coupled finite deformation analysis based on a rate-type equation of motion incorporating the SYS Cam-clay model" *Soils and Foundations*, Vol. 48(6): 771-790.

Noda, T., Nakai, K. and Asaoka, A. (2008). "Delayed failure of a clay foundation-embankment system after the occurrence of an earthquake" *Theoretical and applied mechanics JAPAN*, Vol.57: 41-47.

Nakai, K., Noda, T. and Asaoka, A. (2009). "Numerical simulation of centrifugal model tests on seismic response of embankment-foundation system" *Proc. of 4th International Workshop on New Frontiers in Computational Geomechanics (IWS-Pittsburgh 2008)*, 29-32.

Numerical Investigation into the Arrangement of Clay Core on the Seismic Performance of Earth Dams

Tensay G. Berhe[1], Xue-tao Wang[2] and W. Wu[3].

[1]Doctor, Institute of Geotechnical Engineering, BOKU, A-1180 Vienna, Feistmantel strasse 4; tensay@engineer.com
[2]Doctor, Institute of Geotechnical Engineering, BOKU, A-1180 Vienna, Feistmantel strasse 4; xuetao.wang@boku.ac.at
[3]Professor, Institute of Geotechnical Engineering, BOKU, A-1180 Wien, Feistmantel strasse 4; wei.wu@boku.ac.at

ABSTRACT: During earthquakes, the materials of earthfill dams undergo significant changes in their properties. These modified properties of the soil affect the stability of the dam. The most severe situation is dam failure due to liquefaction of the granular soils in the shoulders. The development of liquefaction is directly related to the excess porewater pressure that would develop during earthquake shaking. The generation and dissipation of excess porewater pressure is a phenomenon that depends on the drainage possibility and length of drainage path. Therefore, with some modifications on the slope of the dam, the clay core can assume different arrangements. These arrangements modify the seismic response of the dam. Numerical codes are useful tools to investigate the safety of dams in seismic prone areas. In this paper FLAC3D numerical tool is used. The influence of the arrangement of the clay cores of the dam on the development of porewater pressure and crest settlement of earthen dams, and hence seismic performance of earthen dams is investigated. Based on the numerical investigations, the performance of earthfill dams increases with increase in the angle of inclination of the center line of the core from the vertical towards the upstream. So the arrangements of the clay core for dams in seismic areas can be taken as one design criteria during earthfill dam design.

INTRODUCTION

During earthquakes, the soil materials of earth dams undergo significant changes in their properties. These modifications in the mechanical and hydraulic properties of the soil in turn affect the stability of the dam. In fact Seed et al. (1978) reported that the seismic performance of earthfill dams is well and the dam can render the service intended for after earthquake. However, they indicated that seismic performance of the dam fails when the dam contains liquefiable materials inside and /or when the dam is founded on liquefiable stratum. One cause for dam failure is failure due to liquefaction of the

granular soils in the shoulders. The development of liquefaction is directly related to the excess porewater pressure that would develop during earthquake shaking. And the generation and dissipation of excess porewater pressure is a phenomenon that depends on the drainage possibility and length of drainage path. Usually, the arrangement of the core of earthfill dams is vertical as shown in FIG.1. And an earthfill dam failure during earthquake concentrates on the upstream portion of the dam as shown in FIG. 2. This is so because the long drainage path does not allow the excess porewater pressure generated to dissipate soon. Therefore, with some modifications on the slopes of the dam, the clay core in the dam can assume different arrangements that can make the drainage path to shorten. These arrangements will alter the seismic performance of the dam.

This paper presents a numerical study that investigates the influence of the arrangement of the clay cores of the dam on its seismic performance. Based on the numerical analysis, design recommendation for the arrangements of the impervious cores for dams in seismic prone areas is obtained.

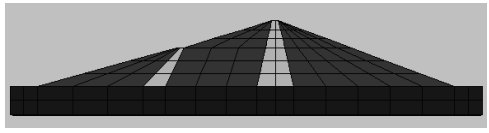

FIG.1. Earthfill dam with clay core placed vertical.

FIG. 2. Typical earthfill dam failure during earthquake.

STATEMENT OF THE PROBLEM

This study deals with the effect of the arrangement of the clay core on development of the porewater pressure and hence the seismic performance of earth dams. The inclination of the clay core is varied from perfectly vertical to totally leaning along with the upstream slope of the dam.

Constitutive model

The seismic concern of an earthfill dam is the development of large displacement that could endanger the safety and serviceability of the dam. For the calculation of these displacements, a 3D finite difference modeling FLAC3D is used during the dynamic analyses. The behaviors of the geomaterials are described by an elastic-plastic

constitutive model.

Numerical Model

The numerical analyses are conducted using the finite difference program FLAC3D. This program is based on a continuum finite difference discretization using the Langrangian approach (FLAC3D, 2005), [1]. In here, the equations of motion are derived for a continuum media and the equations of motion are used to obtain the velocities and displacements from stresses and forces. The strain rates are then calculated according to the new nodal velocities in each element.
To analyze the problem, the strain-rate tensor and rotation rate tensor can be written as follows:

$$\xi_{ij} = \frac{1}{2}\left(v_{i,j} + v_{j,i}\right) \text{ and } \omega_{ij} = \frac{1}{2}\left(v_{i,j} - v_{j,i}\right) \quad (1)$$

where v_i is the deformation velocity and $v_{i,j}$ is the velocity gradient. The equation of motion is written as:

$$\sigma_{ij,j} + \rho b_i = \rho \frac{dv_i}{dt} \quad (2)$$

The elastic-plastic constitutive equation can be written out in general as, [1]:

$$\Delta\breve{\sigma}_{ij} + \alpha\Delta p\delta_{ij} = H_{ij}^{*}(\sigma_{ij}, \Delta\varepsilon_{ij}) \quad (3)$$

$$\breve{\sigma}_{ij} = H_{ij}\left(\sigma_{ij}, \xi_{ij}, \kappa\right) \quad (4)$$

Where $\breve{\sigma}_{ij}$ is the co-rotational stress-rate tensor, H_{ij} is the constitutive function, and κ is a parameter, which takes into account the loading history. The co-rotational stress rate tensor is defined as follows

$$\breve{\sigma}_{ij} = \frac{d\sigma_{ij}}{dt} - \omega_{ik}\sigma_{kj} + \sigma_{ik}\omega_{kj} \quad (5)$$

$\frac{d\sigma_{ij}}{dt}$ is the material time derivative of σ.
The above equations are solved by finite difference method. A coupled calculation with dynamic groundwater flow is performed to determine the excess pore pressure. Regarding the mechanism of porewater pressure generation, an empirical equation that relates the increment of volume decrease, $\Delta\varepsilon_{vd}$ to the cyclic shear-strain amplitude, γ, and accumulated irreversible volume strain , ε_{vd} is used (Byrne 1991), [3]

$$\frac{\Delta\varepsilon_{vd}}{\gamma} = C_1 \exp\left(-C_2\left(\frac{\varepsilon_{vd}}{\gamma}\right)\right) \tag{6}$$

where C_1 and C_2 are material parameters, which vary according to the sand type.

The dynamic loading is applied at the base of the foundation layer as an acceleration time history. The frequency content of the input motion and the velocity of the propagating waves affect the accuracy of the numerical solutions. For appropriate wave propagation through an element, the maximum element size, Δx_{max} has to be smaller than one-tenth to one-eighth of the wave length, λ. This wave length corresponds to the highest frequency component, f, that contains appreciable energy of the input motion. This is according to the recommendation by Kuhlemeyer and Lysmer (1973). Therefore $\Delta x_{max} \leq \lambda/10$ is used in this study. From the seismic record analysis, the highest angular frequency of the input motion is about 15 rad/sec. Accordingly, the grid size or element size for the different materials of the dam body and the foundation are determined.

The Free-Field Boundaries are used to absorb the outward waves originating from the structure. This system of boundary condition involves the execution of free-field calculations in parallel with the main-grid analysis. The lateral boundaries of the main grid are coupled to the free-field grid by viscous dashpots to simulate a quiet boundary and the sigmoidal hysteretic damping is used in the analyses for the energy dissipation through the medium.

Material parameters

The dynamic properties used in this work are taken from Seed et al. (1986), [2]. Except for the lake deposit, the maximum shear modulus of all materials is considered to vary with the mean effective stress according to the formula $G_{max} = 218.7\ K_{2max}(\sigma_m')^{0.5}$ and for the lake deposit $G_{max} = \rho V_s^2$ with the shear wave velocity V_s=1km/sec and the coefficient K_{2max} depends on soil type. The materials that are assumed to liquefy are modeled with the constitutive model proposed by Finn. The other materials are modeled with the Mohr-Coulomb constitutive model. The shear strength envelope is specified by friction angle and cohesion.

Seismic Loading

The earth dam is subjected to the acceleration time history, ATH of the commonly used earthquake, El Centro (California). The base line correction and filtering of this ATH is done and the peak ground acceleration, PGA is scaled to a magnitude of 0.3g. This modified and scaled ATH is then applied at the base of the model.

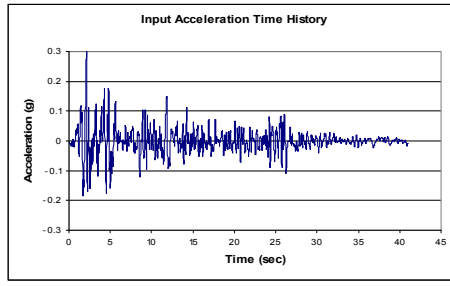

FIG. 3. Modified input acceleration time history.

Dynamic analysis results

The numerical model outlined above has been applied to four different inclination cases of the clay core arrangements as shown in FIG. 4. The dynamic analysis is carried out for the horizontal El Centro earthquake scaled to 0.3g. The results of which are summarized in this section.

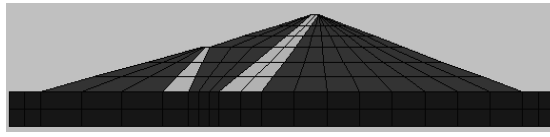

FIG. 4. Earthfill dam with inclined clay core.

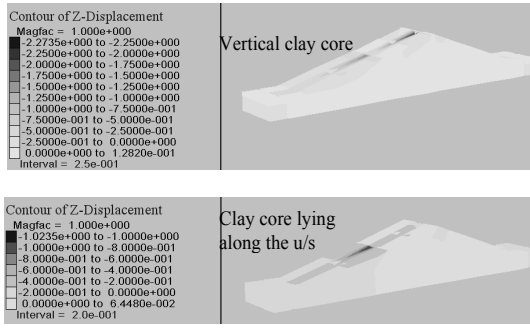

FIG. 5. Crest settlement contour for two of the four cases.

Table 1. Comparison of the predicted crest settlement for the different cases

Arrangement of clay core	Crest settlement (m) (from history node)	Predicted maximum settlement (m).
Vertical (0^0)	-2.27	-2.28
Inclined at 20^0 from the vertical	-1.79	-1.80
Inclined at 45^0 from the vertical	-1.03	-1.50
Resting along the u/s face ($\leq 63^0$)	-0.19	-1.02

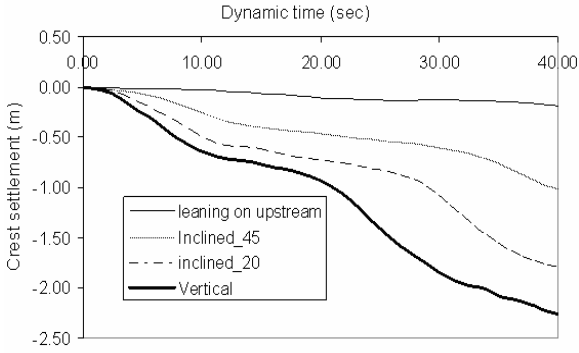

FIG. 6. Crest settlement as function of time for different core arrangements.

As it can be seen in Table 1 and FIG. 6, the magnitude of the crest settlement goes on decreasing with the inclination of the clay core.

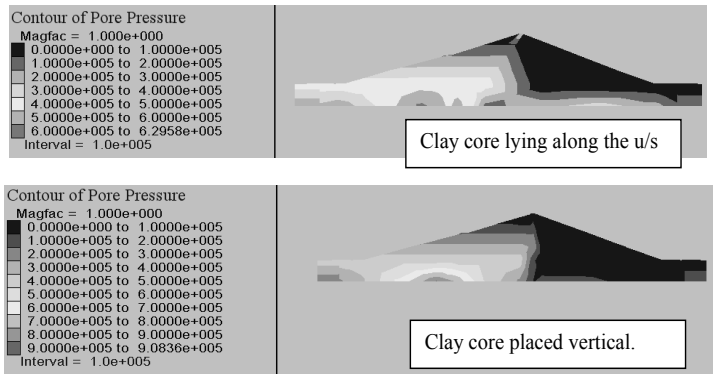

FIG. 7. Typical porewater pressure contour for two of the four cases.

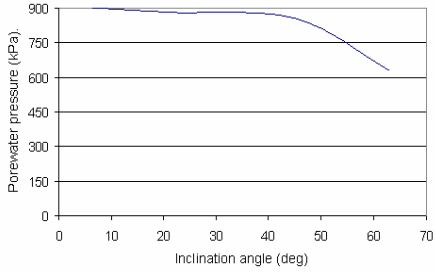

FIG. 8. Max. porewater pressure versus the angle of the impervious clay core.

Moreover, the magnitude of the porewater pressure goes on decreasing with the inclination of the clay core this is shown in FIG. 8.

CONCLUSIONS

In this paper the porewater pressure distribution and the crest settlement are taken as a safety criterion regarding the seismic performance of dams. Based on these criteria and the analysis results obtained, the following conclusions are drawn.

1. The excessive deformation of the shell material in the upstream could be reduced by using inclined core clay towards the upstream rather than the vertical arrangement of the clay core.
2. The magnitude of the excess pore water pressure generated on the upstream can be reduced by using core clay towards the upstream.
3. In general, the seismic performance of the specific earthfill dam considered increases as the impervious clay core is aligned towards the upstream face of the dam. Therefore, the location of the clay core with in the dam can be considered as a design criteria for earthfill dams in seismic prone areas.

ACKNOWLEDGMENTS

The first author wishes to thank Otto Pregl Foundation for Geotechnical Fundamental Research for the generous financial support.

REFERENCES

Itasca Consulting Group, Inc. (2005). “FLAC3D- Fast Lagrangian Analysis of Continua in 3 Dimensions, version 3.0.” Minapealis, Minnesota.

Bull, J.W. (1994). “Soil-structure Interaction Numerical Analysis and Modeling.” First edition: E & FN Spon, UK.

Dawson, E.M etal. (2001). “A practical oriented pore-pressure generation model.” In: Billaux et al. (eds), Proc. of the 2nd Int. FLAC Symposium Lyon, France, Balkema,

Rotterdam, pp. 47-54.
ICOLD (1983). “Seismicity and Dam design, International Commission on Large Dams.” Bulletin 45.

Soil-water Coupled Finite Deformation Analysis of Seismic Deformation and Failure of Embankment on Horizontal and Inclined Ground

Masaki NAKANO[1], Takayuki SAKAI[2], Toshihiro NODA[3]and Akira ASAOKA[4]

[1]Professor, Department of civil engineering, Nagoya University, Chikusa, Nagoya, 464-8603, JAPAN; nakano@civil.nagoya-u.ac.jp, [2]Graduate student, ditto; t-sakai@soil.civil.nagoya-u.ac.jp, [3] Professor, ditto; noda@civil.nagoya-u.ac.jp, [4] Professor, ditto; asaoka@civil.nagoya-u.ac.jp

ABSTRACT: The Noto Hanto Earthquake in 2007 caused large-scale landslide of 11 embankments in NOTO YURYO road, especially the embankment on inclined ground. In order to clarify the cause of the large-scale landslide of embankment, the laboratory tests on the embankment material, the weathering tuff and the seismic response analysis of the embankment on inclined and horizontal grounds by the static/dynamic soil-water coupled finite deformation analysis code, GEOASIA.

The essential results and conclusions are follows; 1) The unconfined strength dramatically decreases by absorbing water beyond the optimum water content. 2) The landslide of the embankment on inclined ground is caused by migration of porewater during/after the earthquake. The soil element of landslide swells both elastically and plastically with structure upgradation and loss of overconsolidation after the earthquake. 3)The embankment on the horizontal ground does not slide but move a little. The soil element did not swell but consolidate after the earthquake due to the generation of the positive porewater pressure in the center of the embankment during the earthquake.

INTRODUCTION

The Noto Hanto Earthquake in 2007 caused large-scale landslide of 11 embankments in NOTO YURYO road (JSCE and JGS, 2007). The landslide mainly occurs in the embankment on inclined ground, and on the contrary the embankment on horizontal ground or the embankment stabilized by lime even on inclined ground deformed a little.

The objective of this study is to clarify the cause of the large-scale landslide of embankment by the Noto Hanto Earthquake in 2007. Firstly, the physical and mechanical properties of a weathering tuff that is the embankment material in NOTO YURYO road will be comprehended by carrying out the experiments and the computations using SYS Cam-clay model. Secondly, a soil-water coupled finite deformation analysis of seismic deformation and failure of embankment on inclined and horizontal ground by the static/dynamic soil-water coupled finite deformation analysis code(GEOASIA, Asaoka and Noda, 2007; Noda et al., 2008).

PHYSICAL AND MECHANICAL PROPERTIES OF EMBANKMENT

MATERIAL, WEATHERING TUFF

Physical properties of the tuff

Figure 1 shows the grain size distribution curves of the weathering tuff as well as typical clay and sand. The grain size of the tuff sample ranges from more than 10 mm to 10^{-3} mm due to weathering. Therefore, the curve is an intermediate between clay and sand.

Figure 2 shows the compaction curve and the unconfined strength for water content. The optimum water content w_{opt} is 26.6%, which is much less than the natural water content w_n in embankment area. The unconfined strength q_u dramatically decreases by absorbing water beyond the optimum water content w_{opt}. The q_u at the natural water content w_n is 68.2kPa, which is about one third of the q_u at the w_{opt}.

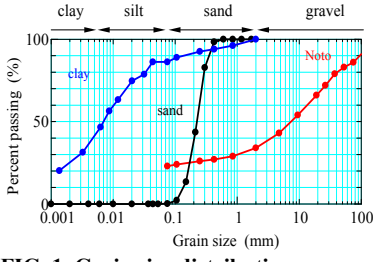

FIG. 1. Grain size distribution

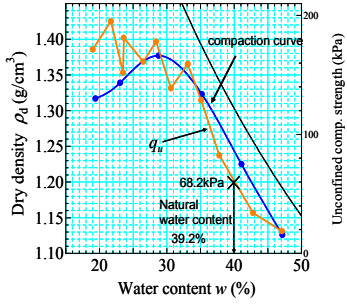

FIG. 2. Compaction curve and q_u

Elasto-plastic interpretation of the mechanical behavior of tuff sample by using SYS Cam-clay model

In order to comprehend the mechanical behavior of the tuff sample, the oedometer test and triaxial compression test were carried out.

Figure 3 shows the triaxial compression test results on the compacted tuff sample and the simulation results by using SYS Cam-clay model (Asaoka et al., 2002). The model describes the mechanical behavior of the natural deposited clays/sands by introducing the concept of the soil skeleton structure (soil structure, overconsolidation and anisotropy). The details of the SYS Cam-clay model can be found in the reference (Asaoka et al., 2002). Figure 4 shows the oedometer test results on the undisturbed tuff sample and its simulation results. The simulation results on both triaxial compression test and oedometer test were in good agreement with the experimental results. The material constants are tabulated in Table 1. Some parameter in Table 1 can also be found in the reference (Asaoka et al., 2002). The evolution parameters mean the action of the soil skeleton structure on the mechanical behavior. The tuff sample used as embankment material can be regarded to be the soil which the decay of soil structure is slow, while the loss of overconsolidation is relatively fast.

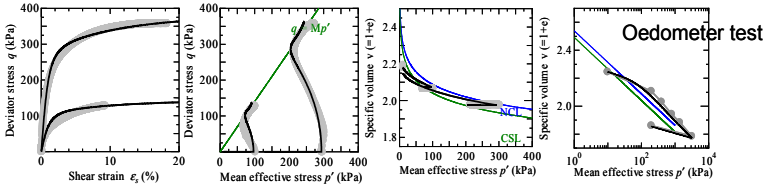

FIG. 3. Triaxial compression and oedometer tests and their simulation results

Table 1. Material Parameters

Elasto-plastic parameters		Evolution rule parameters	
Compression index $\tilde{\lambda}$	0.10	Degradation index of overconsolidation m	1.7
Swelling index $\tilde{\kappa}$	0.03	Degradation index of structure a ($b = c = 1.0$)	0.3
Critical state constant M	1.4	Degradation index of structure c_s	0.1
Specific volume at $q = 0$ and $p' = 98.1$kPa on NCL N	2.09	Evolution index of rotational hardening b_r	0.3
Poisson's ratio ν	0.3	Limit of rotational hardening m_b	0.5

SEISMIC DEFORMATION AND FAILURE ANALYSIS OF EMBANKMENT ON HORIZONTAL AND INCLINED GROUND BY GEOASIA

Calculation conditions and seismic force

The embankments on inclined and horizontal ground were selected as calculation cross-section. For the embankment on inclined ground, large-scale landslide of embankments occurred under the earthquake. The slope gradient of the inclined ground is about 15 degrees. On the contrary, even though the embankment on horizontal ground is near the inclined ground about 40m, the embankment does not slide but move a little.

Figure 5 shows the finite element meshes at the two embankments that were subjected to analysis. The calculations were carried out under the conditions of plane strain over the entire cross-section. The bottom surface was engineering bedrock with a viscous boundary. In addition, the distance to the side surfaces was considered to be sufficient to prevent them from being affected by embankment loading, and they were modeled as periodic boundaries (constant displacement boundaries). The hydraulic boundaries were indicated in Fig.5.

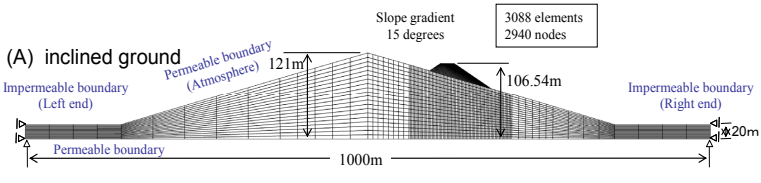

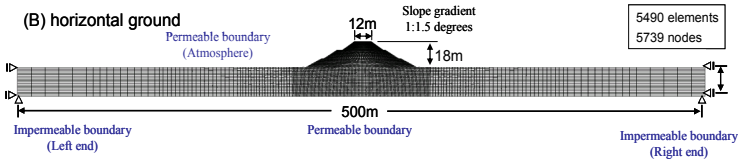

FIG. 5. Finite element mesh with hydraulic boundaries

Table 2 shows the initial conditions for the embankment and soil ground. The ground has the same material constants as the embankment shown in Table 1, because the embankment material was used from the ground. However, the embankment material was disturbed during the construction process and weathered, and therefore the initial condition is different from the one of the ground. As shown in Table 2, the condition of the ground is assumed to be large stiffness.

Table 2. Initial conditions of the embankment and ground

	embankment	ground
Stress ratio η_0	0.55	0.55
Specific volume v_0	2.14	1.60
Degree of structure $1/R_0^*$	7.5	1.2
Degree of anisotropy $\varsigma_0 = \sqrt{3/2\boldsymbol{\beta}_0 \cdot \boldsymbol{\beta}_0}$	0.55	0.55
Soil permeability k (cm/s)	1.0×10^{-7}	1.0×10^{-4}

The seismic input was shown in Fig.6. The amplitude of the seismic input was 0.25 times amplitude of the measured ground surface wave at K-NET Anamizu, which has been set near the embankment calculated in the present study. Through the simulation changing the amplitude of the seismic input, the amplitude ratio of the measured ground surface wave to seismic output was determined. As shown in Fig.7, the seismic output was in good agreement with the measured wave.

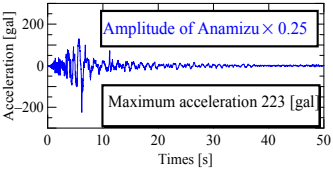

FIG. 6. Seismic input

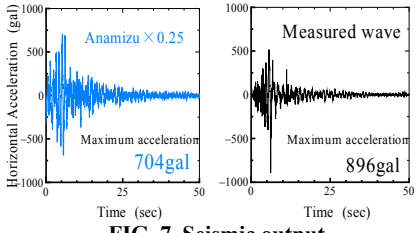

FIG. 7. Seismic output

Seismic deformation and failure of embankment on inclined ground

Figure 8 shows the shear strain after the earthquake. During the earthquake, the shear strain on the boundary between the embankment and the ground dramatically increased to more than 30%. About 2 days after the earthquake, the shear strain developed at the top of the embankment and the sliding surface generated, and the sliding surface was clearly formed in the embankment on 45 days after the earthquake.

Figure 9 shows the behavior of the soil elements at the sliding surface (the circle point). The shear stress of the soil element was large even before the earthquake because the embankment was constructed on the inclined ground. The negative pore pressure generated during the earthquake, and then elastic and plastic swelling with structure upgradation and loss of overconsolidation after the earthquake. In the slip surface, the specific volume increased due to the swelling and the strength decrease in the slip surface, and finally large-scale landslide occurred in the embankment.

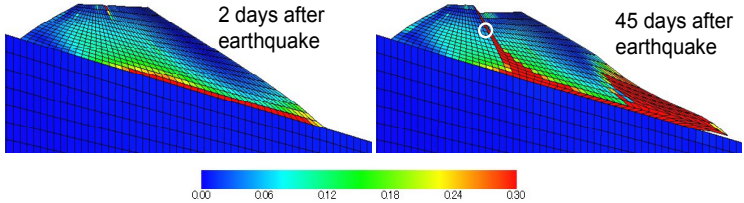

FIG. 8. Shear strain distribution

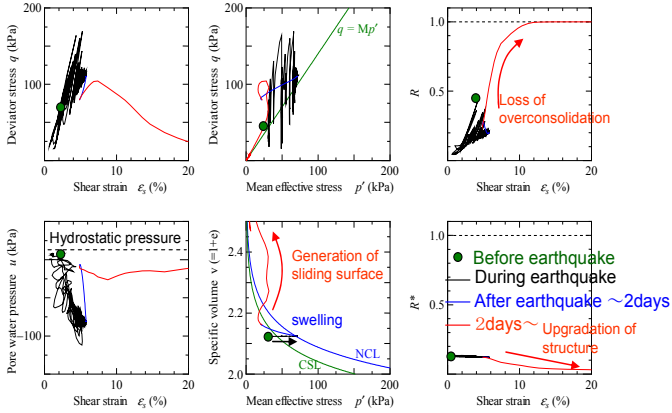

FIG. 9. Element behavior (Inclined ground)

Seismic deformation and failure of embankment on horizontal ground

The embankment on the horizontal ground does not slide but move a little. Figure 10 shows the behavior of the soil elements at the center of the embankment. The shear stress of the soil element was not large before the earthquake. The positive pore pressure generated during the earthquake, and therefore the consolidation progressed after the earthquake. That is the reason why the embankment did not failure.

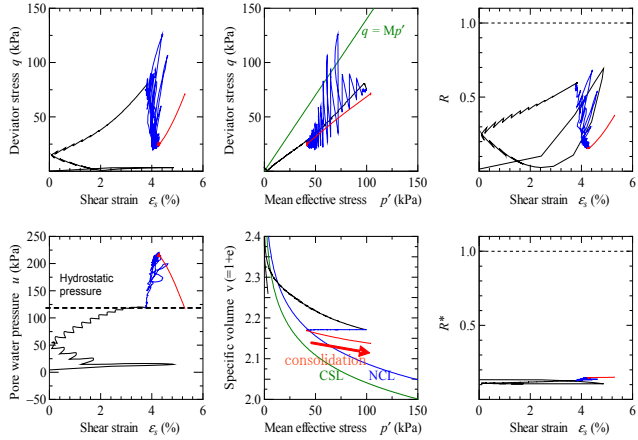

FIG.10. Element behavior (Horizontal ground)

CONCLUSIONS

The essential results and conclusions are follows; 1) The unconfined strength dramatically decreases by absorbing water beyond the optimum water content. 2) The landslide of the embankment on inclined ground is caused by porewater migration during/after the earthquake. The soil element of landslide swells both elastically/plastically with structure upgradation and loss of overconsolidation, and exhibits softening. 3)The embankment on the horizontal ground does not slide but move a little. The soil element of embankment is consolidated after the earthquake.

ACKNOWLEDGMENTS

This work was supported by JSPS, KAKENHI (21226012).

REFERENCES

JSCE and JGS (2007) "The Noto Hanto Earthquake in 2007 damage investigation report."

Asaoka, A., Noda, T., Yamada, E., Kaneda, K. and Nakano, M. (2002). "An elasto-plastic description of two distinct volume change mechanisms of soils." *Soils and Foundations*, Vol. 42(5): 47-57.

Asaoka, A. and Noda, T. (2007). "All soils all states all round geo-analysis integration." *Int. Workshop on Constitutive Modelling - Development, Implementation, Evaluation, and Application*, Hong Kong, China: 11-27.

Noda, T., Asaoka, A. and Nakano, M. (2008). "Soil-water coupled finite deformation analysis based on a rate-type equation of motion incorporating the SYS Cam-clay model." *Soils and Foundations*, Vol. 48(6):771-790.

Deformation Analyses of River Dike on Liquefiable Ground Affected by Different Earthquake Motions

Hiroshi Yokawa[1], Atsushi Yashima[2], Masata Sugito[3], Kazuhide Sawada[4], Masumitsu Kuse[5], Akinori Tanabe[6], and Osamu Nakayama[7]

[1]Graduate student, Department of Civil Engineering, 1-1 Yanagido, Gifu, 501-1193, m3812104@edu.gifu-u.ac.jp
[2]Professor, Department of Civil Engineering, 1-1 Yanagido, Gifu, 501-1193, yashima@gifu-u.ac.jp
[3]Professor, River Basin Research Center, 1-1 Yanagido, Gifu, 501-1193, sugito@gifu-u.ac.jp
[4]Associate Professor, River Basin Research Center, 1-1 Yanagido, Gifu, 501-1193, sawada@gifu-u.ac.jp
[5]Assistant Professor, River Basin Research Center, 1-1 Yanagido, Gifu, 501-1193, kuse@gifu-u.ac.jp
[6]Staff, Structural Engineering Division Tokyo Headquarters, 3-21-1 Nihombashi Hama-cho Chuo-ku, Tokyo, 103-8430, a-tanabe@ctie.co.jp
[7]Senior manager, Research Group for Water Resources Policy, 3-12-1 Toranomon Minato-ku, Tokyo, 105-0001, o.nakayama@jice.or.jp

ABSTRACT: Severe damages of river dikes caused by liquefaction have been often observed. In previous earthquakes, it has been reported that many river dikes were deformed by the liquefaction during earthquake. The river dike in the middle region of Shinano River is built on the loosely deposited sandy layers. Therefore, a large deformation of the river dike by the liquefaction is expected. It is very important to understand the deformation mechanism of the river dike by liquefaction in order to prevent a future damage of river dike along Shinano River.

In this study, effective stress based finite element analyses were carried out by the program code "LIQCA" to reproduce the past damage and to compare the damage of the river dike by different earthquake motions. Three earthquake motions by the 1964 Niigata earthquake, the 2004 Niigataken Chuetsu earthquake and the 2007 Niigataken Chuetsu-Oki earthquake had different duration time and acceleration amplitude. The comparisons among damages by three earthquakes were carried out. As the results, it was confirmed that the duration time and the acceleration amplitude of earthquake motion were key factors which affect the damage of the river dike.

INTRODUCTION

Sever damages of river dikes caused by liquefaction have been often observed in Japan. In previous earthquakes, it was reported that many river dikes were deformed by the liquefaction during earthquake. In order to understand damage mechanism of the river dike, various researches on the liquefaction during earthquake (e.g. Yasuda et al, 2000) have been carried out. The knowledge and experiences acquired by these researches have

contributed to the judgment of liquefaction and several countermeasures against liquefaction. However, earth structures such as river dike have been damaged repeatedly by liquefaction whenever a big earthquake occurs.

In this study, effective stress based finite element analyses were carried out by the program code "LIQCA (Oka et al, 1994)" to understand deformation mechanism of the river dike by liquefaction. The comparisons among damages by three earthquakes were carried out.

RIVER DIKE MODEL

Shinano river right bank 2k-000-point (Tyujyo area) was selected as the target site of analyses because this area was seriously damaged by the 2004 Niigataken Chuetsu earthquake. FIG.1 shows the cross-section of the target dike and soil condition. In this area, three boring investigations were carried out after the 2004 Niigataken Chuetsu earthquake. Table1 shows typical properties of the soil which were acquired from these investigations and laboratory tests. The dike was built on the alternate layer which consisted of sand layer and clay layer. In this cross-section, the loose soil layers where N values are smaller than 10 is distributed in a layer shallower than Ac2. Groundwater level was observed at the altitude of 12.7m which was a river water level immediately after the 2004 Niigataken Chuetsu earthquake (October 21st, 2004 18:00)

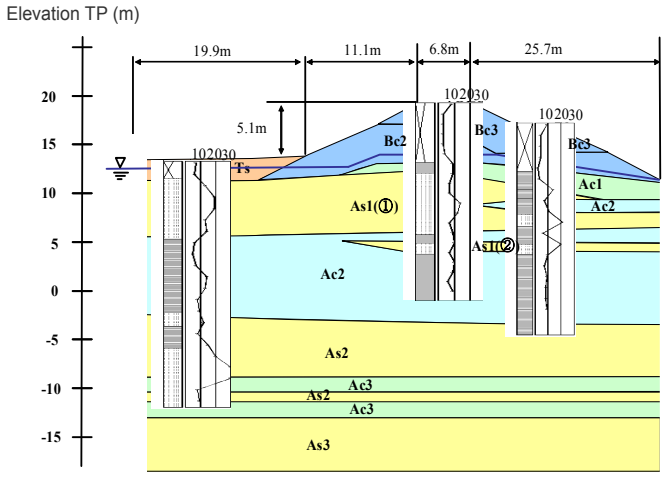

FIG. 1. Cross-section of river dike and soil conditions

Table1 Typical properties of soil

Layer	Soil classification	Wet unit weight γ_t (kN/m^3)	N value	Fine fraction content Fc (%)	Mean grain size D_{50} (mm)	Cohesion c (kN/m^2)	Friction angle ϕ(°)	Coefficient of permeability k (cm/sec)
Ts	Silt	18	7	29	0.30	48	0	2.0×10^{-4}
Bc3	Fine sand	18	4	48	0.35	48	0	2.0×10^{-4}
Bc2	Silty sand	18	4	75	0.31	48	0	8.0×10^{-4}
Ac1	Cohesive soil	14	3	81	0.03	69	0	1.0×10^{-6}
As1(①)	Sandy soil	18	10	6	0.33	0	30	4.0×10^{-3}
As1(②)	Sandy soil	18	20	8	0.35	0	30	4.0×10^{-3}
Ac2	Cohesive soil	17	10	100	0.01	59	0	1.0×10^{-6}
As2	Sandy soil	19	40	18	0.25	0	47	7.0×10^{-4}
Ac3	Cohesive soil	17	15	100	0.01	88	0	1.0×10^{-6}
As3	Sandy soil	19	50	10	0.25	0	47	7.0×10^{-4}

Calculation of input motions

Earthquake motions on earthquake engineering base (Vs=500 (m/sec)) for the 1964 Niigata earthquake, the 2004 Niigataken Chuetsu earthquake and the 2007 Niigataken Chuetsu-Oki earthquake, were calculated using EMPR (Earthquake Motion Prediction on Rock Surface (Sugito et al,2000)). FIG. 2 shows locations of fault and hypocenter for three earthquakes.

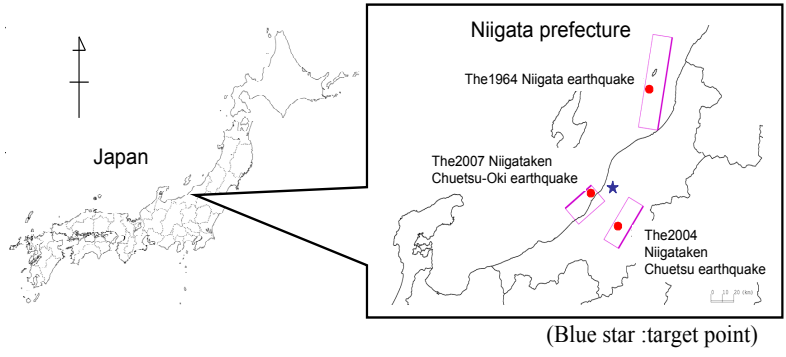

FIG. 2. Locations of fault and hypocenter

FIG. 3 (a) ~ (c) show three acceleration input motions (2E-wave) at the bedrock (Vs=295 (m/sec)) which were calculated from EMPR. The maximum acceleration and the duration time were indicated in these figures. The t_{90} is defined as the duration from 5 to 95 % of the accumulation of acceleration power as shown in Fig. 4.

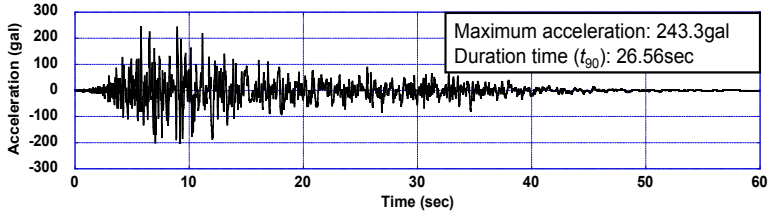

(a) 1964 Niigata earthquake

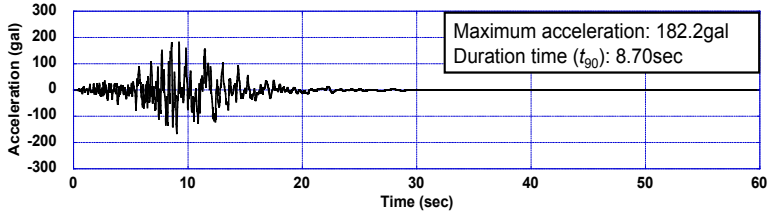

(b) 2004 Niigataken Chuetsu earthquake

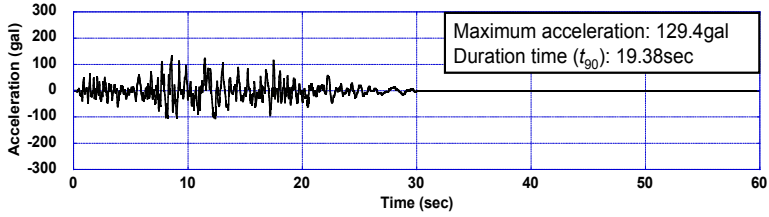

(c) 2004 Niigataken Chuetsu-Oki earthquake

FIG. 3. Acceleration input motions

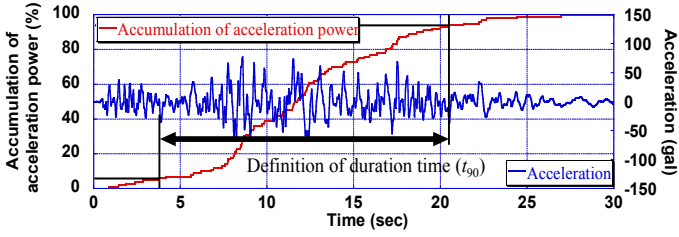

FIG. 4. Definition of duration time (t_{90})

FEM model

The boundary condition is that (a) a viscos boundary is adopted for the bottom nodes, (b) an equal displacement boundary condition is used between the nodes in two sides of the ground and (c) ground water level is set to be a drainage boundary while the other surfaces are impermeable. Just after the kinematic analyses, consolidation analyses are carried out.

FIG. 5 shows FEM mesh which consists of 2498 nodes and 2431 elements. For sandy layers (Bc3, Bc2, As1(①), As1(②), As2, As3 and Ts), a cyclic kinematic elasto-plastic model is adopted. Meanwhile for clayey soil layers (Ac1, Ac2 and Ac3), a cyclic kinematic elasto-visco-plastic model is adopted. The physical properties such as coefficient of permeability, compression index, swelling index, phase transformation stress ratio, and failure stress ratio are determined by the results of the laboratory tests. The liquefaction parameters are determined based on the liquefaction resistance curves estimated from N value (R_{L20}). The Parameters for the constitutive model determined are shown in Table2.

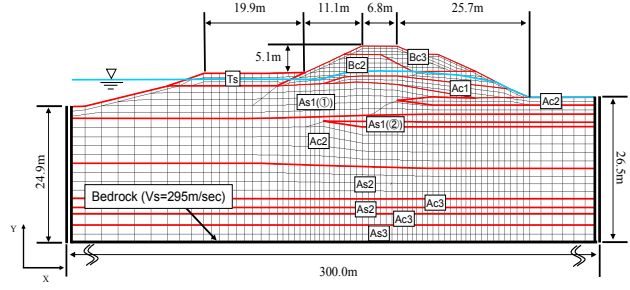

FIG. 5. FEM mesh

Table2. Material parameter for the constitutive model

		Bc3	Bc2	Ts	As1 (①)	As1 (②)	As2	As3	Ac1	Ac2	Ac3
paremeter											
density	ρ (g/cm^3)	1.8	1.8	1.8	1.8	1.8	1.9	1.9	1.4	1.7	1.7
coefficient of permeability	k (m/sec)	2.0E-06	2.0E-06	2.0E-06	2.0E-05	4.0E-05	7.0E-06	7.0E-06	1.0E-08	1.0E-08	1.0E-08
S-wave velocity	Vs (m/sec)	158	158	191	172	217	273	273	158	215	246
a cyclic kinematic elasto-plastic model / a cyclic kinematic elasto-visco-plastic model											
compression index	λ	0.0005	0.0005	0.0008	0.0057	0.0012	0.0460	0.0011	0.0057	0.3280	0.3280
swelling index	κ	0.0002	0.0002	0.0001	0.0001	0.0005	0.0005	0.0006	0.0006	0.0629	0.0629
overconsolidation ratio	OCR	1.5	1.5	1.5	1.5	1.5	1.5	1.5	1	1	1
initial shear modulus ratio	G_0/σ'_m	4300.0	4300.0	5000.0	1183.4	1431.4	1468.6	3020.5	1183.4	287.0	287.0
phase transformation stress ratio	M^*_m	0.909	0.909	0.909	0.909	0.909	0.909	0.909	1.130	1.130	1.130
failure stress ratio	M^*_f	1.150	1.150	1.150	1.150	1.150	1.579	1.579	1.310	1.310	1.310
parameter for hardening function	B^*_0	11000	11000	12000	4000	5000	3500	10000	30	30	30
parameter for hardening function	B^*_1	100	100	100	100	200	100	200	0	0	0
parameter for hardening function	C_f	100	100	100	1000	1500	1000	1000	0	0	0
reference value of plastic shear strain	γ^{p*}_r	0.004	0.004	0.004	0.001	0.002	0.002	0.001	-	-	-
reference value of plastic shear strain	γ^{c*}_r	0.008	0.008	0.008	0.002	0.005	0.004	0.003	-	-	-
parameter of anisotropy disappearance	C_d	2000	2000	2000	2000	2000	2000	2000	-	-	-
parameter for visco plastic	C^*_{01}	-	-	-	-	-	-	-	5.54E-06	5.54E-06	5.54E-06
parameter for visco plastic	C^*_{02}	-	-	-	-	-	-	-	7.76E-07	7.76E-07	7.76E-07
parameter for visco plastic	m^*_0	-	-	-	-	-	-	-	14	14	14
2nd shear modulus ratio for visco-plastic	G/G_2	-	-	-	-	-	-	-	0	0	0

In order to investigate the river dike deformation, several nodes and element are

focused on. These nodes and element are shown in FIG. 5. Node1267 represents the top of slope of protected lowland. Node 748 represents the toe of slope of riverside land. Node2010 represents the toe of slope of protected lowland. Element1031 is located in As1(①) layer.

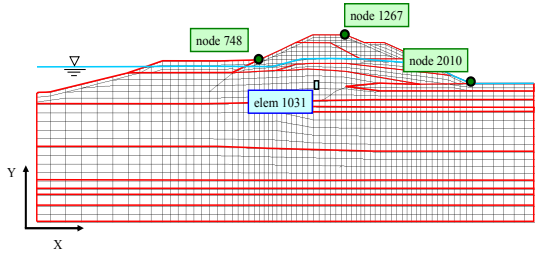

FIG. 6. Attention nodes and element

Influence of different input earthquake motions on settlement of river dike

In this section, in order to understand the influence of the different input earthquake motions on the settlement of the river dike, analyses were carried out using three earthquake motions. FIG. 7 shows the time histories of the settlement at node1267. FIG.8 shows the time histories of the stretch of the river dike calculated from the horizontal displacement at node748 and node2010. FIG.9 shows the time histories of the excess pore water pressure ratio (EPWPR:$\Delta u/\dot{\sigma}_{y0}$) at element1031. The settlement of the river dike at different time is summarized in Table3.

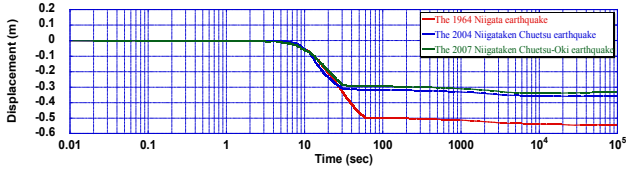

FIG. 7. Time history of settlement (node1267)

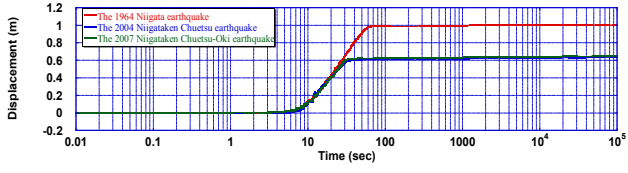

FIG. 8. Time history of stretch between node748 and node2010

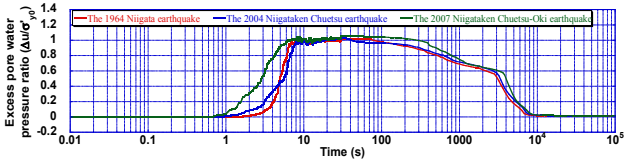

FIG. 9. Time history of EPWPR (elem1031)

Table3. Settlement at time classification

(a) The 1964 Niigata earthquake

time		settlement of crests (m)	rate of total settlement (%)
0.00sec～4.66sec		0.00	0.39
4.66sec～31.22sec	t_{90}	0.34	62.72
31.22sec～60.00sec		0.16	29.51
60.00sec～	consolidation	0.04	7.38
final settlement		0.54	100.00

(b) The 2004 Niigataken Chuetsu earthquake

time		settlement of crests (m)	rate of total settlement (%)
0.00sec～5.72sec		0.00	1.16
5.72sec～14.42sec	t_{90}	0.15	42.36
14.42sec～30.00sec		0.15	42.36
30.00sec～	consolidation	0.05	14.12
final settlement		0.35	100.00

(c) The 2007 Niigataken Chuetsu-Oki earthquake

time		settlement of crests (m)	rate of total settlement (%)
0.00sec～2.84sec		0.00	0.81
2.84sec～22.22sec	t_{90}	0.21	63.12
22.22sec～30.00sec		0.07	21.04
30.00sec～	consolidation	0.05	15.03
final settlement		0.33	100.00

From the results of the analyses, the settlement behavior of the river dike is able to be divided into 2 phases. 1st phase is “during the earthquake (t_{90})”. 2nd phase is “after the earthquake”. From FIG7, it is found that the river dike settles greatly during the main shock (t_{90}). The settlement in 2nd phase was smaller than the settlement in 1st phase. It is also found that the river dike stretches greatly during the main shock (t_{90}) from FIG8.

During 1st phase, due to lateral spreading of the liquefied ground by the earthquake, the stretch of the dike takes place. As the result, the large settlement of the dike occurs. On the other hand, during 2nd phase, the dike only settles by the consolidation of the

liquefied ground.

From FIG.7 and Table3, It is found that the larger the maximum acceleration amplitude is, the larger the settlement of the river dike is. Based on the comparison between the settlements of the 2004 Niigataken Chuetsu earthquake with that of the 2007 Niigataken Chuetsu-Oki earthquake, a big difference is not observed.

As the results, it is confirmed that the duration time and the acceleration amplitude of earthquake motion are key factors which affect the damage of the river dike.

CONCLUSIONS

In order to understand the influence of the different input earthquake motions on the settlement of the river dike, analyses for predicting damage were carried out using three earthquake motions. From analytical results, the following conclusions were derived:

(1) The settlement behavior of the river dike is able to be divided into 2 phases. 1st phase is “during the earthquake”. 2nd phase is “after the earthquake.” The settlement in 2nd phase was smaller than the settlement in 1st phase.

(2) It was confirmed that the duration time and the acceleration amplitude of earthquake motion were key factors which affect the damage of the river dike.

REFERENCES

Biot, M. A. (1962). "Mechanics of deformation and acoustic propagation in porous media." Journal of Applied physics, Vol. 33, No. 4, pp. 1482-1498.

Ministry of Land, Infrastructure, Transport and Tourism (2005). "Investigation report of the damage by the Niigata prefecture earthquake in 2004." Technical Note of National Institute for Land and Infrastructure Management, No.248.

Miyakawa, Y., Nishi, O., Ogawa, S., Oshiki, H. and Suzuki, Y. (2005). "Survey and research on damaged Shinano river embankments caused by Niigataken chuetsu earthquake." Proceedings of River Engineering, JSCE, Vol.11, pp.163-168.

Oka, F. (1992) "A cyclic elasto-viscoplastic constitutive model for clay based on the non liner hardening rule." Proceedings of 4th International Symposium on Numerical Models in Geomechanics, Swansea, pp. 105-114.

Oka, F., Yashima, A., Shibata, T., Kato, M. and Uzuoka, R. (1994). "FEM-FDM coupled liquefaction analysis of a porous soil using an elasto-plastic model." Applied Scientific Research, 52, pp.209-245.

Sugito, M., Furumoto, Y. and Sugiyama, T. (2000). "Strong motion prediction on rock surface by superposed evolutionary spectra." 12th World Conference on Earthquake Engineering, paper No.2111. (CD-ROM)

Uzuoka, R. (2000). "Analytical study on the mechanical behavior and prediction of soil liquefaction and flow" Ph. D. Dissertation, Gifu University.

Yasuda, S., Yoshida, N., Kiku, H. and Uda, M. (2000). "Estimation of Liquefaction-Induced Deformation of River Levees by a Simple Method." Geo-Engineering 2000, pp.1-6.

Elastic Response of Soil-Structure Systems Subjected to Near-Fault Rupture Directivity Pulses

Zeynab Azarhoosh[1], G. Reza Ghodrati Amiri[2]

[1] M.Sc. Student, Department of Civil Engineering, Iran University of Science and Technology, Tehran, Iran, azarhoosh@alum.sharif.edu

[2] Professor, Department of Civil Engineering, Iran University of Science and Technology, P.O. Box 16765-163, Tehran, Iran, ghodrati@iust.ac.ir

ABSTRACT: Generally, in order to evaluate the seismic demand of structures, it is assumed that the structure is located on a rigid soil, with increasing the soil flexibility, there will be significant variations in the structural response, i.e. the effects of Soil-Structure Interaction (SSI). Additionally, ground motions close to active faults have some important characteristics that make them to be different from those recorded in far-fault regions. Forward rupture-directivity velocity pulses, high-frequency acceleration records, and permanent displacement, are notable specifications of records close to ruptured faults. Among mentioned characteristics, forward rupture-directivity effect causes velocity pulses that could potentially exert great damages to buildings in near-fault regions. These pulses possess statistical certainty; hence, researchers tried to present synthetic models for them. In this paper, a parametric study is carried out on the elastic response of soil-structure systems having shallow foundations subjected to a pulse-type motion and near-fault records in order to develop a systematic procedure for assessing near-fault and SSI effects on design of structures. It is concluded that under SSI effects there are clear similarities between elastic demands subjected to pulse-type, and near-fault motions. Consequently, the final form of relationship as a representation of near-fault characterizations under SSI effects is presented.

INTRODUCTION

Soil-Structure Interaction (SSI) phenomenon has been recognized to play an important role in the design of structures subjected to dynamic loads such as seismic excitations. Various researchers in the past four decades showed that for the flexible structure located on a rigid soil; the difference between Foundation Input Motion (FIM) and Free-Field Motion (FFM), i.e. effects of Kinematic Soil-Structure Interaction (KSSI) is negligible. Moreover, due to soil rigidity, flexible structure can be treated as a fixed-base structure, i.e. Inertial Soil-Structure Interaction (ISSI) can be ignored. However, there will be significant variations in the response of a structure relative to fixed-base cases with increasing the soil flexibility. These variations are related to the change in the base

excitation, effects of KSSI, and the change in the dynamic stiffness coefficients such as the natural period, and damping ratio of the system, effects of ISSI. Recent findings have shown that in almost all cases, KSSI can be neglected, as horizontal FIM is smaller than FFM [Stewart, 2000]. Therefore, only the effects of ISSI are being considered in this study. Moreover, ground motions close to a ruptured fault have special characteristics which can be significantly different than those observed further away from the seismic source [Stewart *et al*., 2001].With a tremendous growth of urban areas in seismically active regions, the necessity of their inspections has taken attention of researchers over five decades. The pondering point is that existing standards such as *ATC3-58* [*2009*] and *NEHRP* [*BSSC, 2009*] in the field of SSI are limited to the effects of this phenomenon subjected to ordinary ground motions. However, it appears that some caution should be considered for near-fault strong motions in the forward directivity region [Stewart *et al*., 2004]. Therefore, SSI effects should be taken into account to estimate the strength demands imposed by near-fault motions. Recent research is carried out to relate the SSI effects on structural responses directly to mechanical properties of soil-structure system and near-fault motion characteristics [Zhang, and Tang, 2008]. In this research, a parametric study is carried out on the effects of ISSI on the elastic response of soil-structure systems having shallow foundations. By using the sub-structure method, a simplified discrete model is used to represent the real soil-structure system [Wolf, 1994]. Finally, the whole soil-structure system is analyzed subjected to a mathematical pulse model, and strong motions in the near-fault regions directly in time domain using step by step integration method.

SOIL-STRUCTURE MODEL

Using the sub-structure method, the structure and the soil are modeled separately and then combined to constitute the soil-structure system, as shown in Fig. 1. The structure is replaced by an equivalent linear system. The soil beneath the structure is considered as a homogeneous half-space, and is modeled as discrete model based on the concept of Cone Models, which can be used with sufficient accuracy in engineering practice. More details are available in reference [Wolf, 1994].

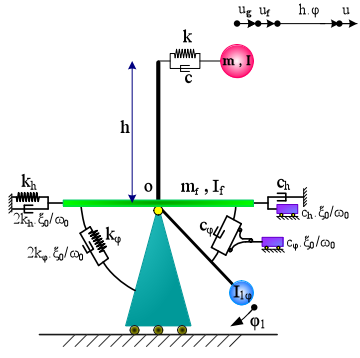

FIG. 1 Soil-Structure Model [Wolf, 1994]

NON-DIMENTIONAL SOIL-STRUCTURE INTERACTION PARAMETERS

Basically, the response of the soil-structure system depends on the size of the structure, its dynamic characteristics, and the soil profile. These effects can be best described by the following non-dimensional parameters [Ghannad *et al.*, 1998]:

1. A non-dimensional frequency, a_0, an index for the structure to soil stiffness ratio defined as:
   $a_0 = \omega_{fix} h / V_s$ (1)
   where ω_{fix}, h, and V_s are the circular frequency, height corresponding to the fundamental mode vibration of the fixed-base structure, and the shear wave velocity, respectively. It can be shown that the practical range of a_0 for ordinary building type structures is from zero, fixed-base structure, to about 3.
2. Aspect ratio of the building, h/r, an index for its slenderness ratio.
3. Material damping ratios of the soil and the structure, ξ_g, ξ_s respectively, Where are set to 5% of the critical damping at the natural frequency of the system.

NEAR-FAULT GROUND MOTIONS EFFECTS

Ground motions close to active faults have some important characteristics that make them different from those recorded in far-fault regions [Somerville, 1997]. Rupture-directivity, high-frequency contents in acceleration records, and permanent displacement, fling-step, are notable specifications of ground motion records close to ruptured faults. Among mentioned characteristics, forward directivity effect causes short-duration and long-period velocity pulses on the near-fault motions. These pulse type motions are generally in the forward direction, where the fault rupture propagates towards the site at a velocity close to shear wave velocity [Somerville, 1997]. As the rupture front propagates from the hypocenter, a shear wave front is formed by the accumulation of the shear waves traveling ahead of the rupture front. When a site is located at one end of the fault and rupture initiates at the other end of the fault and travels towards the site, the arrival of the wave front is seen as a large pulse of motion; a shock wave effect, that occurs at the beginning of the record [Somerville, 1997]. The radiation pattern of the shear dislocation on the fault causes this large pulse of motion to be oriented in the direction perpendicular to the fault plane [Somerville, 2003]. Rupture-directivity pulses could potentially cause great damage to buildings. Due to this fact and statistical certainty of the pulses many researchers have tried to present some analytical models in terms of earthquake and site properties such as magnitude, distance, and soil type in order to simplify dynamic analysis of structures against them. In this study, we have used a simple sine function for velocity pulses similar to those used by Makris [2003]. Ground time histories of this cycloidal pulse are expressed as:

$$\ddot{u}_g(t) = \alpha_P V_P \cos(\alpha_P t), \quad \dot{u}_g(t) = V_P \sin(\alpha_P t), \quad u_g(t) = \frac{V_P}{\omega_P} - \frac{V_P}{\omega_P}\cos(\omega_P t) \qquad 0 \le t \le T_P \quad (2)$$

Where V_p, and $\omega_p = 2\pi/T_p$ are the amplitude and frequency of the velocity pulse respectively. In this study, in order to evaluate effects of SSI on the response of structures subjected to this pulse-type, these ranges are considered:

$50 \le V_P \le 300\ cm/s, \quad 0.5 \le T_P \le 10\ sec$

Showing importance of high-frequency content, in addition to synthetic pulses, four real near-fault records have been used. These records and parameters of their synthetic models, i.e. V_p and T_p, are introduced in Table 1.

TABLE 1 The 1979, Imperial Valley-06 Earthquake Stations and Model Parameters

		Pulse Parameters			Distance (km)		Site
No.	Station	T_P (sec)	V_P (cm/s)	M_W	Closest	Epicentral	Class [S]
1	El Centro Array #4	4.3	60.8	6.5	7.1	27.1	D
2	El Centro Array #5	3.2	70.0	6.5	4.0	27.8	D
3	El Centro Array #6	3.7	100.0	6.5	1.4	27.5	D
4	El Centro Diff. Array	4.3	44.0	6.5	5.1	27.2	D

[S] Site Classification Defined by NEHRP

METHOD OF ANALYSIS

The SSI effect on elastic strength demand is studied by comparing results. For this purpose, a family of 360 soil–structure systems consisting of 30 SDOF structures with fixed-base periods ranging from 0.1 to 3 *sec* having three different values of aspect ratio (h/r = 1, 3, and 5) and three values of non-dimensional frequency (a_0 = 1, 2, and 3) are investigated for each input ground motion. Consequently, at least a total of 1440 independent linear analyses have been carried out for different soil-structure systems subjected to four near-fault motions. In addition, 43200 linear analyses subjected to the synthetic pulses.

NUMERICAL RESULTS

In order to evaluate SSI effects on structural response, variation of normalized elastic strength demand, are presented according to the normalized period of fixed-base structure subjected to near-fault effects. The presented results are valid for all values of V_p, as normalized strength demands have been investigated. Figure 2 displays effects of aspect ratio on normalized elastic demand subjected to the synthetic pulse. The principle effect of SSI is to increase the natural period of the system and usually, to increase its effective damping ratio. As seen, SSI generally causes to reduce structural demand comparing to fixed-base structure, however causes to increase it in lower periods, which amplifies under increasing of h/r. As shown in Fig. 2, elastic demands gradually shift towards up and left when a_0 increases. The shift in the period of maximum strength demand is due to the elongation occurring in the soil-structure period under increasing of a_0. The softer the soil, the larger will be the elongation of period. SSI created higher levels of strength demands after a threshold period ratio; hence, SSI effects are negligible on the structures with very low, $T_{fix}/T_P \leq T_{threshold}/T_P$ or very large, $T_{fix}/T_P \geq 3$ period ratios. The threshold period ratios are listed in Table 2 for each case. Figure 3 displays effects of non-dimensional frequency on elastic demand subjected to the synthetic pulse. As seen, in structures with very low periods, SSI effects in squat buildings, h/r=1, lead to decrease strength demand compared to fixed-base structure due to the increscent occurring in the soil-structure damping, yet by increasing aspect ratio, slender structures, h/r = 3, 5, SSI increases the structural demands, which amplifies under increasing of structure to soil

stiffness ratio. The reason lies in the greater elongation of the system's period that occurs due to the increase in the building's aspect ratio. Slenderizing the structure also leads to considerably lower values of damping for system which well explains more strength demand with large aspect ratio. As mentioned in Fig. 2, the graphs also move up and left. Figure 4 and 5 display the same main features but subjected to real near-fault motions. However, there are two maximum values. One is related to the long-period pulses which may be produced by forward directivity effects, and the other depends on high-frequency content of near-fault motions. Therefore, elastic strength demand graphs show that in contrast with ordinary earthquakes, elastic response near-fault records typically have two distinct local maximum regions, which was mentioned by Ghahari *et al.* [2008].

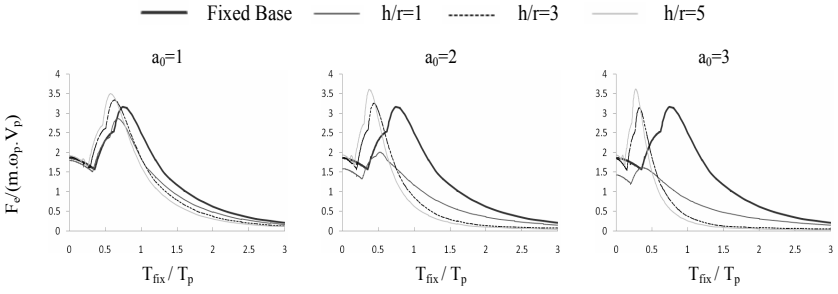

FIG. 2 Effects of Aspect Ratio on Elastic Demands Subjected to the Synthetic Pulse

TABLE 2 Threshold Period Ratios Subjected to the Synthetic Pulse

Category	T_{fix}/T_p	Category	T_{fix}/T_p	Category	T_{fix}/T_p
a_0=1, h/r=1	0.33	*a_0=2, h/r=1*	0.28	*a_0=3, h/r=1*	0.20
h/r=3	0.29	*h/r=3*	0.20	*h/r=3*	0.15
h/r=5	0.26	*h/r=5*	0.17	*h/r=5*	0.12
Fixed-Base	0.36				

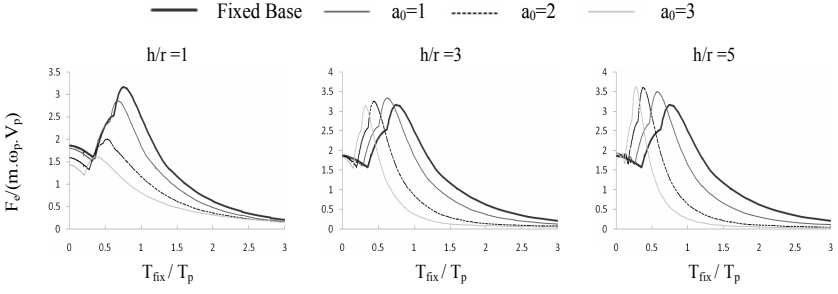

FIG. 3 Effects of Non-dimensional Frequency on Elastic Demands Subjected to the Synthetic

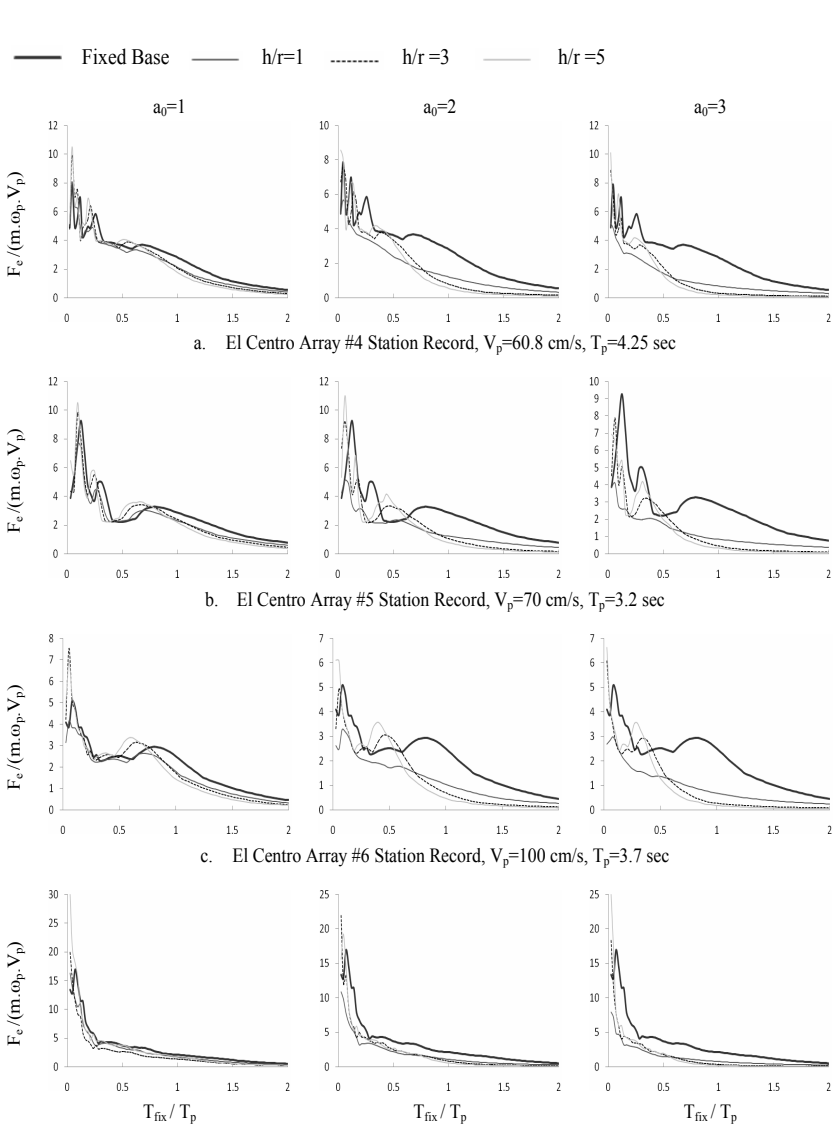

FIG. 4 Effects of Aspect Ratio on Elastic Demands Subjected to the 1979, Imperial Valley-06 Earthquake

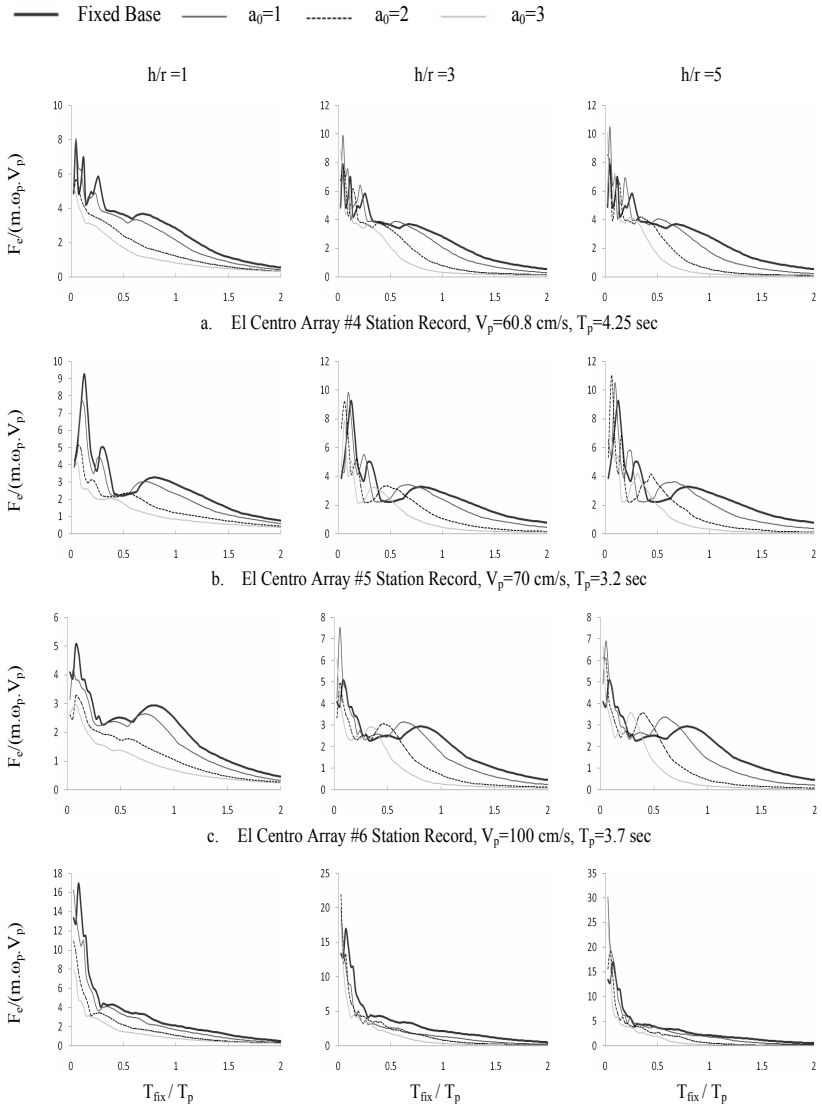

FIG. 5 Effects of Non-dimensional Frequency on Elastic Demands Subjected to the 1979, Imperial Valley-06 Earthquake

SYNTHETIC PULSES AS A REPRESENTATION OF NEAR-FAULT CHARACTERIZATIONS UNDER SSI EFFECTS

As mentioned before, the response of structures subjected to synthetic pulses is very close to the main feature of structural response subjected to near-fault motions under SSI effects, where synthetic pulses can represent near-fault characteristics after a peak period ratio. Structural response typically has two distinct local maximum regions. The first is high period ratio region, $T_{Peak}/T_P \leq T_{fix}/T_P \leq 3$, where fault characteristics can be represented by the pulse-type. The second is low period ratio region, $T_{fix}/T_P < T_{Peak}/T_P$, where only synthetic pulse is not sufficient for quantifying near-fault effects, due to the impossible substitution of high-frequency content of complete near-fault motions in mathematical models. Due to increasing a_0, low period region tends to less than 0.75 for fixed-base case. Consequently, high values of a_0 lead to near-fault characteristics that can be substituted by using the synthetic pulse in the wide period range, which amplifies under increasing of slenderness. The peak period ratios are presented in fourth column of Table 3 for each case. Regarding the replacement of near-fault characterizations by the synthetic pulse, final form of relationship and its coefficients are presented in Eq. 3 and Table 3, respectively. This Eq. is very close to Makris [2003] form when SSI is negligible.

$$\frac{F_e}{m.\omega_p.V_p} = a.e^{-b.(\frac{T_{fix}}{T_p}-c)} \tag{3}$$

TABLE 3 Coefficients Used in Eq. 3

Category	Elastic structural Demand Coefficients		
	a	***b***	$c = T_{peak}/T_p$
a_0=1, h/r=1	2.83	1.31	0.69
a_0=1, h/r=3	3.31	1.52	0.63
a_0=1, h/r=5	3.41	1.62	0.58
a_0=2, h/r=1	1.98	1.00	0.53
a_0=2, h/r=3	2.89	1.82	0.44
a_0=2, h/r=5	3.11	2.05	0.38
a_0=3, h/r=1	1.62	1.00	0.38
a_0=3, h/r=3	2.35	2.00	0.33
a_0=3, h/r=5	2.72	2.37	0.27
Fixed-Base	3.29	1.29	0.75

CONCLUSIONS

SSI created higher levels of elastic strength demands after a threshold period ratio subjected to the pulse-type motion. As a result, SSI effects are negligible on the structures with very low or very large period ratios, as these ratios tend to more and less values under increasing of a_0, and *h/r*, respectively. In addition, under SSI effects there are clear

similarities between elastic demands subjected to synthetic pulses, and near-fault motions. Synthetic pulses can represent near-fault characterizations after a peak period ratio, where fault characteristics can be represented by pulse-type motions. High-frequency content controls response before the peak period ratio which tends to less due to increasing a_0. Thus high values of a_0 lead to near-fault characteristics that can be substituted by using the synthetic pulse in the wide period range, which amplifies under increasing of h/r. Finally, the form of relationship as a representation of near-fault characterizations under SSI effects is presented.

ACKNOWLEDGMENTS

The authors wish to thank Dr. M. A. Ghannad, and S. F. Ghahari of Sharif University of Technology who improved the quality of this paper.

REFERENCES

Ghahari, S. F., Ghannad, M. A., and Jahankhah, H., (2008), "Decomposition of Near-Fault Earthquake Records and their Elastic Response Spectra", *Submitted to Earthquake Engineering and Structural Dynamics*

Ghannad, M. A., Fukuwa, N., and Nishizaka, R., (1998), "A Study on the Frequency, and Damping of Soil-Structure Systems Using a Simplified Model", *Journal of Structural Engineering*; AIJ, Vol. 44B: 85-93

Makris, N., and Black, C., (2003), "Dimensional Analysis of Inelastic Structures Subjected to Near-Fault Ground Motions". *Earthquake Engineering Research Center* (EERC), Report No.05

Somerville, P., Smith, N., Graves, R., and Abrahamson, N., (1997), "Modification of Empirical Strong Ground Motion Attenuation Relations to Include Amplitude and Duration Effects of Rupture Directivity", *Seismological Research Letters*, Vol. 68 (1): 180-203

Somerville, P.G., (2003), "Magnitude Scaling of the Near-Fault Directivity Pulse". Physics of the Earth and Planetary Interiors, Vol. 137: 201-212

Stewart, J.P., (2000), "Variations between Foundation-Level and Free-Field Earthquake Ground Motions", *Earthquake Spectra*, Vol. 16(2), 511-532

Stewart, J.P., Chiou, S J., Bray, J., Graves, R., Somerville, P., and Abrahamson, N., (2001/09), "Ground motion evaluation procedures for performance-based design", *Pacific Earthquake Engineering Research Center* (PEER)

Stewart, J.P., Comartin, C., and Moehle, J. P., (2004), "Implementation of Soil Structure Interaction Model in Performance Based Design Procedures", *Proceeding 3rd UJNR Workshop on Soil-Structure Interaction*, Menlo Park, California, USA, 29-30 March

Wolf, J., P., (1994), "Foundation Vibration Analysis Using Simple Physical Models", *Prentice-Hall*, Englewood Cliffs, New Jersey

Zhang, J., and Tang, Y., (2008), "Dimensional Analysis of Linear Soil-Foundation-Structure System Subjected to Near-Fault Ground Motions", *Structure Congress'08*, Vancouver, Canada, April

Seasonal Freezing Effects on the Dynamic Behavior of Highway Bridges

*Zhaohui "Joey" Yang[1], Qiang Li[2], Gang Xu[3], and J. Leroy Hulsey[4]

[1]Dept. of Civil Engineering, University of Alaska Anchorage, Anchorage. Alaska, USA, afzy@uaa.alaska.edu
[2, 3] University of Alaska Anchorage, Anchorage, Alaska, USA
[4] University of Alaska Fairbanks, Fairbanks, Alaska, USA

ABSTRACT: Frozen ground is significantly stiffer than unfrozen ground. For bridges supported on deep foundations, the bridge stiffness is also measurably increased in the winter months. Significant changes in the bridge pier boundary conditions due to seasonal freezing requires additional detailing to ensure a ductile performance of the bridge during the design earthquake event. This paper reports the latest results obtained from a project aimed at systematically investigating the effects of seasonal freezing on the seismic behavior of highway bridges in cold regions. Presented here are the results obtained from numerical simulation of the overall dynamic performance and field monitoring study of the bridge selected for study in this project. By using OpenSees computational platform, a three-dimensional FE model of the bridge foundation is established to investigate the impact of seasonal frost on the bridge substructure behavior. In the meantime, a bridge is instrumented with a network of accelerometers to monitor its dynamic and seismic behavior. Earthquake-induced vibration data have been collected and analyzed. The results show that seasonal frost has significant impact on the overall dynamic behavior of bridges supported by pile foundations in cold regions, and these effects should be accounted for in seismic design.

INTRODUCTION

Seasonally frozen ground is significantly stiffer than unfrozen ground due to the ice matrix formed during freezing. Stevens (1973) found that the stiffness of soils can change by as much as two orders of magnitude when frozen. By conducting dynamic pile tests in the field, Vaziri and Han (1991) found that the presence of a frozen soil layer, even at a modest thickness of less than 0.5 m, could significantly influence the dynamic responses of piles. For bridges supported on deep pile group foundations, the overall bridge stiffness was found to increase measurably in winter months (Yang et al., 2007). As bridge stiffness increases, seismic demand increases significantly (Sritharan et al., 2007; Suleiman et al., 2006; Yang et al. 2008). However, there is no systematic study of lateral pile behavior considering seasonal freezing nor are there design guidelines to address these effects. A project investigating the effects of seasonal

freezing on the seismic behavior of highway bridges in cold regions has been initiated. As an integral part of this project, a set of reinforced concrete-filled steel pipe piles embedded in soils experiencing seasonal freezing will be tested in an outdoor environment. The results of the single pile performance simulation are presented in this paper. Also reported is the latest results obtained from the field experiments.

DESCRIPTION OF THE PILE EXPERIMENT SITE AND TEST PILES

The pile experiments are to be conducted in Fairbanks, Alaska. Permafrost occurs at 5 m below the ground surface. The maximum depth of seasonally frozen soils in Fairbanks varies depending on surface condition, and is typically 1.5 to 3.0 m. A silt layer extends to the depth of 3 m from the ground surface, which is underlain by a layer of sand with the thickness of 2.9 m; following that is a gravelly sand layer and a gravel layer. Based upon the moisture changes at the ground surface and the partially frozen soil between seasonally frozen layer and the unfrozen layer, transition layers of 0.2 m thickness are assumed for the surface soil and the soil between seasonally frozen layer and the unfrozen layer.

Reinforced concrete-filled steel pipe pile is chosen since it is widely used for bridge foundations in the State of Alaska. The pile diameter and reinforcement configuration are determined considering the limitation of the loading equipment and the common practice in Alaska. The test pile configuration is summarized in Table 1. Two test piles and a reaction pile has been constructed on the site in the summer of 2008. One of the test pile is shown in Figure 1. One test pile will be tested in summer season of 2009 and the other at the end of winter season of 2009-2010. Each pile will be loaded cyclically to failure according to a standard three-cycle, displacement demand protocol.

Fig. 1. A scene of one of the two test piles constructed at the experiment site in Fairbanks, AK

Table 1. Configuration of test piles

Pile Parameter	Value
Total Length	8.4 m
Length Above the Ground Surface	2.4 m
Embedment Depth	6 m
Outside Diameter	406 mm
Number of Reinforcing Bars	8
Steel Pipe Wall Thickness	9.5 mm
Reinforcing Steel Bar Diameter	19 mm (#6)
Planned Load Point Height (above the ground surface)	2.4 m

RESULTS FROM SIMULATION OF THE SOIL-SINGLE PILE SYSTEM

The Open System for Earthquake Engineering Simulation (OpenSees) is a software framework for simulating the seismic response of structural and geotechnical systems (Mazzoni et al., 2006; *http://opensees.berkeley.edu/ index.php*). The details of Finite Element model can be found in Yang et al. (2008). Here summarized are the simulation results.

The pile behavior including lateral force vs. displacement and bending moment obtained at frozen and unfrozen conditions are shown in Figures 2, and 3. With the pile lateral yield lateral force (Vy) defined as the lateral load when the strain in the extreme tension steel fiber reaches first yield, it is observed from Figure 2 that the Vy increases and the lateral displacement capacity at the pile head decreases with the presence of frozen soil. The Vy increases from 75.8 kN at unfrozen status to 99.5 kN at frozen status, or 31% increase; the displacement capacity at the Vy decreases from 0.1 m at unfrozen status to 0.03 m at frozen status, or 70% reduction.

Figure 3 shows the bending moment versus depth for frozen and unfrozen conditions at a pile head deflection (D_x) of 0.3 m, respectively. As before, significantly different pile behaviors for unfrozen and frozen conditions are observed. It is seen from Figure 3 that the locations of maximum moments are founded to be 1.1 and 0.15 m (or 2.75 and 0.38*Pile Diameter) below ground surface for unfrozen case and frozen case, respectively. A comparison of pile behaviors in these two cases is summarized in Table 2. It is also observed in Figures 3 that the plastic hinge length is greatly reduced from 2.9 m in the unfrozen condition to 1.8 m in the frozen condition. The plastic hinge rotation and plastic deflection are also reduced accordingly.

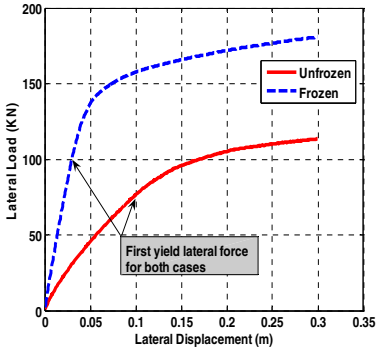

Fig. 2. Lateral load vs. deflection

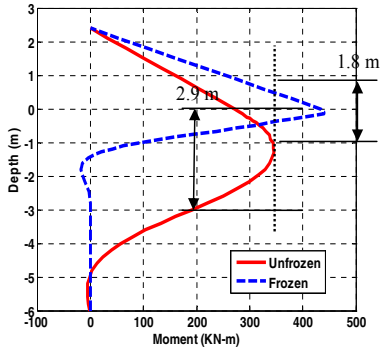

Fig. 3. Bending moment vs. depth (Pile head deflection D_x=0.3 m). Dashed line indicates the yield bending moment.

Table 2. Comparison of pile behavior at unfrozen and frozen conditions (Pile head deflection D_x = 0.3 m)

	Lateral Force at Pile Head (KN)	Max. Bending Moment (KN-m)	Max. Bending Moment Depth (m)
Frozen	181	440	0.15 (0.38*Diameter)
Unfrozen	113.5	345	1.1 (2.75*Diameter)

DESCRIPTION OF THE TEST BRIDGE AND MONITORING FACILITIES

A prestressed reinforced-concrete girder bridge in Anchorage, Alaska has been selected for field experiments for the following reasons: (1) this bridge is supported on extended steel pipe pile-shaft system filled with reinforced concrete; (2) the bridge site consists of original sandy gravelly soils overlaid with a few feet of organic soils; and (3) the water table is within one foot of the ground surface. This bridge provides an excellent test bed for detecting the upper-bound seasonal freezing effects. In order to collect dynamic as well as seismic response data, a network consisting of 11 accelerometers have been installed on the bridge superstructure in November 2008 according to the plan shown in Fig. 4. A 5-ft (1.5 m) deep borehole has been prepared in the site for ground temperature/frost penetration monitoring. Air temperature, frost penetration, ambient vibration data and earthquake-induced vibration data have been collected from January to the end of April 2009.

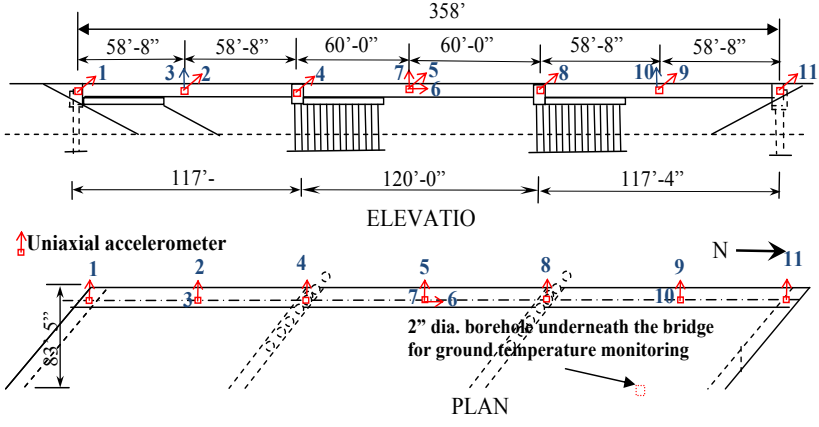

Fig. 4. Schematic of the bridge selected for study and seismic instrumentation

RESULTS FROM FROST PENETRATION MONITORING

A Temperature Acquisition Cable (TAC) with sensors arranged at a pre-defined spacing has been used together with a handheld data collector to collect ground temperature/frost penetration data, as illustrated in Fig. 5. The TAC is brought at times of data collection; the TAC is lowered into the borehole and maintained uninterrupted for at least 60 minutes to ensure that the sensors are fully acclimated before data collection commences. Fig. 6 presents the frost depth vs. monitoring date. The results show that the deepest frost penetration was 4.80 ft. The depth remained at approximately 4.0 ft for the whole month of March.

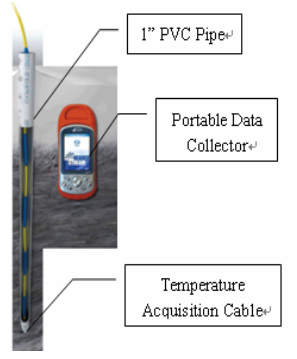

Fig. 5. A temperature acquisition cable used for frost penetration depth monitoring.

Meanwhile, the Berggren's equation was used to provide a continuous assessment of the frost penetration depth (Andersland and Ladanyi 2004). The Berggren Formula is:

$$X = \lambda\sqrt{\frac{48k_{ave}nFI}{L}} \quad (1)$$

where: X is the depth of freeze or thaw (ft), λ is a dimensionless coefficient which takes into consideration the effect of temperature changes in the soil mass and accounts for sensible heat changes, k_{ave} is the thermal conductivity of soil which is the average of frozen and unfrozen in units of $BTU/(hr \cdot ft \cdot {}^oF)$, n is a dimensionless factor for converting the air freezing index to surface freezing index, FI is the air freezing index in , ${}^oF \bullet days$ and L is the latent heat in BTU/ft^3. For comparison purpose, the estimated frost depth is also shown in Fig. 6. It is noted that a value of 0.4 has been used for the dimensionless factor n to produce a better match between the Berggren's formula estimation and the field observation. The difference between the field data versus the estimation can be

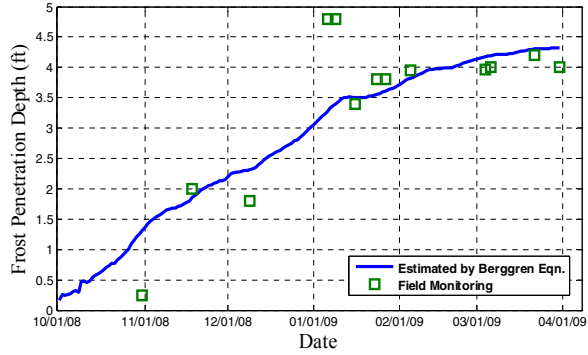

Fig. 6. Comparison of frost depths estimated by using Berggren's Equation and by field monitoring

attributed to the presence of the creek nearby. The creek remained not entirely frozen became a heat source that affected the freezing depths. The actual data ultimately was utilized in the following analysis.

RESULTS FROM MONITORING OF THE TEST BRIDGE

During the data collection period, a total of 8 earthquakes with magnitude varying from 3.3 to 5.7 have triggered the accelerometer network and bridge vibration data have been collected. The raw vibration data have been processed and analyze by using ARTeMIS Structural system identification software to obtain the bridge dynamic properties including modal frequency and mode shape. The modal frequency of the first lateral mode for each earthquake event and the corresponding frost thickness (frost depth minus thaw depth) is presented in Fig. 7. From Fig. 7, it is clearly seen that there is a strong correlation between the frost depth and the structural modal frequency. As the frost thickness remains around 4.0 feet, the first lateral modal frequency oscillates around 7.5 Hz. However, when the frost thickness decreases to 3 ft, i.e. the ground thawed to 1 ft below the surface, the modal frequency decreased significantly to 2.7 Hz, representing a 64% drop.

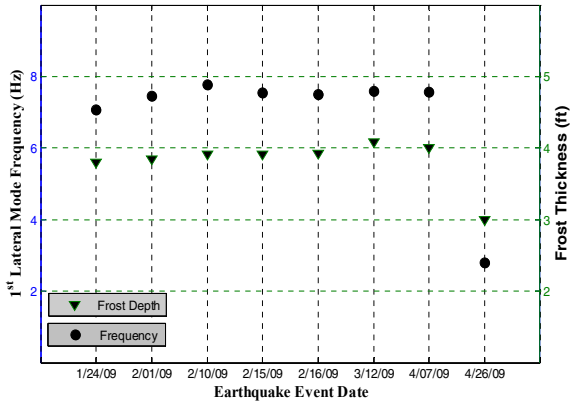

Fig. 7. Frozen Ground Thickness vs. 1st Lateral Modal Frequency

SUMMARY

This paper presents the results obtained from numerical as well as field experiments of highway bridge foundations under the influence of seasonal freezing. The OpenSees simulation platform is used to conduct pushover analyses for the soil-pile system at both unfrozen and frozen conditions. A newly-constructed highway bridge has been instrumented with a network of accelerometers to monitor its dynamic/seismic performance. Results show that seasonal freezing has a great impact on the lateral behavior of the soil-pile system and the overall behavior of the entire bridge system. The pile lateral yield force increases by 31%, and the displacement capacity at the lateral yield force decreases 70%. The maximum bending moment location and plastic hinge location move upward considerably when seasonal freezing occurs. Results also indicate that the plastic hinge length is substantially reduced under the frozen soil condition. It is noted that the numerical simulation results will help establish a testing procedure for the outdoor

testing. The bridge is found to be substantially stiffer at frozen condition than unfrozen condition. Once completed, this project will provide data and guidelines for improved seismic design of highway bridges in cold regions.

ACKNOWLEDGEMENT

This project is jointly funded by Alaska University Transportation Center (AUTC) and Alaska State Department of Transportation and Public Facilities (AK DOT & PF) (AUTC #107014). This support is gratefully acknowledged. Dr. Jinchi Lu, Assistant Research Scientist at the University of California, San Diego provided technical advice on using OpenSees. Dr. Utpal Dutta of School of Engineering, UAA provided software and guidance for strong-motion data processing. The authors are thankful to them.

REFERENCES

Andersland, O. B. and B. Ladanyi (2004). *Frozen Ground Engineering*. 2nd Edition. The American Society of Civil Engineers & John Wiley & Sons, Inc.

Mazzoni, S., F. McKenna, M.H. Scott and G.L. Fenves, et al. (2006). "Open System for Earthquake Engineering Simulation User Command-Language Manual." University of California, Berkeley. (*http://opensees.berkeley.edu/OpenSees/manuals/usermanual/ index.html)*

Stevens, H.W. (1973). "Viscoelastic properties of frozen soils under vibratory loads." *North American Contribution to the Second International Conf. on Permafrost*, 400-409. Yakutsk, U.S.S.R.

Sritharan, S., M.T. Suleiman and D. J. White. (2007). "Effects of seasonal freezing on bridge column-foundation-soil interaction and their implications." *Earthquake Spectra* **23:1,** 199-222.

Suleiman, M.T., S. Sritharan and D.J. White (2006). "Cyclic lateral load response of bridge column-foundation- soil systems in freezing conditions." *J. of Structural Engineering.* **132:11,** 1745-1754.

Vaziri, H. and Y. Han. (1991). "Full-scale field studies of the dynamic response of piles embedded in partially frozen soils." *Can. Geotech. J.* **28,** 708-718.

Yang, Z., U. Dutta, D. Zhu, E. Marx and N. Biswas (2007). "Seasonal frost effects on the soil-foundation-structure interaction system." *J. of Cold Regions Engineering*. **21:4**, 108-120.

Yang Z., F. Xiong, G. Xu, J. L. Hulsey and E. Marx (2008). "Seasonal freezing effects on the lateral behavior of steel pipe piles." *Proceedings from: The 14th World Conference on Earthquake Engineering.* Beijing, China.

Seismic CPTu To Assist the Design on Existing Foundations

Xiong (Bill) Yu[1], Jian Fang[2] and Guoming Lin[3]

[1] Assistant Professor, Department of Civil Engineering, Case Western Reserve University, 10900 Euclid Avenue Bingham 210, Cleveland, OH 44106-7201, xxy21@case.edu
[2] Former Project Engineering, WPC Inc., 2201 Rowland Avenue, Savannah, GA 31404
[3] Vice President, WPC Inc., 2201 Rowland Avenue, Savannah, GA 31404

ABSTRACT: Limited space in urban area makes it attractive to reuse the existing foundation. This paper presents a case study on the use of seismic piezocone penetrometer (SCPTu) to conduct parallel seismic test for the determination of the length of unknown foundation. The tip resistance and side friction by cone penetrometer provide the distribution of mechanical properties of the underground layer. The geophones in seismic piezocone tip acts as seismic wave receiver for parallel seismic test that is commonly used to determine the length of unknown foundation. By fusion of both information, the capacity of pile foundation under existing building can be determined. This testing procedure is very attractive for reuse of existing foundations. A case study is provided on the use of SCPTu in a building expansion project.

INTRODUCTION

This paper describes a case study that involves the use of Seismic Cone Penetrometer (SCPTu) to determine the length of unknown deep foundation. SCPTu is a very useful tool for geotechnical site investigation. The data collected by SCPTu are used to classify soils and determine the soil strength parameters in stratified ground. The seismic function provided by the geophone unit has been traditionally used to perform seismic down hole test for geotechnical seismic hazards assessment. New application scenery was explored in this case study for using SCPTu in a field study program to determine the length of unknown foundation. The geophysical function together with the traditional geotechnical information collected by SCPTu is used to accurately estimate the bearing capacity of unknown foundation. This was incorporated to make recommendations on a building expansion project.

St. Joseph's Hospital is located at 11705 Mercy Boulevard in Savannah, Georgia. The hospital plans to add an additional floor to the existing one-story building located northwest of Hillyer Drive and Mercy Blvd. The one-story building comprises two portions, including a one-story building built in 1966 attached by another one-story building built in 1974 to the south. The entire building is supported on a deep foundation consisting of Augured Cast-in-Place (ACIP) piles. The additional floors will add

additional loads on the pile foundations and therefore it is very important to determine if the design capacities of existing ACIP piles could support additional loads.

Information about the lengths and design capacities of ACIP pile can no longer be located according to the St. Joseph's Hospital. Non Destructive Testing (NDT) methods were used to determine the pile lengths and then the pile design capacities were estimated based on the pile lengths and subsurface information collected through Cone Penetration Test (CPT) soundings performed near the piles. Through the NDT methods, the physical characteristics of ACIP piles were determined without causing any physical damage on them. The SCPTu was used instead of commonly used borehole to perform the Parallel Seismic Method. This method provided good results of pile characteristics. This in conjunction with results of geotechnical investigation by CPTu function was used to determine the bearing capacity of the existing foundation.

GEOTECHNICAL SITE INVESTIGATIONS

Based on the CPT soundings performed at this site and reviewing the existing geotechnical study, the site subsurface primarily consists of medium dense sands (SP), clayey sands (SC) and silty sands (SM) in the upper 64 ft. The ground water was present at depths of 8 to 10 ft below ground surfaces. The average tip resistance is 74-95 tsf. The average SPT blow count is 18-21.

Figure 1 shows an example of the measured results by cone penetrometer equipped with pore pressure measurement unit (CPTu) and Standard Penetration Test (SPT). These include the variations of tip resistance, side friction, pore pressure and SPT blow count with depth. Locations with high pore pressure are typically correspondent to clay layers.

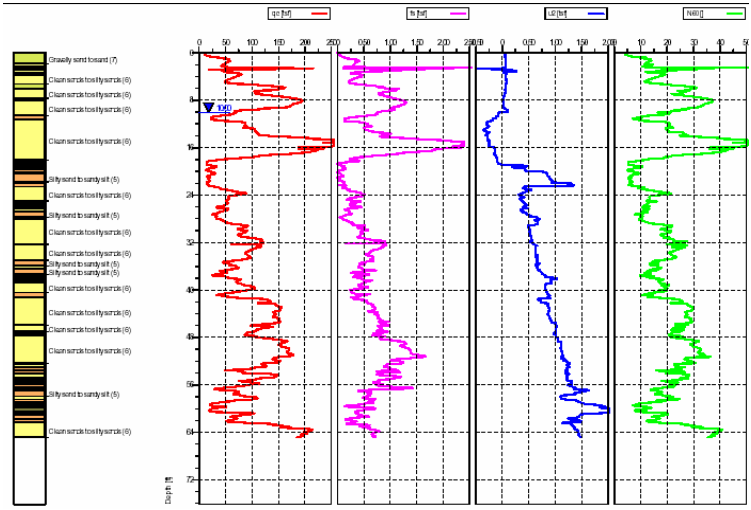

Fig. 1 Example Results of CPTu Test

FIELD SCPT TESTING PROGRAM

Figure 2a shows the outside view of the building wall. It also gives an overview on the locations of NDT tests in reference to the existing buildings. In order to perform the NDT tests, the upper soils below the pile cap and around the piles were removed manually at both outside and inside the walls. The dimensions of pile caps and piles were measured and shown in Fig. 2b. Parallel Seismic Tests were performed for piles installed below Column A3 and Column A19 of the building. The detailed procedures and findings are described and analyzed in the following context.

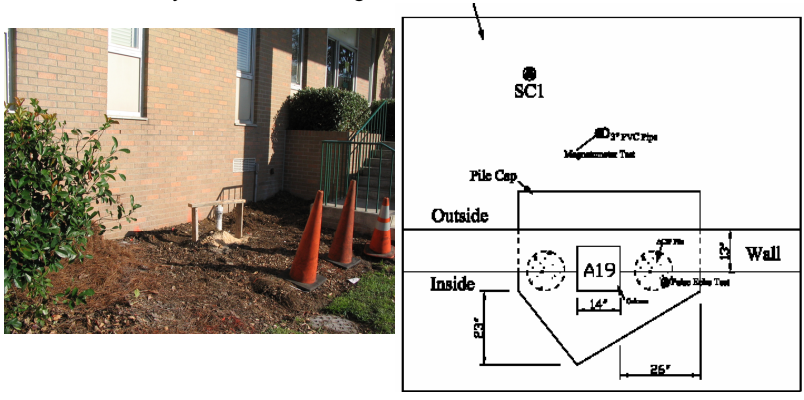

Fig. 2 (a) view of outside building (b) plane view of Column A19 and locations of drilled shaft

Parallel Seismic Tests is a widely accepted procedure to determine the length of unknown foundation (Telford et al. 1976, Olson et al. 1995, Liao et al. 1998, ASTM 2004). Figure 3b shows the conduct of Parallel Seismic Tests with the SCPTu. It typically involves drilling a borehole adjacent to the unknown foundation. Seismic recording units, either by borehole geophones or hydrometer, are lowered down to the borehole at give intervals to certain depths that is beyond the depth of the unknown foundation. At each depth, a seismic wave is sound by using a hammer to tap on the side of the wall or the pile cap. This seismic wave then propagates along the pile and reaches the geophone or hydrophone (Figure 3a). When the group of the seismic waves recorded at different depths is placed together, a systematic change in the trend of the first arrive in the wave train gives an estimation on the depth of the unknown foundation. This test can be performed for concrete, wood, masonry or steel foundations.

In this project, a novel testing procedure was employed. Parallel Seismic Tests are performed by 1) pushing a Cone Penetration Test with a Seismic Element (SCPTu) adjacent to a foundation element; 2) striking the foundation element to generate shear waves, the SCPTu can measure the arrival time of the waves; 3) performing this test at repeated intervals, the length of unknown foundation elements is determined. Figure 3a below shows the settings of a typical Parallel Seismic Test. The SCPTu used here extends beyond its traditional function of determining the soil type and strength data of the bearing stratum. The geophone in the cone tip acts as seismic receiver for the Parallel Seismic Tests.

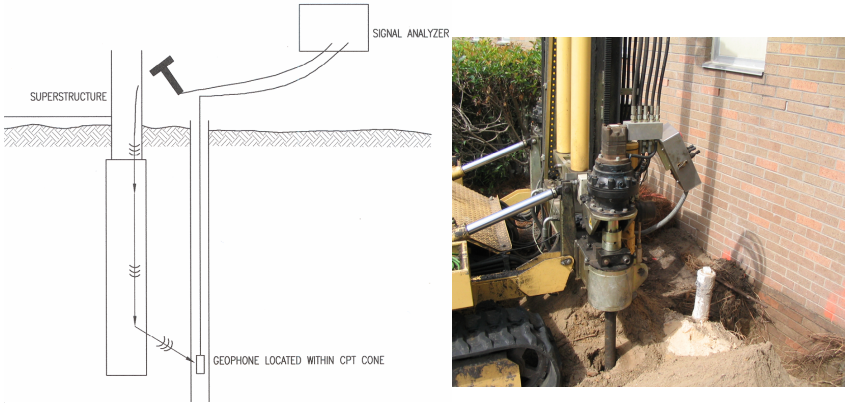

Fig. 3 a) Schematic of Parallel Seismic Testing; b) Parallel Seismic Test Using SCPTu

Parallel Seismic Tests were performed at a distance of approximately 3 ft from the exposed pile cap near Columns A3 and A19 outside the buildings (the schematic location of A19 is shown in Figure 2). A CPT cone instrumented with an accelerometer was pushed into the ground to record the seismic waves at a depth interval of every 3 ft until a depth of 65 ft. At each depth, seismic wave is generated by using a hammer to tap on the side of the wall. The propagating waves were recorded by the geophone embedded in the cone of the SCPTu unit.

RESULTS OF PARALLEL SEISMIC TESTING

Model development to interpret measured signals

Figure 4 shows the recorded signals at different depths near column A3. The processed signals with four major wave trains are also identified and shown in this figure. Four possible types of seismic wave trains are shown in the schematic plot. The first one is the compression wave through concrete pile until arrives at the approximate elevation of the geophone. It then propagates through soil or water to the geophone. The other three types of waves follow similar propagation path. These include the compression wave of water, compression wave in soil and shear wave in soil. The travel times required for the wave trains to arrive at geophone are given in Eq. (1).

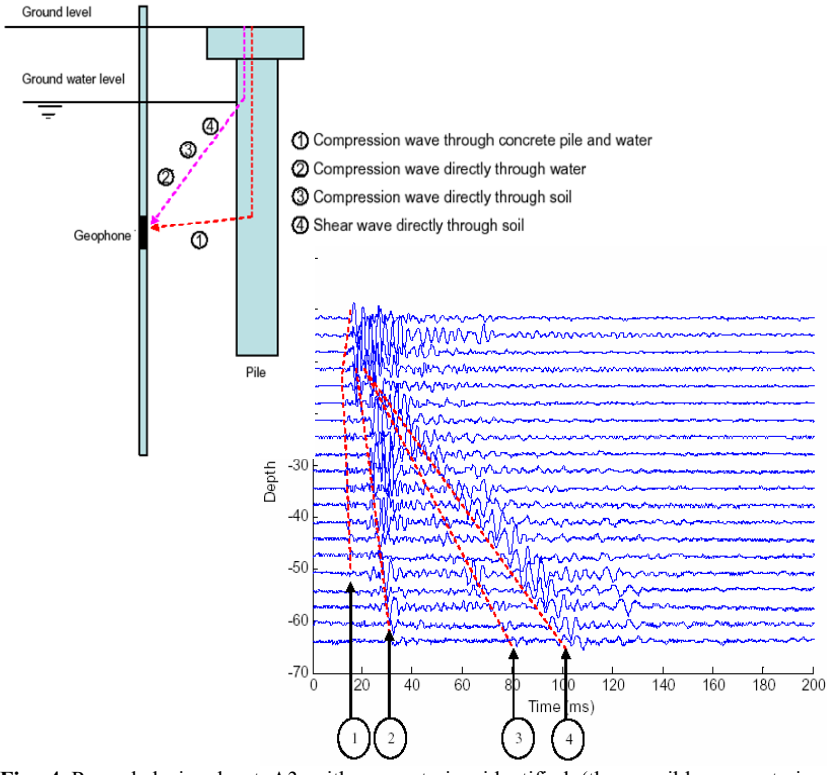

Fig. 4 Recorded signals at A3 with wave trains identified (the possible wave train propagation paths and modes are shown in the schematic drawings)

$$t_{Train,No.1} = \frac{d}{V_c} + \frac{\Delta}{V_{soil}} \tag{1a}$$

$$t_{Train,No.2} = \frac{L}{V_w} \tag{1b}$$

$$t_{Train,No.3} = \frac{L}{V_{c,soil}} \tag{1c}$$

$$t_{Train,No.4} = \frac{L}{V_{s,soil}} \tag{1d}$$

where d is the depth of the geophone, Δ is the horizontal distance between geophone and pile, V_c is the speed of stress wave in concrete, V_w is the speed of compression wave in water, $V_{c,soil}$ is the speed of compression wave in soil, $V_{s,soil}$ is the speed of shear wave in soil.

Estimation of pile length

Estimation of the pile length from the parallel seismic testing can be made by observing the change of the propagation speed of the first wave train; or it can be estimated by observing the change of the amplitude of wave train before and after exceeding the toe of pile. The later approach works when the energy of impact source is controlled or the signals are acquired using a string of geophones together with the same impacting source.

From the testing data collected at A3, the first wave train can be clearly observed up to a depth of 47.6 ft. The speed of this wave train is 12340 ft/sec, which is approximately the speed of wave in concrete. Thus this formation of this wave train corresponds to the travel of seismic wave along the pile. Referring to the principle of Parallel Seismic testing, this implies that the length of the pile foundation is at least up to 47.6 ft.

Similar observations were found on the testing data collected at column A19. The wave trains can be clearly identified up to 50.1 ft.

Under the ideal condition, it should be able to observe the change of slope for the first wave train in the Parallel Seismic testing signals (from speed of traveling in concrete to speed of traveling in pore water). These are illustrated in the predicted signals in Figure 5a. However, this can not be clearly identified from the testing data collected in these tests. The possible causes might be: 1) the interference of background noise. Since the geophone is located in the cone attached to the DCPT rig, the resonance frequency components corresponding to the CPT rod might be a major source of background noise; 2) insufficient amount of energy delivered to the testing pile due to in accessibility to the pile itself; 3) the insufficient depth of investigation compared with the length of pile.

Results of sensitivity analyses using the simplified wave propagation model are conducted to further validate the previous conclusion. Compared with pile length of 50ft, assuming the length are pile 30 ft or 40 ft, they will resulted in the delay of wave train arrival of around 2.4 ms and 1.1 ms respectively (Figure 5b). These difference should have been sufficient large to be identified considering the fact that the quality of signals above 50 ft are clearly edible. The sensitivity analyses further validated that the identification of the pile length based on the speed of the first wave train is sound.

(a)

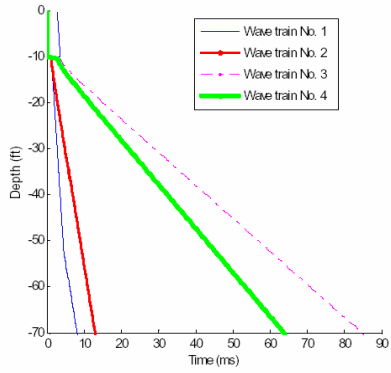

$$t_{Train,No.1} = \frac{d}{V_c} + \frac{\Delta}{V_{soil}}$$

$$t_{Train,No.2} = \frac{L}{V_w}$$

$$t_{Train,No.3} = \frac{L}{V_{c,soil}}$$

$$t_{Train,No.4} = \frac{L}{V_{s,soil}}$$

(b)

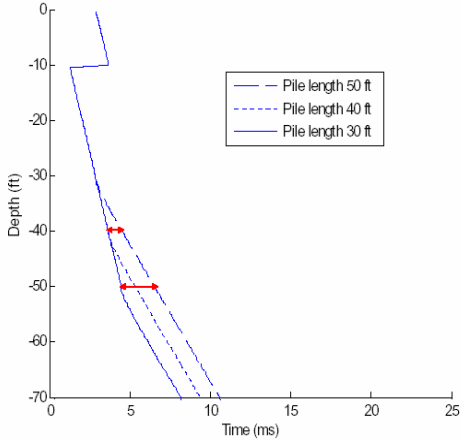

Fig. 5 (a) the predicted first arrival of different wave trains using the propagation paths shown in Figure 4, (b) the sensitivity of the first arrival on the pile length.

In summary: From the testing data collected at column A3, the first wave train was observed up to a depth of 47.6 ft. This implies that the length of the drilled shaft is at least up to 47.6 ft. The testing data collected at Column A19 further validated this assessment. The recorded signals show that first wave train from the Parallel Seismic testing at Column A19 can be clearly identified up to 50.1 ft.

PILE CAPACITY ESTIMATION

Based on the results of parallel seismic test, it is conclude that the ACIP piles are embedded to a depth between 47 and 50 ft below existing grades. After excluding the thickness of pile caps, the ACIP pile should have an embedment length between 44 and 47 ft. To be conservative, a pile length of 44 ft is considered when calculating the pile design capacity. The pile capacity is calculated by using LCPC method (French Method)

based on the CPT sounding data obtained at two sounding locations. Based on the analysis, the existing ACIP pile should have an allowable compression capacity of 50 tons with a factor of safety of 2 (Fig. 6). An uplift capacity of 30 tons may be used for the addition design. Based on the thickness of the pile caps used, it appeared the piles were embedded more than 12 inches into the pile cap, so the piles should behave similar to piles with fixed head connection. A lateral load of 12 kips is recommended as lateral design load for an allowable pile head deflection of 0.25 inches.

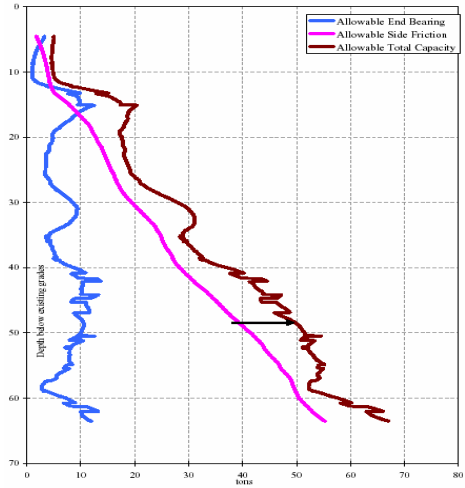

Fig. 6 Pile Net Bearing Capacity With Depth using French Method

SUMMARY AND CONCLUSIONS

This paper introduces the application of seismic piezo-cone SCPTu in parallel seismic test to nondestructively determine the length and bearing capacity of unknown ACIP pile foundation. SCPT was used to perform the parallel seismic test to estimate the length of the unknown ACIP pile. This information was used in conjunction with geotechnical data to estimate the bearing capacity of the existing foundation. Combined application of geophysical and geotechnical functions of SCPTu assisted the decision by the property owner on the building expansion plan. This method combines the function of SCPTu as both geotechnical investigation tool and geophysical survey tool. To ensure the successful application of this method, it is important to conduct a well planned testing program and perform sound interpretations of geophysical signals.

REFERENCES

ASTM Book of Standards, 2004. D5882, vol. 04.09.
Liao, S.-T., Roesset, J.M., Chen, C.-H., 1998. Numerical simulation of nondestructive

Parallel Seismic test for piles. In: The Sixth East Asia-Pacific Conference on Structural Engineering and Construction, Taipei, Taiwan, 1997–2003.

Olson, L.D., Jalinoos, F., Aouad, M.F., 1995. Determination of Unknown Subsurface Bridge Foundations, Report submitted to NCHRP, Transportation Research Board, National Research Council, pp. 129–148.

Telford, W.M., Geldart, L.P., Sheriff, R.E., and Keys, D.A., 1976, Applied Geophysics: Cambridge Press, 155-160.

Effects of Damping and Dynamic Soil Mass on Footing Vibration

H.V. Phuong Truong

Ph.D., P.E. (California), Email: hvptruongya@yahoo.com

ABSTRACT: Effects of different kinds of damping and dynamic soil mass on horizontal and vertical footing vibration, e.g. dynamic stiffness and footing mass, have been analyzed. Total damping should include material damping and geometrical damping. Material damping tends to reduce the dynamic stiffness of the footing. Dynamic soil mass and the effect of footing mass with respect to the geometrical damping have been considered in the vibration analyses. Expressions for total mass, total damping and total dynamic stiffness of the system for horizontal and vertical vibration have been presented in this paper for use in these analyses.

The differential equation for evaluation of these effects and some important circular frequencies for horizontal vibration of a rigid footing on an elastic half space are discussed. The newly presented expressions for total mass, total damping and total dynamic stiffness could be used to calculate whether permanent displacement or resonant frequency and the maximum amplitude of vibration will occur.

INTRODUCTION

Rainer (1975) considered three sources of damping in dynamic structure-foundation interaction: inter-storey damping (not considered here), foundation material damping, and radiation damping. He found the material damping in the foundation soil contributes significantly to the overall damping ratio by comparing the numerical results from two methods of calculating the damping ratio for structures on compliant foundations. One method employs the calculation of the system damping ratio from the dynamic amplification factor; and the other uses the modal damping ratio from energy considerations.

Radiation damping results in energy being removed from the compliant system by the foundation medium during a dynamic disturbance by propagation of waves into the support medium (Rainer 1975). Radiation damping is commonly called geometrical or viscous damping. External viscous damping is caused by the structure moving through surrounding air (or water, in some cases), and it is generally less significant than other sources of damping.

Friction damping is another type of damping considered by many researchers including Richart et al. (1970) who mentioned the footing system comes to rest after some finite time interval, whereas a viscously damped system theoretically never stops moving.

Body-friction damping, also known as Coulomb friction, results from friction between members in contact.

Expressions for geometrical damping and dynamic stiffness for a new forcing function have been developed by Truong (1991a, 1993), and Truong and Moore (1995a). The geometrical damping and the dynamic stiffness have been found inversely proportional to the circular frequency and linearly proportional to the circular frequency, respectively. Similar forms of damping and dynamic stiffness have also been shown by Yan (1981) and Elsabee et al. (1977).

In the present paper some of the theoretical formulae presented by the author in 1990s have now been updated to include dynamic soil mass and material damping, and to show the effect of footing mass on the expression of damping.

TOTAL DAMPING FOR HORIZONTAL AND VERTICAL VIBRATION

A. For horizontal vibration, the total damping has now been updated by using (i) the new expressions of geometrical damping by Truong (1991a, 1993), and Truong and Moore (1995a), (ii) the effect of footing mass on geometrical damping (Truong, 1993), and (iii) material damping proposed by Dobry and Gazetas (1985). From different methods previously presented by other researchers, the total damping could now be expressed as follows:

(a) The Bycroft's method (1956) is now modified to become:

$$C_{th1} = \frac{32(1-\mu)Gr_o}{(7-8\mu)\omega}(1+b) - m_f\omega^2 \qquad (1)$$

Where μ = Poisson' ratio.

m_f = the mass of the footing.

G = Shear Modulus

r_o = the radius of the circular footing

ω = Circular frequency of the footing

b = material damping constant

Note that b is the material damping constant, which is twice the dynamic material damping ratio (Vierck, 1967 and Wolf, 1985). For cohesionless soils, b is equal to 0.05 (Whitman and Richart, 1967).

(b) The method shown by Veletsos and Wei (1971) is now modified to become:

$$C_{th2} = \frac{8Gr_o}{(2-\mu)\omega}(1+b) - m_f\omega^2 \qquad (2)$$

B. Similarly, for vertical vibration, the method for total damping presented by Timoshenko and Goodier (1951) is now modified to become:

$$C_{tv} = \frac{4Gr_o}{(1-\mu)\omega}(1+b) - m_f\omega^2 \qquad (3)$$

DYNAMIC SOIL MASS

Dynamic soil masses for a new forcing function which were described by Truong (1993 and 2009) have increased with the area of the footing, the square root of both shear

modulus and density, and decreased with the circular frequency for both vertical and horizontal vibration. The ratio of the dynamic soil masses for the two modes is equal to the ratio of velocity of Push wave (P-waves), V_p, to that of Shear wave (S-waves), V_s. Dynamic soil mass could be defined as the vibrating soil mass directly under the footing and tends to resist the effects of footing vibrations, especially footing mass.

Note that dynamic soil mass is the "added soil mass" which has been used by many researchers who found that (i) some soils under the foundations, which are so called "added soil masses" or "in-phase soil masses", are vibrating with the foundation and should be added to masses of the foundation in analyses, and (ii) the added soil masses increase with the increase in the area of the foundation, shear modulus and density and decrease with the increase in the circular frequency.

The reasons that the author does not use the term "added soil mass" in the present paper are: (i) the dynamic soil mass, which is based on a new forcing function (Truong, 1991a and 1993), always has a negative sign based on the development for both horizontal and vertical vibration, and (ii) rather than added the dynamic soil mass is actually subtracted from the footing mass. So, the total mass of the footing system for horizontal and vertical vibration can now be expressed, respectively, as follows:

$$M_{th} = m_f - \frac{A\sqrt{\rho G}}{\omega} \tag{4}$$

$$M_{tv} = m_f - \frac{A\sqrt{\rho G}}{\omega s} \tag{5}$$

where A = Area of footing.

ρ = Mass Density of the medium, and

$$s = \frac{\sqrt{(1-2\mu)}}{\sqrt{2(1-\mu)}} \tag{6}$$

TOTAL DYNAMIC STIFFNESS FOR HORIZONTAL AND VERTICAL VIBRATION

A. For horizontal vibration, the total dynamic stiffness based on (i) new expressions of dynamic stiffness by Truong (1991a, 1993) and Truong and Moore (1995a), and (ii) dynamic stiffness with the effect of material damping proposed by Dobry and Gazetas (1985), can now be expressed as follows:

(a) The Bycroft's method (1956) is now modified to become:

$$K_{th1} = \frac{18.4(1-\mu)}{(7-8\mu)}\omega r_o^{\,2}\sqrt{\rho G}\left(1-\frac{b}{2}\right) \tag{7}$$

(b) The method shown by Veletsos and Wei (1971) is now modified to become:

$$K_{th2} = \frac{4.6}{(2-\mu)}\omega r_o^{\,2}\sqrt{\rho G}\left(1-\frac{b}{2}\right) \tag{8}$$

(c) Other dynamic stiffness presented by Truong (1993) is now modified:

$$K_{th3} = \pi\omega r_o^{\,2}\sqrt{\rho G}\left(1-\frac{b}{2}\right) \tag{9}$$

B. For vertical vibration, similarly, the total dynamic stiffness can now be expressed as follows:

(a) The method shown by Timoshenko and Goodier (1951) is now modified to become:

$$K_{tv1} = \frac{3.4}{(1-\mu)} \omega r_o^{\,2} \sqrt{\rho G} \left(1 - \frac{b}{2}\right) \tag{10}$$

(b) Other dynamic stiffness presented by Truong (1993) is now modified:

$$K_{tv2} = \frac{\pi}{s} \omega r_o^{\,2} \sqrt{\rho G} \left(1 - \frac{b}{2}\right) \tag{11}$$

Note that the ratio of two expressions of two dynamic stiffnesses [(Eq.(11) and Eq. (9)] is equal to (i) the ratio of the dynamic soil masses for the equivalent two modes, and (ii) the ratio of velocity of Push wave (P-waves), V_p, to that of Shear wave (S-waves), V_s.

DIFFERENTIAL EQUATION OF PURE HORIZONTAL VIBRATION

The differential equation of motion for the lumped parameter model with a single degree of freedom for a footing having a circular base resting on the soil surface and subjected to pure horizontal vibration can be presented to evaluate the above expressions as follows:

$$M_t \frac{dx^2}{dt^2} + C_t \frac{dx}{dt} + K_t x + F_x = P_o T + P_o \sin \omega t \tag{12}$$

where F_x = Coulomb friction force for horizontal direction
x = the displacement with any time t.
P_o = Constant or Magnitude of Cyclic load
T = Constant
P_o T = Constant load
t = Time Variable

The general solution, x(t), for the equation (12) can be found in any text on differential equations. Note that the total mass and the total damping of the system in Eq. (12) could be equal to 0 with the appropriate circular frequency.

(i) The circular frequency that the total mass of the system becomes zero by using Eq.(4) is

$$\omega_m = \frac{A\sqrt{\rho G}}{m_f} \tag{13}$$

(ii) The circular frequency that the total damping of the system becomes zero by using Eq.(2) is

$$\omega_c^{\,3} = \frac{8}{(2-\mu)} \frac{G r_0}{m_f} (1+b) \tag{14}$$

(iii) The undamped natural circular frequency of the system by using Eq. (9) is

$$\omega_n = \frac{\pi}{m_f} r_o \sqrt{\rho G} \left(2 - \frac{b}{2}\right) \tag{15}$$

Truong (2010) has used the above expressions and also developed new dynamic spring constant to analyze for a vertical single-cylinder compressor shown in the textbook by Richart et al. (1970).

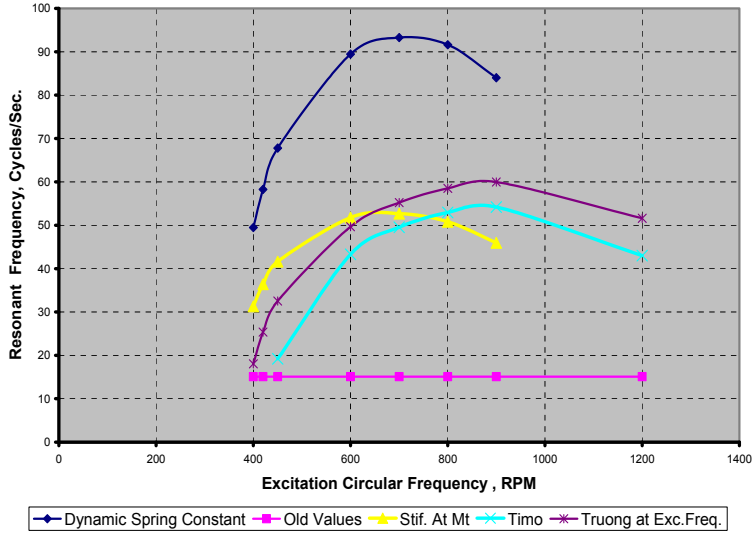

Figure 1: Variation of Resonant Frequencies with Excitation Frequencies.

Truong (2010) has shown that the resonant frequency obtained by using the above expressions varies with the excitation frequency, initially increases with the increase in the small excitation frequencies, and finally decreases with the increase in the larger excitation frequencies. The resonant frequencies from different methods are about 3.6 to 4.0 times the resonant frequency based on the old constant values of stiffness and damping by Richart et al. (1970) (Fig.1).

An analytical treatment of coupled rocking and sliding with vertical vibration has been presented by Truong (1991a, 1991c, and 1993) with the effects of Coulomb friction forces, two-layered system deposits, embedment, material damping, dynamic soil mass, and new expressions of dynamic stiffness and damping parameters for a new forcing function. The analytical results with the above expressions for total mass, total damping and total dynamic stiffness could be used to calculate whether permanent displacement (Truong 1991b, 1991c, and 1991d) or resonant frequency and maximum amplitude of footing vibration (Truong 2010) will occur.

CONCLUSIONS

The total damping of the footing system is equal to the sum of the geometrical damping and material damping, minus the product of the footing mass and square of the circular frequency, for both vertical and horizontal vibration.

The total mass of the footing system is equal to the footing mass minus the dynamic soil mass. The total mass and total damping could be equal to zero with the appropriate non-zero circular frequencies.

The total stiffness of the footing system is the dynamic stiffness minus the effect of material damping on stiffness.

The expressions for the geometrical damping, material damping and dynamic soil mass are inversely proportional to the circular frequency of the footing system. But the expression for the total dynamic stiffness is linearly proportional to the circular frequency.

REFERENCES

Bycroft, G.N. (1956) "Forced Vibrations of a Rigid Circular Plate on a Semi-Infinite Elastic Space on an Elastic Stratum" *Philosophical Trans*., Royal Soc. London, Ser. A, Vol.248: 327-368.

Dobry, R. and Gazetas, G. (1985) "Dynamics Stiffness and Damping of Foundations by Simple Methods" Vibration Problems in Geot. Eng., *Proc.of Symp*. Sponsored by the Geot. Eng. Div. in Conjunction with the ASCE Convention in Detroit, Michigan Oct. 22:75-107.

Elsabee, F., Kausel, E. and Roesset, J.M. (1977) "Dynamic Stiffness of Embedded Foundations" *Proc. Advances in Civil Eng. Through Eng. Mechanics*: 40-43.

Rainer, J.H. (1975) "Damping in Dynamic Structure-Foundation Interaction" *Canadian Geotechnical Journal*, Vol. 12: 13-22.

Richart, F.E. Jr., Woods, R.D., and Hall, J.R. Hall (1970). "Vibrations of Soils and Foundations" *Prentice-Hall*, 414p.

Timoshenko, S.P. and Goodier, J.N. (1951) "Theory of Elasticity" *McGraw Hill Book Co.*, 506p.

Truong, H.V.P. (2010), "Dynamic Spring Constant and Effect of Frequency on Footing Vibration' Proc. *17th Southeast Asia Geotechnical Conference in Taiwan in* May 2010 (In Preparation).

Truong, H.V.P. (2009). "Added Soil Mass and Ratio of Damping For Vertical and Horizontal Vibration", *Proc.11thConference on Science and Technology*, University of Technology in Saigon, Vietnam National University, Vietnam: 24-30.

Truong, H.V.P. and Moore, P.J. (1995b). "Permanent Displacements and Tilting Angle of Small Footings on Sand" *Proceeding 3rd. International Conference on Recent Advances in Geotechnical Earthquake Engineering and Soil Dynamics,* St.Louis, Missouri, USA, Vol.III: 1105-1110.

Truong, H.V.P. and Moore, P.J. (1995a). "Development of New Stiffness and Damping Expressions For Footing Vibrations" *Proceeding 3rd. International Conference on Recent Advances in Geotechnical Earthquake Engineering and Soil Dynamics,* St.Louis, Missouri, USA, Vol.II: 783-788.

Truong, H.V.P (1993). " Behaviour of Small Footings Subjected to Horizontal Vibratory Loading" *Ph.D. Thesis*, The University of Melbourne, Australia.

Truong, H.V.P (1991d). "Movement of Bridge Abutment Due to Cyclic Loading," *Proceeding Ninth Asian Regional Conference on Soil Mechanics and Foundation Engineering*. (9 ARC), Bangkok Thailand: 297-300.

Truong, H.V.P (1991c) "Lotus 1-2-3 In Permanent Displacement*" Proc. Seventh Conference of the International Association For Computer Methods and Advances in Geomechanics,* Cairns, Queensland, Australia: 93-100.

Truong, H.V.P (1991b). "Parametric Study of Horizontal Permanent Displacement on Sand" *Proc. Second International Conference on Recent Advances in Geotechnical*

Earthquake Engineering and Soil Dynamics, St. Louis, Missouri , USA: 675-678.

Truong, H.V.P (1991a). "Lumped Parameters in Permanent Displacement" *Proc. Second International Conference on Recent Advances in Geotechnical Earthquake Engineering and Soil Dynamics*, St. Louis, Missouri, USA: 13-16.

Veletsos, A.S and Wei, Y.T. (1971) "Lateral and Rocking Vibration of Footings" *J. of the Soil Mechanics and Found. Div.,* ASCE, Vol.97, SM9: 1227-1249.

Vierch, R.K. (1967). "Vibration Analysis", *International Textbook Company*, Scranton, Pennsylvania, 387 p.

Whitman, R.V. and Richart, F.E. Jr. (1967). "Design Procedures For Dynamically Loaded Foundations" *J. Soil Mechanics and Foundations Div.,* ASCE, SM6: 16-193.

Wolf, J.P. (1985). "Dynamic Soil-Structure Interaction" *Prentice Hall*, Englewood Cliffs, N.J., 466 p.

Yan, R.J. (1981) "In-Situ Measurement of Coupled Vibration Parameters" *Proc. 10th Inter. Conf. on Soil Mechanics and Found. Eng.*, Vol.3: 327-332.

Ground Vibration Caused by Dynamic Excitation on Pile Foundation

Xuecheng Bian[1], Guang Song[2] and Yunmin Chen[3], Hirokazu Takemiya[4],

[1]Associate professor, Department of Civil Engineering, Zhejiang University, Hangzhou, China, 310058; bianxc@zju.edu.cn
[2]Graduate student, Department of Civil Engineering, Zhejiang University, Hangzhou, China, 310058; songguang49@gmail.com
[3]Professor, Department of Civil Engineering, Zhejiang University, Hangzhou, China, 310058; chenyunmin@zju.edu.cn
[4]Professor, Department of Environmental and Civil Engineering, Okayama University, Tsushima Naka 3-1-1, Japan; e_quakes@cc.okayama-u.ac.jp

ABSTRACT: A computational approach based on pile-soil dynamic interactions was developed to analyze ground response due to excitation on pile foundation. In this work, pile group was assumed to have the concentric arrangement. The geometric and material properties of piles and soils were assumed to be invariable along the azimuth angle by introducing the equivalent stiffness of grouped piles. An axisymmetric finite-element model was employed after taking the Fourier expansion in azimuth for computational convenience. The field test of ground vibration in the vicinity of pile foundation which was subjected to horizontal loading by a shaker at the top of the footing was used to verify the proposed approach. The comparison of the simulated results and the field recorded data showed good agreement. This proved the reliability of the axisymmetric three-dimensional finite element program to predict the field vibrations considering pile-soil interactions.

INTRODUCTION

Viaduct with pile foundation is widely used in high-speed railway. Plenty of works have been done to study viaduct vibration under train's moving loads (Liu, (2009), Ju (2003), Cheng (2001)). But the soil-pile foundation-structure interaction has been paid less attention in these previous works. However, soil-structure interaction significantly affects the dynamic response of viaduct under the high-speed train loading (Takemiya (2007)). Besides, study on ground vibration caused by train running over viaduct is another important issue from environmental amenity considerations. To determine the vibration propagation from pile foundation to adjacent ground soil, soil-pile interaction analysis is indispensible (Yang (2005), Takemiya (2008)).

To evaluate soil-pile interaction in the dynamic sense, Wolf (1978) showed a

substructure method in the finite element formulation in which the soil flexibility with respect to the interface nodes with piles was first computed and the corresponding stiffness as obtained by the inverse was incorporated into the grouped piles analysis. For the computation of soil flexibility, Waas (1981) took an efficient semi-analytical scheme (discretizing the response in the depth and expanding it into the Fourier harmonics in the circumferential direction and adopting the associated analytical solution in the radial direction), and evaluated it by using a Green function for a point loading.

Semi-analytical solution with axisymmetric finite element method is efficient and effective to study the dynamic problem of pile foundation with the ring-like arrangement of pile group (Takemiya (1981,1986)). One of its basic assumptions is that the geometric and material properties are invariable in the angular direction. Then, for the axisymmetric bodies subject to non-axisymmetric loadings, the Fourier expansion is applied both for the displacement components and load components. This solution has advantages in saving the memory and computational efforts, specially for the full three dimensional numerical simulation.

INTERACTION OF PILE FOUNDATION AND SURROUNDING SOIL

In order to formulate the soil-pile foundation system, we model the near field and pile foundation by three-dimensional axisymmetric finite elements, while the far field that extend horizontally by the thin layer elements, as depicted in FIG. 1. By applying the substructure concept, the interaction of soil elements and pile foundation element is depicted in FIG. 2. The model is actually a three dimensional case, but for illustrative convenience, the model is depicted in two-dimensional plane.

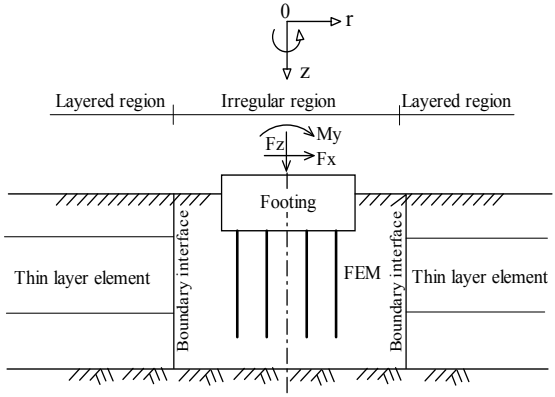

FIG. 1. Soil-pile foundation interaction analysis model

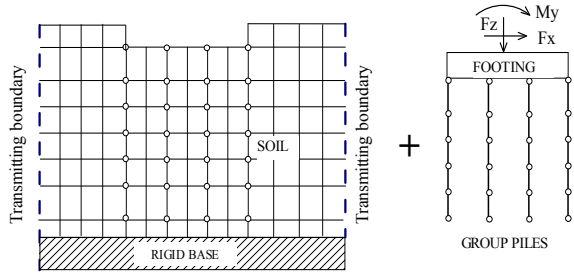

FIG.2. Substructures for the soil and pile foundation interaction

To describe the ground motion under the applied forces, the governing equations are formulated in the cylindrical coordinate system (u,r,θ). Since the displacements and stresses do not vary dramatically around the circumference, the Fourier expansion of the displacement along the circumference is performed and the foundation and ground motions are approximated by the first several series items.

The displacements in cylindrical coordinate system after applying the Fourier expansion can be expressed as

$$\{u(r,\theta,z)\}=\sum_{n=0}^{\infty}\left[H_n^s(\theta)\right]\{u_n^s(r,z)\}+\sum_{n=0}^{\infty}\left[H_n^a(\theta)\right]\{u_n^a(r,z)\} \tag{1}$$

where, the Fourier amplitudes $u_n^{s(a)}(r,z)$ are independent from the azimuth and can be defined as

$$\{u_n^s(r,z)\}=\{u_r^s \quad u_\theta^s \quad u_z^s\}^T, \quad \{u_n^a(r,z)\}=\{u_r^a \quad u_\theta^a \quad u_z^a\}^T,$$

and,

$$[H_n^s(\theta)]=diag.(\cos n\theta,-\sin n\theta,\cos n\theta), \quad [H_n^a(\theta)]=diag.(\sin n\theta,\cos n\theta,\sin n\theta)$$

The superscripts 's' and 'a' stand for the symmetric and anti-symmetric terms, respectively. In case of the smoothly deformed configuration, the n=0 and 1 terms would be enough to describe the pile and soil responses. Namely, the n=0 symmetric harmonic represents a vertical motion in Z-direction as well as a symmetric dilation, while the n=0 anti-symmetric does a torsional motion about Z-axis. The n=1 symmetric harmonic relates a coupled motion of translation along X-axis ($\theta=0^o$) and rotation about Y-axis ($\theta=90^o$), and the n=1 anti-symmetric harmonic does a coupled motion of translation along Y-axis and rotation about X-axis.

Governing equations of ground motions is stated by Navier equations as:

$$\left(\lambda^c+2\mu^c\right)\nabla\left(\nabla\cdot\{u\}\right)-\mu^c\nabla\times\nabla\times\{u\}+\{q\}-\rho\{\ddot{u}\}=0 \tag{2}$$

where $\{u\}$ is ground displacement, and $\{q\}$ is force. ρ is density. λ^c, μ^c are the Lame constants of the soil media including a small part of complex number to consider the ground damping effect.

If β is the internal damping of soil, then the Lame constants can be expressed as,

$$\lambda^c=\lambda(1+2i\beta), \quad \mu^c=\mu(1+2i\beta) \tag{3}$$

According to the prior assumption of the axisymmetric arrangement in the analysis model, the displace and forces vectors can be given after the Fourier expansion along the circumference direction in the cylindrical coordinate system,

$$\{u(r,\theta,z)\}=\sum_{n=0}^{\infty}\left[H_n^s(\theta)\right]\left\{\tilde{u}_n^s(r,z)\right\}+\sum_{n=0}^{\infty}\left[H_n^a(\theta)\right]\left\{\tilde{u}_n^a(r,z)\right\} \tag{4.1}$$

$$\{P(r,\theta,z)\}=\sum_{n=0}^{\infty}\left[H_n^s(\theta)\right]\left\{\tilde{P}_n^s(r,z)\right\}+\sum_{n=0}^{\infty}\left[H_n^a(\theta)\right]\left\{\tilde{P}_n^a(r,z)\right\} \tag{4.2}$$

where $\{u(r,\theta,z)\}=\{u_r \quad u_\theta \quad u_z\}^T$,

and $\left[H_n^s(\theta)\right]=diag\left(\cos n\theta \quad -\sin n\theta \quad \cos n\theta\right)$

$\left[H_n^a(\theta)\right]=diag\left(\sin n\theta \quad \cos n\theta \quad \sin n\theta\right)$

Furthermore, the symmetric mode is independent to the anti-symmetric mode, which makes the motion equations to be decoupled.

To solve the equations for ground system motions with finite element method, $\left\{\tilde{u}_n^s\right\}$, $\left\{\tilde{u}_n^a\right\}$ will be discretized into finite elements with specific Fourier expansion series. In this work, the quadrilateral elements are used to discretize the near field in vicinity of the piled foundation. The displacement field inside the element can be expressed by the node displacement at four nodes $\left\{\tilde{u}_n^e\right\}$ by introducing the interpolation function $\left[N(r,z)\right]$, the finite element formulation can be deduced with the conventional procedure as,

$$\left[K_n\right]\{U\}+\left[M_n\right]\left\{\ddot{U}\right\}=\{P_n\} \tag{5}$$

where $\left[K_n\right]$, $\left[M_n\right]$ and $\left[P_n\right]$ are stiffness matrix, mass matrix and applied force vector respectively. The detailed formulations can be expressed as,

$$\left[K_n\right]=\sum_{\text{element}}\left[\alpha_{1n}\iint[N]^T[B_{1n}]^T[D_1][B_{1n}][N]r\ \mathrm{dr\,dz}+\alpha_{2n}\iint[N]^T[B_{2n}]^T[D_2][B_{2n}][N]r\ \mathrm{dr\,dz}\right]$$

$$\left[M_n\right]=\sum_{element}\iint\rho[N]^T[\alpha_n][N]r\ \mathrm{dr\,dz}$$

$$\{P_n\}=\sum_{element}\left[\iint[N]^T[\alpha_n]\{q_n\}r\ \mathrm{dr\,dz}+\int_S[N]^T[\alpha_n]\{t_n\}ds\right]$$

where,

$$\left[B_{1n}\right]=\begin{bmatrix}\dfrac{\partial}{\partial r} & 0 & 0\\ \dfrac{1}{r} & 0 & -\dfrac{n}{r}\\ 0 & 0 & \dfrac{\partial}{\partial z}\\ \dfrac{\partial}{\partial z} & 0 & \dfrac{\partial}{\partial r}\end{bmatrix} \qquad \left[B_{2n}\right]=\begin{bmatrix}\dfrac{n}{r} & -\dfrac{1}{r}+\dfrac{\partial}{\partial r} & 0\\ 0 & \dfrac{\partial}{\partial z} & \dfrac{n}{r}\end{bmatrix}$$

$$[D_1]=\begin{bmatrix} \lambda^c+2\mu^c & \lambda^c & \lambda^c & 0 \\ \lambda^c & \lambda^c+2\mu^c & \lambda^c & 0 \\ \lambda^c & \lambda^c & \lambda^c+2\mu^c & 0 \\ 0 & 0 & 0 & \mu^c \end{bmatrix}, \quad [D_2]=\begin{bmatrix} \mu^c & 0 \\ 0 & \mu^c \end{bmatrix}$$

The coefficients related to symmetric or anti-symmetric motions are given:

$$\left[\alpha_n^s\right]=diag\left(\alpha_{1n}^s \quad \alpha_{1n}^s \quad \alpha_{2n}^s\right), \quad \left[\alpha_n^a\right]=diag\left(\alpha_{1n}^a \quad \alpha_{1n}^a \quad \alpha_{2n}^a\right)$$

in which,

for $n=0$: $\alpha_{1n}^s=\alpha_{2n}^a=2\pi$, $\alpha_{2n}^s=\alpha_{1n}^a=0$

for $n\neq 0$: $\alpha_{1n}^s=\alpha_{2n}^s=\alpha_{1n}^a=\alpha_{2n}^a=\pi$

MODELING OF PILE WITH BEAM ELEMENTS

A pile foundation mostly comprises a group of piles with a footing on top of them. Therefore, the pile-soil-pile interaction occurs inevitably. A deliberate consideration is made in establishing the equilibrium condition between the discrete piles and the continuum soils. Piles in circular cross sections are assumed to be in a concentric layout, as shown in FIG.3.

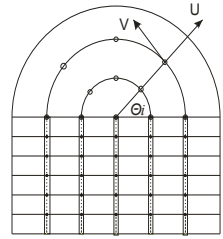

FIG.3. Modeling of pile positioned in concentric layout

The behavior of piles on the same radius from the center is also approximated by the limited Fourier harmonics of n=0 and 1 along the circumferential direction connecting the relevant piles axis. This assumption is reasonable as far as the rings of piles maintain the original axisymmetric configuration during the motion at any depth. In the analysis of the interaction problem between discrete ring-piles and the surrounding continuum soils, the pile element and the neighboring soil element are assumed to have the same translation displacements at the connection nodes. The piles are modeled by the 2-noded 3-dimensional beam elements; the dynamic stiffness of *n*th Fourier harmonic expansion is integrated into the soil stiffness. The original pile properties are used regardless the development of cavity of soil that can be observed in the field.

MASTER-SLAVE RELATION OF RIGID FOOTING AND PILES

A pile foundation has mostly a rather rigid cap (or footing) on top of flexible grouped piles to which the latter are built in. Once the impedance of ring-pile heads and the

corresponding effective input forces are evaluated, the dynamic equilibrium can be established in the Cartesian coordinate system, including the rotational degrees of freedom together with the translational ones at pile cap.

In order to account for all the contribution from each ring of piles to the 6 degrees of freedom of motion by the footing, the master-slave relation of footing and piles is applied as given below.

The rigid motions of a footing in terms of the Fourier series are now derived as the decomposition of the response into independent modes. Namely, vertical and torsional motions, coupled motions of sway and rocking in the perpendicular vertical planes, are expressed in the form of

$$\begin{Bmatrix} u(\theta) \\ \Phi(\theta) \end{Bmatrix} = \sum_{n=0}^{1} \left\{ \mathbf{S}_n^s(\theta)\mathbf{U}_b + \mathbf{S}_n^a(\theta)\mathbf{U}_b \right\} \tag{6}$$

where

$$\overset{3}{\left[S_0^s\right]} = \begin{bmatrix} 0 \\ 0 \\ 1 \\ 0 \\ 0 \\ 0 \end{bmatrix}_{6\times 6}, \overset{6}{\left[S_0^a\right]} = \begin{bmatrix} -r\sin\theta \\ r\cos\theta \\ 0 \\ 0 \\ 0 \\ 1 \end{bmatrix}_{6\times 6} \quad \overset{1}{\overset{5}{\left[S_1^s\right]}} = \begin{bmatrix} 1 & z \\ 0 & 0 \\ 0 & -r\cos\theta \\ 0 & 0 \\ 0 & 1 \\ 0 & 0 \end{bmatrix}_{6\times 6} \quad \overset{2}{\overset{4}{\left[S_1^a\right]}} = \begin{bmatrix} 0 & 0 \\ -1 & -z \\ 0 & r\sin\theta \\ 0 & 1 \\ 0 & 0 \\ 0 & 0 \end{bmatrix}_{6\times 6}$$

elements appearing in the matrices correspond to the influence vector coefficients for the coordinates of x, y, z, ϕ_x, ϕ_y, ϕ_z, while the rest of elements vanish. For the interface nodes with soils, the elements in bottom half of the matrices should be zero in the above matrices.

VERIFICATION OF COMPUTATION MODEL WITH FIELD TESTS

The axisymmetric model yields the response on the cylindrical coordinates. These amplitudes are then transformed into the quantities on the Cartesian coordinates. To verify the proposed computation approach, a pile foundation designed for Taiwan high-speed railway is used.

The soil condition and pile arrange are shown in FIG. 4(a) and 4(b), respectively. The detail of the footing dimension is also depicted. The piles are modeled into two rings of beam elements as shown in FIG.4(c). Because of the high rigidity of the footing structure, it's regarded as a rigid block. The motions of the footing are transferred to the interface soil nodes with the master-slave relation. In the numerical computation, the amplitude of the harmonic exerting load is 10kN to keep accordance with the output force from the shaker in field test.

The transmitting boundary elements are arranged at the side boundary of the near field modeled by finite elements. A rigid bed rock is applied at the bottom of the model.

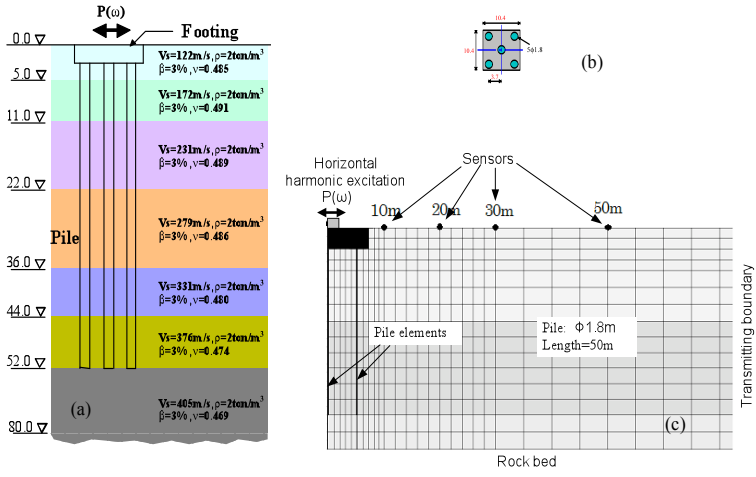

FIG.4. Pile foundation dimensions and site condition

The field test results (Lin (2000)) by the National Earthquake Engineering Center of Taiwan for the foundation in FIG.4 are used to validate the present numerical simulation results. In the shaker tests, the driving frequency varies from 2 to 19 Hz by 0.5 Hz increments. The 3-directional loadings are applied in the two perpendicular horizontal and vertical directions. Since the harmonic exerting force by shakers generally depends on the driving frequency, the measured data were normalized with respect to a fixed maximum excitation force of 10kN for both the horizontal and vertical directions. In this paper, only the results from the horizontal shaking load test are presented, as shown in FIG.5.

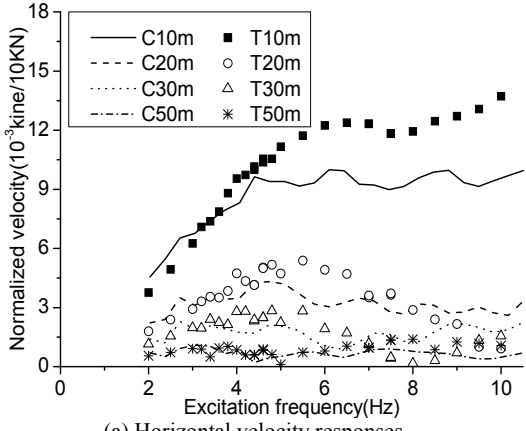

(a) Horizontal velocity responses

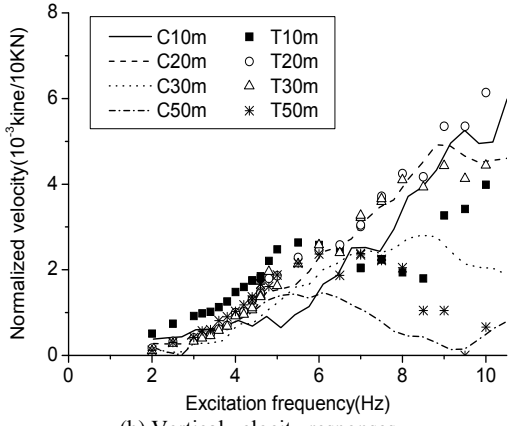

(b) Vertical velocity responses

FIG.5. Comparison of simulated and recorded ground surface velocity responses due to the horizontal loading (Prefix 'C' stands for computation results, 'T' for field test data. Both Computation results and field test data are normalized to 10KN output loading.)

The ground surface responses under the harmonic horizontal loads on the footing top are recorded at the positions of 10m, 20m, 30m and 50m distances. The test data are normalized to 10KN exciting force for all driven frequencies. The horizontal and vertical velocity responses of the simulated results under horizontal loads are also presented in FIG.5 for comparison purpose. Generally, the simulation results fit the field test data quite well. The comparison of the simulation results with the field test data proves the reliability of the proposed computation procedure to evaluate ground responses under pile foundation excitations.

CONCLUSIONS

The ground vibrations due to the dynamic excitation on pile foundation footing are studied with the three-dimensional axisymmetric finite element program. A good agreement is found from the comparison of the simulation results with the field recorded data, which prove the reliability of the proposed axisymmetric three-dimensional finite element computation approach in predicting the field vibration considering pile-soil interactions. This will be the basis for further studying the field vibrations caused by train traffic loadings on viaduct.

ACKNOWLEDGMENTS

The authors appreciate the support of the Natural Science Foundation of China (50538010, 10702063) and Technology Promotion Project of China Ministry of Railway(2008G005-D).

REFERENCES

Liu, K., Reynders, E., et al. (2009). "Experimental and numerical analysis of a composite bridge for high-speed trains." Journal of Sound and Vibration, 320(1-2): 201-220.

Ju, S.H. and Lin, H.T. (2003). "Resonance characteristics of high-speed trains passing simply supported bridges." Journal of Sound and Vibration, 267(5): 1127-1141.

Cheng, Y.S., Au, F.T.K., et al. (2001). "Vibration of railway bridges under a moving train by using bridge-track-vehicle element." Engineering Structures, 23(12): 1597-1606.

Takemiya, H. and Bian, X.C. (2007). "Shinkansen high-speed train induced ground vibrations in view of viaduct-ground interaction." Soil Dynamics and Earthquake Engineering, 27(6): 506-520.

Yang, Y.B. and Wu, Y.S. (2005). "Transmission of vibrations from high speed trains through viaducts and foundations to the ground." Journal of the Chinese Institute of Engineers, 28(2): 251-266.

Takemiya, H. (2008). "Analyses of wave field from high-speed train on viaduct at shallow/deep soft grounds." Journal of Sound and Vibration, 310(3): 631-649.

Wolf, J.P. and Von Arx, G.A. (1978). “Impedance function of group of vertical piles”, Proc. ASCE specialty conf. Soil Dynamics and Earthquake Engineering, 2: 1024-1041.

Waas, G. and Hartmann, H.G.(1981). Analysis of pile foundations under dynamic loads, Conf. Struct. Mech. Reactor Technol. Paris., specialty conf. Soil Dynamics and Earthquake Engineering, 2: 1024-1041.

Takemiya, H. and Yamada, Y. (1981). "Layered Soil-Pile-Structure Dynamic Interaction." Earthquake Engineering & Structural Dynamics, 9(5): 437-457.

Takemiya H.(1986). “Ring pile analysis for grouped piles subjected base motion”. Struct Eng/Earthquake Eng, 1986;3(1):195–202.

Lin T.W., Chen C.H. and Lee Y.J.(2000). Vibration studies for Tainan Science Park due to high-speed train. Evaluation of vibration reduction of train viaduct. National Earthquake Engineering Center Report, NCREE-00-001.

Modeling of Cyclic Plane Strain Response of Toyoura Sand

Md. Raquibul Hossain[1], Mohammed Saiful Alam Siddiquee[1] and Syed Ishtiaq Ahmad[1]

[1]Dept. of Civil Engineering, Bangladesh University of Engineering and Technology, Dhaka 1000, Bangladesh; anup880@yahoo.com

ABSTRACT: Test results of Toyoura sand subjected to plane strain cyclic loading illustrates that it has the memory effect i.e., memory about its last load reversal point in the shear stress-strain plane, which produces a closed hysteretic loop. To simulate this response, a novel formulation of kinematic hardening rule is used here by introducing a framework in which the dimensionless kinematic hardening rate is varied according to the instantaneous stress value at that point along the stress path. When the direction of the loading is reversed, the initial rate of hardening is restored and the rate of variation of hardening is scaled according to extended Masing's law. As a result, a closed hysteretic stress-strain loop is obtained due to cyclic loading. Finally, cyclic plane strain response of Toyoura sand is simulated and compared with available test results.

INTRODUCTION

Geo-materials are often subjected to transient and cyclic stresses due to earthquake or other source of dynamic load. Mathematical modeling of these materials requires robust constitutive models that are capable to simulate the cyclic behavior accurately. Several constitutive models were proposed by the researchers to simulate the response of materials under monotonic loading as well as cyclic loading under the general framework of elasto-plasticity. Amoung them, a number of models have been introduced to simulate the cyclic stress-strain behaviour of materials, such as Prager [1956], Armstrong and Frederick [1966], Mróz [1967], Dafalias and Popov [1975,1976], Ohno and Wang [1993], Hossain et al. [2005], Hossain et al. [2008] etc. These cyclic evaluations of the material are modelled through kinematic hardening, isotropic hardening and/or a combination of both.

Among these constitutive models, Hossain et al. [2008] developed a novel formulation of kinematic hardening rule by extending the one-dimensional Masing's rule to general three dimensional stress-space. To model the cyclic behavior of materials, Masing's rule has great importance, as the cyclic evaluation sometimes resembles this feature. The Masing's rule states that, the unloading curve keeps a homological ratio of two to monotonic one. The extension of this rule, also observed in most materials, is that the modelling process takes place through the initial monotonic curve or through previous

reloading ones when they are intersected (Montáns [2000]). Hossain et al. [2008] simulated the cyclic behaviour by introducing a new framework in which the dimensionless kinematic hardening rate is varied according to the instantaneous stress value at that point along the stress path. When the direction of the loading is reversed, the initial rate of hardening is restored and the rate of variation of hardening is scaled according to modified Masing's law. As a result a closed hysteretic stress-strain loop is obtained due to cyclic loading. Also a new hyperbolic growth function is used to simulate the rate of kinematic hardening.

Masuda et.al. [1999] conducted a set of tests on Toyoura sand subjected to plane strain cyclic loading. Test results showed that Toyoura sand has a memory effect i.e., memory about its last load reversal point in the shear stress-strain plane, which produces a closed hysteretic loop. To simulate this test results, Hossain's [2008] cyclic model is incorporated into a finite element code. A single element stress-strain response illustrated a good simulation of the test results. In this paper, the constitutive model is described and later modeling results are compared with the test results.

KINEMATIC HARDENING RULE

The kinematic hardening rule of the constitutive relation evolves with the accumulative plastic strain. Since the model has been developed within the small strain range, the total strain increment is divided into its elastic and plastic parts as follows:

$$d\varepsilon_{ij} = d\varepsilon_{ij}^{e} + d\varepsilon_{ij}^{p} \tag{1}$$

where, $d\varepsilon_{ij}^{p}$ represents the incremental plastic strain. Now, the increment of the kinematic hardening variable α_{ij} is given as:

$$d\alpha_{ij} = C d\varepsilon_{ij}^{p} \tag{2}$$

where, C is the instantaneous slope of the $\alpha_{ij} \sim \varepsilon_{ij}^{p}$ relationship. For a constant C, the kinematic hardening rule reduces to Prager's linear kinematic hardening rule and results in linear stress-strain curves.

An evaluation rule for C is given as a function of the accumulative plastic strain. Firstly, the loading and unloading skeleton curves are scaled according to a modified Masing's rule upon the reversal of loading to get a closed hysteretic loop (Tatsuoka et al. [2003]). Then from the instantaneous slope of the curve, C is calculated as the model parameter. As a result a closed hysteretic relationship of $\alpha_{ij} \sim \varepsilon_{ij}^{p}$ is found. Thus, the model simulates nonlinear stress-strain relationship which obeys the modified Masing's rule.

Modified Masing's Rule

Tatsuoka et al. [2003] modified the original Masing's rule to simulate the case of unsymmetric loading and unloading skeleton stress-strain curves as well as the case where the unloading curve does not keep a homological ratio of two to the monotonic one.

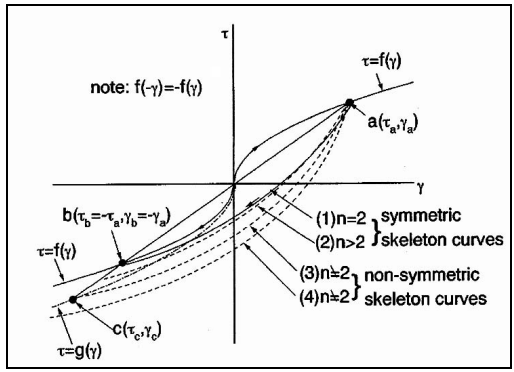

FIG. 1. Schematic diagram explaining the proportional rule (Masuda et al. 1999)

In FIG. 1, stress-strain relationship $\tau = f(\gamma)$ represents the primary loading and unloading curves that are symmetric about the origin i.e., $f(-\gamma) = -f(\gamma)$. When the loading direction is reversed at Point a (τ_a, γ_a), the unloading curve is given as:

$$(\tau - \tau_a)/n = f[(\gamma - \gamma_a)/n] \tag{3}$$

where n=2 (case 1). In this case, the unloading curve joins the unloading skeleton curve at the symmetric point b (τ_b, γ_b) with $\tau_b = -\tau_a$ and $\gamma_b = -\gamma_a$. On the other hand, many experimental results show that the unloading curve from point a does not join the skeleton curve at point b (case 2) (Masuda et al. [1999]). In addition, the primary loading and unloading curves could be largely non-symmetric (case 3 and 4). In these cases, two different functions $\tau = f(\gamma)$ and $\tau = g(\gamma)$ should be assigned for loading and unloading curves. It could be assumed that the unloading curve from point a in this case is given as,

$$(\tau - \tau_a)/n = g[(\gamma - \gamma_a)/n] \tag{4}$$

For example, in case 3 we can find point c (τ_c, γ_c), which is the intersection of straight line passing the reversing point a and the origin and the unloading primary curve $\tau = g(\gamma)$. For unloading curve to join the primary unloading curve at point c, the factor n should be equal to $-(\tau - \tau_c)/\tau_c (\geq 0)$, which is usually different from the constant value two and may be variable during cyclic loading. Therefore, the value of n can be determined by a proportional rule and a drag rule. For the present model the relationship between η and the plastic hardening parameter κ is used to get the instantaneous slope C, where η is a model variable and κ is the measure of the accumulative plastic strain.

Proportional Rule

Tatsuoka et al. [2003] proposed a proportional rule to find the modified n for unsymmetric loading and unloading curves. The proportional rule consists of external and internal rules. Upon the reversal of the loading direction, either external or internal rule is

chosen for a given loading history based on the largeness of the current value of κ relative to the instantaneous maximum (κ_{max}) and minimum (κ_{min}) value of κ. To keep continuity between the external rule and the internal rule, it is assumed that a pair of points having coordinates κ_{max} and κ_{min} is always located on opposite side of the origin O on a straight line passing the origin. The meaning of κ_{min} and κ_{max} is explained below:

1. Suppose that loading starts from the origin and continues until Point A. At Point A, κ_{max} equals to the maximum value of κ ever achieved by loading equals to κ_A. Accordingly, κ_{max} at Point B (located along the first unloading curve from Point A) equals to κ_A. When the current κ value becomes larger than the previous value of κ_{max} (i.e., when $\kappa > \kappa_{max} = \kappa_A$), the previous value of κ_{max} is replaced by the instantaneous κ value.

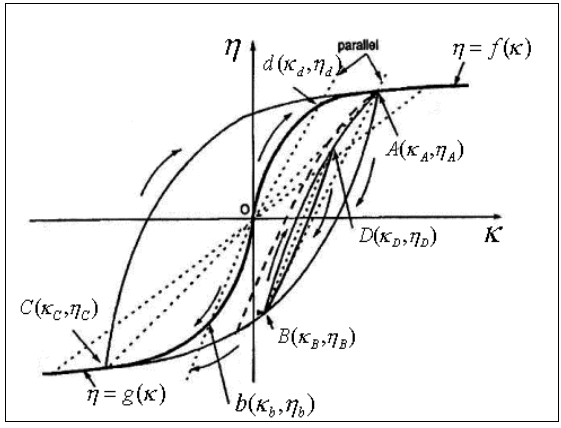

FIG. 2. Details of the proportional rule

2. κ_{min} is defined as the smaller value of (a) the smallest value of κ ever attained during unloading and (b) the value of κ at the intersection of the straight line starting from the point of κ_{max} and passing the origin O with the unloading skeleton curve $\eta = g(\kappa)$. The value of κ_{min} of Point B equals to κ_C (κ at Point C), corresponding to Point A.
3. κ_{max} is defined as larger of (a) the largest value of κ ever attained during loading and (b) the value of κ at the intersection of the straight line starting from the point of κ_{min} and passing the origin O with the loading skeleton curve $\eta = f(\kappa)$.

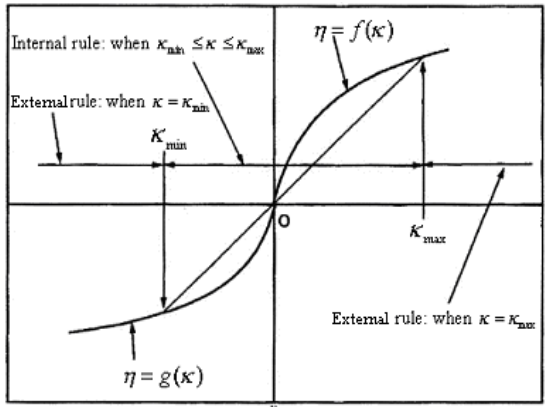

FIG. 3. Rule to choose either external or internal rule for given instantaneous plastic strain κ

The rules to obtain the hysteretic relationship for cyclic loading are described below, referring to FIG. 2 and 3:

1. Curves for reloading and afterwards are obtained as follows:
   - When unloading is reversed to reloading while renewing the κ_{min} value to the instantaneous plastic strain κ, the reloading curve is obtained by following the external rule,
   - When unloading is reversed to reloading with $\kappa_{max} \ge \kappa \ge \kappa_{min}$ maintaining the previous κ_{max} and κ_{min}, the reloading curve is obtained by following the internal rule, and
   - When the loading is continued while renewing the κ_{max} value to instantaneous plastic strain κ, the loading curve $\eta = f(\kappa)$ is followed.
2. Curves for unloading and afterwards are obtained as follows:
   - When loading is reversed to unloading while renewing the κ_{max} value to the instantaneous plastic strain κ, the unloading curve is obtained by following the external rule,
   - When loading is reversed to unloading with $\kappa_{max} \ge \kappa \ge \kappa_{min}$ maintaining the previous κ_{max} and κ_{min}, the unloading curve is obtained by following the internal rule, and
   - When the unloading is continued while renewing the κ_{min} value to instantaneous plastic strain κ, the unloading skeleton curve $\eta = g(\kappa)$ is followed.

The rules are described below more specifically referring to FIG. 2,

1. During the first primary loading from origin O (κ_0,η_0), where $\kappa_{max} = \kappa_{min} = 0$, until Point A, κ_{max} is always equal to κ and the curve follows the loading skeleton curve $\eta = f(\kappa)$. At Point A (κ_A,η_A), we have κ_{max} equals to κ_A and κ_{min} equals to κ_C.
2. When the loading is reversed at Point A, the unloading curve bound for Point C is obtained by following the external rule (with κ_{max} equals to κ_A) and using the known unloading skeleton curve $\eta = g(\kappa)$ and the coordinate at Point C (κ_C,η_C) as,

$$\frac{\eta-\eta_A}{n_1} = g\left(\frac{\kappa-\kappa_A}{n_1}\right) \tag{5(a)}$$

$$n_1 = \frac{(-\eta_C)+\eta_A}{(-\eta_C)} = \frac{(-\kappa_C)+\kappa_A}{(-\kappa_C)} \quad (\geq 0) \tag{5(b)}$$

3. When the unloading continues past Point C, the curve follows the unloading skeleton curve $\eta = g(\kappa)$ with κ_{max} equals to instantaneous κ.
4. Here, the target plastic strain, κ_{target} is introduced, which is defined as the value of κ at that point for which the curve is bound after the loading direction is reversed. For the unloading and reloading curves following the external rule, κ_{target} is equal to κ_{min} and κ_{max}, respectively. In FIG. 2, κ_{target} for the unloading curve starting from Point A bound for Point C is $\kappa_{min} = \kappa_C$.
5. In FIG. 2, when unloading is reversed to reloading at Point B, where κ is between $\kappa_{min} = \kappa_C$ and $\kappa_{max} = \kappa_A$, the reloading curve is obtained by following the internal rule. The target point is assumed to be the same as the last point before Point B (i.e., Point A). Then, this reloading curve is obtained by scaling the loading skeleton curve as,

$$\frac{\eta-\eta_B}{n_2} = f\left(\frac{\kappa-\kappa_B}{n_2}\right) \tag{6(a)}$$

$$n_2 = \frac{\eta_A-\eta_B}{\eta_d} = \frac{\kappa_A-\kappa_B}{\kappa_d} \quad (\geq 0) \tag{6(b)}$$

Where, Point d (κ_d,η_d) is the intersection of the straight line starting from the origin O while parallel to the straight line between Points B and A with the loading skeleton curve $\eta = f(\kappa)$.

6. In FIG. 2, when the loading direction is reversed at Point D, the re-unloading branch, which is bound for the latest previous point (i.e., Point B), is obtained by Equation 5(a), but using another scaling factor n_3 given below,

$$n_3 = \frac{(-\eta_C)+\eta_A}{(-\eta_C)}\frac{\eta_D-\eta_B}{\eta_A-\eta_B} = \frac{(-\kappa_C)+\kappa_A}{(-\kappa_C)}\frac{\kappa_D-\kappa_B}{\kappa_A-\kappa_B} \quad (\geq 0) \tag{7}$$

At Point B, the re-unloading curve does not smoothly rejoin the previous unloading curve $A \rightarrow B \rightarrow C$. The unloading curve beyond Point B follows the curve $A \rightarrow B \rightarrow C$.

7. When following the internal rule, the value of κ_{target} is always equal to the value of κ at the latest previous reversing point (before the current reversing point). For example, κ_{target} is $\kappa_A = \kappa_{max}$ for the reloading branch $B \rightarrow A$ and κ_B for the re-unloading branch $D \rightarrow B$.
8. Whenever the previous reversing point is passed, all the memory of previous cyclic loading history is erased. So, the reloading curve beyond Point B is bound for Point A, and not for Point D.

NONLINEAR STRESS-STRAIN RELATION

The nonlinear $\eta = f(\kappa)$ relationship can be numerically modeled using various nonlinear stress-strain relationships such as Konder [1963], Saenz [1964], Griffith and Prevost [1990], Tatsuoka et al [1993], Tanak [2002], Al-Karni and Alshenawy [2006], Hossain et al [2007] etc. According to Hossain et al [2007], the $\eta \sim \kappa$ relationship for loading is found as follows,

$$\eta = f(\kappa) = \eta_{max} . \frac{\kappa_{max} + a}{\kappa_{max}^2} . \kappa . \left(\frac{\kappa_{max} + a}{\kappa + a} - \frac{a}{\kappa_{max} + a} \right) \quad (8)$$

Where, a is the material parameter which depends on the shape of the curve and can be evaluated from the initial kinematic hardening parameter, C_0 and the material parameters κ_{max} represents the maximum accumulative plastic shear strain and has a direct relevance with the shear strain γ_{max}. η_{max} is the value of η at the peak stress state. Similarly, an unloading $\eta \sim \kappa$ relationship can be found using EQ. 8.

YIELD CRITERIA AND FLOW RULE

A Druker-Prager type conical pressure dependent yield surface has been chosen as follows,

$$f = \sqrt{(S_{ij} - p\alpha_{ij}) : (S_{ij} - p\alpha_{ij})} = 0 \quad (9)$$

Where, the α_{ij} is the centre of the yield function, S_{ij} is the deviatoric stress and p is the hydrostatic pressure.

Tatsuoka et. al. [2003] proposed two different stress-dilatancy relations for loading and unloading. With some modification, the stress-dilatancy relationship becomes,

$$D = b . \frac{-\sin\phi_{mob}(1 + 1/K) + (1 - 1/K)}{\sin\phi_{mob}(1 - 1/K) + (1 + 1/K)} \text{ for loading} \quad (10(a))$$

$$D = b . \frac{\sin\phi_{mob}(1 + 1/K) - (1 - 1/K)}{-\sin\phi_{mob}(1 - 1/K) + (1 + 1/K)} \text{ for unloading} \quad (10(b))$$

Where, $D = \dfrac{d\varepsilon_v^p}{d\kappa}$

$d\varepsilon_v^p$ is the incremental volumetric plastic strain, which is positive for compression and negative for dilation.

$d\kappa$ is the magnitude of the incremental plastic shear strain.

b and K are constants.

And the incremental plastic shear strain is given by,

$$de_{ij}^{p} = \lambda \frac{df}{dS_{ij}} \tag{11}$$

Where, $\lambda = d\kappa$.

Also the hardening rule (EQ. 2.) has been modified for Toyoura sand as follows,

$$d\alpha_{ij} = (1+d)Cde_{ij}^{p} \tag{12}$$

Where, d is a constant.

FINITE ELEMENT MODELING

The model has been incorporated into a finite element code developed using C++ programming language. A four-noded quadrilateral (FIG. 4) plane strain element is chosen for the numerical simulation and for the nonlinear iterative solution of the governing equations dynamic relaxation algorithm is used. Then, the incremental stress-strain relationship is integrated using return mapping algorithm. This element has four degree of freedoms. The confining pressure σ_3 is kept constant to simulate the plane strain behavior and single point Gauss Quadrature integration is chosen to integrate the incremental stress-strain relation.

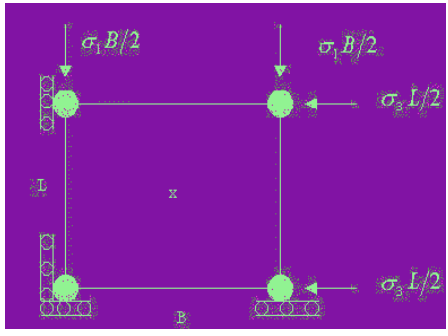

FIG. 4. Quadrilateral Element

SIMULATION OF CYCLIC PLANE STRAIN RESPONSE

The stress-strain relationship of the Toyoura sand is simulated with the constitutive model and compared with the results of Masuda et. al. [1999]. The plane strain compression and extension skeleton curves from the experiment results were not symmetrical and the loops of the $Sin\phi_{mob} \sim \gamma$ relationship were not closed. So, due to the pressure dependency and to simulate the test results a modified hardening rule is applied. The material and the model parameters given in the Table 1 and the parameter d is evaluated using the following algorithm,

For loading and unloading skeleton curve:

The hardening rule: $d\alpha_{ij} = Cde^{p}_{ij}$

Otherwise:

The hardening rule: $d\alpha_{ij} = (1+d)Cde^{p}_{ij}$ with

for loading curve: d = 0

for unloading curve: d = 0.011

Table 1. Material and model parameters

Confining Pressure, σ_3	540 psi
$\kappa_{\max/\min}$	0.01
$\eta_{\max}$	0.75
$\eta_{\min}$	0.99
a	0.0007
b	1.0/3.0
Shear Modulus of Elasticity, G	642,890 psi
Bulk Modulus of Elasticity, K^e	538,990 psi
K for loading/unloading	3.5

The simulated $Sin\phi_{mob} \sim \gamma$ and $R \sim \gamma$ relationships are given in the FIG. 5 and 6. It showed that the simulated results can represent the test results with good accuracy. Then, the volumetric strain vs. shear strain relationship is given in the FIG. 7. Here, a bit of over prediction in the dilatancy behavior is observed.

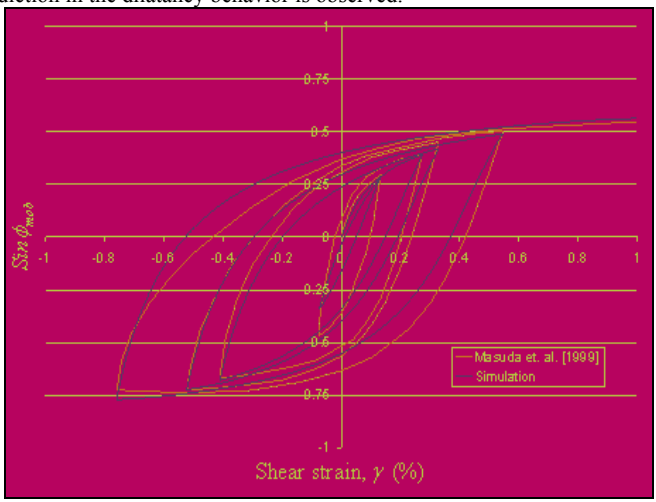

FIG. 5 Comparison of $Sin\phi_{mob} \sim \gamma$ relationship between the test result and the simulation

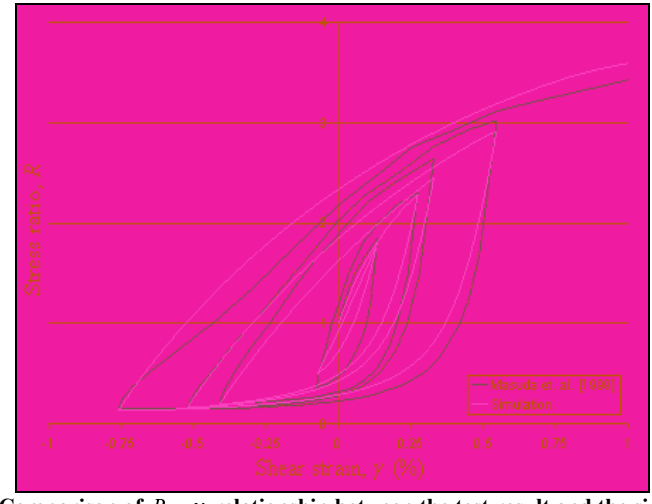

FIG. 6 Comparison of $R \sim \gamma$ relationship between the test result and the simulation

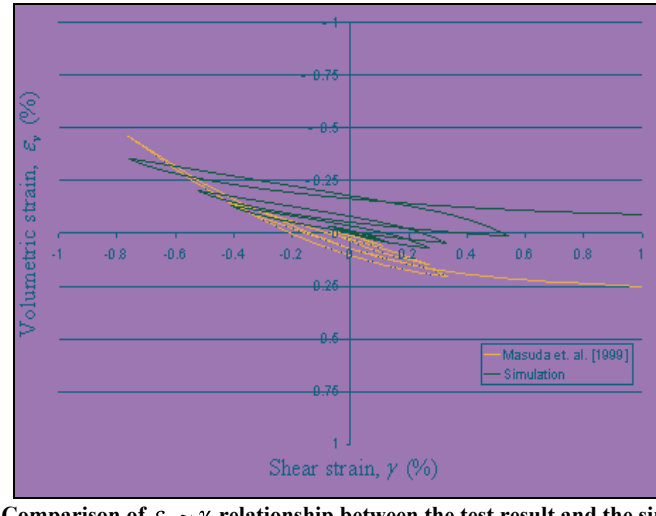

FIG. 7 Comparison of $\varepsilon_v \sim \gamma$ relationship between the test result and the simulation

CONCLUSIONS

The constitutive model proposed by Hossain et al. [2008] is based on a generalized framework of kinematic hardening rule which has been developed by replacing the

constant of Prager's kinematic hardening rule with an instantaneous slope found from a nonlinear skeleton curve. This concept gives rise to a novel robust framework in the field of cyclic plasticity modeling. The model has the ability to simulate fully nonlinear cyclic stress-strain behavior of engineering materials. Also, it has the ability to correctly model Masing's Rule and its extension and can simulate closed loop cyclic stress-strain behavior. As the proposed novel model is based on kinematic hardening rule with a non-dimensional parameter C, it has the ability to simulate the cyclic 3D stress-strain relationship. In the present research, this model is implemented in a finite element code and used to simulate the cyclic plane strain response of Toyoura sand. The simulated stress-strain behavior showed a good correlation between the test results and the simulated results. However, the model over predicts in the dilatancy behavior of Toyoura sand. Further research is going on to improve the performance of the constitutive model.

REFERENCES

Al-Karni, A. and Alshenawy, A. (2006). "Modeling of stress-strain curves of drained triaxial test on sand." *American Journal of Applied Sciences*, 3 11, 2108-2113

Armstrong, P.J. and Frederick, C.O. (1966). "A Mathematical Representation of the Multiaxial Bauscinger Effect." *CEGB Report No. RD/B/N 731*

Dafalias, Y. F., and Popov, E. P. (1975). "A model of nonlinearly hardening materials for complex loadings." *Acta Mech.*, 21, 173–192.

Dafalias, Y. F., and Popov, E. P. (1976). "Plastic Interal Variables formalism of Cyclic Plasticity." *J. Appl. Mech.*, 984, 645-650

Griffith, D.V. and Prevost, J.H. (1990). "Stress strain curve generation from simple triaxial parameters." *International Journal for Numerical and Analytical Methods in Geomechanics*, Vol. 14, 587-594

Hossain, M. R., siddiquee, M. S. A., ahmad, S. I. (2008). "A Novel Kinematic Hardening Rule to Simulate the Cyclic Behavior of Material." *The 12th International Conference of International Association for Computer Methods and Advances in Geomechanics (IACMAG)*,1-6 October, 2008, Goa, India

Hossain, M. R., siddiquee, M. S. A., ahmad, S. I. (2007). "Modeling nonlinear stress-strainrelations of materials." *6th International Symposium on New Technologies for Urban Safety of Mega Cities in Asia*, Dhaka, 2007 (CD-ROM)

Hossain, M.R., Siddiquee, M.S.A, Tatsuoka, F. (2005). "Development Of A Cyclic Model For Pressure Insensitive Soil." *Proceedings of the Japan Bangladesh Joint Seminar on Advances in Bridge Engineering*, August, 2005, Dhaka

Konder, R.L. (1963). "Hyperbolic stress-strain response: cohesive soils." *Journal of Soil Mechanics and Foundation Division*, ASCE, 89SM1, 115-143

Masuda, T., Tatsuoka, F., Yamada, S. and Sato, T. (1999). "Stress strain behavior of sand in plane strain compression, extension and cyclic loading tests." *Soils Found.*, 395, 31-45.

Montáns, F. J. (2000). "Bounding surface plasticy model with extended Masing's behavior." *Comput. Methods Appl. Mech. Engrg.*, 182, 135-162

Mróz, Z. (1967). "On the Description of Anisotropic Workhardening." *J. Mech. Phys. Solids*, 15, 163.

Ohno, N. and Wang, J.D. (1993). "Kinematic Hardening Rules With Critical State Of

Dynamic Recovery, Part I: Formulation And Basic Features For Ratchetting Behavior." *International Journal of Plasticity*, Vol. 9, pp. 375-390

Prager, W. (1956). "A New Method of Analyzing Stresses and Strains in Work Hardening Plastic Solids." *J. Appl. Mech.*, 23, 795-810.

Saenz, L. P. (1964). "Discussion of Equation for the Stress-Strain Curve of Concrete by Desayi and Krishman." *J. Am. Concr. Inst.*, Vol. 61, September, pp. 1229-1235.

Tanaka, T., (2002). "Elasto-plastic strain hardening-softening soil model with shear banding", *em2002*, New York, June, 2002 (http://www.civil.columbia.edu/em2002)

Tatsuoka, F., Masuda, T., Siddiquee, M. S. A. and Koseki, J. (2003). "Modeling the stress strain relations of sand in cyclic plane strain loading." *Journal of Geotechnical and Geoenvironmental Engineering,* ASCE, May

Tatsuoka, F., Siddiquee, M. S. A., Park, C. S., Sakamoto, M. and Abe, F. (1993). "Modeling stress-strain relations of sand." *Soils and Foundations*, Vol. 33, No. 2, 60-81, June

Dynamic Property of Mucky Soil of Subgrade under Cyclic Load

Liu Ganbin*, Kai Qianzheng

College of civil, construction and environmental engineering, Ningbo University, Zhejiang, Ningbo 315211, China; Liugb76@163.com

ABSTRACT: Deformation characteristics of marine sedimentary, which is widely distributed in Ningbo area, are important for the construction of pavement-subgrade system, rail transit-subgrade system, dynamic foundation, and so on. In this paper, FlowTrac II system, a fully automatic bidirectional excitation triaxial testing system produced by GEOCOMP, is used to study the deformation characteristics and the dynamic responses of subgrade in the area covered by rail transit network of Ningbo city. A series of unidirectional cyclic triaxial tests are conducted on remoulded mucky soil samples. Effects of amplitude of dynamic stress, consolidated confining pressure and load repetition on the behaviors of the saturated mucky soil are analyzed. It is shown that the influence of the above factors on the dynamic elastic modulus, damping ratio is great. At last, the envelopes of dynamic shear modulus ratio G/G_{max} versus dynamic strain D for mucky soil are presented.

INTRODUCTION

Due to new high speed transport systems have been developed, which transmit cyclic loading to the subsoil and whose serviceability is very sensitive to differential settlements, the prediction of settlements under cyclic loading under drained conditions has been gained in importance during the last decades of years. In addition, the experimental test is the other method to study the deformation behaviour of soils under very high numbers (i.e. several 10,000 up to several millions) of load cycles.

Results of test series concerning the change of dynamic soil properties due to a cyclic or dynamic loading history could be found in the literatures. Drnevich and Richart(1970) studied the influence of a dynamic torsional prestraining on shear modulus and damping ratio in the resonant column device of using hollow cylinder specimens. Alarcon-Guzman *et al*.(1989) studied the influence of a cyclic strain history on the shear modulus of dry coarse sand using a testing device with integrated resonant column and torsional shear mode. Series specimens of fine sand, dynamically prestrained with an amplitude $\gamma_{\text{prestrain}}$, were performed by Li *et al*(1999). The curves of shear modulus $G(\gamma)$ and damping ratio $D(\gamma)$ were determined. In addition, the test results of free vibration column apparatus on recently deposited soils of flood plain including clay, silty clay, mucky silty clay, silty clay and fine sand interbedded strata, silt and fine sand in Nanjing and its neighboring areas is investigated in detail(Chen and Liu, 2004). The dynamic deformation properties of lightweight clay-EPS beads soil(LCES) were studied by Li and

Gao(2007) using triaxial apparatus, and the effort was focused on the influence of confining pressure, cement content and EPS content.

In this paper, the characteristic of mucky soil under cyclic load is considered. The LoadTrac II/FlowTrac II system for cyclic stress path testing (GEOCOMP) is used to model the cyclic loading, and an undrained dynamic triaxial test on a soil specimen is executed.

TEST APPARATUS

The LoadTrac II/FlowTrac II system for Cyclic Stress Path Testing, as shown in Fig.1, consists of a LoadTrac II load frame, two FlowTrac II flow pumps for controlling cell and sample volume and pressure, a hydraulic pump, a servo valve with a hydraulic cylinder, an external signal conditioning unit and a computer with a network card and an A/D card for test control and data acquisition. The system fully automates the conduct of a Cyclic Stress Path test on a soil specimen. Once a soil specimen is in place and the test conditions selected, the LoadTrac II/FlowTrac II system will run the initialization/ backpressure saturation and consolidation from start to finish,

The system is capable of applying a constant rate of strain or stress at any displacement rate from 0.00003 up to 15mm per minute (0.000001 to 0.6 inches per minute). FlowTrac II is capable of maintaining the desired pressure within 0.35kPa (0.05psi) while monitoring volume changes within 0.001cc. The remarkable advantages of this system is that the vertical and horizontal dynamic loading can be applied and the phase difference of dynamic loading waveform can be adjusted, the frequency range of bidirectional loading is 0.001~5Hz. During the test, the basic factor of dynamic loading is swing, frequency, duration and wave type.

TEST PARAMETERS AND PROCESS

In this paper, the sine wave type is chosen and the stop condition of the cyclic load is that the cyclic load times or the maximum two-amplitude strain of a single cycle reaches the regular value.

(1) Test parameters

1) Amplitude values of dynamic stress

As the stress controlled model is used in this system, the basic requirement of the dynamic stress choosing is to display the dynamic stress-strain curve, and the dynamic stress should not excess the vertical pressure, or the cap will divorced from the test specimen. Considering the low stress amplitude and long circulating action of train loading behavior, the values of stress amplitude and confining pressure is defined as 20kPa, 30kPa and 40kPa.

2) Consolidated confining pressure

The maximum value of consolidated confining pressure should be greater than the effect stress of the ground subject practically. The minimum value of confining pressure can not less than the upper overburden pressure of specimen. According to the test results of dynamic stress attenuated with the depth of railway subgrade, the dynamic stress in the depth of 2.5m is only 20% that of the subgrade surface. To discuss the influence of confined pressure, two values of 50kPa and 100kPa, which can satisfy the demand of engineering, are chosen considering the fact that there is great error in the low confined

pressure.

3) Vibration frequency

As the frequency of train loading is superposed by a series of frequency, which is related to velocity, length of train and wheelbase of train. According to the spectrum of bedding dynamic stress, the fundamental frequency, i.e. the pass frequency of train ($f=V/L$, V is the velocity of train and L is the length of train), has the maximum effect on the subgrade. Therefore, the vibration frequency is defined 2Hz and 3Hz.

(2) Specimen

The test specimen of mucky soil should be natural air drying, then the compaction test is used to make remolded sample. The high of specimen is 100mm and diameter 50mm. The pumping saturation method is used and the saturated degree of the specimen is greater than 95%. The parameter of physical property is listed in table1.

(3) Test process

During the test, the specimen should be installed on the system, and the test program is debugged and run. Then, the dynamic stress is executed and the failure vibration times is distributed in the range of several times, several dozens times and several hundred times. According to the curve of dynamic strength and failure vibration times in different consolidation stress state, the vibration failure load of different initial stress state under equivalent failure vibration can be obtained and furthermore, the dynamic strength parameters can be obtained.

Table 1. The Physical Characteristics of Soil

Water content (%)	Liquid limit ω_L %	Plastic limit ω_p %	Specific gravity	Cohesion kPa	Internal friction angle (°)
55.6	95.2	50.2	2.72	114.4	26.09

TEST RESULT AND ANALYSIS

According to the value of dynamic shear stress τ_d and strain γ_d at the top point of the hysteretic curve, the dynamic shear modulus can be calculated. The maximum dynamic shear modulus $G_{d\max}$ can be defined when γ_d tends to be zero. The curve of $\tau_d \sim \gamma_d$ is close to the hyperbola. Through the process of transpose, the $\tau_d \sim \gamma_d$ can be change to be linear function, the $1/G_d - \gamma_d$ curve is obtained. Beeline fitting method is applied and delayed, and the reciprocal value of ordinate intercept at $\gamma_d = 0$ is $G_{d\max}$. Furthermore, the dynamic elastic modulus E_d can be calculated by using the dynamic stress σ_d and strain ε_d.

$$\gamma_d = \varepsilon_d (1+\mu) \tag{1}$$

$$G_d = \frac{E_d}{2(1+\mu)} \tag{2}$$

Where μ is the Poisson ratio of soil sample, and for saturated soil, μ is equal to 0.4.

The damping ratio D of soil can be defined by using the classical area ratio method

$$D = \frac{A_1}{4\pi A_2} \tag{3}$$

Where, A_1 is the area of the hysteretic curve and A_2 is the area of triangle.

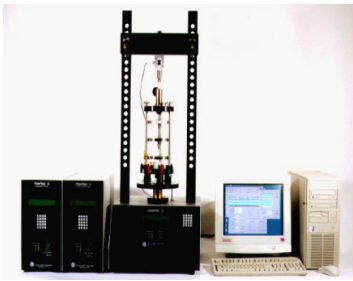

FIG.1 Fully Automated FlowTrac-II/Load Trac-II System for Triaxial Testing

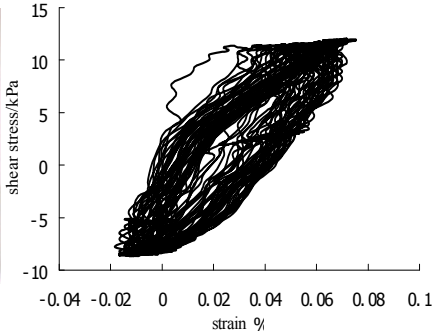

FIG. 2 Loop produced by cyclic loading ($\sigma_3 = 100\text{kPa}$)

The stress-strain curves of mucky soil under dynamic triaxial test condition are a series close hysteretic curve (Fig. 2 is the relation of shear stress and shear strain of specimen under the confining pressure condition of 100kPa). With the increase of cycle times, the hysteretic curve moves to the right of the lateral axis, which shows the increasing of the accumulative plastic strain $\varepsilon_{N,P}$.

(1) Effect of confining pressure on results

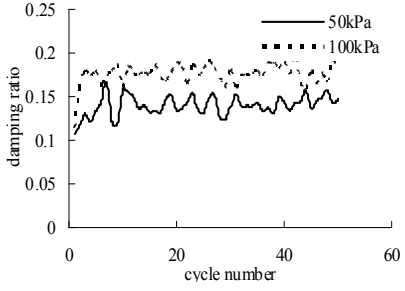

Fig 3 Relation of damping ratio and load repetition

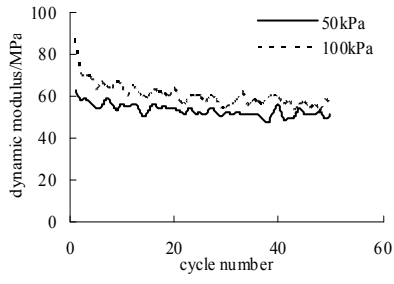

Fig 4 Relation of dynamic modulus and load repetition

The relation curve of damping ratio and dynamic elastic modulus to the cycle number is shown in figure 3 and 4. The damping ratio increases with the increasing of cycle number, in contrary, the dynamic elastic modulus decreases and the softening degree of soil increases. At the initial time, the dynamic elastic modulus decreases with the cycle

number quickly, then the decay rate decreased. With the increasing of confining pressure, the value of damping ratio and dynamic elastic modulus increase. Thus, in the analysis of dynamic characteristics of soil, especially when there is great dynamic stress amplitude, the influence of cycle number should be considered.

(2) Effect of dynamic stress on results

The influence of dynamic stress amplitude on the dynamic modulus and damping ratio are shown in figure 5 and 6. It is indicated in figure 5 and 6, the greater of dynamic stress amplitude σ_d, the smaller of the dynamic modulus on the same load repetition. When the value of dynamic stress is less than the critical cyclic dynamic stress, the modulus tends to be stable with the increasing of cycle number, and vice versa, the modulus is continuously decreased, till the sample failure.

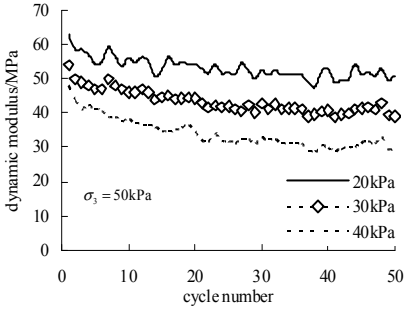

Fig 5 Effect of dynamic stress on dynamic modulus

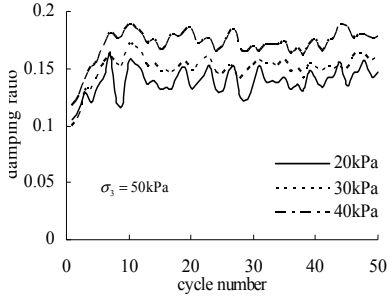

Fig 6 Effect of dynamic stress on damping ratio

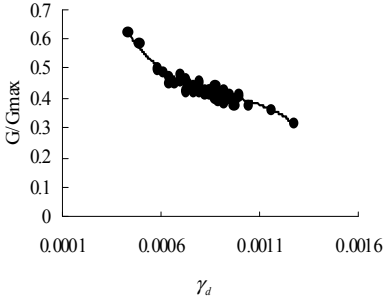

FIG. 7 Curves of G/G_{max}–γ_d under 50kPa confining pressures

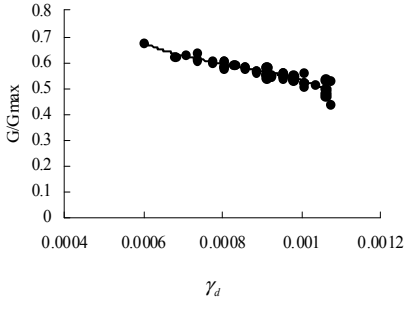

FIG. 8Curves of G/G_{max}–γ_d under 100kPa confining pressures

The relation of damping ratio to load repetition under different dynamic stress is shown in Fig.6. The damping ratio increases with the increasing of dynamic stress amplitude. When the dynamic stress is less than the critical cyclic dynamic stress, the

damping ratio increases linearly with the increasing of load repetition, and tends to be a stable value. Contrarily, the damping ratio is quickly increased, till the sample failure.

The envelopes of dynamic shear modulus ratio G/G_{max} versus dynamic strain γ_d are presented in figure 7 and 8 for remoulded mucky soil when the confining pressure of test is 50kPa and 100kPa respectively. The proposed values can only be used as reference because of the complexity of G. It is shown that the G/G_{max}~γ_d constant increases with the increasing of confining pressure.

CONCLUSION

In this paper, the characteristic of mucky soil under cyclic load is investigated using the LoadTrac II/FlowTrac II system. The influence of the amplitude values of dynamic stress, consolidated confining pressure and load repetition on the dynamic behaviors of the saturated mucky soil is analyzed. In addition, the envelopes of dynamic shear modulus ratio G/G_{max} versus dynamic strain γ_d for mucky soil are presented.

ACKNOWLEDGMENTS

The Project Supported by Scientific Research Fund of Zhejiang Provincial Education Department (20070961).

REFERENCES

Drnevich VP, Richart FE.(1970). “Dynamic prestraining of dry sand.” *J Soil Mechanics Foundation Div*, *ASCE*, Vol, 6: 453-67

Alarcon-Guzman A, Chameau JL, Leonardos GA, Frost JD.(1989). “Shear modulus and cyclic undrained behavior of sands.” *Soils Foundations*. Vol, (4):105-19

Li XS, Cai ZY. (1999). “Effects of low-number previbration cycles on dynamic properties of dry sand.” *J Geotech Geoenviron Engng, ASCE*, Vol,125(11): 979-87

Chen Guoxing，Liu Xuezhu. (2004). “Testing study on ratio of dynamic shear moduli and ratio of damping for recently deposited soils in Nanjing and its neighboring areas.” *Chinese Journal of Rock Mechanics and Engineering,* Vol, 23(8): 1403-1410

Li Bing, Gao Yufeng. (2007). “Experimental study on dynamic deformation characteristics of light weight clay-EPS beads soil.” *Chinese Journal of Geotechnical Engineering*, Vol, 29(7): 1042-1047

Relevance Vector Machine for Evaluating Seismic Liquefaction Potential using Shear Wave Velocity

Pijush Samui[1], and T.G. Sitharam[2]

[1]Postdoctoral Fellow, Department of Civil Engineering, Tampere University of Technology, Tampere, Finland;pijush.phd@gmail.com

[2]Professor, Department of Civil Engineering, Indian Institute of Science, Bangalore, India; sitharam@civil.iisc.ernet.in

ABSTRACT: In this paper, the potential of relevance vector machines (RVM) based classification approach has been used to assess the liquefaction potential from actual shear wave velocity data. RVM is based on a Bayesian formulation of a linear model with an appropriate prior that results in a sparse representation. As a consequence, it can generalize well and provide inferences at low computational cost. It also gives probabilistic output through Bayesian inference. Input parameters of RVM model are effective vertical stress (σ'_{v0}), peak acceleration at the ground surface (a_{max}), earthquake magnitude (M), shear wave velocity (V_s), and soil type. In this study, Gaussian functions are used as kernel for RVM model. The results show that the RVM model predicts liquefaction with accuracy of 98.21%. The developed RVM model provides a viable tool to earthquake engineers in assessing the sites susceptible to liquefaction.

INTRODUCTION

Liquefaction is responsible for large amounts of damage in historical earthquakes around the world. Liquefaction of saturated sandy soils during the past earthquakes has resulted in building settlement and/or severe tilting, sand blows, lateral spreading, ground cracks, landslides, dam and high embankment failures and many other hazards. Damages attributed to the earthquake induced liquefaction phenomenon have cost society hundreds of millions of U.S. dollars. Therefore, the assessment of the liquefaction potential due to an earthquake at a site is an imperative task in earthquake geotechnical engineering. The geotechnical engineering practitioners commonly use the two penetrations based methods (standard penetration tests and cone penetration tests) for assessment of liquefaction potential. On the other hand, shear wave velocity (V_s) may offer geotechnical engineers a third tool that is lower cost and provides more physically meaningful measurements. The present study examines the potential use of the Relevance Vector Machine (RVM) to assess liquefaction potential from V_s. The database collected by Andrus and Stokoe (1997) is used in this study. The RVM introduced by Tipping (2001) produces sparse solutions using an improper hierarchical prior and optimizing over hyper-parameters.

RVM is referred to as a Bayesian kernel method that selects sparse basis sets using an 'Automatic Relevance Determination' (Bishop, 1995) style prior that pushes non-essential weights to zero.

RELEVANCE VECTOR MACHINE METHODOLOGY

The concept of RVM was introduced by Tipping (2001). It allows computation of the prediction intervals taking into account uncertainties of both the parameters and the data (Tipping, 2000). Details about the RVM methodology could be obtained from Tipping(2000); the following paragraph describes the method briefly. A set of targets, Y_i, for the classification problem in the manuscript is occurrence of either *Event 0* defined as "liquefaction" or *Event 1* defined as "no liquefaction". The input parameters for the problem, x_i, are effective vertical stress (σ'_{v0}), peak acceleration at the ground surface (a_{max}), earthquake magnitude (M), shear wave velocity (V_s), and fines content. These input parameters for each experimental specimen test is represented by a basis function $\Phi j(x)$. Thereby the total number of basis functions is the number of samples in the training dataset. Each of this basis function is defined as function of the kernel, K, as

$$\Phi(x_n) = [1, K(x_n,x_1), K(x_n,x_2), \ldots\ldots\ldots K(x_n,x_N)] \quad (1)$$

The kernel, K, is taken as a gaussian function with mean 0 and variance 1. In RVM methodology, usually the set of targets are related to a set of input vectors using the following equation:

$$Y = w_1\Phi_1(x) + w_2\Phi_2(x) + w_3\Phi_3(x) + \ldots\ldots + w_k\Phi_k(x) \quad (2)$$

Where $\Phi_i(x)$ are the basis functions defined above and w_i represent the weight parameters. Gamma priors are introduced to the model weight, w_i, which are governed by set of hyperparameters (maximum likelihood estimations), one associated with each weight, whose most probable value are iteratively estimated from the data. To obtain the probabilistic estimates for the binomial classification problem as given the manuscript, we follow statistical convention and generalize the linear model in equation 2 by applying a logistic sigmoid function $\sigma\{Y(x)\} = 1/(1+ e^{-Y})$ to Y(x).

The dataset consists the information about σ'_{v0}, soil type, a_{max} and M. The dataset represented 88 sites that liquefied and 98 sites that did not liquefy. The data is normalized against their maximum values. In carrying out the RVM formulation, the data has been divided into two sub-sets such as

(a) A training dataset: This is required to construct the model. In this study, 130 out of the 186 data are considered for training.

(b) A testing dataset: This is required to estimate the model performance. In this study, the remaining 56 data is considered for testing.

RESULTS AND DISCUSIION

In this study, width of Gaussian kernel (σ) was chosen by using a trial and error approach. Training and testing performance are calculated by using following equation:

$$\text{Testing / Training performance}(\%) = \left(\frac{\text{No of data predicted accurately by RVM}}{\text{Total data}}\right)\times 100$$

(3)

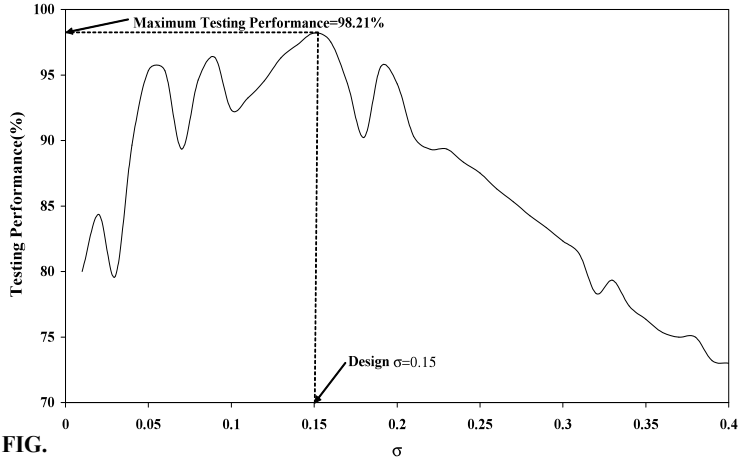

FIG. 1. Variation of testing performance with σ

Figure 1 shows the variation of testing performance(%) with σ value. From Figure 1, it is clear that the design value of σ is 0.15.

Table 1. Performance of testing dataset.

σ'_v	a_{max}	Soil type	M	V_s	Actual class	Predicted Class
58.2	0.36	4	7.7	154	0	0
140.8	0.32	1.5	7.7	199	1	1
35.3	0.12	1	7.1	122	0	0
53.9	0.13	1.5	6.5	127	1	1
123.5	0.32	2.5	7.7	158	0	0
53.9	0.27	1.5	5.9	127	0	0
57.8	0.36	1	5.9	105	0	0
49.4	0.36	4	6.9	109	0	0
38.3	0.36	4	6.9	122	0	0
53.9	0.13	1.5	6.5	124	1	1
35.4	0.22	1.5	6.6	133	1	1
35.4	0.04	1.5	6.2	146	1	1
35.4	0.18	1.5	6.2	127	1	1
35.4	0.16	1.5	7.6	146	1	1
53.9	0.12	1.5	5.9	124	1	1
48	0.03	2	5.9	131	1	1

57.8	0.2	1.5	6.5	115	1	1
48	0.18	2	6.5	133	1	1
60.9	0.14	2	7.1	131	0	0
46.6	0.02	2.5	5.9	164	1	1
40.5	0.36	4	6.9	94	0	0
78.8	0.24	2.5	7.1	146	0	0
81.7	0.24	3	7.1	176	0	0
59.6	0.27	2.5	7.1	125	0	0
62.1	0.19	4	7.1	136	1	1
140.8	0.15	1.5	7.1	200	1	1
120.2	0.06	2	6	195	1	1
46.9	0.25	3	7.1	116	0	0
35.4	0.04	1.5	6.2	130	1	1
140.8	0.32	1.5	7.7	195	1	1
90.1	0.12	1.5	7.1	147	0	0
53.9	0.27	1.5	5.9	124	0	0
46.3	0.36	4	6.9	134	0	0
35.4	0.22	1.5	6.6	146	1	1
35.4	0.18	1.5	6.2	146	1	1
57.8	0.12	1.5	5.9	115	1	1
57.8	0.21	1	6.5	105	1	1
35.4	0.05	1.5	6.2	133	1	1
86.2	0.24	3	7.1	142	0	0
49.8	0.42	2	7.1	158	1	1
58.2	0.19	4	7.1	154	1	1
33.4	0.19	4	8.3	79	0	0
97.7	0.16	3	7.5	163	1	1
46.2	0.36	4	6.9	107	0	0
84.7	0.16	1.5	7.1	135	0	0
46.6	0.03	2.5	5.9	173	1	1
44.5	0.16	3	7.5	118	1	0
48	0.5	2	6.5	133	0	0
82	0.16	2	7.1	148	1	1
123.5	0.15	2.5	7.1	158	1	1
69.2	0.14	2	7.1	136	0	0
35.4	0.18	1.5	6.6	133	1	1
54.4	0.15	3	7.1	153	0	0
53.1	0.25	2.5	7.1	150	0	0
46.6	0.5	2.5	6.5	173	1	1
83.1	0.24	3	7.1	157	0	0

Table 2. Relevance vector and value of weight.

σ'_v	a_{max}	Soil type	M	V_s	Weight(w)
54.8	0.3	2.5	5.9	101	-48.2156
35.4	0.18	1.5	6.6	146	15.5596
83.3	0.16	2	7.1	133	-36.5428
57.8	0.42	2	7.1	135	17.1751
140.2	0.1	2.5	6.5	150	18.683
54.8	0.13	2.5	5.9	101	39.0781
83.7	0.14	2	7.1	157	4.195
140.8	0.15	1.5	7.1	199	3.1159

The developed RVM model has an overall success rate of 98.21%(Training performance=100% and Testing Performance(98.21%), with no errors in training dataset and one data error in the testing dataset. The difference between the performance of training and testing dataset is very marginal. So, developed RVM has the ability to avoid overfitting. Table 1 shows the performance of testing dataset using design value of σ. The number of relevance vector is 8. So, RVM model uses approximately 6% of training data as relevance vectors. This relevance vector is only used for final prediction. So, there is real advantage gained in terms of sparsity. Sparseness means that a significant number of the weights are zero (or effectively zero), which has the consequence of producing compact, computationally efficient models, which in addition aresimple and therefore produce smooth functions.

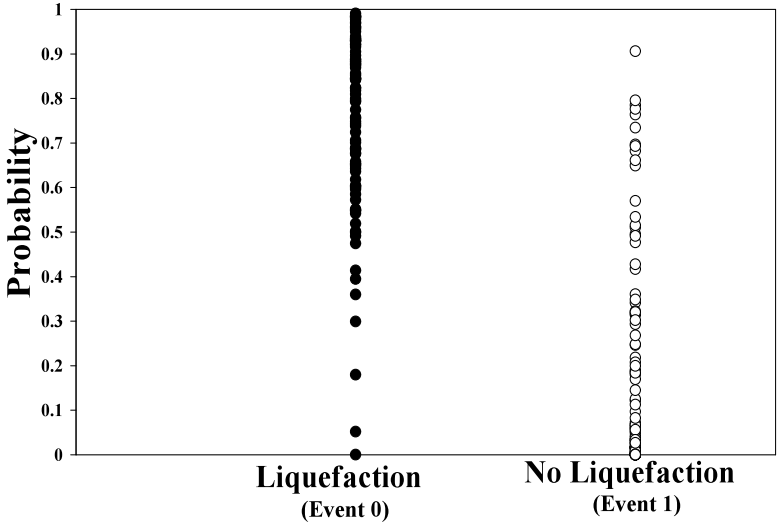

FIG. 2. Probability of training and testing dataset.

Table 2 shows the relevance vector and weight. Figure 2 shows the probability of training

and testing dataset. Probabilistic results from the RVM indicate that most of the liquefiable soil fell within the 0.5 to 1 probability range and most non-liquefiable soil fell within the 0 to 0.5 range. Thus, the RVM probabilistic output can be used to determine the liquefaction susceptibility of soil. If the output is less than 50%, the probability of liquefaction is decreased. If the output is more than 50%, the probability of liquefaction is increased.

Table 3. Performance of Additional dataset for developed RVM model.

σ'_v	a_{max}	Soil type	M	V_s	Actual class	Predicted Class	Probability
39	0.5	1.5	6.9	176	0	0	0.68
38.4	0.5	1.5	6.9	153	0	0	0.78
40.5	0.5	1.5	6.9	183	0	1	0.40
38.2	0.5	1.5	6.9	181	0	0	0.92
31.7	0.5	1.5	6.9	210	0	0	0.84

An additional dataset (as listed in Table 3) which is not part of the training and testing dataset (which was presented earlier)) have been collected from the work of Andrus and Stokoe (1997). The performance of the above RVM developed models has been assessed for this dataset and the same has been reported in Table 3. Only one data has been misclassified. The prediction has been done with radial basis function for both models. The results presented in Table 3 highlights very clearly that RVM is good tool to predict liquefaction resistance of soils.

CONCLUSIONS

This paper investigates RVM model for prediction of liquefaction susceptibility based on shear wave velocity data. The developed RVM model has the ability to model the complex relationship between the seismic parameters and soil parameters. Once the RVM model is developed and trained, it requires only a small amount of computational time and provides promising results. The developed RVM model also estimates uncertainty. It achieves very good generalization performance and yields sparse models. Summarizing, it can be concluded that RVM is a robust model for predicting liquefaction susceptibility of soil based on shear wave velocity data.

REFERENCES

Andrus, R.D., and Stokoe, K. H. (1997). ‘‘Liquefaction resistance based on shear wave velocity,’’ *Proc., NCEER Workshop on Evaluation of Liquefaction Resistance of Soils, Nat. Ctr. for Earthquake Engrg. Res*., State Univ. of New York at Buffalo, 89–128.

Bishop, C. (1995). “Neural Networks for Pattern Recognition.” Oxford: Oxford University Press.

Tipping, M.E. (2001). “Sparse Bayesian Learning and the Relevance Vector Machine.” *J. Mach. Learn*, 1:211-244.

Tipping, M.E.(2000). “The relevance vector machine.” *Advances in Neural Information Processing Systems* , 12:625-658.

Numerical Analysis on co- and Postseismic Behavior of Sandy/Clayey Soil Ground Improved by Sand Compaction Pile Method

Hidekatsu Takeuchi[1], Toshihiro Noda[2], and Akira Asaoka[3]

[1] Research Engineer, Fudo Tetra Corporation, Tokyo, Japan; hidekatsu.takeuchi@fudotetra.co.jp
[2] Professor, Department of Civil Engineering, Nagoya University, Chikusa, Nagoya 464-8603, Japan; noda@civil.nagoya-u.ac.jp
[3] Professor, ditto; asaoka@civil.nagoya-u.ac.jp

ABSTRACT: The co- and postseismic behaviors of typical loose sandy ground and soft clayey ground improved by the sand compaction pile (SCP) method were investigated using a soil-water coupled finite element deformation analysis program incorporating the SYS-Cam clay model. The results indicated that the deformation caused by earthquakes was suppressed in the SCP improved grounds, irrespective of whether they were sandy or clayey. Although the surrounding ground was liquefied in the case of SCP-improved sandy ground, the confining pressure was maintained in the SCP interpile zone because of the compaction effect produced by the cavity expansion of the sand piles. In the case of the SCP-improved clayey ground, negative excess pore pressures appeared in the SCP sand piles because of the hardening that results from plastic expansion and stress was concentrated on them.

INTRODUCTION

The sand compaction pile (SCP) method (Kitazume, 2005) is widely used as a countermeasure against liquefaction of sandy grounds. In loose sandy ground, the cyclic shearing action occurring during construction of sand piles leads to compaction of the original ground, and the resistance to liquefaction is improved. In the case of soft clayey ground, SCP is usually employed as a measure to enhance stability and bearing capacity with respect to static loads. With respect to seismic behavior, many studies have reported that seismic damage to structures built on improved grounds is relatively small. Although improved seismic performance can be expected, a number of points regarding the seismic response characteristics of SCP improved grounds still remain to be clarified. Therefore, design against earthquakes can go only as far as, for example, employing traditional methods such as the circular arc method to determine safety factors through addition of a design horizontal seismic coefficient to the external forces by replacing the seismic forces

with static loads. However, no techniques are available at present to adequately evaluate the effects of seismic waveform characteristics, seismic activity duration, etc.

In this paper, modeling of typical loose sandy ground and soft clayey ground improved by the SCP method was carried out, and their seismic performances were compared and evaluated by examining their co- and postseismic behaviors with respect to an epicentral L2 type earthquake. For this purpose, ***GEOASIA*** (Asaoka and Noda, 2007, Noda et al., 2008), a soil-water coupled finite deformation analysis program mounted with the SYS Cam-clay model (Asaoka et al., 2002, Asaoka, 2003), was employed. This model is an elasto-plastic constitutive model capable of describing the mechanical behavior of all soils ranging from clay or intermediate soil to sand within a single theoretical framework by accounting for the actions of the soil skeleton structure (soil structure, overconsolidation, anisotropy).

SEISMIC PERFORMANCE OF SCP COMPOSITE GROUNDS

(1) Modeling of SCP-improved grounds under plane strain conditions

The seismic performances of SCP-improved grounds are evaluated here using the geo-analysis code ***GEOASIA***. Strictly speaking, 3-dimensional modeling is necessary when considering ground piling when the SCP piles are laid out with low replacement ratios. For the sake of simplicity, however, the modeling in this work is carried out under 2-dimensional plane strain conditions.

The finite element mesh diagram and boundary conditions used the analyses are shown in Figure 1. The material constants and state parameters used in the present analyses are shown in Table 1. The original grounds were assumed to be ones composed of loose sand and soft clay, with the layer thickness being 14 m. The material constants allotted to the sandy ground were those of silica sand No. 6 (Asaoka, 2003). For the clayey ground, the material constants and initial conditions of an actual soft clay ground (Noda et al., 2009) were used. It must be mentioned that the initial values used for the sandy ground were not those obtained by simulating the conditions of an actual site, but were those decided assuming loose conditions. A total of four cases, the original (untreated) sandy and clayey grounds and the two SCP-improved grounds, were analyzed.

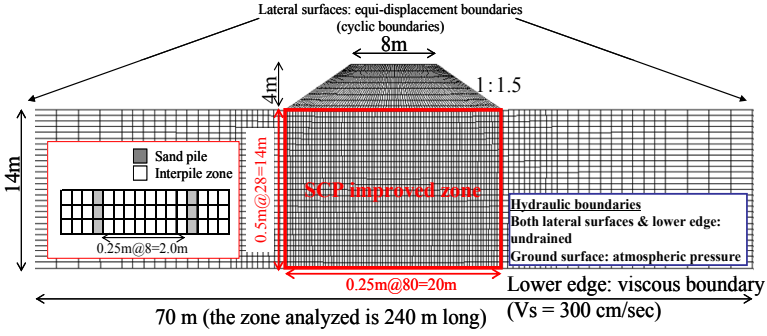

Figure 1 Finite element mesh and boundary conditions

Table. 1 Material constants and initial values of soils

	Sandy ground	Clayey ground	Sand pile	Embankment
＜Elasto-plastic parameters＞				
Compression index $\tilde{\lambda}$	0.05	0.15	0.05	0.04
Swelling index $\tilde{\kappa}$	0.012	0.03	0.012	0.004
Critical state constant M	1.0	1.5	1.0	1.45
Intercept of the line of normal consolidation N	1.98	2.08	1.98	2.40
Poisson's ratio ν	0.3	0.1	0.3	0.4
Permeability k (cm/sec)	1.0×10^{-3}	1.0×10^{-7}	1.0×10^{-3}	1.0×10^{-5}
Density of earth $\rho_s(t/m^3)$	2.80	2.65	2.80	2.65
＜Evolutional parameters＞				
Index of decay of structure a,b,c	2.2,1.0,1.0	0.45,1.0,1.0	2.2,1.0,1.0	10,1.0,1.0
Index of normally consolidated earth m	0.06	2.5	0.06	0.03
Rotational hardening index b_r	3.5	0.05	3.5	0.10
Rotational hardening limit constant m_b	0.7	1.0	0.7	0.65
＜Initial values＞				
Degree of structure $1/R^*_0$	5.0	25.7	1.26	1.18
Specific volume v	1.94	2.416	1.79	2.25
Degree of anisotropy ζ	1.0	0.6	Complies with the interpile zone	0.824
Stress ratio K_0	0.6	0.6	Complies with the interpile zone	0.824

For modeling the SCP-improved zone, the effect of SCP improvement in a 20-m wide region (the area enclosed by the thick lines in Fig. 1), which is situated at the center of the analyzed zone, was considered. The SCP-improved zone is a composite ground consisting of a "sand pile zone" formed by construction of sand piles and an "interpile zone," which refers to the region between the sand piles, that has become compacted because of the shear deformation undergone during build-up of the sand piles. This composite ground condition needs to be simulated by modeling. The sand pile zone was modeled by 25-cm width sand walls placed at 2.0-m intervals (the replacement ratio being equivalent to 12%), and its condition was assumed to be that of dense sand. With respect to the interpile zone, it is necessary to take into account the compaction effect (increase in density) caused by cavity expansion of the sand piles. Therefore, after simulating the compaction process due to cavity expansion of the sand piles under conditions of axial symmetry (Noda et al., 2004), the method of Nakano et al. (2008) was followed to determine the condition of each layer by dividing the interpile zone into seven 2-m thick layers in the vertical direction and utilizing the volume averages of the state parameters for each layer. The values determined by the above method are presented in Tables 2 and 3.

After the above, using the method of finite element mesh addition, embankment loading was carried out at the position corresponding to the improved part of the ground (Noda et al., 2009). After the consolidation deformation subsided, the bottom face viscous boundary (Vs=300 m/sec) was set on the base stratum, and the seismic waveform observed in the Chuetsu earthquake in 2004 was input. The analysis sequence was continued until the deformation subsided.

Table 2 Initial values of the interpile zone in sandy ground

GL	−0 to −2 m	−2 to −4 m	−4 to −6 m	−6 to −8 m	−8 to −10 m	−10 to −12 m	−12 to −14 m
Degree of structure $1/R^*_0$	1.90	1.81	1.75	1.73	1.71	1.70	1.66
Specific volume v	1.927	1.914	1.893	1.876	1.862	1.849	1.836
Degree of anisotropy ζ	0.53	0.68	0.72	0.72	0.73	0.69	0.67
Stress ratio K_0	1.72	0.89	0.79	0.74	0.70	0.68	0.65

Table 3 Initial values of the interpile zone in clayey ground

GL	−0 to −2 m	−2 to −4 m	−4 to −6 m	−6 to −8 m	−8 to −10 m	−10 to −12 m	−12 to −14 m
Degree of structure $1/R^*_0$	21.5	16.4	14.5	13.2	11.9	10.7	9.3
Specific volume v	2.423	2.419	2.408	2.392	2.371	2.347	2.320
Degree of anisotropy ζ	0.70	0.72	0.72	0.72	0.72	0.72	0.72
Stress ratio K_0	2.50	0.85	0.56	0.50	0.51	0.53	0.55

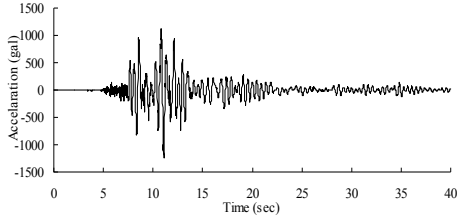

Figure 2 Seismic wave pattern of the free surface of the base stratum (The Mid Niigata Prefecture Earthquake in 2004)

(2) **Results of analyses**

Let us take a look at the results of the computations with respect to the sandy ground first. Figure 3(a) shows time-settlement relationship directly below the center of the embankment from immediately after the start of the earthquake. It can be seen that the SCP-improved ground exhibited as much as a 70% decrease in the amount of settlement compared with the untreated ground. Looking at the results (Fig. 3(b)) of the analysis with respect to the clayey ground next, it can be seen that, although not as prominent as in the case of the sandy ground, the effect of SCP improvement is an approximately 35% reduction in settlement. Usually, the amount of consolidation settlement in a SCP-improved ground is obtained by assuming the improved ground to be a composite ground made up of the original ground and the sand piles and multiplying the amount of settlement of the unimproved ground by a reduction ratio given by $\mathbf{1/\{1+(n-1)*a_s\}}$ (where **n** is the stress sharing ratio, and $\mathbf{a_s}$ is the replacement ratio). For sand piles, the stress sharing ratio is taken as n=3, in which case the reduction ratio becomes 0.8. But in the present analysis, the reduction is greater. When calculated in reverse, the load sharing ratio becomes n=5, indicating that in dynamic loading, there are cases of the share of the stresses born by the sand piles being larger than in static loading. It was also found that almost no long-term settlement occurred in the SCP-improved grounds as a result of the dissipation of pore pressure after the earthquake. The shear deformation distributions after the deformation subsided are illustrated in Figure 4. The effect of the SCP in suppressing deformation is quite evident here.

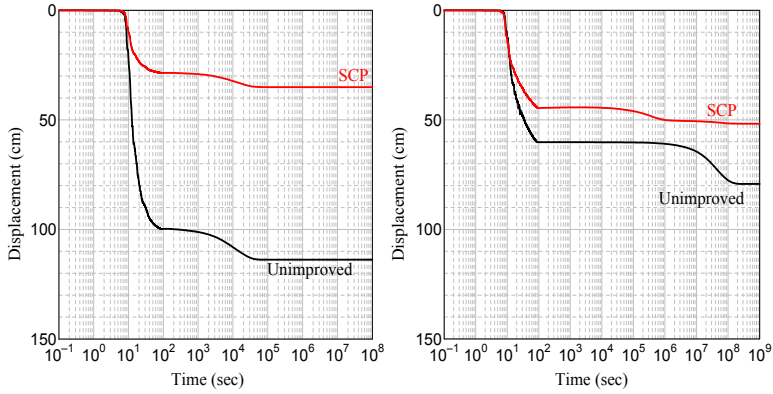

(a) Sandy ground (b) Clayey ground

Figure 3 Time–settlement relationship

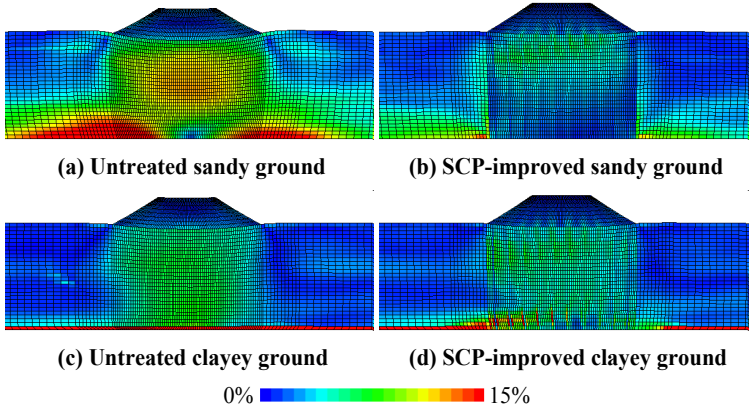

(a) Untreated sandy ground **(b) SCP-improved sandy ground**

(c) Untreated clayey ground **(d) SCP-improved clayey ground**

Figure 4 Shear strain distributions (after the end of consolidation)

Next, we discuss how the mechanism of the effects due to SCP improvement in sandy grounds and clayey grounds differ when an earthquake occurs. Figure 5 shows the mean effective stress distributions during the earthquake (40 seconds after start of the tremors). In both sandy and clayey grounds, large stress concentrations can be observed at the sand piles. Furthermore, because of the unloading caused by the stress concentrations at the sand piles, the stresses in the interpile zone of the clayey ground have reduced in comparison with those in the surrounding original ground. In the sandy ground, because of the compaction effect caused by cavity expansion of the sand piles, the interpile zone is also dense, and the stresses were maintained to a certain extent (repression of liquefaction). For this reason, the effect of SCP improvement on suppression of earthquake deformation is greater in the case of sandy ground than in the case of

untreated ground. The excess pore pressure distributions for the same instant of time as in Fig. 5 are shown in Fig. 6. In the interpile zone of the clayey ground, negative excess pore pressures have arisen. In the sand piles, the dense sand, which undergoes shear due to the earthquake, is hardened due to a positive dilatancy effect, i.e., due to plastic volume expansion (Takeuchi et al., 2009). Because of this, the sand piles bear higher loads even in the case of SCP-improved clayey grounds. Therefore, not only is the resistance to static loads improved, but so is the seismic performance.

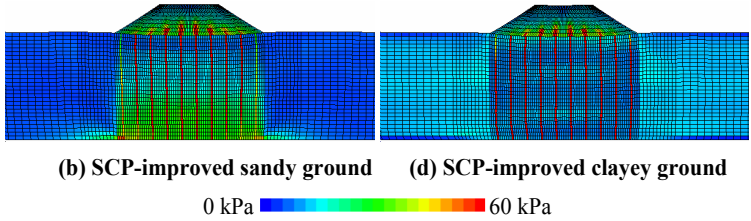

Figure 5 Mean effective stress distributions (during the earthquake, 40 sec. after the start)

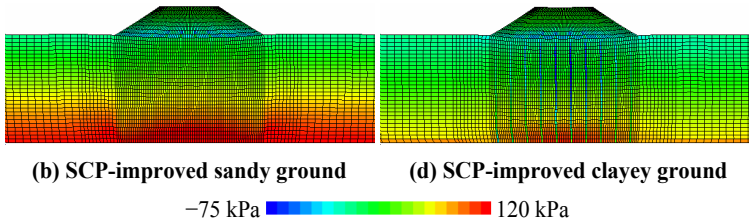

Figure 6 Excess pore pressure distributions occurred by the earthquake (during the earthquake, 40 sec. after the start)

CONCLUSIONS

Using the geo-analysis code ***GEOASIA***, typical loose sandy and soft clayey grounds improved by the SCP method were modeled as composite grounds consisting of sand pile zones and interpile zones, and their co- and postseismic behaviors were investigated in this paper. The main conclusions obtained are outlined below.

1) Compared with untreated grounds, the deformation caused by earthquakes is suppressed in the SCP-improved grounds, both sandy and clayey.
2) It is quite evident that stress concentration occurs at the sand piles in both sandy and clayey grounds. Moreover, because of unloading caused by the stress concentration at the sand piles, the confining pressure in the interpile zone of the clayey ground is reduced compared with that of the surrounding ground. In the sandy ground, because of the compaction effect caused by cavity expansion of the sand piles, the confining pressure is maintained to a certain extent (repression of liquefaction).

3) In the case of a large earthquake, hardening is observed in the sand piles of the SCP-improved clayey ground due to plastic volume expansion occurring under undrained conditions. Because of this, the sand piles are able to bear higher loads, and the seismic resistance of the ground is improved.

ACKNOWLEDGMENTS

This work was supported by JSPS, KAKENHI (Grant-in-Aid for Scientific Research (S):21226012).

REFERENCES

Asaoka, A., Noda, T., Yamada, E., Kaneda, K. and Nakano, M. (2002). "An elasto-plastic description of two distinct volume change mechanics of soils." *Soils and Foundations*, Vol. 42 (5): 45-57.

Asaoka A.(2003). "Consolidation of clay and compaction of Sand - an elasto-plastic description-." Keynote lecture, Proc. of 12th Asian Regional Conf. on Soil Mechanics and Geotechnical Engineering, Leung et al, Singapore, Vol.2: 1157-1195

Asaoka, A. and Noda, T. (2007). "All soils all states all round geo-analysis integration." International Workshop on Constitutive Modelling - Development, Implementation, Evaluation, and Application, Hong Kong, China: 11-27.

Kitazume, M. (2005). "The sand compaction pile method." *Taylor & Francis*.

Nakano, M., Yamada, E. and Noda, T. (2008). "Ground Improvement Reclaimed Land by Compaction through Cavity Expansion of Sand Piles." S*oils and Foundations*, Vol. 48 (5): 653-672.

Noda, T., Asaoka, A. and Nakano, M. (2008). "Soil-water coupled finite deformation analysis based on a rate-type equation of motion incorporating the SYS Cam-clay model." *Soils and Foundations*, Vol. 48 (6): 771-790.

Noda, T., Yamada, E., Yamada, S. and Asaoka, A. (2004). "A soil-water coupled analysis on compaction of sandy ground. " *Geomechanics: Testing, Modeling, and Simulation, Geotechnical Special Publication,* Vol. 143: 269-285.

Noda, T., Takeuchi, H., Nakai, K. and Asaoka, A. (2009). "Co-seismic and post-seismic behavior of an alternately layered sand-clay ground and embankment system accompanied by soil disturbance." *Soils and Foundations*, in printing.

Takeuchi, H., Noda, T. and Asaoka, A. (2009). "Coseismic and postseismic behavior of intermediate soils ground improved by sand compaction pile method." Proc. of International Conference on Performance-Based Design in Earthquake Geotechnical Engineering (IS-Tokyo), Tsukuba, Japan: 1119-1205.

FDTD Simulation of GPR Electromagnetic Wave

Jingwei Zhang[1], Yuancheng Guo[1], Jia Li[2]

[1]School of Civil Engineering, Zhengzhou University, Zhengzhou, China 450002; zhangjw1998@163.com
[2]School of Conservancy and Environment Engineering, Zhengzhou University, Zhengzhou，China 450002; Lijia@zzu.edu.cn

ABSTRACT: The Ground Penetrating Radar (GPR), which is an effective, speedy, continuous and non-destructive testing equipment, its application in pavement has been the international hot subject since 1980s. This paper introduces the basic theory of Finite Difference Time Domain (FDTD) by analyzing the characteristics of electromagnetic wave propagation in pavement, especially from 1-dimension FDTD equation, soft source, effective parameter of layered boundary and Absorbing Boundary Condition (ABC), which have the greatest significance in FDTD simulation of GPR. Then a forward air coupling GPR propagating in layered medium model is established. Moreover, the validity of this forward model is examined through several simulated and actual cases with the maximum error one of 2%. This model develops a new concept for practical and accurate interpretation of GPR reflection data, which can develop a new algorithm to calculate the thickness of pavement's layer, and even develop a new way to measure the moisture and density of pavement's layer in non-destructive testing.

KEY WORDS: Electromagnetic Wave, Finite Difference Time Domain Method (FDTD), Forward Model, Ground penetrating radar (GPR)

1. INTRODUCTION

GPR (Ground Penetrating Radar) systems are used in the detection of objects buried beneath the earth's surface, such as pipes, cables, land mines and hidden tunnels. Although GPR was already recognized as a potential method in geophysical examinations in the first half of this century, it was not used in road inspections until the late 1979s. During the past decade, GPR was widely used in road design, construction and maintenance, due to its speed, nondestructive qualities the capacity of providing continuous profile and high-resolution imaging ability.

Presently, most of the achievements mainly focus on the measurement of pavement thickness. The current GPR data analyzing method for determining pavement thickness provides acceptable results for new asphalt concrete pavement, But, for aged asphalt concrete pavement and cement concrete pavement, the accuracy is not satisfactory because of the theoretical modeling and data acquisition difficulties,. The study of

pavement compaction, moisture content and asphalt content is still in groping stage. Therefore, forward modeling and simulation of GPR systems have been recognized as the preferred means of generating acceptably accurate interpretation of the refection data and enhancing GPR's practical applications, especially the development of software in solving pavement problems. Among the techniques used, the FDTD method has been most popular due to its versatility in solving problems involving EM (Electromagnetic) wave transmitting, scattering and the analysis of antenna arrays. Additional advantages FDTD possesses over the other numerical methods includes:

. Inhomogeneous media is inherently modeled
. Lossy, non-liner and anisotropic media supported
. Boundary conditions are inherently represented
. Computer time and storage saved

In the following context, the working principle and simplified formulations of GPR will be discussed. Next a 1-d FDTD analysis of GPR model from four important aspects will be presented. From that, a practical GPR model is simulated using FDTD method. At last FDTD numerical results will be compared with theoretical and experimental measurements.

2. THE BASIC THEORY OF GPR EM WAVE PROPAGATION IN PAVEMENT

Ground Penetrating Radar (GPR) systems are new type of non-destructive tools using ultra-wide band antenna technique for detecting the structure of layers and objects buried in the earth. GPR special application in road is a system for testing road's thickness, voids, moisture, density etc. The GPR unit contains a transmitting and a receiving antenna. The GPR unit travels above the ground-air interface at a fixed elevation. The transmitter generates the fields, which propagate toward and penetrate the ground with particular polarization. The receiver collects and samples wave reflected from the ground.

The working principle (shown in figure 1) of GPR in road applications is the EM waves are reflected at multi- layer interfaces in the pavement.

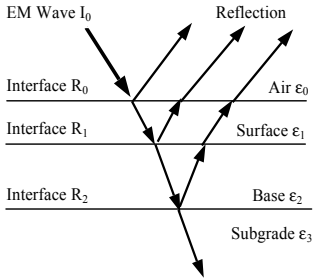

FIG.1 The Working Principle of GPR

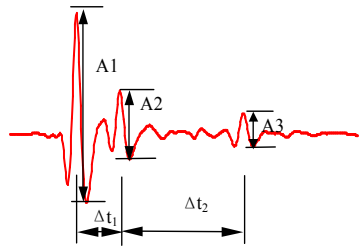

FIG.2 Typical GPR Reflected Waveform for Three layer Pavement

Radar waves have the same characteristics and principle of propagation as other waves. Specially, these waves are reflected at significant layer interfaces with different dielectric value in the pavement. The GPR non-destructive test technique is based on the

characteristics above mentioned. Since reflected waves are captured by the system and displayed as a plot of reflection amplitude (voltage) versus arrival time, this can help to identify the most important sites from the point of view of road construction. Figure 2 shows the typical GPR reflected waveform for three-layer pavement. The largest peak is the reflection from the pavement surface. The second and last are from the base and the subgrade respectively.

3. FDTD SIMULATION OF GPR EM WAVE

3.1 FDTD Discretized Formulations:

First applied to electromagnetic by kane.s.yee in 1966[1], the FDTD technique utilizes a central-differencing scheme to discretize Maxwell's curl equations in space-time. Electric and magnetic field components are evaluated alternately at half-time step intervals. This normally is a 2-d FDTD issue with the reflection of one side being free space and the other being lossy、semi-infinite space. However, an actual pavement system is layered homogeneous and isotropic media so it can be simplified as 1-d FDTD item, which saves computational time and space, and allows the new concept for further studying the backcalculation of pavement dielectric properties and its technical characteristics. Beginning the formulation with the 1-d FDTD lattice, propagation is in the z-direction and only the components Ex and Hy are considered, when $\partial/\partial x = 0, \partial/\partial y = 0$. The yee's algorithm is acquired by discretizing the equations of Ampere's law and Faraday's law .The curl equations of Maxwell's equations in the isotropic medium are given as:

$$\nabla \times H = \frac{\partial D}{\partial t} + J$$

$$\nabla \times E = -\frac{\partial B}{\partial t} - J_m \tag{1}$$

(1) can be discretized as follows

$$E_x^{n+1}(k) = \frac{1-\dfrac{\sigma(m)\Delta t}{2\varepsilon(m)}}{1+\dfrac{\sigma(m)\Delta t}{2\varepsilon(m)}} \cdot E_x^n(k) - \frac{\dfrac{\Delta t}{\varepsilon(m)}}{1+\dfrac{\sigma(m)\Delta t}{2\varepsilon(m)}} \left[\cdot \frac{H_y^{n+1/2}(k+1/2) - H_y^{n+1/2}(k-1/2)}{\Delta z} \right] \tag{2}$$

$$H_y^{n+1/2}(k+1/2) = \frac{1-\dfrac{\sigma_m(m)\Delta t}{2\mu(m)}}{1+\dfrac{\sigma_m(m)\Delta t}{2\mu(m)}} \cdot H_y^{n-1/2}(k+1/2) - \frac{\dfrac{\Delta t}{\mu(m)}}{1+\dfrac{\sigma_m(m)\Delta t}{2\mu(m)}} \cdot \frac{E_x^n(k+1) - E_x^n(k)}{\Delta z} \tag{3}$$

Here, D is the electric flux density and H is the magnetic intensity. The terms J and J_m are often regarded as source terms, and, in that context they are the electric and magnetic current densities, respectively; ε , μ and σ , stand for permittivity, permeability and conductivity , respectively.

3.2 Efficient Source Excitation:

Locating source excitation is a fundamental problem in FDTD simulations. The first source excitation model was applied by Yee in 1966[1]. In 1982, Taflove exemplified

another "hard source"[2]. His simple approach was to fix of the field components at each point with given value for all time steps. However, the "hard" source condition can cause undesired nonphysical reflection. Currently, the simulation of a continuous, effective source excitation by using "soft wave-source" condition is most common. This was developed by An ping zhao in 1996[3]. His method is also very simple, as shown in formulation 4:

$$E_x^{n+1}(k) = E_x^n(k) - \frac{\Delta t}{\varepsilon} \cdot \frac{H_y^{n+1/2}(k+1/2) - H_y^{n+1/2}(k-1/2)}{\Delta z} + E_x^i(k) \tag{4}$$

At each point on this line, the computer first calculates Ex in the normal manner using the algorithm and stores the value in the memory. Then the given value is calculated and added to the stored value Ex. Finally, the modified value of Ex is stored in memory.

3.3 Effective Parameter At Significant Layer Interfaces:

The pavement system is the stratified structure including surface, base and subgrade. Because of the discontinuity at the interface of two dielectric media, the differential form of Maxwell equations are no longer applicable. The FDTD formulation uses the average of the parameters along the two sides of the interface.

$$\left.\begin{aligned} \varepsilon_{eff} &= \frac{\varepsilon_1 + \varepsilon_2}{2} \\ \sigma_{eff} &= \frac{\sigma_1 + \sigma_2}{2} \\ \mu_{eff} &= \frac{\mu_1 + \mu_2}{2} \end{aligned}\right\} \tag{5}$$

3.4 Absorbing Boundary Conditions(ABC):

Another fundamental problem with any finite-difference solution of Maxwell's equations is the treatment of the field vector components at the lattice truncation. Because of limited memory size of calculating ability, the lattice cannot cover a sufficiently large portion of space. Proper truncation of the lattice requires that any out-going wave disappear at the lattice boundary without reflection during the continuous time stepping of the algorithm. Improper truncation results in error for all time steps after the boundary wave reflections return to the vicinity of the scatterer. This is exemplified by Yee's fixing of the field components at each truncation point at zero, for all time steps. This "hard" truncation condition does not take into account the value of the fields of any possible outgoing wave. It causes boundary reflections in a way analogous to reflection at the surface of a conductor.

One way to achieve a "soft" lattice truncation is to assign linearly increasing values of a near the lattice boundary so that absorption of outgoing waves is achieved. However, for a small amount of reflection, the distance over which absorption takes place must be on the order of one wavelength. For many problems, this is an unacceptable assignment of computer storage to points not in the scatterer. In addition, any incident wave propagating parallel to such a lattice boundary must suffer distortion due to the variation of phase velocity along the wavefront. Therefore, this type of truncation is not suitable.

A more desirable soft lattice truncation relates in a simple way the values of the field components at the truncation points to field component values at point. Until late 1994,

the principal ABC's used in FDTD codes were published originally by Mur[4]. This ABC's provided effective outer-boundary reflection coefficients in the range of 0.5%-5.0% for the types of waves, grid resolutions, and scatterer-to-outer boundary distances normally encountered in FDTD simulations. In this paper, the first-order Mur's ABC (equation 6) is chosen because it has the advantages of being local in time and space, but general and extremely accurate over a wide range of group velocities.

$$\varphi^{n+1}(0) = \varphi^{n}(0) + \frac{v\Delta t - \Delta x}{v\Delta t + \Delta x}[\varphi^{n+1}(1) - \varphi^{n}(0)] \tag{6}$$

3.5 Simulation:

The present forward model of GPR electromagnetic wave propagation in pavement system is evolved from the basic theory of electromagnetic through analyzing the propagation characteristics of electromagnetic wave propagation in pavement. In FDTD simulation, we assume: The incident wave makes angle at zero; Materials are non-magnetic and thus the permeability can be neglected. In our formulation, the incident angle is assumed to be zero and the magnetic permeability value of the media is assumed to be one. Based on those assumptions, we can construct the reflection model of multi-layer pavements from EM theory. From the characteristics of the FDTD formulation given above, we can summarize the steps of deducing an EM wave traveling model in a multi-layer pavement as follows:

①Input the parameters of the pavement. Construct the model of the pavement
②Descretize the excitation.
③Use FDTD to calculate the EM wave transmission characteristics in multi-layer pavement, such as reflection, refraction and extenuation. The total field and refraction field are calculated and analyzed separately.
④calculate the reflection field
⑤export the acquired radar reflection signal

4. NUMERICAL RESULTS

A 1-d FDTD code is programmed based on the forward model above mentioned.
Case1: This case is used to test the performance of FDTD code theoretically. The geometry and physical parameters of FDTD simulation are given as follows
$\Delta t = 1\text{x}10^{-12}\text{s}$， $\Delta x = 5\text{x}10^{-3}\text{m}$

Source: the raised cosine function: f(t)=-0.5*(1-cos(2*pi*t/6e-10))

Three -layered pavement system is modeled as:

$$\begin{cases} \varepsilon_1 = 4, \sigma_1 = 0.001\text{S/m}, h_1 = 20cm \\ \varepsilon_2 = 9, \sigma_2 = 0.002\text{S/m}, h_2 = 30cm \\ \varepsilon_3 = 16, \sigma_3 = 0.003\text{S/m}, h_3 = 100cm \end{cases}$$

The FDTD simulation results are shown in Figure 3. Three reflection waves at

significant layer interfaces are very apparent to see. In the following, the amplitude and arrival time are calculated. The theoretical reflection coefficient is calculated based on the data from Figure 3:

$$R = \frac{A_1}{A_m} = \frac{0.333}{1} = 0.333$$

Then the theoretical permittivity is determined based on the theoretical reflection coefficient:

$$\varepsilon_{1c} = \left(\frac{1+R}{1-R} \right)^2 = \left(\frac{1+0.333}{1-0.333} \right)^2 = 3.994$$

This is very close with the value $\varepsilon_1 = 4$ in the model. Also from Figure 3, the two time differences of three reflection waves are determined as:

$$\Delta t_1 = (5.651 - 2.982) = 2.669 ns,$$

$$\Delta t_2 = (11.726 - 5.651) = 6.075 ns$$

The calculated time differences based on formulation 2 are

$$\Delta t_{1c} = \frac{h_1 \times 2}{c/\sqrt{\varepsilon_1}} = 2.67 ns, \Delta t_{2c} = \frac{h_2 \times 2}{c/\sqrt{\varepsilon_2}} = 6 ns$$

The FDTD and calculated result agree well with the maximum error one of 1.25%

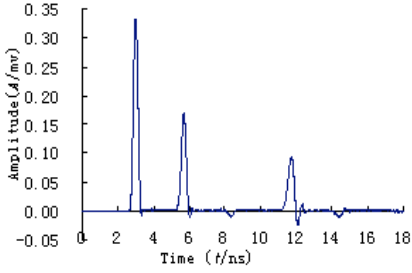

FIG.3 The Calculated Reflected Waveform for Three-layer Pavement

Case 2: A monolayer concrete slab with thickness of 15.5cm is placed on a smooth metal plate. This model is always chosen in simulation because metal reflection is 100% reflection case, so it can measure the thickness of the concrete in the experimentation. The incident waveform is shown in Figure 4. The FDTD simulation results and measured reflected GPR waveform are both shown in Figure.5. The dashed line represents the FDTD results and solid line represents the measured reflection. From studying Figure 5, it is evident that the results are very similar.

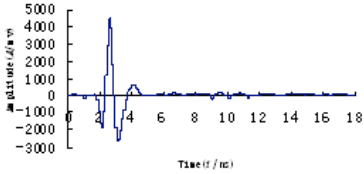

FIG.4 Incident Waveform

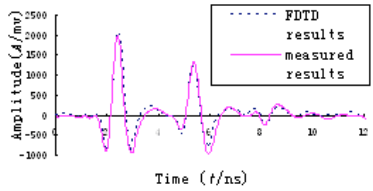

FIG.5 Measured and Simulated Reflected GPR Waveform

Case 3: This case tests how permittivity and conductivity influence the reflected GPR waveform. The conductivity of the monolayer concrete slab with thickness of 15.5cm is assumed to be fixed at value 0.006 S/m so as to determine the influence of dielectric on the reflected waveform. We have its permittivity ε vary 1%, 5%, 10% and 20%, increment as well as decrement, based on the original value 9.5. Such that, we have the following 9 values: 7.6，8.55，9.025，9.045，9.5，9.595，9.975，10.45，11.4.The FDTD simulation results are shown in Figure 6. From Figure 6, it is apparent that permittivity effects the delay time between two peaks of GPR signal. The increment of permittivity can cause the decrement of propagation velocity. When the layer thickness is fixed, the larger the permittivity value, the longer the delay time. However, the change of permittivity causes the change of amplitude of the reflection wave. The increment or decrement of permittivity generates the increment or decrement of the amplitude of the surface and the second boundary reflection waveform. The reflection amplitude is determined by the difference between the permittivity of two media. The larger the value of difference, the larger the reflection amplitude, Vice versa. Since the permittivity of air is 1, the increment or decrement of permittivity causes the increment or decrement of difference between concrete slab and air. Consequently, the larger the value of permittivity, the larger the reflection amplitude.

Still using the same incident waveform shown in Figure 4. Presume the permittivity of the 15.5cm-thick concrete slab is fixed to be 9.5. We have its conductivity σ vary 1%, 5%, 10% and 20%, increment as well as decrement, based on the original value 0.067. Accordingly, the following 9 values were calculated: 0.053，0.06，0.063，0.066，0.067，0.07，0.073，0.08 S/m. Also consider the case of σ =0S/m. From Figure 7, conductivity strongly affects the reflection wave from the pavement structures, except that the reflection value of the surface of the road. The larger the conductivity, the smaller the amplitude of the reflection wave. The reason is the conductivity represents the lossy characteristic of media. The increment of the conductivity value results in the increment of the lossy propagation energy of EM wave. When conductivity is 0, which is the case when an EM wave travels in dielectric material, since the conductivity of PEC (perfect electric conductor) is much larger than that of the concrete slab, the amplitude of the reflection wave achieves its maximum, even exceeds that of the reflection wave

generated at the surface of the slab.

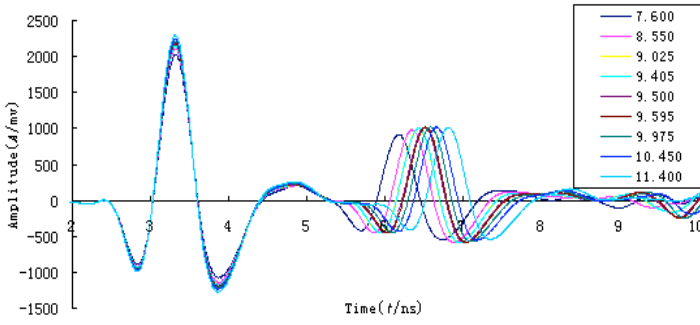

FIG.6 The Influence of Dielectric on GPR Reflected Waveform

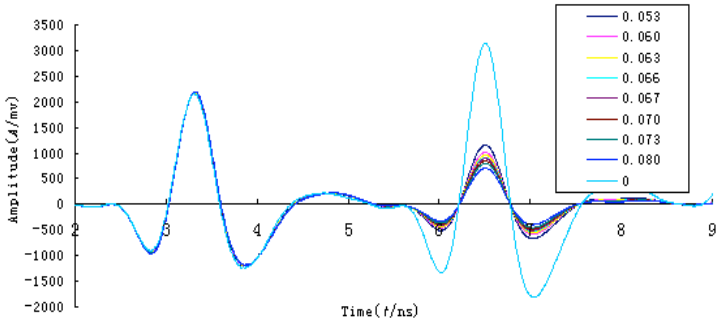

F

IG.7 The Influence of conductivity on GPR Reflected Waveform

Case 4: This case is to test the accuracy of simulated reflection amplitude in lossy media. It compares a group of calculated voltages with FDTD measured values. The conductivity is fixed at the value of 0.005 S/m. The incident waveform is shown in Figure 4 and the results are presented in Table 1. It is apparent that this forward model demonstrated to be successful, with the maximum error of 2%.

No	Calculated reflection waveform w'/(mv)	Incident waveform w/(mv)	Reflection coefficient $R=\frac{w'}{w}$	$\varepsilon_c=\left(\frac{1+R}{1-R}\right)^2$	ε	error θ (%) $\theta=\frac{\lvert\varepsilon_C-\varepsilon\rvert}{\varepsilon}\times 100\%$
1	2997.239	6413	0.467369	7.589733	7.600	0.14
2	3138.722	6413	0.489341	8.510051	8.55	0.47
3	3197.445	6413	0.498588	8.932539	9.025	1.02
4	3198.202	6413	0.498706	8.938156	9.045	1.18

5	3254.824	6413	0.507535	9.370973	9.500	1.36
6	3268.161	6413	0.509615	9.476714	9.595	1.23
7	3366.692	6413	0.524979	10.306301	10.450	1.37
8	3465.051	6413	0.540317	11.228011	11.400	1.50

Table.1 Comparison Theoretical Reflected Waveform with Different Dielectric

5. CONCLUSION

FDTD method based on 1-d Yee's algorithm was implemented in the GPR simulation. The results show the possibility and the accuracy of FDTD simulation of GPR in road system. The importance of this work is it settles the groundwork for simulation of GPR in pavement system. So the future work will focus on the backcalculation of electromagnetic properties and thickness of pavement's layer from GPR data, which can develop a new algorithm to calculate the thickness of pavement's layer, and even develop a new way to measure the moisture and density of pavement's layer in non-destructive testing.

REFERENCES

K. S. Yee(1966), "Numerical solution of initial boundary value problems involving Maxwell's equations in isotropic media", *IEEE Transactions on Antennas and Propagation*, Vol.14(5), 302-307.

Umashankar K.R, A.Taflove(1982), "A novel method to analyze electromagnetic scattering of complex objects", *IEEE Transactions on Electromagnetic Compatibility*, Vol.24(4), 397-405.

An Ping Zhao, Antti V.Raisanen(1996), "Application of a simple and efficient source excitation technique to the FDTD analysis of waveguide and microstrip circuit", *IEEE Transactions on Antennas and Propagation*, Vol.44(9) , 1535-1538.

G. Mur(1981)," Absorbing Boundary conditions for the finite-difference approximation of the time-domain electro-magnetic field equations", *IEEE Transactions on Electromagnetic Compatibility*, Vol.23(4), 377-382.

Cyclic Shear Strength of Clay under Simple Shear Condition

Takeshi Kodaka[1], Kazuo Itabashi[2], Hiroki Fukuzawa[3] and Shinjoro Kato[4]

[1]Professor, Department of Civil Engineering, Meijo University, Nagoya, 464-8502, Japan; kodaka@ccmfs.meijo-u.ac.jp
[2]Trustee, Meijo Univeristy, Nagoya, 464-8502, Japan; itabashi@ccmfs.meijo-u.ac.jp
[3]Graduate student, Department of Civil Engineering, Meijo University, Nagoya, 464-8502, Japan; m0937004@ccmailg.meijo-u.ac.jp
[4]Engineer, JR-Central Consultants, 5-33-10 Meieki, Nagoya, 450-0002, Japan; s-ootake@jrcc.co.jp

ABSTRACT: The aim of the present study is to investigate the cyclic shear behavior of clay, in particular the simple shear conditions. In general, cyclic triaxial tests are performed to evaluate the deformation and the strength characteristics of clay. However, the direction of cyclic loading in triaxial tests is different from the direction of cyclic shear loading in the natural ground. In the present study, therefore, a cyclic simple shear test apparatus has been newly developed and various cases of cyclic simple shear tests have been performed using reconstituted clay and intact natural clay. From the test results, the cyclic shear behavior of clay, which is useful for constitutive modeling, could be precisely obtained. Furthermore, it has been found that the cyclic shear strength of clay can be determined with only the vertical effective stress.

INTRODUCTION

Up to now, various cyclic constitutive models for sand have been developed and proposed to predict liquefaction phenomena using effective stress-based analyses, e.g., Oka et al. 1999 and Asaoka et al. 2000. On the other hand, there are very few cyclic models for clay. Therefore, clay grounds have been modeled as linear or non-linear elastic materials in many cases of numerical seismic analyses. However, in order to predict the seismic behavior of sensitive natural clay more precisely, in particular in the case of huge earthquakes, the constitutive modeling for clay at cyclic loading, including the stress-strain relation, is very important. In general, cyclic triaxial tests are performed to evaluate the deformation and the strength characteristics of clay and to develop the constitutive model, e.g., Oka et al. 2004. However, the direction of cyclic loading in triaxial tests is different from the direction of cyclic shear loading in the natural ground. While hollow cylinder torsional shear tests are effective for obtaining the cyclic shear properties of cohesive geomaterials, they are difficult to perform and require specimens that are relatively large in diameter, e.g., Kodaka et al. 2005. In the present study, a cyclic simple shear test apparatus has been newly developed. The size of the specimen is almost the same as the size of the specimen used in oedometer tests and it is suitable

for thin-wall sampled clay. Thus, the proposed cyclic simple shear tests are very effective for obtaining the cyclic shear characteristics of natural clay.

SIMPLE SHEAR TEST APARATUS

Figure 1 shows the newly developed simple shear test apparatus. A stepping motor and a harmonic reduction gear are adopted to apply the cyclic load without any backlash. Axial strain and shear strain are measured by inner load cells installed in the acrylic pressure cell and the horizontal displacement is measured by a gap sensor. The specimen is 60 mm in diameter and 30 mm in height, which is suitable for the natural clay sampled by the Japanese standard thin-wall tube sampler. Both the upper and the lower pedestals have blades, 1 mm in height, to maintain friction between the pedestals and the clay specimen. The specimen is covered with a thin rubber membrane applied by the confining stress due to water pressure. The shear stress is applied by the lateral movement of the upper pedestal. The slip rings, which are donut shaped and 1 mm in thickness, are set surrounding the membrane-covered specimen in order to allow the specimen to deform with a simple shear mode. Using the developed test apparatus, cyclic simple shear can be loaded to the anisotropically consolidated clay specimen.

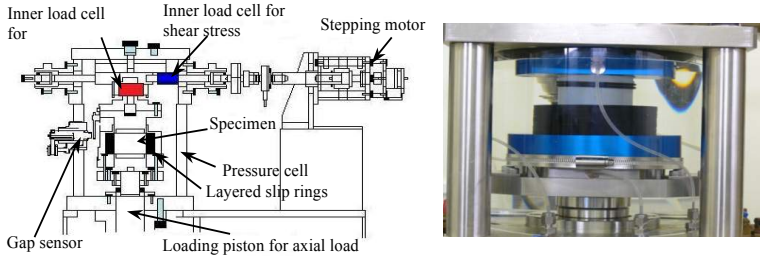

(a) Schematic figure of the apparatus **(b) Enlarged photo of pressure cell**

FIG. 1. Newly developed simple shear test apparatus

TEST SPECIMEN AND TEST PROCEDURE

The clay samples used in this study are reconstituted Yurakucho clay and intact Higashi Osaka clay. The physical properties of these two types of clay are listed in Table 1. The Yurakucho clay was dredged at Tokyo Bay. The reconstituted Yurakucho clay sample was prepared by remolding it in slurry and then pre-consolidating it. Higashi Osaka clay is very sensitive alluvial marine clay called Ma13, which was sampled at Daito City in the East Osaka area by a thin-wall tube sampler without any disturbance.

The clay specimen used in the simple shear tests was trimmed to a cylindrical shape whose radius and height were ϕ=60 mm and h=30 mm, respectively. The test cases are listed in Table 2. All the specimens used in the present study were saturated by the double vacuum method and were acted upon by 200 kPa of back pressure. Firstly, the specimens were isotropically or anisotropically consolidated by the prescribed consolidation pressure. The effective stress path and final state for each case in the

consolidation process are illustrated in Figure 2. The K_0 value expresses the ratio of lateral effective stress σ_3' to vertical effective stress σ_1' in the consolidation process. K_0=1 is an isotropic consolidation case and the others are anisotropic consolidation cases. σ_m' is the mean effective stress. After the consolidation procedure, shear pressure was applied under undrained conditions by moving the upper pedestal with a shear strain control system. For each case listed in Table 2, cyclic loading tests were performed with a constant shear strain rate of 0.5%/min. and by adopting three levels of cyclic shear stress ratio τ / σ_m'.

Table 1. Physical properties of test samples

	Liquid limit (%)	Plastic limit (%)	Plastic index
Yurakucho clay	85.5	31.0	54.5
Higashi Osaka clay	76.2-83.6	32.3-37.0	41.7-46.6

Table 2. Test cases

Case	Sample	K_0	σ_1'	σ_3'	σ_m'
A	Reconstituted Yurakucho clay	1.0	200	200	200
B		0.66	300	200	233
C		0.5	400	200	267
D			200	100	133
E	Intact Higashi Osaka clay	1.0	60	60	60
F		0.5	80	40	53

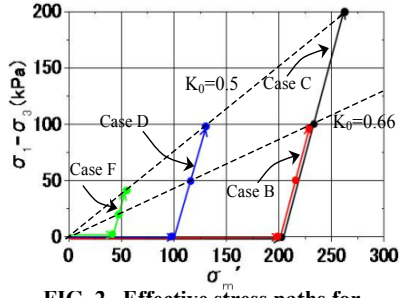

FIG. 2. Effective stress paths for anisotropic consolidation process

TEST RESULTS

Figures 3 and 4 show the cyclic simple shear test results for Cases A and C, respectively. The top and the middle rows of these figures exhibit the shear stress–shear strain relations and the effective stress paths, respectively. The bottom rows illustrate the effective stress paths in terms of the deviator stress. The deviator stress in this paper expresses the second invariant of deviator stress tensor s_{ij}, i.e., $\sqrt{2J_2} = \sqrt{s_{ij}s_{ij}}$, in which each specimen is considered as an element. From the top and the middle rows of each figure, it can be precisely observed that the increase in shear strain and the decrease in mean effective stress develop gradually and symmetrically. In all cases, cyclic loading was applied until a double amplitude of shear strain (DA) of over 10% was reached. The mean effective stress converged to a relatively large value in the final stage of cyclic loading. This behavior is similar to the cyclic mobility for sand. The straight lines illustrated in the effective stress paths are failure lines obtained from monotonic loading tests. In terms of the deviator stress in Case C, i.e., the bottom row in Figure 4, it can be observed from the effective stress paths that the anisotropic effective stress state gradually reaches the isotropic stress state during cyclic shearing. Almost the same tendency was also observed in the other cases, i.e., Cases B and D.

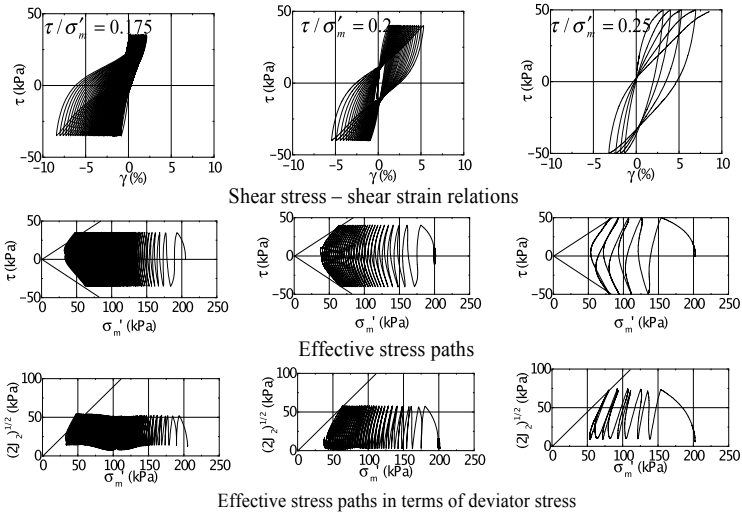

FIG. 3. Test results of isotropically consolidated reconstituted clay, Case A

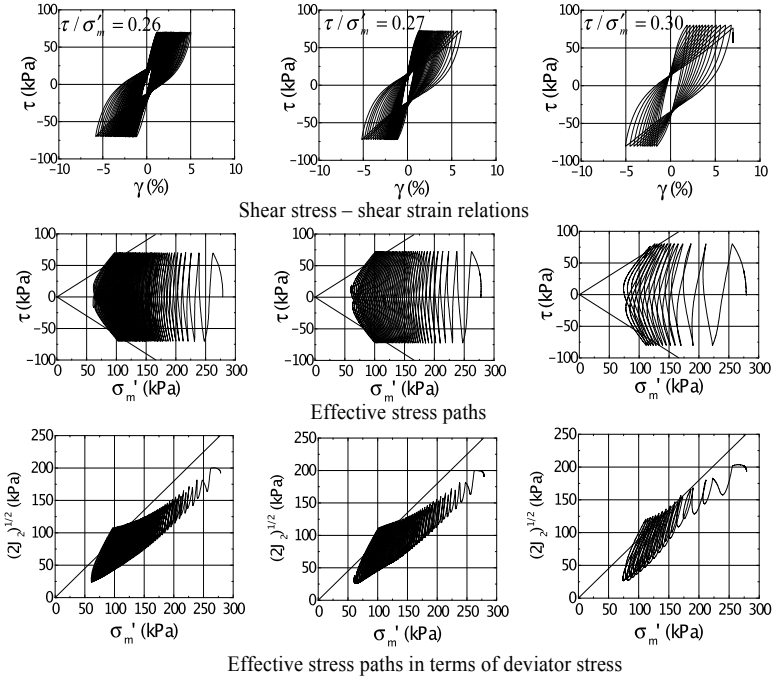

FIG. 4. Test results of anisotropically consolidated reconstituted clay, Case C

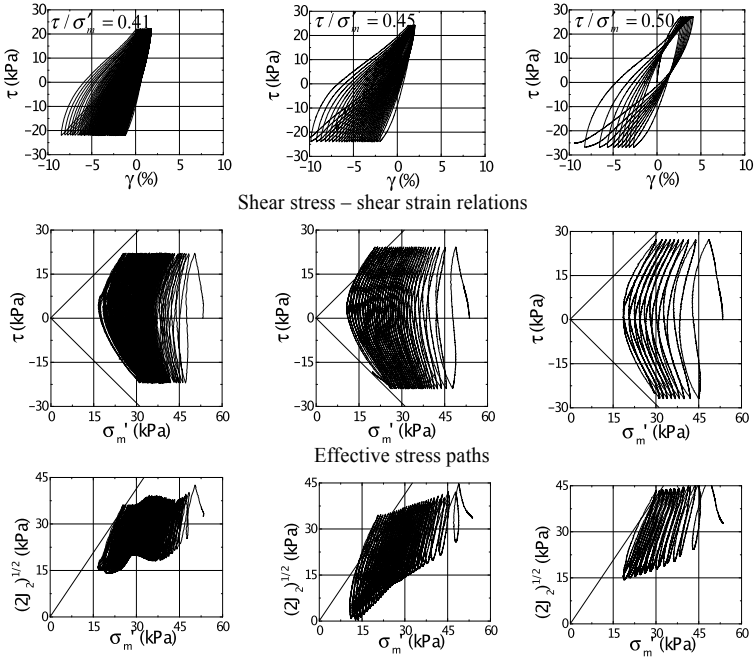

FIG. 5. Test results of anisotropically consolidated intact clay, Case F

Figure 5 shows the test results for Case F. The shear strain could not develop symmetrically in this case. It seems that the imperfection of the initial shear stress easily affects the following shear strain development, since the effective stress state is relatively small. On the other hand, the effective stress decreases with the symmetrical cyclic behavior. In each reloading procedure, in particular in the final stage of cyclic loading, the decrease in mean effective stress is relatively large compared to that of the reconstituted clay. It seems that the structure of natural intact clay was maintained even in the final stage of cyclic loading.

Figure 6 shows the cyclic strength curves, which include all the test results performed in the present study. A vertical axis expresses the cyclic shear stress ratio, defined as τ / σ'_m, and a lateral axis expresses the number of cycles at DA=10%. The definition of the shear stress ratio as τ / σ'_m is the orthodox manner for considering the liquefaction strength of sandy soils. The intact Higashi Osaka clay has relatively large cyclic shear strength compared to the reconstituted Yurakucho clay. In each clay sample, the position of the cyclic strength curve is higher with smaller K_0 values. Hence, the

cyclic shear strength depends on the initial anisotropic consolidation state. Next, the definition of the cyclic shear stress ratio is altered to τ / σ_v', where σ_v' is the initial effective vertical stress. The axial effective stress is used as σ_v' for the cases of the reconstituted Yurakucho clay, and the consolidation yield stress is used for the cases of the intact Higashi Osaka clay. The newly defined cyclic strength curves are shown in Figure 7. The unique cyclic strength curve for each clay sample can be observed; the curves are independent of the K_0 values. These results suggest that the cyclic shear strength can be determined with only the vertical effective stress.

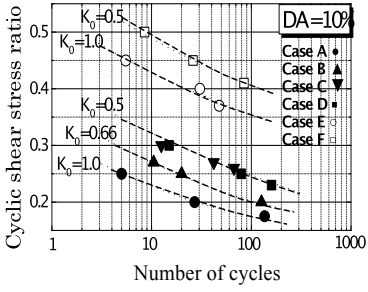

FIG. 6. Cyclic shear strength curves (τ/σm'～N relations)

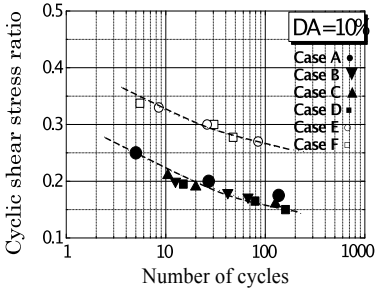

FIG.7. Cyclic shear strength curves (τ/σ1'～N relations)

CONCLUSIONS

A series of cyclic simple shear tests for two types of clay has been performed with the newly developed cyclic simple shear test apparatus. As seen in the results of the present study, the cyclic shear behavior of clay, which is useful for constitutive modeling, could be precisely obtained. The next stage of this study will be to propose a reasonable constitutive model for clay, which can describe the seismic behavior of natural clay grounds.

REFERENCES

Asaoka, A., Nakano, M. and Noda, T. (2000) "Superloading yield surface concept for highly structured soil behavior." *Soils and Foundations*, Vol.40 (2): 99-110.

Kodaka, T., Ohno, Y. and Takyu, T. (2005): "Cyclic shear characteristics of treated sand with colloidal silica grout." *Proc. of 16th ICSMGE*, Vol.2: 404-404.

Oka, F., Yashima, A., Tateishi, A., Taguchi, Y. and Yamashita, S. (1999). "A cyclic elasto-plastic constitutive model for sand considering a plastic-strain dependence of the shear modulus." *Geotechnique*, Vol. 49 (5): 661-680.

Oka, F., Kodaka, T. and Kim, Y.-S. (2004). "A cyclic viscoelastic-viscoplastic constitutive model for clay and liquefaction analysis of multi-layered ground." *Int. J. for Numerical and Analytical Methods in Geomechanics*, Vol. 28 (2): 131-179.

Effect of Cyclic Loading Frequency on Dynamic Properties of Marine Clay

Minmin Jiang[1], Zhengyin Cai[2], Pei Cao[3] and Dan Liu[4]

[1]Ph.D student, Nanjing Hydraulic Research Institute, 34 Hujuguan, Nanjing 210024, China; jiang_mm@hotmail.com
[2]Professor, Nanjing Hydraulic Research Institute, 34 Hujuguan, Nanjing 210024, China; zycai@nhri.cn
[3]Engineer, Nanjing Hydraulic Research Institute, 34 Hujuguan, Nanjing 210024, China; pcao@nhri.cn
[4]Graduate student, Nanjing Hydraulic Research Institute, 34 Hujuguan, Nanjing 210024, China; dliu@nhri.cn

ABSTRACT: A study of the effect of cyclic loading frequency on the dynamic properties of saturated soft marine clay was presented. The research was based on a series of stress-controlled undrained one-way loading cyclic triaxial tests conducted on normally consolidate undisturbed Tianjin soft marine clay. It is found that accumulative axial strain and normalized average pore pressure with number of cycles are strongly affected by cyclic frequency, but the effect of frequency on normalized average pore pressure with accumulative axial strain is not significant, and the frequency is also a less important factor that affects degradation index with number of cycles. Accumulative axial strain, normalized average pore pressure and degradation index with number of cycles were successfully modeled by hyperbolic line, while normalized average pore pressure with accumulative axial strain can be modeled by Hill growth line. These models can be used to estimate the dynamic properties of soft clay under cyclic load reasonably.

INTRODUCTION

Dynamic properties of saturated soft clay under low frequency cyclic load are believed to be important in the design of offshore structures. Although a lot of researches have been done on earthquake and road pavement engineering, the research of ocean wave load on dynamic properties of soil was not begun until 1980s (Andersen et al. 1980). The stress path of offshore structure foundation under wave load is quite complex, however, many engineering problems can be solved with one-way or two-way cyclic load test (Hyde and Ward 1986; Yasuhara et al. 1992; Hyde et al. 1993).

Some researches have been done to study the effect of cyclic frequency on dynamic properties of soils. Matsui et al. (1980) and Zhou et al. (2001) believed that cyclic frequency had a strong effect on dynamic properties of saturated clay, as the frequency increased pore pressure and axial strain decreased. While Hyde et al. (1993) observed

that cyclic pore pressure and axial strain were independent of frequency. Chen et al. (2004) indicated that cyclic frequency had a strong effect on pore pressure and axial strain when they were larger than a threshold value, moreover, the effect of frequency on dynamic strength was not evident when number of cycles was large enough.

In this study, dynamic properties of undisturbed soft marine clay under low frequency cyclic load are investigated with stress controlled cyclic triaxial test, and then empirical models are established.

MATERIAL AND TESTING PROGRAM

The specimens tested represent a clay deposit located in the region off the coast of Tianjin. The samples were recovered with thin wall sampler at the depth of 5~10m below the seabed. The properties of the soil were as follows: specific gravity of solids G_s=2.75, density of dry soil ρ_d=1.01g·cm^{-3}, void ratio e=1.72, liquid limit w_L=52.5%, plastic index I_p=26.5, water content w=62.3% and compressive coefficient a_v=1.46MPa^{-1}. The soil would be defined as high liquid limit clay in plastic chart. The distribution of grain size is shown in Fig.1, it can be seen that grain size below 0.075mm and 0.005mm were about 99.3% and 57.2% respectively.

Cyclic triaxial tests were conducted on GDS cyclic triaxial apparatus. Undisturbed samples were trimmed to a diameter of 39.1mm and a height of 80mm for the test. The specimens were first anisotropically consolidated to a vertical stress of 100kPa and a horizontal stress of 50kPa, and then cyclic load in vertical direction was applied with a single amplitude axial stress of 15kPa under undrained conditions. The cyclic deviator stress was purely compressive, so it was one-way cyclic test. The typical ocean wave period ranged between 5~20s (O'Reilly et al. 1991). In this study, the cyclic periods of 5s, 8s, 12.5s and 20s were chosen for the tests, the total number of cycles was 3000.

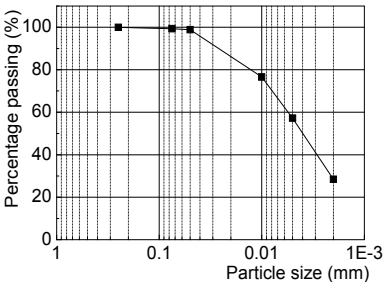

FIG. 1. Grain size distribution chart

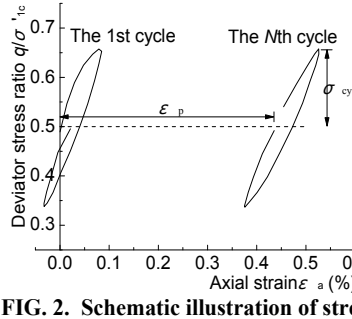

FIG. 2. Schematic illustration of stress and strain components

DEVELOPMENT OF CYCLIC AXIAL STRAIN

The components of stress and strain in cyclic triaxial test are illustrated in Fig.2. Accumulative axial strain ε_p is defined as the axial strain after a certain number of cycles. Accumulative axial strain versus number of cycles for different cyclic period is presented in Fig.3. We can see that, for a given number of cycles, accumulative axial strain

increases with the increase of cyclic period. After 3000 cycles, accumulative axial strain ranged between 1.62% and 2.48%. Accumulative axial strain can be related with number of cycles by hyperbolic equation as follows:

$$\varepsilon_p = \frac{N}{a + bN} \tag{1}$$

Where $1/a$ is the initial slope of ε_p~N curve, $1/b$ is the asymptotic value of ε_p. The fitted line is shown in Fig.3, we can see that the hyperbolic equation can fit the data points reasonably within 3000 cycles. Variation of parameters $1/a$ and $1/b$ with cyclic period are shown in Fig.4. Parameter $1/a$ increases with the increase of cyclic period ranged between 0.0028 and 0.0061. Parameter $1/b$ ranged between 1.94 and 2.84, with T=5s the lowest and T=20s the highest.

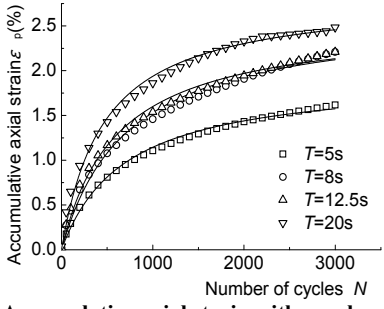

FIG. 3. Accumulative axial strain with number of cycles

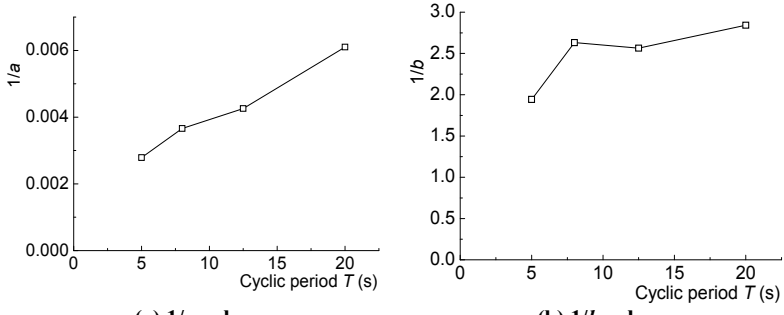

(a) 1/*a* value **(b) 1/*b* value**

FIG. 4. Variation of parameters 1/*a* and 1/*b* with cyclic period

DEVELOPMENT OF CYCLIC PORE PRESSURE

Pore pressure in this study is taken as the average value of each cycle as Matsui et al. (1980) recommended, which can correct the time lag and the gradient of pore pressure in specimen to a certain extent. Normalized average pore pressure is defined as the ratio of

average pore pressure to vertical consolidate stress u/σ'_{1c}. Normalized average pore pressure with number of cycles under different cyclic period is presented in Fig.5. We can see that, under the same number of cycles normalized average pore pressure increases with the increase of cyclic period, and it ranged between 0.132 and 0.179 after 3000 cycles.

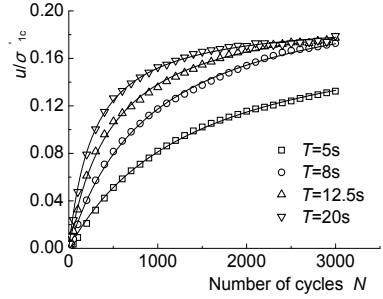

FIG. 5. Normalized average pore pressure with number of cycles

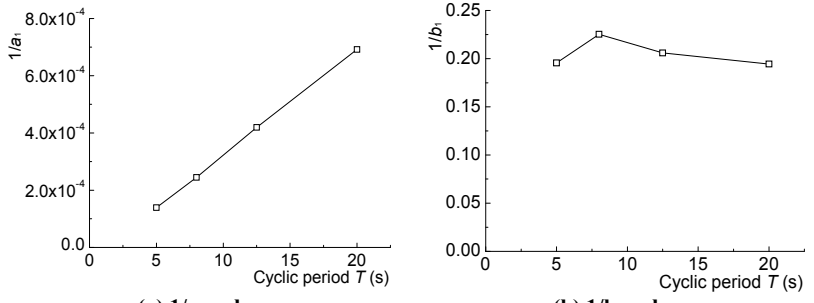

(a) $1/a_1$ value **(b) $1/b_1$ value**

FIG. 6. Variation of parameters $1/a_1$ and $1/b_1$ with cyclic period

The relationship between normalized average pore pressure and number of cycles can be expressed with hyperbolic equation as follows:

$$\frac{u}{\sigma'_{1c}} = \frac{N}{a_1 + b_1 N} \tag{2}$$

Where $1/a_1$ is the initial slope of u/σ'_{1c}~N curve, $1/b_1$ is the asymptotic value of u/σ'_{1c}. Variation of parameters $1/a_1$ and $1/b_1$ with cyclic period are presented in Fig.6. Parameter $1/a_1$ that increases almost linear with cyclic period ranged between 1.39×10^{-4} and 6.92×10^{-4}, and this suggests that normalized average pore pressure developed faster under larger cyclic period in the first several cycles. Parameter $1/b_1$ ranged between 0.194 and 0.225, with T=20s the lowest and T=8s the highest.

Normalized average pore pressure with accumulative axial strain under different cyclic

period is plotted in Fig.7. We can see that, the effect of cyclic period on u/σ'_{1c}~ε_p curve is not obvious. The relationship between normalized average pore pressure and accumulative axial strain under different cyclic period can be fitted with Hill growth function as follows:

$$\frac{u}{\sigma'_{1c}} = u_{\max}\frac{\varepsilon_p^{\ t}}{\varepsilon_p^{\ t} + k^t} \tag{3}$$

Where $u_{\max}$, k and t are parameters, in this study, the fitted parameters are as follows: $u_{\max}$=0.237, k=1.41, t=2.112.

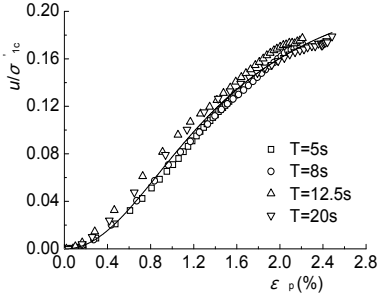

FIG. 7. Normalized average pore pressure with accumulative axial strain

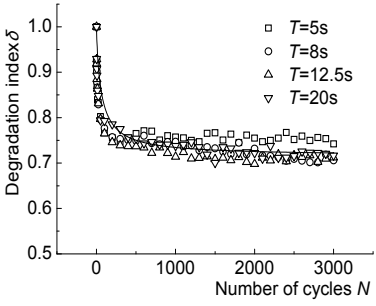

FIG. 8. Degradation index with number of cycles

DEGRADATION OF MODULUS

Degradation index δ is defined as the ratio of secant modulus in the Nth cycle to secant modulus in the first cycle (Idriss et al. 1978). Degradation index with number of cycles under different cyclic period is plotted in Fig.8. We can see that, the effect of cyclic period on degradation index is not significant as well, and after about 3000 number of cycles, the degradation index changed very slowly. Vucetic et al.(1988) established a power function model between degradation index and number of cycles under about 100 cycles, however, the cycle number in this study is 3000, the degradation index with number of cycles under different cyclic period can be simulated with hyperbolic equation as follows:

$$\delta = 1 - \frac{N}{a_2 + b_2 N} \tag{4}$$

Where a_2 and b_2 are parameters, in this study, the fitted parameters are as follows: a_2=235.67, b_2=3.524.

CONCLUSIONS

On the basis of the analysis of one-way cyclic test results performed in this study, the following conclusions can be drawn for cyclic frequency on dynamic properties of Tianjin marine clay:

1. Accumulative axial strain increases with the increase of cyclic period, and accumulative axial strain with number of cycles can be simulated with hyperbolic equation.

2. Normalized average pore pressure also increases with the cyclic period, meanwhile, the normalized average pore pressure with number of cycles can be simulated with hyperbolic equation. The effect of cyclic period on u/σ'_{1c}~ε_p curve is not obvious, and the relation between u/σ'_{1c} and ε_p can be fitted with Hill growth curve.

3. The effect of cyclic period on degradation index is not notable, after about 3000 number of cycles degradation index changed very slowly. The degradation index with number of cycles can be simulated with hyperbolic equation.

REFERENCES

Andersen, K. H., Pool, J. H., Brown, S. F., Rosenbrand, W. F.(1980). "Cyclic and Static laboratory tests on Drammen clay." *J. Geotech. Engrg. Div.*, Vol. 106 (GT5): 499-529.

Chen, Y. M., Ji, M. X., Huang, B. (2004). "Effect of cyclic loading frequency on undrained behaviors of undisturbed marine clay." *China Ocean Engineering*, Vol. 18 (4): 643-651.

Hyde, A. F. L. and Ward, S. J. (1986). "The effect of cyclic loading on the strength of a silty clay." *Mar. Geotech.*, Vol. 6(3): 299-314.

Hyde, A. F. L., Yasuhara, K., and Hirao, K. (1993). "Stability criteria for marine clay under one-way cyclic loading." *J. Geotech. Engrg.*, Vol. 119 (11): 1771-1789.

Idriss I. M., Dobry R., Singh R. D. (1978). "Nonlinear behavior of soft clays during cyclic loading." *J. Geotech. Engrg. Div.*, Vol. 104 (GT12): 1427-1447.

Matsui T., Ohara H., Ito T. (1980). "Cyclic stress-strain history and shear characteristics of clay." *J. Geotech. Engrg. Div.*, Vol. 106 (GT10): 1101-1120.

O'Reilly, M. P., Brown, S. F.(1991). Cyclic loading of soils. Glasgow and London: Blackie, 122-173.

Vucetic, M., Dobry, R. (1988). "Degradation of marine clays under cyclic loading." *J. Geotech. Engrg.*, Vol. 114 (2): 133-149.

Yasuhara, K., Hirao, K., and Hyde, A. F. L. (1992). "Effects of cyclic loading on undrained strength and compressibility of clay." *Soils Found.*, Vol. 32 (1): 100-116.

Zhou, J., Gong, X.N. (2001). "Strain degradation of saturated clay under cyclic loading." *Can. Geotech. J.*, Vol.38 (2): 208-212.

Influence of Soil Saturation on the Free Field Responds of Liquefiable Soils

Hanbing Bian[1], Ali Daouadji[1], Yun Jia[2] and Isam Shahrour[2].

[1]LPMM, FRE CNRS 3236, Université Paul Verlaine Metz, Ile du Saulcy, 57045 Metz Cedex, Francen; hanbing.bian@gmail.com
[2]Laboratory of Mechanics of Lille, Polytech'Lille, Cité scientifique, 59655 Villeneuve d'Ascq, France

ABSTRACT: This paper concerns analysis of the free field response of partially saturated soils to cyclic loading, with a particular attention on liquefaction. Analysis is conducted using a numerical model elaborated for the liquefaction of partially saturated soils together with a cyclic elastoplastic constitutive relation implemented in a finite element program. The paper presents firstly the numerical model, and then the influence of the soil saturation on the free field response for different positions of the water table. Analyses show that the soil saturation degree largely affects the free field response to seismic loading. The decrease in the soil saturation leads to a decrease in the rate of generation of the excess pore-water pressure and consequently to a reduction in the liquefaction risk.

INTRODUCTION

Soil liquefaction was observed in moderate and large earthquakes, for example, Loma 1989, Luzon 1990, Manjil 1990, Kobe 1995, Manzanillo 1995, Chi-Chi 1999, Kocaeli 1999 and Bhuj 2001. It is considered as one of the main causes of economic and human life lost. During the past several decades, intensive efforts have been carried out for evaluating the liquefaction risk. The liquefiable soil layers located below the phreatic surface are not, as usual assumed, fully saturated but in a partially saturated states. Furthermore, the phreatic surface fluctuates with the season and the climate. All these will influence the distribution of water saturation. On the other hand, research results (for example, Martin et al., 1978; Yoshimi et al., 1989) showed that a small reduction in the degree of water saturation of sand could result in a significant increase in liquefaction resistance. The increase of gas content in the pore fluid will enhance the liquefaction resistance. Consequently, it is of major interest to consider the degree of saturation in the analysis of the response of liquefiable soils subjected to seismic loading.

This paper presents a numerical analysis of the influence of the soil saturation on the free field response. Analysis is carried out using the model proposed by Bian and Shahrour (2009) for the analysis of the liquefaction of unsaturated sandy soils. Firstly, the paper

presents the numerical model used in the analysis; then it presents the influence of the soil saturation on the free field response of liquefiable soils.

NUMERICAL MODEL

2.1 Basic assumptions

Based on the theory of Coussy (2004), Bian and Shahrour (2009) proposed a numerical model for analysis of the liquefaction of partially saturated sandy soils. In neglecting the soil suction, the increment of the total stress $\delta\sigma$ and the pore pressure δp_w is expressed in terms of the water flux δm_w and the deformation increment $\delta\varepsilon$, as follows:

$$\begin{aligned} \delta\sigma &= C:\delta\varepsilon - M'\frac{\delta m_w}{\rho_w} I \\ \delta p_w &= \delta p_a = M' tr(\delta\varepsilon) - M'\frac{\delta m_w}{\rho_w} \end{aligned} \tag{1}$$

C is the drained elastic tensor, I is the unit second order tensor. M' stands for the Biot modulus of unsaturated sandy soils, which depends on the water compressibility K_w, the porosity n and the water saturation degree S_w:

$$\frac{1}{M'} = \frac{n_a}{K_a} + \frac{n_w}{K_w} = \frac{n(1-S_w)}{p_w + p_{a0}} + \frac{nS_w}{K_w} \tag{2}$$

It can be observed that the set of equation (1) is similar to the (u-p) formulation proposed for saturated soils by Zienkiewicz (Zienkiewicz & Shiomi 1984), but with a Biot modulus depending on the porosity, the pore pressure and the water saturation. Equation (2) shows that when the saturation degree is equal to 1, the formulation of Zienkiewicz for saturated soil is recovered. It means that this formulation could be used for both saturated and unsaturated soils.

2.2 Field equations

By choosing the displacement and the water pressure as principal variables, the free field response of partially saturated soils is controlled by the following equations: the balance equation, the diffusion equation and the conservation of the mass.

Balance equation

Assuming small perturbation and neglecting the body force, the balance equation is given by:

$$div(\sigma) - \rho\ddot{u} = 0 \tag{3}$$

σ is the total stress tensor and $\ddot{u}$ is the acceleration vectors of soil skeleton. ρ is the soil density; it depends on the soil porosity (n), the soil saturation degree (S_w) and the densities of the solid grains (ρ_s) and pore-water (ρ_w):

$$\rho = (1-n)\rho_s + nS_w\rho_w \tag{4}$$

D*iffusion law*

The generalized Darcy's law is used:

$$\frac{\vec{w}}{\rho_w} = -k_{ins}\frac{k_w^{rl}}{\mu}\left[grad(p_w) + \rho_w \ddot{u}\right] \quad (5)$$

Where $\vec{w}$ is the pore-water mass flux, k_{ins} and k_w^{rl} are the soil intrinsic permeability and the relative permeability associated with water, respectively; μ is the viscosity of pore water. Zero mass flux is assumed for the pore air, so the diffusion equation for the pore water is sufficient. However, the presence of the air significantly affects the diffusion of the pore water. As a soil becomes unsaturated, air replaces firstly the water in the large pores; consequently water flows through small pores with an increased tortuosity. As a result, the permeability with respect to the water phase decreases rapidly as the space available for the water flow reduces. The relative permeability is expressed in terms of the water saturation:

$$k_w^{rl} = \sqrt{S_w}(1-(1-S_w^{\frac{1}{m}})^m)^2 \quad (6)$$

m is a parameter, which can be determined from laboratory measured data.

Conservation of the mass

The expression of the overall mass conservation must take into account the relative masse flow of each fluid phase: pore-water and pore-air. In the absence of overall creation and null gas flux, the overall mass conservation can be written as follows:

$$\dot{m}_w = div(\vec{w}) \quad (7)$$

2.3 Constitutive equation for the soil

The soil behaviour is described using the cyclic elastoplastic constitutive relation MODSOL (Khoshnoudian & Shahrour 2002). This constitutive relation is briefly presented in (Bian and Shahrour 2009).

INFLUENCE OF THE SOIL SATURATION ON THE FREE FIELD

3.1 Problem under consideration

Analyses are conducted for a homogeneous sandy soil layer (Figure. 1a) with Nevada sand, which was used in VELCAS project. The physical properties of the Nevada sand are given in table 1. The constitutive parameters of MODSOL were determined for the sand with relative density as $I_d = 0.4$.

The Finite element modelling was conducted with the following boundary conditions:

(i) the base of soil layer is impervious and its vertical displacement is blocked;
(ii) equivalent displacement and pore pressure are imposed at the lateral boundaries;
(iii) the ground surface is permeable.

A harmonic acceleration is applied at the base of soil layer. It includes 10 cycles at the frequency f = 2 Hz; the amplitude of the acceleration is equal to $a_g = 0.25g$.

3.2 Initial conditions

Nonlinear analysis requires the determination of the distribution of the total stresses

and the pore water pressure prior to the seismic loading. The total initial stress in the soil layer is due to the gravity action. According to equation(4), it can be easily determined from the physical properties of the soil and the water saturation. Generally, underground soils are divided into two distinguished parts by the phreatic surface. Soils below the phreatic surface are considered as saturated, while those above the water table are unsaturated. The position of the water table varies with the climatic conditions and human activities. Above the phreatic surface, the distribution of the soil saturation is controlled by the boundary conditions and the water retention curve of the soil. Analyses were conducted assuming a linear variation of the pore pressure with depth. Above the phreatic surface, suction is assumed to increase with the distance from the phreatic surface (z) as follows:

$$s = \gamma_w z \tag{8}$$

γ_w denotes the specific weight of the pore water. The soil saturation is determined using the following expression for the water retention curve:

$$s = CS_w^{-b} \tag{9}$$

Calculations were conducted with the following values C = 224kPa, b =1.15, which were determined from tests conducted on two sands (Figure. 1b).

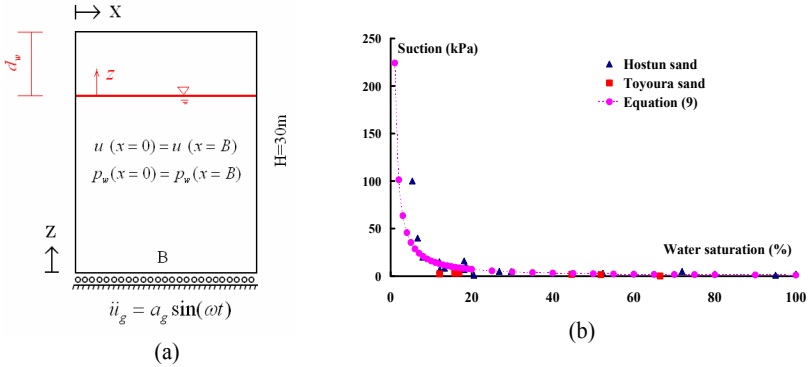

FIG. 1. Free field of partially saturated sandy soil, (a) boundary conditions and (b) the water retention curve of the soils

The soil below the water table is not, as usually assumed fully saturated, but in a partially saturated state due to the presence of residual gas (mixture of dry air and water vapour) in form of small air bubbles. The amount of the residual gas in the soil pore strongly depends on the soil grain size and the distribution of pores. The soil saturation could be assumed uniform if the soil is homogenous. Laboratory and in situ observations confirmed this hypothesis. The degree of water saturation was lower than 77% for the sand piles and 91% for the improved soils below the water table. The partial saturation state could be conserved for long time.

3.3 Numerical results (*loose sand* $I_d = 0.4$)

Firstly, the phreatic table is assumed to coincide with the ground surface (d_w = 0). The influence of the water saturation is investigated by analysing the free field response for the following values of the initial degree of saturation S_{w0} = 100%, 99%, 95% and 90%. Analyses are conducted with the properties of loose Nevada sand ($I_d = 0.4$) (table 2). Figure 2a shows the influence of the soil saturation on the variation of the excess pore-water pressure at depth d = 3m. For the fully saturated case, a steady increase in the pore-pressure is observed; liquefaction occurs at t = 2.0 sec (the excess pore-water ratio $\Delta p_w / \sigma_0^{'}$ is equal to 1, $\sigma_0^{'}$ denotes the initial effective mean stress). For the partially saturated cases, a steady increase in the pore-pressure is also observed but at a rate which decreases with the decrease in the soil saturation. Liquefaction is observed at t=4.0 sec for the initial saturation $S_{w0} = 0.99$. For the initial saturations S_{w0} = 0.95 and 0.90, the load does not cause soil liquefaction. The diminution in the rate of the excess pore pressure with the decrease in S_{w0} is due to the augmentation of the compressibility of the air-water mixture resulting from the decrease in the soil saturation.

Figure 2b shows the influence of S_{w0} on the maximum pore-pressure normalised by the initial effective mean stress ($\sigma_0^{'}$). Liquefaction is observed for the different values of the soil saturation. The decrease in the saturation degree causes a diminution of the liquefied zone. For the fully the saturated case, the liquefaction zone concerns about 20% of the soil layer. For the S_{w0} = 99%, the liquefaction zone is reduced to 10% of the soil layer. At $Z = 0.6$H, the ratio of excess pore-water pressure to the effective mean stress is about 0.42, while this ratio decreases to 0.25, 0.1 and 0.06 for S_{w0} = 99%, 95% and 90%, respectively.

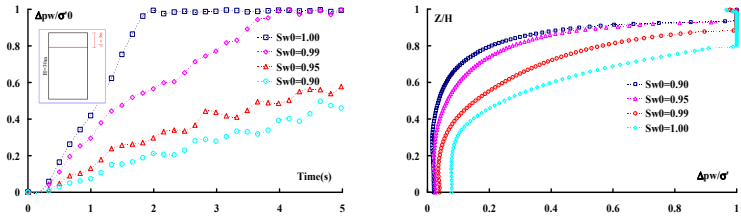

(a) (b)

FIG. 2. Influence of the initial soil water saturation

The influence of the position of the water table on the free-field response is investigated by analysing the response of the soil layer for three values of the depth of the water table d_w = 1m, 2m and 3m. The water saturation below the phreatic surface is assumed equal to $S_w = 0.99$. The distribution of the initial soil saturation was determined using equation(9). It is illustrated in Figure 3a.

Figure 3b shows the influence of the water table depth (d_w) on the excess pore-water pressure at t = 5.0 sec. It can be observed that the increase in d_w leads to an important reduction in the excess pore pressure. Liquefaction is observed for d_w = 0 and 1 m. The

maximum pore-pressure ratio ($\Delta p_w / \sigma_0^{'}$) is equal to 0.8 for d_w = 2 m, and 0.47 for d_w = 3 m. This result shows that the liquefaction risk decreases significantly with the increase in the water table depth.

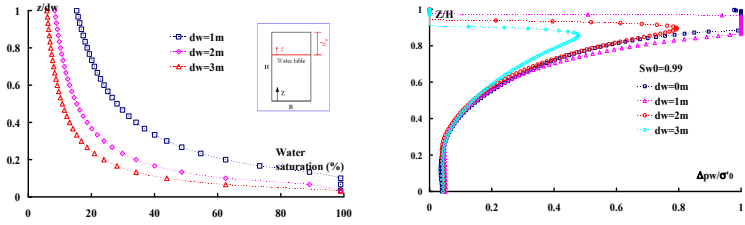

(a) (b)

FIG. 3. Influence of the water table position

CONCLUSIONS

This paper included analysis of the free field response of unsaturated sandy soils to cyclic loading, with a particular focus on liquefaction. This analysis concerns both the soil above the water table and soils located below the water table which are generally in a partially saturated state due to the presence of air bubbles. Analysis is conducted using a numerical model elaborated for the liquefaction of partially saturated soils together with a cyclic elastoplastic constitutive relation implemented in a finite element program. Analyses showed that the soil saturation largely affected the free field response to cyclic loading. The decrease in the soil saturation degree leads to an important decrease in the rate of generation of the excess pore-water pressure and consequently to a reduction in the liquefaction risk.

REFERENCES

Bian H., Shahrour I., (2009) “Numerical model for unsaturated sandy soils under cyclic loading: Application to liquefaction”. Soil Dynamic and Earthquake Engineering, Vol. 29, pp. 237-244.

Coussy O., (2004) “Poro mechanics”, John-Wiley.

Khoshnoudian F. & Shahrour I. (2002) “Numerical analysis of the seismic behavior of tunnels constructed in liquefiable soils”, Journal Soils and Foundations, Vol 42, No 6, pp. 1-8.

Martin G. R., Finn W. D. L. and Seed H. B., “Effects of system compliance on liquefaction testes”, Journal of the geotechnical engineering division, Vol. 104, No. GT4, 1978.

Yoshimi Y., Tanaka K., Tokimatsu K., “Liquefaction resistance of a partially saturated sand”, Soils and foundations, vol. 29, No. 3, pp. 157-162, 1989.

Zienkiewicz, OC. & Shiomi T (1984) “Dynamic behaviour of saturated porous media; the generalized Biot formulation and its numerical solution.” Int. J. for Numerical and Analytical Methods in Geomechanics, Vol. 8, 71-96.

Numerical Analysis of Wave Propagation in Two-Phase Soil Medium

Anna Borowiec[1]

[1]Division of Soil-Structure Interaction, Faculty of Civil Engineering, Cracow University of Technology, ul. Warszawska 24, 31-155 Kraków, Poland; anabo@pk.edu.pl

ABSTRACT: The paper deals with the problem of dynamic consolidation of two-phase soil medium. Finite Element approach is used to calculate tangential stresses and pore pressure and what follows to describe the wave propagation. Biot's formulation, with so called **u** - *p* simplification and Pastor – Zienkiewicz Mark III constitutive relation, is implemented. This model, which treats the soil as an inelastic skeleton saturated with a pore fluid is very close to real behavior of non-cohesive soil under dynamic excitation. Numerical analysis mentioned, is used not only to obtain the result but also to assess them. Cohesion, friction angle and other geotechnical parameters are taken from laboratory tests. Different records of real vibrations along with artificial impulse wave is applied as dynamic loading. Constitutive relations are fully nonlinear and depend on soil type. From numerical calculation we obtain the diagonal shear stress bands which form the typical crosses and pore pressure which responds even after fade of input, proving liquefaction phenomena. The signal processing tool such as Fourier and wavelet transform is used to analyze the results. Two important information such as the time when dominant frequency is reached and the frequencies which are filtered, are retrieved only from wavelet analysis.

INTRODUCTION

Tangential stresses and pore pressure are considered here, because of they importance in creating slip plane and liquefaction in soils.

Main goals of the paper are, to:

- follow the shear stresses behavior of soil layer, under dynamic loading,
- use the signal processing method (especially Wavelet Transform) to assess the results.

From the mechanical point of view, there are two ways of solving the problem mentioned. One is to use the classical wave equations, the other is to formulate Lagrangian system of equations.

In the paper soil layer is modeled as two-phase Biot's porous medium (Biot 1956) with modern contributions (Zienkiewicz et al. 2000) and **u** – *p* simplification. Biot derived his formulation from Lagrangian equation of motion, the kinetic energy and its dissipation. The medium here is considered as a mixture of two phases – solid skeleton and the fluid

(represented by pore pressure), both phases have the separate equation of motion. Dealing with highly inelastic material, like soil, we have to chose the proper constitutive relation. Because of the liquefaction, which takes place in saturated sands, the Pastor-Zienkiewicz Mark III was chosen here.

GOVERNING SYSTEM OF EQUATIONS

Liquefaction and associated shear deformations continue to cause damage during dynamic excitations. In order to study the dynamic response of saturated soil layers as an initial-boundary problem, a Finite Element Method code was considered. The equations of motion for elastic skeleton saturated with a pore fluid, given by Biot, (Biot 1956) consist of two variables' fields: one for pore pressure p and the other for skeleton displacements $\mathbf{u}$. A simplified numerical framework, known as $\mathbf{u} - p$ formulation (Zienkiewicz et al. 2000), implemented here assumes Darcy's flow rule (laminar flow) and neglects the fluid inertia. Applying Voigt notation, widely used in FEM approach, we can write, the overall dynamic equilibrium for soil-fluid mixture:

$$\begin{bmatrix} \mathbf{M} & 0 \\ 0 & 0 \end{bmatrix} \begin{Bmatrix} \ddot{\tilde{\mathbf{u}}} \\ \ddot{\tilde{p}} \end{Bmatrix} + \begin{bmatrix} 0 & 0 \\ \mathbf{Q}^{\mathrm{T}} & \mathbf{S} \end{bmatrix} \begin{Bmatrix} \dot{\tilde{\mathbf{u}}} \\ \dot{\tilde{p}} \end{Bmatrix} + \begin{bmatrix} \mathbf{K} & -\mathbf{Q} \\ 0 & \mathbf{H} \end{bmatrix} \begin{Bmatrix} \tilde{\mathbf{u}} \\ \tilde{p} \end{Bmatrix} = \begin{Bmatrix} \mathbf{f}^{(1)} \\ \mathbf{f}^{(2)} \end{Bmatrix} \tag{1}$$

where $\mathbf{M}$ and $\mathbf{K}$ are the mass and stiffness matrixes, $\mathbf{Q}$ is the discrete gradient operator coupling the soil and fluid phase, $\mathbf{H}$ is the permeability matrix and $\mathbf{S}$ is the compressibility matrix. Vectors $\mathbf{f}^{(1)}$ and $\mathbf{f}^{(2)}$ represent the effect of body forces along with prescribed Boundary Conditions for the solid-fluid mixture and fluid phase.

Taking into account plastic behavior of soil, we are introducing Pastor – Zienkiewicz mark III model (Zienkiewicz et al. 1990). The model described above is the most suitable for soils susceptible to liquefaction. In order to solve system of equations (1) Newton – Raphson iterations must be carried out. Finally using Newmark time integration procedure, we obtain, at each time step, the following set of equations:

$$\begin{Bmatrix} \boldsymbol{\Psi}^{(1)}_{n+1} \\ \boldsymbol{\Psi}^{(2)}_{n+1} \end{Bmatrix}^{i} + \begin{bmatrix} \mathbf{M}_{n+1} + (\mathbf{K}_{\mathrm{T}})_{n+1}\beta_2\Delta t^2 & -\mathbf{Q}_{n+1}\bar{\beta}_1\Delta t \\ \mathbf{Q}^{\mathrm{T}}_{n+1}\beta_1\Delta t & \mathbf{S}_{n+1} + \mathbf{H}_{n+1}\bar{\beta}_1\Delta t \end{bmatrix}^{i} \begin{Bmatrix} \mathrm{d}(\Delta\ddot{\tilde{\mathbf{u}}}_{n}) \\ \mathrm{d}(\Delta\dot{\tilde{\mathbf{p}}}_{n}) \end{Bmatrix}^{i} = 0 \tag{2}$$

where $\mathbf{K}_{\mathrm{T}}$ is tangential stiffness matrix, β_1, β_2 are the Newmark constants. The 'n' index denotes time steps and 'i' – iterations resulting from non-linearity.

Summing up to solve the dynamic fully non-linear problem of porous medium we need to solve at each time step the system of equations (2), which additionally depends on the solution from previous time step. At the same time we have only two variables: pore pressure first derivative according to time and soil skeleton acceleration. The $\mathbf{u} - p$ simplification is the most convenient in numerical analysis. The other, known in the literature, formulations (full $\mathbf{u} - \mathbf{w} - p$ and $\mathbf{u} - \mathbf{u}^{\mathrm{f}}$) are establishing time integration of higher order and are raising the amount of variables.

CONSTITUTIVE RELATION

Pastor – Zienkiewicz mark III constitutive relation was proposed in 1985 by Pastor Zienkiewicz and Leung for saturated soils, mostly sands, subjected to dynamic excitation,

where liquefaction is expected. This Generalized Plasticity model is well known and calibrated. The plastic potential here is defined as:

$$g = q - M_g \cdot p \cdot \left(1 + \frac{1}{\alpha}\right)\left[1 - \left(\frac{p}{p_g}\right)^{\alpha}\right] \tag{3}$$

p_g is the point where the plastic potential crosses the axiator axis p and M_g represents the slope of Critical State Line (see FIG. 1).

Yield function is describe by analogical equation:

$$f = q - M_f \cdot p \cdot \left(1 + \frac{1}{\alpha}\right)\left[1 - \left(\frac{p}{p_g}\right)^{\alpha}\right] \tag{4}$$

In general: $M_f \neq M_g$ and M_f/M_g ratio depends on soil relative density D_r (see Table 1).

Table 1. Plastic properties of Nevada sand

Relative density D_r	M_f / M_g
40%	0,2
70%	0,9

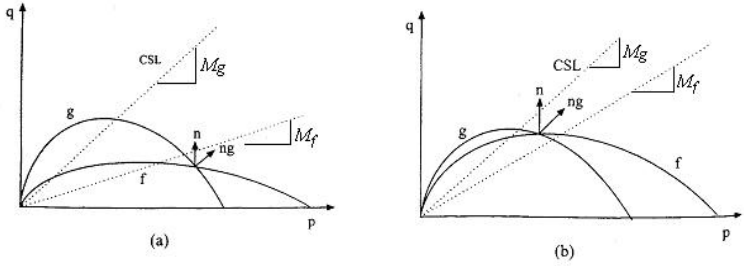

FIG. 1. Yield envelope and plastic potential for sand: (a) loose, (b) dense

NUMERICAL CALCULATION

Program called DIANA – SWANDYNE II is used in the calculations. It is the Finite Element Method program for static and dynamic consolidation with Newmark scheme time integration. The formulation **u** – *p* means that we have two unknown fields of variables - skeleton displacements **u** (vector) and pore pressure *p* (scalar). Because of constitutive law for soil skeleton, we obtain fully nonlinear equations' system, which is solved by iterative Newton – Raphson procedure at each time step. Dynamic load, in the form of accelerations, is applied to the bottom of the layer.

Among several calculated examples, there are two worth attention. Their excitation differ but both are of the same soil type and procedure of establishing frequency spectrum is analogical. These are lose and dense (according to ASTM) sand called *Nevada* sand with geotechnical parameters sited in Table 2.

Layer Geometry and FEM Mesh

Very sudden changes in tangential stresses, cause soil instability and pore pressure excess, leading to liquefaction. In the example sand is treated as a fully saturated layer (11.0 x 17.8 m), under undrained conditions, resting on immovable base (see FIG. 2). Based on numerical experience of Zienkiewicz and Pastor, 4 – node quadrilateral element is used in FEM discretisation (see FIG. 2). Water table reaches the soil surface (small dots at FIG. 2 denoting $p = 0$) and the left and right boundary has the same vertical displacement (tied nodes).

FIG. 2. Sand layer geometry (with BC) and geotechnical parameters used in calculation

Nevada Sand Geotechnical Parameters

The geotechnical parameters for Nevada sand i.e. void ratio e, permeability coefficient k and relative density D_r, as well as the constitutive model parameters, are taken from laboratory tests (Arulmoli K. et al.) conducted under VELACS project. It was international program carried out in the eighties, which results are accessible from several web sites. VELACS stands for VErification of Liquefaction Analysis by Centrifuge Studies. The geotechnical parameters are shown in Table 2.

Table 2. Soil parameters for lose and dense Nevada sand

Soil parameter	Lose	Dense
Void ratio e	0.736	0.624
Permeability coefficient k [m/s]	6.6e-5	4.54e-5
Relative density D_r	40%	70%

Dynamic Excitation

Numerical analysis for dynamic consolidation problems presented previously, can be running for the time longer than the duration of excitation. For the lose sand we assume the time of analysis of about 2 seconds and the time increment equal to 0.002 second (1024 time steps).

The layer of lose sand was subjected to artificial peak wave in the vertical direction. The aim of choosing impulse wave is to induce complete frequency spectrum. To the

dense sand layer the horizontal excitation (lasting about 0.8 s) was applied. FIG. 3 illustrates the records of both loadings.

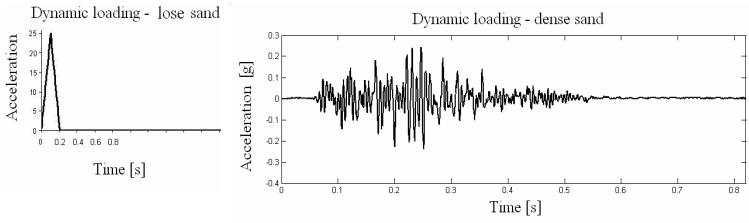

a) **b)**

FIG. 3. Dynamic excitation records for sands: a) lose, b) dense

RESULTS OF NUMERICAL CALCULATIONS

In order to assess the results by means of Wavelet Transform, we are plotting the shear stresses (see FIG. 4) in the reference point (in the middle of layer) and treating them as an input signal for the frequency analysis.

For the lose sand we can observe that the shear wave reaches the middle of the layer suddenly at about 0.3 s which is 0.1 s past the end of impulse loading.

a)

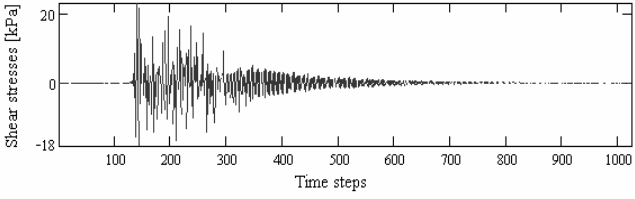

b)

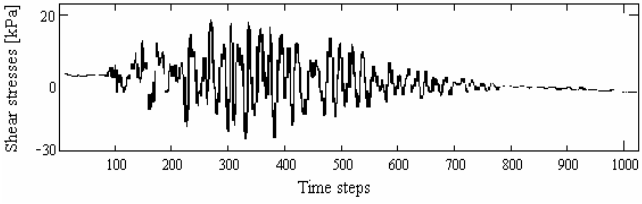

FIG. 4. Tangential stress in the reference point for sand: a) lose, b)dense

The SWANDYNE program calculates shear stress at each Gauss point for each time step, which gives almost 100 000 values for each layer. The SWANDYNE postprocessor is very simple and does not allow for advanced visualizations. In that purpose the 3D

surfaces and contour maps for every 10th step are generated using Surfer. FIG. 5 shows some specific tangential stresses' distributions. Shadings depict stress accumulation thus slip plane and liquefaction location. Comparing stress distribution for this 6 time steps we can detect the creation of diagonal shear bands at the beginning of dynamic excitation and how they propagate later on. Observing the peaks location (at 3D visualizations), we can notice that these bands cross each over. This proves that the phenomena well known under static and quasi-static tests takes place during dynamic excitation either. In the post impulse time shear stresses travel only in the plane perpendicular to the load direction (see 411th and 421st time step at FIG. 5), indicating that the shear waves are still propagating.

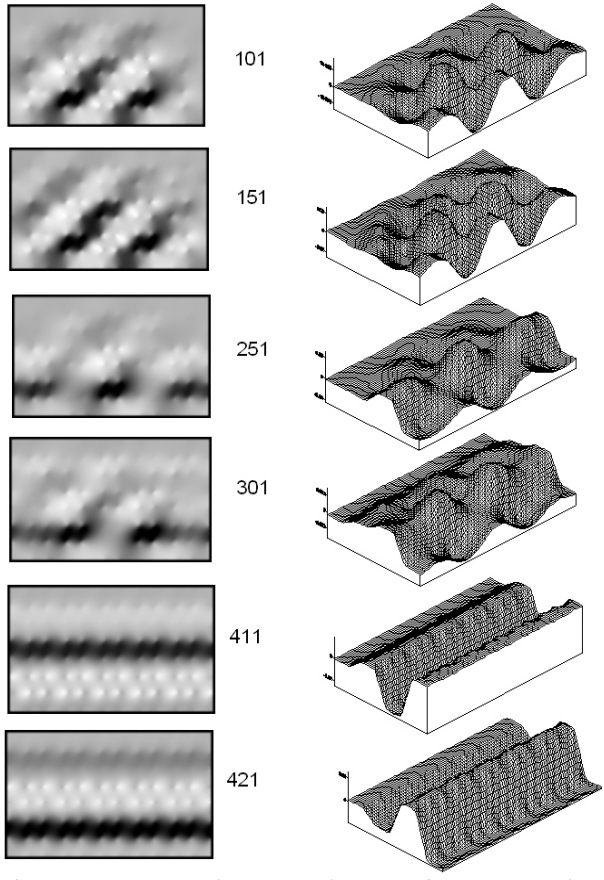

FIG. 5. Shear stress changes in selected time steps for lose sand, visualize as: a) contour maps, b) 3D surfaces

WAVELET ANALYSIS

During geodynamic, earthquake driven processes we dealing with a non-stationary problem, which means that the frequencies varied with time. Then classical signal processing tools such as Fourier transform or spectrograms are insufficient.

The Basis

The wavelet analysis is mainly used in signal (continuous transform) and picture (discrete transform) processing. In general the idea is similar to Fourier analysis only that we are using whole family of wave function instead of sine. Wavelet transform is define as (Daubechies 1992):

$$W[x(t)] = W(a,b) = \frac{1}{\sqrt{a}} \int_{-\infty}^{+\infty} x(t)\, \Psi\left[\frac{t-b}{a}\right] dt \qquad (5)$$

where Ψ is the domain of orthogonal wavelet functions (so called mother or basic wavelets) depending on two parameters: scale a and phase b. The shape and location of basic wavelet is influence by those two parameter (see FIG. 6).

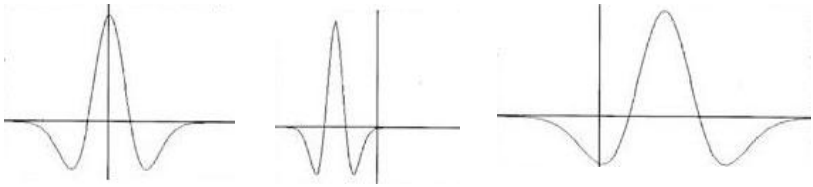

'*mother*' wavelet $a < 1,\ b < 0$ $a > 1,\ b > 0$

FIG. 6. Influence of scale and phase parameters.

Wavelet Analysis Algorithm

Wavelet transform can be described by the following algorithm. After choosing the basic wavelet function we scan the signal, starting from the signal beginning ($t = 0$).

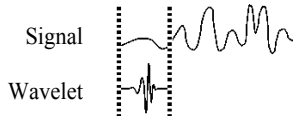

Then we change the phase parameter b while the scale parameter a remains constant.

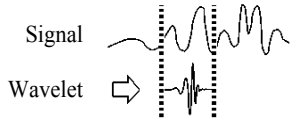

And finally we modify the scale parameter a and repeat the whole procedure for as many scales as wide is the frequency range we want to scan.

Wavelet

The main idea of the transform is to fit tightly wave within the original signal. The measure of this adjustment is fitting function W(a, $b(t)$), the higher values of W the more similar is the wavelet to the signal.

Restrictions For Basic Wavelet

The function $\varphi(t) \in L^2(\Re)$ can not be use as the wavelet unless it fulfills the following condition:

$$C_\varphi = \int_0^\infty \frac{|\Psi(\omega)|^2}{\omega} d\omega < \infty \tag{6}$$

where $\Psi(\omega)$ is Fourier transform of function $\varphi(t)$. Central frequency for Morlet wavelet is equal to one $f_c = 1$, while for fifth derivative of Gauss: $f_c = 0{,}5$.

Frequency – Scale Parameter Relation

The relation between frequency f and scale parameter a is of the great importance, it allows us to follow the frequency changes in time:

$$f = \frac{f_c}{a\,\Delta} \tag{7}$$

where f_c is so called central frequency (unique for every basic wavelet) and Δ is a sampling period (Białasiewicz 2000).

Wavelet Used in Analysis

For purposes presented in the paper the complex Morlet and 'Guss5' basic wavelets are the most suitable. Both basic wavelet are presented on the FIG. 7

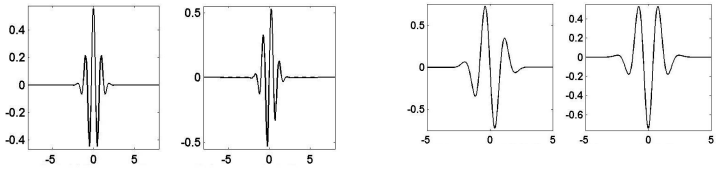

FIG. 7. Real and complex parts of wavelets: a) Morlet, b) 'Gauss5'

They can be presented in the following form:

- Morlet:

$$\varphi(t) = \frac{1}{\sqrt{\pi\, a}} e^{i2\pi b\, t} e^{-t^2/a} \tag{8}$$

- 'Gauss5' – the fifth derivative of Gauss function:

$$\varphi(t) = \frac{d^5}{dt^5}(e^{-t^2} e^{-it}) \tag{9}$$

Wavelet Analysis of the Shear Stresses

Results from SWANDYNE II, here the shear stresses in the reference point, are processed with MathCAD. First the preliminary analysis using Fourier Transform then detailed using Wavelet Transform is carried out (see FIG. 8 and FIG. 9).

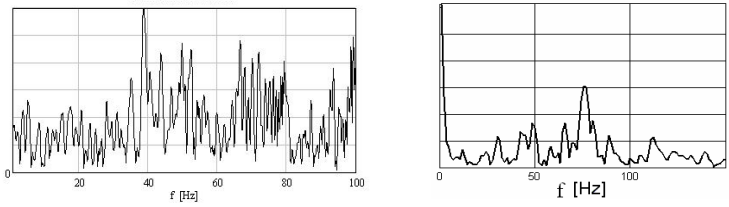

a) **b)**

FIG. 8 Fourier transforms of the shear stresses for sand: a) lose, b) dense

For lose sand - both transforms i.e. Fourier and Wavelet are presented in a similar manner (FIG. 8a and FIG. 9a), so that the frequency axis is a horizontal one. We can easily conclude they give quantitatively comparable frequency spectrum.

a)

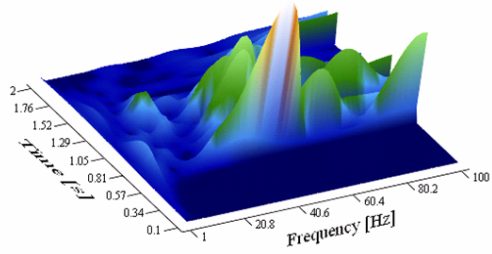

b)

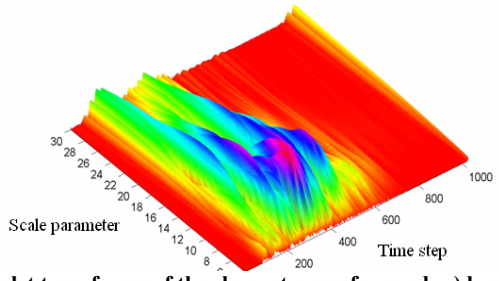

FIG. 9. Wavelet transforms of the shear stresses for sand: a) lose, b) dense

Introducing the wavelet transform we are gaining the information of frequency location

in time. For lose sand (see FIG. 9 a) predominant frequency of 45 Hz appears three times in the response, at about 0.7 s 0.9 s and 1.1 s after the start of the impulse. The second most influential frequency of 80 Hz appears only once during the response that is at 0.9 s. FIG. 10 illustrates more precisely peaks location in time. Not only the 45 Hz frequency but also this of 65 Hz repeats in time. In the other hand low frequencies (below 20 Hz) appear very late or at all.

Dense sand for its excitation responds with higher frequencies and they do not repeat in time.

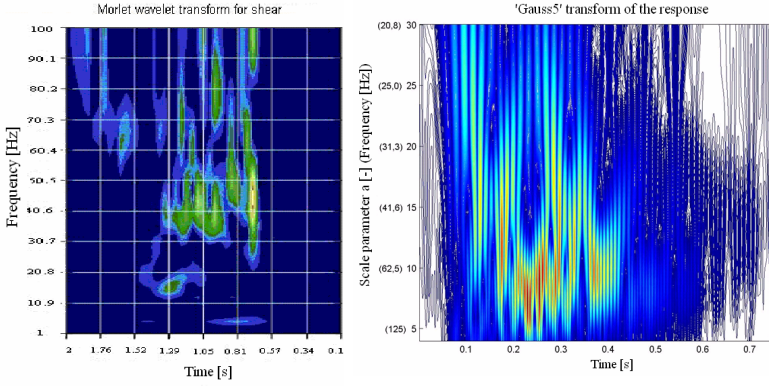

a) **b)**

FIG. 10 Wavelet transforms of the shear stresses – shaded maps – for sand: a) lose, b) dense

CONCLUSIONS

The aim of the paper is to show different methods of analyzing wave propagation in 2-phase porous medium, starting from dynamic consolidation equation of motion and ending with proper wavelet for signal processing.

It was not the point to examine when the liquefaction takes place but to observe the soils in which it is possible to occur. It is well known that liquefaction is generally not an issue for dense sands. As the consequence tangential stresses only for the lose sand are examined for some specific time steps (see FIG. 5). We can conclude that:

- diagonal slip bands relocate with time - proving that the phenomena known in geo-statics takes place in soil-dynamics too,
- after fade of input we still have the response – what indicates to dynamic consolidation of the *Nevada* sand.

In the other hand Ishihara et al. (1975) indicate that liquefaction depends on the angle close to the angle of CSL for monotonic loads and under undrained conditions. And this does not eliminate dense sand form the possibility of being liquefied.

Spectra calculated using wavelets contain similar frequencies as the one obtained from Fourier transform (compare FIG. 8 with FIG. 9). However thanks to wavelet transform

we can retrieve two important information:

- the time when the predominant frequency (highest peak) is reached
- which frequencies appears and/or disappears in time.

ACKNOWLEDGEMENT

To professor A.H.C. Chan for sharing the SWANDYNE source code under the academic license.

REFERENCES

Arulmoli K. et al. (1993). "VELACS Laboratory Testing Program Soil Data Report." National Science Foundation, Washington.

Białasiewicz J. T. (2000). „Falki i aproksymacje." Wydawnictwo Naukowo – Techniczne.

Biot M. A. (1956). "Theory Of Propagation Of Elastic Waves in a Fluid – Saturated Porous Solid." *J. of the Acoustical Society of America* 28 (2): 168-178.

Biot M.A. (1955). "Theory of elasticity and consolidation for a porous anisotropic soil." *J. of Applied Phys*. 26: 182-185.

Daubechies I.(1992). "Ten lectures on wavelets." *CBMS – NSF conference in applied mathematics*, SIAM Ed., Philadelphia.

Detournay E., Cheng A.H.D. (1993). "Fundamentals of poroelasticity." *Comprehensive Rock Engineering: Principles, Practice & Projects*, vol. II, 113–171, Pergamon Press, New York.

Ishihara K., Tatsuoka F., Yasuada S. (1975). "Undrained deformation and liquefaction of sand under cyclic stresses" *Soils and Foundation*, vol. 15, no 1: 29-45.

Zienkiewicz O.C. and Chan A.H.C. and Pastor M. and Paul M. (1990). "Static and dynamic behavior of soils: a rational approach to quantitative solutions. I. Fully saturated problems.". *Proc. R. Soc. Lond.* A 429: 285-309.

Zienkiewicz O.C. and Chan A.H.C. and Pastor M. and Schrefler B.A. and Shiomi T. (2000). "Computational Geomechanics with Special Reference to Earthquake Engineering." John Willey&Sons, New York.

Undrained Long-term Cyclic Degradation Characteristics of Offshore Soft Clay

Shuai Li[1] and Maosong Huang[2]

[1]PhD Student, Department of Geotechnical Engineering, Tongji University, Shanghai 200092, PR China; lishuaipurple@163.com.cn
[2]Professor, Department of Geotechnical Engineering, Tongji University, Shanghai 200092, PR China; mshuang@tongji.edu.cn

ABSTRACT: To design for offshore pile foundations, it is necessary to account for the degradation of stiffness and strength of saturated soft clay under long-term cyclic loading. Hence using the laboratory GDS test apparatus, a series of static and cyclic undrained triaxial tests were conducted on isotropically and anisotropically consolidated natural undisturbed saturated soft clay with the shear wave measured by bender element system during cyclic loading. The experimental results show that under the same consolidated condition the undrained strength and stiffness of soft clay markedly reduce with the increase of the cyclic stress ratio and the progressive number of cycles. On the other hand, anisotropic consolidation and lower effective consolidation pressure decelerate the degradation of stiffness under the same cyclic stress ratio. The dynamic deviatoric stress level was introduced considering the effects of effective confining pressure, consolidated static deviatoric stress and dynamic deviatoric stress. The dynamic deviatoric stress level is further used to describe the reduction of stiffness and strength of saturated soft clay under cyclic loading.

INTRODUCTION

Since the turn of the 21st century, the onshore wind industry has seen a significant growth due to the falling cost of wind generated electricity. This growth has coincided with an interest in the development of offshore wind farms. Wind farms moving from onshore to offshore is the future of wind power development in the trend. Shanghai Donghai-bridge offshore wind farm is the first large scale offshore wind farm in Asia. The wind turbine foundation of this project possesses engineering characteristics of offshore structure, high rising structure foundation, dynamic equipment foundation and complicated soft soil foundation. For any offshore structure, cyclic loads from wind and waves cause significant cyclic loading to be imparted to the foundation. Thus, during the life of the structure, the foundation soil is subjected to many millions of small amplitude load cycles during normal conditions. To design for offshore pile foundations, it is necessary to account for the degradation of stiffness and strength of saturated soft clay under long-term cyclic loading with different low cyclic stress ratios.

The dynamic behavior of soil was examined by many researchers, including dynamic strain, dynamic pore pressure and dynamic strength. Most previous studies have considered only relatively small numbers of cycles, however, as mentioned above the foundations are subject to large numbers of cycles at lower cyclic stress ratio. In an attempt to study the degradation of stiffness and strength of saturated soft clay under long-term cyclic loading, a series of static and cyclic undrained triaxial tests were conducted on isotropically and anisotropically consolidated natural undisturbed offshore saturated soft clay with the shear wave measured by bender element system during cyclic loading. The influences of the effective mean confining pressure, consolidated static deviatoric stress, cyclic stress ratio and cyclic number on the reduction of stiffness and strength of offshore soft clay were mainly analyzed. The dynamic deviatoric stress level was introduced in order to consider the effects of effective mean confining pressure, consolidated static deviatoric stress and dynamic deviatoric stress. The dynamic deviatoric stress level is further used to describe the degradation of stiffness and strength of saturated soft clay under cyclic loading.

SOIL TESTED AND EXPERIMENTAL PROCEDURE

Soil Tested

Soil samples were taken at the construction site of the Shanghai Donghai-bridge offshore wind farm. To ensure homogeneity, all samples were taken from the same layer (about 5-15 m depth). All samples were undisturbed with liquid limit $w_L = 45.1\%$, and plastic limit $w_P = 21.3\%$. Table 1 summaries some of the physical properties of test soil.

Table 1. Physical Properties of Marine Soft Clay

Unit Weight γ (kN/m^3)	Specific Gravity G_s	Water Content w (%)	Degree of Saturation S_r (%)	Void Ratio e
16.6	2.75	52.8	98	1.485

Terminology Used

In this paper, the state of stress is described using "Cambridge $q - p'$" stress invariants, where $q = (\sigma_1' - \sigma_3')$ is the deviator stress, and $p' = (\sigma_1' + 2\sigma_3')/3$ is the effective mean stress, and σ_1' and σ_3' are major and minor principal stresses. The consolidated static deviatoric stress, which is zero for isotropically consolidated samples, is denoted as q_s. During stress controlled cyclic tests, the deviatoric stress is cycled between $q_{\max}$ and $q_{\min}$, giving cyclic deviator stress $q_d = (q_{\max} - q_{\min})/2$. The static deviatoric stress ratio and cyclic stress ratio are denoted as $\eta_s = q_s / p_0'$ and $\eta_d = q_d / p_0'$. q_{ult} is the peak deviator stress during monotonic loading.

Sample Preparation and Test Procedure

The standard of the test is the geotechnique test regulation of CNS (China Nation

Standard). The cylindrical saturated soft clay specimen used in the static triaxial tests had a nominal height of 80mm and a nominal diameter of 39.1mm. However, since bender element tests were performed during cyclic triaxial tests, the size of the cyclic triaxial sample is bigger than the size of the static triaxial sample. The nominal height and diameter of the cylindrical cyclic triaxial specimen were 140mm and 70mm, respectively.

A GDS (Global Digital Systems) multifunction dynamic and static triaxial apparatus with a bender element system was used in the test. Shear-wave velocity measurements were made prior to cyclic loading and after each 1000 cycles using bender elements mounted in the sample end caps, thereby obtain the maximum small strain shear modulus. The bender elements consist of piezoelectric ceramic material that can convert a voltage to mechanical bending. A shear wave was generated from a bender element mounted on one end of the sample, and the received wave was detected at the other end. The shear-wave velocity was calculated from the tip-to-tip distance (Lee and Santamarina 2005) and the travel time of the wave.

Table 2. Summary of Undrained Triaxial Tests on Saturated Soft Clay

Sample	p_0' (kPa)	q_s (kPa)	η_S	q_d (kPa)	η_d	N (Cycles)	f (Hz)
ISU-1	114	0	0	—	—	—	—
ISU-2	228	0	0	—	—	—	—
ASU-1	114	42.86	0.38	—	—	—	—
ASU-2	228	85.72	0.38	—	—	—	—
IRU-1	114	0	0	22.8	0.20	5000	1.0
IRU-2	114	0	0	45.6	0.40	5000	1.0
IRU-3	228	0	0	45.6	0.20	5000	1.0
ARU-1	114	42.86	0.38	11.4	0.10	5000	1.0
ARU-2	114	42.86	0.38	22.8	0.20	5000	1.0
ARU-3	114	42.86	0.38	45.6	0.40	5000	1.0
ARU-4	228	85.72	0.38	22.8	0.10	5000	1.0
ARU-5	228	85.72	0.38	45.6	0.20	5000	1.0

A large number of static and cyclic triaxial tests were studied on both isotropically and anisotropically consolidated samples. A anisotropically consolidated ratio (σ_3'/σ_1') of 0.7 was used to simulate K_0 consolidated soft clay. Cyclic loading was imposed in the vertical direction with a sine wave. In order to study the degradation of undrained strength , the sample was subjected to a monotonically increasing loading after cyclic loading. The rate of monotonic loading is 0.1mm/min for all strain-controlled monotonic triaxial tests. Details of the triaxial tests performed on undisturbed offshore saturated soft clay samples are presented in Table 2.

TEST RESULTS AND ANALYSIS

Undrained Strength of Soft Clay

Based on strength of soft clay can be calculated (Huang et al., 2008). The model parameters are determined by experiments. The initial void ratio e_0 is 1.428; the slopes of virgin consolidation line and swelling line respectively in the $e-\ln p$ space are λ=0.174 and κ=0.036; the Poisson's ratio is 0.377. R is the shape parameter, which controls the ratio of the two major axes of the yield surface. The undisturbed soil samples were taken from the seabed, so a lot of silty sand and shell debris were mixed in the sample, and R is taken as 1.62. α is the slope of yield surface in $p-q$ space, which is the second invariant of anisotropic tensor. In the analysis, the initial value of α is determined by the initial consolidation state of the soil as $\alpha = 3A_0(1-K_0)/(1+2K_0)$, where A_0 is the modified parameter. Fig. 1 shows effective stress paths from undrained monotonic triaxial tests on the samples before cyclic loading and after cyclic loading under various consolidation conditions. Details of the tests can be found in Table 2. The slope of critical state line in triaxial space M can be determined as 1.133. The calculated strength compared with the measured strength is shown in Table 3.

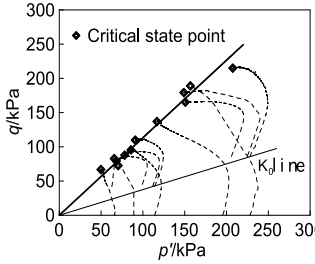

FIG. 0. Effective stress path of undrained monotonic triaxial tests

Table 3. Shear Strength of Undrained Monotonic Triaxial Tests

Sample		ISU-1	ISU-2	ASU-1	ASU-2
q_{ult} (kPa)	**Calculated**	88.00	176.00	112.84	225.68
	Measured	95.83	189.01	112.53	217.52

Undrained Strength Reduction after Cyclic Loading

Fig. 2 shows the stress-strain curves from monotonic tests on the samples of before cyclic loading and after cyclic loading under various consolidation conditions. From Fig. 2, it can be observed that after cyclic loading the undrained peak deviatoric stress reduces after cyclic loading with the increase of the cyclic stress ratio. The degree undrained shear strength reduction can be represented by the normalized shear strength reduction Δ, which is the ratio of the shear strength reduction and the shear strength before cyclic loading, as shown in Table 4. The normalized shear strength reduction Δ increases with the increase of the cyclic stress ratio. The shear strength reduction of anisotropically consolidated soft clay is moderately lower than that of isotropically consolidated soft clay. For an identical cyclic stress ratio applied on either isotropically or anisotropically consolidated samples, the shear strength reduction increases with the accretion of the effective confining pressure.

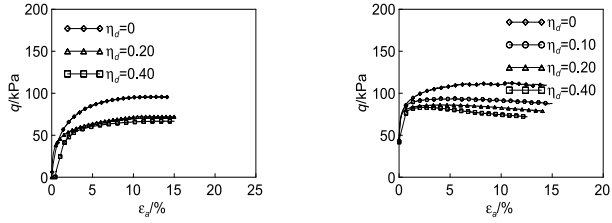

(a) p_0'=114kPa, isotropic consolidation (b) p_0'=114kPa, anisotropic consolidation

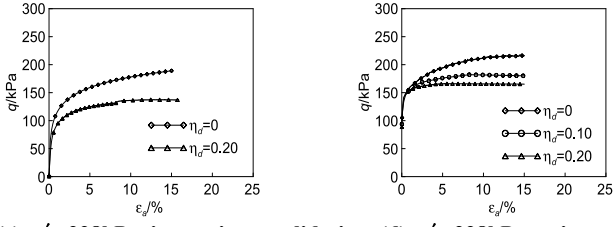

(c) p_0'=228kPa, isotropic consolidation (d) p_0'=228kPa, anisotropic consolidation

FIG. 2. Relationship between deviator stress and axial strain

Table 4. Reduction of Undrained Shear Strength (5000 cycles)

Sample	IRU-1	IRU-2	IRU-3	ARU-1	ARU-2	ARU-3	ARU-4	ARU-5
Δ	0.248	0.305	0.080	0.227	0.253	0.276	0.163	0.236

Stiffness Degradation under Cyclic Loading

The degradation of stiffness after cyclic loading can be represented by the shear modulus reduction of soils. Both bender element tests and cyclic triaxial tests were conducted in order to study the stiffness degradation. Bender element tests were performed during cyclic loading, and the measured shear wave velocities (V_s) were used to calculate the small strain shear modulus $G_{\max}$ as follows:

$$G_{\max} = \rho \times V_s^2 \tag{1}$$

where ρ is the density of specimen.

The hysteresis loops recorded from the cyclic triaxial tests were used to calculate the secant shear modulus at cycle N as follows:

$$G_N = \frac{q_{N,\max} - q_{N,\min}}{\varepsilon_{N,\max} - \varepsilon_{N,\min}} \tag{2}$$

where $q_{N,\max}$ and $q_{N,\min}$ are the maximum and minimum values of the cyclic axial

stresses at cycle N; $\varepsilon_{N,\max}$ and $\varepsilon_{N,\min}$ are the maximum and minimum values of the cyclic axial strains at cycle N, respectively (as shown in Fig. 3).

Stress-strain data for 5000 cycles (intermittent) are shown in Fig. 3. The stress-strain curves show hysteresis and accumulation of irreversible strains with increasing number of cycles. The characteristic features of the hysteresis loops show the degradation of secant stiffness. According to Sharma and Fahey (2003), the normalized shear modulus, which is used to describe the degradation of shear modulus, can be defined as the ratio of the shear modulus at cycles N and 1. Different effects on the degradation of shear modulus can be determined from the test results.

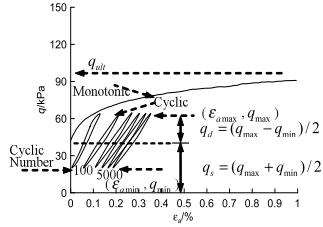

FIG. 3. Stress-strain curves for anisotropically consolidated saturated soft clay and definitions of symbols (p_0'=114kPa, η_d=0.20)

The effect of cyclic stress ratio on the degradation of shear modulus is shown in Fig. 4. The shear modulus decreases with an increase in the number of cycles. The degree of shear modulus degradation becomes large with an increase of the cyclic stress ratio for any given number of cycles.

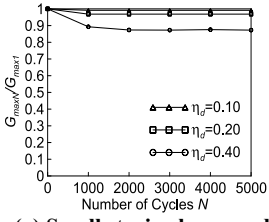

(a) Small strain shear modulus

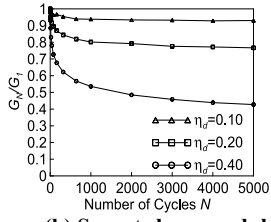

(b) Secant shear modulus

FIG. 4. Normalized shear modulus degradation with cyclic numbers for different cyclic stress ratio at anisotropic consolidation state (p'_0=114kPa)

The relationship between normalized shear modulus and number of cycles for different p_0' is shown in Fig. 5. The degradation degree of shear modulus becomes moderately large with an increase in p_0' under the same cyclic stress ratio and consolidation condition.

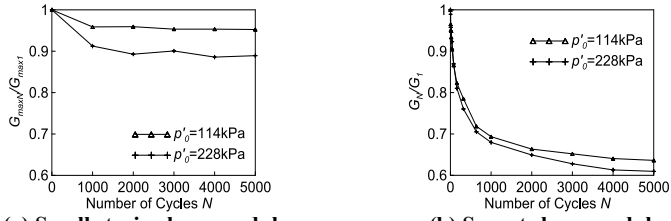

(a) Small strain shear modulus **(b) Secant shear modulus**

FIG. 5. Normalized shear modulus degradation with cyclic numbers for different p'_0 at the same consolidation condition(η_d=0.20,isotropic consolidation)

Consolidated static deviatoric stresses also have an impact on the degradation of shear modulus. Comparisons of the stiffness degradation between isotropically consolidated samples and anisotropically consolidated samples are given in Fig. 6. Compared to isotropically consolidated samples, the stiffness degradation of anisotropically consolidated samples is less significant.

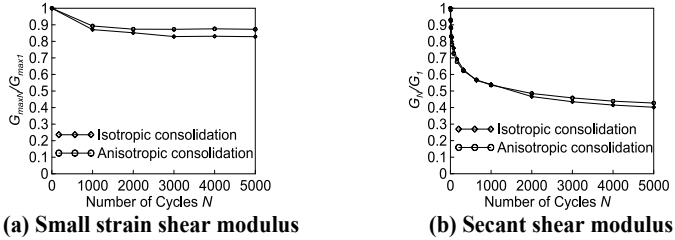

(a) Small strain shear modulus **(b) Secant shear modulus**

FIG. 6. Normalized shear modulus degradation with cyclic numbers for different consolidation conditions (p'_0=114kPa, η_d=0.40)

Reasonable Description of Strength and Stiffness degradation

The effect of cyclic degradation can be expressed by the degradation index δ_d originally proposed by Idriss et al. (1978), which is the ratio of shear modulus at cycle N to that at the first cycle. The value of δ_d decreases with increasing cycles and can be approximately represented as follows:

$$\delta_d = N^{-d} \tag{3}$$

where d is the degradation parameter. Yasuhara et al. (1997) used an approach similar to that of Idriss et al. (1978) for plastic silt, but found that a more linear relationship is obtained if δ_d is plotted against N on a semi-log scale, and proposed the following relationship:

$$\delta_d = 1 - d \lg N \tag{4}$$

The following formula is preferred to describe the relationship between of δ_d and N in this paper:

$$\delta_d = 1 - d \ln N \tag{5}$$

The effects of effective confining pressure, consolidated static deviatoric stress and dynamic deviatoric stress are reflected in the degradation parameter d. To take into account the combined effects of p_0', q_s and q_d, the concept of relative deviatoric stress level D^* was proposed by Huang et al. (2006), where $D^* = q_d/(q_{ult} - q_s)$. However $q_{ult} - q_s$ is not sufficient enough to reflect the influence of q_s. The relative deviatoric stress level D^* weakens the effect of anisotropical consolidation on the cyclic degradation. The so-called dynamic deviatoric stress level D_d as $D_d = q_d / q_{ult}$ is then considered to be a suitable choice. The values of D_d for all tests are given in Table 5.

Table 5. Dynamic Deviatoric Stress Level of Samples

Sample	IRU-1	IRU-2	IRU-3	ARU-1	ARU-2	ARU-3	ARU-4	ARU-5
$D_d = q_d / q_{ult}$	0.259	0.518	0.259	0.101	0.202	0.404	0.101	0.202

The relationship between degradation parameter d and relative deviatoric stress level D_d can be represented using a simple schematic diagram as shown in Fig. 7. It can be observed that the dynamic deviatoric stress level provides a very good correlation between the degradation parameters. Fig. 8 shows an approximately linear relationship between the shear strength reduction ratio and the dynamic deviatoric stress level D_d. Therefore, the dynamic deviatoric stress level D_d introduced here can be regarded as a rational index to describe the degradation of stiffness and strength of offshore saturated soft clay.

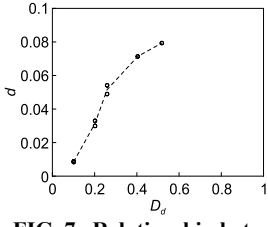

FIG. 7. Relationship between degradation parameter and dynamic deviatoric stress level

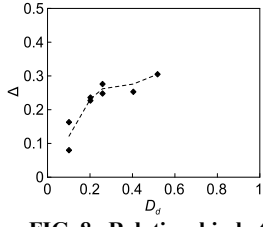

FIG. 8. Relationship between normalized shear strength reduction and dynamic deviatoric stress level

CONCLUSIONS

In order to analyze undrained long-term cyclic degradation characteristics of offshore soft clay, a series of static and dynamic triaxial tests were conducted on natural undisturbed offshore saturated soft clay. The following conclusions can be drawn from the test results and the analysis presented in this paper:

1. The cyclic degradation of stiffness and strength increases with cycles, the effective confining pressure and the cyclic stress ratio. The strength and

stiffness degradation of anisotropically consolidated soft clay is lower than that of isotropically consolidated soft clay.

2. A relationship between the stiffness degradation index and number of cycles was found in isotropically and anisotropically consolidated saturated soft clay. The dynamic deviatoric stress level is presented to reasonably describe the reduction of stiffness and strength of offshore saturated soft clay under cyclic loading.

ACKNOWLEDGMENTS

The authors acknowledge the financial support provided by the National Natural Sciences Funds for Distinguished Young Scholars (Grant No. 50825803).

REFERENCES

Airey, D.W. and Fahey, M. (1991). "Cyclic response of calcareous soil from the North-West Shelf of Australia." *Geotechnique*, 41(1):101-121.

Hyodo, M., Murata, H. and Yasufuki, N. (1991). "Undrained cyclic shear strength and residual shear strain of sataurated sand by cyclic triaxial tests." *Soils and Foundations*, 31(3): 60-76.

Huang, M.S., Li, J.J. and Li, X.Z. (2006). "Cumulative deformation behaviour of soft clay in cyclic undrained tests." *Chinese Journal of Geotechnical Engineering*, 28(4):891-895.

Huang, M.S., Song, X.Y. and Qin, H.L. (2008). "Basal stability of braced excavations in K0-consolidated soft clay by upper bound method." *Chinese Journal of Geotechnical Engineering*, 30(2): 250-255.

Idriss, I.M., Singh, R.D. and Dobry, R. (1978). "Nonlinear behavior of soft clay during cyclic loading." *Journal of Geotechnical Engineering*, ASCE, 104(12):1427-1447.

Lee, J.-S. and Santamarina, J. C. (2005). "Bender elements: Performance and signal interpretation." *Journal of Geotechnical and Geoenvironmental Engineering*, ASCE, 131(9):1063-1070.

Sharma, S.S. and Fahey, M. (2003). "Evaluation of cyclic shear strength of two cemented calcareous soils." *Journal of Geotechnical and Geoenvironmental Engineering*, ASCE, 129(7): 608-618.

Sharama, S.S. and Fahey, M. (2003). "Degradation of stiffness of cemented calcareous soil in cyclic triaxial tests." *Journal of Geotechnical and Geoenvironmental Engineering*, ASCE, 129(7):619-629.

Yasuhara, K., Hyde, A.F.L., Toyata, N., et al. (1997). "Cyclic stiffness of plastic silt with an initial drained shear stress." JARDINE R J, et al, eds. *Proc. Geotechnique Symp. on Prefailure Deformation Behaviour of Geomaterials*, London, UK(Thomas Telford Ltd.),1997:373-382.

Study of Effects of Fines Content on Liquefaction Properties of Sand

Yong Wang[1], and Yanli Wang[2]

[1]Institute of Rock and Soil Mechanics, Chinese Academy of Sciences, State Key Laboratory and Geotechnical Engineering, Wuhan, Hubei 430071, China; wang831yong@163.com
[2]Key Laboratory of Geotechnical and Underground Engineering of Ministry of Education, Tongji University, Shanghai 200092, China; wyldhh@126.com

ABSTRACT: To simulate the effects of fines content on the liquefaction properties of sand, specimens of different fines content were prepared. Based on cyclic triaxial compression tests of these samples, the effects of fines content on the liquefaction properties were analyzed. Results show that for a constant value of dry density, the liquefaction resistance decreases with increasing fines content. Beyond the critical value of fines content of 30% the trend is reversed and the liquefaction resistance increases with increasing fines content. The results are consistent with the variation of relative density with increasing fines content, which verifies the effects of non-plastic fine-grained soils on liquefaction resistance of sandy soil reported by Polito et al. (2001).

INTRODUCTION

Liquefaction is defined as the behavior and process in which the material is changed from a solid state into a liquid state (The Committee, 1978). Liquefaction is one of the primary reasons for field earthquake damage (Zeng 2006). About 50% of the foundation failures are caused by earthquake induced liquefaction (Wang 1997). Destruction of dykes and buildings caused by liquefaction has occurred in several destructive earthquakes in the 1960s and 1970s, which results in great loss. Thus scholars at home and abroad attach great importance to the earthquake induced liquefaction of saturated soil (cohesionless soil and less cohesive soil). Field data shows that soils frequently liquefy are mostly silty sand and sandy silt (Seed et al. 1966 and Youd et al. 1983). This is due to homogeneous clean sand being rare in nature (Dobry and Baziar, 1991). The most problematic deposit of sand in terms of liquefaction is sandy soil, mostly hydraulically deposited sand or sand fill. They are obviously different from pure sand in granulometric composition and they all contain some fines. Sand liquefaction and its influencing factors are important and difficult points in liquefaction study. Domestic and foreign academia and engineers have placed great emphasis on the influences of the fine-grained composition and fines content on the sand in the Seed simplified liquefaction method (Seed and Idriss, 1971). Many researchers have studied the effect of fines content on liquefaction potential, but the research results differ. The reasons for

the discrepancies are probably different soil types, properties, definitions of liquefaction and different testing parameters used (Polito et al., 2003). Based on the above research observations, specimens of different fines content sand were prepared using dry density as the controlling parameter, and tested in cyclic triaxial compression tests to study the effects of fines content on the liquefaction properties of sands.

TESTING DEVICE

The tests were performed at Tongji University using GDS cyclic triaxial testing system (**FIG. 1**). The fundamental characteristics of the testing devices are as follows: the basic triaxial test can be performed to simulate the dynamic response of the soil by controlling stress or strain including earthquake loads, traffic load, the dynamic load and sea wave load. Its main parameters are as follows: (1) the biggest axial force is 7kN; (2) the maximum confining pressure is 1700kPa; (3) The diameters of test specimen in this device can be 39.1mm, 50mm, 70mm and 100mm; (4) The range of load frequency can change from 0 to 5Hz. This device includes brake unit, triaxial stress room, peace instruments, confining pressure controller, the back pressure controller, the signal controller, high-speed data acquisition device and control card.

FIG.1 GDS Soil Cyclic Triaxial Testing System.

SAMPLE PREPARATION

The test used cylindrical specimens with a diameter equal to 39.1 mm and a height of 80 mm. All of the specimens are mixed and air dried, and then sifted out before the preparation. The grains diameter within the scope of 0.075~0.25mm are selected as a skeleton sand (pure sand), and the grains diameter smaller than 0.075mm are fine grains. The fine grained sand is almost composed of non-plastic silt grains. The remolded samples are composed of saturated mixtures of sand and non-plastic fines. They are prepared according to nine different fines contents of 5%, 10%, 15%, 20%, 25%, 30%, 35%, 40% and 45% respectively. Specimens are prepared to a constant dry density

because proper dry density can reflect the traits of the specimens. The dry density should be within the scope of maximum of minimum dry density and minimum of maximum dry density **FIG. 2**, namely 1.30 ~ 1.48 g/cm^3 according to the basic property test. The variation in relative density with fines content for sand specimens with a constant dry density of 1.40 g/cm^3 is illustrated in **FIG. 3**. As observed in the diagram of **FIG. 3**, for a constant value of dry density, the relative density decreased with the addition of non-plastic fines up to a fines content of 30%. Beyond this critical value of fines content the trend was reversed and the relative density increases with an increasing fines content. The relative density reaches a minimum of 29% at a fines content of 30%.

The remolded samples are prepared by using multi-level wet pounding method, and the samples are composed of five layers. According to dry density and the design of each layer of soil moisture content of the soil samples, the weight of each layer is determined and the soil of each layer is compacted to corresponding height. The interface between the two layers is scarified to ensure the upper and lower layers are in good contacts.

TESTING METHOD

The test specimens were saturated by vacuum-pumping method after the completion of the soil specimen preparation, and then frozen. Following this, the specimens were percolated with de-aired water from the bottom of the specimen towards the top while the specimens were subjected to about 20-30kPa effective confining pressure. Then the cell and pore water pressure were slowly increased simultaneously to achieve a B value that was typically greater than 0.95. Pore pressure should increase with the same increments due to the cell pressure increase if the specimen is saturated. Following this, the specimens were isotropically consolidated under an effective confining stress equal to 100kPa. The net volume of the water introduced into the specimen was measured accurately. The standard of isotropically consolidation can be deemed to be reached

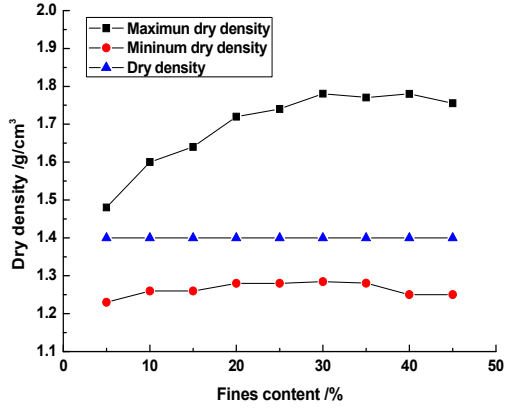

FIG. 2. Variation in Dry Density with Fines Content

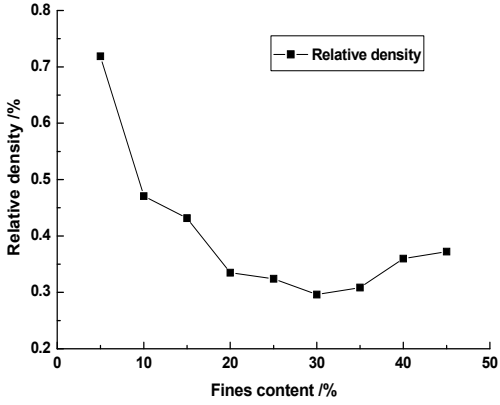

FIG. 3. Variation in Relative Density with Fines Content

when the volumetric change of the specimen keep invariable in 5 minutes. Following consolidation the drainage valves were closed and dynamic triaxial tests were done with different amplitude cyclic loading and a constant frequency of 1.0Hz. During the cyclic loading stage of each test continuous records were obtained such as the excess pore water pressure and axial strain and the axial stress applied to the specimen. Each test was continued until initial liquefaction occurred until the pore water pressure became equal to the confining pressure of the specimen.

RESULTS AND ANALYSIS

Cyclic stress ratio (CSR) required to cause liquefaction is defined as follows:

$$CSR = \frac{\sigma_d}{2\sigma_0'} \tag{1}$$

Where σ_d is axial stress applied to the specimen; σ_0' is the effective confining pressure.

FIG. 4 presents relationships between liquefaction cycles and cyclic stress ratio to cause liquefaction (CSR). As shown in **FIG. 4**, for a constant value of dry density, the liquefaction resistance is maximized (highest CSR) for a fines content of 5 percent and the liquefaction resistance minimized (lowest CSR) for a fines content of 30 percent. To further understand the effects of particle grading on the liquefaction resistance, **FIG. 5** shows the data in **FIG. 4** in terms of (CSR) and fines content for a given value of the number of cycles required to cause initial liquefaction (N_l=20). For this study, cyclic resistance was defined as the cyclic stress ratio(CSR) required to cause initial liquefaction in 20 cycles of loading. As shown in **FIG. 5**, fines content has a significant effects on the liquefaction resistance, and the variation tendency is not monotonic with different fines content. For a constant value of dry density, the liquefaction resistance decreased with the addition of non-plastic fines up to a fines content of 30%. Beyond this critical value of fines content the trend was reversed and the liquefaction resistance increased with an increase in fines content. The results are consistent with the variation in relative density

with the increasing fines content, which further verifies the regularity of the effects of non-plastic fine-grained soils on liquefaction resistance of sandy soil obtained by Polito et al (2001).

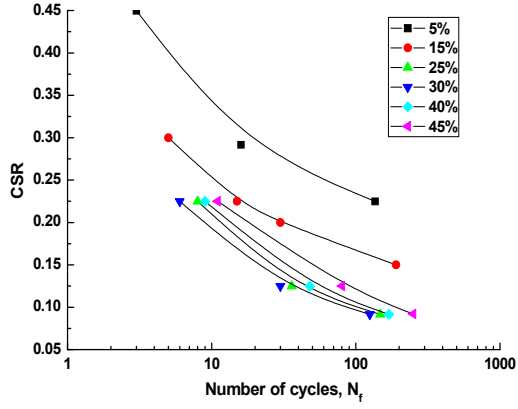

FIG.4. Effects of Fines Content on Curves of Cycles to Initial Liquefaction versus Cyclic Stress Ratio

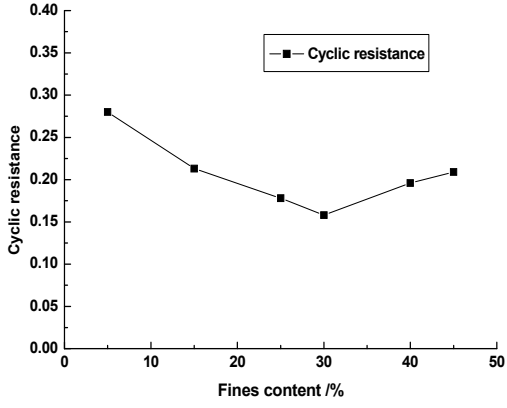

FIG.5. Variation in Liquefaction Resistance with Fines Content for N_l=20

Investigating cause of this behavior suggests microstructure characteristics of coarse grains and fine grains should be analyzed. When the silt mixed into pure sand forming the sand-fines mixtures, because fine sand content is less at the same time, the coarse grained content is more, coarse grains form skeleton voids by mutual arrangement, the fine grains do not occupy the voids between the coarse grains but dissociate in the skeleton voids in a great measure. Liquefaction resistance of sandy soil is manly determined by the coarse grains. When the fine grain content increasing gradually, the voids between the coarse

grains become larger, which makes the mutual contact force of the coarse grains decrease, and the liquefaction resistance of sandy soil also decrease with it. With the further increase of fines content, the fine grains not only occupy the voids between the coarse grains but also wrap up the coarse grains, and the coarse grains do not play a skeleton action. Liquefaction resistance of sandy soil is manly determined by the fine grains, and the void between the fine grains decrease with the increase of the fines content, which makes the mutual contact force of the fine grains increase and the liquefaction resistance of sandy soil also increase with it.

CONCLUSIONS

Through the experimental study of the different content of fine sand in the cycle load conditions, the effects of granulometric composition on dynamic characteristics of sandy soil are obtained. The response law of the effects of the fines content on the characteristics of the liquefaction resistance of sandy soil is verified. This research results are well consistent with the variation tendency of the relative density with the increase of fines content. With a constant dry density, the liquefaction resistance first increase and then decrease with the increase of the fines content, when the relative density reaches the minimum value at the fines content of 30% and the liquefaction resistance also reaches the minimum value at the same fines content.

REFERENCES

Baziar, M.H. and Dobry, R. (1991). "Liquefaction ground deformation predicted from laboratory tests." *Proc. 2nd Int. Conf. on Recent Advances in Geotechnical Earthquake Engineering and Soil Dynamics, St Louis*, 1:451-458.

Polito, C.P. and Martin II, J. R. (2001). "Effects of nonplastic fines on the liquefaction resistance of sands." *J. Geotechnical & Geoenv. Engrg.*, Vol. 127(5):408-415.

Polito, C.P. and Martin II, J. R. (2003). "A Reconciliation of the Effects of Non-Plastic Fines on the Liquefaction Resistance of Sands Reported in the Literature." *Earthquake Spectra*, Vol. 19(3):635-651.

Seed, H.B. and Lee, K.L. (1966). "Liquefaction of saturated sands during cyclic loading." *J. Soil Mech. and Found. Div.*, ASCE, Vol. 92(6):105-134.

Seed, H.B. and Idriss, I.M. (1971). "Simplified Procedure for Evaluating Soil Liquefaction Potential," *J. Soil Mechanics & Foundations Div.*, ASCE, Vol. 97(SM9): 1249-1273.

The Committee soil dynamics of the geotechnical engineering division. (1978). "Definition of terms related to liquefaction." *J. Geotechnical & Geoenv. Engrg. Div.*, ASCE, Vol. 104(GT9) 1197-1200.

Wang, W.S. (1997). *The dynamic strength and liquefaction properties of soil*, China power press, Beijing.

Youd, T.L. and Bennett, M. J. (1983). "Liquefaction sites, Imperial Valley, California." *J. Geotech. Engrg.*, ASCE, Vol. 109(3):440-457.

Zeng, C.N. (2006). "Laboratory test study on the influence of percent fines on silt liquefaction and post-liquefaction." Ph.D. thesis, Civil Engineering, Nanjing: hohai university.

Laboratory Flume Static and Dynamic Experiment for Rock Avalanches

K. Ugai[1], Q. Yang[1], F. Cai[1], Q. Xu[2], A. Ahmed[1,3], Z.Su[4] and M. Yamada[5]

[1] Civil and Environmental Engineering Dept., Gunma University, Japan; ugai@ce.gunma-u.ac.jp
[2] Chinese State Key Laboratory of Geohazard Prevention and Geoenvironment Protection,Chengdu University of Technology, China; xuqiang_68@126.com
[3]Civil Engineering Department, Beni-Suef University, Egypt; aly_76@hotmail.com
[4]Central South University, China, [5]Japan Conservation Engineers Co., Ltd., Japan

ABSTRACT: A series of flume experiments under static and dynamic conditions were conducted to study the Xiejiadian rock avalanche, which was triggered by Wenchuan Earthquake in China. Six influencing factors acting on the run-out of rock avalanches were investigated by releasing three granular materials in a designed flume. Test results under static conditions showed that the coarser sample was of higher fluidity than other types with excessive content of finer particles. Positive correlations were obtained between the following parameters: the angle of flume and the run-out of deposit; the angle and the accumulation of deposit; the mass and the run-out; the mass and the accumulation. In the case of consecutive releases, the traveling length of entire volume was affected mainly by the first release, while subsequent releases only had effects on the height and weight of the main part deposit. The roughness of bottom surface of the flume had a large effect on the finer particles than coarser particles. The run-out of deposit decreased when obstacles were introduced. Dynamic results showed that shaking force has a significant effect on the increase of run-out distance of the deposit compared with results under static. The run-out distance increased with the increase of acceleration amplitudes. Whereas, the run-out distance reduced gradually with the increase of frequency.

INTRODUCTION

On May 12th, 2008, there was a large earthquake shocking most regions of P. R. China, which is named Wenchuan Earthquake, with a magnitude of 8.0. Numerous large and long run-out distance landslides occurred due to the heavy shake of earthquake. It is well known that rock avalanches behave in extraordinary ways unlike other landslides because of rapidity of their triggering and evolution processes (Valentino et al. 2008). Many ‘amazing’ and ‘incomprehensive’ phenomena appearing in long run-out rock avalanches were recorded in literatures, including immense volume, extremely high speed, unexpected movement distance as long as several kilometers, enormous energy, and high fluidity (Cheng et al. 2007). Hypotheses were

proposed to explain these phenomena, such as upward flow of air or hover craft action (Shreve 1966), reduction of basal roughness by grain size separation (Hsü, 1975), lubrication by molten rock (Erismann 1986) or fluidization by particle collision (Hsü 1975). However, these hypotheses remain largely unresolved and controversial (Friedmann et al. 2006), and need to be further validated. In order to clarify the mechanism of earthquake-induced rock avalanche, both field investigations and laboratory experiments are vital that can help study influencing factors and assess parameters of numerical analysis. The influencing factors that have been studied in previous work include material, volume, height of drop, releasing geometry, consecutive releases, inclination and bed obstacle especially in the ways of experiments (Manzella et al. 2008).

This paper focuses on the influencing factors on run-out, such as type of material, angle of slope, mass, consecutive releases, bed roughness, obstacles and shaking force. Therefore, a series of laboratory flume tests were conducted to simulate the Xiejiadian rock avalanche. Actually, it is well known some behaviors of rock avalanches are hard to simulate in the small prototype experimental model. In addition to the main purpose of this work, the results will be obtained that it can be used as useful guidelines for future rock avalanches research.

FIELD INVESTIGATIONS

Xiejiadian rock avalanche as shown in Figure 1 happened right after the first shock of Wenchuan Earthquake. The site of rock avalanche is close to the epicenter of Wenchuan Earthquake, locating in a famous active fault belt named Longmen Mountain fault belt, which has many earthquake activities in history. According to the results of field investigations, it was found that the run-out distance of the debris generated by this event is about 1km, with a deposit volume of about 1 million cubic meter and a fall height of about 400m. A gully was washed out in the deposit in the following rainfall season, the bottom of which was viewed as original ground of this region. Survey results showed that the profile of gully bottom composites of two lines, respectively with angles of 42.5°and 11°, as shown in Figure 2.

FIG. 1. Overview of Xiejiadian rock avalanche

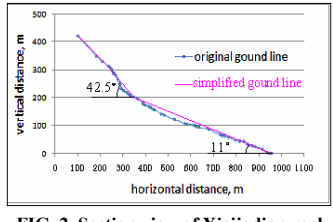

FIG. 2. Section view of Xiejiadian rock avalanche

Many phenomena were revealed from field investigations, including scratches and blow-down-like trees on sidewalls, wavy ground surface, loose rock-and-soil deposit mass, inverse grading of debris, landslide dam, which resulted in changing local geomorphology a lot (Yang et al. 2008). It is puzzling how the failure rock could run

out so long a distance in a gently sloping ground after fall down from a steep position and how their influencing factors work. This paper tried to find some explanations from model experiments.

LABORATORY FLUME EXPERIMENTS

Experimental Set-up under Static Condition

Experiments were performed in a flume as shown in Figure 3 which consists of three straight portions corresponding to the terrain of study site, respectively named as upper inclined portion, lower inclined portion, and flat portion. Each portion of flume was 1500 mm in length and 180mm in width and was connected by hinges in convenience of adjusting the angle of inclination. In order to study the influencing mechanism, the angle of the upper one were changed by 30°, 45°and 60° in many tests, while the angle of the lower one was fixed at 10°. In a few cases, flume bottom was coated with sandpaper to simulate rougher situation, while the roughness of sidewalls was kept small, which would help to maintain the flow in two-dimensional condition (Valentino et al. 2008). Three cases of obstacles were designed to study the influence of obstacles. Each case of obstacle was simulated by wood brick with size of 180 × 20 × 20mm, and was set in different positions. Case-1 was one obstacle located at the joint between the upper portion and the lower one; Case-2 was one obstacle fixed at x=300mm, according to trial results; Case-3 was two obstacle respectively set in x=0mm and x=300mm, the combination of case-1 and case-2.

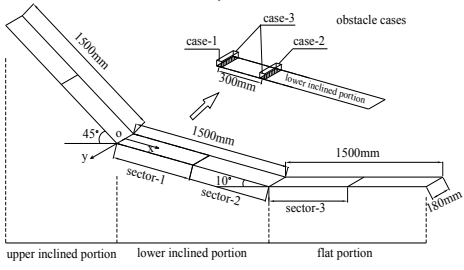

Note: Origin of coordinates is located at the center of the joint between upper inclined portion and lower inclined portion. X-axis is aligned with the dip of lower inclined portion.

FIG. 3. Sketch of testing equipment

Three cohesion-less granular types were used, respectively labeled as sample A, sample B and sample C (see Table 1).

Table 1. Weight ratio of granular materials in each sample

Granular Type	Range of Particle Size		
	10 –20 mm	1-2 mm	0.1-0.2mm
Sample A	10%	30%	60%
Sample B	60%	30%	10%
Sample C	34%	33%	33%

FIG. 4. The photo for experimental set-up in case of dynamic condition

Experimental Set-up under Dynamic Condition

A series of shaking table tests are carried out with the primary objective to study the effect of dynamic factors. The flume is fixed tightly over the shaking table (2.0m×1.0m) by channels to avoid any failure for the flume during shaking process. The same flume which is used under static condition is also used herein and only consisted of two straight potions labeled as the upper and lower inclined portion, respectively. The angle of upper inclined portion is fixed at 45°, while that of lower inclined portion is 10°. The photo for experimental set-up is shown in Figure 4. The rock avalanche is simulated by releasing the same types of granular materials which are used in static condition, held up initially on the upper inclined portion, by a movable wood panel with the same width as the flume. The releasing height of sample in each test was fixed at 0.76m from the flat portion and the mass of sample used is 3.0kg.

TESTING PROGRAM

Rock avalanches were simulated through releasing granular materials, held up initially on the upper inclined portion by a movable wood panel with the same width as the flume. The drop height of sample in each test was fixed at 76cm from flat portion. Each run-out was measured by a tape and the process was recorded by a camera. The measurements were conducted by dividing the deposit materials along the flume to three parts based on the accumulation of particles. The first part represents the huge amount of deposit as one block. The second part represents the deposit which is a layer of one particle height along the second inclination while the deposit particles which reach the flat portion are represented by the third part. These parts can be labeled as sector-1, sector-2 and sector-3 as illustrated before in Figure 3. Summary of all tests under static condition is shown as Table 2.

Table 2. Laboratory flume experiments

Group No.		Sample	Angle	Mass	Release	Roughness	Obstacle
A	A-1	A	45°	3kg	1	wood	Non
	A-2	B					
	A-3	C					
B	B-1	B	30°	3kg	1	wood	Non
	B-2		45°				
	B-3		60°				
C	C-1	B	45°	1.5kg	1	wood	Non
	C-2			3kg			
	C-3			6kg			
D	D-1	B	45°	3kg	1	wood	Non
	D-2				2		
	D-3				4		
E	E-1	B	45°	3kg	1	wood	Non
	E-2					sand paper	
F	F-1	B	45°	3kg	1	wood	case-1
	F-2						case-2
	F-3						case-3

In order to investigate the effect of dynamic factors on the run-out distance, the input of Sin waves and acceleration amplitude are varied. The period of vibration process is kept 3 seconds based on the result of static tests. It is attributed that the whole test process approximately spends 3 seconds from initiation to rest in the static tests. The acceleration amplitude is varied from 0.1g to 0.2g, and the range of frequency is increased from 2 to 10Hz with increasing interval of 2Hz. For each combination of these, five trial tests are run, and the photo and video film for avalanche motion is taken at least one among the number of trials. Repeated performances of a test under the same conditions are done in order to guarantee their accuracy. In most repeated tests, the run-outs are compared.

RESULTS AND DISCUSSION

Type of Granular Material

The morphologies of each deposit body in the tests of Group A as shown in Figure 5 were almost the same but the values of run-out varied.

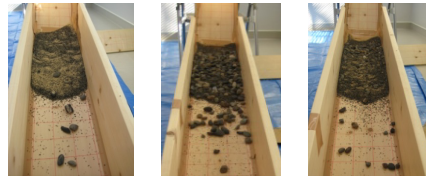

a. Sample A b. Sample B c. Sample C

FIG. 5. Deposit morphology in Group A

As shown in Figure 6, more than 90% of materials deposit in the sector-1, which was found similarly in most of the following tests. Therefore, this paper paid more attention to the run-out of the main part of deposit. The results of Group A which is illustrated in Figure 7 show that the run-out of sample B is the farthest among the three, while sample A is the shortest. As mentioned in Table 1, sample B consisted of considerably more coarse particles than both sample A and sample C. It can be assumed that coarser sample may be with higher fluidity that can go further than other types when they ran on the wood flume. In other words, excessive content of fine particle would be a passive influence on run-out, which may be caused by easier consumption of kinetic energy. This point remains to be clarified in the future.

The results of group B (Figure 8a) show that the longest run-out appeared in experiment B-3 with angle of 60° in upper inclined portion. Positive correlation is obtained between the angle of upper inclined portion and the run-out. However, Okura et al. (2000) expressed that there was an inverse correlation between slope inclination and run-out distance. The accumulation of deposit (Figure 8b) indicates a similar correlation with angle of flume. It should be noted that when the angle of slope is changed from 0° to 90°, the run-out would correspondingly change from 0 to a higher one and then fall to around 0 again: the correlation is not a simple monotonic one.

Mass of Sample

Group C was used to test the influence of sample mass. The results are shown as Figure 9. It is found that both the run-out and accumulation indicate a positive correlation with the mass of sample. It is apparent that the run-out distance depends partly on the mass of materials when it drops at a fixed height.

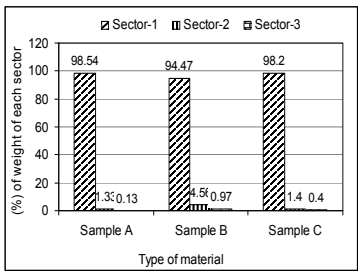

FIG. 6. Weight ratio of each sector in Group A

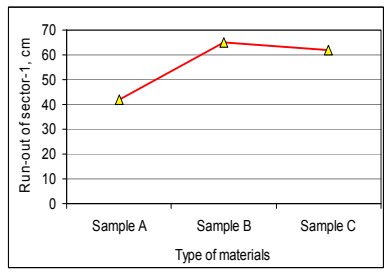

FIG. 7. Run-out in Group A

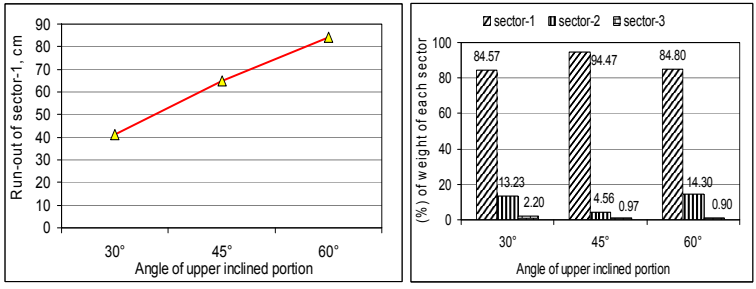

a). Run-out in Group B b). Weight ratio of each sector in Group B

FIG 8. Results of Group B

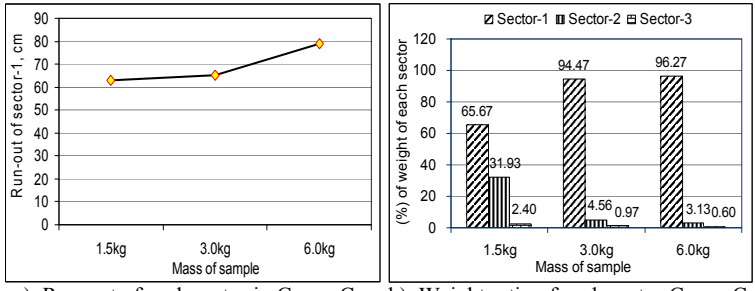

a). Run-out of each sector in Group C b). Weight ratio of each sector Group C

FIG 9. Results of Group C

Consecutive Releases

The influence of consecutive releases was studied by releasing sample B with 3kg in three kinds of manners as following: (a) D-1: once (3.0 kg); (b) D-2: twice (1.5 kg over 1.5 kg); (c) D-3: four times (0.75 kg over 0.75 kg over 0.75 kg over 0.75 kg). Figure 10 revealed the deposit morphology of each release. It is found that the first release formed deposit morphology with three sectors as usual, but subsequent release was just devoted to sector-1, rather than sector-2 and sector-3 and almost all stayed on the deposit of main part of the last release without going further. This result can be explained by the deposit after the first release which behaved as obstacles for the next releases. The first release would mainly affect the travelling length of the entire volume and the subsequent release would add the height and weight of sector-1. Similar phenomena were also recorded by Hutter et al. (1995) and Eberhardt (2004). It is easy to draw the conclusion that the more times it is released, the shorter it would run out, which is validated by these tests.

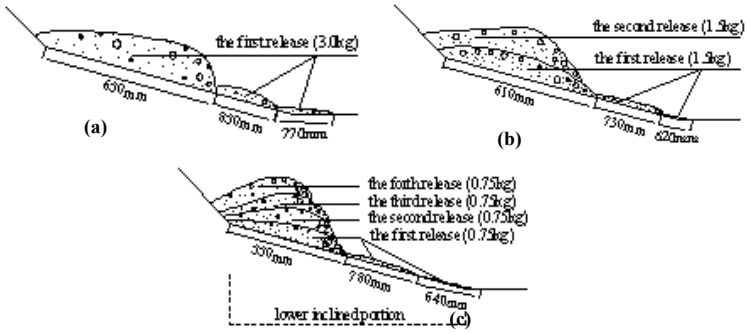

FIG. 10. Deposit morphology of consecutive releases

Bed Roughness

In the experiments of group E, bottom surface of the flume was coated by coarse sandpaper in order to identify the influence of bed roughness on run-out. Most of coarser particles stop at the lower inclined portion (range from 0 to 0.75 m), and the farthest run-out distance is about 1.65 m. Furthermore, it is noticed that almost all the fine sand stop at the upper inclined portion. This phenomenon showed that roughness mainly affects the deposit characteristics of finer particles (with similar dimension as the surface material of sandpaper) rather than coarser particles.

Obstacles

The morphology in each case varied significantly as showin in Figure 11. Both the deposits in case-1 and case-2 jump across the obstacles in their travel path, while in case-3 it stoped behind the further obstacle.

a) case-1 b) case-2 c) case-3

FIG . 11. Deposit morphology in each obstacle case

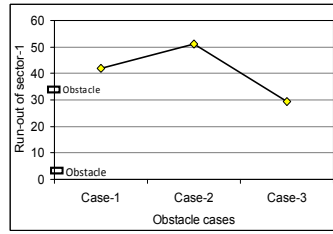

FIG. 12. Run-out of sector-1 in each obstacle case

Figure 12 showed that the run-out of the main part in case-2 was the farthest among the three, while case-3 was the shortest. The run-out in case-2 is a little shorter than the case without obstacle (Figure 7). It is easy to understand the shortest of case-3 because it faced more obstacles and would consume more energy in its traveling. The shorter of run-out in case-1 than in case-2 may partly because of its earlier

encountering of obstacle and its changes of direction. The relation between the position of obstacles and its influence on the run-out of deposit needs to be studied further.

DYNAMIC EXPERIMENTAL RESULTS

Generally, testing results show that more than 90% of materials deposit in the sector-1, which was found similarly in most tests under static and dynamic conditions. Therefore, more attention is paid to the run-out of the main part of the deposit. Figure 13 shows that the run-out reduces gradually with the increase of frequency interval for both acceleration amplitudes 0.1g and 0.2g are used. Also, it is clear from this figure the acceleration amplitude has a significant effect on the run-out of the deposit. The run-out of deposit reduces with the increase the value of acceleration amplitude.

A comparison between static and dynamic results is presented to investigate the effect of dynamic factors for rock avalanche. According to the previous static tests, the average run-out was 65cm. For the same condition but in the case of dynamic tests, the least run-out is 73.125cm when the shaking frequency is 10Hz as shown in Figure 14. Therefore, it can be concluded that the run-out is affected, and presents an increase trend by shaking with the same other conditions.

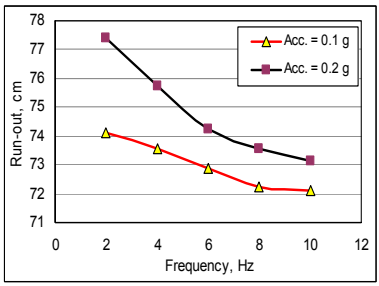

FIG. 13. Run-out of the deposit under dynamic tests

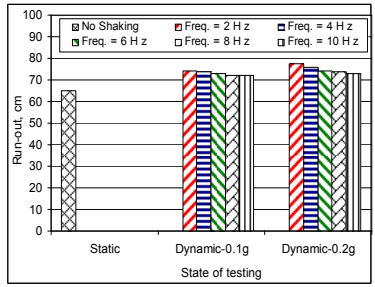

FIG. 14. Effect of dynamic force on the Run-out of the deposit

CONCLUSIONS

Carrying out the laboratory flume experiments has a main purpose to qualitatively identify parameters influencing run-out in a rock avalanche processes which is mainly based on the results of field investigation in Xiejiadian rock avalanche induced by Wenchuan Earthquake. The main conclusions can be drawn as following:

1. For the range of parameters considered in the tests conducted in this paper, coarser sample may be with higher fluidity that can go further than other types with excessive content of fine particle;
2. Positive correlation between the angle of flume and both run-out and accumulation of the deposit.
3. Run-out distance of rockslides depends partly on the mass of materials when it drops at a fixed height and there is a positive correlation between the mass of sample and run-out of deposit, as well as the mass and the accumulation.

4. The travelling length of the entire volume would be affected by the first release, while the subsequent release would add the height and weight of sector-1; the more times it is released, the shorter distance it would run out;
5. When the bottom surface of the flume is coated by sandpaper, roughness mainly affects finer particles rather than coarser particles.
6. The position and number of obstacles would affect the run-out. It is found that earlier encountering of obstacles and the subsequent changes of travel direction would decrease the run-out of deposit.
7. The run-out reduces gradually with the increase of frequency. While acceleration amplitude has a significant effect on the potential of run-out of the deposit, the increase of the acceleration is associated with the increase of run-out of the deposit.

ACKNOWLEDGEMENTS

This work is partly supported by the open study fund project of Scientific Alleviation of Disasters and Home rebuilding [DZJK-0814] from Chinese State Key Laboratory of Geohazard Prevention and Geoenvironment Protection. The support from Prof. R. Huang of Chengdu University of Technology is deeply appreciated.

REFERENCES

Cheng Q., Zhang Z., Huang R. 2007. Study on dynamics of rock avalanches: state of the art report. Chinese Journal of mountain science, 25(1): 72-84. (in Chinese)

Eberhardt E. 2004. Numerical analysis of initiation and progressive failure in natural rock slope: the 1991 Randa Rockslide. Int. J. Rock Mech. Min. Sci. 41, 69-87.

Erismann T. 1986. Flowing, rolling, bouncing, and sliding: synopsis of basic mechanisms. Acta Mech. 64: 101-110.

Friedmann S.J., Taberlet N., Losert W. 2006. Rock-avalanche dynamics: insights from granular physics experiments. International Journal of Earth Sciences, 95(5): 912-919.

Hsü K. 1975. On sturzstorms- catastrophic debris streams generated by rockfalls. Geol. Soc. Am. Bull 86: 129-140.

Hutter K., Koch T. 1995. The dynamics of avalanches of granular materials from initiation to run out. Part 2: Experiments. Acta Mechanica, 109(1-4):127-165.

Manzella I., Labiouse V..2008. Qualitative analysis of rock avalanches propagation by means of physical modelling of non-constrained gravel flows. Rock Mechanics and Rock Engineering, 41(1): 133-151.

Okura Y., Kitahara H., Sammori T., Kawanami A. 2000. The effects of rockfall volume on run-out distance. Engineering Geology, 58(2):109-124.

Shreve R. L. 1966. Sherma landslide. Alaska. Science 154: 1639-1643.

Valentino, R. Barla G., Montrasio L.: Experimental analysis and micromechanical modeling of dry granular flow and impacts in laboratory flume tests. Rock Mechanics and Rock Engineering, 41(1):153-177.

Yang Q., Su Z., Ugai K. Cai F. Yamada M. 2008. Recent landslide disasters induced by earthquakes. Proceeding of 5th International Conference on landslides, slope stability & the safety of infrastructures, Kuala Lumpur, Malaysia, July: 47-52.

Near Surface Soil Characterisation by Passive Ambient Noise HVSR Method

Pavlick Harutoonian[1], Ben Chapman[1], Christopher Neil Young[1], Chin Jian Leo [1] and Ju Jia Zou [1]

[1]School of Engineering, University of Western Sydney, Locked Bag 1797 Penrith South DC NSW 1797; p.harutoonian@uws.edu.au

ABSTRACT: This paper discusses the use of the passive horizontal-to-vertical spectral ratio (HVSR) ambient noise method for near surface characterisation of the soil layers at a proposed building site. The uniqueness of the HVSR method is in having no need for any external excitation sources and cabling, and the setting up time is also very short. In our study, HVSR measurements were taken at spots interspersing the few available bore logs, with each measurement taking no more than 10 minutes. This allows the entire site to be measured very expeditiously. The HVSR spectra were then inverted by fitting measured to theoretical spectra values to obtain the V_s profile of the underlying soil layers, based on an assumed layered soil model. A side benefit of this approach is that the resonance frequencies of the site were also determined without undertaking additional work. In addition to benchmarking the soil profile inverted from the HVSR measurements against the available bore log data to verify its accuracy and correctness, comparisons have also been made with the results from the MASW and ReMi array-based methods. The study shows that the HVSR method performed very well against these surface wave methods. It is thought that the HVSR technique would be especially cost-effective for characterising a large site in conjunction with a few bore logs.

INTRODUCTION

At present, mechanical testing methods such as standard penetrometer testing (SPT), cone penetrometer testing (CPT), down-hole/cross-hole measurements and boreholes are the accepted forms of near surface site characterisation. These methods are used today with confidence to determine shallow soil characteristics but are both time consuming and costly. Alternatively, the use of non-invasive 1D and 2D array surface wave seismic methods such as SASW, MASW, CSW and ReMi have become increasingly popular due to the low cost and short time required to carry out the tests. These non-invasive methods are based on the estimation of the phase velocity dispersion curves to survey the subsurface layering and stratification, through the characterisation of the S-wave (V_s) velocity profiles. The HVSR method is an ambient noise technique which relies on the measurement of microtremors and microseisms which are present in the ground. A study has been initiated by the authors to investigate the possible use of the HVSR single

station technique as a method to characterise an urban development site. The chosen site is on the Penrith campus of the University of Western Sydney (UWS), where there is soon to be the development of a new education centre. It is intended to estimate the V_s velocity profiles and consequent soil layering data. Earlier, it has been shown that single station recordings of the horizontal to vertical spectra ratio of prevailing microtremors and microseisms have allowed the resonance frequencies and site amplifications of a site to be ascertained (e.g. Castellaro & Mulargia 2009; Doanh et al. 2008). The work of Nakamura (1989) is also important in this regard in suggesting that the horizontal to vertical spectral ratio reflect the transfer function of the surface layers. In light of this, the characteristics of the surface layers may be revealed by inversion of HVSR curves either on their own (Arai & Tokimatsu 2004; Fah et al. 2003) or jointly with available dispersion curves (e.g. Arai & Tokimatsu 2005). The estimated V_s profiles may then in turn be correlated to soil data in providing information on the stratified soil layers. Non-invasive shallow geotechnical characterisation by single station HVSR technique holds great potential as an attractive, cost and time efficient method when compared to invasive and other non-invasive methods previously mentioned.

This paper reports and discusses (1) the inverse analysis of the HVSR curves to estimate the V_s velocity profiles for the site (2) benchmarking the inverted HVSR results against the bore log data to verify its accuracy and correctness and (3) comparing the performance of the HVSR method with those of the now well established MASW and ReMi array based methods to assess the viability of the HVSR method.

TEST PROGRAM

(a) Geology and HVSR Measurements at development site

The passive ambient noise HVSR technique was used to conduct an extensive geotechnical survey of a proposed development site on the Penrith campus of UWS. The campus lies on the Cumberland plain to the east of the Blue Mountain plateau within the Sydney Basin. The geology of the campus site is dominated by Bringelly shale of the Wianamatta group. Subsequent weathering of the parent material, and more recent construction activities have resulted in the current soil type especially near the surface. According to available borehole data, the surface of the site consists of highly variable depths of fill ranging from 0.4 m to 2.6 m, assessed to be mostly poorly to moderately compacted silty clay of low to high plasticity. The natural soils underlying the fill consisted of mostly silty and sandy clays, with some of the deeper silty clays close to the bedrock profile containing remnants of the shale structure. The silty and sandy clays are generally of very stiff variety. Very low to low strength weathered shale or bedrock is encountered at depths ranging from 3.6 m to 13.6 m at borehole termination. The locations of the HVSR stations denoted by squares and the available borehole locations are shown in Figure 1. The stations are arranged in three rows by five lines with a total of 116 separate locations. At each station location, a tomograph recording of the ambient noise was made. The tomographs are standalone units, battery operated and able to measure the ambient vibrations in the vertical and two orthogonal horizontal directions (North-South and East-West in this study). Data acquisition frequencies of 128 Hz were implemented throughout the site and passive ambient noise recordings were made for 10

minute period, a duration long enough to capture sufficient good recordings of microtremors at the site. The current testing layout has been implemented due to the availability of prior borehole investigations conducted by UWS.

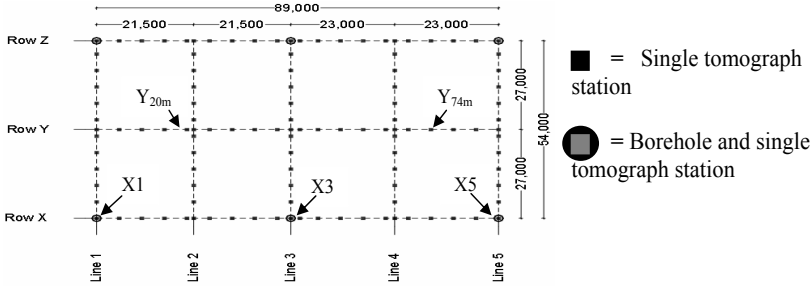

Figure 1: Locations of test stations

(b) Inversion of HVSR measurements

As mentioned previously, establishing the soil profile beneath the ground by bore logging and classical mechanical tests are expensive and protracted, due to the logistics required for such undertakings. A cheaper, more cost-effective alternative is to invert the microtremor measurements to produce the V_s profile using techniques of signal processing, and minimisation of residual error between the synthetic curves and measured values. The soil data of the layers are then estimated by correlating the V_s profile with actual soil parameters. A layered soil model is supposed in generating the theoretical synthetic curve which is required for the inversion of the HVSR data to produce the estimated soil profile.

Arai and Tokimatsu (2004) and Fah et al. (2003) introduced the method for estimating the V_s profile of subsurface soils, based on the inversion of the horizontal-to-vertical (H/V) spectrum of microtremors observed with a three-component sensor. The assumed soil profile consisted of parallel, homogeneous and isotropic layers in a semi-infinite elastic medium. The layers are characterised by shear wave velocity ($V_{s1},....,V_{sn}$), primary wave velocity ($V_{p1},....,V_{pn}$), soil thickness ($y_1, y_2, y_3....,y_n$) and density ($\rho_1,...,\rho_n$). Arai and Tokimatsu's (2004) method has as its theoretical basis the solutions proposed by Harkrider (1964) for both Rayleigh and Love surface waves propagating in a layered half-space. They showed that the computed theoretical or synthetic H/V spectrum could be fitted to the experimental H/V spectrum by minimising the square of the residual error between the two curves by adjusting the estimated V_s and other soil parameters via a least square algorithm. In contrast, Fah et al.'s (2003) inversion proposal is based on a genetic algorithm, owing to the problem being of a non-linear nature. Arai and Tokimatsu (2005) later extended their method to a joint inversion technique which takes into consideration both the HVSR measurements and the dispersion curves of the phase velocity in frequency domain. Thus, much progress has been made in recent years in estimating the V_s profile of a site from the inversion of the microtremor measurements.

(c) Bore logging and non-invasive surface wave techniques

In this study, the geological structure of the UWS Penrith Campus development site has been assessed by 3 alternate means: (1) borehole data (2) the array based MASW technique used together with the passive ReMi technique and (3) the HVSR passive ambient noise technique. The available borehole data was deemed as providing the most reliable basis for geotechnical site characterisation, due to the fact that it can very accurately reveal the thickness and type of soil layers but only at localised spots. Therefore, the bore hole data was used in benchmarking the results from other surface wave and HVSR methods. The MASW and ReMi array based techniques were implemented as an alternative non-invasive method to the HVSR technique as they are well published and recognised. Due to the fact that the HVSR method is passive, the use of a comparative active technique, in this case the MASW, was thought to be particularly apt. The passive based ReMi was used in conjunction with and to reinforce the measurements from the active MASW. Referring to Fig 1, MASW and ReMi measurements were carried out along rows X to Z and lines 1, 3 and 5, generally covering the entire site. An example of the HVSR measurement and the fitted synthetic curve is shown in Figure 2, for the corner X5 (row X, line 5). The soil model associated to the synthetic curve yields the data for the soil layers at this location. Shown in Figure 3 are the corresponding MASW data and the fitted synthetic dispersion curve.

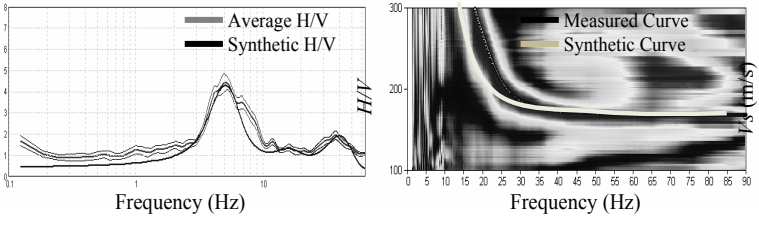

Figure 2 (left): HVSR curve with theoretical plot at the intersection of row X and line 5. Figure 3 (right): Dispersion curve by active MASW along row X

(d) Interpretation of Results

The geological structure at location X5 ascertained from these 3 independent means, summarised and associated to equivalent V_s values, is shown in Figure 4. It can be seen in Figure 4 that the values determined by the HVSR method do in fact correlate well with the benchmark, the data from the borehole located at X5. Although the borehole was terminated at 12.6 m when the stiff bedrock was reached, the available data has shown that the HVSR method satisfactorily estimated the geological structure. The HVSR profile also corresponds quite well with profile established by the MASW and ReMi. The results presented at corner X5 exemplify the general findings at this site.

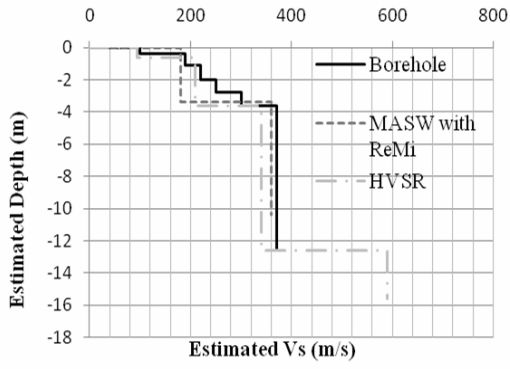

Figure 4: Soil profile by 3 independant techniques

As shown in Figures 5a – 5d, the results at other locations also indicate that the HVSR results have agreed well with borehole data, while also performing very well in comparison with the results achieved by the MASW and ReMi array based methods.

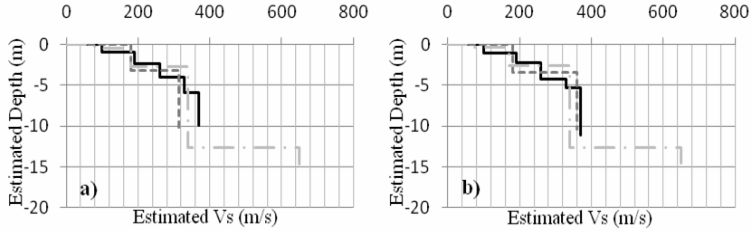

Figure's 5a and 5b: Soil profiles at locations X1 and X3 respectively by borehole, MASW with ReMi, and HVSR. (See legend of Figure 4)

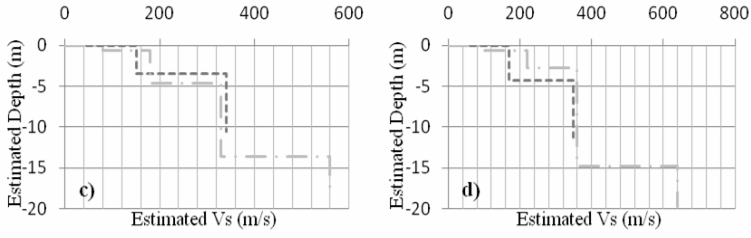

Figure's 5c and 5d: Soil profiles at locations Y_{20m} and Y_{74m} respectively by MASW with ReMi and HVSR. (See legend of Figure 4)

CONCLUSION

This study has demonstrated that the HVSR ambient noise technique used to estimate the geotechnical layer data at the site agrees well with the data obtained from the

boreholes. Moreover, the accuracy of this technique compares very favourably with those of the non-invasive MASW and ReMi methods. This is an indication, as pointed out by earlier investigators, that the HVSR curve is a type of "transfer function" which is strongly correlated to the local geologic structure but not to the excitation source. Thus far, the use of the HVSR method for geotechnical site characterisation has proved to be fast and cost-effective while being able to provide information to depths beyond the capabilities of the array based techniques and mechanical borehole. A single station HVSR recording of microtremors and/or microseisms has the additional benefit of allowing the resonance frequencies and site amplifications of a site to be ascertained.

Acknowledgment

Pavlick Harutoonian is supported by a higher degree research PhD scholarship from the University of Western Sydney.

References

Arai, H. & Tokimatsu, K. 2004, 'S-Wave velocity profiling by inversion of microtremor H/V spectrum', *Bulletin of the Seismological Society of America*, vol. 94, no. 1, pp. 53-63.

Arai, H. & Tokimatsu, K. 2005, 'S-wave velocity profiling by joint inversion of microtremor dispersion curve and horizontal-to-vertical (H/V) spectrum', *Bulletin of the Seismological Society of America*, vol. 95, no. 5, pp. 1766-1778.

Castellaro, S. & Mulargia, F. 2009, 'Vs30 estimates using constrained H/V measurements', *Bulletin of the Seismological Society of America*, vol. 99, no. 2A, pp. 761 - 773.

Doanh, T., Hareb, H., Hans, S., Boutin, C., Anarbaev, M. & Wu, W. 2008, 'Ambient noise site investigation of a representative MSW landfill in Bishkek, Kyrgyzstan', *GeoCongress 2008: The Challenge of Sustainability in the Geoenvironment*, New Orleans, Louisiana, USA.

Fah, D., Kind, F. & Giardini, D. 2003, 'Inversion of local S-wave velocity structures from average H/V ratios, and their use for the estimation of site-effects', *Journal of Seismology*, vol. 7, pp. 449-467.

Harkrider, D.G. 1964, 'Surface waves in multilayered elastic media. Rayleigh and Love waves from buried sources in a multilayered elastic half-space', *Bulletin of the Seismological Society of America*, vol. 54, no. 2, pp. 627-679.

Nakamura, Y. 1989, 'A method for dynamic characteristics estimation of subsurface using microtremor on the ground surface', *Quarterly Report of Railway Technical Research Institute (RTRI)*, vol. 30, no. 1.

Modeling and Seismic Response Analysis of a Reclaimed Artificial Ground

Toshihiro NODA[1], Akira ASAOKA[2] and Kentaro NAKAI[3]

[1] Professor, Department of Civil Engineering, Nagoya University, Furo, Chikusa, Nagoya, JAPAN, 464-8603; noda@civil.nagoya-u.ac.jp

[2] Professor, Department of Civil Engineering, Nagoya University, Furo, Chikusa, Nagoya, JAPAN, 464-8603; asaoka@civil.nagoya-u.ac.jp

[3] Assistant Professor, Department of Civil Engineering, Nagoya University, Furo, Chikusa, Nagoya, JAPAN, 464-8603; nakai@civil.nagoya-u.ac.jp

ABSTRACT: Compared with natural grounds formed by sedimentation over many years, reclaimed artificial grounds are often weak. In this work, modeling of a reclaimed offshore artificial ground and its seismic response analysis were carried out, and the vulnerability of the weak reclaimed layers to seismic activity is pointed out. This study was carried out using a soil-water coupled finite deformation analysis program ***GEOASIA*** incorporating an elasto-plastic constitutive model (the SYS Cam-clay model). This model is capable of describing, within a single framework, the behaviors of sands, clays, and intermediate soils consisting of sand/clay mixtures through their soil skeleton structures (structure, overconsolidation, anisotropy) and its works. In reclaimed sand, lateral flow and upward lifting of lightweight underground structures occur because of liquefaction during an earthquake. In reclaimed clay, long-term settlement, which continues for several years after the earthquake, occurs.

INTRODUCTION

Artificially constructed grounds such as man-made offshore islands and reclaimed grounds are often weak compared with natural grounds formed through many years of sedimentation. In recent years, many important civil engineering structures have been constructed on these kinds of artificially reclaimed grounds. This makes it necessary to evaluate the seismic performance of these grounds with respect to the massive earthquakes that are expected to occur in the near future from a broad perspective that includes not only stability during such earthquakes but also prediction of heavy deformation behavior that may occur due to post-seismic consolidation.

The current study presents the results of numerical analysis carried out to determine the co-seismic and post-seismic deformation behaviors of an artificially reclaimed ground offshore of Nagoya City with respect to the *Tokai-Tonankai-Nankai* multiple-segment type earthquake expected to occur in this region and attempts to identify the weak locations in the ground. The analysis was performed with the aid of a soil-water coupled

finite deformation analysis program ***GEOASIA*** (Asaoka et al., 1994, Asaoka & Noda, 2007, Noda et al., 2008) incorporating an elasto-plastic constitutive model (SYS Cam-clay model, Asaoka et al., 2002). This model is capable of describing, within a single framework, the behaviors of sands, clays, and intermediate soils consisting of sand/clay mixtures through their soil skeleton structures (structure, overconsolidation, anisotropy) and its works, irrespective of whether the behaviors are static or dynamic.

MODELING OF THE ARTIFICIAL GROUND

The finite element mesh used is illustrated in **Fig. 1**. In the analysis, the actual reclamation history, which consisted of 1) construction of a riprap mound, 2) clay filling, and 3) sand filling, was replicated. This was accomplished by simulating the loading in each of the above three stages using soil-water, two-phase type, elasto-plastic finite elements to load a naturally sedimented ground consisting of alternating layers of strong tertiary mudstone and diluvial sand with an N-value of about 30. The reclaimed layers are weak and have low N-values. The concrete revetment constructed on the riprap mound and lightweight underground structure supported by piles were simulated by creating, after the reclamation was completed, a single-phase elastic body whose weight and rigidity were equivalent to those of the actual structures. For the sake of simplification, the piles inserted on the bottom part of the underground structure were simulated here by allotting the constraint condition of invariable distance between the pertinent element nodes. The hydraulic pressure of the ground surface above the water level was always assumed to be zero (atmospheric pressure condition), and the ground surface below the water level was considered to be the drainage boundary subject to pressure corresponding to the static hydraulic pressure. The lateral and bottom faces of the ground were considered to be undrained boundaries.

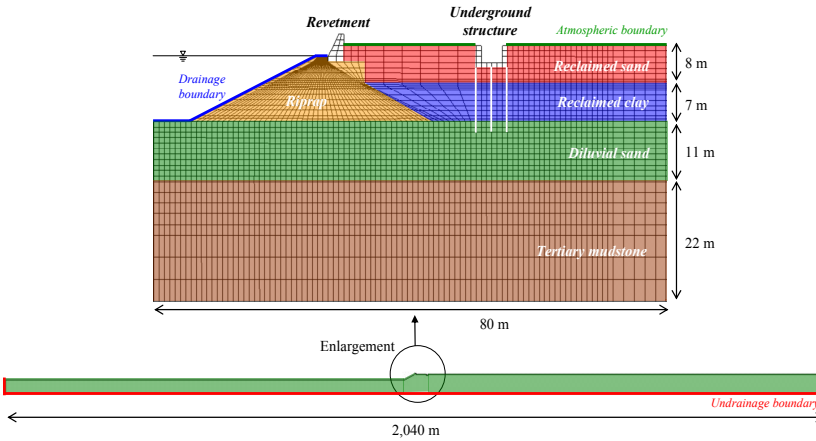

Fig. 1 Modeling of reclaimed offshore artificial ground (finite element mesh)

The list of elasto-plastic parameters (material constants and initial values) used in the

analysis is shown in **Table 1**. These values were determined by simulating, through the SYS Cam-clay model, the mechanical behaviors of undisturbed specimens sampled from the region under consideration. The specific volume and degree of structure within each layer were assumed to be uniform. The overconsolidation ratio was distributed according to the overburden pressure.

Table 1 List of elasto-plastic parameters used in the analysis

	Tertiary mudstone	Diluvial sand	Riprap	Reclaimed clay	Reclaimed sand
Elasto-plastic parameters					
Critical state index M	0.60	1.20	1.85	1.60	1.20
NCL intercept N	2.10	1.985	1.82	2.51	1.985
Compression index $\tilde{\lambda}$	0.17	0.05	0.02	0.21	0.05
Swelling indes $\tilde{\kappa}$	0.003	0.0002	0.0005	0.02	0.0002
Poisson's ratio ν	0.3	0.3	0.33	0.3	0.3
Evolution parameters					
Degradation index of structure a	0.01	2.0	3.0	0.6	2.0
Ratio of $-D_v^p$ to $\|D_s^p\|$ c_s	1.0	1.0	0.95	0.3	1.0
Degradation index of OC m	10.0	0.12	0.06	5.0	0.12
Rotational hardening index br	0.001	1.5	0.01	0.001	1.5
Limitation of rotational hardening m_b	1.0	0.8	0.9	1.0	0.8
Soil particle density ρ_s (g/cm3)	2.707	2.675	2.65	2.754	2.675
Mass permeability index k (cm/s)	1.0×10^{-7}	1.0×10^{-4}	1.0×10^{-3}	2.0×10^{-7}	1.0×10^{-4}
Initial conditions					
specific volume v_0 (unit weight γ_{sat})	1.70 (2.00)	1.79 (1.94)	1.65 (2.00)	2.95 (1.60)	1.916 (1.87)
stress ratio η_0	0.545	0.545	0.0	0.0	0.0
degree of structure $1/R^*_0$	50.0	1.2	1.0	9.0	2.0
degree of OC $1/R_0$	1.3×10^2～ 3.8×10^3	6.8×10^1～ 6.8×10^3	5.7×10^3～ 1.4×10^9	1.5×10^0～ 4.1×10^1	3.9×10^1～ 1.1×10^2
degree of anisotropy ζ_0	0.0	0.0	0.0	0.0	0.0

As earthquake motion, the seismic waveform of the *Tokai-Tonankai-Nankai* 3-segment type subduction zone earthquake (**Fig. 2**) expected to occur in this region was input in the horizontal direction to all finite element nodes at the bottom face of the ground. Based on the results of PS logging, the bottom face viscous boundary (Vs = 600 m/sec) was set at the nodes at the bottom end of the ground. In addition, simple shear deformation boundaries were allocated to the elements at the boundaries on both lateral ends (right and left ends) of the ground.

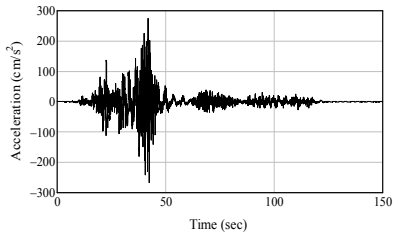

Fig. 2 Seismic waveform used in the analysis

CO-SEISMIC AND POST-SEISMIC GROUND DEFORMATION BEHAVIOR

The variations in the distributions of the mean effective stress p' and shear strain ε_s with time are illustrated in **Figs. 3 and 4**, respectively. In the weak reclaimed sand, p' becomes zero immediately after the start of the earthquake and liquefaction takes place. Because of the long duration of the earthquake, a decrease in p' is seen even in the diluvial sand and reclaimed clay, and consolidation settlement occurs in these soils along with dissipation of the accumulated excess pore pressures after the earthquake. Looking at the ε_s, it is prominent in the diluvial sand directly below the riprap mound during the earthquake. After the earthquake, ε_s in the reclaimed clay increases along with consolidation settlement. It appears that in locations that is subjected to large eccentric loads, such as the area directly below the revetment, ε_s becomes large because the ground becomes disturbed as a result of the earth tremors.

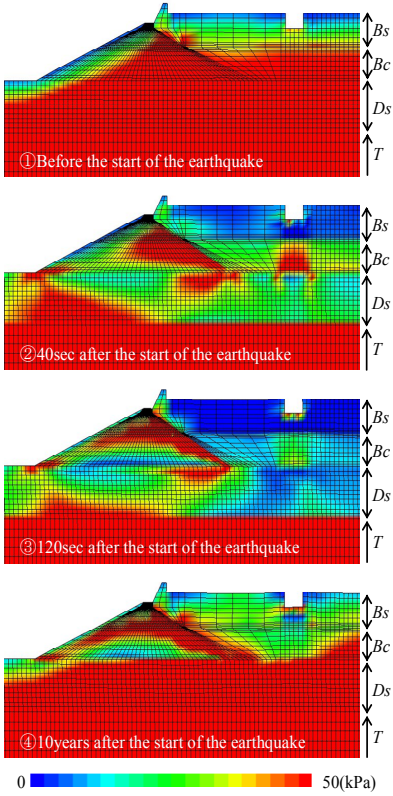

Fig. 3 Mean effective stress distributions

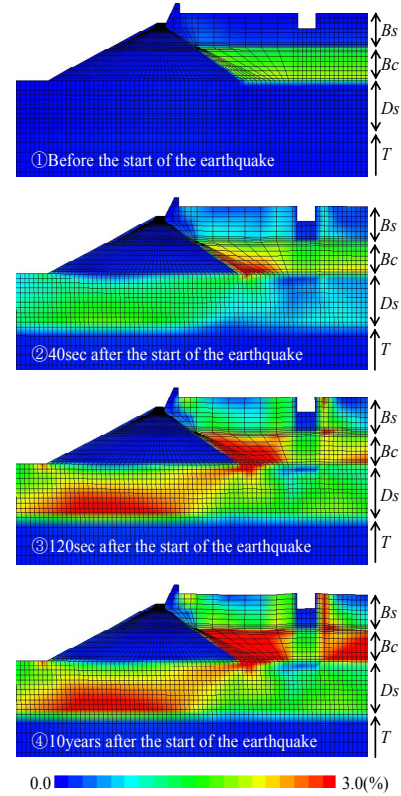

Fig. 4 Shear strain distributions

Figure 5 shows the amount of settlement of the different layers in the flat ground situated 200 meters inland from the revetment. There is no appreciable settlement during the earthquake. However, about 10 cm of settlement occurs in the reclaimed sand over an approximately 3-day period commencing from the time immediately after the end of the earthquake. In the reclaimed clay, about 10 cm of settlement also occurs over an approximately 4-year period beginning from the 3rd day after the start of the earthquake. This shows that large settlement is exhibited not only by the liquefied reclaimed sand, but is also exhibited by the reclaimed clay.

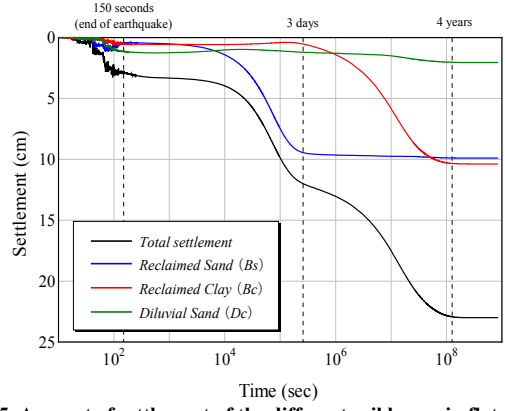

Fig.5. Amount of settlement of the different soil layers in flat ground

The deformations (settlement and displacement) that occur in the revetment and underground structure due to the earthquake are shown in **Table 2**. The case in which the underground structure is not supported by piles (i.e., corresponding to the case of the piles being broken by the earthquake) is also shown in the same Table. Irrespective of the presence of the piles, the revetment exhibits about 8 cm of settlement together with about 40 cm of lateral displacement towards the sea, mainly due to deformation of the diluvial sand directly beneath it. In the case of the underground structure, there is almost no settlement when the piles are there to support it. When there is no pile support, not only does the horizontal displacement become greater, but the structure is also lifted upwards because it is lightweight. This upward lifting is caused by the liquefaction that occurs in the reclaimed sand.

Table 2. Deformations occurring in the revetment and underground structure

		with ***Pile***	without ***Pile***
Revetment	Settlement	7.9cm	8.3cm
	Displacement	40.9cm	38.3cm
Underground structure	Settlement	1.1cm	-23.9cm
	Displacement	29.6cm	41.4cm

CONCLUSION

Modeling and seismic response analysis of a reclaimed offshore artificial ground were carried out in this study. The vulnerability of the weak reclaimed layers to seismic activity was pointed out, and the weak locations were identified. The conclusions obtained are as follows.

1) In the reclaimed sand, lateral flow and upward lifting of lightweight underground structures occurred due to liquefaction during the earthquake.
2) Because of the long earthquake duration, a large decrease in mean effective stress took place in the reclaimed clay, which exhibited long-term settlement that will continue for several years after the earthquake.
3) Compared with flat ground, large deformations occur in locations such as those immediately below revetments, which are subjected to large eccentric loads. This is because of the occurrence of ground disturbance in such areas due to seismic activity.

ACKNOWLEDGMENTS

This work was supported by JSPS, KAKENHI (Grant-in-Aid for Scientific Research (S):21226012).

REFERENCES

Asaoka, A., Nakano, M. and Noda, T. (1994) “Soil-water coupled behaviour of saturated clay near/at critical state” *Soils and Foundations*, Vol. 34(1). 91-105.

Asaoka, A., Noda, T., Yamada, E., Kaneda, K. and Nakano, M. (2002). “An elasto-plastic description of two distinct volume change mechanisms of soils” *Soils and Foundations*, Vol. 42(5): 47-57.

Asaoka A. and Noda T. (2007). “All soils all states all round geo-analysis integration” *International Workshop on Constitutive Modelling - Development, Implementation, Evaluation, and Application, Hong Kong, China*: 11-27.

Noda, T., Asaoka, A. and Nakano, M. (2008). “Soil-water coupled finite deformation analysis based on a rate-type equation of motion incorporating the SYS Cam-clay model” *Soils and Foundations*, Vol. 48(6): 771-790.

The Application of the H/V Spectral Ratio Technique for Estimating the Site Characterization in the South of Iran

Mehdi Mokhberi[1], Mohammad Davoodi[2], Ebrahim Haghshenas[2]

1.Azad Islamic university, Estahban Branch, Iran m-davood@iiees.ac.ir
2.International Institute of Earthquake Engineering and Seismology, Tehran, Iran,
mmmokhberi@yahoo.com, haghshen@iiees.ac.ir

ABSTRACT: As microzonatin studies, microtremor measurements were carried out in many cities in Iran and the resonant frequency of each station was estimated from the peak at the spectral ratio between the horizontal and vertical component. For many of these stations the thickness of the sedimentary cover was known by conducting boreholes or geophysical investigations, and a clear correlation between the resonance frequency and sediment thickness was observed. Three of these cities are located in the southern part of Iran near the sea (Persian Gulf). We attempted to derive a formula to correlate the frequency of the H/V peaks to the soil profiles properties such as thickness, materials properties and shear wave velocity. In addition, by using all of these microtremor measurements and applying the derived relationship, we tried to estimate the basin shape for these areas.

INTRODUCTION

Nowadays, microzonation studies are carried out for site characterization and disaster mitigation in urban areas in several countries. Several methods are used to recognize the soil properties and soil layer profiles. The formal surveying techniques, such as geophysics or boreholes are being used, however, these methods are too expensive and too much time is spending on the exploration and analysis of data**.** It must be pointed out that the new approach introduced by Nakamura (Nakamura, 1989) applied to geotechnical and geophysical researchers and was relayed by several studies emphasizing the stability of the H/V ratios (Lermo and Chavez-Garcia 1994; Duval 1994; Duval et al. 1995, Aki 1957; Milana *et al.* 1996; Bard 1998; Ohmachi and Umezono 1998). Since then, the estimation of the natural frequencies of the soil profiles from horizontal to vertical (*H*/*V*) spectral ratio by use of the single stations method has become common (Kudo 1995; Bard 1998). Although the physical basis of the method and its actual relevancy regarding the estimation of the site effect still remain a controversial issue. The use the H/V technique spreads very rapidly worldwide and many researchers attempted to use this method as a tool for site characterization programs. Moreover, some researchers showed the correlation between frequency and depth (Ibs-Von Seht M. 1999; Parolai 2002; Hinzen, 2004).

Within the framework of extensive microzonation programs in Iran, many cities were studied. The cities were selected in different regions in the south, center and north of Iran. Three of these sites are Bushehr, Gheshm Island and Pars Jonoobi (Site 3), located in the southern part of Iran in the coastal region of Persian Gulf. Some of the stations are near the coast and the others are farther, on the higher parts or on the slopes. The dynamic characteristics of the sites were recognized by geotechnical and geophysical investigations and the soil properties, such as shear wave velocity (V_s), pressure wave velocity (V_p), Electrical resistance, dominant periods (T_0) and SPT numbers. In addition, the predominant frequencies are obtained from horizontal-to-vertical ratio spectrum (H/V) measured by the single station approach. In each site the soil profiles were determined and the depth of seismological bed rock was estimated. The microzonation maps for these sites were prepared. The engineers are using these maps in structural analysis and urban disaster mitigation.

The geotechnical engineers make efforts to obtain the soil log through site investigations. As these methods have been costly and time-consuming, attempts to derive a formula to find the bed rock depth as a function of dominant frequency obtained from the H/V spectra ratio. This paper shows a separate formula for each site, as well as revealing the difference between the seismological coastal characteristics and farther land areas.

H/V SPECTRAL RATIOS AND FUNDEMENTAL FREQUENCIES OF RESONANCE

The microtremors are ambient ground vibrations excited by natural or artificial disturbances such as wind, sea waves, traffic, and industry. They can be recorded using sensitivity seismometers. The predominant frequency of resonance f_0 can be measured with microtremors. The spectral ratio between the recordings on the horizontal and vertical components exhibits a large peak at the fundamental frequency of resonance f_0, as long as the S-wave velocity contrast between the sediments and the bedrock is large. Figure 5 shows a measured H/V spectral ratio at a site with a strong velocity contrast between sediment and bedrock.

In cases where the shear wave velocity of the soft sediments is known from borehole information or seismic measurements, H/V spectral ratios can be used to estimate thickness of the soft sedimentary layer. By knowing the fundamental frequency of resonance, we also qualitatively know the expected amplification as a function of frequency: The expected amplification is in general large at the fundamental frequency of resonance and significant for the frequency range above, but absent in the frequency range below about $f_0/2$.

The amplitude of the H/V spectral ratio at the fundamental frequency f_0 indicates the S-wave velocity contrast between bedrock and sediments, and provides information on the severity of possible resonance effects during earthquakes and the depth of bed rock. The higher the amplitudes, the larger the velocity contrast will be. Furthermore, the amplitude of the H/V ratio depends not only on the velocity contrast but also on the source-depth and source-distance distributions. Therefore, amplitudes of the H/V ratio only qualitatively indicate possible resonance effects.

H/V spectral ratios can be considered a fingerprint of the local structure. By comparing measurements within an area, similar H/V curves are observed for similar local structures

and therefore show similar amplification effects during earthquakes. Such comparison can therefore be used to define a zone.

GEOLOGICAL AND GEOTECHNICAL CONDITON

BUSHEHR CITY:

Bushehr is a large city with a long coast and a harbour in southern Iran. Based on Iran's geological zonation, the Bushehr province is located in the Zagros zone. The Bushehr area has a simple structure which is confined to the NW-SE trending smooth folds, and which is consistent with the Zagros general trend. Mesozoic and Cenozoic units have outcropped; however, the Neogene sediments have mostly covered the area. The information about the Zagros basement originates from the gravitymetry and aeromagnetic measurements on the Arabian plate, the stratigraphic surveys, an amount of data about the Central Iran Basement, the salt domes, and the Hormoz rock fragments. Considering all the data, it is believed that the Zagros basement is the continuation of the N-NE Arabian-Nubian shield that enters Hejaz from NE Africa and is exposed to the western territories and continues to the East of Saudi Arabia under the sediments and lies below the Zagros Basin with a gentle slope related to the Dezful area. The conducted studies in the area have shown that the upper interface of the Zagros basement is too rough and has a complicated topography. The numerous tensional faults have been affected and reflected as surface and or near-surface thrusts. The Persian Gulf coast and its islands should be regarded as a part of the folded Zagros. According to the performed measurements, the lower interface of the basement lies between 35 and 55 km deep. It is known that the basement is 25-50km thick.

The oldest earthquake that occurred in the Bushehr province was recorded in 1925. The longitude and latitude of the earthquake epicentre are 28.54 and 51.82, respectively. Its magnitude is 5.3 on the Mb scale. The latest recorded earthquake in the Bushehr province was in 2004. The longitude and latitude of the earthquake epicentre are 29.68 and 50.36, respectively. Its magnitude is 3.8 on the Mb scale. The powerful earthquake recorded in the Boushehr province was in 1925. The longitude and latitude of this earthquake epicentre are 28.79 and 51.35, respectively. Its magnitude is 6.1 on the Ms scale and 5.6 on the Mb scale.

GHESHM ISLAND:

Qeshm is the largest island in the Persian Gulf. It has the Zagros geostructural and geomorphologic province. The main structures are the anticlines that have different axial trends, posterior axial changes, and salt diapers. The most prominent geological formations added to the Late Proterozoic/Early Paleozoic salt complex of the Namakdan Group (southwest of Island) are the outcrops extended from the Mio-pliocene to the Early Pleistocene and the marly and sandy- to- silty deposits of the Mishan-Agha Jari and younger equivalent formations with the Quaternary coverage, especially the calcareous Marine terraces. In addition to the calcareous Marine terraces, the other important quaternary deposits consist of the unconsolidated sandy alluvial fans, the sandy- to- silty alluvial plains, and the sand dunes.

The recent studies indicate that the region around the Gheshm has experienced 17 events since 1336 A.D. It has been reported that the epicentre of four of them is within the Qeshm Island. It can be declared that one of Iran's most seismically active regions with a

large number of recorded instrumental earthquakes during the 20th century is located in the north of Qeshm Island in the mainland part (the Haji_Abad region, in the north of Bandar-Abbas). Geologically, some reverse and strike-slip faults parallel with the main structure of the island can be observed. The most prominent of them, located inside the island, is the Qeshm thrust fault with a length of 60 km, which passes from the south of the city of Qeshm to the south of Qeshm Airport. The field investigations confirm the existence of a left-lateral strike-slip component for this fault.

PARS JONOOBI (SITE 3):

The Site 3 is a special economic region located in Pars Jonoobi and about 300 KM in the east of the city of Bushehr. Its longitude and latitude are about 53.25 and 26.8, respectively. It has the Zagros geostructural and geomorphologic province. The faulting and folding progress has developed a continuous anticline and syncline the outcrop thereof has two parallel surfaces in the NS and ES directions. This region has the same geostructural features as the other coastlines in the Persian Gulf.

This region is located between two neighbouring provinces, that is, Bushehr and Hormozgan and has been affected by the different earthquakes that had occurred in these regions. The biggest earthquake is the same as that recorded in 1925. The longitude and latitude of the earthquake epicentre are 28.79 and 51.35, respectively as mentioned above. Its magnitude is 6.1 on the Ms scale and 5.6 on the Mb scale.

DATA AND DATA PROCESSING

DATA:

The data used in this study was prepared from two types of approach. First, the seismological bed rock depth was obtained from the soil profile of the microzonation studies. These profiles specify the soil layer properties from the surface to the bottom of the soil log. The shear wave (V_S), pressure wave (V_P), electrical resistance and depth of the bedrock are shown in the soil log. Each site soil profile is produced by several methods i.e. the resistivity method (fig. 2), the refraction (fig. 3), as well as the downhole and microtremor (fig. 4). Second, the resonance frequencies (f_0) were obtained from the H/V spectral curve (fig. 5).

24 stations in the Bushehr site, 19 stations in Gheshm and 35 stations in Pars Jonoobi (Site 3) were selected. By use of these two couples of data, the relationship between the depth and the predominant frequency was determined.

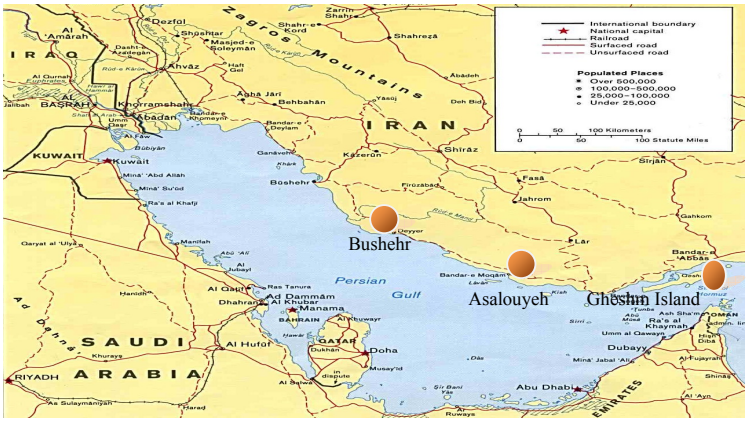

FIG. 1. Location of asaluyeh, Bushehr and Gheshm Island in the Persian Gulf coastal region

DATA PROCESSEING

For all the sites the microtremors were measured and the H/V spectral ratios were calculated by the procedure used in the Geopsy software packages prepared by the SESAME group. These measurements were performed during the microzonation studies measured by Guralp velocimeters (CMG-6TD) in a 30- minute window and by sampling the frequencies of 100 samples per second. The noise windows were selected automatically. In order to be within the safe scope, the non-stationary transients presented on the ambient noise recordings, such as those produced by local traffic, were excluded from the calculation. For sites without specific noise measurements, the H/V ratio was computed using some arbitrary portions in the case of the continuous recording mode. Concerning the minimum number of cycles per window and the minimum number of windows, we did our best to follow the recommendations adopted by the SESAME H/V user guidelines. For each

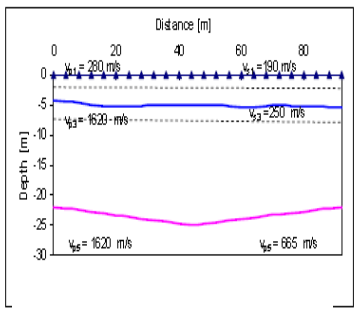

FIG. 3. A sample of refraction profile

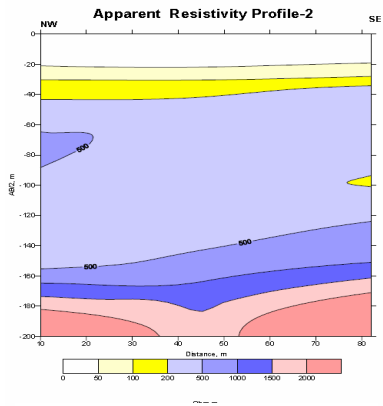

FIG. 2. Typical electrical resistivity profile

station the predominant frequencies (f_0) from the H/V spectrum curve were estimated. The H/V spectrum curves with clear peaks were selected.

Finally, for the three sites, the seismological depth was estimated by the microzonation studies in all the stations. All the data were arranged and the depth and the related predominant frequencies of these stations were selected. Using these couples of data, we analyzed the dynamic soil properties and found the best fit formula that shows the correlation between the depth and the predominant frequencies. The conditions of each site were determined by a certain formula.

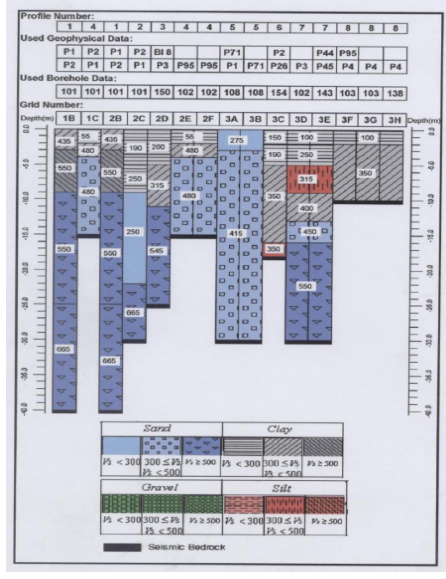

FIG. 4. Some Soil profiles obtained from several methods (IIEES)

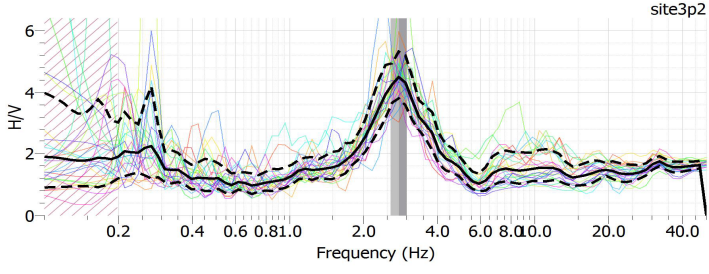

FIG. 5. Typical amplification functions of the spectral analysis category

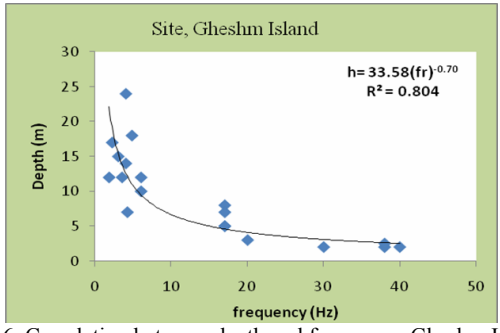

FIG. 6. Correlation between depth and frequency, Gheshm Island

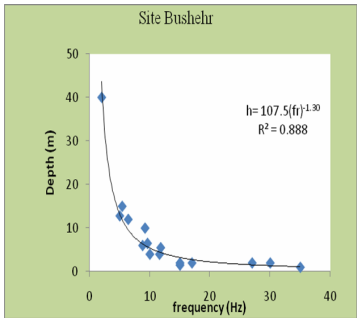

FIG. 7. Correlation formula for Bushehr city

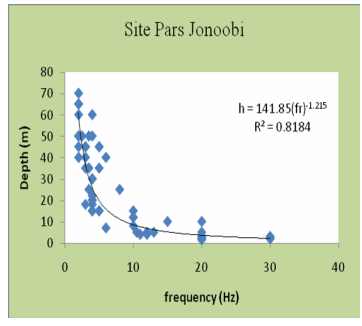

FIG. 8. Correlation formula for site 3

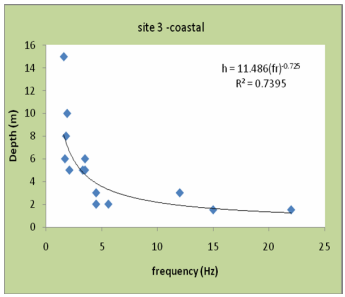

FIG. 9. Correlation Formula for costal region

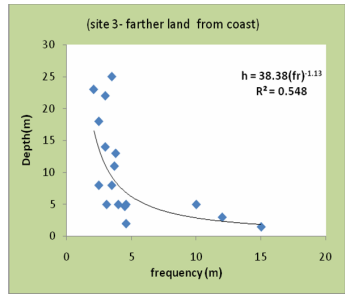

FIG. 10. Correlation Formula for non- coastal region

RESULTS

The evaluation shows a meaningful correlation between the predominant frequencies and the bed rock depth. The results have been summarized as follows:

a) For the site, Bushehr, the correlation formula is:

$$h=107.5(fr)^{-1.30} \quad (1)$$

b) For the site, Gheshm Island, the correlation formula is:

$$h = 33.58(fr)^{-0.70} \quad (2)$$

c) For the site, Pars Jonoobi, the correlation formula is:

$$h = 141.8(fr)^{-1.21} \quad (3)$$

Also, the data on Pars Jonoobi for coastal stations and farther land areas was separated and compared. As can be seen in fig. 7 and fig. 8 the correlated formulas are:

d) For the coastal stations in Pars jonoobi, the correlation formula is:

$$h = 11.48(fr)^{-0.72} \quad (4)$$

e) For farther land areas in Pars jonoobi, the correlation formula is:

$$h = 38.38(fr)^{-1.13} \quad (5)$$

Generally, the best fitted formula for all situations can be written as:

$$h=a(fr)^{-b} \quad (6)$$

The parameters *a* and *b* are not constant and vary with the soil property and layer conditions. These conditions will be evaluated by the studies to come.

CONCLUTION

In this research we evaluated the soil layer properties and the depth of the seismological bed rock and compared them with the predominate frequencies. We arrived at two conclusions. One is that for the three sites i.e. Bushehr City, Gheshm Island and Pars Jonoobi the formulas correlating the depth with the frequencies were derived. The other one is that the formulas related to the coastal regions are alike and the formulas belonging to farther land areas are similar as well. These formulas help engineers to estimate the bedrock depth as well as shear wave velocity without any excavation.

ACKNOWLEDGEMENTS

This paper was funded by the data collection from IIEES (International Institute of Earthquake Engineering and Seismology) , Tehran, Iran. The authors are grateful to the head of the geotechnical faculty, technical staffs and the geotechnical lab due to their collaboration. They also thanks to head of the Islamic Azad University, Estahban Branch for prepare the facilities.

REFERENCES

Bard and the SESAME participants (2004), Practical user guidelines and software for the implementation of the H/V ratio technique: measuring conditions, processing method and results interpretation, 13th World Conference on Earthquake Engineering, Vancouver, Paper No 3132

Ibs-Von Seht M., Wohlenberg J. (1999) Microtremor measurements used to map thickness of soft sediments. Bull. Seism. Soc. Am 89:1, 250–259.

Haghshenas E., Bard P.-Y., Theodulidis N., SESAME WP04 Team (2008) Empirical evaluation of microtremor H/V spectral ratio Bull Earthquake Eng, . 6:1, Jun, 74-108

Haghshenas, M. Khandan Bakavoli and R. Ghods-Azar (2009) Site Effect Evaluation In Qeshm Island (Iran) Using Earthquake Recording and microtremor Measurements. 14th World Conference on Earthquake Engineering, Beijing, Paper No 53

Lermo J. , Chaves-Garcia, F.J. (1993). Site Effect Evaluation Using Spectral Ratios With Only One Station, Bull. Seism. Soc. Am. 83:5, 1574-1594.

Parolai S., Bormann P., Milkereit C. (2002) New Relationships Between Vs, Thickness of Sediments, and Resonance Frequency Calculated by the H/V Ratio of Seismic Noise for the Cologna Area (Germany). Bull. Seism. Soc. Am 92:6, 2521–2527.

Efficient Algorithm Proposed to Generate Non-uniform Ground Motion on Canyon Sites

Reza Tarinejad [1] and Mohammad T. Ahmadi [2]

[1] Assistant Professor, Faculty of Civil Engineering, University of Tabriz, Tabriz, East Azerbaijan Province, Iran ; r_tarinejad@tabrizu.ac.ir
[2] Professor, Department of Civil Engineering, Faculty of Engineering, Tarbiat Modares University, Tehran, Iran ; mahmadi@modares.ac.ir

ABSTRACT: Many huge structures such as dams, plants and bridges located in canyon sites, are subjected to non-uniform ground motions and so their conventional type of analysis (assuming uniform ground motion) may lead to unreasonable responses. There is noticeable difference between the responses of huge structures to uniform and non-uniform ground motions. In order to conduct non-uniform dynamic analysis of this kind of structures, definition of seismic loading is a main challenge. In this research an efficient algorithm based on the numerical analysis of seismic wave components (P, SH and SV) and their combination is proposed using a single point given accelerogram record of the site. Thus, non-uniform seismic acceleration time series could be generated in different points of the site. Special purpose Boundary element code (TDASC) is developed in order to conduct seismic body waves scattering analysis at a canyon of arbitrary shape. Efficiency of this algorithm has been shown by re-generating the 24 October earthquake free-field accelerograms recorded at the Shafaroud dam site canyon in northern Iran. Comparison of the recorded and generated accelerograms for three different components along the canyon shows a good conformity.

INTRODUCTION

Uniform ground motion is an assumption that has often been made for structural analysis of different kinds of structures. However, it has been recognized for many years that the ground motion in a topographic irregularities during an earthquake is changed depending on how the location of the different points is. It is important to understand the nature of the input seismic ground motion to a huge structure such as dams, so realistic dynamic analyses can be performed for the purpose of safety assessment of existing and future dams. The first experience of the non-uniform ground motion effect was obtained at the Pacoima Dam site which was strongly shaken by the 1971 San Fernando earthquake. This site was later on shaken by the 1994 Northridge earthquake too. The acceleration records from both of these events

demonstrate the spatial non-uniformity of the ground motion.

In 1988 Kojic used a two dimensional seismic wave scattering analysis in order to generate non-uniform ground motion time series. The non-uniform ground motion was obtained by solving the two dimensional wave equation via Bessel and Hankel function expansions. Another work has been done recently by Huang. In this research the free field accelerograms along the Feitsui canyon are analysed and modeled by numerical scheme to study the effect of the canyon topography. In 2005 Alves presented an algorithm in order to generate non-uniform ground motions.

Based on the authors' knowledge there still no general algorithm in order to generate non-uniform ground motion from a single point record and all of the aforementioned researches need multiple information which are available only in rare cases. In this research in order to generate non-uniform ground motion at arbitrary points of the canyon topographies, numerical analysis using a single point record is employed. Seismic wave scattering analysis at an arbitrary shape canyon for different types of body waves (P, SH and SV) is used in the frequency domain. One single point ground motion record even in the free-field far from the canyon is sufficient for the proposed algorithm. The main innovation of this research is employment of a single given record of the site to generate ground motion on arbitrary points of the topographies using numerical analysis and a try and error process.

SEISMIC WAVE SCATTERING ANALYSIS

The numerical analysis of the seismic waves scattering from arbitrary shape canyon is carried out by the boundary element method. The arbitrary direction of any incident wave is defined by two θ_h and θ_v angles corresponding to the direction of the normal to the wave front, i.e., with the horizontal *x*- and the vertical *z*-axes. More elaborations could be found in Tarinejad et. al. The main assumptions for the analysis are as follows:

1- The canyon is homogeneous and isotropic.
2- Only body waves (P, SH and SV) is considered.
3- Incidence direction is considered constant for P and S waves.
4- Wave Incident direction is independent of the wave frequencies.
5- Analysis is in the frequency domain.
6- One recorded accelerogram is available along the free-field of the site.
7- Shear waves (SH and SV) are considered in phase.

Amplification function of an arbitrary point located on the canyon relative to the reference point for different kinds of body waves can be obtained in the frequency domain corresponding to each arbitrary wave incidence angle to the canyon site. The reference point can be selected at an arbitrary point along the canyon or on the free-field far from the canyon.

GROUND MOTION GENERATION ALGORITHM

The proposed algorithm includes mainly three parts. The first part of the algorithm is

used in order to approximate the seismic wave incident angle depending on if we know the active fault location or not. If the active fault location is known, the horizontal incident angle of waves can be assumed approximately the angle of the line between the canyon axis and the line connecting epicenter of the earthquake to the site. If we don't have any idea about the active fault location then available ground motion can be used in order to approximate the wave incident angle. In order to do this, first we should divide the recorded ground motion into τ and t-τ parts corresponding to the P- and the S-waves dominance. For P-wave dominant section, the try and error process can be used in order to obtain the incident angles of the seismic waves.

In the second part of the algorithm contribution factors α and β for different shear waves types can be obtained in the form of (αSH+βSV) using the try and error process. In this step the effect of P-wave on the second part of the accelerograms is ignored. In order to obtain factors α and β, a 20 percent increase step is assumed and the try and error process is used to achieve good conformity between the three components of the observed and the generated ground motions. The flowchart of the step by step process of the proposed algorithm is illustrated on Figure 1.

In the third part of the algorithm, the ground motion time series can be obtained from the Fourier transform of the available base record and the transfer functions. Fourier transform of ground motion of the arbitrary point of the canyon is obtained from the multiplication of the Fourier transform of the reference point and the transfer function corresponding to that point. The transfer function of an arbitrary point of the canyon can be obtained using the BEM wave scattering analysis corresponding to a specific type of seismic wave and incident angle. The transfer function for an arbitrary point is the frequency-dependent topographic amplification function which comes from the response amplitude of the arbitrary point relative to the corresponding response of the reference point. The methodology of the ground motion generation from the single reference point and numerical analysis for the specified point along the canyon is illustrated in Figure 2. Figure 3 shows the τ part and t-τ part of the accelerogram in order to approximate the incident angle of the seismic waves if the active fault location is not determined.

THE ASSUMED INVERSE PROBLEM SOLUTION

In order to demonstrate the proposed algorithm application, one simple problem is assumed and the time series at the base and one point along the abutments of the canyon are obtained from the seismic SH wave with specific incident angle. By using the inverse problem we showed that it is possible to re-generate the assumed time series from the proposed algorithm. These analyses showed that this algorithm is applicable and so can be used for real complex problems.

For this trial problem the semi-circular canyon with the points shown on Figure 4 is considered. Assumed time series at points '*f*' and '*a'* are obtained using seismic SH wave with an assumed angle of incident. '*f*' is the point along the free field enough far

from the canyon and used as a free field record, '*a'* is the highest point of the canyon abutment. With these available time series we should show that the proposed algorithm can predict time series for arbitrary points using the single point *f* time series. The normalized transfer functions for point '*a*' relative to '*f*' for different angles of incident are obtained and one case of them is shown in Figure 5. The time series corresponding to each case are obtained and one sample corresponding to the previous results is shown in Figure 6. The results show that good conformity between the assumed time series and the obtained ones is achieved for θ_h=90 and θ_v=60, and this could be accepted as the actual incident angle. This problem also clarified two other important facts.

1. The obtained time series on the base of the canyon is approximately similar to the free field recorded series. So the base records can be used as a reference point.
2. One side of the canyon may show amplification although the other side may show de-amplification depending on the seismic wave incident angle.

RE-GENERATION OF THE 24 OCT 2007 CASPIAN EARTHQUAKE

During the ambient vibration tests on the free field of the Shafaroud canyon in northern Iran when just three seismometers were installed, the 24 Oct 2007 Caspian earthquake with 3.2 magnitude happened. Figure 7 shows the epicenter of the earthquake and the Shafaroud dam site. Figure 8 shows the seismometers location along the free-field canyon. The first three stations (ST1, ST2 and ST3) recorded the earthquake before other stations could be installed. First the baseline corrections and suitable band pass filter were applied on the obtained records. For the corrected time series the corresponding acceleration and displacements were obtained by integration and differentiation on the recorded velocities.

The proposed algorithm was used in order to re-generate the time series of the 2007 earthquake using a single point record. The epicenter of the earthquake from the IIEES (International Institute of Earthquake Engineering and Seismology) site was obtained and so the horizontal incident angle of seismic waves was obtained from the angle of the line between the epicenter and the site. The approximated horizontal incident angle was obtained as 90 degrees.

Geometry of the canyon using the topographic information is defined. The boundary element mesh of the real geometry of the canyon is used for the numerical analyses of seismic wave scattering from the site. To achieve accurate results, the length of the canyon modeled is 5 times the depth of the canyon. The model used here has 2565 nodes and 616 nine-node surface elements.

Different analysis using different vertical incident angle has been done and the results are compared with the recorded ones on the points located along the abutments.

Different transfer functions for the different incident angles and components are obtained and one sample is shown in Figure 9.

The time series obtained from just one type of incident waves didn't show good conformity with the recorded time series. So in order to obtain good conformity it is necessary to combine different components of seismic body waves (SH and SV) with appropriate contribution. In order to achieve the appropriate contribution of seismic shear waves, try and error process has been done and comparison between the generated and recorded response has been done. The results show that there is good agreement between the recorded and generated time series for the contributions of 60 and 40 percents of SH and SV waves respectively. The comparison of time series obtained from the proposed algorithm corresponding to this contribution of seismic waves and recorded time series are shown in the same graph in the Figure 10. The same comparison is done on the response spectrum of the observed and generated ground motion for zero and five percent damping ratios and illustrated on Figure 11. In this research a 20 degrees increment for sweeping the vertical incident angle is assumed. So using these assumptions the maximum total number of the try and error process to get good agreements was about 30. The results show that there is good conformity between the results of the generated and observed ground motions and so the proposed algorithm can be used for real world complex problems with reasonable precision.

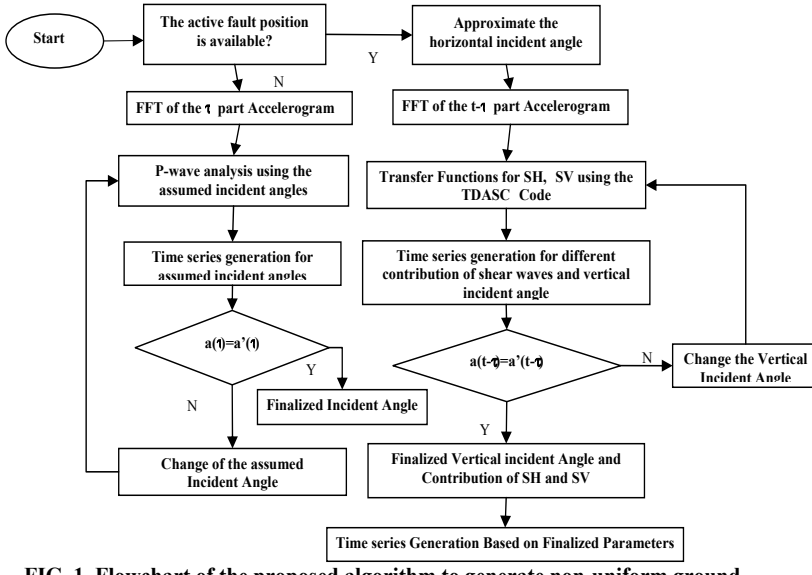

FIG. 1. Flowchart of the proposed algorithm to generate non-uniform ground motion

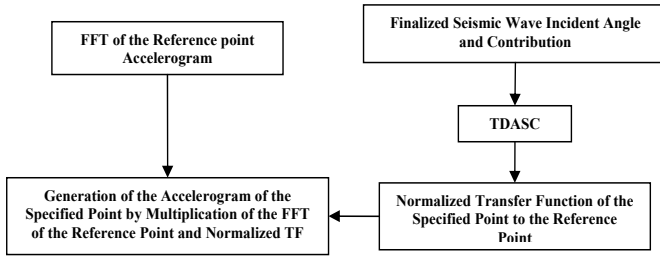

FIG. 2. Time series generation methodology for the specified point from the known time series of a single reference point and Numerical Analysis

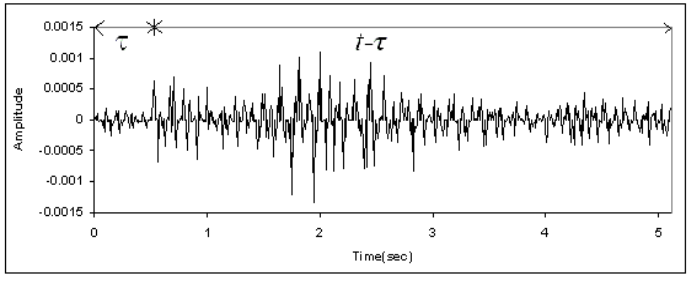

FIG. 3. The two splitted parts of the recorded accelerogram

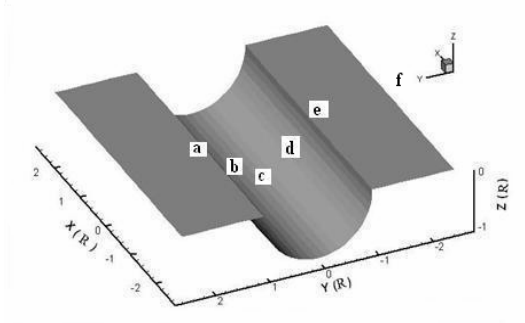

FIG. 4. The semi-circular prismatic canyon for the assumed trial problem

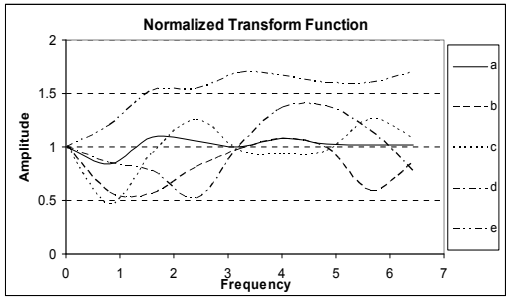

FIG. 5. Transfer functions obtained for different points along the free field of the assumed canyon for SH-wave with θ_h =90 and θ_v =60

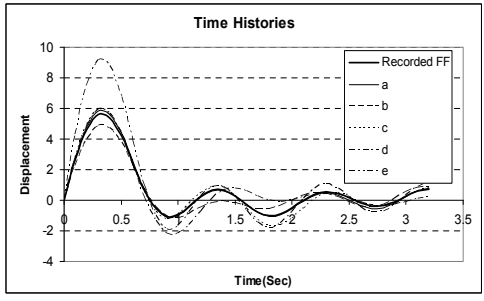

FIG. 6. Generated time series for different points along the canyon for the corresponding transfer functions presented on Figure 5.

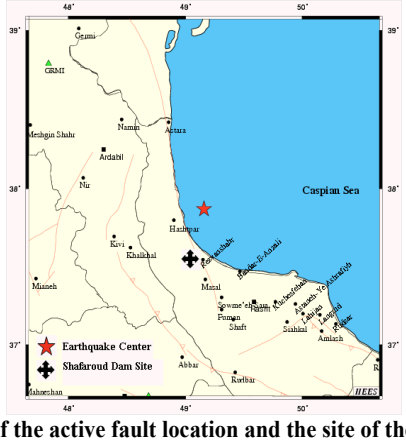

FIG. 7. The map of the active fault location and the site of the Shafroud canyon site

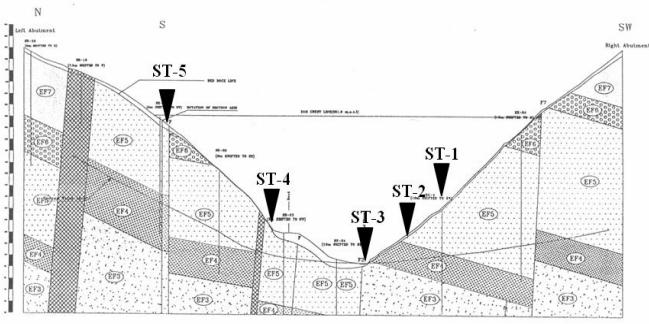

FIG. 8. The Shafaroud canyon cross section and the recording stations location

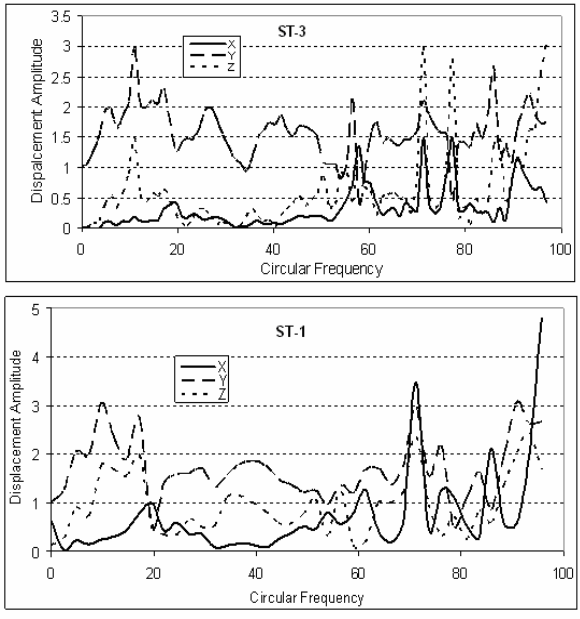

FIG. 9. Transfer functions obtained for two different stations for SV-wave with θ_H=90 and θ_V =0

CONCLUSIONS

A novel algorithm to generate non-uniform ground motion on canyon topographies based on only a single available time series of an arbitrary reference point is proposed. A BEM numerical analysis of the different scattering seismic body waves components

and a try and error process for combining them with appropriate contribution is employed.

The feasibility and efficiency of the proposed algorithm is shown using an inverse problem and also by re-generating of the 24 Oct 2007 earthquake records along the Shafaroud dam site.

If the active fault location is known, the try and error process to generate the time series is reduced significantly. Using suitable increment for sweeping of unknown parameters (contribution factors and incident angle) leads to an acceptable number of try and error process to get good agreements. If the active fault location is not known, more try and error process are needed using the first part of the accelerogram related to p-waves. The seismic wave incident angle will be obtained from this extra process and the same process as previous case will be done in order to generate non-uniform ground motions.

Three dimensional seismic wave scattering analysis from arbitrary shape canyon is done using TDASC code and so this algorithm can be used for the real world complex problems.

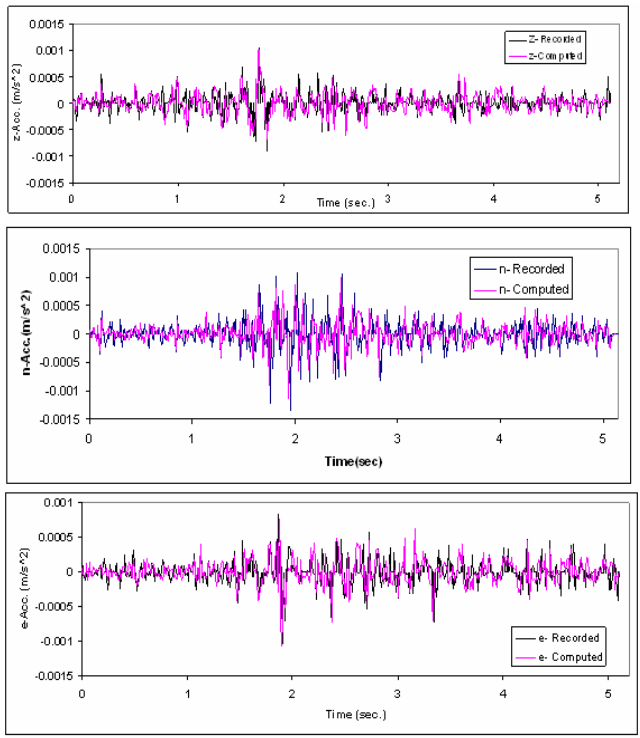

FIG. 10. Comparison of the recorded and computed accelerogram for different components at station 1(ST1) using the reference station records (ST3)

ACKNOWLEDGMENTS

The authors appreciate the help of the International Institute of Earthquake Engineering and Seismology (IIEES) and the Mahab Ghodss Consulting Engineers Company.

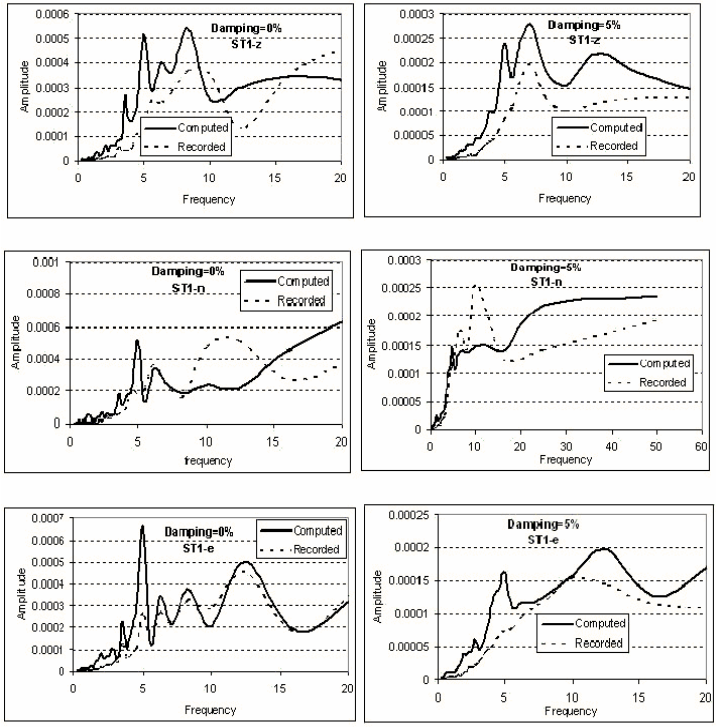

FIG. 11. Comparison of the response spectrum of the recorded and the computed accelerograms for different components at ST1 for zero and 5% damping ratios

REFERENCES

Alves, W.S. (2005). "Nonlinear analysis of Pacoima Dam with spatially Non-uniform Ground Motion", PhD Dissertation, California Institute of Technology.

Huang, H.C. and Chiu, H.C. (1995). "The effect of canyon topography on strong ground motion at Feitsui Damsite:Quantitive Results", Earthquake Engineering and Structural Dynamics, Vol. 24: 977-990.

Kojic,S.B. (1988). "Earthquake response of arch dams to non-uniform canyon motion", PhD Dissertation, Southern California University.

Tarinejad, R., Ahmadi, M.T., and Khaji, N. (2007). "Analysis of topographic amplification effects on canyon sites using 3D boundary element method", JSEE, Spring and Summer, Vol. 9(1): 63-72.

Tarinejad, R. (2008). "Seismic Loading for canyon site structures", Ph.D. Thesis, Tarbiat Modares University, Tehran, Iran.

Earthquake Response Analysis of Soil Layers Using HFTD approach

A. Asgari[1], M. H. Bagheripour[2]

[1]PhD candidate, Civil Eng. Dept., University of Kerman, Kerman, Iran. Corresponding Author, P.O.Box 76175-133, Tel: +98 3413220054, E-mial: ali.asgari111@yahoo.com
[2]Assist. Prof., Civil Eng. Dept., University of Kerman, Kerman, Iran. P.O.Box 76175-133, bagheri@mail.uk.ac.ir

ABSTRACT: Hybrid Frequency Time Domain (HFTD) method is used to evaluate the nonlinear response analysis of soil layers due to the earthquake incident loads. Solution schemes by the frequency and the time domains are rationally combined to achieve an optimum solution procedure. Fast Fourier Transform (FFT) and Inverse Fast Fourier Transform (IFFT) are used for the transformation of the results from one domain to the other and vice versa. A computer program has been developed to calculate the nonlinear ground response based on HFTD concept. A rational iteration procedure is adopted in which the nonlinear effects are updated in time and depth of the soil layer system and convergence is checked to be within an adopted and predefined tolerance. Shear strength of soil is assumed to follow a nonlinear and hyperbolic relation with shear strains. The method developed here is fast and efficient which guarantees satisfactory results with considerable level of accuracy. Examples are solved and the validity of the results is discussed in the paper.

INTRODUCTION

Ground response analysis is usually conducted for prediction of the surface ground motions, developing design response spectrum, determination of dynamic stress and strains, and evaluation of the liquefaction potential. Methods introduced to calculate the ground response are commonly divided to linear, nonlinear and equivalent linear concepts. Unlike the linear analysis in which the shear modulus is basically assumed constant, the equivalent linear method introduced by Schenebel et al (1972) calculates nonlinear response where the soil parameters are repeatedly corrected according to the effective strains developed until an acceptable convergence is reached. Assimaki &Kausel (2002) have used equivalent linear analysis for ground response analysis. Borja et al (1999) have conducted the nonlinear ground response analysis using Finite Element Method (FEM). Using the well known method of Wilson-θapproach, Presti et al (2006) performed similar ground response analysis.

The method of HFTD is, in fact, a procedure that takes the advantages of both the time

domain and the frequency domain methods to optimize the solution particularly for nonlinear problems (Wolf 1986& 1988). In summary, by HFTD method, the equation of motion is solved in frequency domain and the nonlinearities are accounted for by the time domain analysis. Commonly, FFT and IFFT are used for the transformation of the results from one domain to the other and vice versa. A regular iteration scheme based on the well-known Newton-Raphson procedure is adopted in HFTD and in such a way that the variation of stiffness and damping in soil material is rationally followed on the soil's stress-strain curve until the convergence is reached. In the present paper, a software has been developed using MATLAB code of practice for ground response analysis based on HFTD. An advantage of the method is the capability of analysis of multilayer soil systems having diverse material characteristics.

PROBLEM DESCRIPTION AND MATHEMATICAL

A layered soil system including m layers overlain the bedrock is considered. The latter is denoted as $m+1$ th layer and is subjected to a seismic excitation for which the time history of the strong motion is available. A concise review and the main steps in an HFTD procedure developed here are described in the following (Asgari (2009)):

Step1. Performing FFT on the discrete values of the strong motion record, the frequency domain input at the bedrock is established:

$$u_{m+1}(\omega) = FFT\left(u_{m+1}(t)\right) = \sum_{\omega=1}^{N} u_{m+1}(t) w_N^{(\omega-1)(t-1)}\ ,\ w_N = e^{-2\pi i/N}\ ,\ i = \sqrt{-1} \qquad (1)$$

In which ω is the loading frequency and N is the number of discrete acceleration values. u_n is the displacement at the top of the n th layer.

Step2. The solution of the equation of motion based on the 1-D theory of wave propagation in visco-elastic soils is used to calculate the amplitudes of the steady state harmonic waves traveling up and down in the soil layers denoted by A_{n+1}, B_{n+1}:

$$A_{n+1} = \frac{1}{2}\left[A_n(1+\alpha_n)e^{iK_n^* h_n} + B_n(1-\alpha_n)e^{-iK_n^* h_n}\right] \quad B_{n+1} = \frac{1}{2}\left[A_n(1-\alpha_n)e^{iK_n^* h_n} - B_n(1+\alpha_n)e^{-iK_n^* h_n}\right] \qquad (2)$$

In which h_n and ρ_n are thickness and density, K_n^* is the complex wave number which $K_n^* = \omega / v_n^* = \omega\left(\rho_n / G_n\left(1+2i\xi_n\right)\right)^{1/2}$, v_n^* and α_n are the complex shear wave velocity and impedance ratio respectively ($\alpha_n = \rho_n v_{sn}^* / \rho_{n+1} v_{sn+1}^*$) of n th soil layer. At the ground surface $\tau = 0$ which governs the equality of $A_1 = B_1$. Using a recursive iteration scheme and adopting equations 2, we calculate A_2 and B_2 in terms of A_1 and A_3, A_4 in terms of A_2 and so forth … This iteration procedure is continued until A_{m+1}, B_{m+1} are calculated. Since all values of A_{m+1} and B_{m+1} are known, the displacement, stresses and strains are defined at any point of the soil stratum as a function of frequency ω of the steady state harmonic motion. The amplification functions for rigid and elastic bedrock are denoted by $f_{1n}(\omega)$ and $f_{2n}(\omega)$ respectively and are given:

$$f_{1n}(\omega) = \frac{A_n + B_n}{A_{n+1} + B_{n+1}} \qquad and \qquad f_{2n}(\omega) = \frac{A_n}{A_{n+1}} \qquad (3)$$

Step3. At this stage, the bedrock displacement $u_{m+1}(\omega)$ is multiplied by $f_m(\omega)$ which is the amplification function for m th layer. This results in the displacement at the surface of

m th layer known as $u_m(\omega)$. This process is repeated until the displacement at the surface of first layer $u_1(\omega)$ is obtained. Next, the displacements in time domain and at any depth in soil layers and also at any interface between the two adjacent layers, is obtained using IFFT procedure.

$$u_n(\omega) = f_n(\omega) \times u_{n+1}(\omega), \quad 1 \le n \le m \tag{4}$$

$$u_n(t) = IFFT\left(u_n(\omega)\right) = \frac{1}{N}\sum_{t=1}^{N} u_n(\omega) w_N^{-(\omega-1)(t-1)}, \quad w_N = e^{-2\pi i/N} \tag{5}$$

Step4. The shear strain at the middle of any given layer can be calculated as:

$$\gamma_n(t) = \frac{u_n(t) - u_{n+1}(t)}{h_n} \tag{6}$$

Step5. The shear modulus and damping ratio of the soil layers as well as the bedrock are updated using the shear strains obtained above and based on the soil's stress-strain curve shown in Fig 1. The curves in this figure have been proposed for sandy soils and rock by Seed et al (1970).

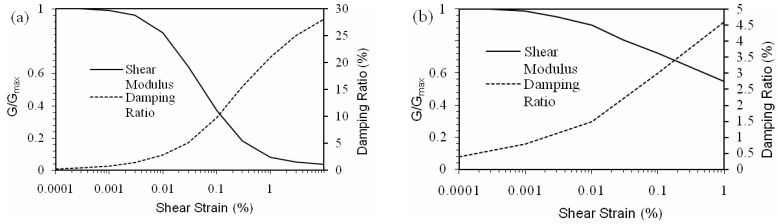

FIG. 1. Variation of shear modulus and damping ratio with shear strain amplitude for (a): sand and (b): rock

Step6. Considering the progressive Newton-Raphson procedure and the regular iteration used for nonlinear analysis, the Pseudo- linear displacements are calculated as:

$$\Delta u_{n,i}(t) = \frac{G_{n,i-1} - G_{n,i}}{G_{n,i-1}} \gamma_{n,i}(t) \times h_{n,i} \tag{7}$$

In which $G_{n,i}$, $\gamma_{n,i}(t)$ and $\Delta u_{n,i}(t)$ are the shear modulus, shear strain and Pseudo linear displacements at n th layer and in i th iteration respectively. In each cycle, the thickness of the layers is assumed to remain constant:

Step7. $\Delta u_{n,i}(t)$ is considered as the new input which is applied to the bedrock and response is calculated at the surface. The steps 1 to 7 above are repeated until the amplitude of $\gamma_{n,i}(t)$ become small enough or less than a prescribed value (i.e. $\gamma_{n,i}(t) \le$ error).

Step8. The sum of the responses obtained at the surface of the layered soil system in all iterations is obtained and is considered as the total nonlinear response of the system.

$$u_{tot}(t) = u_1(t) + \sum_{i=1}^{k} \Delta u_{1,i}(t) \tag{8}$$

In which $u_{tot}(t)$ is the total displacement at the ground surface and k is the number of cycles to reach the convergence.

The consecutive steps described above are integrated into a regular algorithm and a computer program has been developed in MATLAB software. The program receives the input data including the geometrical and mechanical properties of the soil layers as well as the information on loading characteristics. The output of the program includes the surface response including acceleration, velocity, and displacements in time domain and even, if required by user, the response spectrum of the layered soil system.

Example 1

A single soil layer overlain the bedrock is shown in Fig 2. The geometrical and mechanical properties of the soil and bedrock are all shown in Fig 2. In this figure, also the shear stress-strain curve for the soil material is depicted. The bedrock is subjected to a simple harmonic loading function such as $u_r(t) = A\sin(2t)$.

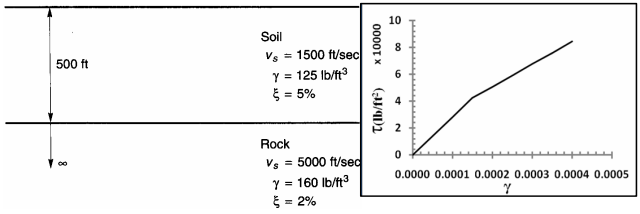

FIG. 2. Properties of Soil and Bed rock

The Fourier Transform of this loading function is obtained as:

$$u_r(\omega) = \sqrt{\frac{2}{\pi}}\int_0^{\infty} u_r(t)\sin(\omega t)dt \tag{9}$$

Substituting $u_r(t)$ in Eq. (9), we obtain:

$$u_r(\omega) = A\sqrt{\frac{\pi}{2}}\delta(\omega - 2) \tag{10}$$

In which ω is the loading frequency and δ is the Dirac function. The amplification function for the soil layer is calculated as:

$$|f(\omega)| = \left[\cos^2(K^*H) + \alpha^2\sin^2(K^*H)\right]^{-1} \tag{11}$$

Using the procedure described in preceding sections and forwarding through the steps 1 to 8 as well as repeating steps 1 to 6 (if necessary for convergence) we obtain the following relation for surface ground motion:

$$u_s(t)_{tot} = 1.359A\sin(2t) \tag{12}$$

In order to make a comparison between the linear analysis and nonlinear one, various frequencies are adopted for which the ground surface response are obtained using both nonlinear HFTD procedure proposed in this paper and conventional linear analysis. The amplification factors ($N(\omega)$) may simply be calculated as the ratio of ground surface displacement to that of the bedrock i.e. $N(\omega) = u_s(\omega)_{tot}/u_r(\omega)$.

The comparison is graphically shown in Fig 3(a). It is seen that by linear analysis, the amplified response in lower frequencies is smaller than that obtained by present nonlinear

HFTD analysis. As the loading frequency increases, the situation is reversed and nonlinear response becomes smaller than that of the conventional linear.

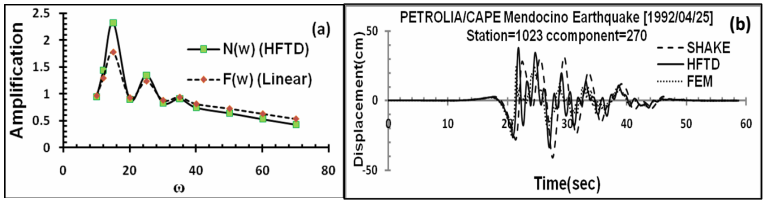

FIG. 3. (a). Comparison of linear and nonlinear amplification (b). Comparison of displacement of surface soil response due to Petrolia Earthquake

Example2

The same soil layer as that studied in example1 is considered again in this example. However, it is subjected to a transient loading. The acceleration time history of the Petrolia 1992 earthquake is adopted as the input and base strong motion. Figure 1 is used as the basic material behavior curve.

The whole soil layer is divided to 20 sub layers of equal thickness 27 ft (H=540ft). The response at the surface of soil layer is obtained using HFTD procedure. The results are also computed with those obtained by SHAKE and QUAKE/W code of practices. The SHAKE software is also used since this software adopts the conventional equivalent linear method for ground response analysis. In addition QUAKE/W is a geotechnical finite element software for the dynamic or seismic analysis of earth structures and makes use of FEM in time domain. Comparison between SHAKE and QUAKE/W with HFTD is shown graphically in Fig 3(b).

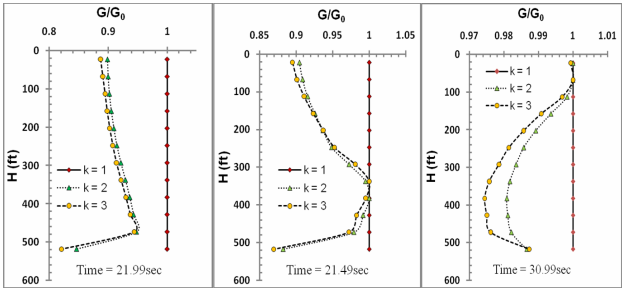

FIG. 4. Variation of shear modulus ratio with depth at difference number of iteration and time

In Fig 4, the variation of the G/G_0 (the ratio of the shear modulus at a given shear strain to the maximum shear modulus) at different depths in soil layer is shown. The number of iteration and time to reach the converged value of G/G_0 is depicted. For interested

readers, more discussion on the results is available in related references particularly in Asgari (2009).

CONCLUSIONS

HFTD approach takes the advantages of both the time domain and the frequency domain methods to optimize the solution procedure particularly for nonlinear earthquake response analysis of layered soil systems. A regular iteration scheme based on the well-known Newton-Rafson procedure is adopted in HFTD and in such a way that the variation of stiffness and damping in soil material is rationally followed on the soil's stress-strain curve until the convergence is reached. Illustrative examples were considered in this paper in which the results obtained by current approach and those obtained by analytical linear and also by other softwares were compared. They showed that HFTD is a reliable, fast, and efficient method and can be applied in variety of the geotechnical earthquake engineering.

REFERENCES

Schnabel, P.B. and Lysmer, J. and Seed, H. B. (1972). "SHAKE: a computer program for earthquake response analysis of horizontally layered sites." Report No. EERC72-12, University of California.

Assimakia, D. and Kausel, E. (2002). "An equivalent linear algorithm with frequency- and pressure-dependent moduli and damping for the seismic analysis of deep sites." *Soil Dynamics and Earthquake Engineering.*,Vol. 22: 959–965.

Borja, R. I. and Chao, H. Y. and Montans, F. J. and Lin, C.H. (1999). "Nonlinear ground response at Lotung LSST site." *J. Geotech Geoen. Engrg*., Vol. 125(3): 187–197.

Presti, L. and Diego, C. F. and Carlo, G. L. and Ignazio, P. (2006). "ONDA: Computer Code for Nonlinear Seismic Response Analyses of Soil Deposits." *J. Geotech Geoen. Engrg*., Vol. 132(2): 223–236.

Wolf, J. P. (1986). "Nonlinear soil-structure-interaction analysis based hybrid frequency-time domain formulation."Lisbon 2, 5.5/25-5.5/32. *Proc. 8th Eur. Conf. Earthquake Eng*.

Darbre, G. R. and Wolf, J. P., (1988). "Criterion of stability and implementation issues of hybrid frequency- time domain procedure for non-linear dynamic analysis."Lisbon 2, 5.5/25-5.5/32. *Proc.8th Eur .Conf. Earthquake Eng*.

Asgari, A. (2009). "Nonlinear Seismic Response Analysis of Soil Layers Using Hybrid Frequency-Time Domain (HFTD) Approach." A Thesis Submitted as a Partial Fulfillment of the Requirements for the Degree of M.Sc. University of Kerman.

Seed, H. B. and Idriss, I. M. (1970). "Soil modules and damping factors for dynamic response analysis." Report No. EERC70-10. university of California, Berkeley.

Earthquake Induced Liquefaction Potential of Reclaimed Areas of Dhaka City

Mohammad Shariful Islam and Md. Tanvir Hossain

[1]Associate Professor, Department of Civil Engineering, Bangladesh University of Engineering and Technology, Dhaka-1000, Bangladesh; mshariful@yahoo.com, msharifulislam@ce.buet.ac.bd
[2]Instructor, Department of Civil Engineering, Military Institute of Science and Technology, BUP, Dhaka, Bangladesh; tanvir5289@yahoo.com

ABSTRACT: Historical seismicity data and recent seismic activities in and around Bangladesh indicate that Bangladesh is at high seismic risk. The capital city Dhaka is situated in the seismic Zone 2, which has a basic seismic coefficient of 0.15g. Over the past 40 years, Dhaka city has experienced a rapid growth of urban population. This high population increase demands rapid expansion of the city. Unfortunately, most parts of the original ground have already been occupied. As a result, both government and private agencies are reclaiming different new areas. In most cases, the practice for developing such areas is just to fill lowlands (3~12 m) by dredged material, which is almost silty sand. This is inviting great liquefaction susceptibility for such reclaimed areas. The field SPT N-value of the filling depth varies from 1 to 13. Mean particle diameter and fines content of the fill materials vary from 0.10~0.32 mm and 6~48%, respectively. Liquefaction potential of selected reclaimed areas of the city has been estimated based on standard penetration test and shear wave velocity. It is found that some parts of the reclaimed sites are susceptible to liquefaction up to the filling depth.

INTRODUCTION

The historical seismicity data and recent seismic activities in and around Bangladesh indicate that Bangladesh is at high seismic risk. Bangladesh including capital city Dhaka is largely an alluvial plain consisting of fine sand and silt deposits with shallow ground water table in most places. Although the older alluvium is less susceptible to liquefaction, the deposits along the river flood plains may liquefy during a severe earthquake. Loose fills, such as those placed without compaction, are very likely to be susceptible to liquefaction. Over the past 40 years, Dhaka city has experienced a rapid growth of urban population. This high population increase demands rapid expansion of the city. Most parts of the city have already been occupied. As a result, new areas are being reclaimed filling low lands (3~12 m). Huge volume of soil is required to fill the lands. Because of severe road traffic congestion around the sites the filling soil has to come through river from adjacent river sources. Soil (which is almost silty sand) is collected from riverbeds by cutter-suction dredging into a barge, which is carried to the nearest river site. Soil is

then pumped through pipes in a slurry form after mixing with water, and transferred to the point of deposition. Lands reclaimed in this way inviting great liquefaction susceptibility.

A few researches have been conducted to estimate the liquefaction possibility in Dhaka city mainly based on Standard Penetration Test (SPT). Researches were also conducted to develop seismic microzonation map of Dhaka city based on site amplification and liquefaction. However, none of these past studies focused on the liquefaction vulnerability of the reclaimed areas of Dhaka city.

Ahamed (2005) evaluated the liquefaction potential of reclaimed areas of Dhaka city based on Standard Penetration Test (SPT). He observed that some parts of the reclaimed areas are susceptible to liquefaction. However, the reliability of the SPT data is questionable. On the contrary, small-strain shear wave velocity, V_s measurements provide a promising alternative, or supplement, to the penetration-based approach. The use of V_s as an index of liquefaction resistance is soundly based, since both V_s and liquefaction resistance are similarly influenced by void ratio, state of stress, stress history and geologic age, etc. As a whole, the precision of different kinds of shear wave velocity tests is higher than that of SPT. It has been, therefore, felt necessary to undertake a study to estimate the liquefaction potential of reclaimed areas of Dhaka city to gain definite knowledge on liquefaction susceptibility of such areas based on both SPT blow-count and shear wave velocity.

EXPERIMENTAL PROGRAM

In this study, liquefaction potential has been estimated based on SPT and shear wave velocity. For this purpose, SPT and shear wave velocity were determined up to 20m and 30m, respectively at different reclaimed sites of the city. During SPT, disturbed and undisturbed samples were collected at the same time water table was also located. Specific gravity, plasticity index and grain size of the samples were determined.

Small Scale Microtremor Measurement (SSMM) procedure of surface wave technique was used for determining the shear wave velocity. 'L' shaped array has been used to get microtremor data in seismograph. Total eleven geophones of 4.5 Hz are placed in an 'L' shaped array at 6 m interval with 30 m base. Total ten waveform data of 60 second duration were taken by seismograph. The seismograph was connected to eleven geophones at one end and with a laptop to the other end to view and record waveform data. Data was converted to shear wave velocity using 'SeisImager'.

ESTIMATION OF LIQUEFACTION POTENTIAL

SPT based evaluation was carried out based on Seed-Idriss simplified procedure (Seed and Idriss, 1971) and Japanese Code of Bridge Design (JRA, 1990). Methods proposed by Andrus and Stokoe (2000) as well as Yunmin et al. (2005) were used to evaluate the liquefaction potential based on shear wave velocity.

All the methods used in this research except the method proposed by Yunmin et al. (2005) defines the factor of safety against liquefaction as stated in Equation 1.

$$F_L = \frac{Cyclic \quad \text{Resistance} \quad \text{Ratio}}{\text{Cyclic} \quad \text{Stress} \quad \text{Ratio}} = \left[\frac{CRR}{CSR} \right] \tag{1}$$

where, F_L is factor of safety, CRR is the cyclic resistance ratio of the soil in question, CSR is the ratio of the equivalent uniform cyclic shear stress.

If $F_L \leq 1.0$, liquefaction is said to occur and otherwise liquefaction does not occur.

Cyclic Stress Ratio (CSR)

In all the methods that are used in this study except the method proposed by Yunmin et al. (2005), CSR is expressed as follows (Seed and Idriss, 1971):

$$CSR = \frac{\tau_{av}}{\sigma'_v} = 0.65\left(\frac{a_{\max}}{g}\right)\frac{\sigma_v}{\sigma'_v}.r_d \qquad (2)$$

where, $a_{\max}$ is peak horizontal ground surface acceleration, g is the acceleration due to gravity, σ_v is total overburden stress at depth z, σ'_v is initial effective overburden stress at the same depth z, r_d is stress reduction coefficient which depends on depth, z.

Cyclic Resistance Ratio (CRR)

1) Seed and Idriss Simplified Procedure (Seed and Idriss, 1971)

For a given $(N_1)_{60_{CS}}$ and earthquake moment magnitude, M_w=7.5 the following equation is used to determine $(CRR_{7.5})_{1_{atm}}$.

$$(CRR_{7.5})_{1_{atm}} = \frac{1}{34-(N_1)_{60_{CS}}} + \frac{(N_1)_{60_{CS}}}{135} + \frac{50}{[10*(N_1)_{60_{CS}}+45]^2} - \frac{1}{200} \qquad (3)$$

Here, $(N_1)_{60_{CS}}$ is the corrected normalized equivalent clean sand SPT blow count.

To adjust the $(CRR_{7.5})_{1_{atm}}$ to magnitudes other than M_w=7.5, the calculated $(CRR_{7.5})_{1_{atm}}$ is multiplied by magnitude scaling factor (MSF) corresponding to the design earthquake of moment magnitude, M_w. The recommended lower bound MSF value is:

$$MSF = \frac{10^{2.24}}{M_w^{2.56}} \qquad (4)$$

To adjust the cyclic resistance ratio to initial effective overburden pressures other than 1.0 tsf, the $(CRR_{7.5})_{1_{atm}}$ is multiplied by a correction factor $K_\sigma = \left(\frac{\sigma'_{vo}}{P_a}\right)^{(f-1)}$.

Finally, cyclic stress ratio is calculated as CRR= $(CRR_{7.5})_{1_{atm}}$ * MSF* K_σ

2) Japanese Code of Bridge Design (JRA, 1990)

Cyclic strength ($\sigma_{DL}/2\sigma_0$) is determined using the Eqns 5 and 6 depending on D_{50}.

For 0.04 mm $\leq D_{50} <$ 0.6 mm; $\left(\frac{\sigma_{DL}}{2\sigma'_0}\right)_{20} = 0.0676\sqrt{N_{1(c)}} + 0.225\log_{10}\left(\frac{0.35}{D_{50}}\right)$ (5)

For 0.6 mm $\leq D_{50} <$ 1.5 mm; $\left(\frac{\sigma_{DL}}{2\sigma'_0}\right)_{20} = 0.0676\sqrt{N_{1(c)}} - 0.05$ (6)

where, D_{50} is the mean particle diameter in mm, $N_{1(c)}$ is corrected SPT value for overburden pressure and fines content. If the plasticity index is higher than 10%, further

correction is made for cyclic strength.

3) Method Proposed by Andrus and Stokoe (2000)

Andrus and Stokoe (2000) proposed the following relation between CRR and V_{sl}:

$$CRR = \left[a\left(\frac{V_{sl}}{100}\right)^2 + b\left(\frac{1}{V_{sl}^* - V_{sl}} - \frac{1}{V_{sl}^*}\right)\right] * MSF \quad (7)$$

where, V_{sl} is overburden stress corrected shear wave velocity (m/s), σ_v' is initial effective overburden stress, (kPa). V_{sl}^* is the upper value of the V_{sl} for liquefaction occurrence(V_{sl}^*= 200 m/s for F_c>35%, V_{sl}^*=208 m/s for F_c=20% and V_{sl}^*=215 m/s for F_c< 5%), a and b are curve fitting parameters (a=0.022, b=2.8); MSF is magnitude scaling factor to account the effect of earthquake magnitude.

Method Proposed by Yunmin et al. (2005)

In this method, shear wave velocity, V_s of the susceptible soil is determined. Then liquefiable shear wave velocity, V_{sliq} has is determined using the following equation:

$$V_{sliq} = \sqrt{\frac{G_{(\max)liq}}{\rho}} = \left(\frac{0.65 a_{\max} z r_d \bar{\rho} F^2(e_{\min})}{r_c K^2 \rho^2}\right)^{1/4} \quad (8)$$

where, $a_{\max}$ is the peak horizontal ground surface acceleration, z is the depth of the soil, r_d is a shear stress reduction coefficient, $\bar{\rho}$ is the average density of the soil above the depth in question, $F(e)$= $(2.17\text{-}e)^2/(1+e)$ is the void ratio function, r_c is a constant to account for the effects of multidirectional shaking with a value between 0.9 and 1.0, and $K = 0.90\times10^{-4}$~1.22×10^{-4} $(\text{kPa})^{-1/2}$. $e_{\min}$ is assumed as 0.65.

Here, liquefaction is said to occur when $V_s < V_{sliq}$

SUB-SOIL CHARACTERISTICS AND SHEAR WAVE VELOCITY

The general soil profile is consists of filling sand layer overlaying a clay layer. However, in some locations a very soft organic layer exists between these two layers. The filling depth of the reclaimed areas varies from 3 to 12 m from Existing Ground Level (EGL). The field SPT N-value of the filling depth varies from 1 to 13. Mean particle diameter and fines content of the soil in the filling depth vary from 0.10 to 0.32 mm and 6 to 48%, respectively. Shear wave velocity of the filling layer varies from 70~125 m/sec. In some locations, soft organic clay layer is found just beneath the filling sand. Thickness of the soft layer varies from 3.0 to7.5 m. Field SPT N-value and organic content of the soft layer vary from 1~4 and 2 to 24%, respectively.

RESULTS AND DISCUSSIONS

Liquefaction potential analysis has been conducted at about 50 borehole locations at six reclaimed sites (Table 1). In the current analysis, the value of peak ground acceleration,

a_{max} has been taken as 0.15g. Some typical results have been presented in Table 1 and Fig. 1. It is seen that some parts of the reclaimed areas are liquefiable. Maximum liquefaction depth was found to be 13.5m below EGL. The mean particle diameter and fines content of the liquefiable soil vary from 0.14 to 0.32 mm and 8 to 27%, respectively. However, liquefaction potential determined using two methods based on SPT are different. Liquefaction potential analysis based on Japanese Code of Bridge Design considers the SPT, mean particle diameter and fines content of the soil in question. But Seed and Idriss method does not consider the effect of particle size. This might be the main reason for the differences in the results.

It is seen that liquefaction potential evaluated using two methods based on shear wave velocity is also different. The procedure proposed by Andrus and Stokoe (2000) is suitable for fine sand to sandy gravels with cobbles. So, this method seems suitable for liquefaction analysis of the study area. On the contrary, it seems that the method stated by Yunmin et al. (2005) is not suitable for sand with high fines content. It needs more investigations and validations for evaluating liquefaction potential for sands with high fines content using this method. However, the value of e_{min} has been assumed as 0.65 for the analysis. It may vary in the field which is yet to be clarified.

CONCLUSIONS

Many reclaimed areas are being developed in and around Dhaka city. Most of the reclaimed areas are being developed by filling dredged materials from riverbed, which is silty sand. Two methods based on SPT N-value and two methods based on shear wave velocity were used to evaluate the liquefaction potential of some selected reclaimed sites. It is found that some parts of the reclaimed sites are liquefiable especially up to the depth of filling (up to 13.5 m below EGL). However, liquefaction potential evaluated from different methods varied significantly. Further research is being conducted to select/develop a suitable method for proper evaluation of the liquefaction vulnerability of such reclaimed areas.

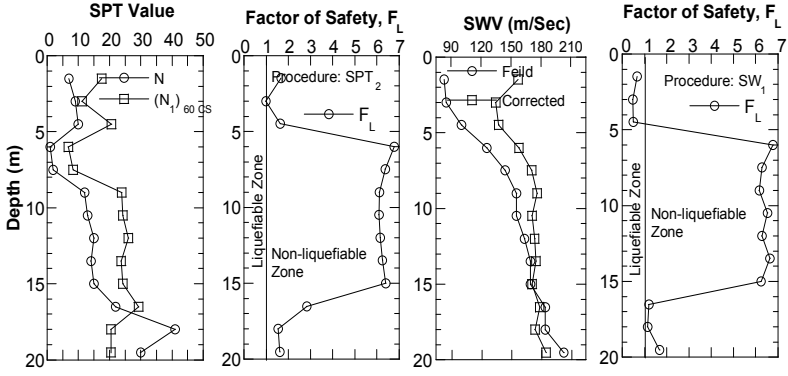

FIG. 1. Liquefaction potential evaluated based on SPT and shear wave velocity.

Table 1. Liquefaction depth and characteristics of the liquefiable soil

Location	BH	Properties of liquefiable soil			Liquefiable zone (m)			
	No.	Soil type	D_{50} (mm)	F_c (%)	SPT1	SPT2	SW1	SW2
Bashundhara	1	Fine sand	0.150	9	–	EGL~12.0	*	*
	2	Fine sand	0.149	10	–	EGL~ 13.5	*	*
	3	Fine sand	0.152	8	9.0~12.0	EGL~12.0	*	*
	4	Fine sand	0.149	18	1.5~4.5	1.5~4.5	*	*
	5	Fine sand	0.144	20	–	EGL~7.5	*	*
	6	Fine sand	0.170	12	–	1.5~4.5	1.5~4.5	–
Banasree	1	Fine sand	0.150	10	EGL~3.0	EGL~3.0	*	*
	2	Fine sand	0.160	19	–	1.5~4.5	EGL~6.0	–
	3	Fine sand	0.170	27	EGL~1.5	EGL~4.5	–	–
Mirpur DOHS	1	Silty sand	0.160	27	EGL ~1.5	EGL ~3.0	*	*
	2	Silty sand	0.160	27	1.5~4.5	1.5~4.5	*	*
	3	Silty sand	0.160	27	3.0~4.5	EGL~4.5	*	*
	4	Fine sand	0.170	19	–	1.5~4.5	EGL~6.0	–
Purbachal	1	Silty sand	0.320	6	1.5~3.0	1.5~3.0	*	*
	2	Fine sand	0.170	18	–	1.5~4.5	EGL~6.0	–
Kamrangirchar	1	Fine sand	0.140	23	EGL~3.0	EGL~3.0	EGL~3.0	–
Adabar	1	Fine sand	0.140	23	EGL~3.0	EGL~3.0	EGL~3.0	–

Note: SPT1: Japanese Code of Bridge Design (JRA, 1990); SPT2: Seed and Idriss (1971) method; SW1: method proposed by Andrus and Stokoe (2000); SW2: method proposed by Yunmin et al. (2005); *data not available.

ACKNOWLEDGEMENTS

The authors would like to acknowledge the cooperation of the Civil Engineering Department of Bangladesh University of Engineering and Technology during the ongoing M.Sc. Engg. research work of the second author. This paper has been prepared on the basis of the findings of the ongoing research. Authors also acknowledge the cooperation of the Geology Department of Dhaka University, Dhaka, Bangladesh for determining the shear wave velocity.

REFERENCES

Ahamed, S. (2005). "Soil characteristics and liquefaction potential of selected reclaimed areas of Dhaka city." M.Sc. Engg. Thesis, Department of Civil Engineering, Bangladesh Univ. of Engg. and Technology, Dhaka, Bangladesh.

Andrus R. D. and Stokoe K. H., (2000). "Liquefaction resistance of soils from shear wave velocity." *J. Geotech Geoenviron. Eng.* Vol. 126, No. 11, pp.1015–25.

Japan Road Association, JRA (1990). Specification for highway bridges, Part V: seismic design, Tokyo, Japan.

Seed, H. B., and Idriss, I. M. (1971). "Simplified procedure for evaluating soil liquefaction potential." *J. Soil Mechanics and Foundations Division*, ASCE, Vol. 97, No. SM9, Proceedings paper 8371, pp. 1249~1273.

Yunmin, C., Han, K. and Ren-peng, C. (2005). "Correlation of shear wave velocity with liquefaction resistance based on laboratory tests." *Soil Dynamics and Earthquake Engineering*, Vol. 25, pp. 461~469.

Seismic Hazard Assessment of Bandar Abbas for Seismic Retrofitting

G. Ghodarti Amiri[1], S.A. Razavian Amrei[2] and B. Mohebi[3]

[1]Professor, Center of Excellence for Fundamental Studies in Structural Engineering, School of Civil Engineering, Iran University of Science & Technology, Tehran, Iran, E-mail: ghodrati@iust.ac.ir
[2]PhD, School of Civil Engineering, Iran University of Science & Technology, Tehran, Iran
[3]PhD Student, School of Civil Engineering, Iran University of Science & Technology, Tehran, Iran

ABSTRACT: This paper presents a seismic hazard assessment of Bandar Abbas in southern of Iran. Four maps have been prepared to indicate the earthquake hazard of this region and its vicinity in the form of iso-acceleration contour lines. They display the probabilistic estimate of Peak Ground Horizontal Acceleration (PGHA) over bedrock for the return periods of 75, 225, 475 and 2475 years, which is the most common criterion in designing and retrofitting of buildings. This region is located at the edge where the Arabian plate pushes forward towards Iran plateau. Southern part of Iran plays an important role in economy of Iran. In this study, seismicity parameters are calculated based on a catalogue of both historical and instrumental earthquakes over an area of 200 km radius around the Bandar Abbas, by Kijko. In order to determine the PGHA, four different attenuation relationships have been used and mixed by using logic tree method. Finally seismic hazard analysis has been performed for region, by SEISRISK III for four hazard levels.

INTRODUCTION

Iran as one of the seismic countries over the Himalayan-Alpide seismic belt is an important region to study for seismicity. It is a country which has high risk of earth quake happening and many catastrophic earthquakes have destroyed and damaged some parts of it and killed many people.

Bandar Abbas located in south of Iran and north of Persian Gulf. Bandar Abbas, as the center of Hormozgan province due to existence of important political, economical and social has more special important than other cities in the south part of Iran. With respect to mentioned reasons, current study has been performed as seismic hazard assessment of Bandar Abbas for seismic retrofitting projects.

In the Iranian code of practice of seismic resistant design of buildings (BHRC, 2005), it has been placed in high seismic risk region and base acceleration of 0.3 g is recommended for Bandar Abbas.

SEISMOTECTONIC STRUCTURE OF BANDAR ABBAS

This region is located at the edge where the Saudi Arabia plate pushes forward towards Iran plateau and situated on the south plateau of Zagros Mountain. In order to evaluate the seismic hazard of a region or zone, all the probable seismic sources must be detected and their potential to produce strong ground motion must be checked. The major faults in Bandar Abbas region are MZRF, MFF, HZF, ZFF, Zendan-Minab, Giroft-Abzevaran, Chah Shirin, Giroft, Bashagard, Beach Makran, Faarooj, Roodan and Minab (IIEES). The location of these faults with respect to Bandar Abbas is shown in Figure 1, and the focal mechanism of main earthquake of Bandar Abbas region is shown in Figure 2.

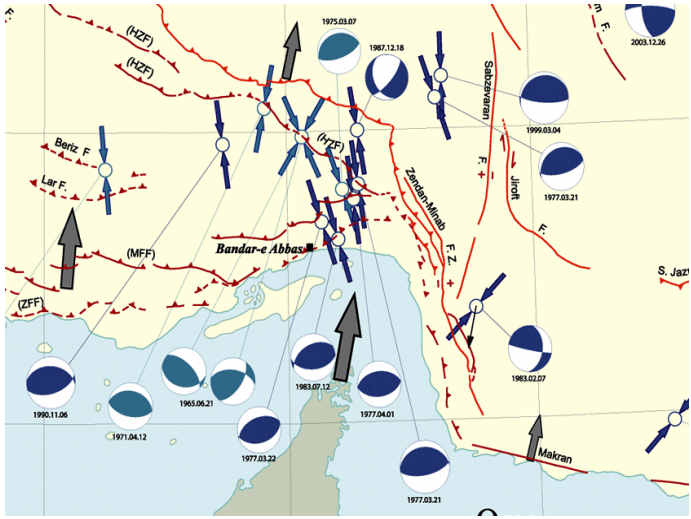

FIG. 1. The active faults of Bandar Abbas (IIEES)

SEISMICITY OF BANDAR ABBAS

The seismicity of each region is indicated by the past earthquakes occurred in that region and to obtain the seismotectonic properties, a thorough list of each region's earthquake events must be collected and studied.

The information of the earthquakes in radius of 200 km of Bandar Abbas, has been gathered from several references. The reason for the application of probabilistic method and its advantage over other methods are for the incompleteness of our seismic data regarding magnitude and focal depth of earthquakes. Seismotectonic and seismicity of Bandar Abbas region is shown in Figure 3. The occurrence of destructive earthquakes like the ones that occurred in 1361 AD Gheshm, in 1497 AD Bandar Abbas, and in 1622 AD Bandar Abbas, all show seismic hazards that threaten the region (Ambrasys and Melvile, 1982).

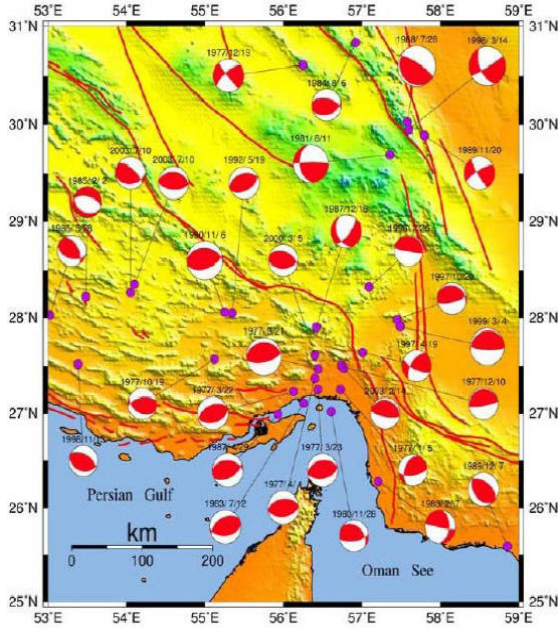

FIG. 2. Focal mechanism of main earthquake of Bandar Abbas region (IIEES)

The types of magnitude scales were not the same. To change these types to one scale, Equation 1, presented by the Iranian Committee of Large Dams IRCOLD (1994) was employed to transfer mb into Ms:

$$M_s = 1.2m_b - 1.29 \quad (1)$$

Where mb and Ms are body wave magnitude and surface wave magnitude.

SEISMICITY PARAMETERS OF BANDAR ABBAS

The evaluation of seismicity parameters is performed based on the seismic data of earthquakes occurred in the region under study and employing probabilistic methods. The seismic catalogue has been collected, assuming that earthquakes follow Poisson distribution. The method which is used to eliminate the foreshocks and aftershocks is the variable windowing method in time and space domains (Gardner and Knopoff, 1974).

Due to the very high importance of the seismicity parameters in seismic hazard evaluation, in this study the new Kijko (2000) method has been employed which is based on double truncated Gutenberg-Richter (1954) relationship and the maximum likelihood estimation method.

In the maximum likelihood estimation method, it is possible to use historic and instrumentally recorded data at the same time.

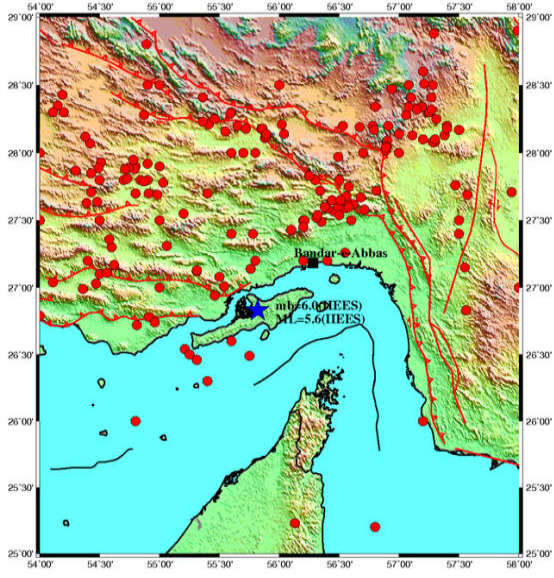

FIG. 3. Seismotectonic and seismicity of Bandar Abbas region (IIEES)

The annual average occurrence rate of earthquake versus magnitude for earthquakes with magnitude greater than Ms=4.0 in the extent of 200 km around Bandar Abbas is shown in Figure 4 based on these investigations and the performed calculations with Kijko method, and the results is shown in Table 1.

Table 1. Seismicity parameters of Bandar Abbas obtained by Kijko method

Catalogue	Parameter	Value	Data Contribution to the Parameters (%)		
			Case 1	Case 2	Case 3
Historical and Instrumental Data	Beta	1.82	44.1	15.8	40.1
	Lambda (Ms=4)	2.56	2.3	13.9	83.8

EVALUATION OF HORIZONTAL SEISMIC HAZARD

In order to evaluate Peak Ground Horizontal Acceleration (PGHA) for the return period of 75, 225, 475 and 2475 years, probabilistic seismic hazard analysis method has been used. In this method, seismicity parameters (β, λ) are given to the seismic sources based on the seismicity investigations, then based on earthquake magnitude, distance of epicenter or hypocenter from site and application of an appropriate attenuation relationship, Peak Ground Horizontal Acceleration (PGHA) at the corresponding site is

evaluated.

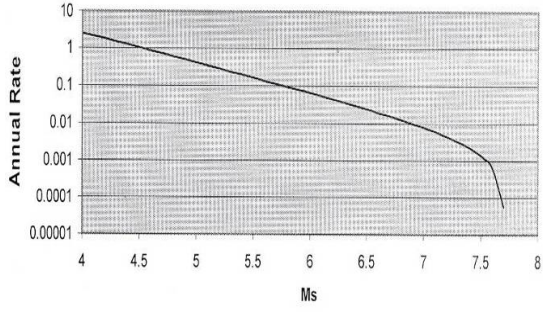

FIG. 4. Annual rates estimated by Kijko method for Bandar Abbas

The relationship between maximum expected magnitude and fault length depends on the understanding of the seismotectonic and geotectonic behavior of the concerned area. Nowroozi (1985) has offered Equation 2 after studying over ten severe earthquakes in Iran and observing active faults ruptures.

$$Ms = 1.259 + 1.244 Log(L) \tag{2}$$

Where Ms and L are surface wave magnitude and rupture length in meters.

ATTENUATION RELATIONSHIP

Selection of appropriate attenuation relationship is very important in validity and reliability of the analysis results. Therefore, there are some important notes that must be paid attention for the selection of attenuation relationship. The most important ones are source specifications, magnitude, fault rupture type, distance to the seismogenic sources, geology and topology of site.

Based on the mentioned remarks, in this research four weighted horizontal attenuation relationships; Ramazi (1999), 0.3; Ambraseys and Bommer (1991), 0.2; Ghodrati et al. (2007), 0.35; and Sarma and Srbulov's (1996), 0.15; in Logic Tree method were employed.

PROBABILISTIC SEISMIC HAZARD ANALYSIS

For the seismic hazard probabilistic evaluation, the software SEISRISK III (Bender and Perkins, 1987) was utilized to calculate the Peak Ground Horizontal Acceleration (PGHA) in the specific hazard level in the structure lifetime. The calculated values can be shown in the form of iso-acceleration lines for each specific hazard level in the structure lifetime. In this study the seismic hazard analysis carried out was based on the assumption of an ideal bedrock case and therefore no influence of local soil condition is taken into consideration. For seismic retrofitting projects, based on the Iranian seismic rehabilitation code of the existing buildings (IIEES, 2002), 4 hazard levels are most

considered: 2%, 10%, 20% and 50% probabilities of exceedence in 50 years. Before the calculations, a grid of sites must be considered in the region where seismic hazard analysis is performed. For this purpose a grid of 18*13 is considered.

As a result, our outputs are Peak Ground Horizontal Acceleration (PGHA) with 2%, 10%, 20% and 50% probabilities of exceedence in 50-year lifetime of structure. The result of the seismic hazard analysis is graphically shown in Figures 5 and 8.

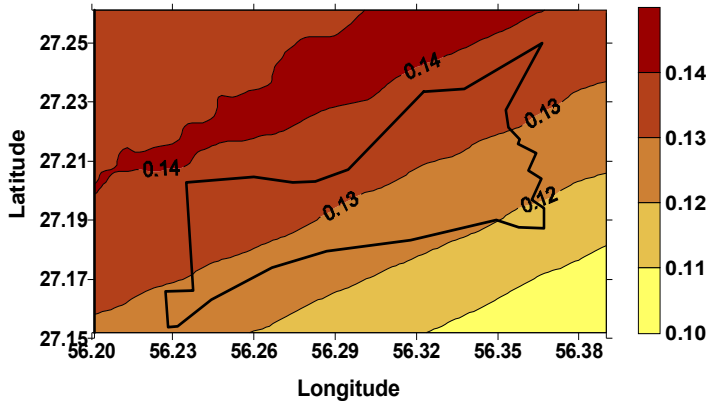

FIG. 5. Horizontal seismic hazard map of Bandar Abbas and its vicinity in g using logic tree for 75 year return period and the border of city (thick line)

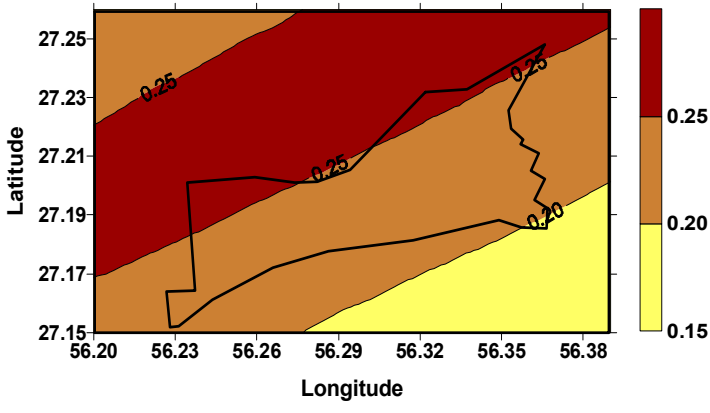

FIG. 6. Horizontal seismic hazard map of Bandar Abbas and its vicinity in g using logic tree for 225 year return period and the border of city (thick line)

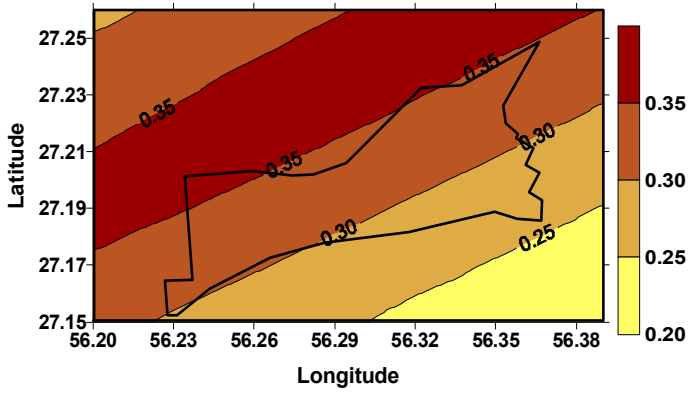

FIG. 7. Horizontal seismic hazard map of Bandar Abbas and its vicinity in g using logic tree for 475 year return period and the border of city (thick line)

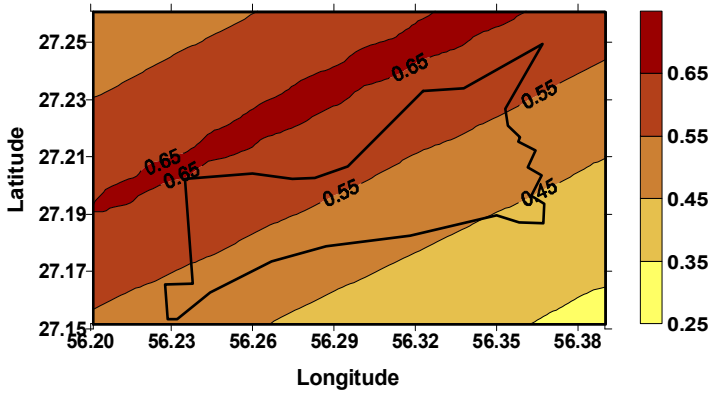

FIG. 8. Horizontal seismic hazard map of Bandar Abbas and its vicinity in g using logic tree for 2475 year return period and the border of city (thick line)

CONCLUSIONS

This paper presents seismic hazard maps of Bandar Abbas and its vicinity based on Peak Ground Horizontal Acceleration (PGHA) for 2%, 10%, 20% and 50% probabilities of exceedence in a time span of 50 years. The significant results of this study can be summarized as:

(1) The contour levels of the horizontal acceleration hazard maps showed that the PGHA for 2% ranges from 0.32(g) to around 0.67 (g), PGHA for 10% ranges from

0.205(g) to around 0.38(g), PGHA for 20% ranges from 0.16(g) to around 0.27(g) and PGHA for 50% ranges from 0.1(g) to around 0.14 (g).

(2) The highest acceleration contours locate in the north and northwest parts of Bandar Abbas.

(3) The smallest accelerations are expected in the southeast of Bandar Abbas.

(4) The comparison of the results with the recommended PGA in Iranian Code of Practice for Seismic Resistant Design of Buildings (BHRC, 2005) (0.30g) shows that the recommended PGA is lower than what it has been achieved in this study for most part of the region. This PGA can cause major structural damage in important structures and lifeline systems.

REFERENCES

Ambraseys, N.N. & Bommer, J.J., (1991), "The attenuation of ground accelerations in Europe," *Earthquake Eng. and Struct. Dynam.*, 20: 1179-1202.

Ambraseys, N.N. & Melville, C.P., (1982), "*A History of Persian Earthquakes,"* Cambridge University Press, Cambridge, Britain.

Bender, B. & Perkins, D.M., (1987), "*SEISRISK-III: A computer program for seismic hazard estimation,"* US Geol. Survey Bull., 1772 .

BHRC, (2005), "*Iranian Code of Practice for Seismic Resistant Design of Buildings, Standard No. 2800,*" 3rd Revision, Building & Housing Research Center, Tehran, Iran. (in Persian).

Gardner, J.K. & Knopoff, L., (1974), "Is the sequence of earthquake in southern California, with aftershocks removed, Poissonian?." *Bull. Seismol. Soc. Am.*, 64: 1363-1367.

Ghodrati Amiri, G. & Mahdavian, A. & Manouchehri Dana, F., (2007), "Attenuation relationships for Iran," *J. Earthquake Eng.*, 11(4): 469-492.

Gutenberg, B. & Richter, C.F., (1954), "*Seismicity of the Earth and Associated Phenomena,"* Princeton University Press, New Jersey.

IIEES, International Institute of Earthquake Engineering and Seismology. http://www.iiees.ac.ir.

IIEES, (2002), "*Seismic Rehabilitation Code for Existing Buildings in Iran*," International Institute of Earthquake Engineering and Seismology (In Persian).

IRCOLD., (1994), "*Relationship between fault length and maximum expected magnitude,"* Iranian Committee of Large Dams, Internal Report (In Persian).

Kijko, A., (2000), "Statistical estimation of maximum regional earthquake magnitude Mmax," In: *Workshop of Seismicity Modeling in Seismic Hazard Mapping,* Poljce, Slovenia, Geol. Survey, pp: 1-10.

Nowroozi, A., (1985), "Empirical relations between magnitude and fault parameters for earthquakes in Iran," *Bull. Seismol. Soc. Am.*, 75: 1327-1338.

Ramazi, H. R., (1999), "Attenuation laws of Iranian earthquakes," In: *Proceedings of the 3rd International Conference on Seismology and Earthquake Engineering*, Tehran, Iran, pp: 337-344.

Sarma, S. K. & Srbulov, M., (1996), "A simplified method for prediction of kinematic soil-foundation interaction effects on peak horizontal acceleration of a rigid foundation," *Earthquake Eng. and Struct. Dynam.*, 25: 815-836.

Effect of Amplification on Seismic Stability of Tailings dam

Sanjay S. Nimbalkar[1] and Deepankar Choudhury[2], M. ASCE

[1]Research Associate, Faculty of Engineering, Univ. of Wollongong, Wollongong City, NSW 2522, Australia; sanjayn@uow.edu.au

[2]Associate Professor, Department of Civil Engineering, Indian Institute of Technology Bombay, Powai, Mumbai - 400 076, India; dc@civil.iitb.ac.in

ABSTRACT: The stability of tailings dams in earthquakes prone areas has become a matter of increasing concern as seismic knowledge has advanced. For the seismic slope stability assessment of tailings dam, majority of current design methodologies rely on the use of pseudo-static approach. However, the crude estimate of finding approximate seismic accelerations makes the pseudo-static approach too conservative to adopt in the stability assessment. In this paper, horizontal slice method is used which considers the seismic inertia forces acting on the sliding wedge of the tailings dam by incorporating the effects of time, phase difference and amplification in shear and primary waves along with the horizontal and vertical seismic accelerations and other soil properties. Results are provided in the graphical form for the stability analysis of tailings dam.

INTRODUCTION

Major earthquakes in the past have caused the failure of numerous tailings dams, to some extent, resulting in human loss. Growing awareness of seismicity and the potential liability associated with tailings dams are raising the requirements for assessing the stability of tailings dams under static and seismic conditions. Many researchers in the past have attempted to investigate the seismic stability of tailings dams and embankments by using pseudo-static method of analysis. Early pioneering work (Newmark, 1965; Sarma, 1975) reported seismic design procedures for earthen dam and embankments. Recently Hou-xiang et al. (2007) and Psarropoulos et al. (2008) analysed stability of tailings dam under static and seismic conditions. However all these investigations were based on pseudo-static method of analysis, which didn't consider the actual dynamic effect with variation of time and propagation of shear and primary wave velocities through the medium. To rectify the shortcomings of the pseudo-static approach, a pseudo-dynamic method has been recently developed (Steedman and Zeng, 1990; Choudhury and Nimbalkar, 2005, 2008, 2009; Nimbalkar and Choudhury, 2008).

Recently, Horizontal Slice Method (HSM) has been formulated (Fakher et al. 2002;

Nouri et al. 2008) to analyse the seismic stability of reinforced slopes and walls based on pseudo-static approach. Considering the non-linear variation of pseudo-dynamic inertia forces, horizontal slice method is extended to investigate stability of tailings dam (Choudhury and Nimbalkar, 2009). In this paper, a complete study has been carried out to investigate the effect of amplification on the seismic stability of the tailings dam considering pseudo-dynamic inertia forces along with other seismic input parameters.

METHOD OF ANALYSIS

The tailings dam, of height H, supporting the compacted tailings overlaid by tailing pond is shown in Fig. 1a. Similar to the pseudo-dynamic approach considered by Choudhury and Nimbalkar (2005, 2009), the finite shear wave velocity (V_s) and primary wave velocity (V_p) are considered in the present analysis. The phase and the magnitude of both the horizontal and vertical seismic accelerations are varying along the depth of the dam. In the present analysis, $V_p/V_s = 1.87$ for $\nu_s = 0.3$ is used (Choudhury and Nimbalkar, 2005). Period of lateral shaking, $T = 2\pi/\omega = 4H/V_s$ is considered in the analysis.

Both the body waves propagating through the dam are considered to be influenced by the soil amplification. Horizontal and vertical seismic accelerations are assumed to linearly vary from the input accelerations at the base to the higher value at the top of the tailings dam, such that $k_h(z = H) = f\, k_h(z = 0)$ and $k_v(z = H) = f\, k_v(z = 0)$, where f is amplification factor. To obtain the critical design values of seismic stability of tailings dam, it is assumed that both the horizontal and vertical vibrations start at exactly the same time without any phase shift between these two vibrations, which is the worst possible combination of earthquake loading. The horizontal and the vertical acceleration at any depth z and time t, below the top of the dam can be expressed as,

$$a_h(z,t) = \left\{1 + \frac{H-z}{H}(f-1)\right\} k_h.g.\sin\omega\left(t - \frac{(H-z)}{V_s}\right) \quad (1)$$

$$a_v(z,t) = \left\{1 + \frac{H-z}{H}(f-1)\right\} k_v.g.\sin\omega\left(t - \frac{(H-z)}{V_p}\right) \quad (2)$$

The total horizontal inertia force $q_{hi}(z, t)$ acting on the i^{th} slice can be expressed as,

$$q_{hi}(z, t) = m_i(z).a_h(z, t) \quad (3)$$

And the total vertical inertia force $q_{vi}(z, t)$ acting on the i^{th} slice can be expressed as,

$$q_{vi}(z, t) = m_i(z).a_v(z, t) \quad (4)$$

Only the critical directions of $q_{hi}(z, t)$ and $q_{vi}(z, t)$ acting on the elemental slice are considered as shown in Fig. 1b. Detailed analysis of pseudo-dynamic inertia forces $q_{hi}(z, t)$ and $q_{vi}(z, t)$ can be found elsewhere (Choudhury and Nimbalkar 2005; Nimbalkar and Choudhury 2008). Similar to 2N+1 formulation (Fakher et al. 2002), equilibrium equations can be written as (Fig. 1b).

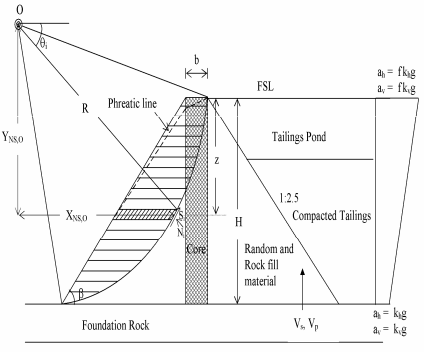

FIG. 1a. Configuration of model tailings dam considered in the analysis.

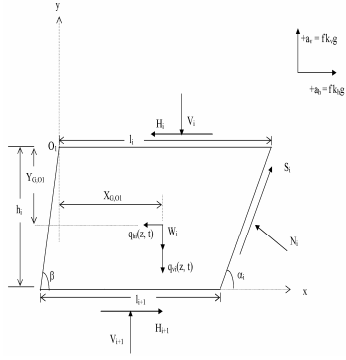

FIG. 2b. Pseudo-dynamic forces acting on single elemental slice.

$\sum F_y = 0$ (For each slice) yields

$$V_{i+1} - V_i - W_i - q_{vi}(z,t) + S_i \sin\alpha_i + N_i \cos\alpha_i = 0 \tag{5}$$

where, V_i and V_{i+1} are vertical inter-slice forces.

Again, $\tau_r = \frac{\tau_f}{FS}$ (For each slice) gives $S_i = \frac{1}{FS}\left(cb_i + N_i \tan\phi\right)$ (6)

Substituting for S_i from eq. (6) into eq. (5),

$$N_i = \frac{V_i - V_{i+1} + W_i + q_{vi}(z,t) - \frac{cb_i}{FS}\sin\alpha_i}{\frac{\tan\phi}{FS}\sin\alpha_i + \cos\alpha_i} \tag{7}$$

Considering 'm' number of slices, $\sum M_O = 0$ (For the whole wedge) gives

$$\sum_{i=1}^{m} \begin{bmatrix} q_{hi}(z,t)\left(Y_{G,O1} + R\sin\theta_i\right) \\ -\left(W_i - q_{vi}(z,t)\right)\left(X_{G,O1} + R\cos\theta_i - l_i\right) \\ -\left(S_i \sin\alpha_i + N_i \cos\alpha_i\right)\left(X_{NS,O}\right) \\ -\left(S_i \cos\alpha_i - N_i \sin\alpha_i\right)\left(Y_{NS,O}\right) \end{bmatrix} = 0 \tag{8}$$

Here, the assumption is made that the normal (N_i) and shear (S_i) forces act at the mid-point of base of each slice and thus,

$$\left.\begin{aligned} X_{NS,O} &= R\cos\theta_i - \frac{h_i}{2\tan\alpha_i} \\ Y_{NS,O} &= R\sin\theta_i + \frac{h_i}{2} \end{aligned}\right\} \tag{9}$$

Substitute S_i and N_i in eq. (8) to obtain the factor of safety (FS). If $q_{vi}(z, t)$ and $q_{hi}(z, t)$ are replaced by constant pseudo-static inertia forces such as k_vW_i and k_hW_i respectively, the expression (8) reduces to the pseudo-static moment equilibrium formulation originally proposed by Fakher et al. (2002).

RESULTS AND DISCUSSIONS

Variations of parameters considered in the present analyses are as follows:

k_h = 0.0, 0.1, 0.2, 0.3; k_v = 0.0, 0.5k_h and k_h; f = 1.0, 1.2 and 1.4; V_s = 100 m/s, V_p = 187 m/s, T = 0.3 s; H = 44 m, b = 4 m, n = 2.5. Table 1 shows input properties used.

Table 1. Input properties for tailings dam (Choudhury and Nimbalkar, 2009)

Zone	Input Parameter		
	Unit weight (γ) (kN/m^3)	Angle of internal friction (ϕ) degrees	Cohesion (c) kN/m^2
Random	18.3	28.0	3.125
Impervious core	16.4	28.0	35.0
Tailing pond	19.0	12.0	14.7
Compacted Tailings	19.0	15.2	14.7
Foundation	18.3	28.0	3.125

Effect of amplification on factor of safety (FS) of tailings dam

Fig. 2 shows the effect of soil amplification on factor of safety (FS) of tailings dam for tailings dam empty and full water condition respectively. The required value of FS decreases with increase in soil amplification factor (f). Considering the tailings dam empty condition, for k_h = 0.2 and k_v = 0.5k_h, FS decreases by 9.8% when f changes from 1 to 1.2 and 20.7% when f changes from 1.0 to 1.4. Similar trend is observed for the effect of amplification on the stability of the tailings dam in full water condition. Thus, the present study reveals the significant influence of amplification of body waves on the stability of tailings dam.

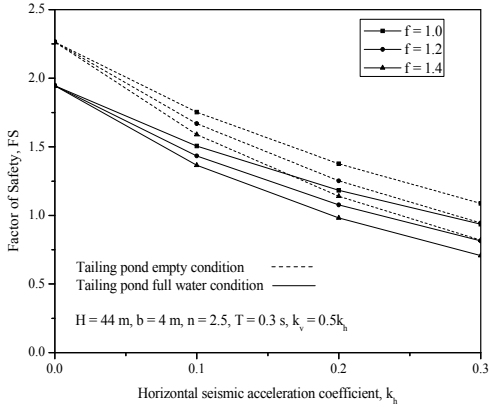

FIG. 2. Effect of amplification on factor of safety, FS with $k_v = 0.5k_h$.

Effect of seismic acceleration coefficients (k_h and k_v) on factor of safety (FS)

Fig. 3 shows the effects of both horizontal and vertical seismic acceleration coefficients (k_h and k_v) on factor of safety (FS) for tailings dam empty and full water condition respectively. FS shows significant decrease with increase in k_h and k_v. For

empty tailing pond with $k_v = 0.5k_h$ and f = 1.2, when k_h changes from 0 to 0.1, FS decreases by about 26.3%. When k_h changes from 0 to 0.2, FS decreases by 44.7%.

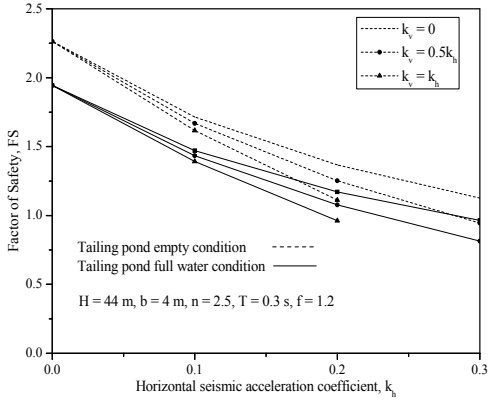

FIG. 3. Effect of horizontal and vertical seismic acceleration coefficients on factor of safety, FS with amplification factor (f) = 1.2.

Similarly when k_h changes from 0 to 0.3, FS decreases by about 58.2%. Also for k_h = 0.2, when k_v changes from 0 to $0.5k_h$, FS decreases by about 8.3% and when k_v changes from $0.5k_h$ to $1.0k_h$, FS decreases by about 11.2%. Tailings dam in full water condition also shows significant reduction in the stability due to increase in seismic acceleration coefficients. Thus, effects of both k_h and k_v are significant in the computation of stability of the tailings dam.

COMPARISON OF RESULTS

The effect of amplification on seismic earth pressures is quite established for the seismic design of rigid retaining walls (Steedman and Zeng, 1990; Nimbalkar and Choudhury, 2008) and for reinforced soil slopes and walls (Nouri et al., 2008). Recently Choudhury and Nimbalkar (2009) analyzed seismic stability of tailings dam without amplification effect. However, the amplification effect using this robust pseudo-dynamic method of analysis was not yet been studied. Hence present results cannot be compared due to scarcity of results in literature.

CONCLUSIONS

The horizontal slice method considering time dependent pseudo-dynamic inertia forces acting within the body of tailings dam is employed to investigate stability of tailings dam. The pseudo-dynamic inertia forces are computed by considering effect of time, phase difference and amplification of vertically propagating shear and primary waves. The present study shows more appropriate consideration of real earthquake

motion parameters compared to conventional pseudo-static methods. The critical design values of safety factors for the tailings dam are reported for tailings dam empty and full water conditions. Present solution reveals that along with the seismic accelerations, the combined effect of the time, phase difference and amplification in body waves significantly changes the design values of the safety factors more towards the unsafe side compared to the static case.

ACKNOWLEDGEMENT

Authors appreciate the financial support received from the sponsored research project no. AERB/CSRP/31/07 by Atomic Energy Regulatory Board, Mumbai, India for carrying out this research.

REFERENCES

Choudhury, D. and Nimbalkar, S.S. (2005). "Seismic passive resistance by pseudo-dynamic method." *Geotechnique* 55(9): 699-702.

Choudhury, D. and Nimbalkar, S.S. (2008). "Seismic rotational displacement of gravity walls by pseudo-dynamic method." *International Journal of Geomechanics* ASCE, USA, 8(3): 169-175.

Choudhury, D. and Nimbalkar, S.S. (2009). "Seismic stability of tailings dam by using pseudo-dynamic method." *17th International Conference on Soil Mechanics and Geotechnical Engineering*, October 5 – 9, 2009, Alexandria, Egypt (in press).

Fakher, A., Nouri, H. and Shahgholi, M. (2002). "Limit equilibrium in reinforced soil walls subjected to seismic loads." *In: Proceedings of the Third Iranian International Conference on Geotechnical Engineering and Soil Mechanics*, Tehran, vol. 3: 281-286.

Hou-xiang, Liu, Ning, Li, Liao, Xue, Cong-shi, Wu and Xu-dong, Pan. (2007). "Effective stress analysis method of seismic response for high tailings dam." *Journal of Central South University of Technology*, 14(1): 129-134.

Newmark, N. M. (1965). "Effects of Earthquakes on Dams and Embankments." *Geotechnique*, 15, 2: 139-160.

Nimbalkar, S.S. and Choudhury, D. (2008). "Effects of body waves and soil amplification on seismic earth pressures." *Journal of Earthquake and Tsunami*, World Scientific Publishing Company, Singapore, 2(1): 33-52.

Nouri, H., Fakher, A. and Jones, C.J.F.P. (2008). "Evaluating the effects of the magnitude and amplification of pseudo-static acceleration on reinforced soil slopes and walls using the limit equilibrium Horizontal Slices Method." *Geotextiles and Geomembranes*, 26(3): 263-278.

Psarropoulos, Prodromos, N. and Tsompanakis, Yiannis. (2008). "Stability of tailings dams under static and seismic loading." *Canadian Geotechnical Journal*, 45(5): 663-675.

Sarma, S.K., 1975. Seismic stability of earth dams and embankments. *Geotechnique* 25: 743–761.

Steedman, R.S. and Zeng, X. (1990). "The influence of phase on the calculation of pseudo-static earth pressure on a retaining wall." *Geotechnique*, 40(1): 103-112.

This page intentionally left blank

Author Index

Page number refers to the first page of paper

Ahmad, Syed Ishtiaq, 194
Ahmadi, Mohammad T., 309
Ahmed, A., 278
Amiri, G. Reza Ghodrati, 153, 332
Amrei, S. A. Razavian, 332
Asaoka, Akira, 125, 139, 218, 294
Asgari, A., 320
Azarhoosh, Zeynab, 153

Bagheripour, M. H., 320
Bai, H. Sharada, 92
Baidya, Dilip Kumar, 50
Berhe, Tensay G., 131
Bian, Hanbing, 246
Bian, Xuecheng, 185
Borowiec, Anna, 252

Cai, F., 278
Cai, Zhengyin, 240
Cao, Pei, 240
Chang, Der-Wen, 109
Chapman, Ben, 288
Chen, Yunmin, 185
Choudhury, Deepankar, 340

Daouadji, Ali, 246
Davoodi, Mohammad, 300

Fang, Jian, 169
Fukuzawa, Hiroki, 234

Gao, Xi-Zhang, 1
Grabe, J., 101
Guo, Yuancheng, 225

Haghshenas, Ebrahim, 300
Han, Dongdong, 85
Han, Y. C., 71
Harutoonian, Pavlick, 288
Ho, Hsing-Chuan, 109
Hossain, Md. Raquibul, 194
Hossain, Md. Tanvir, 326
Huang, Maosong, 32, 263
Hulsey, J. Leroy, 162

Iai, Susumu, 56
Islam, Mohammad Shariful, 326
Itabashi, Kazuo, 234

Jia, Yun, 246
Jiang, Minmin, 240

Kai, Qianzheng, 206
Kato, Shinjoro, 234
Kodaka, Takeshi, 234
Kuse, Masumitsu, 145

Leo, Chin Jian, 288
Li, Jia, 225
Li, Jianhua, 77
Li, Qiang, 162
Li, Shuai, 263
Liao, Xingui, 77
Lin, Bor-Shiun, 109
Lin, Guoming, 169
Liu, Bao-chen, 38
Liu, Dan, 240
Liu, Ganbin, 64, 206
Liu, Nina, 85
Liu, Yang, 85

Manish, A., 92
Manna, Bappaditya, 50
Men, Yuming, 85
Mohebi, B., 332
Mokhberi, Mehdi, 300

Nakai, Kentaro, 125, 294
Nakano, Masaki, 139
Nakayama, Osamu, 145
Narayana, G., 92
Nimbalkar, Sanjay S., 340
Noda, Toshihiro, 125, 139, 218, 294

Peng, Jianbing, 85

Qiu, G., 101

Ren, Q., 32

Sakai, Takayuki, 139
Samui, Pijush, 212
Sawada, Kazuhide, 145
Shahrour, Isam, 246
Siddiquee, Mohammed Saiful Alam, 194
Sitharam, T. G., 212
Song, Guang, 185
Su, Z., 278
Sugito, Masata, 145

Takemiya, Hirokazu, 185
Takeuchi, Hidekatsu, 218
Tanabe, Akinori, 145
Tarinejad, Reza, 309
Tensay, B. G., 118
Tobita, Teteso, 56
Tong, Zhao-Xia, 1
Truong, H. V. Phuong, 178

Ugai, K., 278

Wang, Mingwu, 56
Wang, Xue-tao, 118, 131
Wang, Yanli, 272
Wang, Yong, 272
Wu, Wei, 118, 131

Xu, Gang, 162
Xu, Q., 278

Yamada, M., 278
Yang, Q., 278
Yang, Xiao-li, 38
Yang, Yue, 77
Yang, Ze-Yan, 1
Yang, Zhaohui Joey, 162
Yashima, Atsushi, 145
Yokawa, Hiroshi, 145
Young, Christopher Neil, 288
Yu, Xiong (Bill), 169

Zhang, Jian-Min, 1
Zhang, Jingwei, 225
Zheng, Rongyue, 64
Zhou, Ye, 64
Zhou, Zhong, 38
Zhu, Fangcai, 77
Zou, Ju Jia, 288

Subject Index

Page number refers to the first page of paper

Algorithms, 309
Artificial islands, 294
Asia, 118
Avalanches, 278

Bangladesh, 326
Bridges, highway, 162
Bridges, viaduct, 194
Buried pipes, 225

Canyons, 309
China, 1, 278
Clays, 125, 131, 218, 234, 240, 263
Cyclic loads, 77, 206, 240, 246, 263

Damage, 1
Damping, 178
Dams, 340
Dams, earth, 131
Dams, embankment, 1
Degradation, 263
Design, 169
Dikes, 145
Dynamic analysis, 118
Dynamic properties, 206, 240
Dynamic response, 38, 50, 64, 92, 162

Earth pressure, 109
Earthquakes, 1, 145, 278, 320, 326, 332, 340
Elasticity, 64, 153
Embankments, 125, 139
Estimation, 300
Excitation, 185

Failure modes, 125
Failures, 109, 139
Filters, 252
Finite difference method, 225
Finite element method, 101
Flumes, 278
Footings, 178
Foundations, 77, 92, 101, 125, 169
Frames, 92
Freezing, 162

Geomaterials, 206
Ground motion, 185, 309, 320

Iran, 300, 332

Japan, 139, 145

Laboratories, 278
Landfills, 118
Landslides, 139
Layered soils, 32, 56, 288, 300, 320
Loess, 38

Model tests, 38, 85

Numerical analysis, 131, 218, 252

Pile foundations, 32, 50, 71, 109, 118, 185, 263
Pile groups, 32, 56
Piles, 109, 218
Porous media, 64
Pumps, 77

Radar, 225
Railroad tracks, 64
Rehabilitation, 332
Rivers, 145
Rocks, 278

Sand, Soil type, 194, 218, 272
Saturated soils, 240, 246
Seasonal variations, 162
Seismic design, 101
Seismic effects, 56, 109, 125, 131, 139, 162, 169, 212, 288, 294, 332, 340
Shear strength, 234
Shear waves, 212
Slopes, 38, 139
Soft soils, 263
Soil compaction, 38, 218
Soil consolidation, 252
Soil deformation, 139, 145, 234
Soil liquefaction, 145, 212, 246, 272, 326
Soil nailing, 77
Soil properties, 92, 288, 300
Soil-pile interactions, 185, 194
Soil-structure interactions, 71, 85, 153, 178
Solid wastes, 118
Strain, 194
Structural analysis, 309
Subgrades, 206

Tailings, 340
Three-dimensional analysis, 101
Tunnels, 85

Underground structures, 225

Vibration, 32, 50, 56, 71, 178, 185

Wave propagation, 252
Wave velocity, 212